2012 NCREE Research Programs and Accomplishments

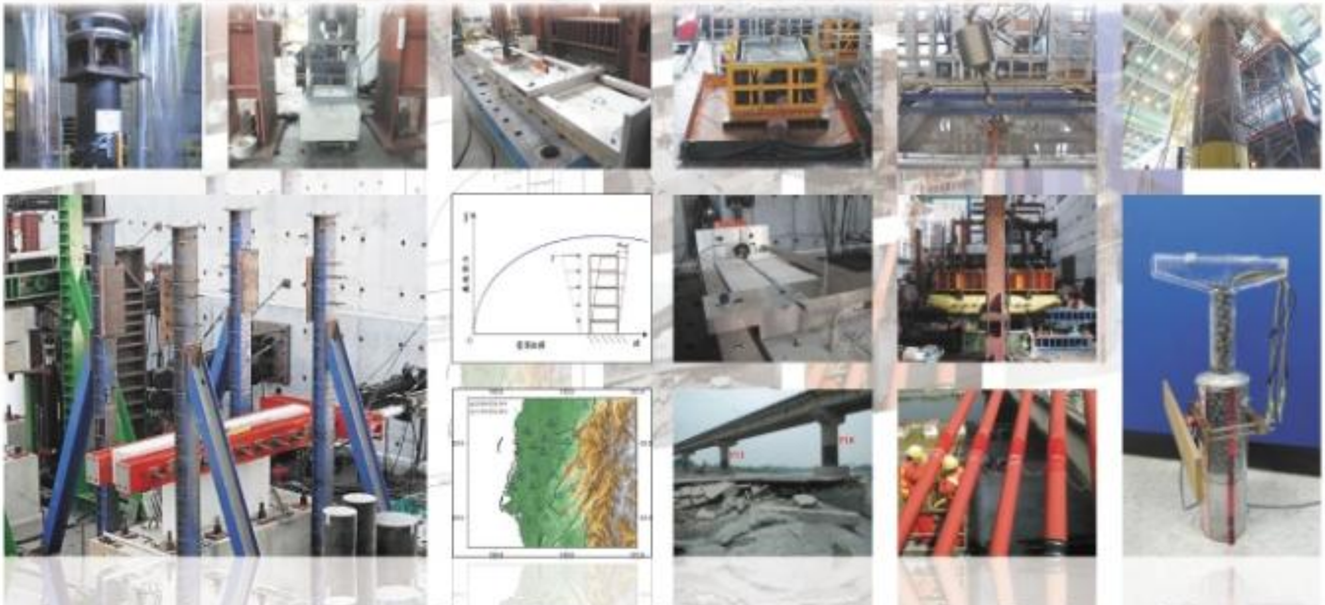

National Center for Research on Earthquake Engineering

2012 NCREE
Research Programs and Accomplishments

Contents

Pushover Analyses for Asymmetrical Buildings

Jui-Liang Lin [1], Keh-Chyuan Tsai [2] and Ming-Chieh Chuang [3]

林瑞良 [1]、蔡克銓 [2]、莊明介 [3]

Abstract

This paper studies the reasons behind four trends in torsional effects in asymmetrical buildings observed in recent literature. It is found that modal eccentricities and the non-proportionality between the modal translations and the modal rotation are key to understanding these trends in torsional effects in asymmetrical buildings. The non-proportionality between the modal translations and the modal rotation leads to the trend that the torsional effects generally decrease when plastic deformations increase. This study also proposes a novel oscillator, referred to as the co-shape oscillator (COSO), which can be effectively used in the nonlinear response history analysis of multistory asymmetrical buildings. For accuracy and simplicity, the incremental dynamic analysis with the use of COSOs, instead of pushover analysis, is proposed for the simplified seismic analyses of asymmetrical buildings.

Keywords:pushover analysis; incremental dynamic analysis; asymmetrical buildings; torsional effects; oscillator

Introduction

Due to architectural and functional requirements, most practical buildings are asymmetrical. However, this type of building is one of the most frequently damaged structures under earthquake loads. The rotational response of asymmetrical buildings leads to unequal displacement demands on the floor diaphragm. The torsional effects, generally represented as the ratio between the displacements of the floor edges to the displacement of the center of mass (CM) are unique to asymmetrical buildings compared with symmetrical buildings. Therefore, identifying torsional effects in a building is a crucial step in several nonlinear static (pushover) analysis procedures for asymmetrical buildings (Fajfar *et al*. 2005).

Fajfar *et al*. (2005) investigated the general trends in the torsional effects in two-way asymmetrical buildings under bi-directional ground excitations. Some trends found in the torsional effects reported in the original paper (Fajfar *et al*. 2005) are re-stated here. First, torsional effects generally decrease when plastic deformations increase. Second, between the two horizontal directions, the torsional effect on displacements in the more flexible direction is smaller than that in the stiffer direction. Third, for the stiff side (SS), it is difficult to make general conclusions. The response of the SS generally has a strong dependence on the effects of several modes of vibration, and on the influence of the ground motion in the transverse direction. The structural and ground motion characteristics in both directions are influential. Finally, transitions from the de-amplification to amplification of the displacement demand may occur on the SS in some cases.

These four trends in the torsional effects in asymmetrical buildings seem difficult to be completely understood by using general intuition. The overall structural parameters that are related to the rotational responses, include the radius of gyration for the mass moment of inertia, the normalized eccentricity and the frequency ratio, *etc*. Nevertheless, it also appears that there is no satisfactory explanation for the aforementioned trends in the torsional effects solely using these overall structural parameters. There is no doubt that

[1] Associate Researcher, National Center for Research on Earthquake Engineering, jllin@ncree.narl.org.tw.
[2] Professor, Department of Civil Engineering, National Taiwan University, kctsai@ntu.edu.tw
[3] Assistant Researcher, National Center for Research on Earthquake Engineering, mcchuang@ncree.narl.org.tw.

the rationale of the torsional effects is an issue deserving of more emphasis. Investigating the reasons behind these trends in torsional effects is helpful not only to understand the seismic responses of asymmetrical buildings but also for the development of suitable seismic assessment procedures.

The present study first used the elastic and inelastic properties of the three-degree-of-freedom (3DOF) modal systems (Lin and Tsai 2008) to explain the trends in the torsional effects in asymmetrical buildings, which were found in the literature (Fajfar *et al*. 2005). It is expected to improve understanding of the characteristics of the seismic behavior of asymmetrical buildings.

In addition, the inelastic dynamic analysis, *i.e.*, the nonlinear response history analysis (NRHA), is widely recognized as a more reliable approach for assessing structural seismic performance when compared with the pushover analysis approach. Nevertheless, the pushover analysis approach is seemingly more popular than the NRHA in engineering practice due to its computational simplicity and efficiency. Krawinkler *et al*. (2011) clearly pointed out that simplicity in modeling is at the core of facilitating the use of the NRHA. Han and Chopra (2006) proposed the simplified approach of performing incremental dynamic analysis, which suggested analyzing the first single-degree-of-freedom (SDOF) modal oscillator, instead of analyzing the finite element model of the multistory building. This again suggests that a simplified and effective inelastic structural model is necessary for promoting the NRHA in engineering practice. The other aim of this study is to construct the co-shape oscillator (COSO), which can be used in the NRHA as a substitute for the finite element model of an inelastic multistory asymmetrical building.

Explanations of the Trends in Torsional Effects

The X- and the Z-axes are the two horizontal axes of the coordinate system used in this study. The direction of the Y-axis is opposite to the direction of gravity. The subscripts x, z, and θ used in this study represent the corresponding quantities associated with the X- and Z-translational and Y-rotational components, respectively.

The first trend in torsional effects is that they generally decrease when plastic deformations increase. Taking the contribution of the nth vibration mode of an elastic two-way asymmetrical building subjected to an X-directional ground motion into consideration, the equations for the torsional effect, defined by the displacements on the flexible side (FS) and SS of the jth floor divided by the corresponding displacement at the CM, are:

$$\frac{u_{FS,nj}^{elastic}}{u_{CM,nj}^{elastic}} = 1 + \left(\frac{b}{2} - e_z\right)\frac{\phi_{\theta n,j}}{\phi_{xn,j}} = 1 + \eta_{FS,nj}^{elastic} \tag{1a}$$

and:

$$\frac{u_{SS,nj}^{elastic}}{u_{CM,nj}^{elastic}} = 1 - \left(\frac{b}{2} + e_z\right)\frac{\phi_{\theta n,j}}{\phi_{xn,j}} = 1 + \eta_{SS,nj}^{elastic} \tag{1b}$$

where b and e_z are the floor diaphragm dimension and the overall structural eccentricity, respectively, and $\phi_{xn,j}$ and $\phi_{\theta n,j}$ are the jth-floor components of the nth mode shape in the X-translational and Y-rotational directions, respectively. The $\eta_{FS,nj}^{elastic}$ and $\eta_{SS,nj}^{elastic}$ are referred to as the elastic torsional indices for the nth vibration mode on the FS and SS of the jth floor, respectively. The larger the absolute value of the torsional index, the more substantial the torsional effect. In an inelastic state, using the concept of "weak coupled vibration modes", the torsional effects on the FS and SS of the jth floor resulting from the nth "vibration mode" are approximated as:

$$\frac{u_{FS,nj}^{inelastic}}{u_{CM,nj}^{inelastic}} \approx 1 + \left(\frac{b}{2} - e_z\right)\frac{\phi_{\theta n,j}}{\phi_{xn,j}}\frac{\mu_{\theta n}}{\mu_{xn}} = 1 + \eta_{FS,nj}^{inelastic} \tag{2a}$$

and:

$$\frac{u_{SS,j}^{inelastic}}{u_{CM,j}^{inelastic}} \approx 1 - \left(\frac{b}{2} + e_z\right)\frac{\phi_{\theta n,j}}{\phi_{xn,j}}\frac{\mu_{\theta n}}{\mu_{xn}} = 1 + \eta_{SS,nj}^{inelastic} \tag{2b}$$

where μ_{xn} and $\mu_{\theta n}$ are the X-translational and Y-rotational ductilities, respectively. The $\eta_{FS,nj}^{inelastic}$ and $\eta_{SS,nj}^{inelastic}$ are referred to as the inelastic torsional indices for the nth vibration mode on the FS and SS of the jth floor. Comparing the elastic and inelastic torsional indices shows that the inelastic torsional indices are equal to the counterpart elastic torsional indices multiplied by $\mu_{\theta n}/\mu_{xn}$. As a reminder, the modal acceleration A_n and the modal displacements D_{xn}, D_{zn}, and $D_{\theta n}$ are computed as (Lin and Tsai 2008):

$$A_n = \frac{V_{bxn}}{\Gamma_{xn}M_n} = \frac{V_{bzn}}{\Gamma_{zn}M_n} = \frac{T_{bn}}{\Gamma_{\theta n}M_n} \tag{3a}$$

and:

$$D_{xn} = \frac{u_{xn,r}}{\phi_{xn,r}}, \quad D_{zn} = \frac{u_{zn,r}}{\phi_{zn,r}}, \quad D_{\theta n} = \frac{u_{\theta n,r}}{\phi_{\theta n,r}} \tag{3b}$$

where $\phi_{xn,r}$, $\phi_{zn,r}$, and $\phi_{\theta n,r}$ are the roof components of the nth mode shape in the three directions; $u_{xn,r}$, $u_{zn,r}$, and $u_{\theta n,r}$ are the roof displacements in the three directions; V_{bxn}, V_{bzn}, and T_{bn} are the base shears and base torque of the original multi-story building pushed using the nth modal inertia force vector; M_n is the modal mass; and Γ_{xn}, Γ_{zn}, and $\Gamma_{\theta n}$ are the modal participation factors in the three directions. Because the pushover force vector keeps proportionally increasing in the three directions, the modal acceleration A_n also proportionally increases in the three directions (Eq. 3a), but the modal displacements, D_{xn}, D_{zn}, and $D_{\theta n}$, are non-proportionally increased (Eq. 3b). Since the translational post-yielding stiffness ratio, α_{xn}, is less than the rotational post-yielding stiffness ratio, $\alpha_{\theta n}$, the value of $\mu_{\theta n}/\mu_{xn}$ is less than one and decreases as A_n increases. Thus, the absolute values of the inelastic torsional indices, $\eta_{FS,nj}^{inelastic}$ and $\eta_{SS,nj}^{inelastic}$, decrease as A_n increases. That is to say, the torsional effect decreases when plastic deformations increase, which explains this first trend in torsional effects (Fajfar *et al.* 2005).

The second trend in torsional effects is that the torsional effect on displacements in the more flexible direction, *i.e.*, the weaker direction, is smaller than that in the stiffer direction (Fajfar *et al.* 2005). Fajfar *et al.* (2005) defined the weaker direction to be the direction in which a building experiences a larger plastic deformation than in other directions. For instance, when α_{zn} is larger than α_{xn}, the X-direction is the "weaker direction". From Eq. 2, the inelastic torsional effects in both the stiff and the flexible directions are equal to its counterpart elastic torsional effects multiplied by $\mu_{\theta n}/\mu_{zn}$ and $\mu_{\theta n}/\mu_{xn}$, respectively. Because α_{zn} is larger than α_{xn}, $\mu_{\theta n}/\mu_{zn}$ is larger than $\mu_{\theta n}/\mu_{xn}$. It consequently explains the second trend of torsional effects.

The third trend of torsional effect is that the seismic responses on the SS generally depend on the influences of several modes of vibration and the ground motion in the transverse direction. Thus, it is difficult to make general conclusions about the torsional effects on the SS. In order to explain this third trend of torsional effects, the relationships between the directions of the modal eccentricities and the trends in unequal modal displacement demands are first discussed in the following contents.

It is clear that the rotational response resulting from structural eccentricity leads to unequal displacement demands on the FS and the SS of the floor diaphragm in asymmetrical buildings. This suggests that the directions of modal eccentricities, *i.e.*, e_{xn} and e_{zn}, are influential on the unequal modal displacement demands on the edges of the floor diaphragm. The beam end with a lumped mass in the 3DOF modal system (Lin and Tsai 2008) is regarded as the FS and the other beam end is regarded as the SS. When a 3DOF modal system with positive e_{zn} and e_{xn} has a positive Y-rotational increment, the displacements of the FS increased in the X-direction and decreased in the Z-direction. That is to say, when the modal eccentricities e_{zn} and e_{xn} are positive, the FS in the X-direction and the SS in the Z-direction face a larger displacement demand than the other side of the floor diaphragm in the same direction. Conversely, when the modal eccentricities e_{zn} and e_{xn} are negative, the SS in the X-direction and the FS in the Z-direction face a larger displacement demand than the other side of the floor diaphragm in the same direction.

It is clear that all structural vibration modes contribute to the structural seismic response of the building. The extent of each mode's contribution depends on the characteristics of the vibration mode and the seismic ground motions; *e.g.*, the frequency content of the ground motions. This brings to light an explanation for the third trend in torsional effects, stating that it is difficult to reach general conclusions about the torsional effects on the SS, which strongly depend on the effects of several vibration modes and is influenced by the ground motion in the transverse direction. A detailed explanation of this trend was given by Lin *et al.* (2012).

The fourth trend found in the torsional effects is that, in some cases, transitions from de-amplification to amplification of the displacement demand may occur on the SS (Fajfar *et al.* 2005). From the discussion of the third trend of torsional effects, it is clear that the displacement demand on the SS is possibly larger than the displacement demand on the FS in the same direction. In addition, the torsional effects on the SS are influenced by ground motions in the transverse direction. Due to the time-varying characteristics of the seismic ground motions, the torsional effect on the SS may, in some cases, change from a de-amplification to an amplification of the displacement demand.

The co-shape oscillator

Each COSO is constructed from the two-degree-of-freedom (2DOF) modal properties of the two specific vibration modes of a one-way asymmetrical building. These two vibration modes consist of an identical number of stationary points in their mode shapes. In addition, the normalized mode shapes of these two vibration modes are very similar. These same unique characteristics of the mode shapes of each pair of vibration modes are the key reasons to name the proposed oscillator as COSO. The first task in developing the COSO is to establish its physical model and its corresponding inelastic properties. The second task is to construct the COSOs representing higher-mode pairs of the multistory asymmetrical building in order to consider the higher-mode effects on its seismic responses.

The concept of using COSOs to estimate the seismic responses of asymmetrical buildings is shown in Fig. 1. The equation of motion for the COSO is:

$$\mathbf{M}^*\ddot{\mathbf{u}}^* + \mathbf{C}^*\dot{\mathbf{u}}^* + \mathbf{K}^*\mathbf{u}^* = -\mathbf{M}^*\iota\ddot{u}_g(t) \tag{4}$$

where:

$$\mathbf{M}^* = \begin{bmatrix} m^* & 0 \\ 0 & I^* \end{bmatrix} = \begin{bmatrix} 1 & 0 \\ 0 & 1 \end{bmatrix}, \quad \mathbf{u}^* = \begin{bmatrix} u_z^* \\ r^* u_\theta^* \end{bmatrix}, \quad \iota = \begin{bmatrix} 1 \\ 0 \end{bmatrix}$$
$$\mathbf{K}^* = \begin{bmatrix} m_1\omega_1^2 + m_2\omega_2^2 \; , & sym. \\ -\sqrt{m_1 m_2}\left(s_2\omega_1^2 + s_1\omega_2^2\right) & I_1\omega_1^2 + I_2\omega_2^2 \end{bmatrix} \tag{5}$$

$\ddot{u}_g(t)$ is the ground acceleration record, and r^* is the mass radius of gyration. The parameters m_n, I_n, and ω_n, where n = 1 and 2, denote the mass, mass moment of inertia, and the circular vibration frequency of the two targeted vibration modes of the original N-story asymmetrical building, respectively. The two targeted vibration modes are the first translational-dominant and the first rotational-dominant vibration modes of the original building. The quantities m_n and I_n, where $n = 1$ and 2, are computed as:

$$m_n = \boldsymbol{\varphi}_{zn}^T \mathbf{m} \boldsymbol{\varphi}_{zn}, , \quad I_n = \boldsymbol{\varphi}_{\theta n}^T \mathbf{I} \boldsymbol{\varphi}_{\theta n}, \quad n = 1,2 \tag{6}$$

where **m** and **I** are the $N\times N$ mass matrix and the $N\times N$ mass moment of inertia matrix of the original building, and $\boldsymbol{\varphi}_{zn}$ and $\boldsymbol{\varphi}_{\theta n}$ are the $N\times 1$ sub-vectors of the nth mode shape of the original building. In Eq. (5), the values of s_1 and s_2, which are equal to either 1 or −1, are determined from the directions of the mode shapes of the two targeted vibration modes. When the directions of the translational component $\boldsymbol{\varphi}_{zn}$ and the rotational component $\boldsymbol{\varphi}_{\theta n}$ of the targeted vibration mode are the same, the corresponding s_n equals 1. Conversely, when $\boldsymbol{\varphi}_{zn}$ and $\boldsymbol{\varphi}_{\theta n}$ have opposite directions, the corresponding s_n equals −1. The elastic and inelastic properties of the springs and dashpots of the COSO are given by Lin *et al.* (2013). The relationships between the seismic responses of the COSO and those of the original multi-story building are also given by Lin *et al.* (2013).

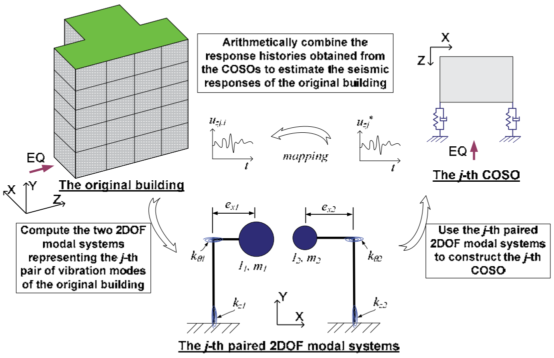

Fig. 1 The concept of using COSOs to estimate the seismic responses of asymmetrical buildings.

Conclusions

This study provided an effective alternative explanation of some of the trends in torsional effects in asymmetrical buildings using the characteristics of 3DOF modal systems. Among the characteristics of the 3DOF modal systems, the modal eccentricities and the non-proportionality between the modal translations and the modal rotation are the keys to reaching the explanations behind the trends in torsional effects.

The properties of each pair of vibration modes pertaining to multistory asymmetrical buildings are used to construct the associated COSO. The COSO consists of a rigid mass block, which has unit mass and unit mass moment of inertia, connected with two spring–dashpot sets. Each spring–dashpot set of the COSO preserves the modal properties belonging to one of the two associated vibration modes. The conventional SDOF oscillator is usually used to represent a single vibration mode of a building, whereas the COSO simultaneously represents a pair of vibration modes in an asymmetrical building. The COSO also possesses an advantage of computational efficiency similar to the conventional SDOF modal oscillator.

References

Fajfar, P., Kilar, V., Marusic, D., Perus, I. (2005), "Torsional effects in the pushover-based seismic analysis of buildings", *Journal of Earthquake Engineering*, 9: 831-854.

Han S.W., Chopra A.K. (2006), "Approximate incremental dynamic analysis using the modal pushover analysis procedure", *Earthquake Engineering and Structural Dynamics*, 35: 1853-1873.

Krawinkler H., Lignos D.G., Putman C. (2011), "Prediction of nonlinear response — pushover analysis versus simplified nonlinear response history analysis", Structures Congress, Las Vegas, Nevada.

Lin, J.L., Tsai, K.C. (2008), "Seismic analysis of two-way asymmetric building systems under bi-directional seismic ground motions", *Earthquake Engineering and Structural Dynamics*, 37: 305-328.

Lin, J.L., Tsai, K.C. and Chuang, M.C. (2012), "Understanding the trends in torsional effects in asymmetric-plan buildings", *Bulletin of Earthquake Engineering*, 10: 955-965.

Lin, J.L., Tsai, K.C. and Chuang, M.C. (2013), "Effective oscillators for the seismic analysis of inelastic one-way asymmetric-plan buildings", *Engineering Structures*, (in press, DOI 10.1016/j.engstruct.2013.02.007).

The Study of the Safety Factor of the Pushover Analysis Procedure Based on the Capacity Spectrum Method

Yeong-Kae Yeh [1] and Te-Kuang Chow [2]

葉勇凱 [1]、周德光 [2]

Abstract

At present, engineers often use pushover analysis based on the capacity spectrum method to work on detailed seismic evaluation of structures in Taiwan. The performance target of the ground acceleration is used to compare with the site peak ground acceleration of a design earthquake with a 475-year return period to evaluate the sufficiency of a structure's seismic capacity. These evaluated results are too conservative as stated in FEMA 440. In this report, the nonlinear dynamic analysis of a single degree structure is used to study the inherent safety factor of the capacity spectrum method and its relationship with the elastic stiffness of the structure, the dispersive hysteretic energy, and the characteristic of input seismic record. From the analysis results, this safety factor is found to be larger than 2 and to have a larger value for less stiff structures. It is also found to be independent of the dispersive hysteretic energy, and to be influenced by the characteristic of the input seismic record.

Keywords: detailed seismic evaluation, nonlinear pushover analysis, capacity spectrum method, nonlinear dynamic analysis,

Introduction

Detailed seismic evaluation procedures are often used to confirm the seismic capacity of existing buildings. Currently the most widely used detailed evaluation method is nonlinear pushover analysis to obtain the capacity curves of structures, namely the establishment of the relationship between the base shear and roof displacement. Based on the building's performance needs, a performance point is set on the capacity curve through a specific procedure to seek a design earthquake that can cause this performance-point roof displacement. This performance target earthquake is presented by its associate 475 year design response spectrum and maximum ground acceleration. The above procedures can be divided into two categories: one is the capacity spectrum method suggested by ATC 40 (ATC, 1996); the other is the coefficient method suggested by FEMA 356 (FEMA, 2000).

In Taiwan the most popular detailed seismic evaluation methods are the "Seismic Evaluation of Reinforced Concrete Structure with Pushover Analysis" developed by the National Center for Research on Earthquake Engineering (NCREE) and the "Seismic Evaluation of RC Buildings (SERCB)" developed by the team led by Prof. I-Chau Tsai from the National Taiwan University. Both of these two methods are based on the capacity spectrum method of ATC 40. The pushover analysis based on the capacity spectrum method is an approximation method to simulate the roof displacement of the structure calculated by nonlinear dynamic analysis. In the FEMA 440 (FEMA, 2005) report, the capacity spectrum method of ATC 40 is noted to be too conservative. The Capacity spectrum method has been widely used in the seismic evaluation and retrofitting of existing buildings in Taiwan, so it is necessary to study the implicit safety factor of the method, and its relationship with the elastic stiffness of the structure, the hysteretic energy dissipation of its elements, and the characteristic of input seismic records.

The analysis results of the capacity spectrum method are dependent on the vertical distribution of the lateral loading and the reference mode (ATC,

[1] Researcher, National Center for Research on Earthquake Engineering, ykyeh@ncree.narl.org.tw
[2] Assistant Technologist, National Center for Research on Earthquake Engineering, tkchow@ncree.narl.org.tw

1996). In order to simply study the relationship between the nonlinear pushover analysis and the dynamic analysis, we use a single degree of freedom structure system as the subject of analysis, so that choice of lateral loading distribution and reference mode can be avoided.

The third edition of the NCREE technology handbook is used to define the nonlinear hinges of the structure, and the software packages ETABS and PERFORM3D are adopted to perform the nonlinear pushover analysis and the nonlinear dynamic analysis respectively.

Capacity Spectrum Method

The actual structure subject to the 475-year design earthquake will develop nonlinear deformation. In order to understand the mechanical behavior of the buildings during the earthquake excitation, the most direct approach is nonlinear dynamic analysis. The most familiar seismic design is to adopt the static elastic analysis where the ductile capacity of the structure is assumed to reduce the design seismic forces. It also uses the elastic response spectrum and the peak ground acceleration to represent the design earthquake. Engineers are more accustomed to static analysis than nonlinear dynamic analysis. So, the static pushover analysis is more commonly used in seismic evaluation to simulate the displacement response of the structure in earthquakes.

The capacity spectrum method for seismic evaluation is suggested by ATC 40 and is also widely adopted by the engineering community. It is based on the nonlinear pushover analysis of a planar frame to establish the capacity curve of the structure. This is done by setting a performance point at the capacity curve and seeking the performance object earthquake that can cause this performance object displacement. The peak ground acceleration of this performance object earthquake is used to compare with the peak ground acceleration of a 475-year design earthquake. If the value of the performance object earthquake is larger, the structure has adequate seismic capacity. Otherwise, the structure needs to be retrofitted to reduce the nonlinear displacement in earthquakes.

The above mentioned capacity curve is developed by the pushover analysis. According equation (1) to set up the lateral loading, the force-deformation curve relating base shear V to roof displacement u_{roof} can be found from a graph as shown in Fig. 1.

$$V_j = V \frac{m_j \phi_{j1}}{\sum_{i=1}^{N} m_i \phi_{i1}} \tag{1}$$

where, m_i is the mass of the i-th floor and ϕ_{i1} is the amplitude of the i-th floor of the first mode.

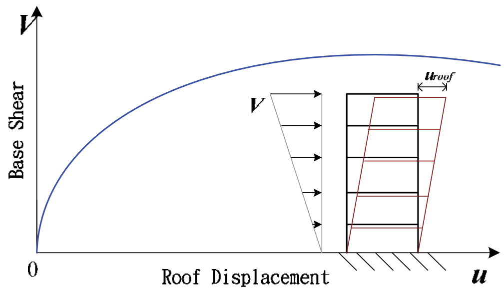

Fig. 1 Capacity curve of the pushover analysis

The capacity curve is then transformed into the capacity spectrum, namely the relation curve of the spectral displacement S_d and the spectral acceleration coefficient S_a. The transform equations are shown as:

$$S_d = \frac{u_{roof}}{PF_1 \phi_{roof,1}} \tag{2}$$

$$S_a = \frac{V}{\alpha_1 \cdot W} \tag{3}$$

where, PF_1 and α_1 are the participation factor and the modal mass coefficient for the first mode of the structure respectively; W is the weight of the structure.

Each performance point (S_{dp}, S_{ap}) of the capacity spectrum can be treated as a response to an equivalent single degree of freedom system at a different level earthquake with an equivalent period and damping ratio. The seismic evaluation procedure seeks a high damping ratio response spectrum which intersects the capacity spectrum at the performance point. The peak ground acceleration (PGA) of this high damping ratio response spectrum is named the performance object ground acceleration A_p . A_p can be calculated as:

$$A_p = \begin{cases} S_{ap} \Big/ \left[1 + \left(\dfrac{2.5}{B_S} - 1\right) \dfrac{T_{eq}}{0.2T_0}\right] & for\, T_{eq} \le 0.2T_0 \\ \dfrac{B_S}{2.5} S_{ap} & for\, 0.2T_0 < T_{eq} \le T_0 \\ \dfrac{B_S T_{eq}}{2.5T_0} S_{ap} & for\, T_0 < T_{eq} \end{cases} \tag{4}$$

where, $T_0 = (S_{D1}B_S)/(S_{DS}B_1)$ is the parting between the short and middle period ranges; S_{DS} is the short period design spectral acceleration at the site; S_{D1} is the site one second period design spectral acceleration; B_S and B_1 are the damping ratio modification coefficients defined in the design code which are dependent on β_{eq} .

Pushover Analysis of a Single Degree of Freedom Structure

As shown in Fig.2, the four-column four-beam single-span single-floor structure is 450 cm long, 450 cm wide, and 330 cm high. The site is set in the eastern part of Tainan City and the site ground is class 2. The reference lines of the columns and beams are the middle centerlines. The offsets of the columns and beams are assumed to be rigid. The properties of the panel zones are the same as the columns. The flexural rigidity EI of the crack section along the weak axis of the columns is 149.4×108 kgf • cm^2. The flexural rigidity EI of beams' crack section is 573.8×108 kgf • cm^2. The properties of the nonlinear moment hinges at both ends of the columns along the weak axis and beams are shown in Fig. 3. The floor has a 12 cm thickness and is set as a rigid diaphragm. The vertical load comes from the self-weight of members and the floor's uniform loading is set at 0.01 kgf/cm^2. The story mass and the mass moment of inertia are 14850 kg and 1.503×109 kg • cm^2 respectively.

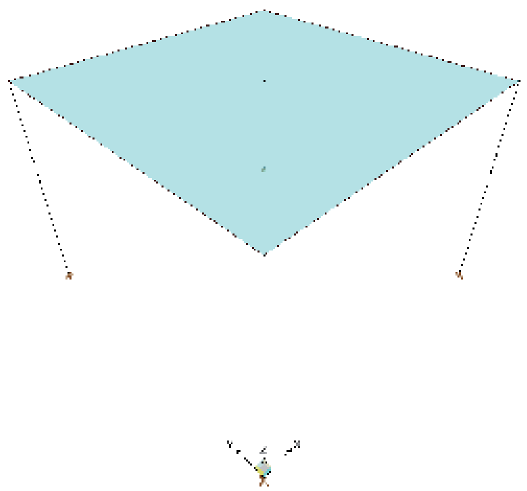

Fig. 2 The four-column four-beam single-span single-floor structure

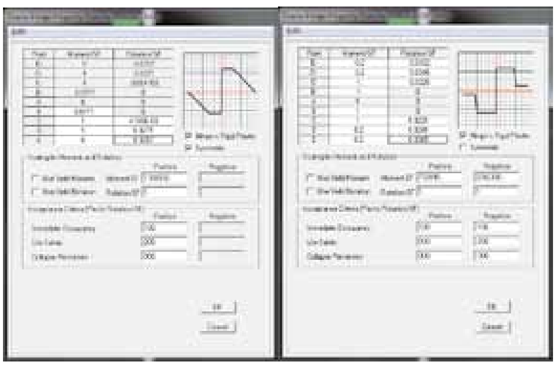

Fig. 3 The moment hinges of the columns and beams

The model is set up in the software ETABS. At first, the vertical loading is applied under force control. Then, under displacement control, the lateral forces are applied at the mass centers of each floor along the X-direction. The capacity curve is shown in Fig. 4. A roof displacement of 7.5 cm is chosen as the performance object displacement. According to the capacity spectrum method, the performance object ground acceleration is calculated as 1.156g, which corresponds to a roof displacement of 7.5 cm in an earthquake with a PGA of 1.156g for this structure. However, the real roof displacement in an actual earthquake will be smaller. The ratio between the estimated roof displacement and the actual is the studied safety factor.

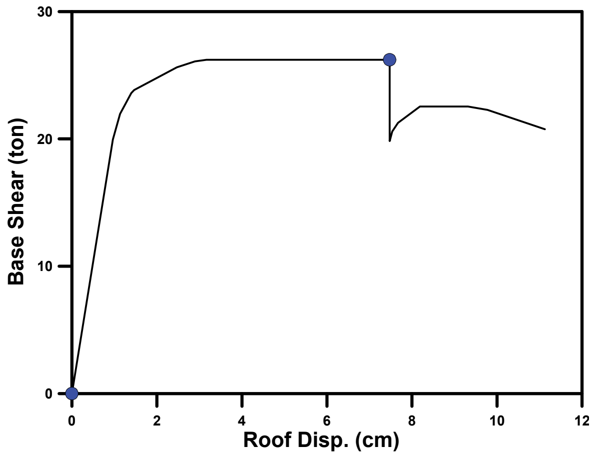

Fig. 4 Capacity curve of the single-span single-floor structure

Nonlinear Dynamic Analysis of a Single Degree of Freedom Structure

The software PERFORM3D is used to perform the nonlinear dynamic analysis for this study. The model is same as that used in the pushover analysis. We have two types of hysteretic behavior: one where the stiffness does not degrade during the analysis as shown in Fig.5, and another where the stiffness does degrade as shown in Fig. 6.

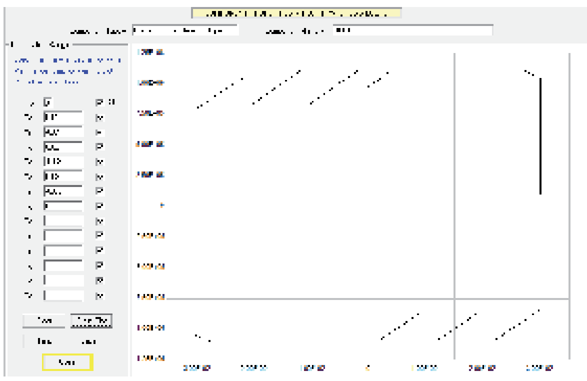

Fig. 5 Hysteretic behavior of nonlinear hinge of columns with no stiffness degradation

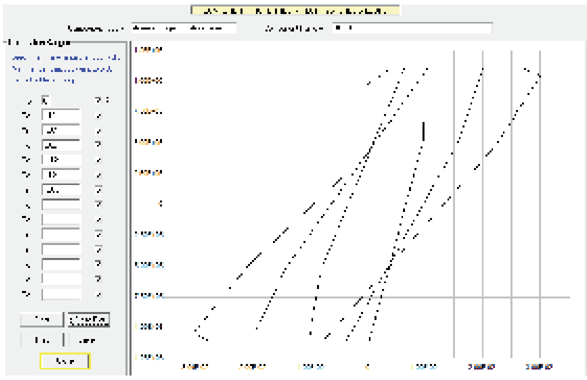

Fig. 6 Hysteretic behavior of nonlinear hinge of columns with stiffness degradation

The input earthquakes are chosen from the seismic databank of the Central Weather Bureau. The seismic intensity for all twenty seismic records is larger than 6 and the seismic stations are all located on class 2 ground. The peak ground accelerations of these records lie between 250gal and 550gal. Their response spectrums and the average spectrum are shown in Fig. 7.

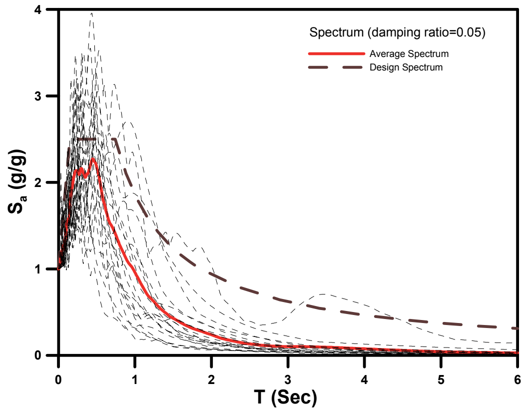

Fig. 7 Response spectrums of 20 chosen earthquakes

As shown in Table 1, the average roof displacement of the cases with no stiffness degradation is 1.64 cm, which is much smaller than the performance object displacement 7.5 cm, and the ratio 4.5 is the implicit safety factor; the average roof displacement of the cases with stiffness degradation is 1.73 cm, which is also smaller than the performance object displacement, and the implicit safety factor is 4.3. From the comparison, we can conclude that conservation of the capacity spectrum method is not dependent on the stiffness degradation.

Conclusions

This study shows the capacity spectrum method to be a very conservative method and to overvalue the importance of stiffness degradation in hysteretic cycles.

Table 1 The analysis of the roof displacements in nonlinear dynamic analyses

Earthquake	Disp.(cm) (No Degradation)	Disp.(cm) (Degradation)
21	1.12	1.12
22	1.32	1.59
23	1.24	1.24
24	1.76	1.87
25	1.37	1.52
26	2.11	2.52
27	2.28	2.38
28	1.35	1.41
29	1.24	1.25
30	1.40	1.40
31	2.00	2.00
32	1.15	1.15
33	1.85	2.26
34	1.55	1.54
35	2.55	2.55
36	2.50	2.70
37	1.27	1.29
38	1.45	1.45
39	1.83	1.83
40	1.56	1.56
AVE	1.64	1.73
STD	0.44	0.50

References

Applied Technology Council (ATC) (1996), "ATC-40 Seismic Evaluation and Retrofit of Concrete Buildings", prepared by the Applied Technology Council, Redwood City, Calif.

Federal Emergency Management Agency (FEMA) (2000), "Prestandard and Commentary for the Seismic Rehabilitation of Buildings (FEMA Publication 356)", prepared by the American Society of Civil Engineers, Washington, D.C.

Federal Emergency Management Agency (FEMA) (2005), "FEMA 440 Improvement of Nonlinear Static Seismic Analysis Procedures", prepared by the Applied Technology Council for the Federal Emergency Management Agency, Washington, D.C.

Verification of Simplified Pushover Analysis of School Buildings by In-Situ Tests

Lap-Loi Chung[1], Lai-Yun Wu[2], Yao-Sheng Yang[3], Ting-Yu Ku[3], Yong-An Lai[3], and Chun-Ting Huang[3]

鍾立來 [1]、吳賴雲 [2]、楊耀昇 [3]、顧丁與 [3]、賴勇安 [3]、黃鈞鼎 [3]

Abstract

During the Chi-Chi Earthquake in Taiwan, 786 school buildings were damaged and 43 school buildings collapsed. Unfortunately, elementary schools and junior high schools sustained the majority of the damage. As there is a lack of seismic capacity for existing school buildings, solving this problem has become an important issue in Taiwan. For this purpose, various seismic evaluation methods were proposed by researchers to determine whether existing school buildings needed retrofitting. However, some of these methods require complicated calculations and packaged software. Therefore, a simple and efficient seismic evaluation method for estimating the seismic capacity of existing school buildings needs to be developed.

Based on post-earthquake reconnaissance reports, school buildings in Taiwan typically collapsed along the direction of the corridor during an earthquake. Therefore, only the seismic resistance along the direction of the corridor is considered in this study. In order to realize how school buildings subjected to lateral forces behave, many in-situ pushover tests of school buildings have been completed in Taiwan by the research team at the National Center for Research on Earthquake Engineering (NCREE).

The Simplified Pushover Analysis (SPA), based on the assumption of shear buildings, is used in this study to verify the seismic capacity of Ruei-Pu elementary school by in-situ pushover tests. The results show that the analytical pushover curves agree with the in-situ pushover tests. Thus, this analysis will benefit engineers when predicting the seismic capacity of typical school buildings in Taiwan.

Keywords: simplified pushover analysis; in-situ pushover test; weak columns and strong beams

Introduction

School buildings in Taiwan are typically two or three stories high, and are classified as low-rise buildings. According to field investigation and in-situ tests after the Chi-Chi earthquake, column failure is the main factor contributing to the fact that school buildings were seriously damaged, while little damage was observed on beams. This phenomenon is called “weak-column-and-strong-beam failure mode”. As RC slabs and RC beams are constructed together, the stiffness of beams becomes stronger than expected.

Based on the behavior of weak columns and strong beams, this study uses the Simplified Pushover Analysis (SPA) method, which refers to nonlinear behaviors of concrete columns to predict the seismic capacity of typical school buildings. It is reasonable to assume that typical school buildings in Taiwan can be categorized as shear buildings due to their weak-column-and-strong-beam failure mode.

To verify the feasibility of SPA, the base shear versus roof displacement curve, called seismic capacity, is calculated by the proposed method, and compared with the results obtained from an in-situ pushover test of Ruei-Pu elementary school.

[1] Researcher, National Center for Research on Earthquake Engineering,
Professor, National Taiwan University, chung@ncree.narl.org.tw
[2] Emeritus Professor, Department of Civil Engineering, National Taiwan University
[3] Student, Department of Civil Engineering, National Taiwan University

Behavior and Failure Mode of Column

Before implementing the SPA, it is important to characterize the nonlinear behavior of the structure. From observing the school buildings that damaged in Chi-Chi Earthquake, the failure behavior was caused by weak columns and strong beams. Columns played the main role in resisting the earthquake. For this reason, the nonlinear behavior of school buildings is established by the nonlinear behavior of RC columns.

From previous researches, columns are categorized into three different failures conditions: flexural failure, shear failure, and flexural shear failure. The three types of failure conditions are proposed by Elwood and Moehle [1,2], and the failure condition of columns is determined by the ratio between lateral strength due to flexure and that due to shear (V_m / V_n). The lateral strength due to flexure V_m and due to shear V_n can be calculated[3], respectively, using Eqs. (1) to (4):

$$V_m = 2M_n / H \tag{1}$$

$$V_n = V_c + V_s \tag{2}$$

$$V_c = 0.53(1 + P/140A_g)\sqrt{f_c'}bd \tag{3}$$

$$V_s = A_{st} f_{yt} d(\cot\alpha)/s\ . \tag{4}$$

where, M_n is the nominal flexural strength; H is the clear height of the reinforced concrete column; V_n is the nominal shear strength; V_s is the nominal shear strength provided by shear reinforcement; V_c is the nominal shear force provided by concrete; P and A_g are the axial force and the gross area of the reinforced concrete column, respectively; f_c' is the compressive strength of concrete; b and d are the width and the effective depth of the columns, respectively; A_{st} is the area of transverse reinforcement; f_{yt} is the specified yield strength of the transverse reinforcement; s is the transverse reinforcement spacing; and α is the angle of the shear cracks as calculated using Eqs. (5)

$$\alpha = 45^\circ - \frac{1}{2}\tan^{-1}\left(\frac{\sigma}{2f_t\sqrt{(1+\sigma)/f_t}}\right) \tag{5}$$

where, $\sigma = P/A_g$; and f_t ($f_t = 1.06\sqrt{f_c'}$) is the tensile strength of the concrete. The flexure-to-shear force ratio and failure conditions of column are defined as follows:

$$\begin{cases} V_m / V_n < 0.6 & \textit{flexural failure} \\ 0.6 \le V_m / V_n \le 1.0 & \textit{flexural-shear failure} \\ V_m / V_n > 1.0 & \textit{shear failure} \end{cases}$$

In this study, the ratio between the lateral strengths due to flexure and shear of all columns are smaller than 0.6, calculated based on the data collected from in-situ pushover tests of Ruei-Pu elementary school. Therefore, the failure conditions of all columns are flexural failure, and the relationship of lateral force-displacement of columns is defined in Fig 1.

When the flexural strength of a column is developed, the displacement is Δ_y, which can be calculated using Eq. (6):

$$\Delta_y = V_m / k_c \tag{6}$$

where, k_c is lateral stiffness of the column, equal to $0.35 \times (12E_c I_g / H^3)$. When the column transits from flexural to shear failure, the displacement is Δ_s which can be calculated using Eq. (7):

$$\frac{\Delta_s}{H} = \frac{3}{100} + 4\rho'' - \frac{1}{40}\frac{v_m}{\sqrt{f_c'}} - \frac{1}{40}\frac{P}{A_g f_c'} \ge \frac{1}{100} \tag{7}$$

where, ρ'' is the ratio of transverse reinforcement defined as A_{st}/bs; and v_m is the maximum nominal shear stress in MPa , defined as V_m / bd.

When the column appears to be in axial failure, the displacement is Δ_a calculated using Eq. (8):

$$\frac{\Delta_a}{H} = \frac{4}{100}\frac{1 + (\tan\theta)^2}{\tan\theta + P\dfrac{s}{A_{st} f_{yt} d_c \tan\theta}}\ . \tag{8}$$

where d_c is the depth of the column core from the center line to the center line of the ties; θ ($\theta = \tan^{-1}(H/h)$) is the maximum crack angle, where h is the depth of the column, and θ is less than 65 degrees. The seismic capacity established by column behavior and their failure conditions can be performed using SPA.

Simplified Pushover Analysis

In SPA, the seismic capacity of typical school buildings in Taiwan is obtained by the following procedures:

1. The lateral force-displacement curve of all columns for each story should be established;
2. The lateral force-displacement curve of each story should be established, and the lateral force is obtained by superimposing the lateral force of all the columns in the same story by consistent displacement. It should be noted that the lateral strength of each story is not calculated by adding the maximum strength of all columns in the story directly;
3. When the building is subjected to lateral earthquake loading, the lateral force applied and distributed at each story is in the form of an inverted triangle based on the seismic code in Taiwan and can be calculated using Eq. (9):

$$F_i = \frac{(V_{bs} - F_t)W_i}{\sum_{i=0}^{n} W_j h_j} \tag{9}$$

where, V_{bs} is base shear; W_i and W_j are the weight of level i and j; and for low-rise buildings, F_t is equal to zero. The corresponding lateral force of each story can be calculated using Eq. (10):

$$V_{Fi} = \sum_{k=i+1}^{n} F_{Fk} \tag{10}$$

4. Based on Eq. (10), the corresponding story drift can be obtained. The roof displacement Δ_{RF} is the summation of each story drift Δ_i, which can be calculated using Eq. (11):

$$\Delta_{RF} = \sum_{i=1}^{n} \Delta_i \tag{11}$$

Database of Ruei-Pu Elementary School

The in-situ pushover test of Ruei-Pu elementary school is chosen to be verified by implementing the SPA method. The database of the building is as follows:

Ruei-Pu elementary school is located in Taoyuan, Taiwan. It is a 2-story RC building, with two classrooms and 17 columns in each story. The total length of the school building is 18.6m, and the total width is 10.8m as shown in Fig 2. The height of each story is 3.6m, with a total building height of 7.2m, as shown in Fig 3. Column sections of the specimen are divided into two sizes, C1 with dimension of 35cm×40cm and C2 with dimensions of 24cm×40cm, respectively. The cross section details of columns are shown in Fig 4.

The properties of the materials used are as follows: the compressive strength of concrete is 113kgf/cm^2; the yield strength of longitudinal reinforcements is 3204kgf/cm^2; and the yield strength of transverse reinforcements is 4386kgf/cm^2. These material properties are the average values of the test results.

Test Results

The test result of the school building is shown in Fig. 5. The school building is cut into two sections: one for monotonic testing and the other for cyclic testing, where the latter is used to simulate a real earthquake. The comparison of the maximum base shear shows that the maximum base shear of the cyclic loading test is 97% of that of the monotonic loading test.

Fig. 6 shows the maximum strength of 1FL and 2FL obtained by SPA.

Fig. 7 presents the comparison between results from the pushover test and analysis.

The maximum base shear from the in-situ pushover test was 117.7 tf, as the roof displacement reached 3.78cm. When the base shear was dropped to 0.8 times the maximum base shear, the roof displacement reached 10.73cm.

The maximum base shear from the SPA was 108.4 tf, as the roof displacement reached 2.80cm. When the base shear was dropped to 0.8 times the maximum base shear, the roof displacement reached 6.14cm.

The maximum analysis base shear is 7.9% less than the test one, and the displacement corresponding to the maximum base shear by analysis is 26% less than the test one. The SPA is conservative in its base shear and displacement predictions.

Conclusion

Seismic capacity obtained from the SPA by superposing the lateral force-displacement curves of all columns was verified with in-situ pushover tests of Ruei-Pu elementary school in Taiwan. The verification indicates that

1. The analysis result demonstrates conservative predictions of the base shear and displacement, where the base shear prediction is 92% of the test result, and the displacement corresponding to the maximum base shear from the analysis is 74% of the test value;
2. Most of the columns failed due to flexural failure conditions, which agree with the test results;
3. It is an effective analytical tool to obtain the seismic capacity of shear buildings.

Reference

Elwood, K.J. and Moehle, J.P., “Drift Capacity of Reinforced Concrete Columns with Light Transverse Reinforcement,” Earthquake Spectra, Vol. 21, No. 1, pp. 71-89, 2005.

Elwood, K.J. and Moehle, J.P., “Axial Capacity Model for Shear-Damaged Columns,” ACI Structural Journal, Vol. 102, No. 4, pp. 578-587, 2005.

ACI Committee 318, Building Code Requirements for Structural Concrete (ACI 318-05) and Commentary (ACI 318R-05). American Concrete Institute, Farmington Hills, MI, 2005.

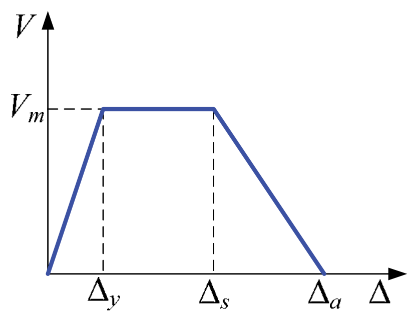

Fig. 1 Lateral Force-Displacement of Flexural Failure

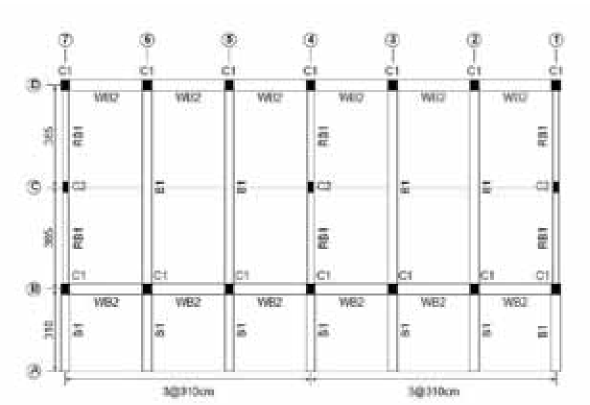

Fig. 2 Plan View of the School Building

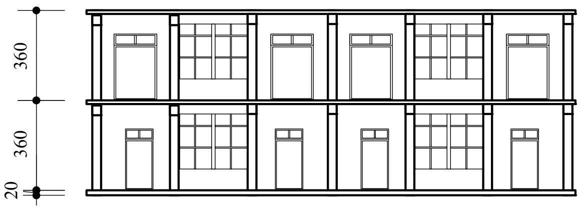

(a) the front of elevation view

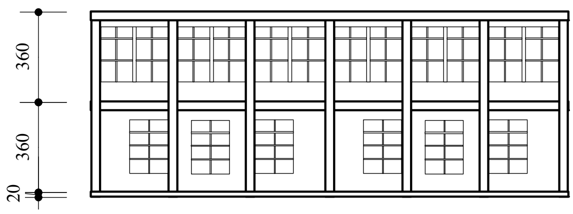

(b) the back of elevation view

Fig. 3 Front and Back Elevation View of the School Building

Serial numbers of columns	C1	C2
Cross-Section detial	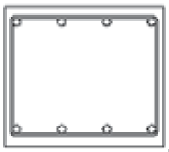	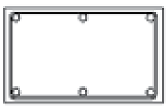
Main reinforcement	∘ 8－D19	∘ 6－D19
Transverse reinforcement	D10@25cm	D10@25cm
Size	35cm×40cm	24cm×40cm

Fig. 4 Cross Section Details of Columns

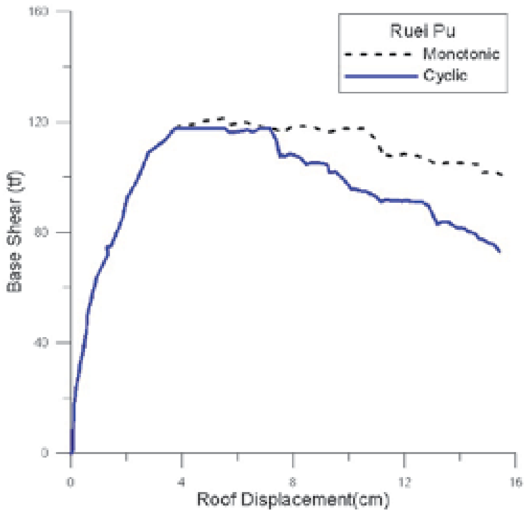

Fig. 5 Experimental Capacity Curve

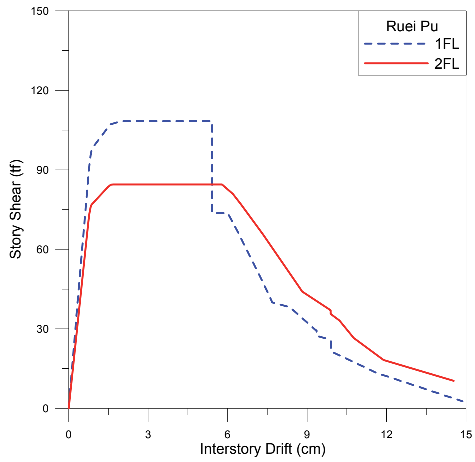

Fig. 6 Analytical Lateral Force-Displacement Curve of Each Story

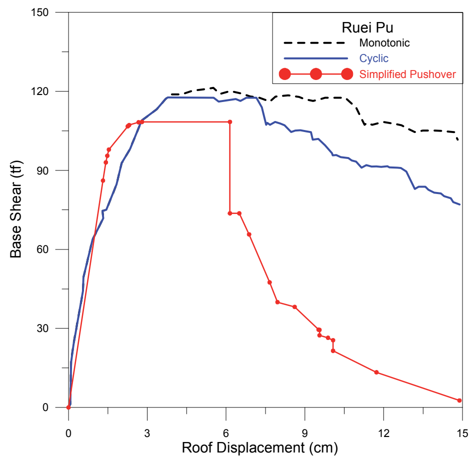

Fig. 7 Comparison between Experimental and Analytical Capacity Curves

Verification of Seismic Preliminary Evaluation of School Buildings by In Situ Tests

Lap-Loi Chung[1], Lai-Yun Wu[2], Kun-Wei Lin [3], and Yao-Sheng Yang[3]

鍾立來 [1]、吳賴雲 [2]、林琨偉 [3]、楊耀昇 [3]

Abstract

Preliminary evaluation is a screening stage for the seismic performance of existing school buildings. This method is simple, fast, objective, and effective to reduce the magnitude of a problem of seismic deficiency. From data regarding the seismic zone, the importance factor, the dimensions of the structure and its members, the seismic capacity and demand of a school building can be estimated by preliminary evaluation. The priority of a school building to enter the next stage, that of detailed evaluation, is determined according to the seismic capacity and demand ratio. However, a preliminary evaluation should be conservative enough to avoid overestimation of the performance of school buildings. Unlike in laboratory tests, the material strength, reinforcement detailing, construction quality, and foundation boundary conditions of in situ tests of a school building are realistic. In this study, the results of in situ pushover tests of Ruei-Pu Elementary School are used. From the configuration and capacity curve (the relationship between lateral force and lateral displacement) of the school building, the ultimate base shear, the weight per unit floor area, the fundamental vibration period, the allowable ductility capacity, and the fundamental seismic performance (the ratio of seismic capacity and demand) are found. Based on the results of the in situ tests of the school building, the results of the preliminary evaluation are examined. Even though the compressive strength of concrete is quite low and the thickness of the concrete cover is quite high in the specimen, the preliminary evaluation of the school building is found to still be conservative.

Keywords: school building, seismic performance, preliminary evaluation, in situ experiments

Introduction

Seismic capacity is a common problem for school buildings currently in use in Taiwan. To reduce risks to students, upgrading the seismic performance of school buildings has become a serious issue. Following the procedures of preliminary evaluation, detailed evaluation, retrofit design and construction, the seismic capacity of school buildings can be upgraded effectively and the risk to teachers and students can be reduced during an earthquake event.

Due to the importance of the safety of the school buildings, the Taiwanese government allocated a budget of $17.6 billion NTD in the economy revival plan to upgrade the seismic capacity of public elementary, junior and senior high school buildings from 2009 to 2011. Preliminary seismic evaluation was one of the procedures in the project.

According to structure types, seismic weakness, failure modes, and experimental data, the National Center for Research on Earthquake Engineering (NCREE) developed an evaluation method that is simple and objective. The main purpose of this method is to quickly determine which school buildings have a lower seismic capacity and to provide school teachers, engineers, and government officials with necessary information to decide on a plan for each school.

[1] Researcher, National Center for Research on Earthquake Engineering, Professor, National Taiwan University, chung@ncree.narl.org.tw
[2] Emeritus Professor, Department of Civil Engineering, National Taiwan University
[3] Student, Department of Civil Engineering, National Taiwan University

Database of Ruei-Pu Elementary School

Located in Taoyuan, Ruei-Pu Elementary School was established in the era of Japanese occupation. In 1979, the two school buildings were rebuilt into a two-story buildings made of reinforced concrete. Each floor consisted of four classrooms and a unilateral hallway without exterior columns.

Each specimen [1] contained two classrooms on a single floor, including three partition brick walls of 25 cm thickness. Each classroom consisted of three spans that lay along the longitudinal direction. Each floor was 3.6 m high; the total length along the corridor was 18.8 m and the transverse width was about 8 m. The specimen had seventeen columns on a single floor with two different types of sectional detailing: fourteen C1-columns with dimensions of 35 cm × 40 cm, and three C2-columns, located in the three brick walls, with dimensions of 24 cm × 40 cm. There were three types of beams: an RB1- beam with dimensions of 24 cm × 35 cm, a WB2- beam with dimensions of 40 cm × 40 cm, and a B1- beam with dimensions of 35 cm × 60 cm. The compressive strength of the concrete was 113 kgf/cm^2, and the yielding strength of the rebar and stirrup were 3204 and 4386 kgf/cm^2, respectively. A photo, structural plan, and an elevation plan are shown in Fig. 1.

The two buildings were used as specimens for a monotonic loading test and a cyclic loading test, respectively [2]. Comparing the capacity curves of the monotonic test and the cyclic loading test in Ruei-Pu Elementary School, the maximum base shear of the cyclic loading test was 97% of that of the monotonic test. After the maximum base shear was reached, the increment of roof displacement of the specimen under the cyclic loading test was half of that under the monotonic loading test. In this study, the capacity curve under a monotonic loading test was modified to simulate the cyclic one and used to verify the seismic preliminary evaluation.

Maximum Base Shear of School Building

The seismic performance of the school buildings can be evaluated from their seismic capacity to demand ratio [3]. The seismic capacity of the school buildings is computed by superimposing the shear strength of various vertical members, such as walls and columns. The seismic demand is determined from the weight and location of the school building. In order to simplify the evaluation method, fundamental assumptions, based on the characteristics of typical school buildings in Taiwan, are made. Transverse to the corridors, classrooms are typically partitioned by walls, which are continuous in the direction of gravity. However, along the corridors, there are windows and doors for entrances and provision of natural light. Because the walls are seldom continuous in the direction of gravity, damage and collapse of school buildings occurs only along the corridors.

Thus, seismic performance is evaluated along the corridor direction only. Since the demand of seismic shear force at the first story is larger than at other stories, and as school buildings are quite regular from story to story, the seismic resistance of the first story is the most critical. Therefore, the seismic vulnerability of the first story needs to be evaluated. Due to the presence of the concrete slab and the lintel above the window, the beams were strongly confined, becoming stronger and stiffer than the columns. School buildings are often founded to be damaged or collapsed due to the failure of the vertical members. Therefore, only columns and walls are taken into account in the evaluation of seismic resistance. The total base shear strength $V_{\mathrm{bs,PE}}$ from preliminary evaluation is shown below:

$$V_{\mathrm{bs,PE}} = \beta(\tau_{\mathrm{CI}} A_{\mathrm{CI}} + \tau_{\mathrm{CII}} A_{\mathrm{CII}} + \tau_{\mathrm{CIII}} A_{\mathrm{CIII}}) \tag{1}$$

where $\beta = 0.9$ is the reduction factor; and τ_{CI}, τ_{CII}, and τ_{CIII} are the ultimate strengths per unit cross sectional area of the classroom columns (at the front and back frame of the classroom), corridor columns (at the exterior side of the corridor), and partition columns (embedded in the partition wall) in the first floor, respectively. Meanwhile, A_{CI}, A_{CII}, and A_{CIII} are the total cross-sectional areas of the classroom columns, corridor columns, and partition columns in the first floor, respectively.

In Ruei-Pu Elementary School, the total cross-sectional area of the classroom columns was 19,600 cm^2 and that of the partition columns was 2,880 cm^2. The maximum base shear strength from preliminary evaluation was 140.80 tf. From the in situ test, the maximum base shear of the specimen was 117.71 tf. Therefore, the preliminary evaluation overestimates the maximum base shear strength; it is found to be 119.6% of the experimental value.

Weight of School Building

The actual weights of the roof and the second floor were calculated to be 145.27 and 168.46 tf, respectively. The total weight of the specimen was 313.73 tf. The actual weights per unit floor area on the roof and the second floor were $w_{\mathrm{RF,EX}} = 723$ and $w_{\mathrm{2F,EX}} = 839\,\mathrm{kgf/cm^2}$, respectively.

From preliminary evaluation, the total weight of school building can be estimated as:

$$W_{\mathrm{PE}} = \sum_{i=2}^{N_{\mathrm{F}}} w_{i\mathrm{F,PE}} A_{i\mathrm{F}} + w_{\mathrm{RF,PE}} A_{\mathrm{RF}} \tag{2}$$

where $A_{i\mathrm{F}}$ is the floor area on the *i*-th floor and $w_{i\mathrm{F,PE}}$ is the weight per unit floor area on the *i*-th floor. In the preliminary evaluation, the weight per unit floor area on the roof and the *i*-th floor are assumed to be $w_{\mathrm{RF,PE}} = 750$ and $w_{i\mathrm{F,PE}} = 900\,\mathrm{kgf/cm^2}$, respectively.

The total weight of the building estimated from the preliminary evaluation was 331.45 tf, 105.7% of the actual weight. The weight per unit floor area on the roof and the second floor estimated from preliminary evaluation were 103.7% and 107.3% of the actual values.

Fundamental Vibration Period

The first mode shape of the school building can be assumed to be $\boldsymbol{\varphi}_1 = \begin{bmatrix}1 & 0.5\end{bmatrix}^{\mathrm{T}}$. The first modal weight $\overline{W}_1$ can be calculated as:

$$\overline{W}_1 = \boldsymbol{\varphi}_1^{\mathrm{T}} \mathbf{W} \boldsymbol{\varphi}_1 = W_{\mathrm{RF,EX}} + 0.25 W_{\mathrm{2F,EX}} \tag{3}$$

In the in situ test, the proportion of the applied lateral force on the roof and the second floor was $F_{\mathrm{RF}} : F_{\mathrm{2F}} = 1:0.5$. The relationship between the lateral force and the displacement can be shown as:

$$\begin{bmatrix} F_{\mathrm{RF}} \\ F_{\mathrm{2F}} \end{bmatrix} = \mathbf{K}\boldsymbol{\varphi}_1 \Delta_{\mathrm{RF}} = \mathbf{K}\begin{bmatrix} 1 \\ 0.5 \end{bmatrix}\Delta_{\mathrm{RF}} \tag{4}$$

where $\mathbf{K}$ is the stiffness matrix of the building. And Δ_{RF} is the roof displacement.

After pre-multiplying by $\boldsymbol{\varphi}_1^{\mathrm{T}}$, the above equation can be transformed to:

$$1.25 F_{\mathrm{RF}} = \overline{K}_1 \Delta_{\mathrm{RF}} \tag{5}$$

where $\overline{K}_1$ is the first modal stiffness of the structure. The base shear V_{bs} is the summation of the lateral forces on the roof and second floor:

$$V_{\mathrm{bs}} = 1.5 F_{\mathrm{RF}} = \frac{1.5 \overline{K}_1 \Delta_{\mathrm{RF}}}{1.25} \tag{6}$$

From Eqs. (3) to (6), the actual fundamental vibration period from the in situ test is:

$$T = 2\pi \sqrt{\frac{1.5(W_{\mathrm{RF}} + 0.25 W_{\mathrm{2F}})\Delta_{\mathrm{RF}}}{1.25 \mathrm{g} V_{\mathrm{bs}}}} \tag{7}$$

In the in situ test, as the base shear V_{bs} developed to 0.7 times the maximum base shear $V_{\mathrm{bs,EX,max}}$, the corresponding roof displacement was $\Delta_{\mathrm{RF}} = 1.739\,\mathrm{cm}$. The actual fundamental vibration period was $T_{\mathrm{EX}} = 0.437\,\mathrm{s}$.

Since the school building was a reinforced concrete structure without reinforced concrete walls or stiffened members, the fundamental vibration period of the building was estimated in the preliminary evaluation as:

$$T = 0.070 h_n^{3/4} \tag{8}$$

where h_n is the height of the structure. The structural period of the building was estimated in the preliminary evaluation to be $T_{\mathrm{PE}} = 0.308\,\mathrm{s}$, 70.4% of the experimental value.

Allowable Ductility Capacity

The capacity curve can be transformed to an equivalent elastic, perfectly plastic curve. The slope of the curve is determined by the secant stiffness when the base shear rises to 0.7 times the maximum base shear. When the base shear has already reached its maximum value and drops to 0.8 times the maximum base shear, the corresponding roof displacement is the ultimate displacement $\Delta_{\mathrm{RF,u}}$. The ductility capacity $R_{\mathrm{EX}} = \Delta_{\mathrm{RF,u}} / \Delta_{\mathrm{RF,y}}$ is the ratio of the equivalent ultimate roof displacement and the yielding displacement. From the in situ test results, the ductility capacity R_{EX} can be obtained as:

$$\frac{1}{R_{\mathrm{EX}}} = 1 - \sqrt{1 - \frac{2U_{\mathrm{V\Delta}}\Delta_{\mathrm{RF,0.7Vmax}}}{0.7 V_{\mathrm{bs,EX}} \Delta_{\mathrm{RF,u}}^2}} \tag{9}$$

The school building was located at the site other than in the Taipei Basin, so the allowable ductility capacity $R_{\mathrm{a,EX}}$ was:

$$R_{\mathrm{a,EX}} = 1 + (R_{\mathrm{EX}} - 1)/1.5 \tag{10}$$

In the in situ test, as the base shear V_{bs} rose to 0.7 times the maximum base shear, the corresponding roof displacement was $\Delta_{\mathrm{RF,0.7Vmax}} = 1.739\,\mathrm{cm}$. As the base shear dropped to 0.8 times of the maximum base shear, the corresponding roof displacement was $\Delta_{\mathrm{RF,u}} = 10.728\,\mathrm{cm}$. The experimental and allowable ductility capacity are $R_{\mathrm{EX}} = 4.515$ and $R_{\mathrm{a,EX}} = 3.343$, respectively. From the preliminary evaluation, the allowable ductility capacity is assumed to be $R_{\mathrm{a,PE}} = 2.2$, 65.8% of the experimental value.

Fundamental Seismic Performance

According to the seismic design code [4], the design lateral strength can be calculated as:

$$V = \frac{S_{\mathrm{aD}} I}{1.4 \alpha_{\mathrm{y}} F_{\mathrm{u}}} W \tag{11}$$

where S_{aD} is the design spectral acceleration. I is the importance factor. W is the total weight of the building. α_{y} is the amplification factor for the first yielding in the building, and F_{u} is the reduction factor due to the structural system. After rearranging the above equation, the capacity-to-demand ratio can be expressed as below:

$$R_{\mathrm{CD}} = \frac{1.4 \alpha_{\mathrm{y}} V}{S_{\mathrm{aD}} I W / F_{\mathrm{u}}} = \frac{V_{\mathrm{bs}}}{S_{\mathrm{aD}} I W / F_{\mathrm{u}}} \tag{12}$$

In order to express this more clearly, the capacity-to-demand ratio is enlarged 100 times the fundamental seismic performance index E:

$$E = 100 R_{\mathrm{CD}} = (100) \frac{V_{\mathrm{bs}} F_{\mathrm{u}}}{S_{\mathrm{aD}} I W} \tag{13}$$

In the in situ test, the maximum base shear was $V_{\mathrm{bs}} = 117.71\,\mathrm{tf}$. The importance factor was $I = 1.25$ for a normal school building. The total weight of the specimen was $W = 313.73\,\mathrm{tf}$. The structural period of the specimen T was 0.437 s. The spectral response acceleration parameters at short period, $S_{\mathrm{S}}^{\mathrm{D}}$, and at 1-s period, S_1^{D}, were 0.6 and 0.35, respectively. The near-fault modification factors, N_{A} and N_{V}, were

1.0. The site coefficients were $F_a = 1.1$ and $F_v = 1.4$. Therefore, the design spectral response acceleration parameters at short period, S_{DS}, and at 1-s period, S_{D1}, were 0.66 and 0.49, respectively. The corner period of the design spectrum was $T_0^D = S_{D1}/S_{DS} = 0.742\,\mathrm{s}$. The design spectral response acceleration was $S_{aD,EX} = 0.66$. The allowable ductility capacity $R_{a,EX}$ was 3.343, so that the reduction factor due to the structural system F_u is 2.385. The fundamental seismic performance E can be calculated to be 108.5.

In the preliminary evaluation, the maximum base shear $V_{bs,PE}$ was 140.80 tf. The total weight of the specimen W_{PE} was 331.45 tf. The design spectral response acceleration $S_{aD,PE}$ was 0.66. The allowable ductility capacity $R_{a,PE}$ is 2.2. The reduction factor due to the structural system $F_{u,PE}$ was 1.844. The fundamental seismic performance E can be estimated to be 94.9, 87.5% of the experimental one.

Conclusion

In this paper, the results of an in situ test on Ruei-Pu Elementary School was used to verify the accuracy of the preliminary seismic evaluation. Because the actual compressive strength of concrete was less than that assumed for the preliminary evaluation and as the clear cover of column was too thick, the maximum base shear found in the preliminary evaluation was slightly larger than the experimental value. The allowable ductility capacity assumed for the preliminary evaluation was 65.8% of the calculated value. The total weight in the preliminary evaluation was 105.7% of the actual weight. As a whole, the fundamental seismic performance from the preliminary evaluation was 87.5% of that from the experiments. Therefore, the preliminary evaluation is confirmed to be conservative.

Reference

Chung LL, Wu LY, Lin KW, Yang YS, Lien KH. Verification of Seismic Preliminary Evaluation of School Buildings by In situ Tests. Journal of the Chinese Institute of Civil and Hydraulic Engineering 2012; 24(3):299- 311.(In Chinese)

Weng YT, Lin KC, Hwang SJ, Chiou TC. In situ pseudo-dynamic test and cyclic pushover test of existing school buildings. Report number NCREE 08-004, National Center for Research on Earthquake Engineering, Taiwan, 2008. (In Chinese)

Su, Keng-Li, "Preliminary Seismic Evaluation Method for Typical School Buildings in Taiwan", National Taiwan University, 2008. (in Chinese)

Construction and Planning Agency, "Seismic Design Specifications and Commentary of Buildings", Ministry of the Interior, Taiwan, 2004. (in Chinese)

(a) Photo of specimen

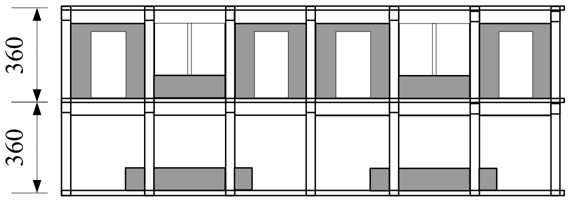

(b) Elevation plan

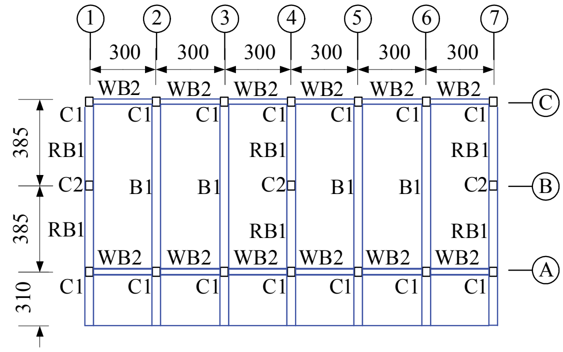

(c) Structural plan

Fig. 1 (a) Photo, (b) elevation plan and (c) structural plan of the building specimen

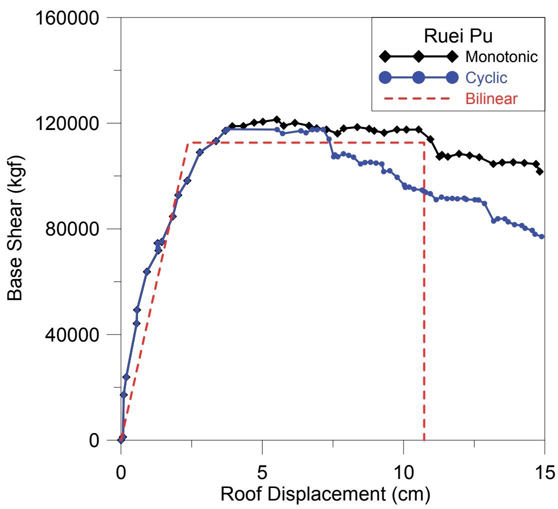

Fig. 2 Capacity curve of the building specimen

Dazhi Bridge Safety Monitoring Demonstration Project

Zheng-Kuan Lee [1]

李政寬

Abstract

Technology for the real-time monitoring of bridge safety is required by bridge management authorities and one task the National Center for Research on Earthquake Engineering (NCREE) has continually researched and developed. How to conduct real-time monitoring of long-range, multi-span bridges economically and effectively has remained the most significant challenge for related research and development. The NCREE has significantly improved the manufacturing of fiber optic sensor instruments, fiber optic welding technology, and communication capabilities in recent years, allowing the center to conduct real-time monitoring of long-range, multi-span bridges. Last September NCREE obtained approval from the Taipei City government to establish a fiber optic monitoring system on Dazhi Bridge. We hope that by using this project as an example, we can introduce a new generation of comprehensive full-bridge fiber optic monitoring technology to bridge management authorities throughout Taiwan.

Keywords: optic fiber sensors, bridge health monitoring, cable-stayed bridge, bridge elevation profile

Bridge Situation in Taiwan

Currently, approximately 28,000 bridges exist in Taiwan. These bridges are subjected to frequent earthquakes and typhoons, in addition to overloading and material fatigue. Concerns are growing regarding the durability and safety of bridges. Thus, bridge safety inspections are becoming increasingly important. Therefore, the development of an economical monitoring system is needed to monitor bridges simultaneously at all times and facilitate bridge safety inspections. This study, as an example of optic-fiber bridge monitoring system, demonstrates the integrated FBG-sensors applied on Dazhi Bridge.

Introducing Dazhi Bridge

Dazhi Bridge crosses the Keelung River, connecting to Binjiang Street in the south and Dazhi District in the north. It is an important bridge in the Zhongshan District of Taipei City. The bridge was completed and opened to traffic on June 23, 2002. Dazhi Bridge is beige with a total of 11 spans. The three spans in the north are box-shaped steel beams and the five spans in the south are pre-stressed concrete box-shaped beams. The middle three spans are fishing rod-style cable-stayed steel beams. The cable-stayed bridge section features striking red steel cables, and is considered a landmark of Taipei (Fig. 1).

Fig. 1 Dazhi Bridge landscape

Introducing the Comprehensive Full-Bridge Fiber Optic Monitoring System Developed by the NCREE

To fulfill the safety monitoring requirements for long-range, multi-span bridges, the NCREE developed a comprehensive full-bridge fiber optic monitoring system following years of research, development, and integration. The goal was to assist bridge management authorities in controlling

[1] Associate Researcher, National Center for Research on Earthquake Engineering, zklee@ncree.narl.org.tw.

the state of bridge safety at all times, which includes managing the flood levels, expansion joint distance changes, bridge elevation, the steel cable tension of the cable-stayed section, and other monitoring data directly related to safety (Fig. 2).

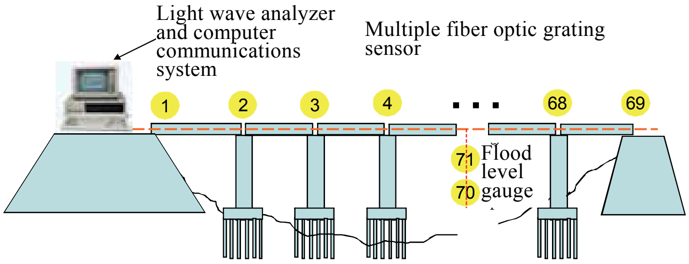

Fig. 2 Long-range, multi-span bridge safety monitoring

The comprehensive full-bridge fiber optic monitoring system can be used to monitor bridges for (1) routine bridge testing operations; (2) earthquake and post-earthquake bridge safety; and (3) flooding and post-flood bridge safety. This monitoring system can be considered specifically designed for disaster prevention and rescue management (Fig. 3).

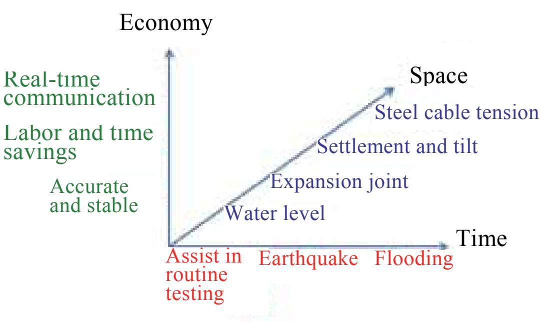

Fig. 3 Monitoring system characteristics

Table 1 Comparisons on the current commercial optical sensors and those sensors developed this study

	Current commercial product	Features of this study
Charts and comparisons	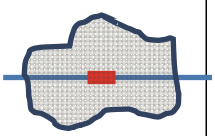	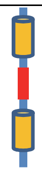
	Gratings are attached to or embedded into the bridge as a strain gauge	Prestressed-clamp FBG in the instrument components, combining physical principles to assemble the sensor
Numbers of gratings	On-site welding a single optical fiber cable with more than ten gratings is relatively difficult because of adverse circumstances	This research improves the welding techniques. One optical fiber cable possesses up to thirty gratings
Features and signal interpretation	Receiving the strain of the local structures; however, monitoring the performance of the entire bridge is difficult	The designed sensor possesses physical meanings. Numerous sensors facilitates the safety control of long bridges

Introducing Fiber Optic Settlement and Tilt Sensor Gauge

Fiber optic settlement and tilt sensor gauge can monitor bridge elevation, which is the monitoring system's most prominent characteristic. This system applies the communicating vessels principle and the buoyancy principle to monitor changes in bridge elevation (Fig. 4). According to the design dimensions, the instrument accuracy is up to 1 mm, and the high resolution is extremely beneficial for monitoring the bridge pier settlement or tilt.

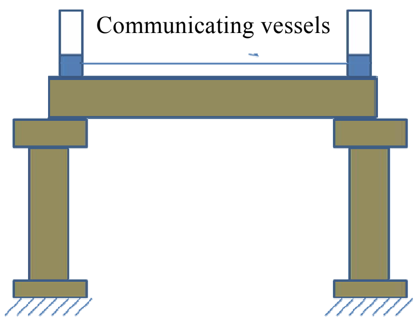

Fig. 4 Fiber optics settlement and tilt sensor gauge

Layout of the Comprehensive Full-Bridge Fiber Optic Monitoring System for Dazhi Bridge

This study installed steel-cable vibration meters, bridge Altimeter, angle gauges, expansion joint displacement meters, and flood level gauges throughout Dazhi Bridge. The instantiation and layout are shown in Table 2, Fig. 5(a) and Fig. 5(b).

Table 2 The instrument type, purpose, and quantity installed throughout Dazhi Bridge

Sensor	Purpose	Quantity
Steel cable vibration meter	Tension analysis	22
Altimeter (Fig. 5)	The girder's elevation and bridge pier settlement	7
Two-axis gauge	Bridge pier tilt	3
Displacement meter	Expansion joint displacement	10
flood level gauge	Warning flood level Action flood level	2

Displacement gauge

Flood level gauge

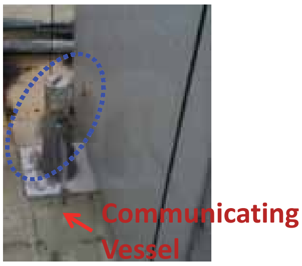

Altimeter
(Subsiding and tilting)

Vibration meter

Fig. 5(a) The installation of FBG sensors on Dazhi Bridge

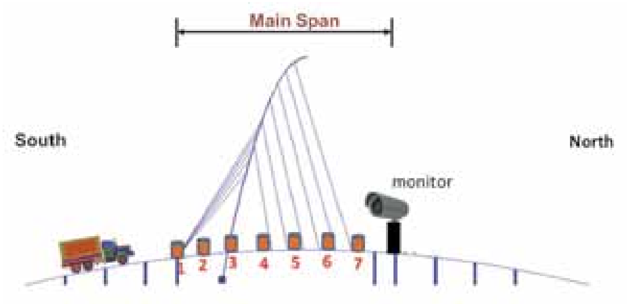

Fig. 5(b) Altimeter layout

Monitoring Data Analysis

After data transmission to the NCREE, the real-time monitoring data are immediately analyzed. The monitoring data are illustrated in Fig. 6(a). The top image is the vibration of the longest steel cable, the middle image shows the rotation of the girder in the traffic direction, and the bottom image shows the elevation profile of the girder. Dynamic messages are rendered in real time. Fig. 6(b) shows those real-time signal and image on mobile devices.

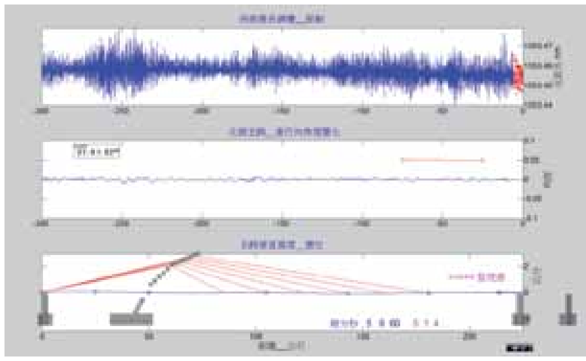

Fig. 6(a) Illustration of monitoring data: the top image shows the steel cable vibration, the middle image shows the girder's rotation, and the bottom image shows the girder's elevation

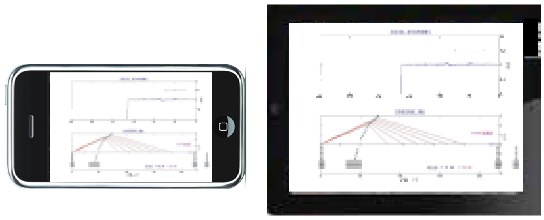

Fig. 6(b) The real-time signal and bridge elevation profile on mobile devices

Cost and Effect

The cost of this system is approximately half to one third that of conventional electronic monitoring systems. In Taiwan domestic market, currently the conventional electronic monitoring systems are imported, whereas the software and hardware of the studied system, excluding the datalog, are developed and manufactured by NCREE. In addition, the following techniques of this new system are unprecedented in Taiwan, and currently no similar product can be found domestically: automatic elevation measuring system, visualization of the dynamic deformation response for the bridge structure, synchronous measurement of the vibrations of multiple cables, and monitoring the expansion joints of long bridges with multiple spans.

Practical Application in the Future

The integrated sensing system could be applied to various transportation systems with verdict bridges, such as the high-speed railway, the highways, the Metro, the railways.

Conclusion

After many years of research, development and system integration, the NCREE can finally self-produce sensors and integrate communication systems, facilitating the achievement of long-range, multi-span bridge safety monitoring.

The Development of a Smart Sensing System for Bridge Health Monitoring

Kung-Chun Lu [1], Chin-Hsiung Loh [2] and Pei-Yang Lin[3]

盧恭君 [1]、羅俊雄 [2] 林沛暘 [3]

Abstract

Bridges are very important types of infrastructure that connect communication and transportation between cities. In recent years, torrential rain has induced damage to the structural safety of cross-river bridges; therefore, health monitoring and damage detection of bridges is of utmost importance. A pioneering step in the study of this issue is to collect and observe structural response signals under different environmental conditions. A flexible sensing solution is required to provide an effective and robust way to collect the structural response of bridges under harsh climate conditions. The objective of this paper is to develop a Smart Sensing System to provide a flexible sensing solution for bridge health monitoring. The Smart Sensing System was developed to fulfill the requirements of bridge health monitoring, which include 1) a flexible and reliable data transmission in a field environment; 2) autonomous and long-term measurement under harsh climates; 3) high sensitivity signal sampling to extract structural ambient responses; 4) on-site signal processing and analysis. The performance of the Smart Sensing System was examined during a field experiment at Niudou Bridge during the FANAPI typhoon period.

Keywords: wireless sensing, structural health monitoring, bridge monitoring

Introduction

In recent years, increasingly serious natural hazards have endangered the structural safety of bridges; therefore, bridge health monitoring has become an important issue in the mitigation of the effects of natural hazards on the transportation infrastructure as well as the protection of the lives and property of citizens. The first step in monitoring a bridge structure is to assess its dynamic behavior; a flexible long-term measurement system is required for this purpose. The application of wireless sensing technology on civil infrastructure was initially proposed by Straser and Liremidjian,1998, and several structural health monitoring (SHM) applications with wireless sensors have been developed using both scale models and full-scale structures. Moreover, Lynch et al., 2002, have extended their work to include computational microcontrollers in the hardware design of wireless sensors so that various system identification and damage detection algorithms can be embedded for local execution by the sensor. Through these pioneering studies, the concept of wireless sensing is widely accepted in the monitoring of civil infrastructure. For example, wireless sensing has been used in the monitoring of the Alamosa Canyon Bridge (New Mexico), the Geumdang Bridge (Korea), the WuYuan Bridge (China), and the Voigt Bridge (California). Recently, Hongki Jo, et al., 2012, proposed the concept of a wireless smart sensor network and Junhee Kim, et al., 2012, proposed the concept of a smart wireless sensor network, where both studies examined the production of a wireless sensor for the realistic application of SHM. The aim of this study is the development of a smart sensing system and is focused on the integration of software (SHM analysis) and hardware (long-term monitoring system).

In this study, the concept of a smart sensing system was applied to bridge health monitoring. The Sensor Node (NTU-WSU) of a smart sensing system

[1] Assistant Researcher, National Center for Research on Earthquake Engineering, kclu@ncree.narl.org.tw.
[2] Professor, National Taiwan University, lohc0221@ntu.edu.tw
[3] Researcher, National Center for Research on Earthquake Engineering, pylin@ncree.narl.org.tw

was adapted to version 0.2b in order to consider bridge monitoring and the use of a medium cost accelerometer instead of a high cost ambient velocity-meter.

The Concept of the Smart Sensing System

The Smart Sensing System (S^3) was designed for civil engineering applications. We must first define the function of the Smart Sensing System before deciding on the hardware. **Figure 1** shows the concept of the Smart Sensing System; there are three nodes in this system, the Sensor Node, the Server Node and the User Node. Based on the application scenario of automatic bridge health monitoring, the structural vibration responses of the bridge is routinely measured and buffered by the Sensor Node. In order to implement the arranged health monitoring procedure, the Sensor Node offers distributed computing functions and wireless communication to process the measured data and communicate with the Server Node. Therefore, the Sensor Node is a smart sensor that includes three major functions: signal sampling, distributed computing, and wireless communication.

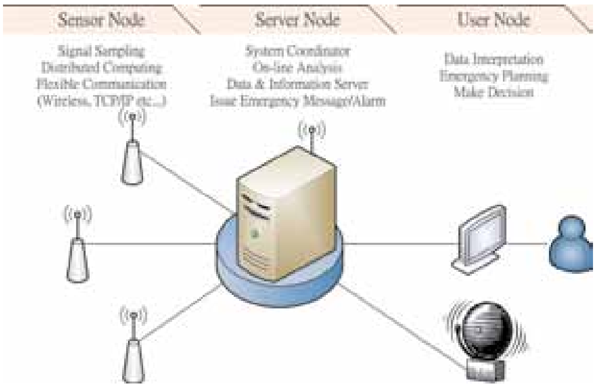

Fig. 1 The concept of the Smart Sensing System

From past experiences, bridges are considered to be large-scale structures and most of them are subjected to heavy traffic loading; these conditions make both instrumentation and maintaining a traditional wired sensing system on a bridge structure difficult. Linking the sensors to a central data logger on a large-scale structure requires lengthy signal cables that are very expensive and expend a lot of manpower on the installation and maintenance of the cables. Noise disturbance and signal attenuation effects of the lengthy signal cables are difficult to constrain; moreover, these effects cause a serious deterioration in the quality of sensor signals, especially when the measured target is a very weak signal, for example, structural ambient vibration responses. The sensor network of the Smart Sensing System adopts wireless communication technology to avoid the above deficiencies of a wired system; also, wireless communication provides an efficient and economical way to link the Sensor Node and the Server Node of the Smart Sensing System and overcome the communication limitations of large-scale bridge structures.

The system coordinator of the Smart Sensing System is a Server Node that coordinates the wireless sensor network and manages the system status and the assigned working procedure. After the Sensor Node feeds the data back to the Server Node, the arranged on-line SHM analysis is executed to calculate the monitoring results and the identified structural information on the Server Node. Two information distribution pathways are built into the Server Node: 1) Issue the emergency message or alarm, and 2) Data and Information Server. The User Node is an interface for engineers and others who are interested in the structural safety status. To provide a conventional interface for the user, the User Node is designed to be a common general-purpose electoral information machine (e.g., PC, Laptop, PDA, Smart Phone) that allows the user to easily retrieve information from the Smart Sensing System, i.e., the interface between the Smart Sensing System and the Wide Area Network must follow standard internet protocols (e.g.. TCP/IP, FTP, Webpage).

The Revised Sensor Node (WSU_V02b)

The following section focuses on the hardware improvements made to the Smart Sensing System.

Most SHM methods are based on the analysis of structural vibration responses; furthermore, many output-only system identification methods use the assumptions of the white noise process. The structural ambient responses are closest to these assumptions; its frequency contents are mainly distributed over the low frequency band (in general, it is around 0.1 ~ 30Hz), and the peak-to-peak range is generally smaller than 1gal. Therefore, the transducer of the Sensor Node must be a sensitive vibration sensor that satisfies the specifications of high sensitivity and the broad-frequency band. In order to keep costs at a minimum, this new wireless sensing unit (WSU) version was integrated with a medium cost accelerometer (AS-2000). In order to adopt the AS-2000 sensor into the ambient structural vibration measurement, a signal conditioner is required to prevent high frequency noise and the anti-aliasing effect.

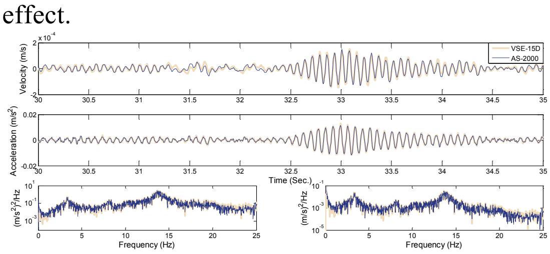

Fig. 2 A signal comparison of the VSE-15D and AS-2000

An analog low-pass filter whose filter type and implemented topology are 8^{th} order butter-worth (fc = 50Hz) and the Sallen-Key topology was integrated into the Smart Sensing System to enhance the performance of the AS-2000 sensor in the measurement of ambient structural responses. To evaluate the sensor performance, the VSE-15D and AS-2000 with a signal conditioner were collocated, and these two signals were recorded by the Sensor Node (NTU-WSU V0.2b). Figure 2 shows a comparison of these two sensors.

The main improvement in the signal sampling of version 0.2b is the oversampling process. This process achieves ADC sampling with a rarely encountered high speed (the speed is limited by the performance of the ADS8341EB and is about 100 kHz) and reduces the sample by the process of downsampling to the configured sampling rate (Fs). The oversampling process has three advantages for signal sampling: avoiding aliasing, improving resolution, and reducing noise. Version 0.2b provides 5 different sampling rates, Fs, (50, 100, 200, 500, 10k Hz) and when the oversampling function is achieved, the oversampling number D is 128 for 50Hz, 64 for 100Hz, 32 for 200Hz, 16 for 500Hz, and 1 for 10kHz. Figure 3 shows the oversampling process of the Sensor Node; the output signal of the AS-2000 accelerometer is first filtered by a low-pass filter to avoid the aliasing effect; this filtered signal is held and quantized by an analog-to-digital converter (ADC) with the sampling rate D*Fs; the microcontroller unit (MCU) processes these digitalized data using the oversampling process (averaging and down-sampling), and generates the row data.

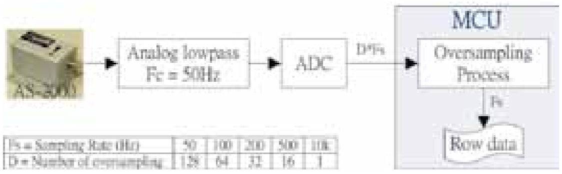

Fig. 3 Oversampling process of WSU

Considering the sensor signal sampling, the new version 0.2a provides two signal adjustment stages. The first stage is an amplifying signal with optimal gain and the second stage is a scaling and shifting signal to the sampling range of the ADC. There are four sensor input channels in the Sensor Node and all of them have the same amplification gain settings which are controlled by the general purpose input/output (GPIO) (PD6 and PD7) of the ATmega128; this does not make sense in real application scenarios where each channel should be adjusted individually to get the best signal quality. Version 0.2b is capable of this requirement. In version 0.2b, each channel is controlled by the ATmega128 with individual GPIO pins and each channel is set through the software interface of the Server Node.

Version 0.2b also places emphasis on the wireless communication performance; the data rate and the RF signal strength are improved in this version. The universal asynchronous receiver/transmitter (UART) is the interface between the microcontroller and the wireless module, and its data rate depends on the clock frequency of the MCU. The data rate capacity of the UART interface of the 9XTend module is 115.2kbps, but this capacity is constrained by the mapping error of the UART interface of the MCU and is only 57.6kbps in version 0.2a. To obtain the maximum data rate, version 0.2b adopts a 16MHz oscillator to replace the original one (8MHz) in version 0.2a. This increases the data rate of version 0.2b to 115.2kbps, twice as fast as version 0.2a and six times faster than a wireless modular monitoring system (WiMMS); this faster data rate shortens the data collection time of the Smart Sensing System considerably. Another issue is the RF signal strength; in order to obtain the highest transmission power of the 9XTend module, the power system of the Sensor Node was revised and is shown in Figure 4.

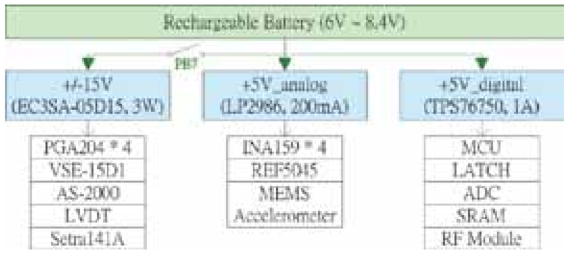

Fig. 4 The power system of the Sensor Node

The revised power system of the Sensor Node is divided into three power circuits, +5V for the analog device, +5V for the digital device, and +/-15V for the sensing interface, to prevent the noise effect which is produced by the current sink. The 5V digital power source was designed according to the requirements of the 9XTend module, and a 1-A low-dropout voltage regulator, TPS76750, was adopted in this power circuit. The main feature of TPS76750 is its ultralow typical quiescent current (85μA) which improves the power efficiency of the Sensor Node and also allows the 9XTend achieve the highest transmission power. To reduce the power consumption of the sensors, the sensor power of Version 0.2b is switched by the GPIO (PB7) of the MCU, and the Sensor Node turns the sensor off when a sensor signal is not requested; this mechanism extends the battery life of the Sensor Node substantially.

Field Experiment at Niudou Bridge

Niudou Bridge crosses the Lanyang River and is located in Sanxing Township, Yilan County, Taiwan. Niudou Bridge is a dangerous bridge with serious foundation soil scouring. The bridge is a simple supported bridge with 7 spans and 6 piers; the length of the deck in each span is 36.5m and the total length of this bridge is 256m; the width of this bridge is 5m.

FANAPI was a medium-strength typhoon; its center made landfall in the Hualien area and its storm hit Taiwan between the 19th and the 21st of

September 2010. The typhoon's outer bands gave rise to extremely heavy rain in the east and southeast of Taiwan, and the Lanyan River became swollen as a result.

Fig. 5 Photos of the Smart Sensing System on Niudou Bridge

The objective of this field experiment was to collect the structural responses of the Niudou Bridge under serious flood loading to obtain the foundation soil scouring and the flood loading induced structural vibration characteristics. There were a total of 5 NTU-WSU units installed on the 2nd to 6th deck of the Niudou Bridge and a local site (Host Node) was installed on this bridge. Each NTU-WSU was connected to two ambient sensors that measured the vertical and transverse vibrations at the center point of the deck, and a total of 10 ambient sensors were installed on this bridge. The site of the Niudou Bridge has 3G Mobile Internet (Chunghwa Telecom) signal coverage, with a signal strength of about 30%. The position of the user node was not limited; in this experiment, the user node was a laptop installed in a hotel at Niudou.

This system was installed before the land warning of FANAPI, and continuously collected the structural responses of the Niudou Bridge during the typhoon period. The system was set to collect data every 15 minutes and each record had 15000pts (@ 200Hz) of structural responses. The data was saved as a MS EXCEL file and labeled with the current time and date. A remote user could observe the system status and the recorded data over the internet from a safe place during this typhoon period.

Figure 5 shows photos of the Smart Sensing System on the Niudou Bridge; Figure 5(a) shows the Sensing Node installed on the deck of the Niudou Bridge, (b) shows the Server Node, and (c) shows the contents of the Sensing Node, which includes a NTU-WSU, two VSE-15D sensors, and a Li battery (which supplied over 3 days of power with full loading of the Sensing Node); an acrylic housing with an aluminum plate was used to protect the Sensing Node and was mounted on the bridge deck. Figure 5(d) shows the serious flood acting on the foundations of the Niudou Bridge.

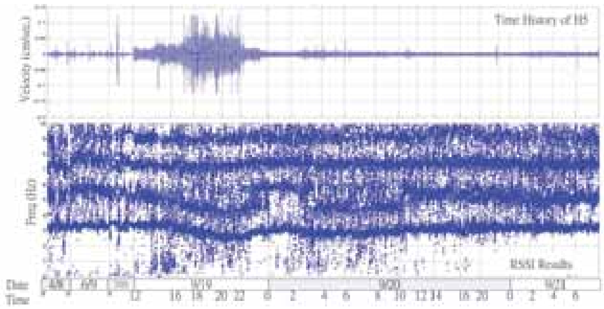

Fig. 6 The time history of H5 and the analysis results of RSSI

The structural responses of the Niudou Bridge were collected during the FANAPI typhoon event with the reference database established before this event. Based on the data, Figure 6 shows the rough results of the RSSI analysis which was performed by Dr. J. H. Weng who also worked on this project. In this figure, the response data includes 4/8, 6/9, 7/23, and the period during typhoon FANAPI. The RSSI results show that the frequencies of the Niudou Bridge changed during the typhoon period.

Conclusions

The new version of the Sensor Node, NTU-WSU V0.2b, provides: 1) a more flexible adjustment range of the sensor signal; 2) high quality and accurate signal sampling through the oversampling process; 3) high speed data rates for wireless communication, twice as fast as Version 0.2a; 4) more reliable wireless communication and a larger RF transmission range through the enhanced power design of the Sensor Node; 5) a low cost measuring solution of ambient structural responses through the extended compatibility of the medium cost accelerometer, AS-2000. Through this study, the concept of the Smart Sensing System was extended to cover the application of bridge health monitoring. Such a flexible monitoring system is a good solution for bridge structures. The experiment at the Niudou Bridge during the FANAPI typhoon period demonstrates that the Smart Sensing System is fit for field experiments in harsh climate conditions. The modifications of the system design (software and hardware) of the Smart Sensing System were shown to be successful during this experiment. The system setup on the Niudou Bridge only took about 30 minutes, and the robustness of the system allowed for its continuous function during the FANAPI period, which was approximately three days.

References

Kung-Chun Lu, Chin-Hsiung Loh, "Development of Wireless Sensing System for Structural Health Monitoring", Earth&Space 2010, 12th International Conference on Engineering, Science, Construction, and Operations in Challenging Environments, Honolulu, Hawaii, March 14-17.

Phase Controlled Semi-active Tuned Mass Dampers for Vibration Reduction under Base Excitation

Lap-Loi Chung[1], Yong-An Lai[2], Ting-Yu Ku[2], Lai-Yun Wu[3]

鍾立來 [1]、賴勇安 [2]、顧丁與 [2]、吳賴雲 [3]

Abstract

The vibration suppression effect of phase controlled semi-active tuned mass dampers (SATMD) under base excitation is proposed in this study. The phase control algorithm applies the variable friction force to slow down the mass block at specific moments when the phase lag of the SATMD with respect to the structure is off the optimal 90 degrees, returning the SATMD back to the desired phase lag, i.e., a -90 degree phase deviation, so that the SATMD has maximum power flow to reduce the structural vibration. A single-degree-of-freedom structure with phase controlled SATMD is simulated to be subjected to sinusoidal base acceleration, random base acceleration, and earthquakes. Under the sinusoidal base acceleration, the results show that the SATMD has a broader range of excitation frequency in reducing structural vibration than the optimal passive tuned mass damper. The SATMD also has better robustness of its design parameters especially the frequency ratio under random base accelerations. The earthquake excitation shows that although the SATMD is not very effective in reducing the peak value of structural response but it is still able to reduce root-mean-square responses.

Keywords: tuned mass damper, phase control, semi-active control, base excitation

Introduction

According to the power flow theory (Soong, and Dargush, 1997), tuned mass dampers (TMD) have the best performance in suppressing the vibration when the TMD has a 90° phase lag (or -90° phase deviation) to the structure. Therefore, attempts have been made to control the phase of TMD (Chung, et al., 2012). To induce the TMD mass block movement to have a 90° phase lag to the structure, a variable friction force is applied to slow down the TMD mass block velocity. The effectiveness of the proposed control algorithm is observed.

In this paper, the device for a semi-active tuned mass damper (SATMD) is assumed to be a variable friction device with a variable normal force to slow down the mass block velocity. This semi-active friction device acts like a brake mechanism to create friction force to adjust the phase lag. A single-degreed-of-freedom (SDOF) structure with SATMD phase control is simulated to be subject to sinusoidal base accelerations, random base accelerations, and earthquakes. Under the sinusoidal base acceleration, the results show that the SATMD has broader range of excitation frequencies to reduce the structural vibration than the optimal passive tuned mass damper. The SATMD is also found to have better robustness in its design parameters especially in the frequency ratio under random base accelerations. The earthquake excitation shows that although the SATMD is less effective in reducing the peak value of the structural response, it is still able to reduce the root-mean-square responses.

Motion Equation

As a SATMD is attached to a SDOF structure, as shown in Fig. 1, it becomes a 2DOF system. The equation of motion of the system can be expressed as:

[1] Researcher, National Center for Research on Earthquake Engineering,
Professor, National Taiwan University, chung@ncree.narl.org.tw
[2] Student, Department of Civil Engineering, National Taiwan University
[3] Emeritus Professor, Department of Civil Engineering, National Taiwan University

$$\mathbf{M}\ddot{\mathbf{x}}(t)+\mathbf{C}\dot{\mathbf{x}}(t)+\mathbf{K}\mathbf{x}(t)=\mathbf{b}u(t)+\mathbf{e}w(t) \quad (1)$$

where $\mathbf{M}=\begin{bmatrix} m_\mathrm{d} & 0 \\ 0 & m_\mathrm{s} \end{bmatrix}$ is the mass matrix of the system, m_d is the TMD mass, m_s is the SDOF structural mass; $\mathbf{C}=\begin{bmatrix} c_\mathrm{d} & -c_\mathrm{d} \\ -c_\mathrm{d} & c_\mathrm{d}+c_\mathrm{s} \end{bmatrix}$ is the damping matrix of the system, c_d is the TMD damping coefficient, c_s is the SDOF structural damping coefficient; $\mathbf{K}=\begin{bmatrix} k_\mathrm{d} & -k_\mathrm{d} \\ -k_\mathrm{d} & k_\mathrm{d}+k_\mathrm{s} \end{bmatrix}$ is the stiffness matrix of the system, k_d is the TMD stiffness and k_s is the SDOF structural stiffness; $\mathbf{x}(t)=\begin{bmatrix} x_\mathrm{d}(t) \\ x_\mathrm{s}(t) \end{bmatrix}$ is the displacement vector of the system, $x_\mathrm{d}(t)$ and $x_\mathrm{s}(t)$ are, respectively, the TMD displacement and the SDOF structural displacement; $u(t)$ is the semi-active friction force; $\mathbf{b}=\begin{bmatrix} 1 \\ -1 \end{bmatrix}$ is the friction force location vector; $w(t)$ is base acceleration; $\mathbf{e}=\begin{bmatrix} -m_\mathrm{d} \\ -m_\mathrm{s} \end{bmatrix}$ is the base excitation location vector.

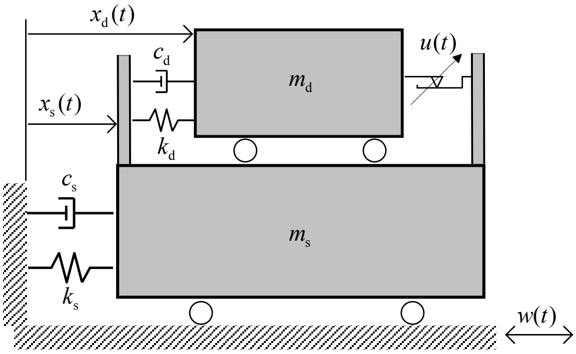

Fig. 1 Model of SDOF structure with the attached SATMD

The motion equation can be expressed as state-space form:

$$\dot{\mathbf{z}}(t)=\mathbf{A}\mathbf{z}(t)+\mathbf{B}u(t)+\mathbf{E}w(t) \quad (2)$$

where $\mathbf{z}(t)=\begin{bmatrix} \mathbf{x}(t) \\ \dot{\mathbf{x}}(t) \end{bmatrix}$ is the state vector; $\mathbf{A}=\begin{bmatrix} \mathbf{0} & \mathbf{I} \\ -\mathbf{M}^{-1}\mathbf{K} & -\mathbf{M}^{-1}\mathbf{C} \end{bmatrix}$ is the system matrix; $\mathbf{B}=\begin{bmatrix} \mathbf{0} \\ \mathbf{M}^{-1}\mathbf{b} \end{bmatrix}$ is the state-space friction force location vector; $\mathbf{E}=\begin{bmatrix} \mathbf{0} \\ \mathbf{M}^{-1}\mathbf{e} \end{bmatrix}$ is the state-space wind force location vector.

It can be assumed that the semi-active friction force, $u(t)$, and the base acceleration, $w(t)$, in a single sampling period, Δt, both are piecewise constants. The discrete-time state-space equation can be expressed as:

$$\mathbf{z}[k+1]=\mathbf{A}_\mathrm{d}\mathbf{z}[k]+\mathbf{B}_\mathrm{d}u[k]+\mathbf{E}_\mathrm{d}w[k] \quad (3)$$

where $\mathbf{A}_\mathrm{d}=e^{\mathbf{A}\Delta t}$ is the discrete-time system matrix; $\mathbf{B}_\mathrm{d}=\mathbf{A}^{-1}(\mathbf{A}_\mathrm{d}-\mathbf{I})\mathbf{B}$ is the discrete-time friction force location vector; $\mathbf{E}_\mathrm{d}=\mathbf{A}^{-1}(\mathbf{A}_\mathrm{d}-\mathbf{I})\mathbf{E}$ is the discrete-time base excitation location vector.

Phase Control Algorithm

When the external force resonates with the structure, the TMD has the best performance at a 90° phase lag to the structure. For this case, the flowing characteristic is observed: when the displacement of the structure is 0, the relative displacement (stroke) of the TMD is at a maximum (the relative velocity of the TMD is 0). Once the external force stops resonating with the structure, the TMD loses its efficacy. In this case, the phase deviation of the TMD to the structure is no longer at -90°. When the frequency of the external sinusoidal force is lower than the natural frequency of the structure, the phase deviation is between -0° and -90° (phase leading). When the frequency of the external force is higher than the natural frequency of structure, the phase deviation is between -90° and -180° (phase lagging). Therefore, the control strategy for the SATMD to bring the mass block back to a 90° phase lag for the cases of "phase leading" and "phase lagging" is proposed as follows:

1. The responses of the TMD relative displacement and structural displacement when the external frequency is 0.95 times of the structural frequency are shown in Fig. 2 (a). At specific moments (A) and (B) in Fig. 2 (a), the TMD relative displacement is at a maximum (the TMD relative velocity is 0) and the structural displacement is still decreasing but not at 0. At these moments, the phase of the TMD to the structure is between -0° and -90° (phase leading), not simply a 90° phase lag. Therefore, a friction force is applied to stop the TMD motion at these moments in order to keep the TMD relative velocity at 0 until the structural displacement is 0. Thus, the TMD will return to a 90° phase lag to the structure.

2. The responses of the TMD relative displacement and structural displacement when the external frequency is 1.05 times of the structural frequency are shown in Fig. 2 (b). At specific moments (C) and (D) in Fig. 2 (b), the structural displacement is 0 but the TMD's relative displacement is still increasing (the TMD relative velocity is decreasing, but not 0). The phase of the TMD to the structure is between -90° and -180° (phase lagging). Thus, the friction force is applied to stop the TMD motion at these moments in order to decrease the TMD relative velocity to 0. Therefore, the TMD will head back towards the 90° phase lag to the structure.

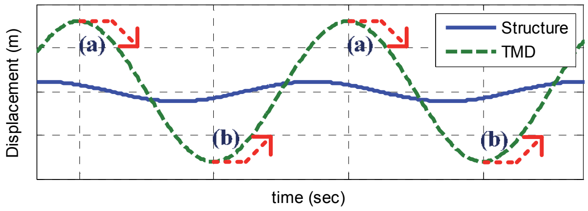

(a) Phase leading

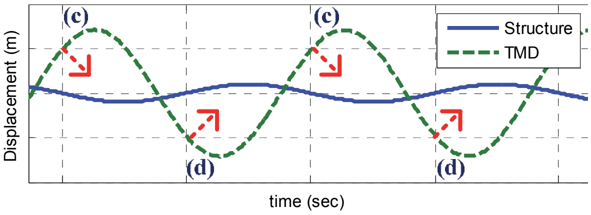

(b) Phase lagging

Fig. 2 TMD relative displacement (stroke) and structural displacement time history

Therefore, no matter whether the TMD is "phase leading" or "phase lagging", it is found that a friction force can be applied to slow down the TMD relative velocity to 0 at specific moments: "the signs of structural displacement and the TMD relative velocity are opposite, and the signs of the structural velocity and the TMD relative displacement are also opposite". To determine this, the sign convention, G is introduced as:

$$G=\frac{1}{2}\{1-\mathrm{sgn}(\dot{x}_s[k+1])\times \mathrm{sgn}(x_d[k+1]-x_s[k+1])\}\times \frac{1}{2}\{1-\mathrm{sgn}(x_s[k+1])\times \mathrm{sgn}(\dot{x}_d[k+1]-\dot{x}_s[k+1])\} \quad (4)$$

When $G=1$, the control force is applied to stop the TMD movement ($u[k]\neq 0$). When $G=0$, no control force is applied ($u[k]=0$).

To determine whether the friction force is to be applied at the current step k, the states of the next step $\hat{\mathbf{z}}[k+1]$ are estimated by neglecting the external disturbances to be:

$$\hat{\mathbf{z}}[k+1]=\mathbf{A}_d\mathbf{z}[k] \quad (5)$$

By eq. (5), the estimated structural displacement $x_s[k+1]$, TMD relative velocity $\dot{x}_d[k+1]-\dot{x}_s[k+1]$, structural velocity $\dot{x}_s[k+1]$ and TMD relative displacement $x_d[k+1]-x_s[k+1]$ can be calculated. Then the control opportunity can be determined by eq. (4).

Next, the friction force $u[k]$ can be calculated by assuming the next step (k+1-th step) in the TMD relative velocity to be 0:

$$\mathbf{d}_1\mathbf{z}[k+1]=0 \quad (6)$$

where $\mathbf{d}_1=[0\ \ 0\ \ 1\ \ -1]$ is the TMD relative velocity location vector.

Substituting eq. (3) into eq. (6), the friction force $\hat{u}[k]$ is estimated by neglecting the external disturbances term to be:

$$\hat{u}[k]=-(\mathbf{d}_1\mathbf{B}_d)^{-1}\mathbf{d}_1(\mathbf{A}_d\mathbf{z}[k]) \quad (7)$$

The semi-active device output power may not achieve the estimated friction force. For this reason, the actual outputs of the semi-active friction force have to be limited by the maximum output u_{max}:

$$u[k]=\frac{1}{2}\hat{u}[k]\times\left[1+\mathrm{sgn}(u_{max}-|\hat{u}[k]|)\right]+\frac{1}{2}\mathrm{sgn}(\hat{u}[k])u_{max}\times\left[1+\mathrm{sgn}(|\hat{u}[k]|-u_{max})\right] \quad (8)$$

Therefore, the control strategy is as follows: once measuring the states at the current step, by eq. (5) to estimate one step states, by eq. (4) to judge whether the friction force is applied or not, then by eq. (6) to eq. (8) to calculate and apply the friction force.

Numerical Verification

A SDOF structure with structural frequency 0.33 Hz and structural damping ratio 0.02 is installed with a SATMD and subjected to sinusoidal base acceleration, random base acceleration, and earthquakes, respectively. In order to show the effect of SATMD, a linear optimal passive tuned mass damper (PTMD) is also simulated for comparison. The PTMD and SATMD design parameters are show in Table 1.

Table 1 PTMD and SATMD design parameters

PTMD mass ratio	0.02
PTMD frequency ratio	0.9678
PTMD damping ratio	0.0702
SATMD mass ratio	0.02
SATMD frequency ratio	1
SATMD damping ratio	0.01

Sinusoidal Base Acceleration Excitation

A SDOF structure is subjected to sinusoidal base accelerations to plot the frequency response functions. The sinusoidal base accelerations frequency range is assigned to be 0.8 to 1.2 times of the structural frequency. Fig. 3 shows the structural displacement and absolute acceleration frequency response functions. The frequency response of the SATMD is always smaller than the optimal PTMD and the peak of frequency response of the SATMD is almost only half of the optimal PTMD. Like MTMDs (Multiple Tuned Mass Dampers), the effective range of SATMD is broadened to 0.88 to 1.15 times of the structural frequency.

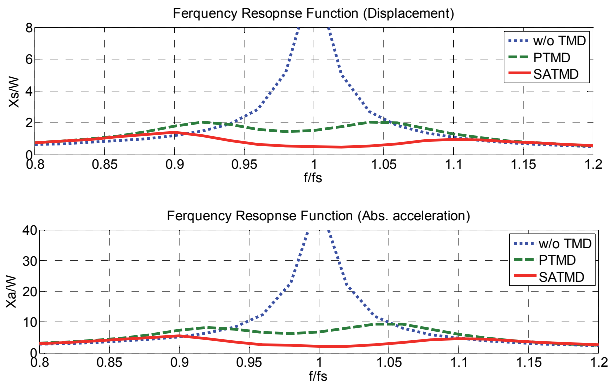

Fig. 3 Frequency response functions of the structural displacement and absolute acceleration

Random Base Acceleration Excitation

The SDOF structure is subjected to random base accelerations to study the design parameter sensitivity. As Fig. 4 shows, the SATMD is less sensitive to the frequency ratio. The off-tuned effect can be minimized. The SATMD friction device can fully replace the damping device in its energy dissipation function. The defect can be overcome if the design damping is less than optimal.

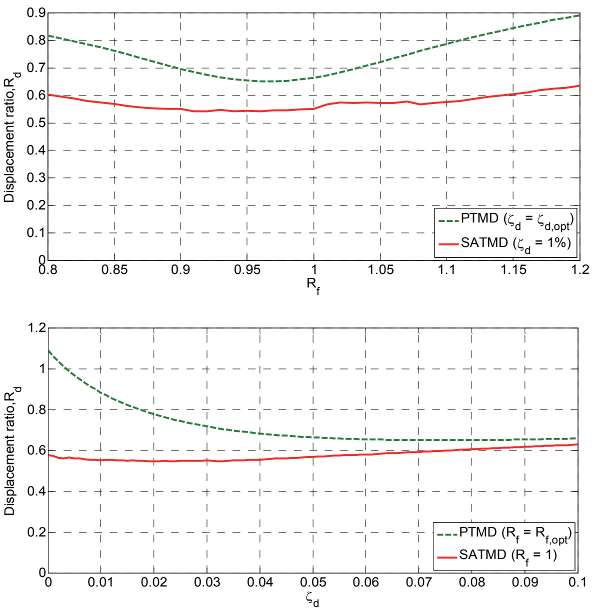

Fig. 4 Sensitivity analysis of frequency ratio and damping ratio

El Centro Earthquake Excitation

The responses under El Centro earthquake excitation are shown in Fig. 5. Without the use of the TMD, the peak values of the structural displacement and absolute acceleration are 0.3854 m and 1.6923 m/s^2 respectively. The root mean square of the structural displacement and absolute acceleration are 0.1759 m and 0.7723 m/s^2. After installing the PTMD, the peak value of the structural displacement and absolute acceleration are 0.2674 m and 1.1660 m/s^2. The root mean square of the structural displacement and absolute acceleration are 0.1013 m and 0.4556 m/s^2. After installing the SATMD, the peak value of the structural displacement and absolute acceleration are 0.2644 m and 1.1522 m/s^2. The root mean square of the structural displacement and absolute acceleration are 0.0874 m and 0.3935 m/s^2. The SATMD therefore, seems to be less effective in reducing the peak value of the structural responses but is able to reduce the root-mean-square responses.

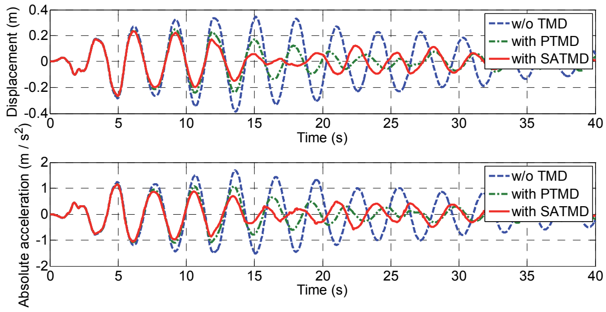

Fig. 5 Time histories of the structural displacement and absolute acceleration under El Centro earthquake

Conclusion

In this paper, the phase control for semi-active tuned mass dampers (SATMD) is presented under base excitation. According to the results of the numerical simulations, the phase controlled SATMD have good performance and the conclusions that are drawn are as follows:

1. The frequency response functions of the SATMD with phase control are smaller than optimal PTMDs and the peak of frequency response functions of the SATMD are only half of that of optimal PTMDs. The effective frequency range of SATMD can be broadened under a phase control like the MTMD.

2. According to the sensitivity study under random base acceleration excitation, SATMD with phase control can improve the weakness of PTMDs in their sensitivity to the frequency ratio. Thus, the off-tuning effect can be minimized.

3. The El Centro earthquake simulation results show that the SATMD is less effective in reducing the peak value of structural responses but is able to reduce root-mean-square responses.

Reference

Soong, T.T. and Dargush, G.F., Passive Energy Dissipation Systems in Structural Engineering. Wiley, New York, 1997.

Chung, L.L., Ku, T.Y., Lai, Y.A. and Wu, L.Y., Application of Optimal Passive and Phase-Control Semi-active Tuned Mass Dampers for Vibration Reduction under Base Excitation. NCREE-12-004, 2012.

Shaking Table Tests on Sloped Rolling-Type Isolation Devices

Shiang-Jung Wang[1], Chia-Yi Shiau[2], Wang-Chuen Lin[3], Jenn-Shin Hwang[4]
and Kuo-Chun Chang[5]

汪向榮 [1]、蕭佳益 [2]、林旺春 [3]、黃震興 [4]、張國鎮 [5]

Abstract

Seismic simulation tests on sloped rolling-type isolation devices with different design parameters such as sloping angles and supplemental sliding friction capabilities, together with a isolated raised floor system were conducted in this study. Not only is the efficiency of the isolation devices in seismically protecting the objects studied, but also a validation of the derived theory in predicting the seismic responses of the isolation devices is experimentally investigated. From the study, it is evident that the sloped rolling-type isolation device has excellent potential for the mitigation of seismic risks posed to critical equipment and facilities.

Keywords: Seismic isolation, Sloped rolling-type isolation device, Isolated raised floor, Twin-flag mathematical model, Shake table test, Numerical verification

Introduction

Based on the derived theory for sloped rolling-type isolation devices (Wang et al., 2012; 2013), a simplified twin-flag mathematical model to represent the hysteretic characteristics of the isolation bearing has been developed. In the isolation device, both surfaces of the intermediate bearing plate are V-shaped sloping while the upper and lower bearing plates have either V-shaped sloping surfaces (Type A isolation device) or flat surfaces (Type B isolation device) in contact with cylindrical rollers, as shown in Figure 1. A total of four equations of motion were derived for Type A and Type B isolation devices along the horizontal direction. For Type A isolation devices, when the roller is moving within the fixed curvature range, the equation of motion is given by:

$$\begin{aligned}&M\ddot{x}_1+\frac{1}{2R}M\left(g+\ddot{z}_g\right)\mathrm{sgn}\left(x_1\right)x_1\\&+\left(\mu_r N+F_D\right)\mathrm{sgn}\left(\dot{x}_1\right)=-M\ddot{x}_g\end{aligned} \quad (1)$$

When the roller is moving away from the fixed curvature range, it is written as:

$$\begin{aligned}&M\ddot{x}_1+\frac{1}{2}M\left(g+\ddot{z}_g\right)\sin 2\theta\,\mathrm{sgn}\left(x_1\right)\\&+\left(\mu_r N+F_D\right)\cos\theta\,\mathrm{sgn}\left(\dot{x}_1\right)=-M\ddot{x}_g\end{aligned} \quad (2)$$

For Type B isolation devices, when the roller is moving within the fixed curvature range, it is given by:

$$\begin{aligned}&M\ddot{x}_1+\frac{1}{4R}M\left(g+\ddot{z}_g\right)\mathrm{sgn}\left(x_1\right)x_1\\&+\left(\mu_r N+F_D\right)\mathrm{sgn}\left(\dot{x}_1\right)=-M\ddot{x}_g\end{aligned} \quad (3)$$

When the roller is moving away from the fixed curvature range, it is written as:

$$\begin{aligned}&M\ddot{x}_1+\frac{1}{2}M\left(g+\ddot{z}_g\right)\sin\theta\,\mathrm{sgn}\left(x_1\right)\\&+\left(\mu_r N+F_D\right)\cos\theta\,\mathrm{sgn}\left(\dot{x}_1\right)=-M\ddot{x}_g\end{aligned} \quad (4)$$

where $\ddot{x}_g$ and $\ddot{z}_g$ are the horizontal and vertical acceleration excitations, respectively; x_1, $\dot{x}_1$ and $\ddot{x}_1$ are the horizontal relative displacement, velocity and acceleration responses of the protected object,

[1] Associate Researcher, National Center for Research on Earthquake Engineering, sjwang@ncree.narl.org.tw
[2] Assistant Researcher, National Center for Research on Earthquake Engineering, cyshiau@ncree.narl.org.tw
[3] Assistant Researcher, National Center for Research on Earthquake Engineering, wclin@ncree.narl.org.tw
[4] Deputy Director General, National Center for Research on Earthquake Engineering, jshwang@ncree.narl.org.tw
[5] Director General, National Center for Research on Earthquake Engineering, kcchang@ncree.narl.org.tw

respectively; g is the acceleration due to gravity; M is the total seismic reactive mass of the protected object together with the device components; μ_r is the ratio of the rolling resistant coefficient (δ) to the roller radius (r) (Shames, 1996); N is the normal force acting between the bearing plate and the roller, which can be approximated as Mg; F_D is the sliding friction force acting parallel to the slope of the bearing plate; R is the curvature radius in the range between two inclines of the V-shaped surface of the bearing plate; and θ is the sloping angle of the V-shaped surface of the bearing plate.

In this study, Type A and Type B isolation devices with multi-rollers (Chang et al., 2011) and an isolated raised floor system were tested using a shaking table. In addition to experimentally investigating the dynamic behavior of the isolation devices with different design parameters, the efficiency of the isolation devices in their seismic protection of the equipment and the validity of the proposed simplified hysteretic model in predicting the seismic responses of the isolation devices are demonstrated.

(a) Type A

(b) Type B

Fig. 1 The sloped multi-roller isolation devices (Test Scheme I)

Seismic Simulation Test

The upper, intermediate and lower bearing plates of the tested sloped multi-roller isolation devices, as shown in Figure 1, are made of aluminum with heat treatment. The bearings have a plan dimension of 600*mm* by 600*mm*. The cylindrical rollers are made of stainless steel and have a sectional radius (r) of 17.5*mm* and a longitudinal length of 600*mm*. The maximum allowable displacement of the isolation devices is designed to be 250*mm*. An arc length of 19*mm* (±9.5*mm*) with a curvature radius (R) of 100*mm* is provided at the intersection of the two inclines of the V-shaped surfaces of the bearing plates to prevent undesired instant pounding as the rollers pass through the sharp angles of the V-shaped surfaces.

The supplemental friction damping mechanism is composed of a vulcanized rubber pad with a thickness of 2*mm* attached to the surfaces of the upper, intermediate and lower bearing plates sliding against the stainless steel surface of the side plate. The tested dynamic friction coefficient varies approximately between 0.2 and 0.25. The friction mechanism can be renewed effortlessly if needed by replacing the rubber pad. The required normal force for the supplemental sliding friction is provided by the compression of linear spring modules installed in the side plates.

A total of two test schemes were conducted in this study. In Test Scheme I, four sloped multi-roller isolation devices including Type A and Type B bearings, respectively denoted as Bearings A-1, A-2, B-1 and B-2 hereafter and detailed in Table 1, are designed to investigate the effects of the design parameters on the seismic performance of the isolation devices. The difference between Bearings A-1 and A-2 as well as Bearings B-1 and B-2 is that supplemental friction damping mechanism is provided in Bearings A-2 and B-2. In Bearings A-2 and B-2, two sets of linear spring modules with a constant compression length of 6*mm* are installed in each side plate so that the normal force for sliding friction applied to each side plate is about 332.52*N*. The to-be-protected equipment above the isolation devices is simulated by lead blocks with a total seismic reactive mass of 500 $N-sec^2/m$. The setup is shown in Figure 1.

Table 1 Design parameters of different sloped multi-roller isolation devices

Bearing No.	Design parameter		
	Sloping angle of V-shaped surface		Sliding friction
	Upper and lower bearing plates	Intermediate bearing plate	
A-1	6.25 degrees	6.25 degrees	w/o
A-2	6.25 degrees	6.25 degrees	with
B-1	flat	6.25 degrees	w/o
B-2	flat	6.25 degrees	with

As summarized in Table 2, the recorded ground motion of the 1940 El Centro earthquake, denoted as I-ELC270 hereafter, is used for the seismic simulation test. In addition, two generated acceleration histories compatible with the required response spectra of AC156, denoted as AC156-TAP090 and AC156-TCU054 hereafter, are also adopted in the test.

Table 2 Acceleration excitation program

Test name	Excitation direction		Targeted input peak acceleration (g)
I-ELC270	Unilateral	X	0.36
	Bilateral	X/Y	0.36/0.21
AC156-TAP090	Unilateral	X	0.50
	Bilateral	X/Y	0.50/0.45
AC156-TCU054	Unilateral	X	1.00
	Bilateral	X/Y	1.00/0.96

The comparison of the horizontal acceleration and displacement response histories together with the hysteresis loops for Bearings A-1, A-2, B-1 and B-2 under unilateral I-ELC270 is illustrated in Figure 2.

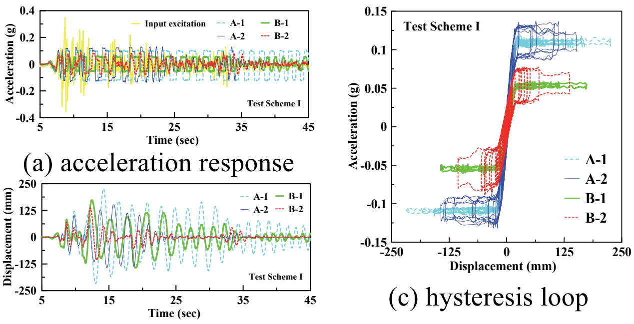

(a) acceleration response

(b) displacement response

(c) hysteresis loop

Fig. 2 Comparison of seismic responses of the isolation devices with different design parameters subjected to unilateral I-ELC270

It is of no surprise that the increase in supplemental sliding friction mechanism (i.e. energy dissipation capability) will lead to a reduction in maximum horizontal displacement responses but will also result in the augmentation of the maximum horizontal transmitted acceleration responses. In addition, the oscillations after the input excitations will be damped out more quickly. As a consequence, the displacement and acceleration performances should be mutually compromised when designing the supplemental damping mechanism. Furthermore, it was indicated (Wang et al., 2012; 2013) that without considering rolling and sliding friction for the isolation device, the horizontal transmitted acceleration responses can essentially remain constant corresponding to the constant inclined surface angle (θ) when the roller moves away from the fixed curvature range. Besides, the dynamic behavior of Type A isolation devices in which the roller is sandwiched between two V-shaped surfaces with a sloping angle of θ is identical to that of Type B isolation devices in which the roller is sandwiched between a flat surface and a V-shaped surface with a sloping angle of 2θ. In this test program, assuming that the rolling friction contribution is very limited, the maximum horizontal transmitted acceleration response of Bearing A-1 is larger than and about twice ($\sin(2\theta)/\sin(\theta) \approx 2$ where θ is 6.25 degrees) that of Bearing B-1.

More importantly, the test results show that the maximum horizontal displacement response of Type B isolation devices is less than that of Type A isolation devices under the same excitations. It implies that an increase in the sloping angle of bearing plates (or potential energy capability) may not result in the reduction of maximum horizontal displacement responses of the isolation device, which agrees with the previous analytical results for highway bridges equipped with sloped rolling-type isolation bearings (Ou et al., 2010). This may be clarified using the definition of the equivalent damping ratios (ξ_{eq}) shown in Equation (5) and Figure 3, in which E_D is the total energy dissipated by the isolation device and E_S is the maximum potential (or strain) energy of the isolation device. When Type A and Type B isolation devices have the same horizontal displacement responses (that is, when D_1 and D_2 respectively represent the rollers moving within and away from the fixed curvature range), the calculated equivalent damping ratios of Type B isolation devices ($\xi_{eq,B}$) are found to be more significant than those of Type A isolation devices ($\xi_{eq,A}$) due to the smaller strain energy in Type B isolation devices. In other words, under the same damping conditions, Type B isolation devices should have a smaller horizontal displacement response than Type A isolation devices.

$$\xi_{eq} = E_D / 4\pi E_S \qquad (5)$$

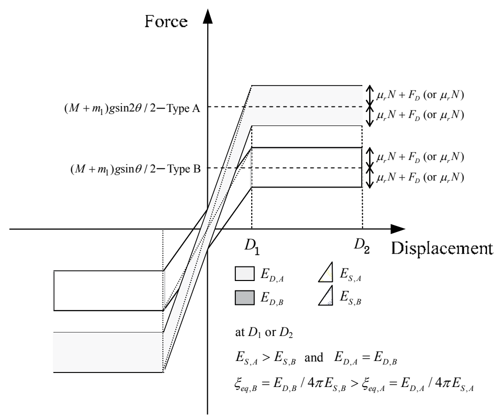

Fig. 3 Approximation of equivalent damping ratios for Type A and Type B isolation devices

In Test Scheme II, the effectiveness of Type B devices with the supplemental friction mechanism is investigated on a seismically isolated raised floor system with a plane dimension of 3*m* by 3*m*. For the four isolation devices underneath the raised floor system, the sloping angle (θ) of the V-shaped surfaces of the intermediate plate is designed to be 6 degrees. A steel frame composed of 200×150×6×9 (*mm*) H beams is designed to connect the raised floor to the isolation devices. The total seismic reactive mass of the raised floor system is about 1420 $N-sec^2/m$. The equipment to be protected, placed above the isolated raised floor system, is simulated by lead blocks with a total seismic reactive mass of 1000 $N-sec^2/m$. The setup is shown in Figure 4.

Fig. 4 Isolated raised floor system in Test Scheme II

The X directional acceleration response histories transmitted to the isolated raised floor system and the X directional hysteresis loops of the isolated raised floor system under bilateral AC156-TAP090 and bilateral AC156-TCU054 are depicted in Figures 5 and 6, respectively. It is evident that the maximum acceleration response transmitted to the isolated raised floor system can be drastically reduced in comparison to the input peak acceleration and can reveal an acceptably steady level. Since the supplemental sliding friction is engaged, the hysteresis loops shown in Figure 6 reveal an excellent energy dissipation capability. The test results also disclose that the isolated raised floor system has an excellent plane rotation control.

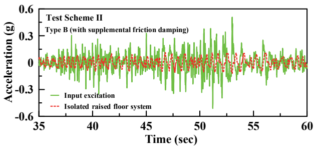

(a) AC156-TAP090

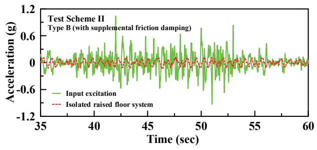

(b) AC156-TCU054

Fig. 5 X directional acceleration response histories of isolated raised floor system

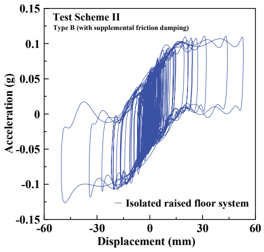

(a) AC156-TAP090

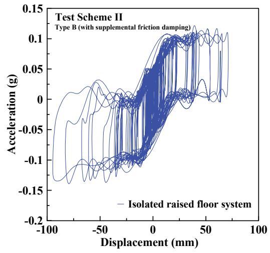

(b) AC156-TCU054

Fig. 6 X directional hysteresis loops of isolated raised floor system

Numerical Verification

When the test models are subjected to horizontal acceleration excitations, the dynamic behavior of a single degree of freedom (SDOF) system equipped with the sloped multi-roller isolation devices can be numerically predicted using the simplified twin-flag hysteretic model (Wang et al., 2012; 2013). The comparison of the experimental results and the numerical predictions for Bearing B-2 subjected to unilateral AC156-TAP090 is presented in Figure 7. It is found that the numerical predictions using the proposed simplified mathematical hysteretic model have an excellent agreement with the seismic simulation test results, including the predictions of amplitude and phase responses.

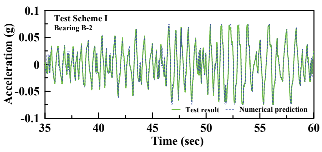

(a) acceleration response

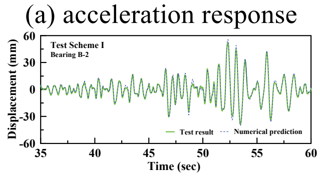

(b) displacement response

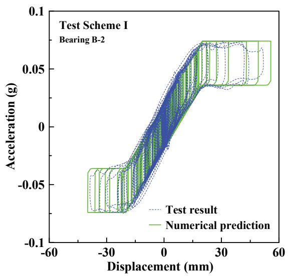

(c) hysteresis loop

Fig. 7 Comparison of experimental results and numerical predictions

Conclusions

The sloped rolling-type isolation device features a standardized design irrespective of input motions, which addresses one of the most important design concerns for critical equipment or facilities if the maximum acceleration response is selected as the seismic performance criterion. In this study, a series of seismic simulation tests on isolation devices with different design parameters and an isolated raised floor system subjected to the recorded ground motion and spectrum compatible floor acceleration histories were conducted to demonstrate the seismic performance of the isolation device. The high efficiency of employing the isolation devices in reducing seismic demands (or seismic damage potential) of the protected objects is experimentally verified. The test results also clarify the influences of different sloping angles and supplemental sliding friction on the dynamic behavior of the isolation devices. Moreover, the excellent agreement between test results and numerical predictions shows a validity and practical applicability of the proposed twin-flag mathematical model in characterizing the hysteretic behavior of the isolation devices. As a consequence, the sloped rolling-type isolation device is capable of effectively mitigating seismic risks posed to the critical equipment and facilities.

References

Chang KC, Hwang JS, Wang SJ, Hwang CH, Tsai MS. Adaptable Seismic Isolation Bearing System. Patent Application 100125835, WOOD & WU Patent and Trademark Office, Taiwan, 2011.

Ou YC, Song J, Lee GC. A parametric study of seismic behavior of roller seismic isolation bearings for highway bridges. Earthquake Engineering and Structural Dynamics, 2010; 39(5): 541-559.

Shames IH. Engineering Mechanics: Dynamics. 4th Ed, Eaglewood Cliffs (NJ): Prentice-Hall Inc., 1996.

Wang SJ, Chang KC, Hwang JS, Tsai MS, Hsiao JY, Yu CH. Development of Sloped Rolling-Type Isolation Devices for Seismic Protection of Important Equipment and Facilities. Proceedings of the 15th World Conference on Earthquake Engineering (15WCEE), Lisbon, Portugal, September 24-28, 2012.

Wang SJ, Hwang JS, Chang KC, Shiau CY, Tsai MS, Hong JX. Sloped rolling-type isolation devices for seismic protection of equipment and facilities: theoretical study. Earthquake Engineering and Structural Dynamics, 2013. (under review)

Feasibility Study of Smart Carbon Fiber Reinforced Concrete for Structural Monitoring

Fang-Yao Yeh[1], Kuo-Chun Chang[2], Wan-Yu Lien[3] and Wen-Cheng Liao[4]

葉芳耀 [1]、張國鎮 [2]、連婉佑 [3]、廖文正 [4]

Abstract

Structural monitoring systems are important in civil engineering. Traditional structural monitoring systems have some disadvantages such as a shorter sensor life span than the structures. This research uses CFRC (Carbon Fiber Reinforced Concrete) as a structural monitoring sensor to extend the life of the sensor to match that of the structure. There are some known advantages of carbon fiber reinforced concrete, such as high tensile strength and high ductility which increases the seismic capacity and security of structures. However, CFRC has functionality similar to piezoresistive materials which can be used as a self-sensing material for strain measurement and damage detection. This property is based on the reversible effect of the strain on the volume of electrical resistivity and the irreversible effect of material damage on its resistivity. The strain sensing behavior is such that the resistivity decreases reversibly upon compression due to the slight inward push of crack-bridging fibers and the consequent decrease in the contact electrical resistivity of the fiber-cement interface. Similarly, the resistivity increases reversibly upon tension due to the slight outward pull of crack-bridging fibers and the consequent decrease in the contact resistivity. To consider the economic benefits, the fiber content is only 0.2 vol. % which is less than half of the amount used in other references (0.48 vol. %). The experimental results show that the conductivity of current materials is significantly improved by CFRC and that it can be used for strain measurement and damage detection with fiber content of 0.2 vol. %. Moreover, the experimental results of CFRC coated beams can be kept in a database for applications in the future.

Keywords: CFRC, Self-sensing, Strain measurement, Damage detection

Introduction

This article shows that once carbon fiber is added to concrete to become carbon fiber reinforced concrete (CFRC) it has functionality similar to piezoresistive materials that can be used as self-sensing materials for strain measurement and damage detection. This functionality is based on pairing the reversible effect of strain on the volume's electrical resistivity with the irreversible effect of damage to the resistivity. The strain sensing behavior is such that the resistivity decreases reversibly upon compression due to the slight inward push of crack-bridging fibers and the consequent decrease in the contact electrical resistivity of the fiber-cement interface. Similarly, the resistivity increases reversibly upon tension due to the slight outward pull of crack-bridging fibers and the consequent decrease in the contact resistivity [Wen and Chung, 2007; Han and Ou, 2007]. The self-sensing ability of CFRC cement-based composites has been well demonstrated under compression and under flexure. Using the electrical resistance change of CFRC and the appearance of structural cracks, we are able to derive an integration of sensors, and which possesses the material smartness quotient of self-sensing, stability, and repetitiveness.

1 Researcher, National Center for Research on Earthquake Engineering, fyyeh@ncree.narl.org.tw
2 Director, National Center for Research on Earthquake Engineering, kcchang@ncree.narl.org.tw
Professor, Department of Civil Engineering, National Taiwan University, ciekuo@ntu.edu.tw
3 Master, Department of Civil Engineering, National Taiwan University, quietskycrystal@gmail.com
4 Assistant Professor, Department of Civil Engineering, National Taiwan University, wcliao@ntu.edu.tw

Experimental Investigations

Preparation of Materials

The design concrete strength was set to 500 kgf/cm^2. The cement was a blended Portland cement and the specimens were made from a mix with the following ratios: water-cement ratio (w/c) = 0.4; sand-cement ratio (s/c) = 0.75; silica fume 15% by weight of cement; methylcellulose 0.4% by weight of cement and carbon fiber 0.2% by of total volume. The fiber diameter was 7μm. The nominal fiber length was 15mm. A standard mixing procedure was used. A rotary mixer with flat beater was used for mixing. After pouring the mix into oiled molds, an external electric vibrator was used to facilitate compaction and decrease the amount of air bubbles.

Specimens and Test Setup

From the aforementioned concrete mixture, 5 CFRC bone-shaped specimens, 4 CFRC cylinders and 8 different styles of CFRC beams were produced for testing at 28 days of age. The bone-shaped specimens had dimensions of 455×50×20mm and were prepared for uniaxial tension testing. The cylinders had dimensions of 100×200mm and were prepared for uniaxial compression testing. With the same concrete mixture, 8 concrete beams were produced. These beams had dimensions of 550×150×150mm and were prepared for three-point bending testing. The test setup is shown in Fig. 1.

Uniaxial Tension Test

A monotonous tensile loading was applied to the specimen shown in Fig. 1(a). The tensile strain of the CFRC specimen was measured using an LVDT under a gauge length of 105mm. The electrical resistance measurements were conducted using the four-probe method, with silver paint in conjunction with copper wires for electrical contacts and the electrode distance was 75mm (Fig. 1(a)). A Keithley 2000 digital multimeter was used to measure the electrical resistance of the specimens.

Uniaxial Compression Test

A monotonous compressive loading was applied to the specimen shown in Fig. 1(b). The compressive strain of the CFRC specimen was measured by an LVDT under a gauge length of 100mm. The electrical resistance measurements were also conducted using the four-probe method, with silver paint in conjunction with copper wires for electrical contacts and the electrode distance was 90mm (Fig. 1(b)).

Three-point Bending Test

Cyclical loading was applied to the CFRC beam specimen shown in Fig. 1(c). The dynamic strain of the CFRC beam was measured by the strain gauge, the central deformation was measured by an LVDT, and the electrical resistance was measured by the Keithley 2000 digital multimeter under a gauge length of 120mm (Fig. 1(c)).

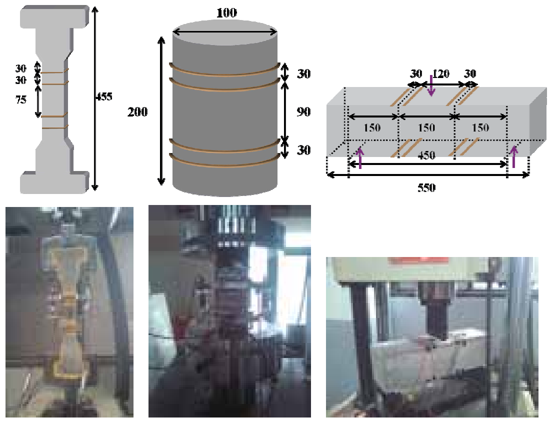

(a) (b) (c)

Fig. 1 Test setup, (a) uniaxial tension test, (b) uniaxial compression test, and (c) bending test

Results and Discussion

Uniaxial Tension Test

The test results of the 28 day old specimens are shown in Fig. 2. Fig. 2(a) shows the relationships between the fractional change in electrical resistance of the CFRC and the strain measured by LVDT at the middle portion of the specimens. This data depicts a linear relationship between the fractional change in electrical resistance of the CFRC and the strain measured by LVDT before a proportional limit. If the limit is exceeded, the fractional change in the electrical resistance decreases due to the increase in electrical resistance in the CFRC specimen caused by microstructure changes. This causes the micro crack density to increase and damage occurs.

In order to relate the fractional change in electrical resistance to tensile strain, we define the gauge factor (GF) as being the fractional change in electrical resistance per unit strain. When under the proportional limit, there is a strong linear relationship ($R^2 \fallingdotseq 1$) between the fractional change in electrical resistance and the tensile strain in the T1 to T5 specimens (Fig. 2(a)). The similarity between the fractional change in the electrical resistance and tensile strain under uniaxial tension testing means that CFRC can be used as a kind of self-sensing material for strain measurement within the proportional limit.

Based on the different variations in the fractional change in electrical resistance, three regions are considered in this paper: (1) region-I - the linear region where strain sensing via fractional change in electrical resistance has a linear relationship and is reversible; (2) region-II - the plastic region where the strain sensing via fractional change in electrical resistance is still with some proportional relationship and partial reversibility, owing to crack occurrence and damage accumulation in the specimen, but is not as obvious in the tensile specimens; (3) region-III - the damaged region where the strain sensing via fractional change in electrical resistance is meaningless, owing to the damage and material failure in the specimen. The fractional change in the electrical resistance changes very rapidly and can be used for damage detection.

Fig. 2(b) shows the variation in tensile stress and the fractional change in electrical resistance with tensile strains. The fractional change in electrical resistance has a linear relationship with tensile strain in region-I and rapidly decreases in region-III because of the fast electrical resistance increase, due to damage accumulation. The slope of fractional change against tensile strain is a good indicator for damage detection under tensile loading.

The test results are summarized in Table 1. Before the proportional limit, there exists a strong linear relationship between the fractional change in electrical resistance and tensile strain. The range of the R^2 values is between 0.93 and 0.97. The similarity of the fractional change in electrical resistance and tensile strain under uniaxial tension tests means that CFRC can be used for strain measurement. The gauge factors are 9.5 to 19.5 and the measurement ranges are 57.8% to 83.33% of the ultimate tensile strain.

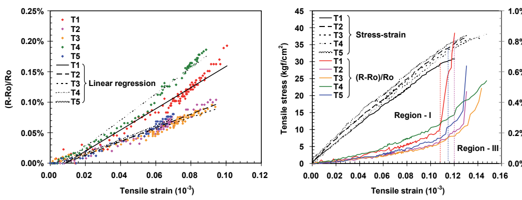

(a) (b)

Fig. 2 Tension test, (a) comparison between the fractional change in electrical resistance and strain measured by LVDT in linear region, and (b) variation of the tensile stress and fractional change in electrical resistance with tensile strain

Table 1 Results of the uniaxial tension tests

Unit / Spec.	f_t (kgf/cm^2)	ε_u (10^{-3})	Ro (Ω)	GF	R^2	$(\Delta R/Ro)_L$ (10^{-3})	MR %
T1	30.79	0.120	26.47	15.4	0.95	0.1	83.33
T2	37.29	0.173	25.03	10.0	0.94	0.1	57.80
T3	32.14	0.137	29.23	9.5	0.96	0.1	72.99
T4	38.22	0.147	36.54	19.5	0.97	0.1	68.03
T5	37.70	0.130	24.87	11.5	0.93	0.1	76.92

Uniaxial Compression Test

The test results from the 28 day old specimens are shown in Fig. 3. Fig. 3(a) shows the relationships between the fractional change in electrical resistance of the CFRC and the strain measured by the LVDT at the middle of the specimens. This data showed a bi-linear relationship between the fractional change in electrical resistance of the CFRC and the strain measured by the LVDT before the proportional limit. If the proportional limit is exceeded, the fractional change in electrical resistance decreases due to an increase in electrical resistance in the CFRC specimen caused by the microstructure changes. In addition, micro crack density increases and damage occurs.

When under the proportional limit there is a bi-linear relationship between the fractional change in electrical resistance and the compressive strain. Fig. 3(b) shows that the relation between the fractional change in electrical resistance and compressive strain is smaller than 2×10^{-4} and that the gauge factor of the C1 to C4 specimens are 200 to 250. Fig. 3(c) shows the relation between the fractional change in electrical resistance and the compressive strain to be between 5×10^{-4} and the proportional limit and that the gauge factor of the C1 to C4 specimens are 20 to 30. The similarity in the fractional change in electrical resistance and the compressive strain under uniaxial compression tests demonstrates that CFRC can be used as a self-sensing material for strain measurement within a proportional limit.

Fig. 3(d) shows the variation in the compressive stress and fractional change in electrical resistance as compressive strain varies. The fractional change in electrical resistance has a linear relationship with the compressive strain in region-I and region-II where GF1 and GF2 are used for compressive strain measurement. The fractional change in electrical resistance rapidly decreases in region-III because the electrical resistance increases quickly due to the damage accumulation. The slope of the curve is a good indicator for damage detection under compressive loading.

The test results are summarized in Table 2. Before reaching the proportional limit, there exists a strong bi-linear relationship between the fractional change in electrical resistance and compressive strain. The range of R^2 values is greater than 0.94. The similarity between the fractional change in electrical resistance and compressive strain under uniaxial compressive testing can be used for strain measurement. The gauge factors range from 187.1 to 240.6 (for GF1) and 20.9 to 24.9 (for GF2) and the measurement range lies between 71.15% and 88.32% of the ultimate compressive strain.

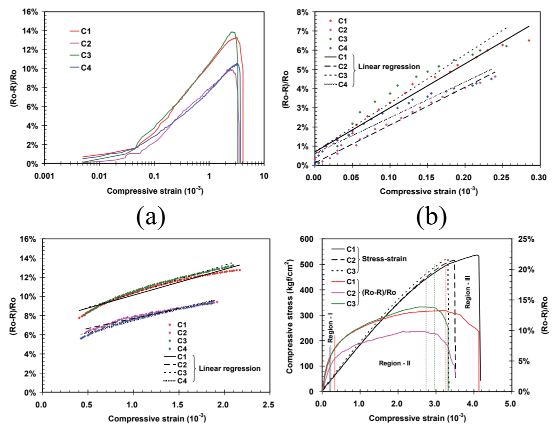

(a) (b)

(c) (d)

Fig. 3 Compression test, (a) comparison between the fractional change in electrical resistance and strain measured by LVDT, (b)(c) comparison between the fractional change in electrical resistance and the strain measured by LVDT in linear region, and (d) variation of compressive stress and fractional change in electrical resistance as compressive strain changes

Three-point Bending Test

The test results of 28 day old three-point bending specimens are shown in Table 3. The different types of specimen shown in Table 3 include a pure CFRC beam without steel reinforcement (P), a pure CFRC beam with steel reinforcement (PS), a concrete beam coated with a CFRC layer without steel reinforcement (Co) and a concrete beam coated with a CFRC layer with steel reinforcement (CoS).

From Table 3, the following results were observed: (1) from a comparison of the two pure CFRC beams, the strain in both the tension and compression side of the P specimens are found to be smaller than the PS specimens, but the electrical resistance (Ro) and gauge factor (GF) are found to be larger in the P specimens; (2) from a comparison of the two CFRC coated beams, the gauge factor of the CoS specimens are found to be greater than the Co specimens; (3) from a comparison between the pure CFRC beams and the CFRC coated beams, the gauge factor of the CFRC coated beams (Co and CoS) are found to be larger in the pure CFRC beams (P and PS). Generally, the CoS specimens were found to have the greater gauge factor.

Summary and Discussion

To consider the economic benefits, the fiber content of the CFRC is only 0.2 vol. % which is less than half the amount used in the cited references (0.48 vol. %). The experimental results of the uniaxial tension tests, the uniaxial compression tests and the three-point bending tests show that the conductivity of materials significantly improved and that CFRC can be used for strain measurement and damage detection at a fiber content of 0.2 vol.%.

From the tension tests, we observed that due to the similarity between the fractional change in electrical resistance and tensile strain under uniaxial tension testing, the material can be used as a self-sensing material for strain measurement within the proportional limit. The slope of the fractional change against tensile strain curve is a good indicator for damage detection under tensile loading.

From the compression tests, we also observed that due to the similarity between the fractional change in electrical resistance and compressive strain under uniaxial compression testing, the material can be used as a self-sensing material for strain measurement within the proportional limit. The slope of the fractional change against compressive strain curve is a good indicator for damage detection under compressive loading.

From the three-point bending tests, the gauge factor of the concrete beams coated with a CFRC layer with steel reinforcement was found to be greater than that of a concrete beam coated with a CFRC layer but without steel reinforcement and pure CFRC beams with or without steel reinforcement. Moreover, the experimental results of the coated beams can be kept in the database for applications in the future.

Self-sensing of the tensile strain, compressive strain, and damage detection was found to be effective in CFRC under monotonous loading. The self-sensing ability of CFRC, as shown in the sensing of strain and damage detection, is demonstrated in this paper.

References

Sihai Wen and D. D. L. Chung "Piezoresistivity-based strain sensing in carbon fiber-reinforced cement", *ACI Materials Journal,* Vol. 104, No. 2, pp 171-179, 2007.

Baoguo Han and Jinping Ou "Embedded piezoresistive cement-based stress/strain sensor", *Sensors and Actuator*, A138, pp 294-298, 2007.

Table 2 Results of the uniaxial compressive tests

Unit / Specimen	E	f_c'	ε_u	Ro	GF1	R^2	GF2	R^2	$(\Delta R/Ro)_L$	MR
	(tf/cm^2)	(kgf/cm^2)	(10^{-3})	(Ω)					(10^{-3})	%
C1	178.18	536.77	4.09	19.63	240.6	0.98	24.9	0.97	2.91	71.15
C2	181.18	514.87	3.49	31.38	197.2	0.99	20.9	0.97	2.57	73.64
C3	189.66	523.62	3.30	31.17	253.0	0.94	29.3	0.98	2.89	87.58
C4	179.65	519.65	3.68	19.93	187.1	0.95	24.7	0.98	3.25	88.32

Table 3 Results of the three-point bending tests

Bending		Specimen	Strain (10^{-3})		Ro (Ω)		GF		R^2		Force
			c	t	c	t	c	t	c	T	kN
CFRC	w/o Rebar	P1	-0.08	0.040	36.8	53.3	175	220	0.97	0.81	7
	w Rebar	PS1	-0.17	0.075	14.7	18.9	52	87	0.96	0.90	10
		PS2	-0.15	0.075	15.3	15.9	78	89	0.92	0.89	10
Coated	w/o Rebar	Co1	-0.11	0.075	54.1	51.1	252	160	0.97	0.91	8.5
		Co2	-0.15	0.060	31.9	35.7	49	78	0.88	0.95	8.5
	w Rebar	CoS1	-0.15	0.060	81.9	49.7	1031	497	0.95	0.94	13
		CoS2	-0.06	0.045	40.6	84.3	603	844	0.98	0.93	13
		CoS3	-0.08	0.050	31.8	47.8	445	516	0.94	0.93	13

Development of Damage Evaluation Techniques for Geotechnical Structures (II) - A Case Study of the old Jhong-Jheng Bridge in Hsinchu

Yung-Yen Ko[1] Ya-Han Hsu[2]

柯永彥 [1]、許雅涵 [2]

Abstract

This report presents a verification of damage evaluation techniques for geotechnical structures based on structural dynamic responses developed in previous years through an actual case study. In Taiwan, several failures of highway bridges related to foundation scour occurred in recent years, which have caused considerable casualties and property loss. Therefore, the focus of this study is on the damage evaluation of bridge foundations, and the old Jhong-Jheng Bridge in Hsinchu, of which the caisson foundations have suffered severe exposure due to scouring, was adopted as the object of study. Firstly, microtremor measurements were made on the superstructure of the bridge, and the influence of foundation scouring was revealed by spectrum analysis and modal analysis. In addition, because the design drawings were unavailable and the foundation depth is thus unknown, the impulse response method was utilized to estimate the depth of the caisson foundation and a satisfactory result was obtained. According to all the above results, the feasibility of the non-destructive testing methods in the damage evaluation of structural foundations can be validated.

Keywords: geotechnical structures, damage evaluation, foundation scour, microtremor measurement, impulse response

Introduction

In Taiwan, several major highway bridge failures occurred in recent years. The majority of these failures were related to the exposure of the pier foundation due to scouring, which reduces its bearing capacity. For example, a pile foundation of the Kao-Ping Bridge settled in 2000, and a caisson foundation of the Hou-Fong Bridge tilted in 2008, causing the collapse of their superstructures. In both cases, the foundations were significantly exposed due to scouring. In 2009, Typhoon Morakot hit Taiwan with record-breaking rainfalls. An over 200-year-recurrence flood occurred in the watershed of the Kao-Ping River, and several bridges, including the Liu-Gui Bridge, the Ci-Wei Bridge, the Da-jin Bridge, and the Shuang-Yuan Bridge, experienced severe scour and were destroyed.

These disasters led to considerable casualties and property loss, yet they could have been preventable if the damage or insufficient capacity of the foundation could have been detected in advance, and repairs and retrofitting works or the implementation of restraints on the usage of the bridge were timely executed. Although it is possible to inspect the exposure of the foundation using instruments installed on it, these instruments might be destroyed in flood conditions. Therefore, it is necessary to develop indirect damage evaluation techniques for the foundations.

The geotechnical structure can be regarded as a soil-structure system. Its structural dynamic responses exhibit the global characteristics of the system and also reflect the boundary conditions. Thus, measuring the dynamic responses of a geotechnical structure helps to detect its damage. This kind of damage evaluation is classified as non-destructive testing. It is easy to perform, data processing is well developed, and many vulnerability indices have been proposed. Hence, it is a research subject worthy of development. Since the disaster mitigation of bridges has become an important issue, the focus is on bridge foundations.

[1] Associate Researcher, National Center for Research on Earthquake Engineering, yyko@ncree.narl.org.tw
[2] Assistant Researcher, National Center for Research on Earthquake Engineering, yhhsu @ncree.narl.org.tw

The old Jhong-Jheng Bridge in Hsinchu, which crosses the Tou-Cian River, used to be a vital roadway and has been in operation for more than 30 years. The riverbed nearby is mainly composed of mudstone or inter-layered mudstone and sandstone. Thus, scouring and erosion has formed many gullies and has caused several piers to suffer foundation exposure (NCTU, 2005). Although many anti-scour protective works for the bridge foundations have been completed, the strong current induced by the heavy rainfall of Typhoon Saola in August 2012 still caused the caisson foundation of pier P9 to be severely exposed, as shown in Fig. 1. Because of the possible insufficiency of the structural stability, this bridge has been closed since then, and a new bridge is to be constructed.

Taking advantage of this opportunity, microtremor measurements were performed on the superstructure of the old Jhong-Jheng Bridge during the closed period to investigate the influence of the foundation exposure on the dynamic behavior of the bridge. In addition, the impulse response method was utilized to examine the length of the caisson foundation. Through this case study, non-destructive testing methods for the damage evaluation of foundations can be verified.

Fig. 1 The scouring condition of the old Jhong-Jheng Bridge (August 2012)

Testing and Analysis Methods

The testing techniques adopted in this study and their corresponding analysis methods are as follows:

1. Microtremor Measurement:

Microtremors are randomly generated by natural and civilian activities in the environment and have a wide frequency range. If the input microtremors and the excited structural responses are simultaneously measured, the transfer function can be deduced for system identification. If no input motion is available, the structure can be characterized only by its excited response, assuming microtremors as the white noise.

The vibration characteristics of a structure, such as its natural frequency, damping, and modal shape, are related to its structural properties and integrity. Since damage of a structure lowers its natural frequency due to stiffness reduction, the natural frequency is often adopted for damage evaluation. Moreover, the modal shape of a damaged structure would be changed because of the stiffness redistribution. Therefore, the modal shape would help to locate the damage.

In order to identify the dynamic properties of the bridge–foundation–ground system using microtremor measurements, the analysis methods adopted include:

(a) Average spectrum analysis

When long-term field vibration measurements are made, the vibration characteristics at various moments show a certain variance since the environment and the vibration source are not consistent. To eliminate the dispersion, the concept of Samizo et al. (2007) was used. Sections with a fixed duration are extracted from the overall record, and each is partially overlapped with the next. The Fourier spectrum is calculated in each section and an averaged spectral curve is then obtained as a representative as shown in Fig. 2. Thus, the influence of abnormal events can be diluted and the structural characteristics are better described.

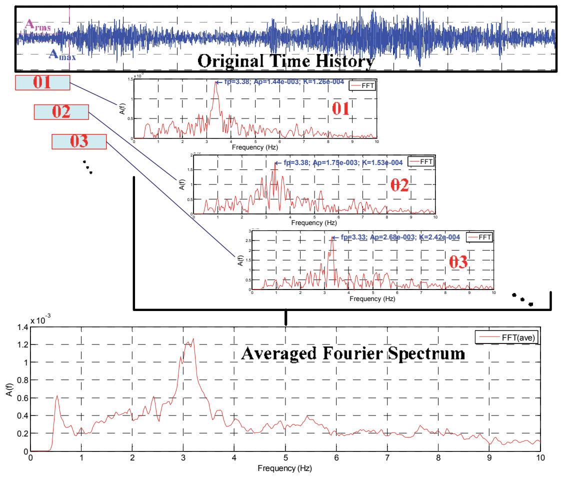

Fig. 2 Procedures of average spectrum analysis.

(b) Modal analysis

In this study, the correlation analysis method is adopted for modal analysis. Considering the time histories of two random vibration signals, $x(t)$ and $y(t)$, their cross-correlation is defined by the function:

$$r_{yx}(t) = \int_{-\infty}^{\infty} y(\tau)x(t+\tau))d\tau \qquad (1)$$

The cross-correlation of $x(t)$ with itself is usually called as auto-correlation.

If the Fourier transform is performed on the cross-correlation function, a cross-power spectrum can be obtained, which is exactly the dot product of $x(t)$ and $y(t)$ in the frequency domain:

$$S_{yx}(\omega) = \int_{-\infty}^{\infty} r_{yx}(\tau)e^{-i\omega t}d\tau = Y(\omega)\cdot\overline{X}(\omega) \qquad (2)$$

where $Y(\omega)$ and $X(\omega)$ are the Fourier transform of $x(t)$ and $y(t)$, and $\overline{X}(\omega)$ is the conjugate of $X(\omega)$.

Similarly, if the auto-correlation function is transformed into the frequency domain, the auto-power spectrum is acquired, which is exactly the dot product of $x(t)$ and itself in the frequency domain.

Accordingly, a reference point is first chosen. Then the cross- and auto-power spectra of the vibrations in a certain direction at all the measuring points (including the reference point) with respect to the vibration of the reference point are calculated. Thus, the mutual peaks of these power spectra are considered to be the fundamental (natural) frequencies of the principal modes of the system. Based on the amplitude ratio and the phase differences among all the points at the fundamental frequency of a specific mode, the corresponding modal shape is obtained.

2. Impulse Response Method:

The impulse response method is based on the recognition of the reflected compressive wave and is often used to inspect the pile integrity. As shown in Fig. 3, the pile top is impacted by an impulse hammer, inducing a transient impulse propagating downward along the pile. When the impulse reaches the discontinuities of the pile, such as the pile tip or the deflections in the pile body, reflection occurs. Then, the pile length or the location of the deflections can be estimated according to the response of the reflected wave measured by the accelerometer on the pile head.

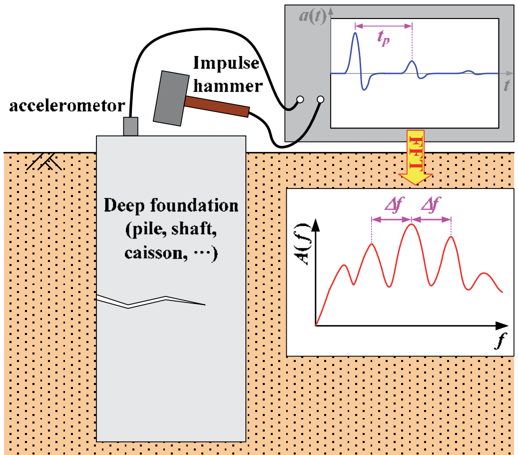

Fig. 3 Test scheme of the impulse response method.

The data processing procedures for the impulse response method are described as follows:

(a) Time domain analysis

Since the stiffness of the pile body is relatively higher than the supporting soil below the pile tip or the deflections, the reflected wave induced by these discontinuities will be in phase with the incident wave, as shown in Fig. 3. The travelling distance of the impulse can be calculated by the time lag between the incident and reflected waves passing the pile head and the P-wave velocity in the pile. Thus, the pile length or the location of deflections can be deduced.

The time lag between incidence and reflection can be estimated directly by the peaks on the time-history curve. However, the reflected waves may not be easily recognized due to environmental conditions, impact quality, and material inhomogeneity. In this case, Eq. (1) can be introduced to perform an auto-correlation analysis for the measured response, and the maximum of the correlation function, apart from the one at $t = 0$, can be identified at $t = t_p$. Then, t_p is considered to be the duration of the impulse travelling back and forth along the pile. If the discontinuity is at the pile tip, then the pile length L can be calculated as below:

$$L = \frac{v_P t_P}{2} \tag{3}$$

where v_p is the propagating velocity of the impulse.

(b) Frequency domain analysis

Based on elastic theory, a prismatic pile has a consistent interval between the intrinsic frequencies of the resonant modes, which is a function of L and v_p, provided that the induced wavelengths are greater than the diameter of the pile. Therefore, if the Fourier spectrum of the impulse response on the pile head is obtained, then the frequency interval Δf can be estimated accordingly, as shown in Fig. 3. Then the pile length L can be calculated by the following equation (Finno and Gassman, 1998):

$$L = \frac{v_P}{2\Delta f} \tag{4}$$

Microtremor Measurement of the old Jhong-Jheng Bridge

During the closed period of the old Jhong-Jheng Bridge, a microtremor measurement was conducted on its superstructure. The measuring points were located at pier P9, where the foundation exposure was the most severe, and at neighboring piers P10 and P11, as shown in Fig. 1. Velocity-type vibro-sensors were adopted and were installed on the deck beside the expansion joint. At the measurement, the exposed depth of the caisson of pier P9 was estimated at around 15 m using a plumb bob and measuring tape.

Using an averaging scheme, the average Fourier spectrum of the horizontal transverse (HT, parallel to the flow direction) vibrations can be obtained, as shown in Fig. 4. A majority of the vibrations at piers P10 and P11 are concentrated in the frequency range of 2–4 Hz, with predominant frequencies of 2.8 Hz and 3.3 Hz, respectively. For pier P9, an obvious peak is noted at the frequency of 1.5 Hz. The predominant frequency of P10 is found to be lower than that of P11, where the protective works remained intact, probably because the protective work was partially damaged. Meanwhile, pier P9, which was severely scoured, has a lower predominant frequency than P10 and P11. It is therefore concluded that the exposure of the foundation will cause the predominant frequency of vibration of the pier to be apparently decreased.

In addition, modal analysis was performed using the microtremor measurement data. The fundamental frequency of the 1st mode is found to be 1.47 Hz, conformable to the predominant frequency of the microtremors of pier P9. The corresponding modal shape is shown in Fig. 5, in which the maximum vibration amplitude is observed for pier P9. Consequently, the stiffness of pier P9, which had suffered severe scour and significant foundation exposure, is found to belower than the neighboring piers as expected. Thus, it will show a larger response when subjected to external loads, leading to stability concerns in terms of settlement and overturning.

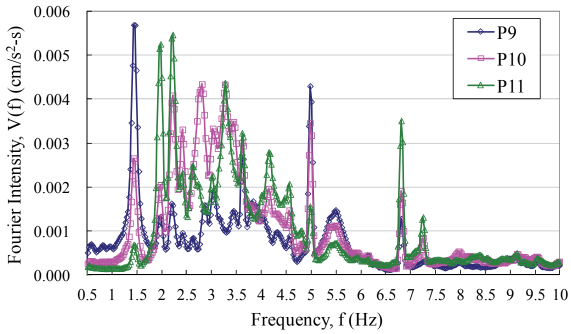

Fig. 4 Average Fourier spectra of HT vibrations.

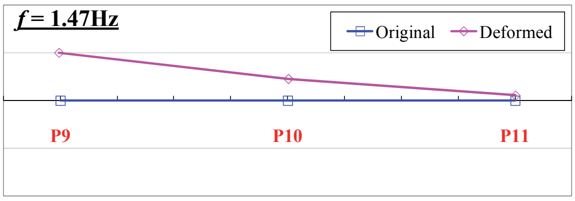

Fig. 5 Modal shapes of the bridge section P9~P11

Impulse Response Testing on the Caisson Foundation of the old Jhong-Jheng Bridge

The caisson foundations were used for the old Jhong-Jheng Bridge. However, the design drawings are unavailable and the foundation depth is unknown, so the influence of the foundation exposure on the stability of the pier cannot be evaluated. Therefore, the impulse response method was adopted for the testing of the caisson length of pier P11. The test situation is as shown in Fig. 6. An impulse hammer was used to hit the top of the caisson, an accelerometer was placed on the top to measure the incidence and reflection of the induced impulse wave, and another accelerometer was installed on the side of the caisson 1.85 m below the top to estimate the wave velocity.

Fig. 7(a) depicts the time history of the impulse response at the top of the caisson. The waveforms of the incident and reflected waves are identifiable and t_p can be obtained using the correlation method. Several high-quality hits were chosen to obtain an average $t_p = 1.053\times10^{-2}$ s as a representative. In addition, from the time lag of the impulse passing between the two accelerometers, the v_p can be estimated to be around 4975 m/s. From this, the length of the caisson can be calculated by Eq. (3), and is about 26.2 m. Fig. 7(b) gives the Fourier spectrum of the impulse response. Similarly, an average Δf of about 96.0 Hz was acquired. Then the caisson length was calculated using Eq. (4), and is 25.9 m, close to that found from the time domain analysis.

As mentioned, the exposed depth of the P9 caisson was close to 15 m. If the length of the P9 caisson is the same as that of P11, the exposure exceeds half of the caisson length. Therefore, the foundation stability of pier P9 might be insufficient.

Fig. 6 Impulse response testing on P11caisson.

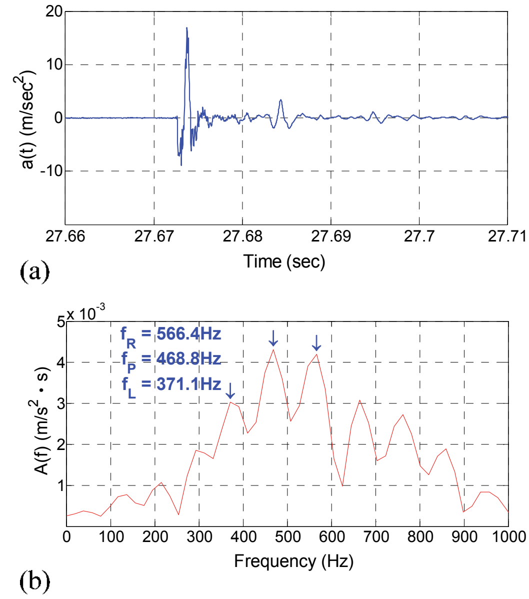

Fig. 7 Impulse response on the top of P11 caisson: (a) time history curve; (b) Fourier spectrum.

References

Finno, R.J., and Gassman, S.L. (1998), “Impulse response evaluation of drilled shafts”, J. Geotech. Geoenviron. Eng, ASCE, 124(10), pp. 965-975.

NCTU (2005), The Study on the Impact of Jhong-Jheng Bridge and the Other Existing Flood Control Structures to the Overall Characteristics of Tou-Cian River, MOEA/WRA Report.

Samizo M, Watanabe S, Fuchiwaki A and Sugiyama T. (2007), “Evaluation of the structural integrity of bridge pier foundations using microtremors in flood conditions”, Quarterly Report of the Railway Technical Research Institute, 48(3), pp. 153-157.

Shaking Table Tests on Model Pile in Saturated Sloping Ground

Chia-Han Chen[1], Tzou-Shin Ueng[2] and Cheng-Hsing Chen[3]

陳家漢[1]、翁作新[2]、陳正興[3]

Abstract

For the study of soil-structure interaction, including the effect of lateral spreading, in a saturated sloping ground during earthquake, shaking table tests on a model pile in an inclined large biaxial laminar shear box filled with saturated clean sand were conducted at the National Center for Research on Earthquake Engineering (NCREE), in Taiwan. The pile tip was fixed at the bottom of the shear box to simulate the condition of a pile foundation embedded in a firm stratum. The pile top was mounted with 6 steel disks to simulate the superstructure. Input shakings including sinusoidal and recorded earthquake accelerations were imposed either perpendicular or parallel to the slope direction. Strain gauges and accelerometers were placed on the pile surface to obtain the response of the pile under shaking. The near-field and far-field soil responses, including pore water pressure changes, accelerations, and settlements were also measured. The lateral spreading displacement of the soil and pile behavior were observed and evaluated while soil liquefaction was triggered under shakings in either direction.

Keywords: shaking table test, liquefaction, lateral spreading, pile

Introduction

Pile foundations within liquefiable and laterally spreading ground have suffered extensive damages in many large earthquakes such as the 1964 Niigata Earthquake, the 1989 Loma Prieta Earthquake, the 1995 Kobe Earthquake, the 1999 Chi-Chi Earthquake, the 2011 Christchurch Earthquake and the 2011 Great East Japan Earthquake. Previous studies on soil-pile interactions have been conducted in order to understand the mechanism of the dynamic loading on the piles (soil-pile interaction) and their responses under earthquake loading. Lateral loading tests in the field or in the laboratory and shaking table tests on model piles within soil specimens, under either 1 g or centrifugal condition, have been used to investigate the pile behaviors and soil-pile interaction in saturated soil (e.g. Dobry et al. 2003, Tokimatsu et al., 2005, Ashford et al., 2006, Brandenberg et al., 2006, Cubrinovski et al., 2006, Madabhushi et al., 2010, Ueng and Chen, 2010). The results of these studies, including failure mechanisms, bending moments of pile in laterally spreading ground, pore water pressure variation around the piles, p-y relations for soil-pile interaction, and pile cap effect, can provide information on performance criteria for aseismic design of structures with pile foundations.

However, there are still uncertainties concerning the soil-pile interaction issues in laterally spreading ground, including (1) the kinematic loading on pile foundation due to lateral spreading; (2) the relationship between the mobilized lateral pressure and the ground displacement; and (3) the transient responses of the surrounding soil and pile during soil liquefaction. In this study, a large biaxial laminar shear box developed at the National Center for Research on Earthquake Engineering (NCREE) was used as the soil container and an instrumented aluminum model pile was installed inside the shear box filled with saturated sand. The biaxial shear box with the model pile in a saturated sloping ground was placed on 1 g shaking table and one dimensional sinusoidal and recorded earthquake accelerations were applied perpendicularly or parallel to the slope direction. The soil and pile responses and their

[1] Assistant Researcher, National Center for Research on Earthquake Engineering, chiaham@ncree.narl.org.tw
[2] Professor Emeritus, Department of Civil Engineering, National Taiwan University
[3] Professor, Department of Civil Engineering, National Taiwan University

interaction, including the inertial and kinematic actions on the model pile, under these types of shakings were studied.

Model Pile and Sand Specimen

The model pile was made of an aluminum alloy pipe, with a length of 1600 mm, an outer diameter of 101.6 mm, and a wall thickness of 3 mm. Its flexural rigidity, $EI = 75\ kN \cdot m^2$, was obtained by flexural testing. Strain gauges and mini-accelerometers were placed at different locations to respectively measure bending strains and accelerations along the model pile. The shear box was inclined 2° to the horizontal, simulating a mild infinite slope. The sloping direction of this model was in the X-direction. The pile was vertically fixed at the bottom of the shear box. Hence, this physical model can be used to simulate the condition of a vertical pile embedded in sloping rock or within a sloping stratum of firm soil. In addition, 6 steel disks, 226.14 kg, were attached to the top of the model pile to simulate the superstructure.

A clean fine silica sand ($G_s = 2.65$, $D_{50} = 0.31$ mm) from Vietnam was used in this study for the sand specimen inside the laminar shear box. The maximum and minimum void ratios are 0.918 and 0.631, respectively. The sand specimen was prepared using the wet sedimentation method after the placement of the model pile and the instruments inside the shear box. The sand was rained down into the shear box filled with water to a pre-calculated depth. The size of the sand specimen is 1.880 m × 1.880 m in plane and about 1.31 m in height before shaking tests. The relative density of the sand is about 10 %. Details of the biaxial laminar shear box and the sand specimen preparation are described in Ueng et al. (2006).

Shaking Table Tests

Shaking table tests were first conducted on the model pile without sand specimen in order to evaluate the dynamic characteristics of the model pile itself. Sinusoidal and white noise accelerations with amplitudes from 0.03 to 0.05 g were applied in X- and/or Y-directions. In the two-dimensional (multidirectional) sinusoidal shakings, there is a 90° phase difference between the input acceleration in X- and Y-directions, i.e., a circular or ellipse motion was applied. The model pile in saturated sloping ground was then tested under one dimensional sinusoidal (1-8 Hz) and the recorded accelerations during Chi-Chi Earthquake and Kobe Earthquake with amplitudes ranging from 0.03 to 0.15 g. Input motions were mainly imposed perpendicular to the slope direction for the study of kinematic effect on the pile foundation (lateral spreading force) independently, and also tested in another direction parallel to the slope to investigate the resultant force on the pile foundation including the inertial and kinematic effect. White noise accelerations with amplitude of 0.03 g were also applied in both the X- and Y-directions to evaluate the dynamic characteristics of the model pile within the soil and the sand specimen. Figure 1 shows a picture of the shaking table test on a model pile with 6 steel disks on its top.

Fig. 1 A model pile with 6 steel disks on its top in saturated sloping ground on the shaking table

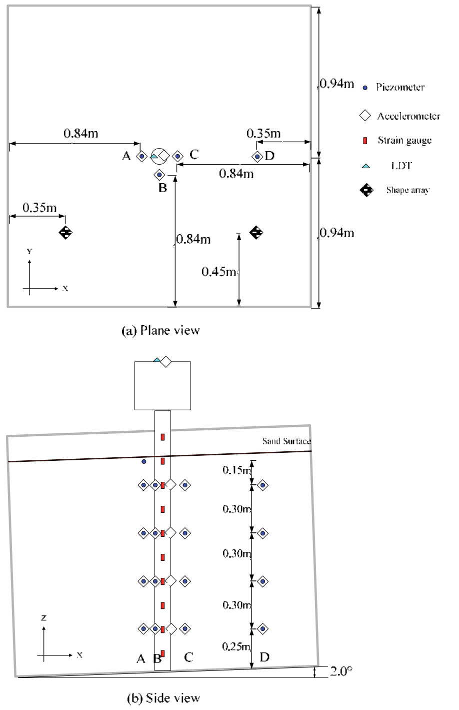

Fig. 2 Instrumentation on the pile and within the sand specimen

The pile top displacements, strains and accelerations at different depths on the pile, and the pore water pressures and accelerations in the sand specimen (near-field and far-field) were measured during each shaking, as shown in Fig. 2. In addition, the frame movements at different depths of the laminar shear box were also recorded to evaluate the responses and liquefaction of the sand specimen using displacement transducers and accelerometers. Pore water pressures inside the sand specimen were measured continuously until sometime after the end of shaking to observe the dissipation of the water pressures. The height of the sand surface after each test was obtained for the settlement and density of the sand specimen. Soil samples were taken using short thin-walled cylinders at different depths and locations after completion of the shaking tests to obtain the densities of the sand specimen.

Preliminary Results

Characteristics of model pile

Shaking table tests on the model pile without sand specimen were conducted to evaluate the dynamic characteristics of model pile itself. The behavior of model pile on the shaking table can be regarded as a single-degree viscously damped system. Hence, the amplification curve was obtained from the Fourier spectral ratio of the measured acceleration of the pile top and the input motion. Table 1 lists the predominant frequencies of the model pile according to the test data. The damping ratio of the model pile ranges from 0.7 % to 1.2 % obtained by the back-calculations from the free vibration and forced vibration.

Table 1 Predominant frequencies of the model pile

Mass on pile top	Aluminum pile
	Freq., Hz
No mass	22.9
6 steel disks	2.1

Dynamic characteristics of soil and soil-pile system under small amplitude of shaking

The dynamic characteristics of soil stratum and soil-pile system were evaluated by a series of shaking table tests on the model pile within the saturated sand specimen with small amplitude. Table 2 lists the predominant frequencies of the soil and the soil-pile system for the model pile (with 6 steel disks on its top) in soil of various relative densities. It can be seen that the predominant frequency of soil increases with the relative density, but that of pile increase slightly with the relative density. In addition, the predominant frequency of soil-pile system is significantly lower than that of the soil specimen. Comparing the predominant frequencies of the model pile without and within soil specimen (Table 1 and Table 2, respectively), one can find that, except for the case without mass on the pile top, the predominant frequencies of the model pile in the soil specimen were higher than those without soil due to the constraint of the soil on the pile. Hence, the response of the pile was mainly governed by the inertia force from the 6 steel disks.

Table 2 Predominant frequencies of the soil and the aluminum pile in soil of different relative densities

Density of soil	Predominant frequency , Hz	
Dr, %	Soil	Pile in soil
11.9	10.92	4.61
26.0	11.7	4.64
42.4	12.7	4.65
70.1	13.8	4.67

Response of model pile under laterally spreading

A shaking table test under one-dimensional sinusoidal acceleration with frequency of 8 Hz and amplitude of 0.068 g in the Y-direction (i.e. the input motion was imposed perpendicular to the slope direction) was conducted to study the kinematic effect on the pile foundation in a saturated sloping ground with relative density of 13.6 %. The depth of liquefaction was determined based on the measured pore water pressures in the sand specimen and accelerometers on the frames (Ueng et al., 2010). In this test, the liquefied depth of the sand specimen reached about 112.6 cm. Figure 3 shows a distinct lateral spreading displacement after the shaking. (Compared with Figure 1)

Fig. 3 Liquefaction-induced lateral spreading displacement in X direction

The time histories of relative displacement and trajectory of the pile top are shown in Fig. 4. The X-displacement of the model pile is mainly caused by lateral spreading, whilst the displacement in the other direction is induced by the shaking. Hence, the force exerted on the model pile due to lateral spreading (X-direction) can be extracted from this kind of test. It is also observed that the pile response in the X-direction can be divided into three stages during the shaking. (i) The first stage is only small movement and rebound at 2.2 to 3 seconds. The response of pile is due to the small amount of movement and softening at the shallower depth of soil. (ii) The second stage, pile has the maximum displacement and rebound again at 3 to 4.2 seconds. At this stage, the model pile suffers the majority of liquefaction-induced lateral ground displacement (Fig. 5), and it has its maximum displacement at 3.618 seconds. After this time, the pile rebounds again because of the reduction in lateral force on the pile when the specimen was liquefied. (iii) The pile response at this stage demonstrates a free vibration motion at 4.2 to 8 seconds. The predominant frequency of the acceleration on the pile top in the X-direction is about 2 Hz. Comparing this result with the predominant frequency of the model pile without soil specimen (Table 1), one can find that the predominant frequency of the model pile within liquefied soil was almost the same as that of model pile without soil specimen. This inferred that the stiffness of the soil had nearly dissipated when soil liquefaction occurred.

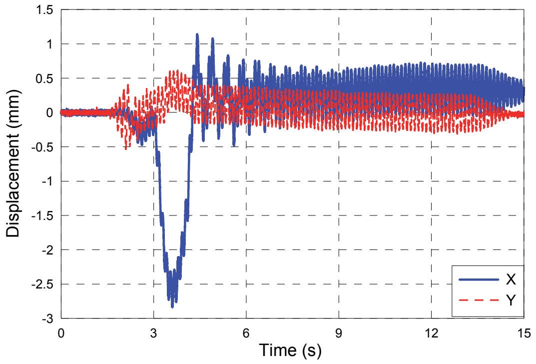

Fig. 4 The time histories of relative displacement of the pile top

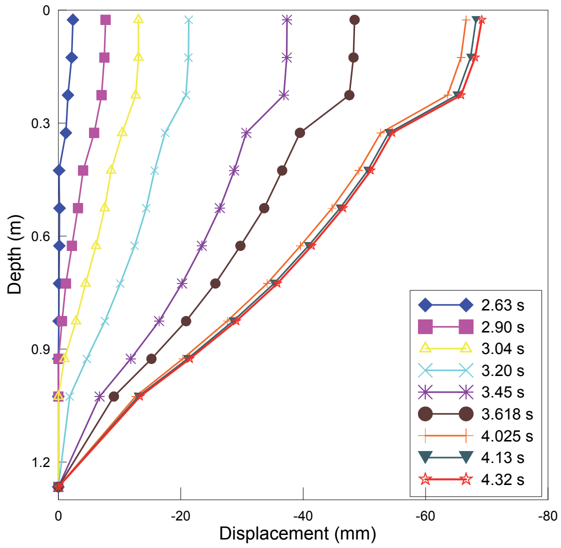

Fig. 5 Profiles of free-field ground at various times in X direction

Conclusions

Shaking table tests were conducted on an aluminum model pile in saturated sloping ground using the biaxial laminar shear box. Analyses of the dynamic behavior of the model pile and the soil stratum were conducted during the shaking tests according to observations. Lateral spreading displacements of the soil and pile behavior were observed while soil liquefaction was triggered under the shaking. It was also found that the kinematic loading on the model pile due to lateral spreading during shaking can be separated individually in a suitable way by using the biaxial shear box. Further analyses of the test data will be performed to obtain more information on the relationship between the mobilized lateral pressure on the pile and the ground movement and the evaluation of bending moment of pile in design.

References

Ashford, S. A., T. Juirnarongrit, T. Sugano and Hamada, M. (2006). "Soil–pile response to blast-induced lateral spreading I: Field Test," Journal of Geotechnical and Geoenvironmental Engineering, Vol.132, No.2, pp.152-162.

Brandenberg, S. J., Boulanger, R. W., Kutter, B. L., and Chang, D. D. (2005). "Behavior of pile foundations in laterally spreading ground during centrifuge tests," Journal of Geotechnical and Geoenvironmental Engineering, Vol.131, No.11, pp.1378-1391.

Cubrinovski, M., Kokusho, T., and Ishihara, K. (2006). "Interpretation from large-scale shake table tests on piles undergoing lateral spreading in liquefied soils," Soil Dynamics and Earthquake Engineering, Vol.26, No.2-4, pp.275-286.

Dobry, R., Abdoun, T., O'Rourke, T. D., and. Goh, S. H.(2003). "Single piles in lateral spreads: field bending moment evaluation," Journal of Geotechnical and Geoenvironmental Engineering, Vol.129, No.10, pp.879-889.

Haigh S. and Madabhushi, G.(2005). "The effects of pile flexibility on pile-loading in laterally spreading slopes," Seismic performance and simulation of pile foundations in liquefied and laterally spreading ground. Vol I.

Madabhushi, G., Knappett, J., and Haigh S. (2010). Design of pile foundations in liquefiable soils, Imperial College Press, U.K.

Tokimatsu, K., Suzuki, H. and Sato, M. (2005). "Effect of inertial and kinematic interaction on seismic behavior of pile with embedded foundations," Soil Dynamics and Earthquake Engineering, Vol.25, No.7-10, pp.753-762.

Ueng, T. S., Wang, M. H., Chen, M. H., Chen, C. H., and Peng, L. H. (2006). "A large biaxial shear box for shaking table tests on saturated sand," Geotechnical Testing Journal, Vol.29, No.1, pp.1-8.

Ueng, T. S., and Chen, C. H. (2010). "Multidirectional shaking table tests on model piles in saturated sand," Seventh International Conference on Physical Modelling in Geotechnics, Vol II pp.1445-1450.

Ueng, T. S., Wu, C. W., Cheng, H. W., and Chen, C.H. (2010). "Settlements of saturated clean sand deposits in shaking table tests," Soil Dynamics and Earthquake Engineering. Vol.30, No.1-2, pp.50-60.

Using the ANSYS/LS-DYNA to Investigate the Seismic Response of Dry Storage Facility for Spent Nuclear Fuel

Cheng-Hsing Chen[1] Hsuan-Chih Yang[2] Yung-Yen Ko[3] Shang-Yi Hsu[4]

陳正興 [1]、楊炫智 [2]、柯永彥 [3]、許尚逸 [4]

Abstract

The management and storage of the high radioactive waste has always been an important subject to maintain the security and running continuously of nuclear power plants. The planning of spent fuel storage including three steps: (1) short term storage; (2) interim storage; and (3) long-term storage. The concept of dry storage system means the spent fuel was stored in cask which is freestanding on a concrete pad. This leads to stability concerns in terms of sliding, rocking or tipping over in an earthquake event. In this study, the ANSYSLS/LS-DYNA code is adopter to analyze the seismic response of the dry storage facility. A 3D coupled finite element model was established, which consisted of a freestanding cask, a concrete pad, the interface friction coefficient and an artificial earthquake. The results show that there is a threshold value of friction coefficient control the fist move of cask to slide or rotation. The friction coefficient between freestanding cask and concrete pad will influence the seismic behavior of cask. The cask will slide and rotation but not tip over during the artificial earthquake. The design and analysis of dry storage facility need to consider the influence of friction coefficient.

Keywords: dry storage facility, friction coefficient, ANSYSLS/LS-DYNA

Introduction

The management and storage of highly radioactive waste has always been an important issue in the safe and continuous operation of nuclear power plants. In Taiwan, the available space of spent fuel pools for short-term storage will be exhausted in a few years, and the location of the final disposal facility has yet to be decided. Therefore, the installation of dry storage facilities for interim storage is necessary. In dry storage facilities, the spent fuel is stored in dry-type storage casks or modules, and these casks/modules are usually free-standing on a concrete pad rather than anchored like other ordinary civil structures. This leads to stability concerns in terms of sliding and rocking in the event of an earthquake [1]. The main considerations for the seismic safety of the free-standing casks/modules are the possible collision between casks/modules due to their horizontal displacement and tipping-over due to the rocking response of the cask during an earthquake [2]. The coefficient of friction must be greater than the breadth-height ratio of the body in order to initiate rocking motions. If the coefficient of friction at the interface is small enough, a rigid block resting on a floor subjected to a strong horizontal ground motion will not jump. A strong dependency relationship between the stability, the aspect ratio (h/r), and size (R) has been established [3、4]. Rabbat etc. also indicate that the coefficient of friction can be influenced by the presence of the mill scale on the steel surface, as well as by the normal pressure applied to the interface [5]. According to previous studies, the coefficient of friction at the interface between the cask and the pad is crucial when determining the seismic response of a free-standing vertical cylindrical cask. However, the difference in the value of the coefficient of friction is considerable between different materials.

In this paper, the seismic behavior of a free-standing vertical cylindrical cask (VCC), which has been widely used in practice, will be investigated

[1] Professor, Department of Civil Engineering, National Taiwan University
[2] Associate Researcher, National Center for Research on Earthquake Engineering
[3] Associate Researcher, National Center for Research on Earthquake Engineering
[4] Associate Researcher, National Center for Research on Earthquake Engineering

for various coefficients of friction. Firstly, a quasi-static equilibrium analysis of the cask was performed to examine the basic physics of a VCC. Then, the ANSYS/LS-DYNA code was adopted to analyze the seismic response of a dry storage facility with a VCC. A 3D finite element (FE) model consisting of a VCC and a concrete pad was established with the simulation of the nonlinear frictional contact at their interface. Artificial earthquake motions, which are compatible with the design spectra, was adopted as input motions. The characteristics of the seismic response of a VCC and the influence of the coefficient of friction at the cask/pad interface will be presented and discussed herein.

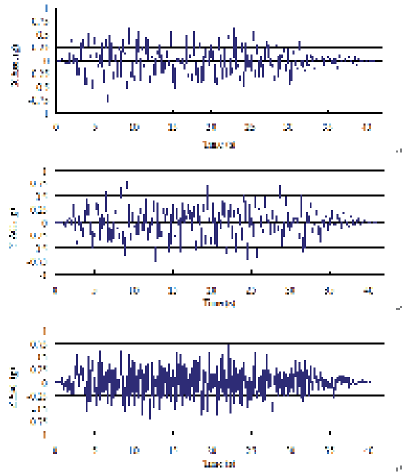

Fig. 1 Pad motions based on the design spectrum in the X, Y, and Z directions

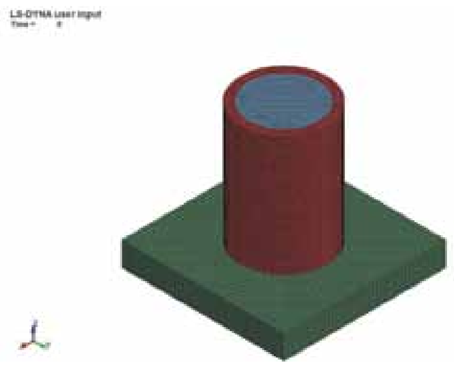

Fig. 2 Finite element model of a cask standing freely on a pad.

Analysis Model and Parameters

Although it is well known that ground motions are one of the most important factors affecting the dynamic response of a shaken system, only one set of time-histories will be specified and inputted to the pad in the current analyses. A 40 second duration artificial earthquake compatible with the design spectrum was established. This is compatible with the design response spectrum of a selected VCC project in Taiwan as shown in Fig. 1. The peak ground accelerations in the X-, Y-, and Z-directions were all scaled to 0.78 g. This is considered to be a very conservative value for this parameter.

A prototype VCC that will be used in Taiwan was selected as an example VCC. The VCC is of a cylindrical type with a diameter of 4.25 m and a height of 5.95 m. It is assumed to be standing freely on a rigid concrete pad with dimensions of 8 m × 8 m and a thickness of 1.2 m. An FE mesh of the model is shown in Fig. 2. The minimum element length was about 0.1 m and the time step for explicit time integration was 2.84×10^{-5} sec. Both of these satisfy the basic requirements for numerical accuracy and stability. In order to save computational effort, the material in the inner cylinder of the cask was assumed to be rigid (Φ3.83 m) and the outer part was assumed to be elastic concrete. Concerning the modeling of the highly nonlinear contact behavior at the interface between the cask and the pad, the "contact_automatic_single_surface" algorithm provided in the LS-DYNA code was used, and Coulomb's law of friction was adopted for the modeling of friction. The coefficients of friction chosen in this analysis were 0.2, 0.5, and 0.8

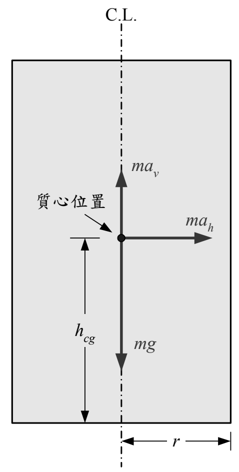

Fig. 3 Free body diagram of a free-standing cask

Fig. 3 shows the free body diagram of a cylindrical cask. The height from the cask base to the center of gravity (CG) is denoted as h_{cg}, and the radius of the cask is denoted as r. The forces applied to the cask include the gravitational force, mg, the horizontal seismic inertial force, ma_h, and the vertical seismic inertial force, ma_v; where m denotes the mass of the cask, g is the acceleration due to gravity, a_h is the horizontal ground acceleration, and a_v is the vertical ground acceleration. The more conservative case of an upward a_v is considered here, and the effective compressive normal force acting on the cask base is $m(g-a_v)$.

When the horizontal seismic inertial force on the cask exceeds the maximum static frictional force at the cask/pad interface, the cask will slide relative to the pad, i.e.,

$$ma_h \geq \mu(mg - ma_v) \;\; \Rightarrow \mu \leq \frac{a_h}{g - a_v} = a_c \qquad (1)$$

When the overturning moment generated by the horizontal seismic inertial force on the cask exceeds the stabilizing moment provided by the effective weight of the cask, one side of the cask will be lifted (rocking) against the contact point between the two bodies, i.e.,

$$ma_h h_{cg} \geq (mg - ma_v)r \;\; \Rightarrow \frac{r}{h_{cg}} \leq \frac{a_h}{g - a_v} = a_c \qquad (2)$$

For cases with $\mu > (r/h_{cg})$, the rocking motion of the cask will be induced whenever $a_c > (r/h_{cg})$. For the VCC model selected, since r=2.125 m and h_{cg}=2.975 m, the ratio of r/h_{cg} is 0.714 in this case. According to the quasi-static equilibrium analysis, this can be regarded as a borderline value of the frictional coefficient, differentiating the motion type of the cask between sliding and rocking. Therefore, the response of the cask is pure sliding without any tip-over for cases with μ = 0.2 and 0.5, while it is dominated by a rocking type motion at μ = 0.8. This can be verified via the dynamic analysis.

Seismic Responses of the VCC

For the corresponding cases, the loci of horizontal displacements at the center of the base and the center of the top of the cask are plotted in Fig. 4, in which the solid line represents the loci of horizontal displacements at the center of the base of the cask, and the dotted line represents the loci of horizontal displacements at the center of the top of the cask. For all analyzed cases, the maximum and residual translational displacements at the center of the base of the cask are summarized in Table 1. The maximum rocking angle and the maximum and residual rotational angles of the cask were also calculated and are shown in Table 1.

To characterize the response of the cask under the conditions of various coefficients of friction, the key response to be considered is the vertical (Z) displacement. From the results shown in Figs. 4 and Table 1, it can be noted that the vertical (Z) displacements at the center of the base of the cask are equal to zero for cases with μ = 0.2 and 0.5, and are not equal to zero for cases with μ = 0.8. The former means that the cask's motion type is purely sliding and the latter means that the cask's motion includes the rocking response

Table 1 Maximum and residual seismic responses of the cask

	Relative displacement (m)					Rocking angle (deg)	
μ	X		Y		Z	X-dir.	Y-dir.
	Max	Final	Max	Final	Max		
0.2	0.40	-0.12	0.40	0.03	-	-	-
0.5	0.17	0.02	-0.12	0.08	-	-	-
0.8	-0.41	0.21	-0.27	0.03	0.28	7.16	-4.90

Fig. 4(a) and 4(b) show that the loci of horizontal displacements at the center of the top of the cask coincide with those at the center of the base of the cask. Therefore, the responses of the cask are almost purely sliding with minimal rocking motion for cases with μ = 0.2 and 0.5. When μ = 0.2 and 0.5, the magnitude of the maximum horizontal displacement of the cask decreases significantly as the coefficient of friction increases. This is due to the fact that the resisting force of friction at the cask/pad interface increases with the magnitude of the coefficient of friction. However, no significant relationship between the residual displacement and the coefficient of friction was observed. Since the residual displacement is the accumulation of the dynamic response (back and forth) of the cask during the foundation excitation, it is not necessarily related to the coefficient of friction.

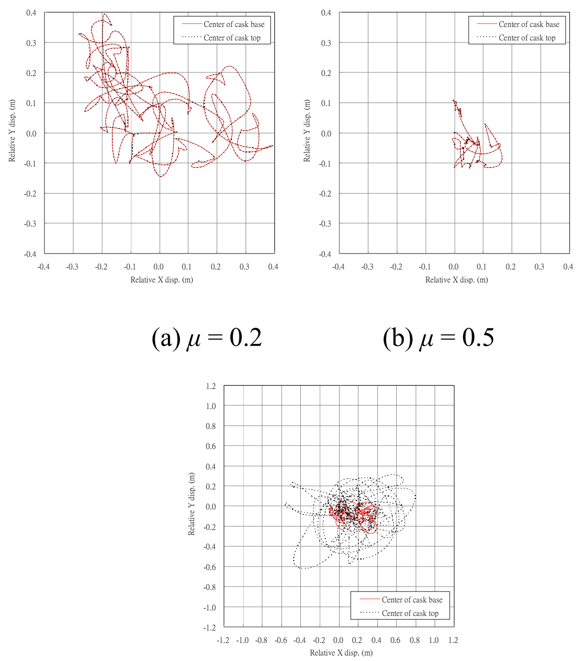

(a) μ = 0.2 (b) μ = 0.5

(c) μ = 0.8

Fig. 4 Horizontal displacement locus of the cask for μ = 0.2, 0.5 and 0.8

.

Fig. 4(c) shows the loci of horizontal displacements at the center of the top and the center of the base of the cask for the case of $\mu = 0.8$. The larger Z-displacement implies that the response of the cask was dominated by the rocking motion, yet the significant horizontal displacements may not result from sliding. The cask top experienced a much larger displacement than the base due to the rocking motion. In addition, the cask exhibited a rolling behavior following the rocking motion. That is, when the cylindrical cask was uplifted on one side, it could roll along the circumference of the cask's bottom edge.

As mentioned in the previous section, the ratio r/h_{cg} is a borderline value of the coefficient of friction that differentiates the motion type of the cask at the onset of motion between sliding and rocking from the rigid-body quasi-static equilibrium analysis. For the cask adopted in this case study, the value of r/h_{cg} was 0.714. Therefore, from the results of the dynamic analysis, the motion of the VCC during the excitation changed from a sliding to a rocking response when the coefficient of friction changed from 0.6 to 0.8.

Conclusions

Based on the results obtained in this study, some general conclusions can be drawn as follows:

1. According to the rigid-body quasi-static equilibrium analysis, the r/h_{cg} value of a vertical cylindrical cask (VCC) represents a borderline value of the coefficient of friction that differentiates the motion type of the cask at the onset of motion between sliding and rocking.
2. The results of the case study show that for $\mu = 0.2$ and 0.5, the cask response was almost purely sliding, and the maximum horizontal displacement of the VCC decreased significantly as the coefficient of friction increased.
3. For the aseismic design of a dry storage cask, it is suggested to allow the sliding motion but to prevent the rocking motion. This can be achieved by setting an appropriate coefficient of friction at the cask/pad interface

References

Toshiari Saegusa, Genki Yagawa, and Masanori Aritomi, "Topics of research and development on concrete cask storage of spent nuclear fuel," Nuclear Engineering and Design, Vol. 238, pp. 1168-1174 (2008).

Yuji Ishiyama, "Motions of Rigid Bodies and Criteria for Overturning by Earthquake Excitations," Earthquake Engineering and Structural Dynamics, Vol. 10, pp. 635-650 (1982).

Lin Yanheng and Shi Baoping, "Response of 3D Free Axisymmetrical Rigid Objects under Seismic Excitations," New Journal of Physics, arXiv:0807.2101v3 (2008).

Antonio Scalia and Mezhlum A. Sumbatyan, "Slide Rotation of Rigid Bodies subjected to a Horizontal Ground Motion," Earthquake Engineering and Structural Dynamics, Vol. 25, pp. 1139-1149 (1996).

B. G. Rabbat, M. ASCE and H. G. Russell, "Friction Coefficient of Steel on Concrete or Grout," Journal of Structural Engineering. ASCE, Vol. 111, No. 3, pp. 505-515 (1985).

Centrifuge Shaking Table Tests on the Seismic Responses of Geosynthetic Reinforced Earth Embankments

Wen-Yi Hung [1] , Yi-Zeng, Chiou[2], Jin-Hung Hwang[3], Chung-Jung Lee[4] and Jiunn-Shyang Chiou[5]

洪汶宜 [1] 邱益增 [2] 黃俊鴻 [3] 李崇正 [4] 邱俊翔 [5]

Abstract

A series of centrifuge shaking table tests are performed to study the seismic behavior of geosynthetic reinforced earth (GRE) embankments. From the test results, for an 8-m-high GRE embankment, the natural frequency is found to be about 5.7 Hz and has no significant relationships with the reinforcement material, the reinforcement arrangement, or the facing batter. The amplification of the acceleration increases with increasing elevation and with increasing frequency of the input motion. At the same elevation, the amplification inside the reinforced earth zone is found to be larger than that inside the retained soil zone.

Keywords: Centrifuge; embankment; natural frequency; amplification

Introduction

Reinforced earth is generally constructed with backfill and manufactured materials, such as metal strips, geosynthetic sheets or grids, known as reinforcements. The reinforcements sustain the forces resulting from the deformation of reinforced earth structures and external loadings. The biggest advantage of reinforced earth structures over reinforced concrete structures is in their flexibility and capacity to absorb deformation due to poor foundations and seismic loadings. A series of centrifuge modeling tests were performed by Viswanadham and Kong (2009) to investigate the effect of differential settlement in the foundation on a reinforced earth slope with a flexible facing. The advantages of geosynthetic reinforced structures were verified from the test results. It was indicated that even after inducing a differential settlement of 1.0 m in prototype dimensions, the reinforced soil structure was not found to experience a collapse failure.

In addition, observations made after the Chi-Chi earthquake in Taiwan or the Hanshin-Awaji earthquake in Japan showed that most reinforced soil structures survived without serious damage, demonstrating an earthquake-resistant capability. The seismic behaviors of reinforced earth walls and slopes were studied by Nova-Roessig and Sitar (2006) using a centrifuge shaking table. The models were subjected to maximum input accelerations of up to 1.08 g. The experimental results showed that reinforced slopes move under small input motions and that significant lateral and vertical deformations occur under strong shaking, but the distinct failure surfaces were not observed. The magnitude of the deformations is related to the backfill density, the reinforcement stiffness and spacing, and the slope inclination.

It was also found from other past studies that the design of the reinforcement, including its length, spacing, and strength, significantly affects geosynthetic reinforced earth (GRE) structures (Hu et al., 2010; Chen et al., 2007). Therefore, in this research, a series of centrifuge shaking table tests was performed in a 50 g acceleration field to investigate the effects of the reinforcement design on the seismic response of GRE embankments, including the natural frequency and the amplification of acceleration.

[1] Associate technologist, National Center for Research on Earthquake Engineering, wyhung@ncree.narl.org.tw
[2] Master, Department of Civil Engineering, National Central University, h87727@yahoo.com.tw
[3] Professor, Department of Civil Engineering, National Central University, hwangjin@ncu.edu.tw
[4] Professor, Department of Civil Engineering, National Central University, cjleeciv@ncu.edu.tw
[5] Researcher, National Center for Research on Earthquake Engineering, jschiou@ncree.narl.org.tw

Testing Equipment and Materials

This experimental work was undertaken in the centrifuge modeling laboratory at the National Central University (NCU) of Taiwan. The NCU centrifuge has a nominal radius of 3 m and a one-dimensional servo-hydraulically controlled shaker is installed in a swing basket. It has a maximum nominal shaking force of 53.4 kN with a maximum table displacement of ±6.4 mm and it operates at up to an 80 g centrifugal acceleration with a model weight of 400 kg. The operating frequency range is 0 Hz to 250 Hz. A rigid model container with inner dimensions of 767 mm × 355 mm × 400 mm (L × W × H) is used for dry soil models.

The sand used to prepare the uniform sandy model consists of fine quartz. The quartz sand is pluviated into the rigid model container and the falling height was maintained at 0.6 m to prepare the uniform models with a relative density of about 60%. Two very weak geosynthetic materials with tensile strengths, T_u, of 1.25 kN/m and 2.24 kN/m were selected to simulate the prototype reinforcement materials with strengths of 62.5 kN/m and 112.0 kN/m, respectively, in a 50 g acceleration field.

Table 1 The configurations of GRE embankment models

No.	Width (m)	Height (m)	Slope	s_v (m)	T_u (kN/m)
GREE4	18.35	8.0	1:1.0	0.8	112.0
GREE5	18.35	8.0	1:0.5	0.8	112.0
GREE6	18.35	8.0	1:0.5	0.8	62.5
GREE8	18.35	8.0	1:1.0	0.5	112.0
GREE9	18.35	8.0	1:0.5	0.5	112.0

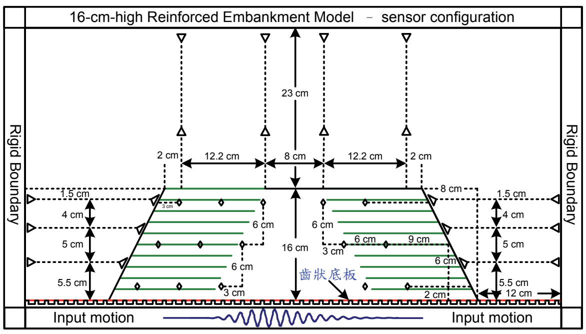

Fig. 1 The profile and the configuration of sensors for model GREE5

Model Setup and Testing Procedures

The GRE embankment models were wrapped-face with 100% coverage of reinforcement material. The purpose of this study was to investigate the effects of the reinforcement spacing, s_v, and the face inclination on the seismic response of the GRE embankment induced by different input motions. In the design of GRE embankment models, the external and internal stabilities of the structure must be ensured. Consequently, a tooth-shaped aluminum alloy plate was installed at the bottom of the rigid model container to prevent the model sliding during shaking. Above the tooth-shaped plate, the 10-mm-thick sandy foundation was firm.

The configurations of five GRE embankment models are shown in Table 1 in prototype scale. The height and the top width of the GRE embankment models were made to be 160 mm and 367 mm, respectively, to scale the model to GRE embankment prototype, which is 8-m-high and 18.35-m-wide. The reinforcement length was 0.71 times the height and the overlap length was 0.4 times the reinforcement length. Two face inclinations of 1.0:1.0 (vertical:horizontal) and 1.0:0.5 (vertical:horizontal) and two reinforcement spacings of 16 mm and 10 mm, which correspond to 0.8 m and 0.5 m in the prototype, respectively, were selected.

For instance, Figure 1 shows the profile and the configuration of the sensors for model GREE5. For each model, seven accelerometers were installed, including one fixed onto the shaking table to monitor the input motion, and two accelerometer arrays were instrumented inside the retained soil zone (A6–A4–A12) and inside the reinforced earth zone (A11–A13–A10). Eight linear variable differential transformers were placed to measure the settlement on top of the embankment and the horizontal displacement of the facing.

During the construction of the GRE embankment model, several pieces of hard Styrofoam boards were piled up in front of the model to provide lateral support. For each reinforcement layer, the reinforcement material was placed first followed by pluviating the sand to construct the retained soil and the reinforced earth zones until the desired reinforcement spacing was attained. The accelerometers were placed in their proper positions inside the model simultaneously. Then the reinforcement was wrapped to produce the facing and embedded into the backfill. This process was repeated until it reached the design height. Finally, the weight of the model was measured to check its relative density. The completed model was then put on the platform and fixed on the shaking table to start the centrifuge modeling processes.

The completed model was accelerated stepwise to 50 g, with an increment of acceleration in each step of 10 g. The model was maintained and preserved for 3 minutes at each step to ensure the consolidation of the sand model at the current overburden pressure. At 50 g, the model was then excited with a series of one-dimensional seismic events. First, white noise input motion was applied to detect the natural frequency of the GRE embankment system. Next, two series of seismic events with frequencies of 1 Hz and 4.8 Hz (in the prototype) were applied to the models with a sinusoidal input motion consisting of 15 cycles.

Natural Frequency of the GRE Embankment

The acceleration histories obtained from the white noise input motion were adopted and the Fast Fourier Transform was used to transfer the data to the frequency domain. Then, the Fourier spectrum of each accelerometer was divided by that of the base input motions to create transfer function, which gives the amplification of the acceleration at different frequencies. The frequency at the first peak of the transfer function was at the natural frequency of the GRE embankment system. Based on these calculations, it was found that the natural frequency for all the models was about 5.7 Hz, meaning that the reinforcement spacing and the face inclination did not affect the natural frequency of the GRE embankment. Thus, the natural frequency for an 8-m-high GRE embankment is also about 5.7 Hz. On the other hand, the transfer function at the 1 Hz input motions for different elevations were close to 1, illustrating that the acceleration was not amplified. At a 4.8 Hz frequency, significantly different values of the transfer functions were observed, leading to different amplifications of acceleration at varying elevations. In the following section, the amplifications of accelerations are calculated directly from the acceleration responses of different seismic events.

Amplification of Acceleration of the GRE Embankment

There are 30 data points for each accelerometer in each seismic event, including the positive and negative peaks of the 15 cycles. The peak values of input motion and the measurements by the accelerometer are converted to absolute values and plotted in Figures 2, 3, and 4 according to the top, middle, and bottom of the GRE embankment, respectively. Figures 2(a) and 2(b) indicate the relationships between the base input motion and the responses of acceleration at the top of the retained soil zone and reinforced earth zone, respectively. In these figures, the circular, triangular, diamond and inverted triangular symbols represent the peak accelerations for the models GREE4, GREE5, GREE8, and GREE9, respectively. The hollow and solid symbols represent the input motions of 1 Hz and 4.8 Hz, respectively. If the symbols are located at the left of the solid black line, this means that the acceleration was amplified. By comparing Figures 2, 3, and 4, it can be seen that the trends of all the hollow symbols are almost parallel to the solid line. Consequently, the different reinforcement spacing and the face inclination do not seem to affect the amplification of the acceleration significantly for GRE embankments subjected to 1 Hz seismic loadings.

On the other hand, when comparing Figures 2(a), 3(a), and 4(a), or Figures 2(b), 3(b), and 4(b), it can be seen that the accelerations are amplified with increasing elevations inside either the retained soil zone or the reinforced earth zone for GRE embankments subjected to 4.8 Hz seismic loadings. Nevertheless, the amplifications inside the reinforced earth zone were slightly larger than those inside the retained earth zone. There are several solid symbols located in the intermediate zone surrounded by a red ellipse in Figures 2(a), 2(b), 3(a), and 3(b). These are the first peak accelerations of seismic events with a frequency of 4.8 Hz and are usually smaller than the peak values in the other cycles. Aside from the data points of the first cycle, the trend for all solid symbols seems to lie on a line that is steeper than the black line. This shows that the seismic response of the GRE embankment is not related to the reinforcement spacing and the face inclination.

The measurements of each seismic event are divided into the responses of the retained soil zone and the reinforced earth zone, as shown in Figures 5 and 6, respectively. Figure 5 shows the relationships between the elevation normalized by height and the mean values of the amplification for the retained soil zone. The hollow symbols in Figures 2, 3, and 4 are graded into three input motions with a frequency of 1 Hz. These grades are relative: small, middle, and large accelerations which correspond to mean accelerations of 0.056 g, 0.111 g and 0.199 g labeled in the figures as hollow circles, squares, and triangles, respectively. It can be seen that the mean amplifications increase slightly with increasing elevation. In addition, a smaller input acceleration seems to lead to larger amplification. The maximum amplification was found to be about 1.3 at the top of the retained soil zone for an 8-m-high GRE embankment subjected to 1 Hz at an approximately 0.056 g seismic loading. The solid symbols in Figures 2, 3, and 4 are also graded into three input motions with a frequency of 4.8 Hz. The mean accelerations are 0.015 g, 0.037 g, and 0.086 g and are labeled by solid circles, squares, and triangles, respectively. It can be observed that, in these tests, the mean amplification increases dramatically with increasing elevation when the input motion frequency was raised to 4.8 Hz. The amplification at the top was about 4.5 for the input motion of 0.037 g, which is larger than that for the input motion of 0.086 g.

Figure 6 shows the relationships between the elevation normalized by height and the mean values of the amplification for the reinforced earth zone. It also can be seen that the mean amplifications increase slightly with increasing elevation. The smaller input acceleration leads to the larger amplification with a maximum value of 1.4 at the top of the reinforced earth zone for an 8-m-high GRE embankment subjected to 1 Hz and 0.056 g seismic loadings. The mean amplification increases dramatically with increasing elevation for input motions with a frequency of 4.8 Hz. The maximum amplification at the top is about 5.5 for the input motion of 0.037 g.

Consequently, if a constant amplification of acceleration is used to design a GRE embankment, the results would underestimate the seismic behavior at the top portion of the GRE embankment as the frequency of the input motion is close to the natural frequency of system.

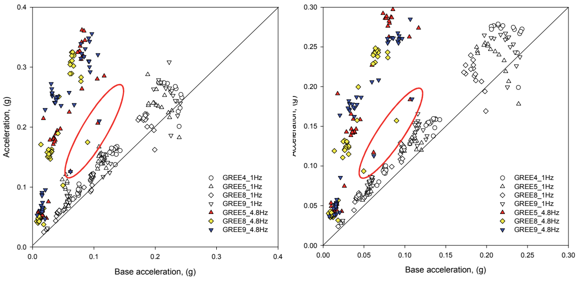

Fig. 2 The relationships of the base input motion and the acceleration measured at the top of (a) retained soil zone; (b) reinforced zone

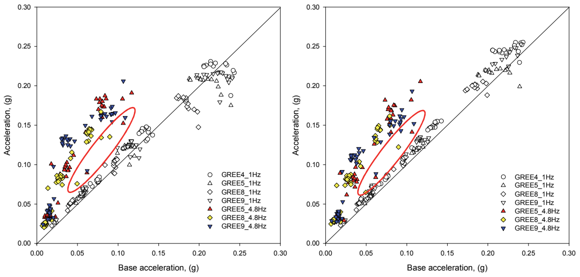

Fig. 3 The relationships of the base input motion and the acceleration measured at the medium of (a) retained soil zone; (b) reinforced zone

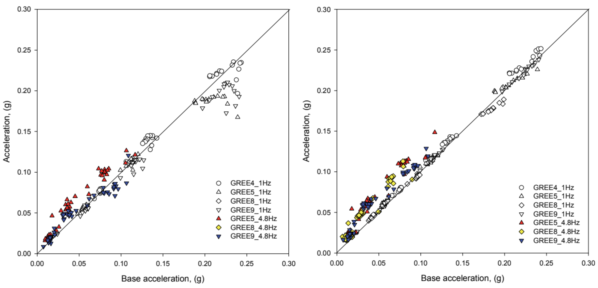

Fig. 4 The relationships of the base input motion and the acceleration measured at the bottom of (a) retained soil zone; (b) reinforced zone

Conclusions

A series of centrifuge shaking table tests was performed to investigate the seismic response of geosynthetic reinforced earth (GRE) embankment with different reinforcement spacing and face inclination. The test results show that for an 8 m-high GRE embankment, the natural frequency is about 5.7Hz and has no significant relationships with the reinforcement material, the reinforcement arrangement and the batter of facing. The amplification of acceleration increases with the increasing elevation and with the increasing frequency of input motion. At the same elevation, the amplification inside the reinforced earth zone is larger than that inside the retained soil zone. It tells that the uniform distribution of amplification with height assumed in the current design guidelines may underestimate that at top of GRE embankment and result in overestimating the local stability.

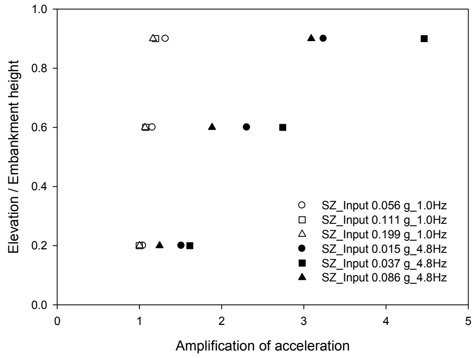

Fig. 5 The amplification of acceleration inside the retained soil zone for different input motions

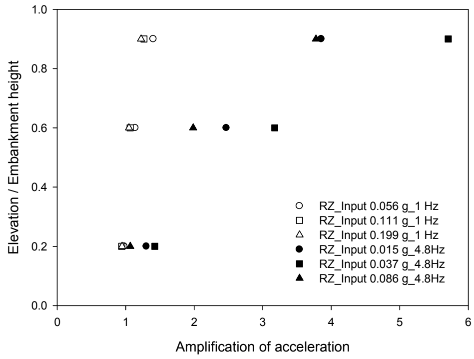

Fig. 6 The amplification of acceleration inside the reinforced zone for different input motions

References

Chen, H.T., Hung, W.Y., Chang, C.C., Chen, Y.J and Lee, C.J, (2007) "Centrifuge modeling test of a geotextile-reinforced wall with a very wet clayey backfill." *Geotextiles and Geomembranes*, 25(6), pp. 346–359.

Hu, Y., Zhang, G., and Lee, C.F., (2010) "Centrifuge modeling of geotextile-reinforced cohesive slopes," *Geotextiles and Geomembranes*, 28, pp.12-22.

Nova-Roessig, L., and Sitar, N., (2006) "Centrifuge model studies of the seismic response of reinforced soil slope," *Journal of Geotechnical and Geoenvironmental Engineering*, ASCE, 132(3), pp.388-400.

Viswanadham, B.V.S., and Kong, D., (2009) "Centrifuge modeling of geotextile-reinforced slopes subjected to differential settlements," *Geotextiles and Geomembranes*, 27, pp.77-88.

Earthquake Source Parameters of Active Faults for Seismic Potential Assessment in the Chianan Region of Taiwan

Che-Min Lin[1], Tao-Ming Chang[2], Hung-Hao Hsieh[3], Yi-Zen Chang[4], Chun-Hsiang Kuo[5], and Kuo-Liang Wen[6]

林哲民 [1]、張道明 [2]、謝宏灝 [3]、張議仁 [4]、郭俊翔 [5]、溫國樑 [6]

Abstract

The Chiayi and Tainan (Chianan) regions in southwestern Taiwan are scattered by several active faults that have induced massive earthquakes. The seismicity is generally quite high and widespread in this region. The potential of disastrous earthquakes is expected to be high in the near future. Therefore, the present study aims to monitor micro-earthquakes activity in the Chianan region for three years. The monitoring data will provide important information about recent seismicity and the source parameters of active faults, which are indispensable in assessing the seismic potential for the Chianan region. Twenty-one highly-sensitive broadband stations were installed to develop a regional network covering the Chiayi County and City, Tainan City, and adjacent foothills, as well as the adjoining major seismogenic area. Almost 1,200 earthquakes were observed by this network in the first two years. The data were processed and analyzed periodically to evaluate the seismicity of the Chianan region. The earthquake relocations and focal mechanism solutions were also studied to understand the probable seismogenic structures and source ruptures.

Keywords: earthquake monitoring, active fault, earthquake location, focal mechanism

Introduction

The Chiayi and Tainan (Chianan) region in southwestern Taiwan has witnessed numerous serious disasters caused by massive earthquakes, including the Meishan Earthquake in 1906, Chungpu Earthquake in 1941, Hsinhua Earthquake in 1946, Paiho Earthquake in 1964, Rueyli Earthquake in 1998, and the Chiayi Earthquake in 1999, all occurring within the last century. More recently, the Jiasian Earthquake occurred in Kaohsiung with a magnitude of M_L 6.7 and also caused damage to some buildings in the Chianan region. According to the paleoseismological research of the National Science Council (NSC), the Meishan Fault in Chiayi has the highest short-term probability of experiencing a characteristic earthquake amongst all active category one faults in Taiwan. The probabilities of earthquakes from faults with magnitudes of 7 or more within 10 and 50 years are respectively 9.75 % and 45 %. Additionally, there are still four other active category one faults of the first category and four category two faults rooted in the Chianan region. Since potential disastrous earthquakes in the region are expected in the near future, it is imperative to understand the characteristics of the active faults in the Chianan region.

Based on the Central Weather Bureau (CWB) earthquake catalog and the micro-earthquake monitoring in the Southern Taiwan Science Park from the end of 2006 to 2010 (Lin et al., 2010), the seismicity was widely distributed over the Chianan region. The earthquakes were not restricted only to the faults but occurred frequently between the foothills on the east side and the coastal plain on the west. The

1 Associate Researcher, National Center for Research on Earthquake Engineering, cmlin@ncree.narl.org.tw
2 Associate Researcher, National Center for Research on Earthquake Engineering, tmchang@ncree.narl.org.tw
3 Assistant Researcher, National Center for Research on Earthquake Engineering, hhhsieh@ncree.narl.org.tw
4 Assistant Researcher, National Center for Research on Earthquake Engineering, yzchang@ncree.narl.org.tw
5 Associate Researcher, National Center for Research on Earthquake Engineering, chkuo@ncree.narl.org.tw
6 Professor, Dep. of Earth Science, National Central University and Division Manager, National Center for Research on Earthquake Engineering, wenkl@ncree.narl.org.tw

western seismicity beneath the coastal plain was thought to result from the tectonic escape behavior of plate collision. However, the thick alluvial cover on the surface limits understanding of the underground seismogenic structures.

Therefore, this study planned to monitor micro-earthquakes in the Chianan region for three years. The objects that were monitored were not only the active faults, but also blind faults and other seismogenic structures beneath the wide coastal plain. A study of micro-earthquakes will help researchers to understand the probable fault planes and rupture mechanisms of major faults. The source parameters of characteristic earthquakes will be estimated to assess the seismic potential of the Chianan region. The preliminary results of the monitoring in the first two years will be discussed in this article.

Micro-Earthquake Monitoring Network in the Chianan Region

The development and planning of the micro-earthquake monitoring network in the Chianan region was based on the distributions of historical earthquakes and major fault lines. Twenty-one stations were installed to develop the network in the second half of 2011. In addition, several real-time stations were also installed in the Chianan region. Each real-time station was installed with a broadband velocimeter and an accelerometer. The combined monitoring data provides complete ground motion information for the region.

Figure 1 shows the distributions of all seismic stations, including the National Center for Research on Earthquake Engineering (NCREE) strong-motion and micro-earthquake networks, used in this study. Because the seismicity was widely distributed over the Chianan region, the integrated network covered the Chiayi County and City, Tainan City, and adjacent foothills over which the faults were spread. The network provides a complete ability to monitor the seismicity for research on the characteristics of faults and seismic sources in the Chianan region.

This study benefitted from the rich experience that the group acquired conducting installations and monitoring of micro-earthquakes in the Science Parks over the past few years. A standard operating procedure was created to avoid artificial noise. The station locations were all chosen with caution and the background noise was continuously accounted for to ensure the data quality. Then, the seismometer, set in a bucket, was buried at a depth of at least 1 m. To increase the quality of the incident seismic waves, a cement foundation sat on the bottom of the bucket and several long nails were used to fix the bucket in the bottom of the hole. In doing so, the rims of the bucket, in which the seismometer was placed, were able to avoid touching the surrounding soils of the hole and decrease the surface noise. The moisture proofing and heat insulation aided in keeping a stable monitoring operation.

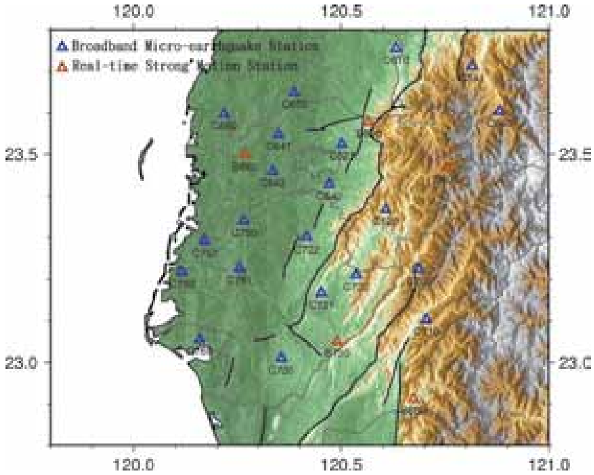

Fig. 1 The distribution of the monitoring networks in the Chianan region

Because this project concentrated on small earthquakes with magnitude lower than 3 in order to observe potential insignificant tremors related to the faults, high-sensitivity broadband seismometers (CMG-6TD, Guralp Systems Ltd) were used in the micro-earthquake network to collect the weak seismic waves. The recording was carried out continuously with a sampling rate of 100 points per second to avoid missing any micro-earthquakes. A set of solar energy equipment and a GPS antenna were installed at each station to supply electricity and correct the internal clock of the seismometer. The photos in Fig. 2 show the installation set up of a station in the field. For a real-time strong motion station, a broadband seismometer and an extra accelerometer (Etna, Kinemetrics), which was installed in a FRP station, were set up together.

Fig. 2 Photos of the micro-earthquake monitoring stations

Data Processing

The data processing was based on a program developed by NCREE for the micro-earthquake monitoring network (Chang, 2009). The data conversion, earthquake selection, arrival time picking and earthquake location are all included in the program. The preliminary location for each earthquake was determined using the program HYPO 71 (Lee and Lahr, 1972) to estimate the origin time, epicenter location, focal depth and duration magnitudes (M_d) based on the arrival times of the P- and S-waves. Every two months, the data were collated and processed to locate any observed micro-earthquakes. The monthly micro-earthquake activity was compared against the CWB seismic catalog to assess the current status and any variation in the seismicity in the Chianan region.

To reduce location errors, a double-difference hypocenter location program (hypoDD) was used to relocate the earthquakes observed by the network. This program incorporates ordinary absolute travel-time measurements and cross-correlation P- and S-wave differential travel-time measurements to determine high-resolution hypocenter locations for an earthquake sequence. The location method collapses diffuse locations into sharp images of seismicity and reveals seismogenic structures.

Micro-earthquake Activity

Figure 3 shows the distribution of almost 1200 micro-earthquakes located by the Chianan network before November, 2012. The micro-earthquakes observed this year exhibited a widespread and frequent distribution within the monitoring scope of the network, as expected. In the northern part of the monitoring region, the Chiayi region, the earthquakes concentrated in the eastern side of the Tachienshan and Chukou Faults. Some earthquakes also took place east of Chiayi City. Meanwhile, the seismicity was quiet near the Meishan and Hsinhua Faults, which were dislocated and have induced destructive earthquakes in the past. In Tainan City, in the southern part of the region, high seismicity was heavily located along the Chukou, Muchiliao, and Liuchia Faults and extended to the southeast of the northern Chishan Fault. Earthquakes occurred on both sides of these faults and were uniformly concentrated along the fault traces to form a wide NW–SE trending seismic zone. The seismic zone extends to the border between Kaohsiung and Taitung. The high seismicity may result from a broken local structure.

The mainshock region of the Jiasian earthquake, which occurred on 3rd March 2010, in the south of the network continued to induce small earthquakes. The small earthquakes show a NW–SE trend from the middle of the Chishan Fault that crosses the Liukuei and Chaochou Faults. It indicated that the seismogenic structure of the Jiasian earthquake is still active to release the tectonic stress.

Some 368 earthquakes were relocated by hypoDD and are shown in Fig. 4. There are two obvious lines of relocated earthquakes, including the seismicity along the east side of the Chukou Fault and the mainshock region, which has just been discussed. The Chukou Fault is an active thrust category one fault. The revised length of this fault is 28 km. It connects with the Tachienshan Fault at the northern end. The original southern part of the Chukou Fault, with the length of 48 km, has been renamed as the Lunghou Fault and is believed to be inactive. The east side of the Chukou and Lunghou Faults shows dense seismicity in comparison to the west side. The earthquake linearity begins at the northern end of the Chukou Fault and stops at the Zengwun River at southern Lunghou fault.

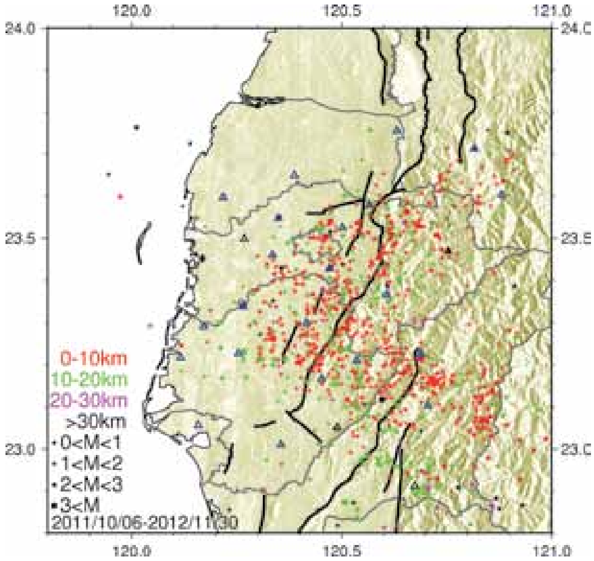

Fig. 3 The earthquakes located by the Chianan micro-earthquake monitoring network before November, 2012

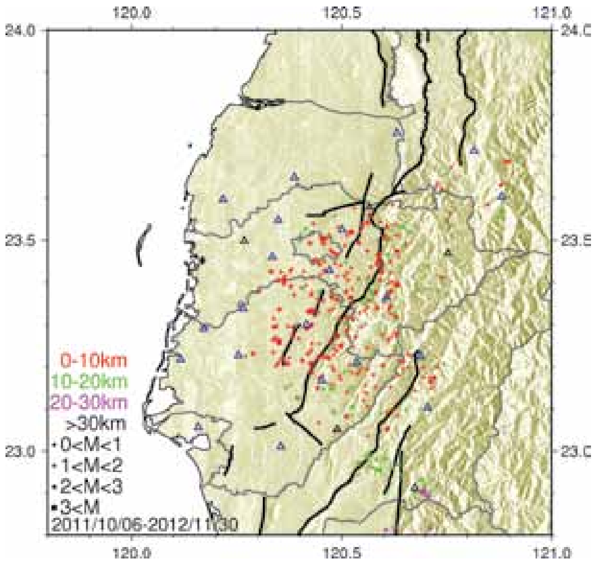

Fig. 4 Double-difference locations of earthquakes

Furthermore, a M_L 4.2 earthquake occurred at the eastern side of the northern end of the Chukou Fault on 18th January 2012 (Fig. 5). The Chianan micro-earthquake monitoring network observed some aftershocks over the next few days. The mainshock focal mechanism and the double-difference hypocenter relocations of the aftershocks are shown in Fig. 6. An E–W cross-section view of the hypocenters is shown in Fig. 7. The relocated aftershocks indicate an E–W–striking source rupture plane dipping toward the east with a high angle. The rupture plane agrees with the mainshock focal mechanism. The upward extension of the plane is close to the fault trace of the Chukou Fault on the surface. These verify that the M_L 4.2 earthquake and its aftershocks were induced by the partial activity of the Chukou Fault.

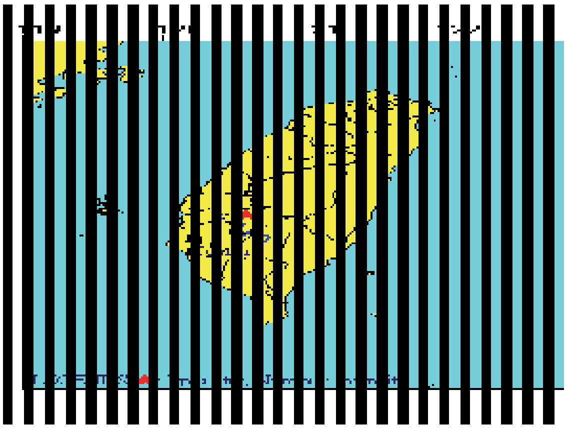

Fig. 5 The CWB report for the M_L 4.2 earthquake that occurred on 18th January 2012

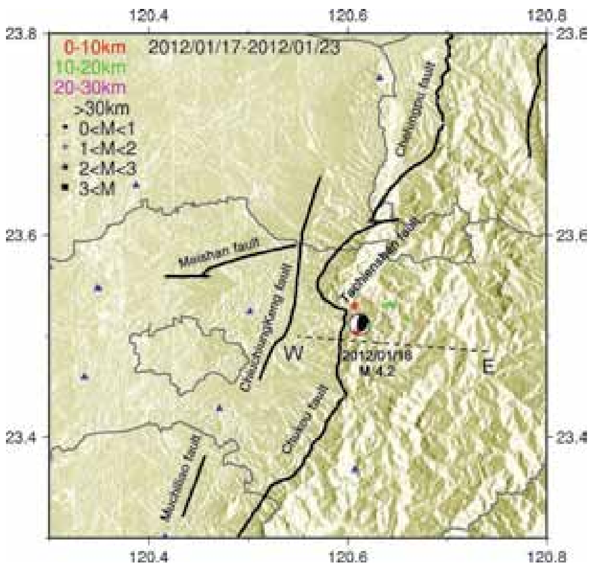

Fig. 6 The CWB mainshock focal mechanism and aftershocks, relocated by this study, of the 18th January 2012 M_L 4.2 earthquake.

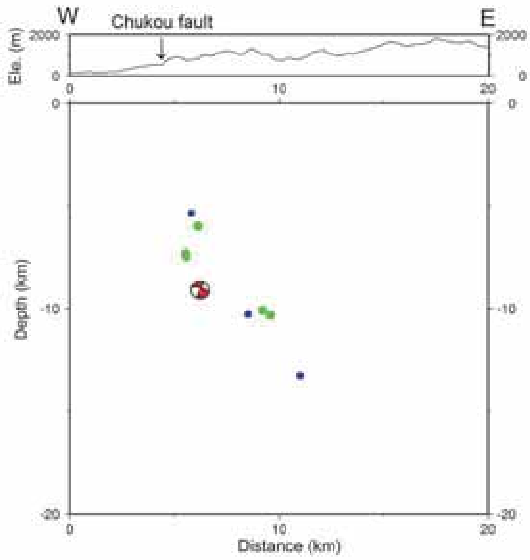

Fig. 7 The E–W cross-section of the dashed line in Fig. 6

Conclusions

The establishment of the Chianan micro-earthquake monitoring network has been accomplished for long-term, high-resolution, seismic monitoring. The network is currently able to detect abnormal seismicity in order to achieve the goals of disaster prevention. The earthquake relocations and the focal mechanism solutions were also studied to understand the seismogenic structures and source ruptures in the region. The monitoring data will provide important information on recent seismicity and the source parameters of active faults that will be indispensable in assessing the seismic potential for the Chianan region.

References

Chang, T. M. (2009), “Earthquake data processing system installation and using guide”, NCREE Rep., NCREE-09-066. (In Chinese)

Lee, W.H.K. and Lahe, J. C. (1972), “Hypo71：A computer program for determining hypocenter, magnitude, and first motion pattern for local earthquakes”, USGS open file Rep., 100pp.

Lin, C. M., Chang, T. M., Wen, K. L., Hsienh, H. H., Chen, A. B., Chang, L. C., and Kuo, C. H. (2010), “Micro-Earthquake Monitoring of Science Parks in Taiwan”, NCREE Rep., NCREE-10-020. (In Chinese)

Waldhauser, F. and Ellsworth, W. L. (2000), "A double-difference earthquake location Algorithm: method and application to the northern Hayward fault, California", Bull. Seism. Soc. Am., 90, 1353-1368.

Analysis of Site Effects using Microtremor in Kaohsiung and Pingtung

Chun-Hsiang Kuo[1], Kuo-Liang Wen[2], Che-Min Lin[3], and Hung-Hao Hsieh[4]

郭俊翔 [1]、溫國樑 [2]、林哲民 [3]、謝宏灝 [4]

Abstract

Microtremor is one of noninvasive methods which are usually used to estimate site effects. The Engineering Geological Database for TSMIP (EGDT) was used in this study as well as measured microtremor at free-field strong motion stations in Kaohsiung and Pingtung to analyze site effects. The dominant frequencies of the Horizontal to Vertical Spectral Ratio (HVSR) of microtremor were proportional to the Vs30 value. The stations considered in this study are classified according to the Building Seismic Safety Council (BSSC). The Vs30 values indicate that differences exist between shear wave velocities (Vs) in the shallow part of thick sediments at stations of class D and E, but this is difficult to estimate using HVSR. The main advantage of HVSR is its ability to detect discontinuities in velocities such as the interfaces of engineering bedrock and seismic bedrock. Most of the strong motion stations are located in plane areas and are classified as class D, showing no significant variation in Vs at depths. Stations of class C are mainly distributed in piedmonts and show a larger variation in their Vs values. Vs values at class B stations are relatively low; only one station in this study had a Vs30 value higher than 1000 m/s. Two stations from the total 62 drilled stations in this area are classified as class E. The distribution pattern of dominant frequencies was found to be comparable with the Vs30 map provided by the EGDT. The dominant frequency was lower than 2 Hz in the plane area, over 4 Hz in the mountains, and lower than 1 Hz for several near the coast. One exception was the station labeled KAU003 which had a coastal location and a dominant frequency of over 10 Hz. This exception is due to the limestone geology at this station. The similarity between the dominant frequency and Vs30 maps demonstrates that HVSR can recognize different seismic site conditions by indicating changes in sedimentary depths.

Keywords: HVSR, microtremor, free-field strong motion stations, S-wave velocity, site classification

Introduction

The so called site effect is the study of seismic wave amplification by local unconsolidated sediments at specific frequencies during strong ground motions. It is an important consideration in both seismology and earthquake engineering. The fact that different seismic site conditions are able to cause varied site effects was first recognized in the 19th century (Milne, 1898). It was noted that “it is an easy matter to select two stations within 1000 feet of each other where the average range of horizontal motion at the one station shall be five times, and even ten times, greater than it is at the other”. This indicates that the site effect can be evident even at two nearby stations.

Microtremors are caused by various natural and artificial signals. These signals exist perpetually and thus the time of measurements is very short in comparison with that for earthquakes. After Nakamura (1989) proposed the HVSR method, microtremor became a popular tool to assess site response to

[1] Associate Researcher, National Center for Research on Earthquake Engineering, chkuo@ncree.narl.org.tw
[2] Professor, Dep. of Earth Science, National Central University and Division Manager, National Center for Research on Earthquake Engineering, wenkl@ncree.narl.org.tw
[3] Associate Researcher, National Center for Research on Earthquake Engineering, cmlin@ncree.narl.org.tw
[4] Assistant Researcher, National Center for Research on Earthquake Engineering, hhhsieh@ncree.narl.org.tw

ground motions, i.e., the resonance frequency and amplification factor at a specific site. The EGDT was constructed by the NCREE and CWB, and includes logging data at over 400 stations. The Vs30 data and site classification of the drilled stations has also been accomplished (Kuo et al., 2011; 2012) according to the criteria of BSSC (2001). The site classification is a pre-requisite for the present study of developing HVSR models for different seismic site conditions in this study.

In this study, microtremors were measured at 74 free-field TSMIP stations in Kaohsiung and Pingtung (Fig. 1). Old data from the EGDT in the area was reviewed, the Vs30 of KAU048 was corrected, and the site was reclassified from class E to class D. The Vs30 value of the station KAU086 was derived from the N-value and was classified as class D. Finally, the Vs30 data for 62 stations in the area was used in this study. This included 6 stations of class B, 10 stations of class C, 44 stations of class D, and 2 stations of class E.

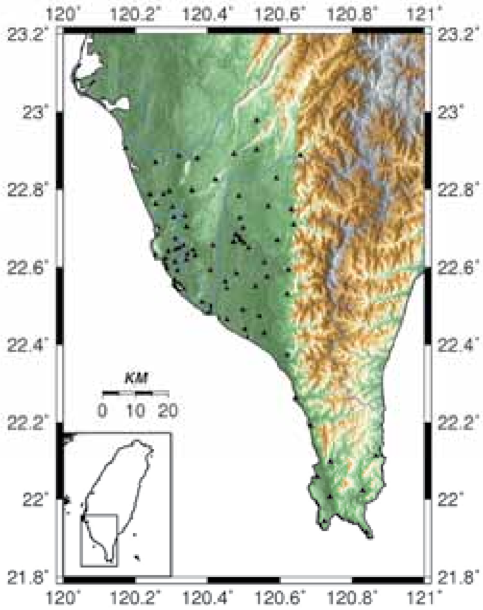

Fig. 1 Distribution of the measured stations (black triangles) in the KaoPing area

Microtremor Measurements and Data Processing

A SAMTAC-801B (recorder) and a VSE311C (sensor) manufactured by Tokyo Sokushin were the instruments used in the study. The sampling rate was 200 points per second and the recording period was 18 minutes for each measurement. The microtremor measurements were located at the side of each station to ensure that the geological conditions were identical. The instrumental response was eliminated in the HVSR procedure. Multi-windows with a length of 8192 points were utilized to partition the microtremor recordings, and a 6% cosine taper was implemented at both ends of each window. The recordings should be checked so that the windows contaminated by unusual noise can be deleted in advance; however, the number of selected windows should be more than 20 to make sure that the averaged result will be stable. A geometric mean of the horizontal Fourier spectra was calculated, smoothed 5 times, and then divided by the smoothed vertical Fourier spectrum to derive a single HVSR. After averaging the single HVSR of each window, the mean HVSR at a station was finally derived.

Properties of Microtremors

In the studied area, most of the strong motion stations are located in plane area and are classified as class D without significant variation in Vs at depths. Stations of class C are mainly distributed in piedmonts with larger variations in Vs. Class B stations have relatively low velocities; only one station has a Vs30 higher than 1000 m/s (Fig. 2).

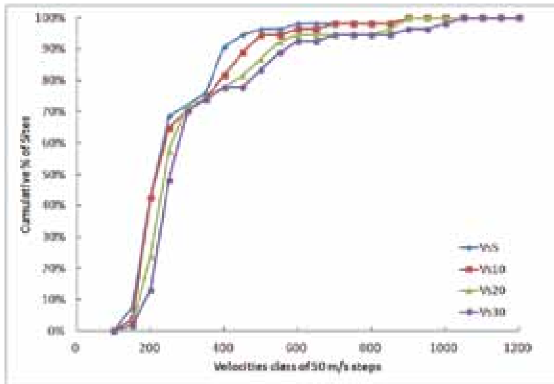

Fig. 2 Cumulative percentage of sites in velocity steps of 50 m/s

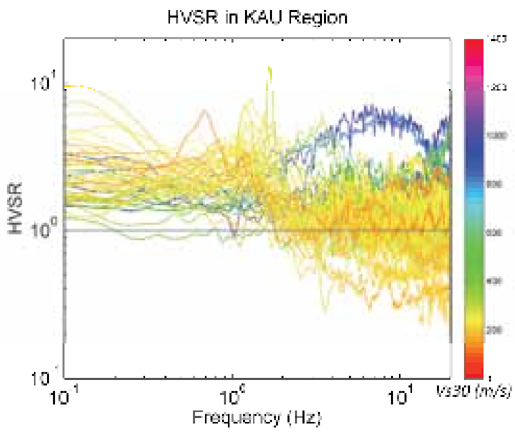

Fig. 3 HVSR of the 61 measured stations at different seismic site conditions with different colors corresponding to Vs30

HVSRs at the 61 strong motion stations were derived following the standard data processing steps introduced in the above section. The HVSRs were plotted using different colors according to the Vs30 values from logging data (Fig. 3). The dominant frequencies increased with Vs30. Moreover, these HVSRs were categorized into classes of B, C, D, and E according to the site classification of Kuo et al. (2011; 2012); in addition, two stations were reclassified by N-value as explained above (Fig. 4). The similarity of HVSRs in each class is consistent and the differences between each class are also quite clear.

Stations in class B are situated on hard rocks or sometimes covered with a thin regolith and therefore the dominant frequencies of HVSR are unremarkable or relatively higher than those at other stations. The stations of class C, which are situated on soft rocks or stiff soils, have obvious amplification at comparatively lower resonant frequencies than those of class B. The HVSRs of classes D and E are evidently amplified at relatively lower resonant frequencies.

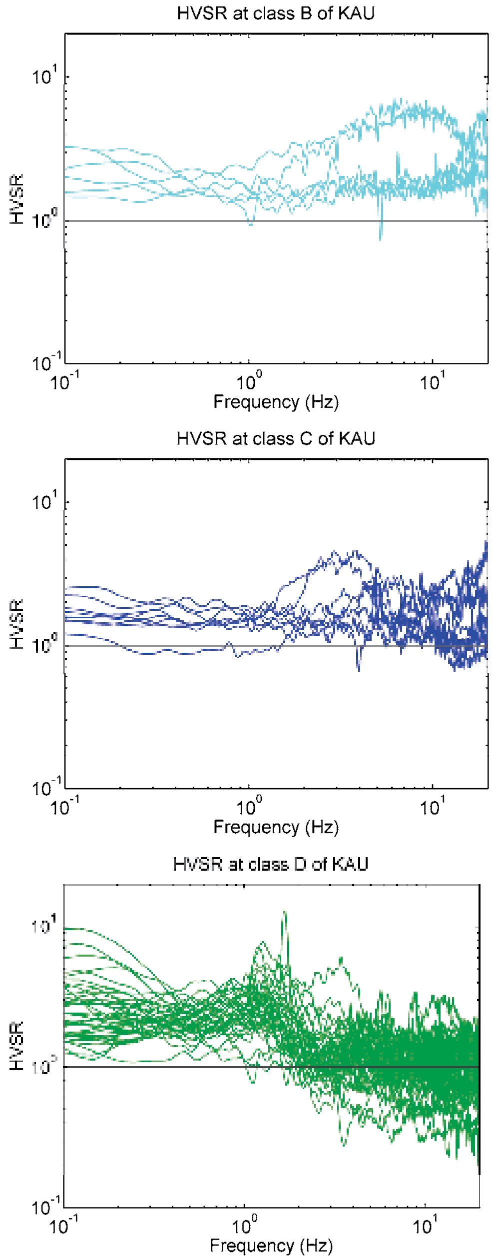

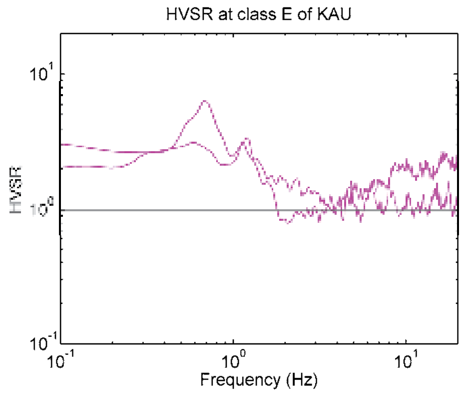

Fig. 4 The categorized HVSR curves according to logging data. From top to bottom, they are class B, class C, class D, and class E

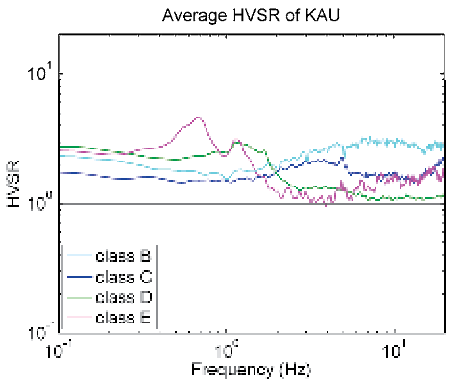

Fig. 5 Averaged HVSRs of each class

Additionally, Fig. 4 also shows the phenomenon of "deamplification", which could be observed in many of the HVSR curves in class D, class E, and several class C (Kuo et al., 2013).

Fig. 5 shows the average HVSR of the four classes. In this figure, the difference in shape and dominant frequencies are very clear. However, the HVSR of class E was only available at two stations; therefore the average HVSR in this class may not be very reliable. The deamplification of HVSRs was also averaged but cannot be seen in Fig. 5. However, the trend of decreasing ratios is still apparent in the average curves of class D and E.

Dominant frequency and Vs30 maps

The dominant frequencies of the microtremor HVSRs are proportional to the measured Vs30 values in the KaoPing area as shown in Fig. 6. Our recent study (Kuo et al., 2013) in the Taipei area showed the outstanding reliability of site classification using HVSRs of microtremor. This approach analyzed the similarity of HVSRs between the site of interest and the average HVSRs of each class using the Spearman's rank correlation coefficient as well as adopting the dominant frequency, deamplification, and relative amplification as weightings to assess the site class of a station. The accuracy of this approach is better than previous results using surface geology parameters.

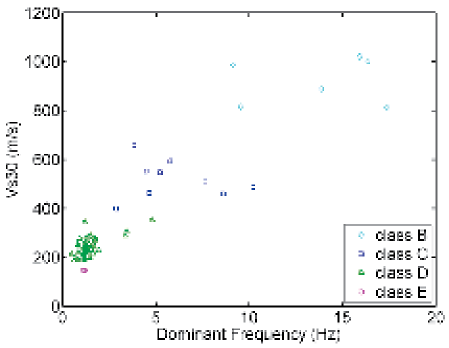

Fig. 6 The correlation between Vs30 and the dominant frequency

Conclusions

This study conducted microtremor measurements in Kaohsiung and Pingtung, and considered the EGDT logging data to analyze the site effects. Fig. 7 shows the distribution of the dominant frequencies of microtremor at 74 measured KAU stations. The pattern is comparable with the surface geology in Fig. 1. The dominant frequency was lower than 2 Hz in the plane area, over 4 Hz in the mountains, and lower than 1 Hz for several near the coast. One exception is station KAU003 that is located near the coast but had a dominant frequency of over 10 Hz. The geology at the station is mainly limestone with higher velocity characteristics.

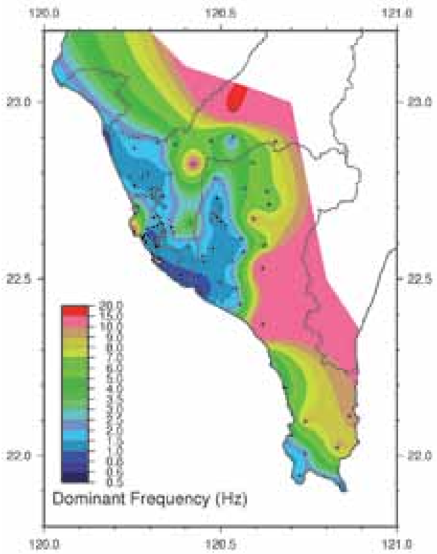

Fig. 7 Dominant frequency map from 74 measured KAU stations

The Vs30 map (Fig. 8) in this area was plotted using the results of Kuo et al. (2012). However, it also includes the stations in Tainan and Taitung. It also displays similarities to the distribution pattern in Fig. 7, indicating that the dominant frequencies of microtremor are able to detect the variation in the main interface of different velocities. When the sedimentary depth of a site is less than 30 meters, it may be class B or C; on the contrary, when the sedimentary depth becomes larger than 30 meters, it may be class D or E. The HVSRs indicate several stations with dominant frequencies lower than 1 Hz near the coast. This may be caused by very thick sediments in this region and also demonstrates a better recognition than Vs30 for deeper interfaces.

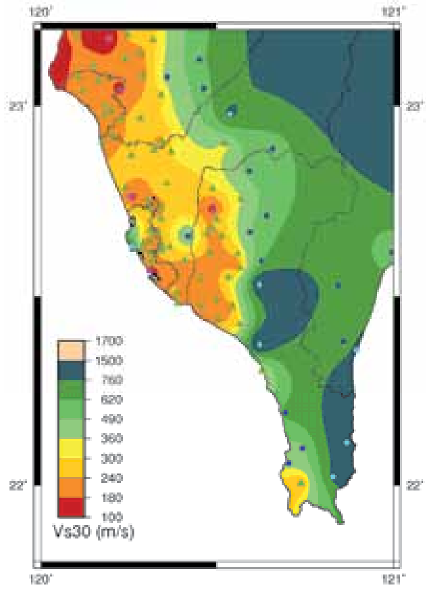

Fig. 8 Vs30 map derived from the EGDT results

References

Building Seismic Safety Council, BSSC (2001), "NEHRP Recommended Provisions for Seismic Regulations for New Buildings and Other Structures", Washington, DC.

Kuo, C. H., K. L. Wen, H. H. Hsieh, C. M. Lin, and T. M. Chang (2011), "Characteristics of Near-Surface S-wave Velocity", National Center for Research on Earthquake Engineering, NCREE-11-022, 82 p. (In Chinese)

Kuo, C.H., Wen, K.L., Hsieh, H.H., Lin, C.M., Chang, T.M., and Kuo, K.W. (2012), "Site Classification and Vs30 estimation of free-field TSMIP stations using the logging data of EGDT", *Engineering Geology*.

Kuo, C. H., Wen, K. L., Lin, C. M., Huang, J. Y., and Chang, T. M. (2013), "Analysis of HVSR of Microtremor on Different Seismic Site Conditions", *10CUEE Conference Proceedings*, 151-157, Tokyo, Japan.

Milne, J. (1898), Seismology. London, K. Paul, Trench, Trubner & co., ltd. 320 p.

Nakamura, Y. (1989), "A method for dynamic characteristics estimation of subsurface using microtremor on the ground surface", *Quarterly Report of Railway Technical Research Institute*, 30 (1), 25-33.

Ground Motion Selection for Engineering Applications

Hsun-Jen Liu[1] , Wen-Yu Jean[2] , and Yu-Wen Chang[3]

劉勛仁 [1]、簡文郁 [2]、張毓文 [3]

Abstract

In practice, for new structures of major importance (rock-filled dams, nuclear power plants), complexity (soil-structure systems, irregular buildings), inelasticity and geometrical nonlinearity (base-isolated structures), dynamic time-history analysis is very beneficial for obtaining inelastic structural responses that are close to reality. In the past, dynamic time-history analysis frequently used records from significant earthquakes, such as El Centro (1940), Kobe (1995), and Chi-Chi (1999), or used artificial records based on random vibration theory. During the last decade, however, due to experience of severe earthquakes and massive earthquake records, modern seismic codes prescribe general guidelines that input motions, either real or artificial, must be selected to represent regional seismicity and must conform to design earthquakes. This paper aims to use real earthquake records to establish magnitude-distance (M–R) bins for different site conditions, and to match these with target spectral shapes defined by ten corner periods (T_c). Comparisons of record spectra from M–R bins for different hazard sources, and a review of record spectra versus design spectra from the Taiwan Building Code are discussed. The results of applied ground motion selection for the Taiwan region are presented.

Keywords: selection of real records, spectral matching, design spectra, seismic code

Introduction

The main purpose of ground motion selection is to select real records that satisfy both design levels and seismic hazards. In other words, the selection of real records should reflect site conditions and anticipated earthquake scenarios, so that the reliability, safety, and economy of seismic design can be improved. With advances in technology, new systems and special construction methods have been widely used in the building industry, so that dynamic analysis using smooth response spectra is insufficient to understand the nonlinear behavior of such structures. According to current seismic design trends, linear or nonlinear dynamic analysis requires recorded time histories as seismic input.

In this study, magnitude-distance (M–R) bins for different site conditions have been developed to estimate the characteristics of response spectra corresponding to various hazard sources. M-R bins can also be used as seed motions for response analyses. Meanwhile, ten target response spectra with different corner periods (T_c) from the Taiwan Building Code have been employed to select ground motions for spectral matching and, as such, can be utilized in the framework of performance-based design.

Code for Seismic Input

Most contemporary seismic codes, such as the New Zealand Standards (NZS 1170.5), the Italian Code (OPCM 3274), the Greek Seismic Code (EAK 2000) and Eurocode 8, describe relatively similar procedures for seismic inputs to be used as dynamic loadings in structures. Most frequently, seismic inputs can be represented by real, artificial, or simulated records, while some important seismological parameters, such as earthquake magnitude, distance, the seismotectonic environment, and the local soil conditions, should reflect local seismic scenarios.

In the scope of the nuclear industry, the regulatory or standards such as RG 1.208, NUREG-0800, and NUREG/CR-6728 by NRC, and ASCE 4-98 and

[1]Assistant Researcher, National Center for Research on Earthquake Engineering, hjliu@ncree.narl.org.tw
[2] Researcher, National Center for Research on Earthquake Engineering, wychien@ncree.narl.org.tw
[3]Assistant Researcher, National Center for Research on Earthquake Engineering, ywchang@ncree.narl.org.tw

ASCE/SEI 43-05 by ASCE, require more criteria for developing seismic inputs. For example, RG 1.208 requires ground motions that are generated to “match” or “envelop” given design response spectral shapes and should comply with the majority of the following:

(1) The average ratio of the spectral acceleration calculated from the recorded time history to the target, *i.e.*, the record-to-target ratio (RTR), where the ratio is calculated frequency-by-frequency, is only slightly greater than one.

(2) Time histories should have a time increment of at most 0.01 seconds, and a total duration of 20 seconds. The total duration of the record can be increased by zero-packing to satisfy these frequency criteria.

(3) The computed 5 percent damped response spectrum of the average of all accelerograms should not fall more than 10 percent below the target spectrum at any one frequency, and should not exceed the target spectrum at any frequency by more than 30 percent. That is, the RTR at any frequency should be between 0.9 and 1.3.

(4) To be considered statistically independent, the directional correlation coefficients between pairs of time histories should not exceed 0.16.

Ground-Motion Database

For ground motion selection and M–R bins development, the use of an informed ground-motion database is important. The earthquake data used in this study are from Taiwan Strong Motion Instrumentation Program (TSMIP), which is operated by the Central Weather Bureau (CWB). The TSMIP system, composed of more than 700 stations that are spaced approximately 5 km apart in populated areas, is widely used in the Taiwan area.

The station information is from the Engineering Geological Database for TSMIP (EGDT), which is co-established by both the CWB and the National Center for Research on Earthquake Engineering (NCREE). CWB and NCREE carried out a free-field strong-motion station drilling project to construct the EGDT (Kuo *et al*., 2011). Up to 2010, the site investigation at 469 TSMIP stations was completed and all of the results of this investigation were systematically organized in the EGDT project. With a detailed subsurface soil profile and quantitative soil properties (SPT-N values and wave velocities) at a station site, the site effect of the ground motions can be thoughtfully analyzed for a certain class of site conditions.

According to data sufficiency and the designed ground motion level, the earthquake records in the ground-motion database complied with the following two conditions: (1) the earthquake events included were from 1991 to 2010 and (2) the local magnitude (M_L) was greater than 4.5. Considering engineering applications, some ground motion parameters are also included in the ground-motion database, such as cumulative absolute velocity (CAV), strong motion duration (T_d), and Arias intensity (I_a).

Response Spectra Characterization

Ground-motion frequency content is one of the most important aspects of free-field motion as it affects structural responses, and is strongly dependent on specific factors pertaining to both the earthquake and the site. Three particularly important characteristics of ground motions are earthquake magnitude, epicentral distance, and the average shear-wave velocity in the top 30 m (V_{s30}). Therefore, the response spectra characterization of hazard-consistent scenario earthquakes is very important for

Table 1 M–R bins of V_{s30} between 360 and 760 m/s.

距離(R, km) / 規模(M)	0 – 25	25 – 50	50 – 75	75 – 100	100 – 125	125 – 150	150 – 175	175 – 200
5.50 – 5.75	[illegible]	[illegible]	[illegible]	[illegible]	N/A	[illegible]	N/A	N/A
5.75 – 6.00	[illegible]	[illegible]	[illegible]	N/A	N/A	N/A	N/A	N/A
6.00 – 6.25	[illegible]	[illegible]	[illegible]	[illegible]	N/A	N/A	N/A	N/A
6.25 – 6.50	[illegible]	[illegible]	[illegible]	[illegible]	N/A	[illegible]	N/A	N/A
6.50 – 6.75	[illegible]	[illegible]	[illegible]	[illegible]	[illegible]	N/A	N/A	N/A
6.75 – 7.00	[illegible]	[illegible]	[illegible]	[illegible]	[illegible]	[illegible]	[illegible]	N/A
7.00 以上	[illegible]	[illegible]	[illegible]	[illegible]	[illegible]	[illegible]	[illegible]	[illegible]

seismic design.

Based on the statistics method of time histories that is adopted in NUREG/CR-6728, Table 1 shows M–R bins for V_{s30} between 360 and 760 m/s. Each bin represents the total data, mean of the magnitude and epicentral distance, range of V/A ratio, PGA, $S_{a(0.3s)}$, $S_{a(1.0s)}$, and CAV. The observations are as follows: (1) according to data scattered in the M–R bins, the hazard-consistent earthquake scenario should consider the larger magnitude with both close-field and far-field; (2) larger M_L values were accompanied by a higher V/A ratios, so large earthquake events obviously induce a long-period effect; and (3) the closer the distance and the larger the magnitude, the higher the PGA, V/A ratio, CAV, and S_a.

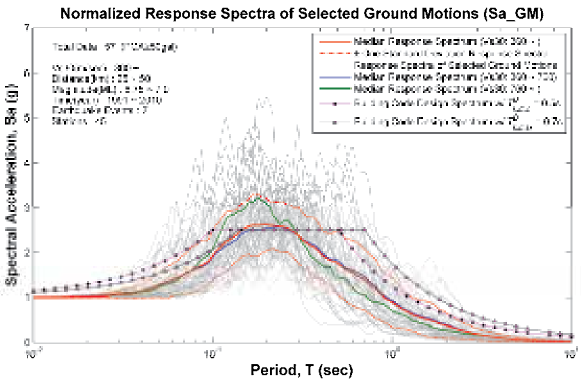

Fig. 1 Design response spectra (T_c = 0.5 s, 0.7 s) *vs*. recorded response spectra from M–R bins (M: 6.75–7.0, R: 25–50 km).

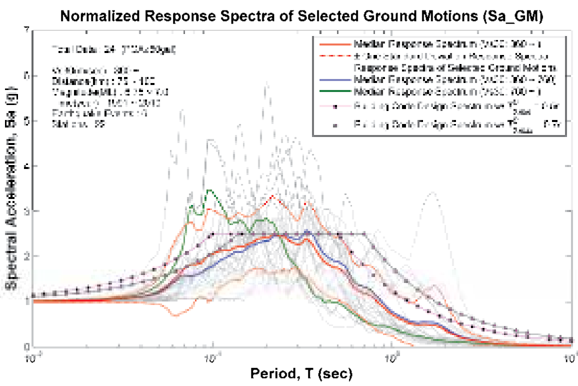

Fig. 2 Design response spectra (T_c = 0.5 s, 0.7 s) *vs*. recorded response spectra from M–R bins (M: 6.75–7.0, R: 75–100 km).

In order to estimate the characteristics of the response spectra for various seismic hazards in terms of earthquake magnitudes and distances, Fig. 1 and Fig. 2 show comparisons between design response spectra (T_c = 0.5 s, 0.7 s) based on the Taiwan Building Code and recorded response spectra from the M–R bins. The observations are as follows: (1) the average record spectrum is close to code-based spectra, so it seems that design spectra from the Taiwan Building Code can be applied for firm sites; (2) lower V_{s30} values are characterized by narrow-banded response spectra and high frequencies in comparison to higher V_{s30} values; and (3) the farther the distance of large-magnitude earthquake event, the higher the predominant period.

Applied Ground Motion Selection

Spectral matching is a commonly used code-based selection process. In this procedure, two parameters should be used: (1) the scale factor (F), a mean value of all RTRs applied to the entire recorded response spectrum; and (2) the mean squared error (MSE), represents a difference between the target spectrum and the recorded response. The MSE and scale factor were calculated in terms of the natural logarithm scale as follows:

$$F = \sum_{i}^{N} \left[\ln\left(SA_{target}(t_i)\right) - \ln\left(SA_{record}(t_i)\right) \right] \Big/ N \qquad (1)$$

$$MSE = \sum_{i}^{N} \left[\ln\left(SA_{target}(t_i)\right) - \ln\left(F \times SA_{record}(t_i)\right) \right]^2 \Big/ N \qquad (2)$$

In the above, 87 points were near-uniformly spaced over the log period scale from 0.01 s to 10 s, so the value of N will change in different period ranges.

The design spectra, as defined by the Taiwan Building Code, satisfied the following conditions: the return period of 475 years, full site classification, and no consideration of near-fault effects. As above, ten target spectral shapes defined by T_c have been grouped as shown in Table 2. The corner period can not only be used to judge the frequency content and site conditions, but also can be used instead of the parameters S_s and S_1 related to the spectral shape to illustrate the response spectrum.

Table 2 The T_c groups of code-based design spectra.

Site Class	S_S^D	S_1^D	F_a	F_v	S_{DS}	S_{D1}	T_c	Zone	Section Point of T_c
TAP1	–	–	–	–	0.60	0.96	1.60	TAP1	1.60
TAP2	–	–	–	–	0.60	0.78	1.30	TAP2	1.30
TAP3	–	–	–	–	0.60	0.63	1.05	TAP3	1.05
SC1	0.6	0.30	1.0	1.0	0.60	0.30	0.50	SC1-P1	0.50
	0.7	0.35	1.0	1.0	0.70	0.35	0.50	SC1-P1	0.50
	0.8	0.40	1.0	1.0	0.80	0.40	0.50	SC1-P1	0.50
	0.8	0.45	1.0	1.0	0.80	0.45	0.56	SC1-P2	0.60
	0.7	0.40	1.0	1.0	0.70	0.40	0.57	SC1-P2	0.60
	0.6	0.35	1.0	1.0	0.60	0.35	0.58	SC1-P2	0.60
	0.5	0.30	1.0	1.0	0.50	0.30	0.60	SC1-P2	0.60
	0.5	0.35	1.0	1.0	0.50	0.35	0.70	SC1-P3	0.70
SC2	0.8	0.40	1.0	1.3	0.80	0.52	0.65	SC2-P3	0.70
	0.6	0.30	1.1	1.3	0.66	0.43	0.68	SC2-P3	0.70
	0.8	0.45	1.0	1.2	0.80	0.54	0.68	SC2-P3	0.70
	0.7	0.35	1.0	1.4	0.70	0.49	0.70	SC2-P3	0.70
	0.6	0.35	1.1	1.4	0.66	0.49	0.74	SC2-P4	0.80
	0.7	0.40	1.0	1.3	0.70	0.52	0.74	SC2-P4	0.80
	0.5	0.30	1.1	1.5	0.55	0.45	0.82	SC2-P5	0.85
	0.5	0.35	1.1	1.4	0.55	0.49	0.89	SC2-P6	0.90
SC3	0.6	0.30	1.2	1.8	0.72	0.54	0.75	SC3-P4	0.80
	0.7	0.35	1.1	1.7	0.77	0.60	0.78	SC3-P4	0.80
	0.8	0.40	1.0	1.6	0.80	0.64	0.80	SC3-P4	0.80
	0.6	0.35	1.2	1.7	0.72	0.60	0.83	SC3-P5	0.85
	0.7	0.40	1.1	1.6	0.77	0.64	0.83	SC3-P5	0.85
	0.8	0.45	1.0	1.5	0.80	0.68	0.85	SC3-P5	0.85
	0.5	0.30	1.2	1.8	0.60	0.54	0.90	SC3-P6	0.90
	0.5	0.35	1.2	1.7	0.60	0.60	1.00	SC3-P7	1.00

An example case for comparison between the design spectrum of the second microzonation of the Taipei basin (TAP2) and all horizontal records in the ground-motion database is presented in Fig. 3. It seems that the top five recorded spectra of the best spectral fit to the target spectrum can be applied as seismic input, but some problems obviously can occur, as follows: (1) the stations do not belong to TAP2 and (2) the higher the scale factor, the smaller the spectral amplitude of the record compared to the design level. This shows that the MSE is applied to select the conformed ground motions along with the target spectrum, not to select the records appropriate to the anticipated earthquake scenario. In other words, some criteria and parameters consistent with characteristics for the controlling earthquake and site conditions should accommodate the selection.

Fig. 4 shows the selection results, according to records from the Taipei basin, with PGA greater than 50 gal, and periods range from 0.07 s to 3 s. The results ranked in ascending order of MSE are shown in Table 3. This information could be provided to develop seismic inputs for dynamic analyses. In order to estimate the criteria for developing time histories in RG 1.208 applied to a real case, Fig. 4 also shows 1.3 and 0.9 times the target spectral shapes in the period range from 0.07 s to 3 s in order to represent the restricted RTR. It is obvious that real records cannot comply with any RTR between 0.9 and 1.3. Even if the upward scale factor to satisfy the most parts of criteria, it is still hard to satisfy the criteria with any RTR lower than 1.3.

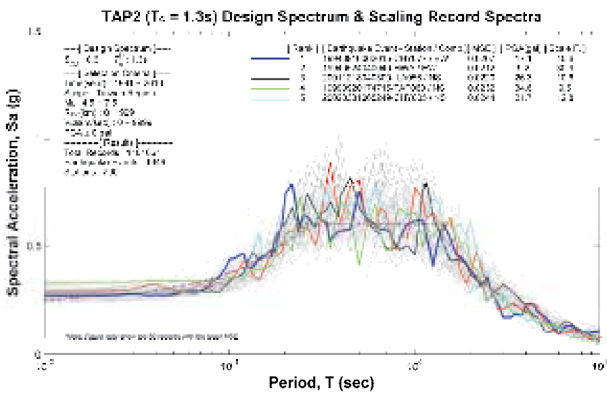

Fig. 3 Comparisons of TAP2 design spectra *vs.* all record spectra of the database (T: 0.01–10 s).

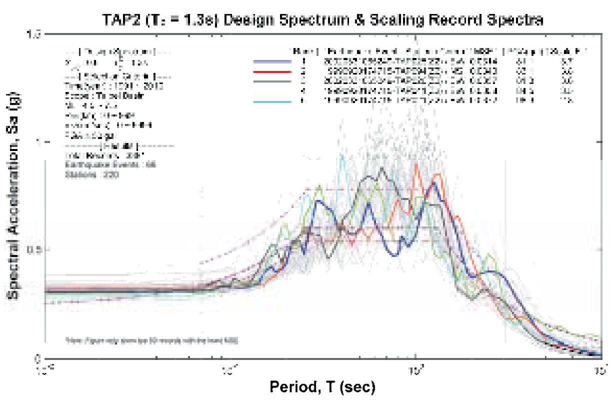

Fig. 4 Comparisons of TAP2 design spectra *vs.* record spectra of the Taipei basin (T: 0.07–3 s)

Table 3 The top twenty selection results for TAP2.

[Design Spectrum] TAP2 (S_{DS} = 0.6, T_c = 1.3s) [Period Range] 0.07s~3.0s [PGA]≥50gal [Sorting By] MSE

Rank	Matching Index		Earthquake Parameters				Station Parameters			Ground Motion Parameters					
	MSE	Scale Factor	Time (UTC)	M_L	R_{hyp} (km)	Depth (km)	Station (comp)	Comp	V_{s30} (m/s)	PGA (gal)	PGV (cm/s)	PGD (cm)	CAV (gal-sec)	V/A (sec)	T_d (sec)
1	0.0314	3.7	2002/03/31 06:52:49	6.8	120.7	13.8	TAP025 (2)	EW	201.8	91.1	19.4	8.2	0.49	0.23	29.8
2	0.0348	3.8	1999/09/20 17:47:15	7.3	158.4	8.0	TAP034 (2)	NS	408.2	83.1	17.0	8.3	0.58	0.21	23.8
3	0.0357	3.8	2002/03/31 06:52:49	6.8	119.2	13.8	TAP028 (2)	EW	201.7	81.3	15.8	8.3	0.49	0.19	29.7
4	0.0368	5.5	1999/09/20 17:47:15	7.3	168.1	8.0	TAP041 (1)	EW	374.1	84.5	20.6	24.1	0.68	0.24	33.9
5	0.0372	2.8	1999/09/20 17:47:15	7.3	151.3	8.0	TAP021 (1)	EW	187.8	98.3	29.6	12.2	0.76	0.29	28.6
6	0.0379	4.4	1999/09/20 17:47:15	7.3	168.1	8.0	TAP041 (2)	NS	374.1	63.0	18.1	11.8	0.53	0.29	29.2
7	0.0399	2.9	2002/03/31 06:52:49	6.8	128.4	13.8	TAP103 (1)	EW	–	114.8	22.7	18.7	0.81	0.20	23.2
8	0.0402	5.2	2002/03/31 06:52:49	6.8	131.9	13.8	TAP052 (2)	NS	309.7	61.0	15.5	5.8	0.42	0.25	33.3
9	0.0407	5.6	2002/03/31 06:52:49	6.8	123.1	13.8	TAP095 (2)	NS	162.7	51.8	12.5	8.3	0.38	0.24	22.8
10	0.0409	3.7	2002/03/31 06:52:49	6.8	128.3	13.8	TAP006 (2)	NS	202.8	87.0	20.1	7.8	0.42	0.23	19.8
11	0.0415	3.4	1999/09/20 17:47:15	7.3	158.1	8.0	TAP042 (2)	EW	–	85.5	17.2	14.1	0.68	0.20	22.2
12	0.0438	2.6	1999/09/20 17:47:15	7.3	153.3	8.0	TAP014 (1)	EW	194.6	104.6	27.4	18.1	0.86	0.26	38.8
13	0.0446	4.3	1999/09/20 17:47:15	7.3	152.8	8.0	TAP051 (2)	NS	408.1	62.6	16.0	12.6	0.58	0.26	28.4
14	0.0463	4.9	2002/03/31 06:52:49	6.8	128.3	13.8	TAP005 (1)	EW	202.8	67.2	12.9	5.2	0.34	0.19	21.8
15	0.0471	3.2	2002/03/31 06:52:49	6.8	118.3	13.8	TAP109 (1)	NS	–	88.6	16.8	4.7	0.58	0.19	17.4
16	0.0478	4.1	2002/03/31 06:52:49	6.8	139.3	13.8	TAP041 (1)	EW	374.1	73.2	25.7	18.6	0.41	0.35	20.8
17	0.0479	2.4	2002/03/31 06:52:49	6.8	118.3	13.8	TAP109 (2)	EW	–	147.3	28.4	8.8	0.86	0.19	15.3
18	0.0486	4.3	2002/03/31 06:52:49	6.8	121.9	13.8	TAP019 (2)	EW	229.8	84.0	14.8	8.3	0.46	0.23	25.2
19	0.0487	3.9	1999/09/20 17:47:15	7.3	158.1	8.0	TAP042 (1)	NS	–	95.0	15.8	16.8	0.61	0.16	34.3
20	0.0507	2.5	2002/03/31 06:52:49	6.8	118.7	13.8	TAP015 (2)	EW	209.8	137.8	32.3	8.3	0.63	0.25	19.8

Conclusions

In this study, magnitude–distance (M–R) bins of different site conditions and the application of ten target spectra to select ground motions have been presented. Several comments can be made as follows:

(1) M–R bins can be used to assess the characteristics of controlling earthquake. In addition, M–R bins and the selection results of ten target spectra defined by T_c can be applied to develop seismic inputs for dynamic analyses.

(2) Spectral matching between the design spectrum and the response spectrum of a selected record is commonly required in practice. However, with some parameter settings, these criteria should be considered in the selection process.

(3) Because of ground motion diversity, it is difficult to comply with RG 1.208 criteria. The issue of how to select time histories appropriately and to modify ground motion to serve as seismic input will be discussed in future research.

References

Kuo, C. H., Wen, K. L., Hsieh, H. H., and Kuo, K. W. (2011). "Introduction of the Geological Database for TSMIP," *8CUEE Conference Proceedings*, Tokyo, Japan, pp. 157-163.

McGuire, R. K., Silva, W. J., and Costantino, C. J. (2001). "Technical Basis for Revision of Regulatory Guidance on Design Ground Motions: Hazard- and Risk-Consistent Ground Motion Spectra Guidelines," NUREG/CR-6728, *U.S. Nuclear Regulatory Commission*.

RG 1.208, (2007). "A Performance-Based Approach to Define the Site-Specific Earthquake Ground Motion," *U.S. Nuclear Regulatory Commission*.

CPAMI, (2011). "Seismic Design Code for Buildings in Taiwan", Construction and Planning Agency, Ministry of the Interior, Taiwan. (in Chinese)

De-Noising the Influence of Meteorological Parameters on Geochemical Monitoring Data: Pre-processing for Earthquake Precursory Research

Vivek Walia [1] Arvind Kumar [2] Baldev Raj Arora [3] Shih-Jung Lin [4]
Hsiao-Hsien Chang [5] Tsanyao Frank Yang [6] Kuo-Liang Wen [7]

瓦里亞 [1] 亞耳文 [2] 艾若拉 [3] 林世榮 [4] 張效賢 [5] 楊燦堯 [6] 溫國樑 [7]

Abstract

The present work is focused to investigate the relation of geochemical precursors to earthquakes through a network soil-gas radon stations in the multiple-plate collision setting of Taiwan. Geochemical variations of soil-gas composition are recorded at established geochemical observatories along the Hsincheng fault (HC) in Hsinchu area, Hsinhua fault (HH) in Tainan and at Jaosi in Ilan areas of Taiwan, respectively, to determine the influence of enhanced concentrations of soil gases on the tectonic activity in the region and to test the proposed tectonic setting based model from data generated at earthquake monitoring stations during the observation period. In addition to the continuous monitoring, in an effort to reduce the noise level which may be due to meteorological parameters especially for the rainfall, statistical filters have been applied to a selected data segment for both HC and HH monitoring stations. An attempt has been made to derive noise free synthetic curve on the data segment of the HC monitoring station.

Keywords: Soil-gas, Earthquake, Radon, Meteorological Parameters, Singular Spectral Analysis (SSA), Single Value Decomposition (SVD)

Introduction

Studies on earthquake precursory signals related to soil-gas anomalies have accelerated during the past few decades. Gases like radon, helium and carrier gases like carbon dioxide, nitrogen, methane etc. with different origins in soil have been used to trace various fault systems (Fu et al., 2005; Walia et al, 2009a, 2010) and in earthquake precursory studies (Kumar et al., 2009; Walia et al., 2005; Yang et al., 2006). The process of gases migration in the soil is apparently controlled by the interaction of geological, pedological, climatic and meteorological factors. Radon concentration variations have been established as a major contributor for seismic surveillance. While other gases have also been considered as possible earthquake precursors, however, bulk of reports in the scientific literature is focused on radon. As the stress build-up increases, the rocks in the impending focal zone experience opening of micro-cracks. With the opening of the cracks exposed surface area of rocks increases that leads to enhanced emanation of radon. If this increase in radon intensity can be measured at the surface, it can serve as a possible precursor to earthquakes. Diffusion is the simplest mechanism, but owing to its short half-life, radon cannot travel more than a few meters. The second mechanism, the advection mechanism, is mostly dominated in fault zones and fractured systems and convection can occur when a sufficient thermal gradient is available

[1] Researcher, National Center for Research on Earthquake Engineering, walia@ncree.narl.org.tw
[2] Associate Researcher, National Center for Research on Earthquake Engineering, kumar@ncree.narl.org.tw
[3] Visiting Professor, National Center for Research on Earthquake Engineering, arora@ncree.narl.org.tw
[4] Assistant Researcher, National Center for Research on Earthquake Engineering, sjlin@ncree.narl.org.tw
[5] Assistant Researcher, National Center for Research on Earthquake Engineering, seanchang@ncree.narl.org.tw
[6] Professor, Department of Geosciences, National Taiwan University, tyyang@ntu.edu.tw
[7] Professor, National Center for Research on Earthquake Engineering, wenkl@ncree.narl.org.tw

within the soil, depending on many local parameters, such as viscosity, porosity, permeability and so on. The transport by means of a carrier gas (Yang et al., 2003, 2011) is particularly important inside a volcanic edifice, where gases, such as, CO_2, H_2 SO_2 and H_2S etc. are abundantly present and can be good carriers of radon, reaching the surface at very high rates. Radon monitoring across the seismic active zone is motivated by these physical processes. In addition, change of soil moisture (capping effect), squeezing of water (rinsing effect) and the rise & fall of water table following the events of rainfall produce fluctuations in radon intensity. The real assessment and quantification of these influences is a major pre-requisite in the isolation of precursory signals.

Taiwan is a product of the arc-continent collision between Philippine Sea plate and Eurasian plate which makes it a region of high seismicity. In the southern part of the island, the Eurasian plate is subducting under the Philippine Sea plate while in the northern part of the island, the Philippine Sea plate bounded by the Ryukyu trench is subducting beneath the Eurasian plate. Behind the Ryukyu trench, the spreading Okinawa trough has developed. The northern part of Taiwan Island is located at the western extrapolation of the Okinawa trough. These collisions are generally considered to be the main source of tectonic stress in the region which is, thus, densely faulted and seismically active.

In last few years, we focused on the temporal variations of soil-gas composition at established geochemical observatories along the Hsincheng fault (HC) in Hsinchu area, Hsinhua fault (HH) in Tainan and at Jaosi (JS) in Ilan areas of Taiwan, respectively, to determine the influence of enhanced concentrations of soil gases to monitor the tectonic activity in the region and to test the previously proposed tectonic setting based model (Walia et al, 2009b, Walia et al, 2012) from data generated at earthquake monitoring stations during observation period. The stress-induced variations due to impending earthquakes in radon are contaminated by meteorological changes (i.e. atmospheric temperature, pressure, precipitation etc.) and, hence assessment and quantification of these influences is a major pre-requisite in the isolation of precursory signals. The present study is aimed at the appraisal and filtrations of these environmental/ meteorological parameters. Detailed geology and tectonic features of the monitoring stations are reported elsewhere (see the previous reports).

Methodology

Temporal soil-gases compositional variations were measured regularly at continuous earthquake monitoring stations using RTM2100 (SARAD) for radon and thoron measurement following the procedure as described in Walia et al, 2009b. Seismic parameters (viz. earthquake parameters, intensity at a monitoring station etc.) and meteorological parameter data were obtained from Central Weather Bureau of Taiwan (www.cwb.gov.tw).

To carry out the present investigation, a segment of soil-gas radon data for the station HC and HH was selected for its continuity, availability of corresponding atmospheric pressure, temperature, humidity and rainfall data from Central Weather Bureau. Single Value Decomposition (SVD) in the form of Singular Spectral Analysis (SSA) was applied to isolate respective variations.

Results and Discussions

Long term time series data are fundamental to try various numerical tools to quantify the influences of meteorological parameters as well as critical to re-validate the developed methodology using some recent segments of the data. As per the present practice, the data from various stations are examined synoptically to evaluate earthquake precursory signals against the backdrop of rainfall and other environmental factors (see the previous reports). Various guidelines are developed to identify the nature of precursory signals almost in real time. A tectono-physical model to isolate precursory radon signals and to issue a provisional forecast for future academic assessment and integration with other precursory signals has already been proposed (Walia et al, 2009b, Walia et al, 2012). In earthquake prediction research it is extremely important to estimate the size and shape of the earthquake preparation zone. We calculated effective/strain radius (D) for the earthquake preparation zone using Dobrovolsky (1979) formula:

$$D=10^{0.43M}$$

where, M is the magnitude of the earthquake.

Taiwan is one of the most active seismic regions of the world with an average of about 20,000 earthquakes occurring every year in or around as reported by the Central Weather Bureau of Taiwan (www.cwb.gov.tw). Therefore, it is essential to define some selection criteria to identify threshold earthquakes for this study. Based on the anomalous signatures from particular monitoring stations we are in a state to identify the area for impending earthquakes of magnitude ≥ 5. For selection criteria, earthquakes having local intensity ≥ 1 at the monitoring stations with epicentral distance (R) < 150 kms having D/R ratio ≥ 1 with focal depth < 40 kms are considered.

After careful examination of all available data from a network of 3 stations, a segment of soil-gas radon data for the station HC, corresponding to a period of about 7 months, i.e., from August 11, 2009 to March 5, 2010, was selected for applying the statistical filtrations. The 15 minute data were carefully edited for rare duplicate sampling, gaps and discontinuous jump following intervals of mal-functioning of equipments. Since allied meteorological data were available with hourly sampling, 15-min radon were also reduced to hourly averages. It is to note that time series is dominated by two classes of variations; (i) periodic variations at diurnal frequencies, (ii) aperiodic signals with a time scale of less than 30 days, the formulation of Single Value Decomposition (SVD) in the form Singular Spectral Analysis (SSA) was applied to isolate respective variations. The decomposed eigen values in the radon show absence of variations determined by earth tides. Aperiodic signals in radon, in period band of 2-30 days, show some control of temperature, pressure and rainfall (Fig. 1). It has been noted that sharp changes in radon are correlated with rainfall occurrence, although with some phase lag. However, it has been observed that radon variations are not significantly influenced by temperature and pressure variations.

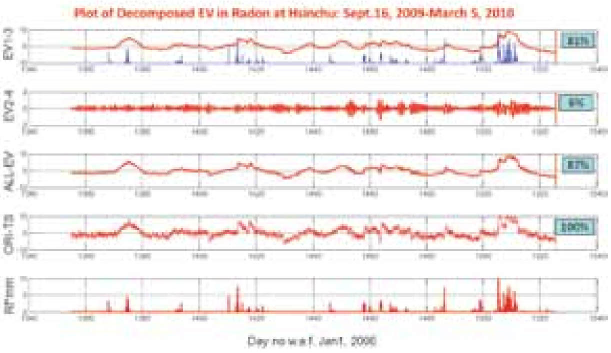

Fig. 1 Sum Plots of aperiodic (EV1&EV3) and periodic (EV2&EV4) decomposed Eigen Values (EV) together with the sum of all EV and original time series (ORO-Ts) in Radon at station Hsinchu during September 16, 2009 - March 5, 2010. The lower panel shows the distribution of rainfall (Rf). Percentage variance accounted for by combined EV are shown in boxes.

With an objective to identify earthquake related perturbation in radon, the residual radon variations corrected for temperature, pressure and rainfall indicated changes are compared in relation to earthquake occurrence. Amongst the various meteorological parameters, the influence of rainfall on radon is found to be the strongest. Radon at the onset of rainfall shows a step-jump that attain peak in 12-15 hours. This is attributed to increased flow of radon to measuring chamber as increased soil moisture prevents escape of radon into the atmosphere (capping effect). After the rainfall, radon shows regular recession in a complex manner. The intensity of radon decreases rapidly first and then shows slow decrease which continued for the next several days. In addition, radon variation shows long-term modulations which appear to be due to ground level variations. After testing linear and exponential decay pattern, the overall recession could be approximated in terms of double exponential decay and internal loading could reproduce the most salient perturbation seen during the intervals of rainfall (Fig. 2a). The residual radon series shows some definite deviations in respect of earthquake occurrences which are in agreement with

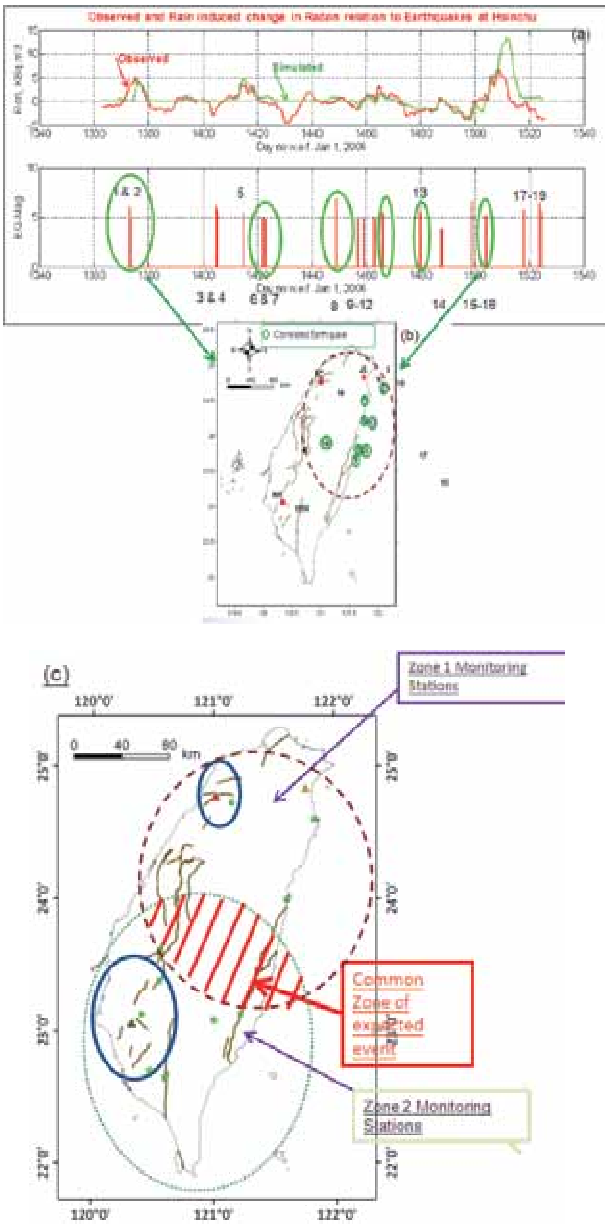

Fig. 2 (a) Relation of significant perturbations in observed and rainfall induced changes in radon with 19 earthquakes occurring within radius of 150 km of the monitoring station at Hsinchu during the selected observation period (b) Corelated earthquakes with radon monitoring station at Hsinchu (c) Proposed tectonic based model.

the signatures inferred from long term synoptic observations (Fig. 2). It can be noted that many of the strong perturbations in radon are the manifestation of the rainfall induced effects. Allowing for these correspondences, still a number of anomalies can be related to earthquake occurrences. It is obvious that all earthquake occurrences within 150 km of the recording stations produce anomalies. Some of the significant anomalies are consistent with earthquakes numbered 1, 2, 6, 7, 8, 12, 13 as well as 15-16 (Fig. 2b) and these fit well in the proposed model (Fig. 2c).

In order to check the efficiency of applied methodology, we have also applied SSA filter to a selected data segment (i.e. Nov. 2011 to Feb 2012) for the HH monitoring station (Fig. 3). The The singular value decomposition (SVD) results show that radon varations at HH stations is more influenced by periodic variations corresponding to diurnal and semi-diurnal variation (about 25%) which are found to be less at HC monitoring station (6%) data. It may be attributed to the daily temperature variations. Further, it has been noted that radon variation is not much effected by rainfall during the observation period, although no heavy rainfall was recorded during that period. Same kind of synthetic curve will be developed for this and other monitoring stations.

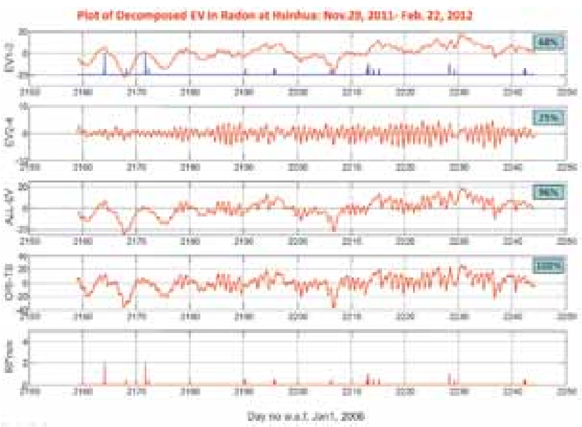

Fig.3 Sum Plots of aperiodic (EV1&EV3) and periodic (EV2&EV4) decomposed Eigen Values (EV) together with the sum of all EV and original time series (ORO-Ts) in Radon at station Hsinhua during November 29, 2011 – Feburary 22, 2012. The lower panel shows the distribution of rainfall (Rf). Percentage variance accounted for by combined EV are shown in boxes.

References

Etiope G., Calcara, M., Quattrocchi, F. (1997). “Seismogeochemical algorithms for earthquake prediction: an overview”. *Annali Di Geofisica*, 40(6), 1483-1492.

Dobrovolsky, I.P., Zubkov, S.I. and Miachkin, V.I. (1979). “Estimation of the size of earthquake preparation zones”. *Pure and Appl. Geophys*., 117, 1025-1044.

Kumar, A., Singh, S., Mahajan, S., Bajwa, B.S., Kalia, R., Dhar, S., (2009). “Earthquake precursory studies in Kangra valley of North West Himalayas, India, with special emphasis on radon emission”. Appl. Radiat. Isot. 67, 1904-1911.

Fu, C.C., Yang, T.F., Walia, V., Chen, C.H. (2005). “Reconnaissance of soil gas composition over the buried fault and fracture zone in southern Taiwan”. *Geochemical Journal*, 39,427-439.

Walia, V., Yang, T.F., Lin, S.J., Hong, WL., Fu, C.C., Wen, K-L.,Chen, C-H. (2009a). “Geochemical variation of soil-gas composition for fault and earthquake precursory studies along Hsincheng fault in NW Taiwan”. *Appl. Radiat. Isotopes, 67, 1855- 1863*.

Walia, V., Yang, T.F., Lin, S.J., Hong, W.L., Fu, C.C., Wen, K.L.,Chen, C.H. (2009b). “Continuous temporal soil.gas composition variations for earthquake precursory studies along Hsincheng and Hsinhua faults in Taiwan”. *Radiat. Meas.,* 44, 934.939.

Walia, V., Virk, H.S., Yang, T. F., Mahajan, S., Walia, M. and Bajwa, B.S. (2005). “Earthquake prediction studies using radon as a precursor in N.W Himalayas, India: a case study”. *TAO*, 16(4), 775.804.

Walia, V., Lin, S-J.,Yang, T.F., Fu, C-C., Hong, W-L., Wen, K-L.,Chen, C-H. (2010). “Soil-gas monitoring: A tool for fault delineation studies along Hsinhua Fault (Tainan) Southern Taiwan.” *Applied Geochemistry, 25,* 602-607.

Walia, V., Yang, T.F., Lin, S-J., Kumar, A., Fu, C-C., Chiu, J-M., Chang, H-H., Wen, K-L.,Chen, C-H. (2012). “Temporal variation of soil gas compositions for earthquake surveillance in Taiwan.” *Radiat. Meas.,* http://dx.doi.org/10.1016/j.radmeas.2012.11.007.

Yang, T.F., Chou, C.Y., Chen, C.H, Chyi, L.L., Jiang, J.H. (2003). “Exhalation of radon and its carrier gases in SW Taiwan”. *Radiat. Meas.* 36, 425.429.

Yang, T.F., Fu, C.C., Walia, V., Chen, C.H., Chyi, L.L., Liu, T.K., Song, S.R., Lee, M., Lin, C.W., Lin, C.C., (2006). Seismo-geochemical variations in SW Taiwan: multi.parameter automatic gas monitoring results, *Pure Appl. Geophys.*, 163, 693.709.

Yang, T.F., Wen, H.-Y., Fu, C.-C., Lee, H.-F., Lan, T.F., Chen, A.-T., Hong, W.-L., Lin, S.-J., Walia, V., (2011). “Soil radon flux and concentrations in hydrothermal area of the Tatun Volcano Group, Northern Taiwan”. *Geochem. J.*, 45, 483-490.

From P Wave Attenuation to Study 2006 Taitung Earthquake

Yi-Zeng Chang [1], Strong Wen [2], Chau-Huei Chen [3], and Kou-Liang Wen [4]

張議仁 [1]、溫士忠 [2]、陳朝輝 [3]、溫國樑 [4]

Abstract

Amplitude attenuation and attenuation dispersion are the two main methods used in the study of seismic wave attenuation, especially the attenuation dispersion obtained from single stations. When the seismic wave is propagating, its geometric spread and inelastic absorption would affect the amplitude as well as related factors such as the rock porosity, lithology, temperature and pressure conditions, rock particle size, viscosity, and the saturation of the medium. According to the continuous relaxation model, based on the assumption that the attenuation material is a linear viscoelastic solid, we picked up the first cycle of the P arrival wave from the vertical component in a single station to calculate the delay time of the group velocity using the multiple filter technique and then adopted the Genetic Algorithm (GA) method to investigate the related parameters of the Qp value. In this study, we calculated the temporal variation of Qp with the stations near to the 2006 Taitung earthquake epicenter (M6.2). We explored each quadrant of the Qp value changes with different stations and the consistency in different orientations of the stations. The results confirmed each other to enhance the observable characteristics of strong earthquake forecasting.

Keywords: Attenuation dispersion, Qp

Introduction

The purpose of this study is to make use of the attenuation dispersion of seismic waves to investigate the characteristics of the medium before a strong earthquake event. This includes the study of the differences in regional characteristics, how the size of the main shock shows the correlation between a strong earthquake and the dispersion property, the relationship between the size of the main shock and the Q value, the temporal variation in Q value anomaly distribution, the Q value abnormal direction and many other related issues. If a correlation between a strong earthquake event and the Q value can be found, a seismogenic zone could be detected through surveying. Since real-time waveform data and related earthquake information cannot be obtained immediately, this study firstly investigated large historic earthquakes. Enough stations were located near the main shock, allowing the production of good quality data that could be used to analyze bigger magnitude events. Since the crust medium exhibits non-uniform and non-elastic characteristics, the use of the attenuation property of the seismic wave can help us obtain information when seismic waves passing through the path bring out the medium component, status, and the temperature distribution. The study of attenuation dispersion is suitable for the study of smaller events. In that way, more of the available seismic data can be used and the distribution of small earthquake locations, depths, and epicenter distances can make our study more comprehensive.

Methodology

The attenuation dispersion model was based on the continuous relaxation model, which was proposed by Correig and Mitchell (1989). The Q value can be

[1] Assistant Researcher, National Center for Research on Earthquake Engineering, yzchang@ncree.narl.org.tw

[2] Associate Researcher, National Center for Research on Earthquake Engineering, scwen@ncree.narl.org.tw

[3] Professor, Dept. of Earth and Environment Sciences, National Chung Cheng Univ., seichen@eq.ccu.edu.tw

[4] Professor, Dept. of Earth Science, National Central Univ.,wenkl@ncree.narl.org.tw

expressed by the following equation：

$$Q^{-1}(\omega) = \frac{2}{\pi} Q_m^{-1} \arctan \left[\frac{\omega(\tau_1 - \tau_2)}{1 + \omega^2 \tau_1 \tau_2} \right] \qquad (1)$$

ω : Angular Frequency

τ_1, τ_2 : Long and Short Relaxation Times

Q_m^{-1} : Constant representing the flat part of the spectrum (Liu et al., 1976)

If the attenuation medium can be referred as the linear viscoelastic solid, then the phase velocity can be showed as (Ben-Menahem and Singh, 1981)：

$$C(\omega) = C_\infty \left\{ 1 + \frac{1}{\pi} Q_m^{-1} \left[\ln \frac{\tau_1}{\tau_2} + \frac{1}{2} \ln \left(\frac{1 + \omega^2 \tau_2^2}{1 + \omega^2 \tau_1^2} \right) \right] \right\}^{-1} \qquad (2)$$

C_∞ : Phase Velocity at Infinite Frequency (the Perfectly Elastic Case)

Correig (1991) used formula (1) to express the relationship between group velocity and phase velocity ：

$$U(\omega) = \frac{C(\omega)}{1 - \frac{\omega}{C(\omega)} \frac{dC(\omega)}{d\omega}} \qquad (3)$$

Then, the delay time of group velocity is the following:

$$\Delta t_g = t_g(\omega) - t_g(\omega_r) \text{ (Correig, 1991)：}$$

$$\Delta t_g = \frac{t}{\pi Q_m} \left[\frac{1}{2} \ln \frac{(1 + \omega^2 \tau_2^2)(1 + \omega_r^2 \tau_1^2)}{(1 + \omega^2 \tau_1^2)(1 + \omega_r^2 \tau_2^2)} + \frac{\omega^2 (\tau_1^2 - \tau_2^2)}{(1 + \omega^2 \tau_1^2)(1 + \omega^2 \tau_2^2)} - \frac{\omega_r^2 (\tau_1^2 - \tau_2^2)}{(1 + \omega_r^2 \tau_2^2)(1 + \omega_r^2 \tau_2^2)} \right] \qquad (4)$$

t : The Travel Time of the Signal at Infinite Frequency

ω_r : Reference Frequency

We obtain the delay time of the group velocity from multiple filter techniques and apply this to formula (4) with the travel time of the P wave. Finally, we can obtain Q_m, τ_1 and τ_2 through the Genetic algorithm (GA) inversion。

Data processing

In Figure 1, the study area is illustrated along with the station distribution (the blue triangles), the red star indicates as the location of epicenter of the 2006 Taitung earthquake (2006/04/01, M6.2) and the red lines are the fault traces. This study used the data from the CWBSN to search the attenuation parameters.

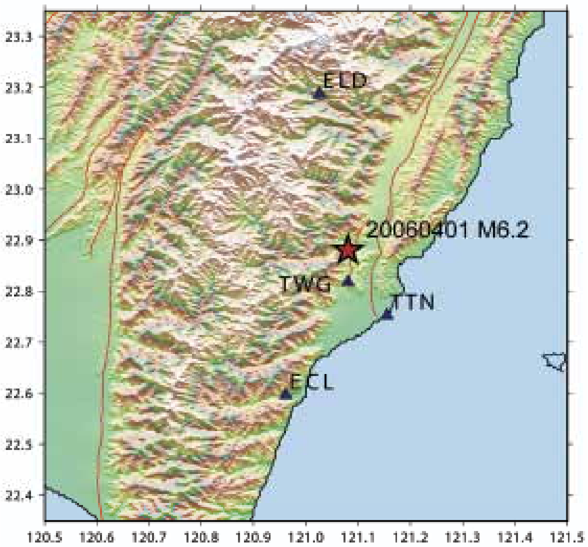

Fig. 1 The study area where includes Taitung earthquake and the related stations.

1. Choosing data

We choose the vertical component data having a magnitude lower than 3 from October 2005 to March 2006 for each station. We must take into account that the larger the earthquake, the lower the angular frequency becomes. Therefore, even while using smaller events, the angular frequency can still fall into the frequency range. As a side-note, a relatively large number of smaller events can help us study the surrounding environment of the measuring stations. The main factor of high frequency energy attenuation is the propagation distance so the data accessed was for the selected epicenter and the focal depth was within 30 km of the station. Regional stress accumulations are within a limited range before a strong earthquake hits, and longer wave propagation paths tend to weaken the seismic waves to bring abnormal characteristics from seismogenic areas. But for these factors, this study would have used ECL and ELD stations that were over 30 km from the epicenter. Therefore, the epicenter distance of these two stations are changed to 40 and 50 km, respectively. In addition, the seismic data received by the TTN station exhibited a high noise ratio, so the poor quality data from this station cannot be used in this study. Figure 2 shows the selected events near the TWG station.

2. Resample and filter the signal

The waveform was resampled at 1000 points by using the Newton Interpolation method and the band-pass filter.

3. Cut the first cycle of P wave

According to the theory in Cong and Mejia (2000) and Correig (1991), the first cycle of the P wave is enough to obtain information on the medium and is quite resilient to interference from other phase signals. Therefore, we cut the first cycle of the P wave in our calculations. In Figure 3, the waveform of the first cycle of the P wave with duration of 0.1~0.2 seconds is shown.

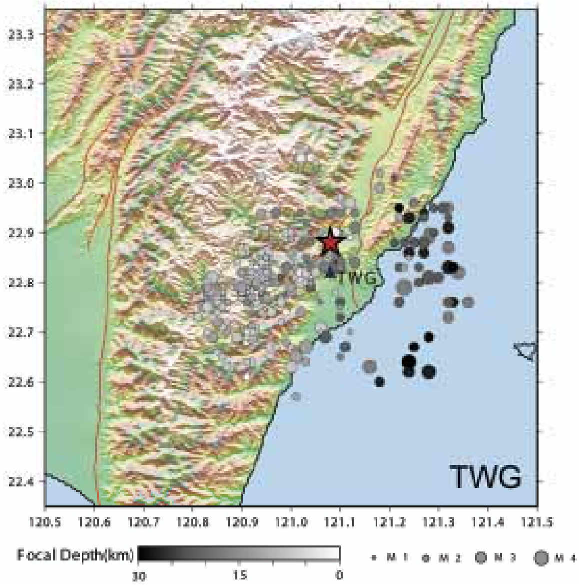

Fig. 2 The distribution of earthquakes near by TWG station

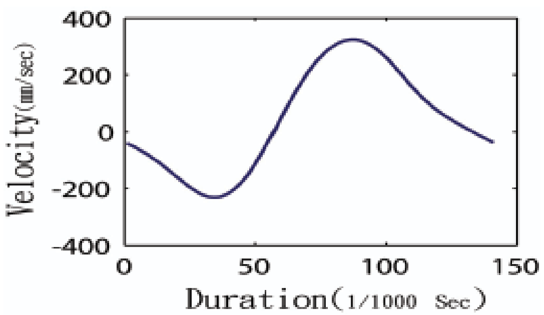

Fig. 3 Cutting the first cycle of P wave

4. Calculating the Group Velocity Delay Time Spectrum from Multiple Filter Method and using GA to Invert the Attenuation Factors Qp

The interception of the first cycle of the P wave would adopt multiple filters to obtain the group-velocity delay time-frequency spectrum. In Figure 4, the horizontal axis is the frequency, and the ordinate is the time, the red circle represents the magnitude of the energy corresponding to the different frequencies. If the waveform data is disturbed, then the time-frequency spectrum would exhibit chaotic behavior and the data would not be used. Finally, we use GA to search for optimal solutions (shown in red lines) to produce , and in formula (4). Finally, each seismic Q value statistic obtained by the stations is converted into a distribution diagram corresponding to its time and an appropriate average is taken to show the temporal variation in attenuation factor changes due to the tectonic seismogenic process in the station's vicinity before strong earthquakes.

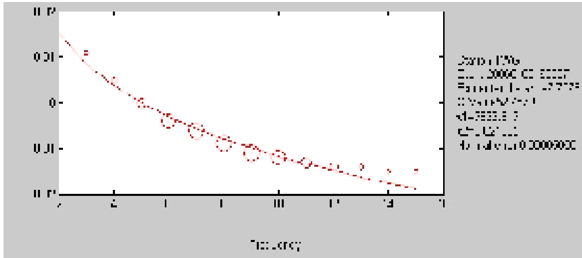

Fig. 4 The spectrum with the group velocity delay time

Results and Discussions

In this study, the chosen stations (TWG, ECL, and ELD) were near the 2006 Taitung earthquake epicenter (M6.2) but the TTN station was not used due to poor quality waveform data. The distances of the ECL and ELD stations from the epicenter of the Taitung earthquake (M6.2) are more than 30 and 40 km, respectively, thus, these results in a smaller weighting on the path of the seismic wave propagated through the source area of the strong earthquake and the selected events are weighted less. Therefore, since the variation of the Qp value is not as obvious, this report omitted the results of the two stations.

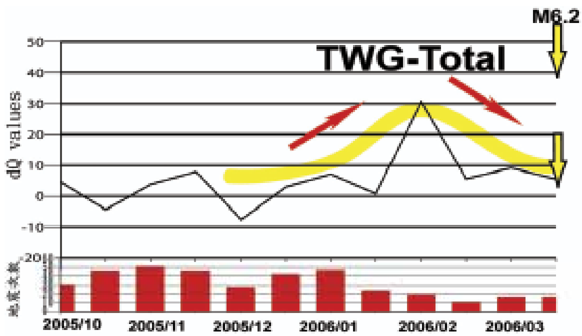

Fig. 5 TWG station: The variation of temporal average in δQ. The yellow arrow indicates the occurrence of the Taitung earthquake and the red histogram indicates the number of events.

According to the Qp study in Cong et al (2000), the Qp value increases with epicenter distance. Therefore, this study adopted linear regression to obtain a linear trend with the epicenter distance erasing the effect of epicenter distance to obtain the residual of Qp (see Figure 5). Moreover, in order to investigate the change in the path effect related to the δQ, we used the station as the center to divide the seismic data into different orientations to explore the changes in δQ (see Figure 6).

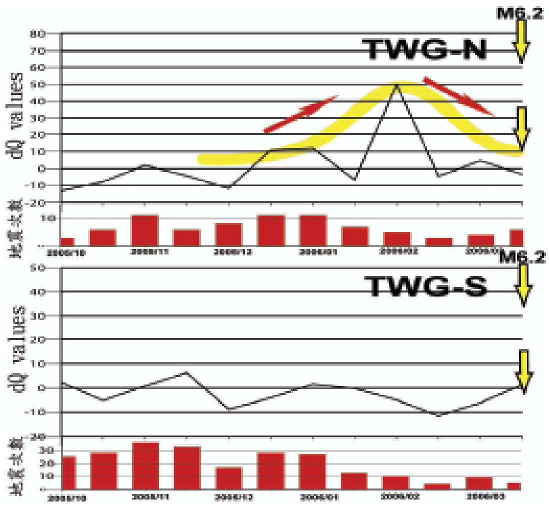

Fig. 6 The variation of δQ in TWG station.

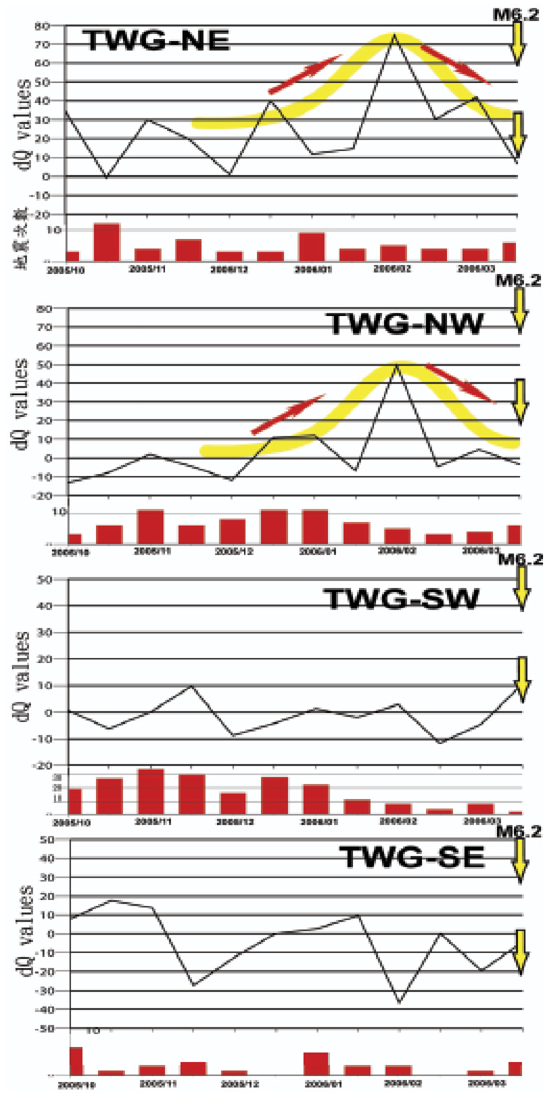

Fig. 7 The azimuth variation of δQ in TWG station.

The study adopted the temporal average of 0.5 months as a unit to display the variation of δQ . This value is mainly related to the number of earthquakes because the finer sorting corresponds to the number of events. Figure 5 shows the value to be slightly higher in February since the Qp value is related to the path. Therefore, we try to separate the north side from the south side based on the TWG station in Figure 6. From the results, the peak value becomes more apparent in north side of TWG in February while the south side is relatively stable. In the study area, the Taitung earthquake (M6.2) is located to the north of the TWG. This makes it reasonable for the north side to exhibit anomalies in its data. This also confirms the high values that the TWG station observed in February (Figure 5), and their absence in the south side. For finer classification, the azimuth is mainly limited by time - number of earthquakes. This study further divided the data into four regions to analyze (Figure 7). In Figure 7, the TWG-NE and TWG-NW both appear to have high values in February. This phenomenon is understood to occur from the Taitung earthquake (M6.2) being located in the north side of the TWG station.

Conclusions

In this study, the high quality of waveform data is a necessity, and having a sufficient number of earthquakes within the time unit is also important. Using small-scale earthquakes to increase the number of natural earthquakes can make this data useful in enhancing the data quality. Moreover, analyzing real time seismic data is also a major problem owing to the limitations in data processing, which includes the data download and location procedures. If more stations were available to monitor the study area, we could use the azimuth variation in δQ to identify the same area with different stations. This can provide us with important information of precursors to strong earthquakes.

References

Ben-Menahem, A., and S. J. Singh (1981). Seismic Waves and Sources,Springer-Verlag, New York, 1108 pp.

Correig, A. M., and B. J. Mitchell (1989). Attenuative dispersion at La Cerdanya, eastern Pyrenees, Phys. Earth Planet. Int. 57, 304-310.

Correig, A. M. (1991). On the measurement of body wave dispersion, J. Geophys. Res. 96, 16,525-16,528.

Cong L, J. Mejia, B. J. Mitchell (2000). Attenuation dispersion of P waves in near the New Madrid seismic zone, Bull. Seism. Soc. Am. 90 (3), 679-689.

Liu, H. P., D. L. Anderson, and H. Kanamori (1976). Velocity dispersion due to anelasticity: implications for seismology and mantle composition, Geophys. J. R. Astron. Soc. 47, 41-58.

Rapid on-site peak ground acceleration estimation based on SVM and P-wave features in Taiwan

Ting-Yu Hsu[1] , Shieh-Kung Huang[2], Yu-Weng Chang[3], Chun-Hsiang Kuo[4], Che-Min Lin[5], Tao-Ming Chang[6], Kuo-Liang Wen[7], Chin-Hsiung Loh[8]

Abstract

This study extracts pressure wave (P-wave) features from the first few seconds of recorded vertical ground acceleration at a single station. These features include the predominant period, peak acceleration amplitude, peak velocity amplitude, peak displacement amplitude, cumulative absolute velocity, and the integral of the squared velocity. The support vector regression method is employed to establish a regression model, which can predict the peak ground acceleration according to these features. Some representative earthquake records of the Taiwan Strong Motion Instrumentation Program from 1992 to 2006 are used to train and validate the support vector regression model. Then the constructed model is tested using entire earthquake records from the same period as well as the 2010 Kaohsiung earthquake with a magnitude of 6.4 ML. The effects on the performance of the regression models using different P-wave features and different lengths of time window to extract these features are studied. The results illustrate that, if the first three seconds of the vertical ground acceleration are used, then the standard deviation of the predicted peak ground acceleration error for the entire 15 years of earthquake records tested is 20.89 gal. The time window can be shortened, e.g., to 1 second, increasing the prediction error slightly, in order to lengthen the lead-time before destructive shear waves reach the station.

Keywords: earthquake early warning, single station method, on site, support vector machine, peak ground acceleration

Introduction

In an earthquake early warning system, an on-site warning issues an alarm within a few seconds after triggered, based on initial pressure wave (P-wave) motion at a single station. Nakamura (1988) developed an earthquake early warning system named UrEDAS that predicted potential damage according to the estimation of magnitude and location based on the calculated predominant frequency, back azimuth, vertical-to-horizontal ratio, and amplitude level. Nakamura (1998) further developed the Compact UrEDAS which estimated potential damage based on the calculation of destructive intensity defined as the logarithm of the absolute value of the inner product of acceleration and velocity. Odaka et al. (2003) tested another approach to estimate magnitude and epicenter distance based on the P-wave amplitude and the fitting parameter of the waveform envelope. Kanamori (2005) proposed another predominant frequency of P-wave which is similar to the one developed by Nakamura (1988) to estimate the magnitude. He proposed the combination of both the predominant frequency and peak ground displacement (PGD) of the P-wave measured in the vertical direction to recognize damaging earthquakes. Bose et al. (2012) estimated

[1] Associate Researcher, National Center for Research on Earthquake Engineering, dysheu@ncree.narl.org.tw.
[2] Assistant Researcher, National Center for Research on Earthquake Engineering, sghuang@ncree.narl.org.tw.
[3] Assistant Researcher, National Center for Research on Earthquake Engineering, ywchang@ncree.narl.org.tw.
[4] Associate Researcher, National Center for Research on Earthquake Engineering, chkuo@ncree.narl.org.tw.
[5] Associate Researcher, National Center for Research on Earthquake Engineering, cmlin@ncree.narl.org.tw.
[6] Associate Researcher, National Center for Research on Earthquake Engineering, tmchang@ncree.narl.org.tw
[7] Professor, Department of Earth Sciences and Institute of Geophysics, National Central University, wenkl@earth.ncu.edu.tw.
[8] Professor, Department of Civil Engineering, National Taiwan University, lohc0220@ntu.edu.tw

the magnitude, epicenter distance and peak ground velocity (PGV) based on the three-component waveforms of acceleration, velocity and displacement. In summary, in the above-mentioned literature, an on-site earthquake early warning is issued according to the estimated magnitude, location, PGV, and/or vulnerability of the earthquake.

However, the peak ground acceleration (PGA) is also a representative parameter for earthquake early warning. Following an earthquake, the seismic intensity scale measured at each station can be calculated according to the measured PGA. For example, in Taiwan, the Central Weather Bureau calculate the seismic intensity scale based on an equation of the form $I = a\log(PGA) + b$, where a and b are constants. Similarly, the Japan Meteorological Agency also reports the earthquake intensity level based on the ground acceleration. The United States Geological Survey can also report the Modified Mercalli Intensity (MMI) scale at each station for smaller events based on the measured PGA using the relationship developed by Worden et al. (2012). Besides, for practical concerns, the PGA threshold is one of the main criteria for earthquake emergency reactions in many applications. For instance, the Taiwan high-speed rail uses PGA as the main criterion for emergency stops. Nuclear power plants also use PGA as the criterion for emergency shutdowns.

Therefore, in this study, PGA is chosen as the target to be estimated. The P-wave features including predominant frequency, peak ground acceleration, peak ground velocity, peak ground displacement, cumulative absolute velocity, and integration of the squared velocity, will be extracted from the initial P-wave motion of the vertical component at a single station. The support vector regression (SVR) method is employed to establish a regression model to predict the PGA according to these P-wave features. In order to gain more lead-time on the on-site warning, the effect of the length of the initial P-wave motion on the performance of the SVR model is also studied.

In addition, the databases used in the literature to establish and validate an empirical regression model between the initial P-wave motion and the final peak ground motion is usually limited to some selected records of some representative events; the epicenter distance is also restricted in some cases. As a result, the applicability of the established empirical regression model could be restricted to only the selected events. Furthermore, since the established empirical regression model has never been validated through the earthquake events of an entire period, e.g., 10 years, the estimated error in practice has never been revealed. Therefore, in this study, earthquake records between 1992 and 2006 from the Taiwan Strong Motion Instrumentation Program (TSMIP) (Liu et al. 1999) will be used to test the proposed approach. The database includes the catastrophic 1999 Chi-Chi earthquake and several damaging earthquake events as well as more than ten thousands records of non-damaging earthquakes.

Methodology

The on-site earthquake early warning technique takes advantage of the different velocities of propagation of P-waves and S-waves. In other words, the expected ground shaking dominated by S-waves can be estimated based on the recorded early informative P-wave of a single station. This is usually accomplished through empirical regressions between the P-wave features extracted from the measurements of the first few seconds and the final earthquake intensity at the same site. Satriano et al. (2011) reviewed the concepts, methods and physical backgrounds of earthquake early warning systems. The P-wave features used to estimate the final earthquake size were also summarized in the same paper. These P-wave features include the peak measurement, predominant period and integral quantities. The P-wave features used to estimate final earthquake intensity in this study are briefly introduced in the following paragraphs.

Firstly, the peak measurement of acceleration, velocity and displacement in the vertical direction t_p seconds after the P-wave's arrival are considered. These features are denoted as P_a, P_v, and P_d, respectively and can be calculated in a straightforward manner. These parameters correlate to the PGA, PGV and PGD of the entire measured time history of ground motion at the same station. Next, the effective predominant period T_c proposed by Kanamori (2005) is employed. This parameter is correlated to the earthquake magnitude. Finally, two more integral quantities are used; the cumulative absolute velocity (CAV) and the integral of the squared velocity (IV2). The CAV is used as a threshold value to determine whether a damaging earthquake is coming. The IV2 is correlated to earthquake magnitude. In this study, the above-mentioned six P-wave features extracted from the vertical component of ground motion after P-wave arrival are used for rapid estimation of PGA.

SVR, which is a supervised learning method based on statistical learning theory, is very effective for solving multivariate problems. Moreover, it has outstanding advantages over other methods, such as no local minimum problem and reliability at underfitting, overfitting, or in high noise conditions. Owing to these merits, this paper employs the SVR algorithm to establish a nonlinear regression model between several P-wave features and PGA. The details for employing SVR to establish a regression model are given by Hsu et al. (2013).

Earthquake data and preprocessing

Approximately fifteen years of TSMIP data between the 29th of July 1992 and the 31th of December 2006 recorded by the Central Weather Bureau are employed in this paper. A total of 91,142 sets of data, named "Testing Earthquake Data", are used in this study to estimate the general performance of the proposed approach. In order to reduce the time required for training the SVR model, 71 earthquake events with local magnitudes, M_L, between 3.0 and 7.3 are selected for all focal depths (2.8 ~ 282.8 km). In this study, only half of the strong ground motion records of the 71 earthquake events will be used to train the SVR model. As a result, the database for training the SVR model consists of 4,166 sets of data, which are named "Representing Earthquake Data". The original strong ground motion records are acceleration signals. The zero-mean normalization of the records was applied. The records were integrated once and twice to obtain velocity and displacement signals, respectively. The second-order 0.075Hz high-pass Butterworth filter was applied to remove the low-frequency drift after integration. The Short-Term Average/Long-Term Average algorithm was applied to determine the P-wave arrival time automatically.

Results and conclusions

Figure 1 compares the real PGA and the predicted PGA for the "Testing Earthquake Data" using the SVR model of all six P-wave features. The regions enclosed by the blue lines and the red lines are within zero- and one-level difference of the seismic intensity scale of Taiwan for reference, respectively. It can be observed in the figure that the predicted PGA approximates the real PGA. The standard deviation of the predicted PGA errors is 20.89 gal, and the ratio of the predicted PGA located within one-level difference from the real PGA is 99.22%. Note that the predicted PGA is generally lower than the real PGA, which means the predicted PGA of the SVR model is in the non-conservative side. The predicted PGA could be scaled up to the conservative side for practical application, which is not considered in this paper.

Next, the effect of the length of time window t_p was studied. Although a longer t_p achieves higher reliability, the lead-time of early warning is sacrificed. As discussed, the lead-time is the crucial factor in an effective earthquake early warning system which should issue an early warning before the arrival of destructive seismic waves, instead of issuing an alarm with very high reliability after or during the incoming destructive seismic waves.

The length of the time window t_p ranges from 0.1 to 10 seconds in intervals of 0.1 second. The results show that the standard deviation of the predicted PGA errors of the "Testing Earthquake Data" decreases as t_p increases, as shown in Figure 2. The standard deviation of predicted error diminishes very quickly from about 34 gal to 23 gal within the first second. It continues to decrease gradually thereafter to less than 18 gal. In addition, the ratios of the predicted PGA located within one-level difference from the real PGA are also plotted in the same figure. The one-level predicted ratios increase dramatically from about 91% to 97% within the first 0.4 seconds and then continue to increase rapidly to almost 99% until $t_p = 1$, which is already quite close to the maximum value saturated at around $t_p = 4$. It appears that t_p could be less than 3 seconds for practical application using the proposed approach. Thus, the extent of the region without lead-time could be reduced and valuable response time could be gained.

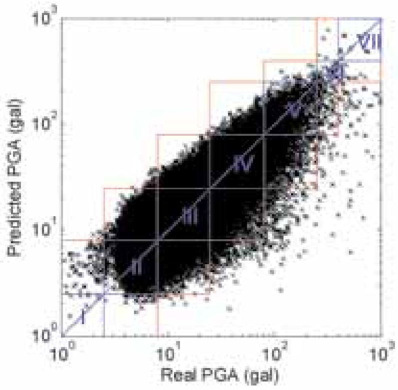

Fig. 1 Real PGA and the predicted PGA of the 91,142 sets of "Testing Earthquake Data" using the SVR model of six P-wave features with $t_p = 3$. The Roman numerals "I" to "VII" represent the seismic intensity scale in Taiwan. The regions enclosed by the blue lines represent the fact that seismic intensity of the predicted PGA is the same as the real one, while the regions enclosed by the red lines represent the seismic intensity of the predicted PGA is within ±one-scale of the real one.

Finally, the feasibility of the proposed SVR model is studied through the application of the 2010 Kaohsiung earthquake which is absent from the "Testing Earthquake Data". The Kaohsiung earthquake with magnitude $M_L = 6.4$ and focal depth 22.6 km caused injuries to 96 people and different levels of damage to hundreds of buildings. The maximum PGA was 463.03 gal measured at the CHY062 station about 30.48 km from the epicenter, while the minimum PGA was 5.16 gal measured at the TAP057 station about 254.46 km from the epicenter. Again, the overall approximate relationship between real PGA and the predicted PGA can be observed.

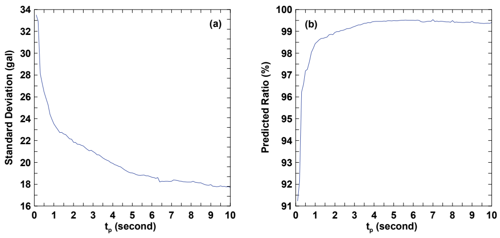

Fig. 2 The performance of the SVR model of the "Testing Earthquake Data" using different length of time window: (a) standard deviation of the predicted PGA errors and (b) ratio of the predicted PGA located within one-level difference from the real PGA.

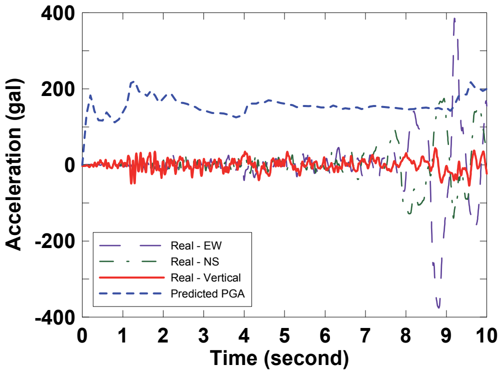

Fig. 3 The predicted PGA of the SVR models with t_p ranges between 0.1 and 10 seconds in intervals of 0.1 second at station: (a) KAU020, (b) KAU018, (c) CHY062, and (d) CHY063. The measured acceleration time-history of three directions at each station is also plotted.

The performances of the SVR models at several stations close to the epicenter are also studied. According to the reconnaissance report of the National Center for Research on Earthquake Engineering in Taiwan (NCREE), four stations, i.e. KAU020, KAU018, CHY062 and CHY063, within a short distance from the epicenter of 18.46, 24.8, 30.5 and 37.2 km, respectively, were accompanied by severe or moderate damage of nearby buildings and non-structural items (NCREE 2010). The predicted PGA at the CHY063 station using the SVR models with different lengths of time window, i.e. $t_p = 0$ to $t_p = 10$, and the measured acceleration time-history of three directions is plotted together in Figure 3. It can be observed that after the arrival of a P-wave, the predicted PGAs at different times are larger than 80 gal or 92 gal, which corresponds to intensity V on the Taiwan scale and intensity VI on the MMI scale (Worden et al. 2012), respectively. In other words, if the warning is issued based on these intensities, the region close to the station could be alerted directly after the arrival of a P-wave. However, in practice, due to the higher uncertainty of the predicted PGA using less P-wave information, the warning could be postponed until the first second if a higher reliability is required. Furthermore, if the warning is issued at the first second after the arrival of a P-wave, the response time before the strike of the largest seismic wave of the station is about 6 seconds.

References

Böse M, Heaton T, Hauksson E (2012) Rapid estimation of earthquake source and ground-motion parameters for earthquake early warning using data from a single three-component broadband or strong-motion sensor. Bull Seism Soc Am 102(2): 738–750.

Kanamori H (2005) Real-time seismology and earthquake damage mitigation. Annu. Rev Earth Planet Sci 33: 195–214.

Liu KS, Shin TC and Tsai YB (1999) A free-filed strong motion network in Taiwan: TSMIP TAO 10(2): 31-50.

Nakamura, Y. (1988). On the urgent earthquake detection and alarm system (UrEDAS). Proc 9th World Conf Earthquake Eng (7): 673–678.

Nakamura Y (1998) A new concept for the earthquake vulnerability estimation and its application to the early warning system. Proc Early Warning Conf Potsdam, Germany.

National Center for Research on Earthquake Engineering (2010) Reconnaissance report on Jiaxian earthquake in Kaohsiung on March 4, 2010. Taipei, NCREE-10-010 (in Chinese).

Odaka T, Ashiya K, Tsukada S, Sato S, Ohtake K, Nozaka D (2003) A new method of quickly estimating epicentral distance and magnitude from a single seismic record. Bull Seism Soc Am 93(1): 526–532.

Satriano C, Wu YM, Zollo A, Kanamori H (2011) Earthquake early warning: Concepts, method and physical grounds. Soil Dyn Earthq Eng 31: 106-118

Vapnik VN (1995) The nature of wtatistical learning theory. Berlin, Springer-Verlag

Worden CB, Gerstenberger MC, Rhoades DA, Wald DJ (2012) Probabilistic relationships between ground-motion parameters and Modified Mercalli Intensity in California. Bull Seism Soc Am 102(1): 204–221.

Hsu T.Y., Huang S.K., Chang Y.W.,Kuo C.H., Lin C.M., Chang T.M., Wen K.L., Loh C.H., "Rapid on-site peak ground acceleration estimation based on support vector regression and P-wave features in Taiwan." Soil Dynamics and Earthquake Engineering (2013), Volume 49, June 2013, Pages 210 – 217, DOI: 10.1016/j.soildyn.2013.03.001.

Investigation of Buried Pipelines under Large Fault Movements by Small-Scale Testing and Numerical Methods

Tsu-Jung Lin (林祖榕)[1]

Abstract

This paper investigates the responses of buried pipelines under large fault movements using numerical models and small-scale experiments. Well-designed small-scale shear boxes experiments can induce the soil-pipeline interaction under fault displacements. Numerical models built by the ABAQUS commercial software were able to simulate the behavior of small-scale shear box experiments at different soil depths. Comprehensive and reliable numerical simulation of this problem requires experimental data to calibrate and verify the three dimensional responses of pipelines subjected to axial and flexural loadings. Finally, recommendations and future works are proposed for the design of small-scale experiments and numerical models.

Keywords: small-scale experiment, fault movement, pipeline, local buckling

Introduction

Earthquakes can damage pipelines near the fault influencing the function of the water supply system. Thus, the structural behavior of buried pipelines under fault lines has gained attention from engineers and researchers. O'Rourke et al. (2008) addressed the large-scale testing of pipeline responses to earthquake-induced ground ruptures and pipeline system performance after earthquakes. Vazouras et al. (2010) presented a rigorous FEM model to investigate the mechanical behavior of buried steel pipelines under strike-slip faults. In Vazouras' research, the interacting soil-pipeline system was modeled by finite elements, which can account for large strains and displacements, nonlinear materials and special contact on the soil and pipelines interface. Due to the high cost and time consumption of large-scale experiments, such as the one shown in Fig. 1, small-scale experiments are often used since they are more convenient to set up and can be conducted as preliminary experiments to large-scale experiments. In this study, small-scale experiments were conducted in National Center for Research on Earthquake Engineering (NCREE) laboratory. Only strike-slip fault movements were applied by the shaking table. The selection of pipelines in the experiment has some limitations with regard to the materials and sizes due to the size restrictions of the small-scale experiments. The axial strains of pipelines and fault movement displacements can be measured during the experiments. The responses of the buried pipelines subjected to large strike-slip fault movements are investigated by finite element analysis (ABAQUS 2011). Geometric and material nonlinearities are taken into account in the simulation.

Fig.1 Large-scale soil-pipeline test at Cornell University

Test Set-up

The small-scale soil-pipeline tests were set-up at the laboratory at the National Center for Research on Earthquake Engineering (NCREE). The shear boxes used were 60 cm in length, 23 cm in width, and 32 cm in height. Fig. 2 shows that one of the shear boxes was placed on a small shaking table with a small hydraulic structural actuator (maximum forces

[1] Associate Researcher, National Center for Research on Earthquake Engineering, tjlin@ncree.narl.org.tw

of 15kN allowed) which can provide a one-way stroke displacement of 14 cm. Another shear box was set up on a small manufactured platform that can be adjusted to the same height as the shear box on the shaking table. The two shear boxes were fabricated to ensure good contact in order to prevent sand leaking issues and also to allow free movement under fault displacements. The shear boxes were initially offset to allow for maximum soil pressure acting on the pipelines, as shown in Fig. 3.

Fig.2 Shear boxes set-up

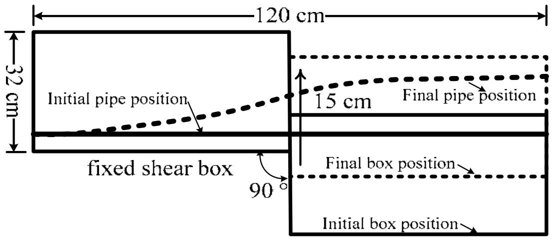

Fig. 3 Plan view of the small-scale pipeline test with key dimensions and geometry

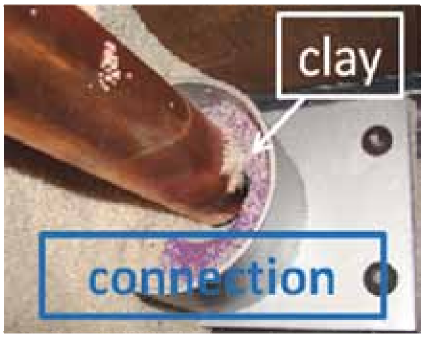

Fig. 4 The end of the pipeline.

Fig. 5 Shear boxes with loadings on the top of the sand surface.

Test Methods

All tests were conducted with partially saturated silica sand imported from Vietnam. During production, the full test set-up was completed by the following steps: 1) pipeline installation in the test basin, 2) structure adjustment at the boxes, 3) soil placement and compaction. Tests were performed using the static monotonic loading method at a 0.5mm/sec speed (slow). Twenty instances of data per second could be recorded. A long steel strip was placed on the bottom of the shear boxes to prevent sand leaking outside the boxes from the location of fault movement.

Compared to large-scale experiments, the small-scale soil-pipeline interaction experiments may bring size effect issues. The choice of pipeline size, soil properties in the small shear boxes and boundary conditions at the ends of the pipeline needed to be considered in the test set-up. The pipeline size chosen in the current tests was 40 mm in diameter with a 0.5 mm copper thickness. The buried depth was 125 mm. Both ends of the pipeline were surrounded by soft clay in order to appropriately reflect the real site situation, as shown in Fig.4. Several lead weights (each one 54 Kg) were placed on the top of rigid plates to increase the soil pressure surrounding the pipelines, as shown in Fig. 5. Eleven strain gauges were placed on each side of the pipeline surface including two yield strain gauges to detect large deformations.

Fig. 6 Local buckling occurred on the pipeline.

Test results

In this case, five lead weights were placed on the top of each shear box. The total lead weight was equal to 270Kg, which gave an additional 0.96m buried depth if the density of dry sand is 1.56. From Fig. 6, local buckling behavior can be observed occurring on the pipeline at both sides of the faults. In Fig. 7(a) and (b), it can be seen that the local buckling occurred at around 20 cm to the fault. The maximum compressive strain occurred at a fault movement of 7 cm. After this movement, the compressive strain decreased gradually because the pipeline had been extended by the fault movement.

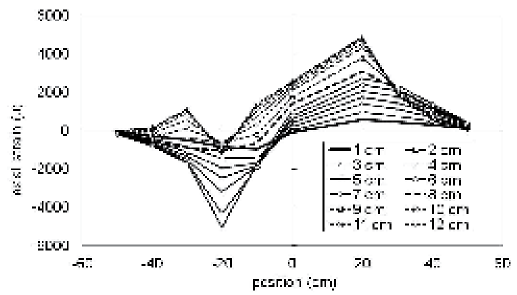

(a)

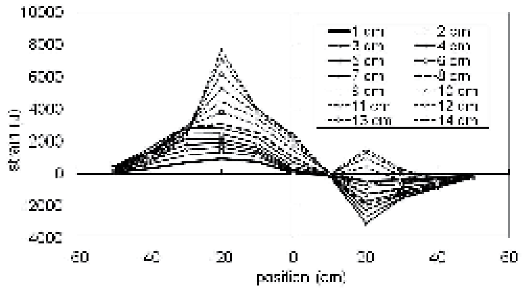

(b)

Fig. 7 The relationship between axial strain and position under different fault movements.

Numerical model and results

The commercial finite element package software ABAQUS was adopted to numerically simulate the mechanical behavior of the buried pipe. The surrounding soil medium and the soil-pipeline interaction were studied in a rigorous manner with consideration to the nonlinear geometry of the soil and the pipe. An elongated prismatic model was considered, as shown in Fig. 8, in which the pipelines were embedded in the soil. The eight-node reduced-integration brick elements (type C3D8R) were used to simulate the surrounding soil. The seismic fault plane divided the soil in two equal parts and was considered perpendicular to the pipeline axis at the middle section of the pipeline. The pipeline was modeled by four-node reduce-integration shell elements (S4R) which easily expressed the local buckling behavior of the pipelines. The pipeline axis was assumed to be horizontal and normal to the fault plane.

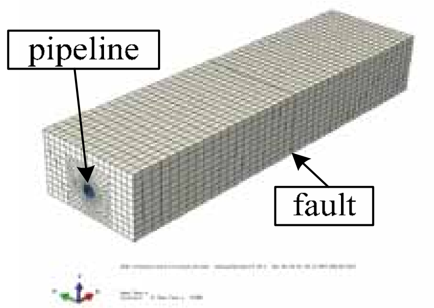

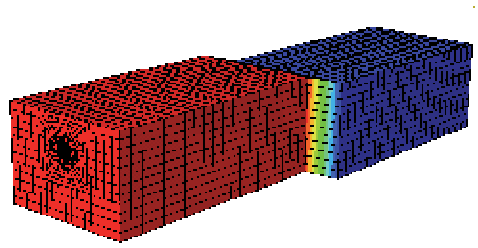

Fig. 8 Numerical model: soil (brick elements); pipeline (shell elements); gap opening at the soil-pipe interface induced by fault movement.

Fig. 9 depicts the shape of the deformed pipeline at a fault displacement of d = 8 cm in the area near the fault where localized deformation at point A is referred to as local buckling. Due to the skew-symmetry of the problem, a similar local deformation occurred at point B, on the hidden side of the pipeline.

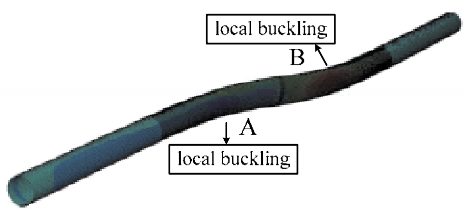

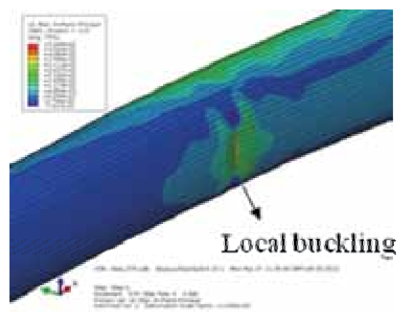

Fig. 9 Local buckling at the pipeline

By conducting the small-scale pipeline-soil interaction tests, the structural behavior of the buried pipeline crossing the strike-slip fault was investigated. Through the commercial FEM software, the effects of the size of the shear boxes, soil material properties and boundary conditions, which might affect the behavior of pipelines, can be discussed in the future. Besides, the parameter calibration of the numerical models can be achieved by using experimental data.

Conclusions

By conducting small-scale pipeline-soil interaction tests, the structural behavior of buried pipelines crossing a strike-slip fault was investigated. However, size effects, which might affect the behavior of pipelines such as, the size of pipelines, soil pressures, and boundary conditions set up at both ends of the pipeline, needed to be considered in the small-scale experiments. In the set up of the current tests, some problems that needed to be considered were: 1) the reduction of the thickness of the pipelines, a characteristic that might be helpful in the observation of local buckling behavior of pipelines; 2) the introduction of steel plates on the top of soil surfaces to produce adequate soil pressure, as well as designing devices to accurately measure the soil pressure; 3) the shaping of the boundary conditions at the two ends of the pipeline in order to simulate the real world behavior of endless pipelines. Using advanced finite element simulation tools, the numerical models of the soil (solid elements) and pipelines (shell elements) were built by the ABAQUS commercial software. The contact algorithm between the soil and pipeline was taken into account. This model can be used to complete the investigation of several soil and pipe parameters on the pipeline deformation and strength. As small-scale experiments are limited to the size of the shear boxes, numerical models are a relatively convenient method to investigate the size effect, which will be part of the future work of this study. The realistic soil material properties of sand measured accurately from the shear boxes will also be applied to the numerical model. A parametric study of the numerical model can be calibrated by using the experimental data in the future.

References

ABAQUS version 6.10 (2011). Analysis Users Manual. Providence, RI: Dassault Systèmes Simulia Corporation.

Abdoun, T. H., Ha, D., O'Rourke, M. J., Symans, M. D. O'Rourke, T. D. Palmer, M. C. and Harry, E. S. (2009). Factors influencing the behavior of buried pipelines subjected to earthquake faulting. *Soil Dyn. Earthqu. Eng.* **29:3**, 415-427.

American Lifelines Alliance-ASCE (2001). Guidelines for the design of buried steel pipe (with addenda through February 2005).

Elhmadi, K. and O'rourke, M. J. (1990). Seismic damage to segmented buried pipelines. *Earthqu. Eng. Struct. Dyn.* **19:4**, 529-539.

Joshi, S., Prashant, A., Deb, A. and Jain, S. K. (2011). Analysis of buried pipelines subjected to reverse fault motion. *Soil Dyn. Earthqu. Eng.* **31:7**, 930-940.

Ha, D., Abdoun, T. H., O'Rourke, M. J., Symans, M. D. O'Rourke, T. D., Palmer, M. C. and Harry, E. S. (2008a). Buried high-density polyethylene pipelines subjected to normal and strike-slip faulting-a centrifuge investigation. *Can. Geotech*. J. 45(12), 1733-1742.

Ha, D., Abdoun, T. H., O'Rourke, M. J., Symans, M. D. O'Rourke, T. D. Palmer, M. C. & Harry, E. S. (2008b). Centrifuge modeling of earthquake effects on buried high-density polyethylene (HDPE) pipelines crossing fault zones, *ASCE J. Geotech. Geoenviron. Eng.* **134:10**, 1501-1515.

Karamitros, D. K., Bouckovalas, G. D. and Kouretzis, G. P. (2007). Stress analysis of buried steel pipelines at strike-slip fault crossings. *Soil Dyn. Earthqu. Eng.* **27:3**, 200-211.

Kennedy, R. P., Chow, A. W. and Williamson, R. A. (1977). Fault movement effects on buried oil pipeline. J. Transp. *Eng. Div.*, ASCE. **103:15**, 617-633.

Newmark, N. M. and Hall, W. J., (1975). Pipeline Design to Resist Large Fault Displacements, Proc. US National Conference on Earthquake Engineering, Ann Arbor, Michigan.

Olson, N. (2009). Soil Performance For Large Scale Soil-Pipeline Tests. PhD, Thesis. Cornell University.

O'Rourke, T. D., Jezerski, J. M., Olson, N. A., Bonneau, A. L., Palmer, M. C., Stewart, H. E., O'Rourke, M. J., Abdoun, T. (2008). Geotechnics of pipeline system response to earthquakes, *Proceedings of the Geotechnical Earthquake Engineering and Soil Dynamics IV Congress.*

Palmer, M. C., O'Rourke, T. D., Olson, N. A., Abdoun, T. H., Ha, D. and O'Rourke, M. J. (2009). Tactile pressure sensors for soil-structure interaction assessment, *ASCE J. Geotech. Geoenviron. Eng.* **135:11**, 1638-1645.

Trifonov, O. V. and Chernify, V. P. (2010). A semi-analytical approach to a nonlinear stress-strain analysis of buried steel pipelines crossing active faults. *Soil Dyn. Earthqu. Eng.* **30:11**, 1298-1308.

Vazouras, P., Karamanos, S. A. and Dakoulas, P. (2010). Finite element analysis of buried steel pipelines under strike-slip fault displacements. *Soil Dyn. Earthqu. Eng.* **30:11**, 1361-1376.

Wang, L. R. L. and Yeh, Y. (1985). A refined seismic analysis and design of buried pipeline for fault movement. *Earthqu. Eng. Struct. Dyn.* **13:1**, 75-96.

Seismic Damage Estimation and Database Construction for the Railway Transportation System in Taiwan

Chin-Hsun Yeh[1], Gee-Yu Liu[2], Lee-Hui Huang[3] and Hsi-Hung Chang[4]

葉錦勳 [1]、劉季宇 [2]、黃李暉 [3]、張錫宏 [4]

Abstract

The objective of this study is to evaluate the seismic risk and retrofit feasibility of railway bridges and to improve the safety of the entire railway system for the Taiwan Railways Administration (TRA). The around-Taiwan railway system is a ring network with some branches. It comprises structural elements such as rail tracks, bridges, tunnels, station buildings, and electrical facilities. The railway database was constructed according to structural elements types, and the relevant parameters were adjusted according to actual damage results and earthquake damage assessments of the railway system. Based on the developed seismic scenario simulation technology and refer to the framework of the Thway (TELES for highway system) software, an integrated software (Trail) was developed for application in the estimation of earthquake damage and economic loss for the railway transportation system. The software is primarily used to evaluate railway bridge damage and turnover loss caused by interruptions to railway bridges following an earthquake event.

Keywords: Railway system, Seismic damage estimation, Turnover loss.

Introduction

The TELES (Taiwan Earthquake Loss Estimation System) software has been developed by the National Center for Research on Earthquake Engineering (NCREE) over many years. It is used to assess potential earth science hazards and possible damage and loss induced by earthquakes. The framework of TELES includes modules of seismic hazard analysis, structural damage assessment, earthquake-induced secondary disaster evaluation, and social economic loss estimation. Traditionally, the analysis modules for buildings, bridges, the water system, and so forth, are all integrated into the TELES software. Each module was often divided into sub-modules for specific research purposes or according to the needs of TELES users. Subsequently, even though its performance has been upgraded continually, the operation of the software has become more complicated. This is sometimes inconvenient for users. Moreover, most users only made use of certain parts of the TELES's functions and modules, with other parts never being used. This may reduce the willingness of users to use the TELES software since time is lost in learning how to operate all the functions and modules of TELES.

Recently, the TELES software has been further developed to allow customization depending on the specific needs of users. For example, an earthquake risk assessment (ERA) module has been developed to meet the unique demand of the Taiwan Residential Earthquake Insurance Fund (TREIF). This module can provide objective evaluations of residential earthquake exposure and calculate the insurance premiums and references for insurance brokers. Similarly, a module for earthquake loss assessment of the water system (Twater) was developed as a standalone module from TELES. It provides hydraulic model analysis and post-earthquake performance assessment for use by water departments of the government.

With participation in research projects such as the "Seismic assessment and retrofit feasibility for highway bridges" (Directorate General of Highways, MOTC, 2009), and the "Development of early seismic

[1] Researcher and Division Manager, National Center for Research on Earthquake Engineering, chyeh@ncree.narl.org.tw
[2] Associate Researcher, National Center for Research on Earthquake Engineering, karl@ncree.narl.org.tw
[3] Assistant Researcher, National Center for Research on Earthquake Engineering, lhhuang@ncree.narl.org.tw
[4] Associate Researcher, National Center for Research on Earthquake Engineering, hhchang@ncree.narl.org.tw

loss estimation module and database for highway bridges" (Liu, et al., 2010), TELES now has the ability to estimate the seismic damage of highway bridges. In this study, the seismic damage estimation module for railway bridges was constructed mainly based on the development experience obtained from the analysis module for highway bridges. However, the superstructures of railway bridges are different from those of highway bridges, as they include rail tracks, roadbeds, electrical facilities, loading types, and so on. Hence, parameters such as the replacement cost, damage ratio, repair time, and the fragility curve have to be modified appropriately for the railway system. At this stage, TELES has included 708 railway bridges, rail tracks, and turnover data for the damage assessments of railway bridges and rail tracks, as well as the estimation of the turnover loss caused by interruption to railway bridges after an earthquake.

Database Construction

Recently, with the participation in the TRA project, "Planning of total examination and seismic retrofit of railway bridges", which was primarily executed by Sinotech Engineering Consultants, the structural database of 708 railway bridges and the GIS database of bridge culverts, rail tracks, and train stations has been obtained. These databases are sufficient for the development of seismic damage estimation of railway bridges and tracks in the railway system, in which the structural elements of culverts and underground passages are a major part of the railway bridge database. Since the properties of these structural elements are different from the regular bridge classification in the highway system, one extra class was added for the culverts and the underground passages in the bridge classification of the railway system.

Regarding the economic loss estimation of the railway system, a simplified module was applied to calculate the distribution of the average daily turnover between any pair of train stations using the TRA annual turnover data of all train stations. Accordingly, one can then obtain the possible turnover loss of the disconnected train stations caused by interruption to railway bridges after an earthquake.

In order to examine the reliability of the estimation parameters and the outcomes of the damage and the turnover loss assessment modules for railway bridges, some survey reports of the railway system suffering from earthquake and typhoon disasters in recent years, including the cases of the 921 Chi-Chi Earthquake in 1999, Typhoon Morakot, and Typhoon Parma in 2009, were also collected for analysis. By comparing the compiled information of damage states, restoration times and repair costs of the railway bridges following actual disasters with the scenario simulation results from the assessment modules, reasonable and reliable parameters for the analysis modules of the railway system were then drawn up.

Damage Estimation of Railway Bridges

The methodology and analysis procedure of seismic damage estimation for railway bridges are similar to those for highway bridges. However, the characteristics and basic requirements of the seismic capacity, replacement cost, restoration time, and repair time between these two engineering structures are different. Hence, it is necessary to appropriately review and modify the relevant parameters of damage assessment for railway bridges.

The classification of bridges is primarily based on the following structural characteristics: seismic design, span continuity, and abutment type. Before 1999, there was no seismic design code in place for railway bridges in Taiwan. In order to understand the seismic capacity of domestic railway bridges, Sinotech Engineering Consultants selected 38 railway bridges with different seismic designs and structural types for the seismic capacity analysis using the pushover method, in which the analysis of railway bridges before 1999 are carried out according to the version of the 1987 seismic design code for highway bridges. After comparing these results with the real damage situation that occurred during the 921 Chi-Chi Earthquake, one can define the fragility parameters of railway bridges, culverts, and underground passages for the railway system.

In contrast to highway bridges, the replacement cost of railway bridges comprises the costs of both civil structures and track facilities, which are denoted by C_{str} and C_{track}, respectively. In other words, the track facilities of rail tracks, roadbeds and electrical facilities in the railway system could be damaged from ground shaking and ground failure in addition to the civil structures. Similar to the estimation formula for the highway system, the replacement cost of the civil structures for each bridge type is given by:

$$C_{str} = A_{bridge} \times C_{unit} , \tag{1}$$

in which A_{bridge} denotes the bridge area, and C_{unit} is the replacement cost per unit deck area.

The replacement cost of the track facilities includes the costs of roadbeds, rail tracks, and electrical facilities. According to practical experience, the replacement cost is NT$30,000 per meter per track for regular roadbeds and rail tracks, and is about NT$35,000 per meter per track for concrete roadbeds. The replacement cost of the electrical facilities is NT$23,500 per meter per track. When a railway bridge requires rebuilding, a temporary rail track would have to be established beside the bridge in order to retain the normal operation of the railway transportation. Thus, it is necessary to include the cost of the temporary track in this situation. Furthermore, when the segment of the rail track on a bridge is damaged and needs to be replaced, other rail tracks nearby would also be affected and need to be replaced concurrently. In this study, we assume that the segment length of the affected rail tracks is about 150 meters. As a result, the total value of rebuilt tracks for the track facilities includes the temporary tracks and the nearby affected tracks. The replacement cost is given by:

$$C_{track} = (L_{bridge} \times (N_{track} + 1) + 150) \times (3.5 + 2.35), \quad (2)$$

where N_{track} represents the number of rail tracks to be replaced and L_{bridge} denotes the length of a damaged railway bridge.

The definition of the damage ratio is the proportion of the repair cost to the replacement cost of a structural system. The relevant parameters of the damage ratio are determined according to the actual loss of each damage state for different types of railway bridges from field investigation. Under the assistance of the TRA, material data and information regarding the damage situations of railway bridges suffering from earthquake and typhoon disasters (such as the 921 Chi-Chi Earthquake, Typhoon Morakot and Typhoon Parma) in recent years were collected from the construction sections, and were compiled in a database in an appropriate format for TELES. According to the practical experience of the TRA, the repair cost of rail tracks and electrical facilities subjected to slight, moderate, or extensive damage is very small. The major repair cost is spent on civil structures in these damage states. However, the difference among the repair costs of bridge structures, rail tracks, roadbeds, and electrical facilities are not significant in the complete damage state. Herein the damage ratio is determined based on the above rules in order to evaluate the economic loss to the railway bridges under different kinds of damage states.

Restoration Time or Intercept Time

The definition of the intercept time (or the restoration time) is the time period for the restoration of damaged railway bridges. The intercept time has an important influence on the operation of the railway transportation system: the longer the intercept time, the more turnover loss is produced. It is therefore necessary to assess the intercept time caused by the interruption to railway bridges after an earthquake before evaluating the turnover loss of the railway transportation system.

The railway transportation system in Taiwan is a ring network. When a railway bridge on a certain section of the railway system is damaged, all the trains that pass through this section will be affected. When a railway bridge located on a section between two adjacent train stations is damaged, the passage between these two train stations will fail. In other words, the greater the number of railway bridges located on a section between two adjacent train stations, the greater the demand of the average intercept time since each railway bridge on this section may be damaged by an earthquake event. Under the assumption that the intercepts of damaged railway bridges are sample events independent of each other and without considering the damage probabilities of the rail tracks or the other facilities, the failure probability of one section is a function of the failure probabilities of the railway bridges on this section only. The failure probability of the section can be expressed as follows:

$$\hat{p}_f = 1 - \prod_k (1 - p_f^k), \quad (3)$$

where p_f^k denotes the failure probability of the k th railway bridge.

Eq. (3) implies that the passage probability of a section is the product of the passage probabilities of all the railway bridges on that section. Assume that the average intercept time of one section under the failure condition, $\hat{T}_f$, is defined by the weighting average of the average intercept times of all the railway bridges on the section under the failure condition, we have

$$\hat{T}_f = \frac{\sum_k p_f^k \cdot T_f^k}{\sum_k p_f^k}, \quad (4)$$

from which the average intercept time of the section is given by

$$\hat{T}_1 = \hat{p}_f \cdot \hat{T}_f. \quad (5)$$

Moreover, if one of the railway bridges on a section requires a long time to be restored, the average intercept time of this whole section may be controlled by this one railway bridge. This implies that another way to determine the average intercept time of one section is to choose the maximum average intercept time among the railway bridges on the section, yields

$$\hat{T}_2 = \max(p_f^k \cdot T_f^k, \quad \forall k). \quad (6)$$

In summary, in this study, the larger value from Eq. (5) and Eq. (6) is chosen to be the average intercept time of one failed section.

The existence of a failed section would interrupt the passage between any pair of train stations that pass through this section. Specifically, when the railway segment between one pair of train stations contains many sections, any section's failure would interrupt the passage of the railway segment. Similar to the calculation of the average intercept time of a failed section containing many railway bridges, the average intercept time of a failed railway segment containing many sections can be evaluated accordingly. The average intercept time of the railway segment between any pair of train stations can be displayed in the form of a matrix, as shown in Table 1.

Table 1 Average intercept time of railway segment between pairs of train stations under failure conditions

	Taipei	Taoyuan	Hsinchu	Taichung	Chiayi	Tainan	Kaohsiung
Taipei	0	$T_{r,21}$	$T_{r,31}$	$T_{r,41}$	$T_{r,51}$	$T_{r,61}$	$T_{r,71}$
Taoyuan	0	0	$T_{r,32}$	$T_{r,42}$	$T_{r,52}$	$T_{r,62}$	$T_{r,72}$
Hsinchu	0	0	0	$T_{r,43}$	$T_{r,53}$	$T_{r,63}$	$T_{r,73}$
Taichung	0	0	0	0	$T_{r,54}$	$T_{r,64}$	$T_{r,74}$
Chiayi	0	0	0	0	0	$T_{r,65}$	$T_{r,75}$
Tainan	0	0	0	0	0	0	$T_{r,76}$
Kaohsiung	0	0	0	0	0	0	0

Turnover Loss Evaluation

To evaluate the turnover loss caused by interruption to railway bridges, the transportation revenues between pairs of train stations were obtained by analyzing the 2011 transportation revenue of each train station provided by the TRA. The transportation revenue between each pair of train stations along a main railway line is expressed in a matrix form, and is called the Daily Turnover Matrix. According to the railway transportation operation type, the Taiwan railway system is divided into four main railway lines: West-sea line, West-mountain line, East line, and South line. As such, one can construct the daily turnover matrices for the four main railway lines, in which each element represents the daily turnover between one pair of train stations.

For example, if one section between the Taoyuan and Hsinchu stations fails, it is necessary to suspend all the trains travelling through this section. As shown by the red circle in Table 2, the trains that set out from the Taipei or the Taoyuan station toward the southern stations after the Hsinchu station are required to be suspended, and vice versa for the trains travelling in the direction to the northern stations. The trains not passing through the failed section will remain in operation. The summation of the turnovers in the red circle in Table 2 represents the total turnover loss caused by the failed section between the Taoyuan and Hsinchu stations.

Table 2 Turnover loss for a failed section between the Taoyuan and Hsinchu stations

	Taipei	Taoyuan	Hsinchu	Taichung	Chiayi	Tainan	Kaohsiung
Taipei	0	L_{21}	L_{31}	L_{41}	L_{51}	L_{61}	L_{71}
Taoyuan	0	0	L_{32}	L_{42}	L_{52}	L_{62}	L_{72}
Hsinchu	0	0	0	L_{43}	L_{53}	L_{63}	L_{73}
Taichung	0	0	0	0	L_{54}	L_{64}	L_{74}
Chiayi	0	0	0	0	0	L_{65}	L_{75}
Tainan	0	0	0	0	0	0	L_{76}
Kaohsiung	0	0	0	0	0	0	0

Conclusions

Regarding the transportation system, the TELES software already contains a module to estimate the earthquake damage of the highway system. This study developed the evaluation methodology of economic loss for railway bridges, railway turnover loss, and the average intercept time for each railway section of the Taiwan railway system. However, the damage estimation module of tunnel structures for the railway and highway systems has not yet been established due to the lack of a database relevant to the tunnel structures. Hence, in order to improve the integrity of the transportation system module for TELES, data collection and the development of the damage estimation of tunnel structures will be the primary focus of work in the future.

References

RMS (Risk Management Solutions, Inc.), 1999, Earthquake Loss Estimation Method -HAZUS99 Technical Manual, National Institute of Building Sciences, Washington, D.C.

Directorate General of Highways, MOTC (2009). *Seismic Assessment and Retrofit Feasibility for Highway Bridges*, Final report, CECI Engineering Consultants, Inc., Taipei. (in Chinese)

Liu, G.-Y., Yeh, C.-H., Chang, K.-C., Jao, C., Hung, H.-Y., Huang, L.-H., Liu, Y.-N., Chen, C.-L., Lin, C.-C. (2010). *Development of Early Seismic Loss Estimation Module and Database for Highway Bridges*, Institute of Transportation, Ministry of Transportation and Communications, Taipei. (in Chinese)

Yeh, C.-H. (1999). *Application of Geographical Information System on Seismic Hazard Analysis and Loss Estimation*, Technical Report NCREE-99-035, National Center for Research on Earthquake Engineering, Taipei. (in Chinese)

Yeh, C.-H. (2002). *Integration Study on the Earthquake Disaster Scenario Simulation and its Application Software*, Technical Report NCREE-02-009, National Center for Research on Earthquake Engineering, Taipei. (in Chinese)

Seismic Testing and Grading of Ductile Iron Water Pipes

Gee-Yu Liu[1], Lap-Loi Chung[2] and Pao-Ching Chou[3]

劉季宇 [1]、鍾立來 [2]、周寶卿 [3]

Abstract

Ductile iron is widely adopted as a material for buried water pipes due to its mechanical and chemical properties, such as its high toughness, strength, and resistance to corrosion. Ductile iron pipes (DIP) are fabricated in segments, normally 6 meters long, in workshops, and are connected by joints one-by-one on site. During an earthquake, they are inevitably subjected to ground shaking and deformation. Damage may occur in the pipe wall or at the pipe joint under excess seismic actions. In this research, seismic testing of DIPs is performed. DIPs with three different joint types, namely K-type, A-type, and flange, are tested. Pipe specimens filled with pressurized water were deformed separately under tension, compression, and bending loads. It is observed that DIPs with either a K-type or an A-type joint have good deformation capacity, but fail to prevent disengagement at the pipe joint under very small tensile action. DIPs with a flange joint, albeit with very high strength, have very poor deformation capacity and may leak easily once opened or bent slightly. Finally, according to the classification suggested by ISO 16134, the seismic capacity of DIPs with each of the three joints is classified with respect to their expansion, contraction, slip-out resistance, and joint deflection performance, respectively.

Keywords: water pipes, ductile iron, seismic capacity, ISO 16134

Introduction

Taiwan is located in an earthquake-prone area. Disastrous inland earthquakes take place every 10 years on average. The expected earthquake losses have become increasingly significant as a result of a highly developed environment. The seismic safety of the water system is evidently critical to the welfare of citizens. Ductile iron is a widely adopted material used for buried water pipes, due to its mechanical and chemical properties, such as its high toughness, plasticity, and resistance to corrosion. Ductile iron pipes (DIP) are fabricated in segments, normally 6 meters long, in workshops, and are connected by joints one-by-one on site. During an earthquake, DIPs are inevitably subjected to ground shaking and deformation. Damage may occur in the pipe wall or at the pipe joint under excess seismic action. Evidence from the 1999 Chi-Chi earthquake showed that DIPs were mostly damaged at the joints. The vulnerability of DIPs is highly dependent on pipe size and joint type.

ISO 16134 now serves as a major reference for the earthquake- and subsidence-resistant design of DIPs; following this reference, practitioners can design a water pipe according to the seismic demands of a site. Nevertheless, very limited research work has focused upon how to quantify the seismic capacity of a pipe through a testing process. In this study, a testing process to determine the seismic capacity of ductile iron water pipes with various types of joints was investigated experimentally. Pipe specimens with a nominal diameter of 400 mm were assembled using K-type, A-type, and flange joints, as illustrated in Fig. 1. Recently in Taiwan, pipes with a K-type joint have become widely used in water pipes. However, pipes with A-type joints outnumber those with K-type joints due to the fact that the former have been used for a long time in buried DIPs. Flange joints are commonly used for the connection of valves and meters.

For each type of joint, six specimens were prepared for testing under different types of loading: two for tension, two for compression, and two for

[1] Associate Researcher, National Center for Research on Earthquake Engineering, karl@ncree.narl.org.tw

[2] Researcher, National Center for Research on Earthquake Engineering, chung@ncree.narl.org.tw

[3] Assistant Researcher, National Center for Research on Earthquake Engineering, pcchou@ncree.narl.org.tw

bending. The specimens were closed with end plates and filled with pressurized water. The water pressure was controlled to maintain a prescribed level. Failure of the specimen was defined as the point at which leakage occurred and the water pressure could not be kept at this prescribed level. The stiffness, strength, ductility, and failure mode of each joint were investigated. The seismic performance of each joint was classified, in terms of resistance to tension, displacement capacity, and rotation capacity according to ISO 16134.

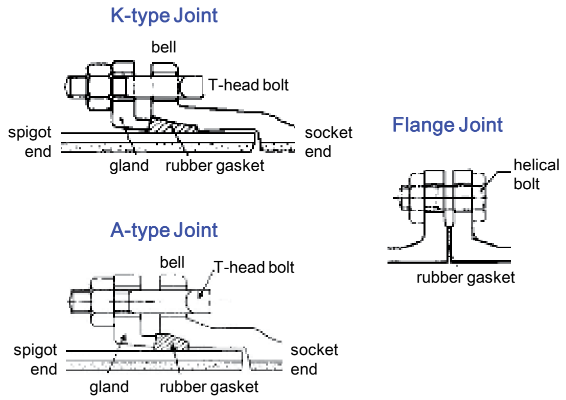

Fig. 1 DIPs with various types of joints

Test Methods

For the tension and compression tests, the specimens had a length of four times their nominal diameter (4DN). Each specimen consisted of a pair of pipes, one with a socket end and the other with a spigot end. After the assembly of the pipes at a joint, the edge of the socket end was positioned exactly at the mid-height of the specimen. It was mounted vertically to the universal testing machine with a capacity of 500 tf through fixtures, as depicted in Fig. 2. The test was conducted under displacement control. During testing, the specimen's axial force and displacement were measured using the internal load cell and the LVDT of the universal testing machine. The relative displacements at the two sides of the pipe joint were measured by a pair of external LVDTs. Knowing that K-type and A-type joints both have very low slip-out resistance, an additional 50-tf load cell was installed with the same alignment during the tension tests to ensure that the measurement of the axial force had adequate resolution.

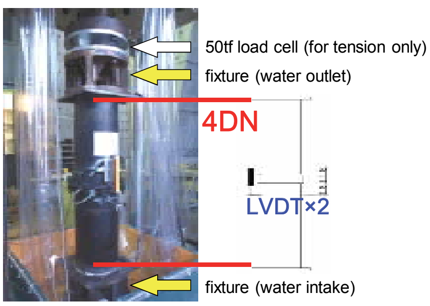

Fig. 2 Setup of the tension and compression tests

For the bending tests, the specimens had a length of eight times their nominal diameter (8DN). Again, each specimen consisted of a pair of pipes, one with a socket end and the other with a spigot end, and the edge of the socket end was positioned exactly at the mid-span of the specimen after the assembly of the pipes at the joint. The specimen was mounted horizontally at the ends on a pair of hinge supports. With a portal frame, a cross beam and a 100-tf actuator, the test was set up in such a way that the specimen was loaded with four-point bending, as depicted in Fig. 3. The 100-tf actuator gradually extended and the specimen was bent in a flexural way. During testing, the actuator load and extension were measured using its internal load cell and LVDT. Four 50-tf load cells were employed to measure the reaction of each hinge support. The bent specimens were also instrumented with tilt meters to record the rotation along the pipes' springline.

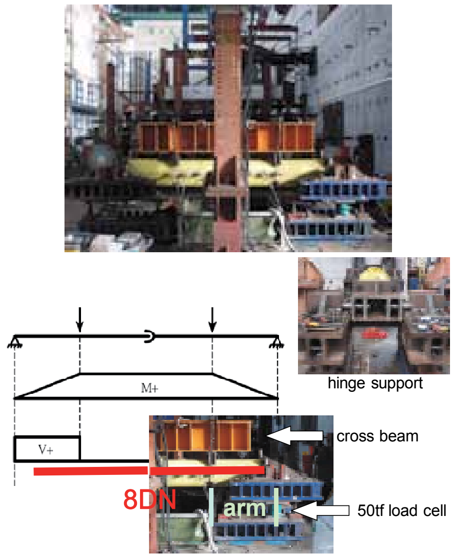

Fig. 3 Setup of the bending test

Since the A-type joint is very old and no longer used in new pipeline installations, the only available socket ends for this kind of joint were from the cross pipes with an A-type joint in stock. Therefore, the specimens were actually an assembly of such cross pipes and the spigot ends of straight DIPs, as depicted in Fig. 4. The pipe thickness of the former was about twice that of the latter. In addition, the cross pipes weren't fabricated by centrifugal casting, which resulted in a poor precision of the sockets' geometry.

Fig. 4 DIP specimens with an A-type joint.

During each test, the specimen was filled with water that was then pressurized. This was achieved by using a water pressure control system specially fabricated for this study, as depicted in Fig. 5. The deformation of the specimen (axial displacement or rotation) was increased monotonically until the specimens began to leak and the water pressure was no longer maintained. According to ISO 2531 (2009), the leak-tightness of DIP joints to internal pressure should be tested at a pressure of (1.5 × PN + 5) bar. Taking 2 kgf/cm^2 for the working pressure PN, water pressure throughout the testing was supposed to be within 8 ± 0.5 kgf/cm^2, with an additional tolerance of 0.5 kgf/cm^2 to accommodate for the variation of water pressure in the specimen due to the change of its volume during deformation.

Fig. 5 Water pressure control system

Test Results and Pipe Grading

The detailed test results of this experimental study can be found in the technical reports of the Taipei Water Department (2012) and the Water Resource Agency, MOEA (2012). Regarding the quantitative results, Fig. 6 depicts the axial force–specimen displacement curves of DIP specimens under tension, while Table 1 further summarizes all the test data in detail. It can be seen that both K-type and A-type joints have good deformation capacities. The former can withstand deformations of up to around 110 mm without any leakage (K-1 and K-2), and the latter 75 mm (A-1 and A-2). However, these specimens failed to prevent disengagement at the pipe joint under very small tensile actions of around 40 kN, which is merely the friction between the rubber gasket and the spigot end. Flange joints, although having very high strength, have very poor deformation capacity and may leak easily once opened slightly (F-1 and F-2).

Regarding the qualitative results, in K-type joints, water tightness was achieved in such a way that the rubber gasket was pressed firmly into the socket by the gland. The tensile strength of this joint was low but the tensile deformation capacity was fully developed. Water tightness was maintained until the axial displacement was as large as the splice length of the spigot and socket ends. The compressive strength was high but the compressive deformation was limited. The bending strength was low but the rotation deformation capacity was good.

As mentioned earlier, in the specimens with an A-type joint, the socket end was actually a cross pipe and the spigot end was a straight pipe. The thickness of the former was about twice that of the latter. The tensile strength of the specimen was very low, and once the strength reached its maximum, it degraded very fast. The compression results of the two specimens were very different. The compatibility of the two different pipes connected together may be the reason for the variation of the test results. The bending strength was very low.

In the specimen with a flange joint, two single flange pipes were connected with a rubber gasket as the interface. Because the resilience of the rubber gasket was bad, the tension and bending deformation capacities were very small, not exceeding 1 mm and 0.15°, respectively, and the corresponding tension and bending strengths were very low. The compressive strength was high but water began to leak from the pipe when the compression force was totally unloaded.

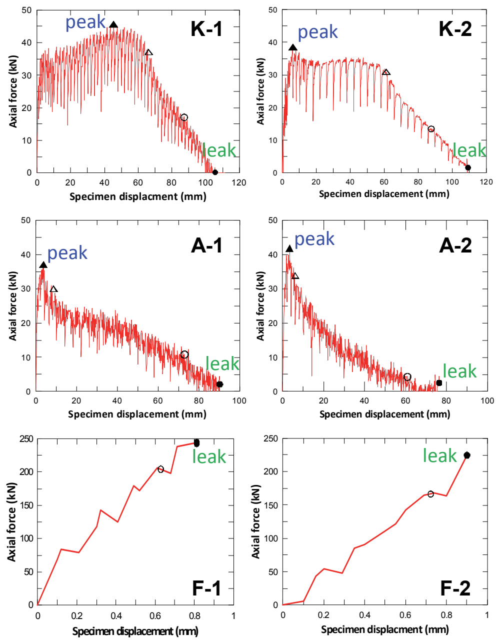

Fig. 6 The axial force-specimen displacement curves of DIP specimens under tension

In the technical report of the Water Resource Agency, MOEA (2012), a procedure was proposed to grade DIPs and joints seismically according to ISO 16134 (2006). It is based upon the reduced deformation capacity of the pipe and joint, which can be decided from the pipe's deformation at peak load and the moment it begins to leak. Following this procedure, the seismic grading of all DIP specimens can be determined as shown in Table 2. For example, the K-type joint's reduced deformation capacity has proven to be larger than 1% of the pipe's nominal length (6000 mm) in the tension test. Its expansion capacity can be graded as S-1. However, its slip-out resistance is well below 0.75d or 300kN, and can only be graded as D.

Table1 Test results for the DIPs.

Joint Type	Test Type	Speci. No.	Peak Load	Peak Deform.	Leak Load	Leak Deform.
K-Type Joint	Tension	1	45.24	45.53	1.64	111.45
		2	38.19	5.98	0.32	109.25
	Comp.	1	2698	7.56	1881	17.43
		2	2594	9.67	1885	17.07
	Bending	1	20.81	10.14	3.86	14.85
		2	28.29	14.20	5.90	17.18
A-Type Joint	Tension	1	37.1	3.59	3.15	90.35
		2	41.95	3.49	3.6	76.2
	Comp.	1	2815	12.45	615	23.01
		2	-	-	96.15	2.09
	Bending	1	9.62	7.85	0.78	9.34
		2	4.4	3.04	1.88	9.39
Flange Joint †	Tension	1	‡	‡	243.5	0.81
		2	‡	‡	223.4	0.92
	Comp.	1				
		2				
	Bending	1	‡	‡	18.89	0.06
		2	‡	‡	44.23	0.14

†: compressive strength beyond capacity of testing machine and too high to be decided
‡: no peak load or deformation
Units: kN (peak load and leak load in tension and compression testing), kN-m (peak load and leak load in bending testing), mm (peak deformation and leak deformation in tension and compression testing), degree (peak deformation and leak compression in bending testing).

Table 2 Seismic grading of the DIPs.

Joint Type			K-Type Joint		A-Type Joint		Flange Joint †	
Specimen No.			1	2	1	2	1	2
Item	Seismic Class.	Range						
Expansion Capacity δ (mm)	S-1	δ≥1%L	√	√				
	S-2	0.5%L≤δ<1%L						
	S-3	δ<0.5%L			√	√	√*	√*
Contraction Capacity δ (mm)	S-1	δ≥1%L						
	S-2	0.5%L≤δ<1%L						
	S-3	δ<0.5%L	√	√	√	√		
Slip-out Resistance F (kN)	A	F≥3d						
	B	1.5d≤F<3d						
	C	0.75d≤F<1.5d						
	D	F<0.75d	√	√	√	√	√*	√*
Joint Deflection Capacity θ (deg)	M-1	θ≥15°						
	M-2	7.5°≤θ<15°	√	√				
	M-3	θ<7.5°			√	√	√	√

L: nominal pipe length (mm)
d: nominal pipe diameter (mm)
†: compression strength too high to be decided;
*: leak load/deformation while failing to maintain water pressure.

Conclusion

According to the test results, K-type joint ductile iron pipes (DIP) are so flexible that their tensile and bending deformation capacities are good but their corresponding strengths are low. A-type joint DIPs are easily disengaged under either axial tension or bending loads. Flange-joint DIPs, due to extremely high joint rigidity, have very low tensile and flexural deformation capacities, and leakage may occur as a result of the poor elasticity of the rubber gaskets. Due to their poor seismic performance, existing A-type joint DIPs should be replaced as soon as possible. Flange-joint DIPs, due to poor deformation capacity, should not be used for the purposes of water transmission and distribution; regarding other usages, their water tightness should be inspected regularly.

References

ISO 16134, 2006, “Earthquake- and Subsidence-Resistant Design of Ductile Iron Pipelines”, First Ed.

ISO 2531, 2009, “Ductile Iron Pipes, Fittings, Accessories and Their Joints for Water Applications”, Sixth Ed.

Taipei Water Department, 2012, “Seismic Deflection and Leakage Testing of Segmented Water Pipes,” Technical Report, Project No. 10131056S04, Taipei.

Water Resource Agency, MOEA, 2012, “A Study on Upgrading Earthquake Loss Estimation Technology for Water Utilities and Seismic Testing Platform and Procedure for Water Pipes,” Technical Report, Project No. MOEAWRA-1010381, Taipei.

Seismic Damage Simulation on Taiwan Water Supply Networks with Negative Pressure Treatment

Kuang-Wu Chou[1], Gee-Yu Liu[1], and Chin-Hsun Yeh[2]

周光武[1]、劉季宇[1]、葉錦勳[2]

Abstract

This work is to develop a tool for simulating seismic damages on water supply networks in Taiwan. The tool is based on TELES's potential earth science analysis and a Taiwan-applicable pipeline repair rate formulation proposed by Liu et al. (2012). The development of the tool follows the seismic damage simulation methods from GIRAFFE, especially the negative pressure treatment. The EPANET library is integrated into the tool to create, update, and analyze the hydraulic model of a water supply network. Graph Theory is employed to remove the solution obstacle: no-flow sub-networks derived by either the modeling of network seismic damages, or the removal of negative pressures.

Keywords: hydraulic analysis, EPANET, GIRAFFE, boost, Graph Theory, TELES

Introduction

EPANET as the industrial standard is reliable to solve the hydraulic behaviors of water supply systems. The software, however, couldn't conduct seismic damage simulation on water supply networks. For damaged pipes in such simulation, the modeling of leaks or breaks could cause water loss that greatly exceeds the whole water supply of the network; negative pressures would thus occur in the EPANET solution of the hydraulic analysis. Negative pressures are incorrect prediction unless the network keeps air-tight (any damaged water system with leaking or broken pipes cannot be air-tight). If those negative pressures cannot get some treatment, the network's ability of supplying water will be misestimated.

Ballantyne et al. (1990) assumed that all nodes with negative pressures have no flow to pass through. Shinozuka et al. (1981) suggested removing such nodes and their adjacent links before running the hydraulic analysis. Markov et al. (1994) classified the negative-pressure nodes as no-flow or partial-flow. The no-flow nodes are to remove, and the no-flow node of the highest negative pressure is removed first. The pressure of each partial-flow node will be modified towards 0 by decreasing the roughness of the full-flow pipe walls. The node removal and pressure modification repeat until no negative pressure is shown. GIRAFFE (Cornell University, 2008) proposed a simpler procedure that removes only the node of the highest negative pressure as well as its adjacent links, and then runs the hydraulic analysis again. The procedure repeats unless negative pressure disappears. GIRAFFE, however, couldn't be directly applied to the water systems in Taiwan, because it is based on the experience of seismic damages of the water systems in USA. So there is a need to develop a tool that utilizes Taiwan's experience to grasp the serviceability of Taiwan's water systems after earthquake. This work tries to fulfill the need by following the seismic damage simulation methods that GIRAFFE proposed.

Seismic Damage Simulation for Water Supply Networks

As shown in Fig. 1, this work proposes a method of simulating seismic damages on a water supply network. The first step is to create the network's hydraulic model by using the EPANET library to read an input text that describes the model. To this model, the Monte Carlo method is applied, which performs a loop of 100 random simulations. The entry of the loop is the pipeline seismic damage simulation that is based

[1] Associate Researcher, National Center for Research on Earthquake Engineering

[2] Researcher and the Head of the Earthquake Disaster Simulation Division, National Center for Research on Earthquake Engineering

on a Taiwan-applicable pipeline repair rate formulation proposed by Liu et al. (2012). The step utilizes the result of TELES's potential earth science hazards (PESH) analysis, the pipe diameter, and the pipe material type to randomly determine if the pipe is undamaged, broken, or in leakage. The outcome of the pipeline damage determination will be used in the damage modification of the hydraulic network model.

In the step of modifying the network model, the pipeline damage modification applies GIRAFFE's hydraulic models that simulate pipe breaks and leaks. Because the break model works by cutting a pipe, a network where any pair of nodes are connected may be divided into several sub-networks that are mutually disconnected (on the other hand, it won't change the connectivity of the network to apply the leak model). As long as any sub-network without water supply exists, the whole network cannot be solved in hydraulic analysis. Fortunately, removing all such no-flow sub-networks may make the network solvable again. In this work, the no-flow sub-networks can get identified; they are removed from the network model in the step of modifying the network model. How to identify no-flow sub-networks will be explained in the section of no-flow sub-network identification.

After all no-flow sub-networks get removed, the hydraulic analysis may be carried out on the trimmed network model without obstacle in solution. The hydraulic solution of a damaged network, however, would contain negative pressures that need to be conducted after hydraulic analysis.

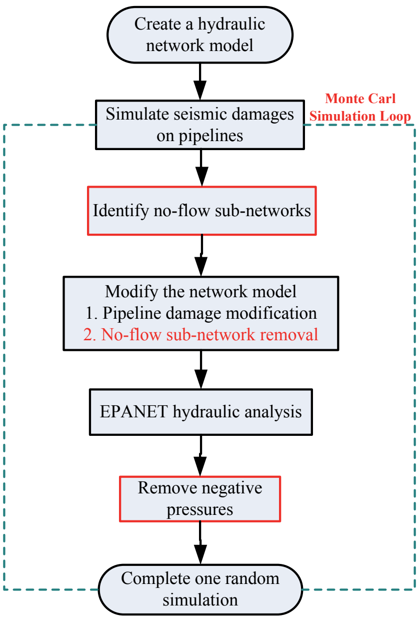

Fig. 1 Procedure of simulating seismic damages on a water supply network

Negative Pressure Removal

The negative pressure removal, at first, finds the node owning the minimum pressure from the result of the hydraulic analysis on a network model modified with seismic damages (See Fig. 2). The removal procedure completes if the minimum is not negative. Otherwise, the node and its adjacent links (including pipes and pumps) are removed from a graph copy of the current network model (why we employ the graph copy here will be explained in the section of no-flow sub-network identification). But as cutting a pipe, removing links may cut the current network into sub-networks containing no-flow ones so that the network cannot be solved in hydraulic analysis. As a result, identifying and then removing the no-flow sub-networks are also required for modifying the network model in the procedure of removing negative pressures.

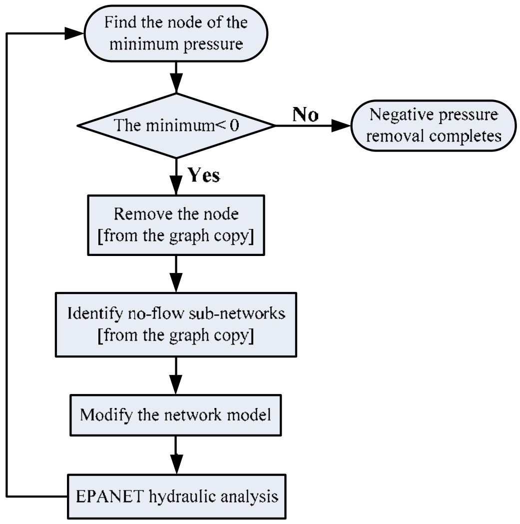

Fig. 2 Procedure of removing negative pressures

EPANET and Hydraulic Network Model Modification

EPANET offers an application, source code files, and a dynamic link library. The dynamic link library, as the EPANET programmer's toolkit, is used in this work. Still, the library needs reading an EPANET input to create a hydraulic network model. Updating a model also requires modifying the EPANET file and then feeding the library with the modified file. In Fig. 1, the library creates a hydraulic network model by reading an EPANET file. In Fig. 1 and Fig.2, the library modifies a hydraulic network model by reading and writing EPANET input files. That means reading or writing files could be performed over one thousand times by the Monte Carlo loop that executes 100 random simulations; if more than 10 negative-pressure nodes are removed in each simulation. In fact, it consumes most file operations in the network seismic damage simulation to repeat trimming the network model within the negative pressure removal procedure.

No-flow Sub-network Identification

Graph Theory is utilized to identify sub-networks resulting from cutting or removing pipes. This theory helps find from a network graph all the connected components as the sub-networks. The required procedures are implemented with the boost graph library (BGL).

The first step of identifying sub-networks is to create a graph copy for the hydraulic network. each vertex and each edge of the graph copy have one-to-one correspondence with each node and each link of the network. Thus the removal of a vertex or edges from the graph copy may simulate removing a node or cutting pipes from the network, respectively. The trimmed graph copy is then given to BGL's connected_component method. This method will find out all the connected components or sub-networks. The method returns the number of sub-networks, and labels each vertex a number that is used to identify which sub-network where this vertex belongs.

The final task is to pick out the sub-networks without water supply. A simple approach is employed as what follow: ask each node about if it is a tank or reservoir; if the condition is true the sub-network where the node resides is identified as having water supply. After all nodes are visited, the sub-networks never confirmed as owning water supply are considered no-flow (without water supply).

Example

A seismic damage simulation is carried out on the water supply network in Taiwan's Lan-Yang area. A simplified hydraulic network model is employed, which was proposed by Sinotech engineering consultants (2009). In the simplified model, 358 nodes and 439 links (comprising pipes and pumps) are defined; 85 nodes are given demands, responsible for supplying water.

An earthquake is simulated by TELES with a Richter magnitude 7.3. The epicenter is at latitude 24.48°N and longitude 121.88°E, in Yilan's offshore. The focal depth is 20Km. The earthquake source is described as a north-south-trending line source. Fig. 3 shows the result of TELES's PESH analysis on the earthquake, the result in the Lan-Yang area.

The outcome of the seismic damage simulation is presented with the serviceability of the water supply network. The serviceability is obtained by dividing the summation of all demands of the model of an undamaged system by that of all available demands of the system model trimmed and modified with damages.

Given the PESH analysis result, the seismic damage simulation brings out the serviceabilities of the water supply network subjected to the simulated earthquake. Fig. 4 shows the town serviceabilities averaged from the 100 Monte Carlo random simulations. The right part of Fig. 4 presents the town serviceabilities computed after the whole simulation procedure is completed. The left part represents the town serviceabilities computed before the negative pressure removal. And the serviceability computation follows the negative pressure treatment proposed by Ballantyne et al. (1990): the demands of all negative-pressure nodes are disregarded in demand summation. Besides, the right and the left of Fig. 4 show the same tendency. The worst serviceabilities are in Touching (頭城), 0.4346 and 0.2552. The second worst are in Jiaoxi (礁溪), 0.6664 and 0.5951. The smaller in any of the two pairs are by the negative pressure removal.

In the 100 Monte Carlo simulations, the 44-th and the 93-th brings out the maximum serviceability of the whole network and the minimum: 0.9555 and 0.7670. Their town serviceabilities are shown in Fig. 5. Fig. 6 shows the maximum's model modifications before and after the negative pressure removal, Fig. 7 the minimum's. As expected, the network gets greater modification after the negative pressure removal than it gets before. In addition, the model modification with the minimum serviceability is more severe than that with the maximum.

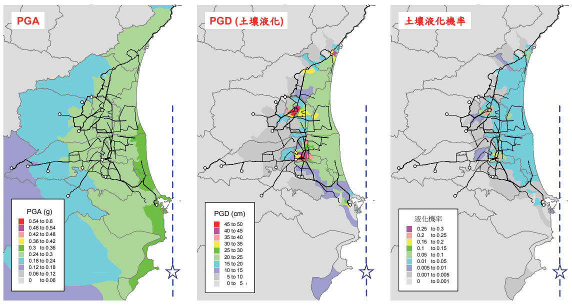

Fig. 3 Distributions of the simulated PGAs, PGDs by soil liquefaction, and soil liquefaction probabilities over the Lan-Yang area (from left to right)

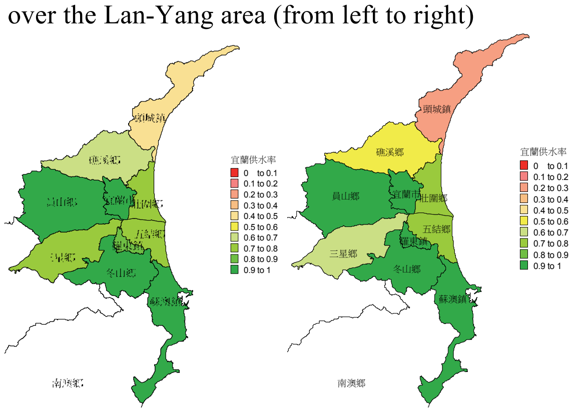

Fig. 4 Town serviceabilities in the Lan-Yang area (left: the negative pressure removal is by-passed)

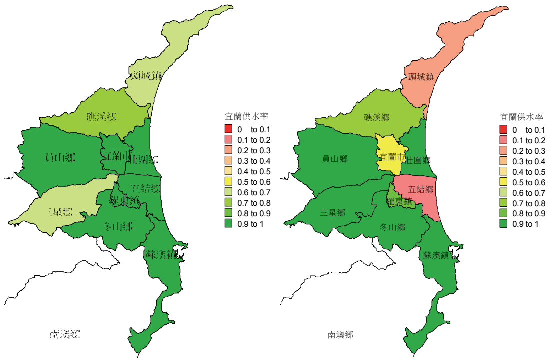

Fig. 5 Town serviceabilities with the maximum whole-network serviceability (left) and that with the minimum (right)

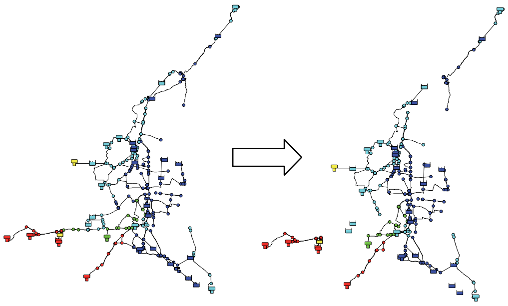

Fig. 6 Network model modification before and after the negative pressure removal, with the maximum whole-network serviceability

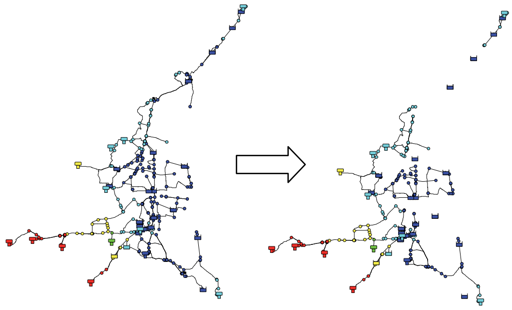

Fig. 7 Network model modification before and after the negative pressure removal, with the minimum whole-network serviceability

Conclusions

A tool for simulating seismic damages on Taiwan's water supply networks is developed. The tool could modify a hydraulic network model modification and remove negative pressures as GIRAFFE does. GIRAFFE couldn't identify no-flow sub-networks itself, however. GIRAFFE needs to run an EPANET hydraulic analysis that finds the disconnected nodes or links for GIRAFFE to remove. The tool works with a different approach. The tool applies Graph Theory to damaged networks so that the tool can identify and then remove no-flow sub-networks from a hydraulic network model. With the help of Graph Theory, the tool depends less on EPANET than GIRAFFE does, and could seize the connectivity of any water supply network.

Nevertheless, the employment of the reliable EPANET library confines the efficiency of modifying a hydraulic network model. The model modification must be performed through reading and writing files that consumes more CPU time than the memory operations do. In this work, the time consumption is observable. We will try to resolve this issue to improve the performance of the tool. Application of the EPANET source codes might be considered.

References

Ballantyne, D. B., Berg, E., Kennedy, J., Reneau, R., and Wu, D. (1990), "Earthquake Loss Estimation Modeling of the Seattle Water System", Technical Report, Kennedy/Jenks/Chilton, Federal Way, WA.

Cornell University (2008). GIRAFFE User's Manual, School of Civil & Environmental Eng., Cornell University, Ithaca, NY.

Markov, I., Grigoriu, M., and O'Rourke, T. (1994), "An Evaluation of Seismic Serviceability Water Supply Networks with Application to the San Francisco Auxiliary Water Supply System", Technical Report NCEER-94-0001, National Center for Earthquake Engineering Research, Buffalo, NY.

Shinozuka, M., Tan, R. Y., and Toike, T. (1981), "Serviceability of Water Transmission Systems under Seismic Risk", Lifeline Earthquake Engineering", the Current State of Knowledge, ASCE, New York, NY.

Liu, G.-Y., Chung, L.-L., Yeh, C.-H., Chou, K.-W., Chang, K.-C., Hung, H.-Y., Chou, P.-C., Lin, T.-J., Chou, C.-H., Chen, J.-C., Chen, C.-H, Kuo, C.-W., and Uang, P.-Y. (2011), "A Study on Upgrading Earthquake Loss Estimation Technology for Water Utilities and Seismic Testing Platform and Procedure for Water Pipes", Technical Report MOEA- WRA-1010381, Water Resources Agency, Ministry of Economic Affairs, Taipei.

Sinotech Engineering Consultants (2009), "Establishment Planning for the Surface-Ground Water Allocation and Management System in Lan-Yang Area", Technical Report MOEA-WRA-0980193, Water Resources Planning Institute, Water Resources Agency, Ministry of Economic Affairs, Taichung.

Constructing Scour Fragility Curves for Piled Bridge Piers from Flume Experiment Data

Chun-Chung Chen [1], Chi-Ying Lin [2], Kuo-Chun Chang [2], and Ming-Yi Shen [2]

陳俊仲 [1]、林其穎 [2]、張國鎮 [3]、沈明毅 [4]

Abstract

The escalating scale of natural disasters increasingly threatens civil infrastructure. In particular, earthquakes and floods are two major types of disasters that can result in damage to key civil structures such as bridges. This preliminary study proposes a procedure for constructing scour fragility curves from flume experiment data for piled bridge piers. Several experiments were conducted and the variation in the scouring process was observed. The scour depths observed were used to develop scour fragility curves for the piled bridge piers. A methodology to construct the scour fragility curves was presented. The main purpose of this paper is to show how to use the flume experiment data to build the scour fragility curves defined as a function of the pile length embedded ratio. The measured trend of the curve is consistent with the general scouring process and the realistic behavior of the piled bridge pier damage sequence. This paper has shown a feasible methodology to construct the scour fragility curves from flume experiment data. However, further studies are necessary in order to find solutions for the problems mentioned in the preliminary study.

Keywords: bridge scour, flume experiment, fragility curves,

Introduction

Earthquakes and floods are two major types of disasters that severely affect bridge structures. Floods can intensify the scouring to bridges and the submerged debris deepens the scour depth. In Taiwan, most bridges cross the river so scouring has been a leading possibility of failures. Therefore, predicting bridge damage due to scouring is much needed and fragility curves can help us to express the probability of damage due to the effects of certain hazards.

A methodology to construct the scour fragility curve from flume experimental data was presented. The scour fragility curve is defined as a function of the pile length embedded ratio. A piled bridge pier model was set up in the flume for scour testing under certain flows. The variations in scour depth and the pier settlement were recorded. Afterwards, the settlement was used to define the damage states. The fragility surface giving a conditional probability of exceeding different scour states given the occurrence of specific flow conditions at certain flow velocities and water levels was constructed in this paper.

Scour Fragility Curves

Applying the fragility curve to predict the possible extent of earthquake-induced damage has been developing for a long time in earthquake engineering. This curve shows the probability of structural damage as a function of the seismic parameter. Conducting a seismic fragility curve requires synergistic use of the following methods (Shinozuka et al, 2001): (1) professional judgment, (2) quasi-static and design code consistent analysis, (3) utilization of damage data associated with past earthquakes, and (4) numerical simulation of bridge seismic responses. Due to the complex condition of bridge scouring, much time and

[1] Associate Researcher, National Center for Research on Earthquake Engineering, ccchen@ncree.narl.org.tw.
[2] Research Assistant, Department of Civil Engineering, National Taiwan University
[3] Director, National Center for Research on Earthquake Engineering
Professor, Department of Civil Engineering, National Taiwan University
[4] Student, Department of Civil Engineering, National Taiwan University

effort is required to simulate the real scouring mechanism. For this reason, few studies have focused on developing the fragility curves for scoured bridges. The procedure to develop seismic fragility curves is a good template for finding scour fragility curves.

The numerical and the empirical approach are two ways to estimate seismic fragility. In the numerical approach, ground motion records were selected and a bridge pier model was constructed. The fragility curve was generated by damage probabilistic analysis (Karim et al, 2001 and Chiou et al, 2011). In the empirical approach, the actual damage data were selected (Sarabandi et al, 2004), and the damage data and seismic parameters were sorted into damage ranks. By relating each damage rank with their damage ratio, the empirical fragility curve could be constructed (Yamazaki et al, 2000).

This paper established its scour fragility curve by a similar procedure to the empirical approach through a series of experiments. Since the fragility curve is a function of defined damage parameters and exceeding probability of specified failure, defining the damage states is the first step in this work. In this study, the vertical displacement of the bridge pier is selected to discriminate the damage states because it correlates to the scouring around the pile. Once the displacement changes and the scour depths are recorded, we can then define the damage states. It can be anticipated that more severe critical damage states would lead to a deeper scour depth. Repeating the experiment provides the experimental data to develop the scour fragility curves.

For the preliminary study, the data includes the mean and the standard deviation of the pile length embedded ratio, R_l, which is equal to the embedded depth of the pile, L_e, over the full length of the pile, L. As the scour depth, D_S, was observed and recorded, at the moment when the vertical displacement of the bridge pier reaches the value of the defined damage state, we can obtain:

$$R_{l,i} = \frac{L_{e,i}}{L} = \frac{(L-D_{S,i})}{L} \quad (1)$$

The parameter *i* indicates the experiment number. The experimental statistical data, the mean and the standard deviation of the pile length embedded ratio are calculated more precisely as we increase *i*. As mentioned, the vertical displacement of the pier is selected to discriminate the damage states. Three differentiated damage states were defined: 1mm, 3mm and 5mm. Generally, the structure is considered to be at failure when the vertical displacement exceeds 10 percent of the pile diameter. But owing to the scale effect of the scale model experiments, this factor is not clearly understood. This study takes the broader range of the displacement of the pile into the consideration.

The cumulative probability P_f of the occurrence of the damage states according to the pile length embedded ratio is given as:

$$P_f = \Phi\left[\frac{lnR_{l,j}-\lambda_j}{\xi_j}\right] \quad (2)$$

where, Φ is the standard normal distribution; j indicates the specific damage rank; λ and ξ are the mean and the standard deviation of $\ln R_l$. These two parameters are obtained to develop the scour fragility curves. A detailed description of the procedures can be found in Karim et al, 2001.

Flume Experiments

The experimental setting is simplified so that we can focus on the bridge pier structure failure behaviors. The material strength and the column tilt are relatively unnecessary. Bearing capacity failure is the most controllable failure mode. The self-weight and the soil conditions are the major factors affecting the bearing capacity. The load transfer mechanisms of the pile structure are the point bearing capacity and the friction between the pile and the sediment. The soil bearing capacity fails mostly through punching.

The reduced scale model that was used in this study is shown in Figure 1. It includes a bridge column (2.5cm in diameter) and a cap beam (25cm in length, 5cm in width, 5cm in height) made from stainless steel, and an acrylic pile cap (10cm in length x 10 cm in width x 5cm in height) on top of four replaceable stainless steel piles (1cm in diameter and 20cm in length). An inner camera was installed to observe the scour depth. The hydraulic flume is 0.6 meter wide by 1 meter high with a total length of 7 meters (see Figure 2). The average flow velocity is 0.3 m/sec and the water level is 20 cm above the initial sediment level. Mass blocks were added to provide the vertical loading to accomplish the failure mode of the scoured bridge pier. A weight of 25kg was evaluated and used in this study.

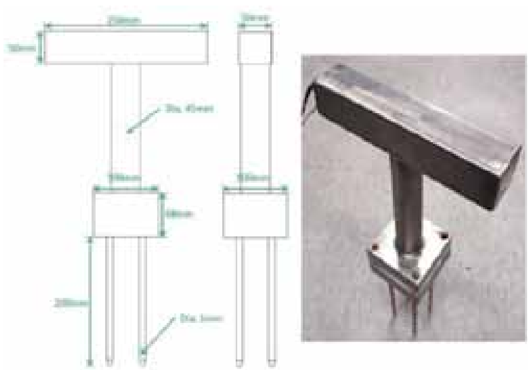

Fig. 1 Pile foundation bridge pier model used in the flume experiment

Figure 3 shows the measuring instruments. The scour depth was recorded by the inner camera. Two magnetic displacement transducers were installed on the top of the cap beam to record the vertical translational displacement. Ambient vibration sensors were also deployed in the experiments, but the change of the dynamic properties of the pier during the scouring process is not discussed in this paper. Some photos of the experiments are shown in Figure 4.

Fig. 2 The hydraulic flume used in this study (Left) Top view of flume channel (Right) Test section of the experimental flume

Fig. 3 Layout of the measuring instruments (Left) Measuring instruments (Right) Sketch of the instruments

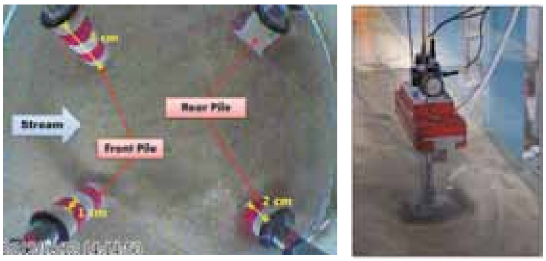

Fig. 4 Photos of the flume experiments (Left) View from the inner camera (Right) Bridge model

Preliminary Results and Discussions

The recorded curves of the embedded length ratio of the pile (R_l) versus time are shown in Figure 5. Only three repeated flume experimental results are presented in this paper because more experiments are still being conducted. The result shows a feasible methodology to construct the scour fragility curve. Figure 6 shows the curves of the vertical translational displacement versus time measured during the experiment. Note that the recorded starting time is the same for the embedded length change observation as it is in the displacement measurement.

Figure 5 indicates that the embedded length will decrease during the experiment. This trend is consistent with the general scour process. The curves also show the variation in the data that accounts for the unavoidable uncertainty of the boundary conditions while setting up the model. The jumps of each curve are caused by the lack of bearing capacity at the pile. The record time of each jump that corresponds to the time of the discontinuities of slope in the vertical translational displacement curves are shown in Figure 6. About 9% - 24% of the depth of the initial sediment around the pier was washed away. The curves of Experiment No. 1 and 2 have similar trends but the curves in Experiment No.3 show a different result. There are several minor settlement events in Experiment 1 and 2. However, Experiment 3 only shows one major settlement event. Thus, it is difficult to find a proper numerical model with natural variability for the full process of bridge scouring. Also, the failure mechanisms of the structure are quite complicated.

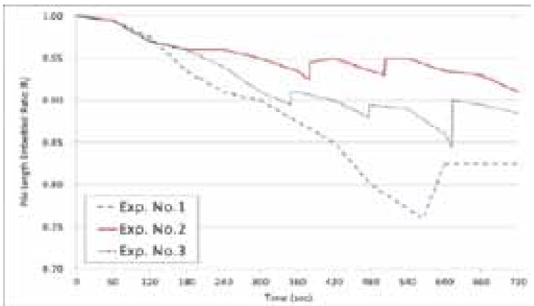

Fig. 5 Curves of the embedded length ratio of the pile versus time

Vertical translational displacement increases along with the movement of the pier. As it can be seen in Figure 6, the settlement occurs in sequence, which describes the realistic behavior of bridges. In Figures 5 and 6, one can see a similar outcome for the different experiments conducted.

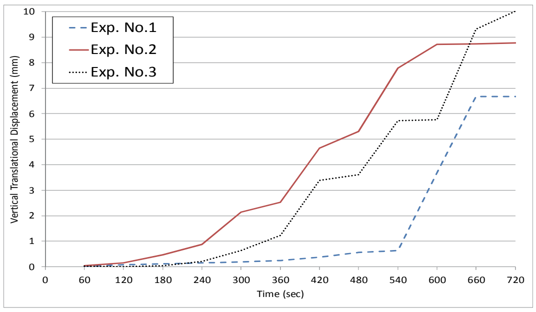

Fig. 6 Curves of the vertical translational displacement versus time

The maximum vertical translational displacement is between 6.8mm to 10mm. If we define the major damage rank directly using the maximum value of the displacement, the damage state of the piled bridge might be overestimated. As mentioned previously, the discriminated values of vertical displacement are 1mm, 3mm and 5mm. These values correspond to minor scour damage, moderate scour damage and major scour damage respectively. We can then obtain the time of occurrence for each of the defined damage ranks from Figure 6 and find the corresponding pile length embedded ratios from Figure 5. Then the experimental statistical properties, the mean and the standard deviation, are calculated to develop the fragility curve by using Equation 2. Finally, the cumulative probability of occurrence for each of the damage states can be obtained. The constructed scour fragility curves are shown in Figure 7. This figure shows the plots of the fragility curves for the defined damage states for the bridge pier model with respect to the embedded length ratio of the pile. In Figure 7, the range of the pile embedded length ratio is from 0.60 to 1.10, where 1.10 is the embedded length of the pile is over the length of the pile itself, which does not happen in reality.

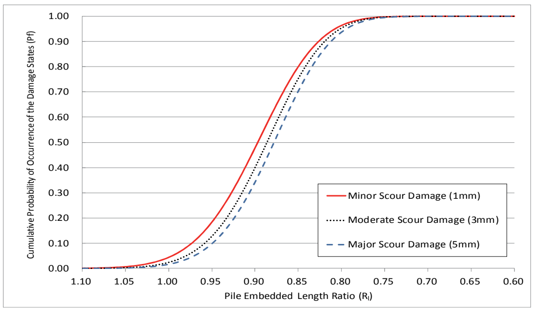

Fig. 7 Scour fragility curves constructed from experimental data in this study

One of the possible reasons why the ratio exceeded 1.0 is that experimental data used in this paper is limited as it was from only three experiments. More experiments are currently being conducted to provide more data to construct the fragility curves. Another possible reason could be that there is an inevitable inaccuracy in the procedure of developing the fragility curves. The simplest solution for the inaccuracy is to set a lower limit for the pile embedded length ratio so that the starting point of the fragility curve would be at 1.0. Further studies are necessary in order to find conclusive solutions for the problems mentioned.

Discussing the preliminary results in this paper, it can be seen (Figure 7) that the developed fragility curves of the minor scour damage (1mm), moderate scour damage (3mm) and major scour damage (5mm) show a different level of damage probability with respect to the pile embedded length ratio. As the pile embedded length ratio decreases, the constructed fragility curves of the major damage rank show a lower level of damage probability compared to that of the moderate damage rank and the minor damage rank in an understandable order. An interesting result was also observed in Figure 7 regarding the spacing between each of the fragility curves with the same level of damage probability. The difference between each discriminated value of the vertical translational displacement is the same but the spacing between fragility curves was not constant. The moderate damage curve is closer to the major damage curve than the minor damage curve. This indicates that the level of minor damage probability is more sensitive to the damage rank criteria. Furthermore, the cumulative probability of occurrence of the damage state reaches 1.0 as long as the pile embedded length ratio is not over 0.75. In other words, we can say that the bridge model will have at least a 5mm vertical translational displacement as the scour depth reaches 25% of the pile length.

Summary and Remarks

A methodology to construct the scour fragility curves from flume experimental data was presented in this preliminary study. The main purpose of this paper is to show how the flume experimental data were used to build the scour fragility curve defined as a function of the pile length embedded ratio. The curve of the embedded length ratio of the pile over time and the curve of the vertical translational displacement over time were observed and recorded through flume experiments. The measured decreasing trend of the curve is consistent with the general scouring process and the realistic behavior of the piled bridge pier damage sequence. The constructed fragility curves were presented and discussed. This paper has shown a feasible methodology to construct the scour fragility curve from flume experiment data. However, further studies are necessary in order to find solutions for the problems mentioned in the preliminary stage.

Reference

Reddy, D. R., 2006, "Bridge Scour Detection", Proceedings of National Conference on Advanced in Bridge Engineering (ABE), March 24-25.

Shinozuka, M., Feng, M. Q., Kim, H., Uzawa, T., Ueda, T. 2001 "Statistical Analysis of Fragility Curves." Technical Report MCEER, Department of Civil and Environmental Engineering, University of Southern California Los Angeles, California 90089-2531

Karim, K. R., Yamazaki, F. , 2001,"Effect of earthquake ground motions on fragility curves of highway bridge piers based on numerical simulation." Earthquake Engng Struct. Dyn., 30:1839-1856

Chiou, J. S., Chiang, C. H., Yang, H. H., Hsu, S. Y. , 2011, "Developing fragility curves for a pile-supported wharf." Soil Dynamics and Earthquake Engineering, 31:830-40

Sarabandi, P., Pachakis, D., King, S., Kiremidjian, A. ,2004, "Empirical Fragility Functions from Recent Earthquakes." 13th World Conference on Earthquake Engineering, Paper No.1211

Yamazaki, F., Motomura, H., Hamada, T., 2000, "Damage Assessment of Expressway Networks in Japan based on Seismic Monitoring." 12th World Conference on Earthquake Engineering, CD-ROM, Paper No. 0551

Modal Analysis of a Nuclear Reinforced Concrete Containment Vessel

Shu-Hsien Chao[1], Chiun-Lin Wu[2], Hsuan-Chih Yang[3] and Kuo-Chun Chang[4,5]

趙書賢 [1]、吳俊霖 [2]、楊炫智 [3]、張國鎮 [4,5]

Abstract

In this study, a finite element model of a reinforced concrete containment vessel (RCCV) in an advanced boiling water reactor (ABWR) was constructed using the commercial program ABAQUS ver.6.12. The modal analysis was performed to derive the modal properties of an RCCV, such as the frequency and mode shape of each mode, in order to clarify the dynamic behavior of the RCCV while it is subjected to earthquake excitation. The effect of different mesh sizes and element types on the modal analysis results was examined. The modal frequencies of the first four dominant modes are 7.3Hz, 15.2Hz, 18.2Hz, and 23.6Hz, with the first one representing the horizontal mode, the second being the torsional mode, the third being the inner-shell deformation mode, and the fourth being the vertical mode. It is suggested that the mesh size can be defined as half of the RCCV thickness, and the quadratic element with a reduced integration point can be used to derive accurate results under the limitations of the hardware environment.

Keywords: finite element method, modal analysis, advanced boiling water reactor, reinforced concrete containment vessel

Introduction

The safety of a nuclear power plant is always an issue of major public concern, especially after the Japanese earthquake on the 11th March 2011. The earthquake induced a tsunami which caused devastation to the Fukushima plant in Japan. The impact of the damage to the Fukushima plant on society, life, the economy, and the environment was massive. Therefore, assessing and re-evaluating the seismic capacity of structures, components, piping systems, and equipment in a nuclear power plant has become essential. In the past, the seismic demand of components, piping systems, and equipment in a nuclear power plant was determined through linear time history analysis using a simplified lumped mass model. However, many general dynamic properties, such as 3-D mode, torsional mode, and torsion-coupled mode cannot be represented by this simplified lumped mass model.

In this study, a finite element model of a reinforced concrete containment vessel (RCCV) of an advanced boiling water reactor (ABWR) was constructed using the commercial program ABAQUS ver.6.12. The modal analysis was performed to derive the modal properties of an RCCV, such as the frequency and the mode shape of each mode, to clarify the dynamic behavior of the RCCV while subjected to earthquake excitation. The effect of different mesh sizes and element types on the modal analysis result was also studied.

Description of Structure and Model

Fig. 1 shows a sketch of the advanced boiling water reactor building [1]. It is a 7-story building with a total height of 63.4m. It comprises an underground section (3-story, 25.7m height) and an aboveground section (4-story, 37.7m height). The dimensions of the basemat are 60m×57m. The building contains an

1 Assistant Researcher, National Center for Research on Earthquake Engineering, shchao@ncree.org.tw
2 Associate Researcher, National Center for Research on Earthquake Engineering, clwu@ncree.org.tw
3 Associate Researcher, National Center for Research on Earthquake Engineering, hcyang@ncree.org.tw
4 Director, National Center for Research on Earthquake Engineering, kcchang@ncree.org.tw
5 Professor, Department of Civil Engineering, National Taiwan University

RCCV, an outer reinforced concrete (RC) box wall, and inner RC shear walls. The entire RCCV and a section of the basemat were considered in this study. The RCCV is a cylindrical wall structure, with an inner diameter of 29m and an outer diameter of 31m. The thickness of the cylindrical wall is 2m. The RCCV should resist earthquake excitation and other types of loading in order to keep harmful radiation inside it during a reactor core accident. It is the final line of defense of a nuclear power plant's safety system. The height of the RCCV is 31.9m and the height of the basemat is 5.5m.

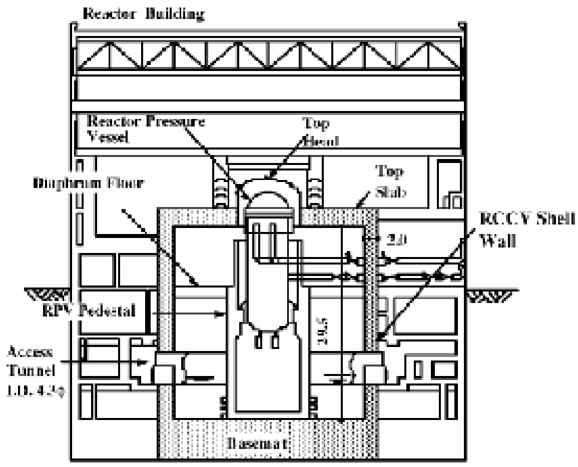

Fig.1 A sketch of the Advanced Boiling Water Reactor Building [1]

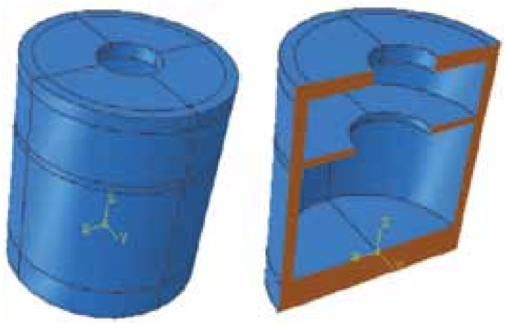

Fig. 2 Illustration of the RCCV model

A finite element model of the RCCV using real dimensions including a part of the basemat was constructed using ABAQUS, as shown in Fig. 2. The analysis model was assumed to be composed of an isotropic linear elastic material. The elastic modulus and Poisson's ratio were assumed based on the design concrete properties. The ultimate compressive strength of the design concrete, f_c', of the RCCV was 350kgf/cm^2. According to design codes [2], the elastic modulus of concrete can be derived as:

$$E_c = 15000\sqrt{f_c'} \quad \cdots\cdots\cdots\cdots \quad (1)$$

where the unit of f_c' is kgf/cm^2 and the Poisson's ratio of the concrete was assumed to be 0.2. Only the self-weight of the structure was considered in the model. The density of concrete was assumed to be 2.4t/m^3. The displacement at the bottom of the basemat was assumed to be zero during the modal analysis. All modal properties associated with modal frequencies from 0Hz~33Hz were evaluated.

Mesh and Element Type

Generally, more accurate results can be derived by using a finer mesh size; however, a finer mesh size is accompanied by a larger amount of nodes and elements in the model, which will increase computational efforts. Due to hardware capability limitations, it is unwise to make the mesh size arbitrarily finer. Therefore, it is very important to investigate the effect of the mesh size on the modal analysis results and to determine the appropriate mesh size for a particular engineering problem. In this study, a finite element model with four different mesh sizes was constructed. The outline of this model along with the four different mesh sizes is shown in Fig. 3. The mesh size was defined according to the thickness of the RCCV cylinder wall. The element sizes of mesh type I~IV as shown in Fig. 3 correspond to 200%, 100%, 50%, 25% of the RCCV cylindrical wall thickness respectively.

In ABAQUS ver. 6.12, the solid element is classified into linear elements and quadratic elements according to the element node number. A linear solid element has 8 nodes, and a quadratic solid element has 20 nodes, as shown in Fig. 4. According to the number of integration points, the solid element is classified into full integration and reduced integration elements, as shown in Fig. 4. Therefore, four kinds of solid elements can be used in ABAQUS ver. 6.12. They are:

1. Linear element with reduced integration (C3D8R): this element has 8 nodes and 1 integration point for each face.
2. Linear element with full integration (C3D8): this element has 8 nodes and 4 integration points for each face.
3. Quadratic element with reduced integration (C3D20R): this element has 20 nodes and 4 integration points for each face.
4. Quadratic element with full integration (C3D20): this element has 20 nodes and 9 integration points for each face

In this study, a total of 16 finite element models were constructed for the RCCV according to different mesh sizes and element types. The number of nodes and elements of each model is shown in Table 1. The computational effort for the full integration element is heavier than that for the reduced integration element even if the number of elements is the same. As shown in Table 1, if the mesh size is reduced to 50%, the number of nodes and elements increases by four to five times, and will result in a considerable increase in computational effort.

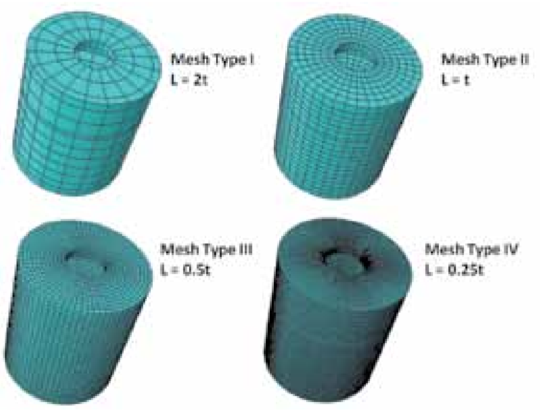

Fig. 3 Different Mesh Types

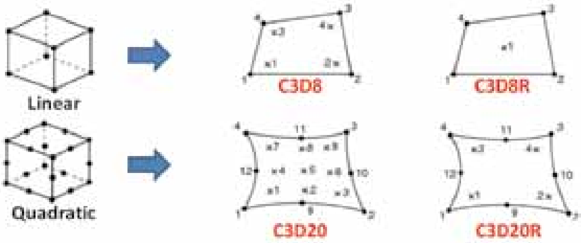

Fig. 4 Linear and quadratic solid elements with full and reduced integration points [3]

Table 1 Number of nodes and elements for 16 different finite element models

Number of Node				
	Mesh Type I	Mesh Type II	Mesh Type III	Mesh Type IV
C3D8R C3D8	775	3044	16085	116128
C3D20R C3D20	2719	10807	59719	444956
Number of Element				
C3D8R C3D8	408	1700	11508	96661
C3D20R C3D20	408	1700	11508	96661

Modal Analysis Result

The modal frequencies of the first four dominant modes for each model are shown in Fig. 5(a) ~ 5(d) respectively. From these figures, it is found that:

(1) The modal frequency analysis results of the quadratic element are more stable than those of the linear element. The mesh size of mesh type II, III, or IV for the quadratic element with full or reduced integration can be used to derive an accurate analysis result.

(2) The modal frequency calculated from the linear element with reduced integration proves lower because of the element's hourglass problem [3]. This makes the analyzed model more flexible than its real counterpart. Besides, higher modes (third mode and fourth mode) cannot be well represented when the mesh size is too coarse (mesh type I and type II). One should use a fine mesh (mesh type IV) to derive an accurate analysis result while using this element.

(3) The modal frequency calculated from the linear element with full integration proves higher because of the element's shear locking problem [3]. The analyzed model has higher stiffness while using this element type and a fine mesh (mesh type IV) is necessary to derive accurate results.

The parametric analysis results suggest that the quadratic element with reduced integration (C3D20R) is favorable for modeling the RCCV. The mesh size can be selected as a half of the RCCV cylinder wall thickness. In this way, accurate results together with affordable computational effort can be assured. In the next section, the analysis result of the C3D20R model with mesh type II is used to illustrate the RCCV modal properties.

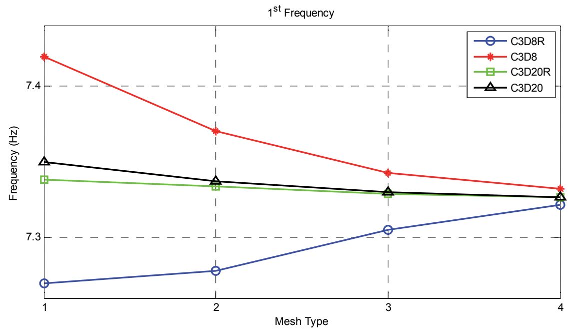

Fig. 5(a) 1st modal frequency of 16 different finite element models

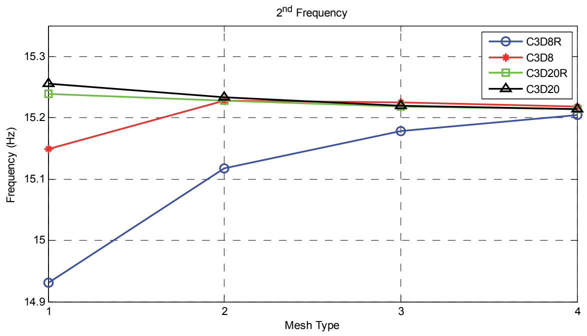

Fig. 5(b) 2nd modal frequency of 16 different finite element models

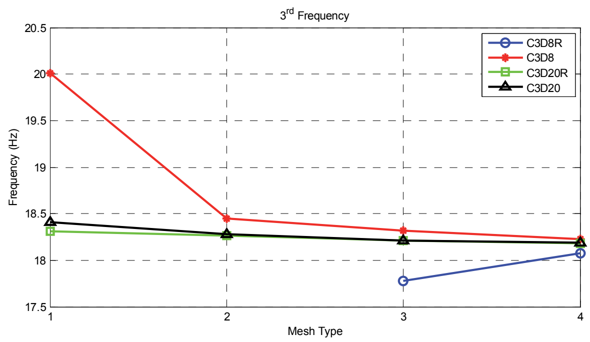

Fig. 5(c) 3rd modal frequency of 16 different finite element models

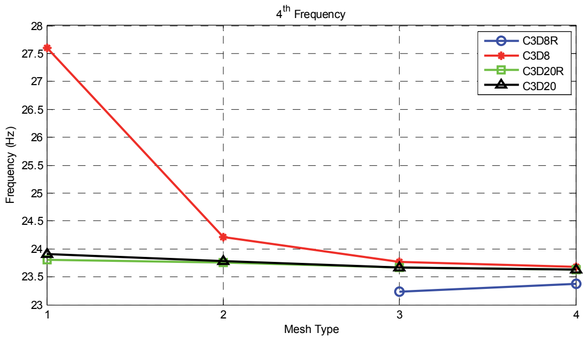

Fig. 5(d) 4th modal frequency of 16 different finite element models

Figure 6 shows the mode shapes of the first four dominant vibration modes of the RCCV. The modal frequencies are 7.3Hz, 15.2Hz, 18.2Hz, and 23.6Hz, respectively. The first mode corresponds to the horizontal mode, and the second represents the torsional mode; the third is the inner-shell deformation mode, and the fourth is the vertical mode.

A key parameter of the concrete material yield function is the von Mises stress. Therefore, the von Mises stress of each element is discussed in this study. The definition of the von Mises stress is:

$$\sigma_{mises} = \sqrt{\frac{(\sigma_1 - \sigma_2)^2 + (\sigma_2 - \sigma_3)^2 + (\sigma_1 - \sigma_3)^2}{2}} \quad .....(2)$$

where $\sigma_1 \sim \sigma_3$ is the first, second, and third principal stress at the integration point. Figure 7 shows the maximum von Mises stress distribution of each element for each mode. The results show that the stress is concentrated at the bottom of the RCCV for the first and second modes, at the middle plate of the RCCV for the third mode, and at the top plate and the bottom of the RCCV for the fourth mode.

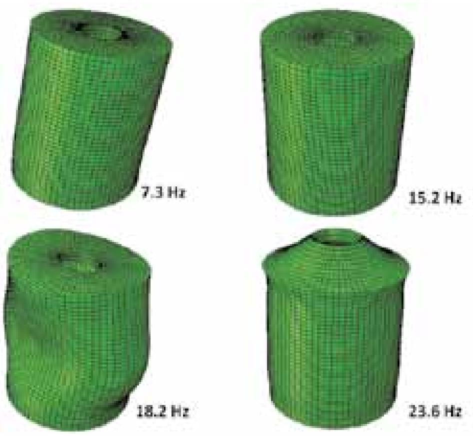

Fig. 6 Mode shape of each mode

Conclusions

In this study, a finite element model of a reinforced concrete containment vessel (RCCV) of an advanced boiling water reactor (ABWR) was constructed using the commercial program ABAQUS ver.6.12. The modal analysis was performed to derive the modal properties of the RCCV, such as the frequency and mode shape of each mode, to clarify the dynamic behavior of the RCCV while subjected to earthquake excitation. The effect of different mesh sizes and element types on the modal analysis result was studied. The modal frequencies of the first four dominant vibration modes are 7.3Hz, 15.2Hz, 18.2Hz, and 23.6Hz. The first is the horizontal mode, the second is the torsional mode, the third is the inner-shell deformation mode, and the fourth is the vertical mode. It is suggested that the mesh size can be defined as a half of the RCCV thickness, and the quadratic element with reduced integration point can be used to derive accurate results under hardware limitations.

In this study, only the RCCV substructure from an ABWR building was investigated. In the near future, a finite element model for a complete ABWR building will be considered to realize its dynamic behavior comprehensively. The differences between the analysis results of the finite element model and the simplified lumped mass model will be discussed to validate the application of the simplified lump mass model in our subsequent studies.

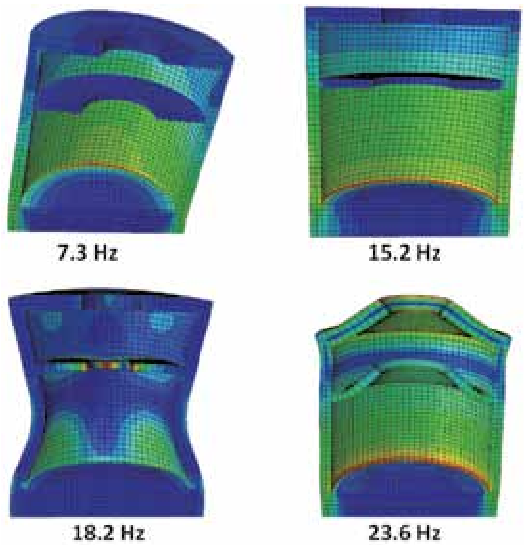

Fig. 7 Stress distribution of each mode

References

Hirama T. et al. (2005a). “Seismic proof test of a reinforced concrete containment vessel (RCCV) Part 1: Test model and pressure test.” *Nuclear Engineering and Design*, 235, 1335–1348.

土木 401-93 (2004)，“混凝土工程設計規範與解說”，中國土木水利工程學會，ISBN: 957-655-394-6.

Hibbitt, Karlsson and Sorensen, Inc. “Abaqus Analysis User’s Manual”, Version. 6.3.

Seismic Probabilistic Risk Assessment of Nuclear Power Plants

Chang-Ching Chang[1], Ying-Hsiu Shen[2], Yin-Nan Huang[3] and Kuo-Chun Chang[4]

張長菁[1]、沈盈琇[2]、黃尹男[3]、張國鎮[4]

Abstract

Seismic Probabilistic Risk Assessment (SPRA) determines the annual frequency of unacceptable seismic performances of a nuclear power plant (NPP), such as core melt and release of radiation, and has been recognized as an important tool for assessing the seismic risk of NPPs. In this study, the procedures of conventional SPRA methodologies are explored and the seismic risk of a sample NPP for one of the accident sequences is computed using conventional SPRA methodologies. SPRA methodologies typically involve the use of component fragility curves defined as a function of ground-motion parameters, such as peak ground acceleration and spectral acceleration. In future studies, the conventional SPRA procedure will be compared with the new SPRA procedure proposed by Huang et al. (2011), where the component fragility curves are defined as a function of structural-response parameters, such as floor spectral acceelration, and the advantages and disadvantages of those two methodologies are discussed.

Keywords: seismic probabilistic risk assessment, fragility curve, nuclear power plant.

Introduction

The United States Nuclear Regulatory Commission (USNRC) issued Supplement 4 to Generic Letter No. 88-20 (USNRC 1991) in 1991 requiring nuclear power plant (NPP) utilities to perform an Individual Plant Examination of External Events (IPEEE). They also issued NUREG-1407 (Chen et al. 1991) to help guide the IPEEE. NUREG-1407 identified Seismic Probabilistic Risk Assessment (SPRA) as an acceptable methodology for the examination of earthquake-induced risks. The purpose of a SPRA is to determine the probability distribution of the frequency of occurrence of adverse consequences (e.g. core damage, radiological release and off-site consequences). In conventional SPRA methodologies, fragility curves express the conditional probability of failure of a structure or component for a given ground-motion parameter, such as peak ground acceleration (PGA) or spectral acceleration.

In this study, the prodedures of conventional SPRA methodologies are explored, and the seismic risk of a sample NPP for one of the accident sequences is computed using conventional SPRA methodologies. In future work, the conventional SPRA prodedure will be compared with the new SPRA procedure proposed by Huang et al. (2011), where the component fragility curves are defined as a function of structural-response parameters, such as floor spectral acceelration. The results of risk computed using conventional and new SPRA methodologies are compared and the advantages and disadvantages of the new methodology will be futher discussed.

Steps in Seismic Probabilistic Risk Assessment

NUREG/CR-2300 (USNRC 1983) provides general guidance for performing SPRA for NPPs. The

[1] Assistant Researcher, National Center for Research on Earthquake Engineering, ccchang@ncree.narl.org.tw.
[2] Assistant Researcher, National Center for Research on Earthquake Engineering.
[3] Assistant Professor, Department of Civil Engineering, National Taiwan University.
[4] Professor, Department of Civil Engineering, National Taiwan University &
Director, National Center for Research on Earthquake Engineering.

guideline describes two SPRA methods: (1) "Zion" and (2) the "Seismic Safety Margin Research Program" (SSMRP). The Zion method requires less computational effort than the SSMRP method and is currently the most popular SPRA procedure. In the Zion method, the component fragility curves are defined in terms of ground-motion parameters, such as peak ground acceleration and spectral acceleration at a given period. The four steps of SPRA are briefly described in the following subsections.

1. Seismic Hazard Analysis

The seismic hazard used in a SPRA is characterized using Probabilistic Seismic Hazard Analysis (PSHA). A PSHA generates a family of hazard curves, which describe the frequency of exceedance for a ground-motion parameter (e.g., PGA and spectral acceleration at a given period) at a specific site. The following four steps that comprise a seismic hazard analysis are as below: (1) identify of sources of earthquakes; (2) evaluation of earthquake history in the region surrounding the site; (3) development of ground motion attenuation relationships; and (4) integration of the above to obtain the frequency of exceeding different ground motion intensities.

2. Plant-System and Accident-Sequence Analysis

There may be a series of elements in a NPP that are required to function in order to prevent core damage. These elements are analogous to the links in a chain. If one link in the chain fails, then the chain fails to perform its function and if a further element fails, then core damage occurs. More formally, the plant logic model takes the form of event trees and fault trees. Event trees display the success or failure of various safety systems leading to a failure event. On the other hand, fault trees answer the question of how a particular system fails. Thus, for each of the systems in an event tree, there is a corresponding fault tree that relates the various structure and equipment failures in a logical manner. The branches of a fault tree proceed downward in increasing refinement, until the most basic failure events are reached. Through the logic of the event and fault trees, the fragilities of the basic events are related by a Boolean equation for the failure event under consideration. Thus, the frequency of failure for the individual structures and equipment are combined to produce the frequency of failure, such as core melt.

3. Component Fragility Evaluation

Seismic fragility curves for structural and nonstructural components in NPPs are needed in a SPRA to estimate the frequencies of occurrence of initiating events and the failures of different safety systems. The lognormal distribution has become the most widely used distribution for developing fragility curves. A lognormal distribution for a random variable can be fully defined by two parameters: the median and logarithmic standard deviation. The latter parameter represents the dispersion in the variable. The sources of the dispersion are distinguished into two types for developing fragility curves for structural and nonstructural components in NPPs: (1) "epistemic uncertainty", for the variability due to the lack of knowledge for the procedure and variables used in the analysis process, for example, the variability in the strength of a shear wall, which could be tested to eliminate the uncertainty; and (2) "aleatory randomness", for the variability that is inherent in the used variables and cannot be reduced practically, for example, the variability in peak ground acceleration for a given earthquake magnitude and distance.

Reed and Kennedy (1994) presented a methodology for developing fragility curves used in a SPRA, and apply a double lognormal model in order to consider the two types of variability separately. The model is shown as:

$$A = \bar{A} \cdot \varepsilon_r = \hat{a} \cdot \varepsilon_u \cdot \varepsilon_r \tag{1}$$

where A is the random variable for the capacity of the component and the capacity is defined in terms of a ground-motion parameter, such as peak ground acceleration or spectral acceleration at a given period; $\bar{A}$, which is equal to $\hat{a} \cdot \varepsilon_u$, is a random variable for the median capacity of the component; $\hat{a}$ is a deterministic value representing the median of $\bar{A}$; and ε_u and ε_r are two lognormally distributed random variables with medians both equal to one and logarithmic standard deviations of β_u and β_r, respectively. Variables ε_u and ε_r represent the uncertainty and randomness in A, respectively. In this model, the median capacity of the component is considered uncertain. The model of (1) can be used to generate a family of fragility curves for each structure, system and component (SSC) in NPPs. As an example, the fragility curve is developed as shown in Fig. 1. The conditional failure frequency for a peak ground acceleration of $2g$ is calculated as 0.29.

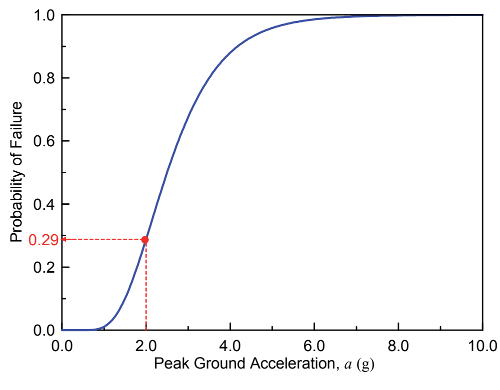

Fig. 1 Component Fragility Curve

In estimating the fragility parameters, it is convenient to work in terms of an intermediate random variable called the factor of safety. The factor of safety, F, on ground acceleration capacity above the safe shutdown earthquake level specified for design, A_{SSE}, is defined as follows:

$$A = F \cdot A_{SSE} \quad (2)$$

The basic variables are presented for structures first and are followed next by a discussion of the basic variables that effect equipment.

(1) Basic Fragility Analysis Variables for Structures

For structures, the factor of safety can be modeled as the product of three random variables:

$$F = F_S F_\mu F_{RS} \quad (3)$$

where the strength factor, F_S, represents the ratio of ultimate strength or strength at loss-of-function to the stress calculated for A_{SSE}; the inelastic energy absorption factor, F_μ, accounts for the fact that an earthquake represents a limited energy source and many structures or equipment are capable of absorbing substantial amounts of energy beyond yield without loss-of-function; and the structure response factor, F_{RS}, is modeled as a product of factors influencing the response variability.

$$F_{RS} = F_{SA} F_{GMI} F_\delta F_M F_{MC} F_{EC} F_{SSI} \quad (4)$$

where F_{SA} is the spectral shape factors; F_{GMI} is the ground motion incoherence factor; F_δ is the damping factor; F_M is the modeling factor; F_{MC} is the mode combination factor; F_{EC} is the earthquake component combination factor; and F_{SSI} is the factor to account for the effect of soil-structure interaction including the reduction of input motion with depth below the surface.

(2) Basic Fragility Analysis Variables for Equipment

For equipment and other components, the factor of safety is made up of three parts consisting of a capacity factor, F_C; a structure response factor, F_{RS}; and an equipment response factor, F_{RE}. Thus,

$$F = F_C F_{RE} F_{RS} \quad (4)$$

The capacity for the equipment may be evaluated as the product of the strength factor, F_S and the inelastic energy absorption factor, F_μ. The equipment response factor, F_{RE}, is the ratio of equipment response calculated in design to the realistic equipment response. Both the responses are calculated for the design floor spectra. F_{RE} is the factor of safety inherent in the computation of equipment response. It depends upon the response characteristics of the equipment, as it is influenced by some of the variables listed under Eq. (4). These variables differ according to the seismic qualification procedure. For equipment qualified by analysis, the important variables that influence response and variability are qualification method, spectral shape, modeling, equipment damping, combination of modal responses, and combination of earthquake components. The structural response factor, F_{RS}, is based on the response characteristics of the structure at the location of the component (equipment) support. The applicable variables are spectral shape, ground motion incoherence factor, damping, modeling, mode combination, and soil-structure interaction effect including the reduction with depth of seismic input, and are almost the same as Eq. (4).

4. Consequence Analysis

Once the hazard curves for the site and the fragility curves for a failure event are obtained, two curves, one from each of the two sets, are selected to compute the frequency of the failure event, P_f, using the following equation:

$$P_f = -\int_0^\infty P_{f/a} \left| \frac{d\lambda_H(a)}{da} \right| da \quad (5)$$

where $P_{f/a}$ is the fragility curve that characterizes the probability of the occurrence of the failure event for a given a value of the parameter a; and λ_H represents the seismic hazard curve. The range of integration should be wide enough to cover all of the earthquake intensities with significant contributions to P_f. The use of (5) requires that the fragility and seismic hazard curves be a function of the same parameter.

Example of Seismic Risk Calculations for One of the Accident Sequences in NPPs

In this study, the seismic risk of a sample NPP for one of the accident sequences is computed using conventional SPRA methodologies. The hazard curve for this sample NPP is shown as Fig. 2.

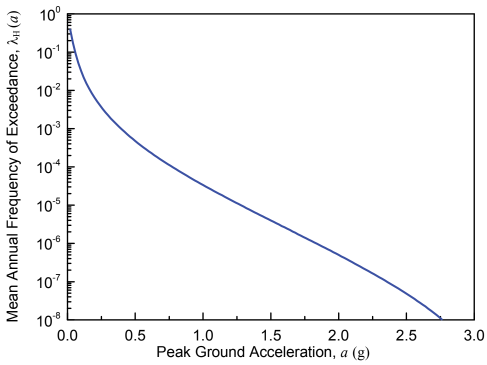

Fig. 2 Hazard Curve for the Sample NPP

One of the accident sequences for the sample NPP is presented in Fig. 3. The accident sequence starts from a seismic event, ends at core damage and consists of a series of safety systems in between. The accident sequence is triggered by a seismic event, which results in a loss of off-site power (LOP). Although all the safety-related structures maintain their integrity during the earthquake, the service water system (SW) fails, which results in the failure of emergency diesel generator. The swing diesel generator has its own service water system and survives in this accident sequence. Scram succeeds in representing that the process of safety control rod insertion is finished. Under these conditions, the Reactor Core Isolation Cooling System (RCIC) provides core cooling for approximately 8 hours as designed. Subsequently, the reactor is depressurized to permit the AC Independent Water Addition System (ACIWA) to inject water into the reactor. In the accident sequence of Fig. 3, ACIWA fails which results in core damage. Therefore, the failure event is LOP, SW, and ACIWA in the sample accident sequence.

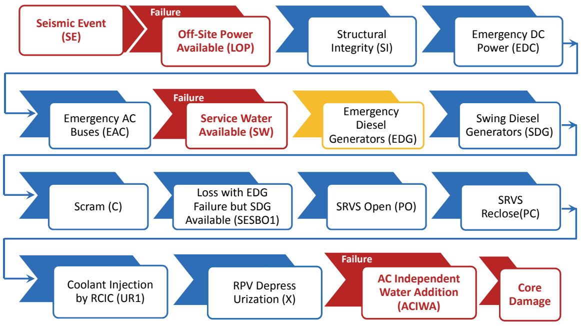

Fig.3 Accident Sequence

In this example, fragility curves express the conditional probability of failure of a structure or component for a PGA using the Zion method. For the accident sequence of Fig. 3 in the sample NPP, the fragility curve is calculated as shown in Fig. 4. Then, the seismic risk P_f can be obtained by numerical convolution of the seismic hazard curve and fragility curve, using Eq. (5). In this sample, the frequency of core damage for this accident sequence is calculated as 8.78×10^{-6}.

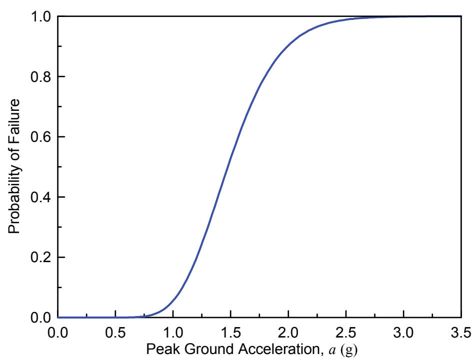

Fig. 4 Fragility Curve for the Accident Sequence

Conclusions

In conventional SPRA methodologies, fragility curves express the conditional probability of failure for a structure or component for a given ground-motion parameter, such as PGA or spectral acceleration. In this study, the seismic risk for one of the accident sequences in NPPs is calculated and the component fragility curves are defined in terms of PGA. However, the damage and failure of NPP components are more closely tied to structural response parameters than to ground motion parameters. The use of ground motion parameters greatly increases the dispersion in the fragility curves. Moreover, the median and dispersion of a component fragility curve expressed in terms of ground-motion parameters are dependent on both the capacity of the component and the response (demand) of the structure where the component is attached.

In future studies, the conventional SPRA procedure will be compared with the new SPRA procedure proposed by Huang et al. (2011), where the component fragility curves are defined as a function of structural-response parameters, such as floor spectral acceleration. The results of risk computed using conventional and new SPRA methodologies are compared and the advantages and disadvantages of the new methodology will be further discussed.

References

Chen, J. T., Chokshi, N. C., Kenneally, R. M., Kelly, G. B., Beckner, W. D., McCracken, C., Murphy, A. J., Reiter, L., and Jeng, D., "Procedural and submittal guidance of individual plant examination of external events (IPEEE) for severe accident vulnerabilities." NUREG-1407, U.S. Nuclear Regulatory Commission, Washington, D.C., 1991.

Huang, Y.-N., Whittaker, A. S., and Luco, N., "A probabilistic seismic risk assessment procedure for nuclear power plants: (I) Methodology." *Nuclear Engineering and Design*, 241(9), pp3996-4003, 2011.

Huang, Y.-N., Whittaker, A. S., and Luco, N., "A probabilistic seismic risk assessment procedure for nuclear power plants: (II) Application." *Nuclear Engineering and Design*, 241(9), pp3985-3995, 2011.

Pickard, Lowe, and Garrick, Inc., and Westinghouse Electric Corporation, Fauske & Associates, Inc., "Zion Probabilistic Safety Study." prepared for Commonwealth Edison Company, Chicago, 1981.

Reed, J. W., and Kennedy, R. P., "Methodology for developing seismic fragilities." TR-103959, Electric Power Research Institute, Palo Alto, CA. 1994

U.S. Nuclear Regulatory Commission (USNRC). "PRA procedures guide." NUREG/CR-2300, USNRC, Washington, D.C., 1983.

Pushover Analyses for Asymmetrical Buildings

Jui-Liang Lin [1], Keh-Chyuan Tsai [2] and Ming-Chieh Chuang [3]

林瑞良 [1]、蔡克銓 [2]、莊明介 [3]

Abstract

This paper studies the reasons behind four trends in torsional effects in asymmetrical buildings observed in recent literature. It is found that modal eccentricities and the non-proportionality between the modal translations and the modal rotation are key to understanding these trends in torsional effects in asymmetrical buildings. The non-proportionality between the modal translations and the modal rotation leads to the trend that the torsional effects generally decrease when plastic deformations increase. This study also proposes a novel oscillator, referred to as the co-shape oscillator (COSO), which can be effectively used in the nonlinear response history analysis of multistory asymmetrical buildings. For accuracy and simplicity, the incremental dynamic analysis with the use of COSOs, instead of pushover analysis, is proposed for the simplified seismic analyses of asymmetrical buildings.

Keywords: pushover analysis; incremental dynamic analysis; asymmetrical buildings; torsional effects; oscillator

Introduction

Due to architectural and functional requirements, most practical buildings are asymmetrical. However, this type of building is one of the most frequently damaged structures under earthquake loads. The rotational response of asymmetrical buildings leads to unequal displacement demands on the floor diaphragm. The torsional effects, generally represented as the ratio between the displacements of the floor edges to the displacement of the center of mass (CM) are unique to asymmetrical buildings compared with symmetrical buildings. Therefore, identifying torsional effects in a building is a crucial step in several nonlinear static (pushover) analysis procedures for asymmetrical buildings (Fajfar *et al*. 2005).

Fajfar *et al*. (2005) investigated the general trends in the torsional effects in two-way asymmetrical buildings under bi-directional ground excitations. Some trends found in the torsional effects reported in the original paper (Fajfar *et al*. 2005) are re-stated here. First, torsional effects generally decrease when plastic deformations increase. Second, between the two horizontal directions, the torsional effect on displacements in the more flexible direction is smaller than that in the stiffer direction. Third, for the stiff side (SS), it is difficult to make general conclusions. The response of the SS generally has a strong dependence on the effects of several modes of vibration, and on the influence of the ground motion in the transverse direction. The structural and ground motion characteristics in both directions are influential. Finally, transitions from the de-amplification to amplification of the displacement demand may occur on the SS in some cases.

These four trends in the torsional effects in asymmetrical buildings seem difficult to be completely understood by using general intuition. The overall structural parameters that are related to the rotational responses, include the radius of gyration for the mass moment of inertia, the normalized eccentricity and the frequency ratio, *etc*. Nevertheless, it also appears that there is no satisfactory explanation for the aforementioned trends in the torsional effects solely using these overall structural parameters. There is no doubt that

[1] Associate Researcher, National Center for Research on Earthquake Engineering, jllin@ncree.narl.org.tw.
[2] Professor, Department of Civil Engineering, National Taiwan University, kctsai@ntu.edu.tw
[3] Assistant Researcher, National Center for Research on Earthquake Engineering, mcchuang@ncree.narl.org.tw.

the rationale of the torsional effects is an issue deserving of more emphasis. Investigating the reasons behind these trends in torsional effects is helpful not only to understand the seismic responses of asymmetrical buildings but also for the development of suitable seismic assessment procedures.

The present study first used the elastic and inelastic properties of the three-degree-of-freedom (3DOF) modal systems (Lin and Tsai 2008) to explain the trends in the torsional effects in asymmetrical buildings, which were found in the literature (Fajfar *et al*. 2005). It is expected to improve understanding of the characteristics of the seismic behavior of asymmetrical buildings.

In addition, the inelastic dynamic analysis, *i.e.*, the nonlinear response history analysis (NRHA), is widely recognized as a more reliable approach for assessing structural seismic performance when compared with the pushover analysis approach. Nevertheless, the pushover analysis approach is seemingly more popular than the NRHA in engineering practice due to its computational simplicity and efficiency. Krawinkler *et al*. (2011) clearly pointed out that simplicity in modeling is at the core of facilitating the use of the NRHA. Han and Chopra (2006) proposed the simplified approach of performing incremental dynamic analysis, which suggested analyzing the first single-degree-of-freedom (SDOF) modal oscillator, instead of analyzing the finite element model of the multistory building. This again suggests that a simplified and effective inelastic structural model is necessary for promoting the NRHA in engineering practice. The other aim of this study is to construct the co-shape oscillator (COSO), which can be used in the NRHA as a substitute for the finite element model of an inelastic multistory asymmetrical building.

Explanations of the Trends in Torsional Effects

The X- and the Z-axes are the two horizontal axes of the coordinate system used in this study. The direction of the Y-axis is opposite to the direction of gravity. The subscripts x, z, and θ used in this study represent the corresponding quantities associated with the X- and Z-translational and Y-rotational components, respectively.

The first trend in torsional effects is that they generally decrease when plastic deformations increase. Taking the contribution of the nth vibration mode of an elastic two-way asymmetrical building subjected to an X-directional ground motion into consideration, the equations for the torsional effect, defined by the displacements on the flexible side (FS) and SS of the jth floor divided by the corresponding displacement at the CM, are:

$$\frac{u_{FS,nj}^{elastic}}{u_{CM,nj}^{elastic}} = 1+\left(\frac{b}{2}-e_z\right)\frac{\phi_{\theta n,j}}{\phi_{xn,j}} = 1+\eta_{FS,nj}^{elastic} \tag{1a}$$

and:

$$\frac{u_{SS,nj}^{elastic}}{u_{CM,nj}^{elastic}} = 1-\left(\frac{b}{2}+e_z\right)\frac{\phi_{\theta n,j}}{\phi_{xn,j}} = 1+\eta_{SS,nj}^{elastic} \tag{1b}$$

where b and e_z are the floor diaphragm dimension and the overall structural eccentricity, respectively, and $\phi_{xn,j}$ and $\phi_{\theta n,j}$ are the jth-floor components of the nth mode shape in the X-translational and Y-rotational directions, respectively. The $\eta_{FS,nj}^{elastic}$ and $\eta_{SS,nj}^{elastic}$ are referred to as the elastic torsional indices for the nth vibration mode on the FS and SS of the jth floor, respectively. The larger the absolute value of the torsional index, the more substantial the torsional effect. In an inelastic state, using the concept of "weak coupled vibration modes", the torsional effects on the FS and SS of the jth floor resulting from the nth "vibration mode" are approximated as:

$$\frac{u_{FS,nj}^{inelastic}}{u_{CM,nj}^{inelastic}} \approx 1+\left(\frac{b}{2}-e_z\right)\frac{\phi_{\theta n,j}}{\phi_{xn,j}}\frac{\mu_{\theta n}}{\mu_{xn}} = 1+\eta_{FS,nj}^{inelastic} \tag{2a}$$

and:

$$\frac{u_{SS,j}^{inelastic}}{u_{CM,j}^{inelastic}} \approx 1-\left(\frac{b}{2}+e_z\right)\frac{\phi_{\theta n,j}}{\phi_{xn,j}}\frac{\mu_{\theta n}}{\mu_{xn}} = 1+\eta_{SS,nj}^{inelastic} \tag{2b}$$

where μ_{xn} and $\mu_{\theta n}$ are the X-translational and Y-rotational ductilities, respectively. The $\eta_{FS,nj}^{inelastic}$ and $\eta_{SS,nj}^{inelastic}$ are referred to as the inelastic torsional indices for the nth vibration mode on the FS and SS of the jth floor. Comparing the elastic and inelastic torsional indices shows that the inelastic torsional indices are equal to the counterpart elastic torsional indices multiplied by $\mu_{\theta n}/\mu_{xn}$. As a reminder, the modal acceleration A_n and the modal displacements D_{xn}, D_{zn}, and $D_{\theta n}$ are computed as (Lin and Tsai 2008):

$$A_n = \frac{V_{bxn}}{\Gamma_{xn}M_n} = \frac{V_{bzn}}{\Gamma_{zn}M_n} = \frac{T_{bn}}{\Gamma_{\theta n}M_n} \tag{3a}$$

and:

$$D_{xn} = \frac{u_{xn,r}}{\phi_{xn,r}},\quad D_{zn} = \frac{u_{zn,r}}{\phi_{zn,r}},\quad D_{\theta n} = \frac{u_{\theta n,r}}{\phi_{\theta n,r}} \tag{3b}$$

where $\phi_{xn,r}$, $\phi_{zn,r}$, and $\phi_{\theta n,r}$ are the roof components of the nth mode shape in the three directions; $u_{xn,r}$, $u_{zn,r}$, and $u_{\theta n,r}$ are the roof displacements in the three directions; V_{bxn}, V_{bzn}, and T_{bn} are the base shears and base torque of the original multi-story building pushed using the nth modal inertia force vector; M_n is the modal mass; and Γ_{xn}, Γ_{zn}, and $\Gamma_{\theta n}$ are the modal participation factors in the three directions. Because the pushover force vector keeps proportionally increasing in the three directions, the modal acceleration A_n also proportionally increases in the three directions (Eq. 3a), but the modal displacements, D_{xn}, D_{zn}, and $D_{\theta n}$, are non-proportionally increased (Eq. 3b). Since the translational post-yielding stiffness ratio, α_{xn}, is less than the rotational post-yielding stiffness ratio, $\alpha_{\theta n}$, the value of $\mu_{\theta n}/\mu_{xn}$ is less than one and decreases as A_n increases. Thus, the absolute values of the inelastic torsional indices, $\eta_{FS,nj}^{inelastic}$ and $\eta_{SS,nj}^{inelastic}$, decrease as A_n increases. That is to say, the torsional effect decreases when plastic deformations increase, which explains this first trend in torsional effects (Fajfar *et al*. 2005).

The second trend in torsional effects is that the torsional effect on displacements in the more flexible direction, *i.e.*, the weaker direction, is smaller than that in the stiffer direction (Fajfar *et al*. 2005). Fajfar *et al*. (2005) defined the weaker direction to be the direction in which a building experiences a larger plastic deformation than in other directions. For instance, when α_{zn} is larger than α_{xn}, the X-direction is the "weaker direction". From Eq. 2, the inelastic torsional effects in both the stiff and the flexible directions are equal to its counterpart elastic torsional effects multiplied by $\mu_{\theta n}/\mu_{zn}$ and $\mu_{\theta n}/\mu_{xn}$, respectively. Because α_{zn} is larger than α_{xn}, $\mu_{\theta n}/\mu_{zn}$ is larger than $\mu_{\theta n}/\mu_{xn}$. It consequently explains the second trend of torsional effects.

The third trend of torsional effect is that the seismic responses on the SS generally depend on the influences of several modes of vibration and the ground motion in the transverse direction. Thus, it is difficult to make general conclusions about the torsional effects on the SS. In order to explain this third trend of torsional effects, the relationships between the directions of the modal eccentricities and the trends in unequal modal displacement demands are first discussed in the following contents.

It is clear that the rotational response resulting from structural eccentricity leads to unequal displacement demands on the FS and the SS of the floor diaphragm in asymmetrical buildings. This suggests that the directions of modal eccentricities, *i.e.*, e_{xn} and e_{zn}, are influential on the unequal modal displacement demands on the edges of the floor diaphragm. The beam end with a lumped mass in the 3DOF modal system (Lin and Tsai 2008) is regarded as the FS and the other beam end is regarded as the SS. When a 3DOF modal system with positive e_{zn} and e_{xn} has a positive Y-rotational increment, the displacements of the FS increased in the X-direction and decreased in the Z-direction. That is to say, when the modal eccentricities e_{zn} and e_{xn} are positive, the FS in the X-direction and the SS in the Z-direction face a larger displacement demand than the other side of the floor diaphragm in the same direction. Conversely, when the modal eccentricities e_{zn} and e_{xn} are negative, the SS in the X-direction and the FS in the Z-direction face a larger displacement demand than the other side of the floor diaphragm in the same direction.

It is clear that all structural vibration modes contribute to the structural seismic response of the building. The extent of each mode's contribution depends on the characteristics of the vibration mode and the seismic ground motions; *e.g.*, the frequency content of the ground motions. This brings to light an explanation for the third trend in torsional effects, stating that it is difficult to reach general conclusions about the torsional effects on the SS, which strongly depend on the effects of several vibration modes and is influenced by the ground motion in the transverse direction. A detailed explanation of this trend was given by Lin *et al*. (2012).

The fourth trend found in the torsional effects is that, in some cases, transitions from de-amplification to amplification of the displacement demand may occur on the SS (Fajfar *et al*. 2005). From the discussion of the third trend of torsional effects, it is clear that the displacement demand on the SS is possibly larger than the displacement demand on the FS in the same direction. In addition, the torsional effects on the SS are influenced by ground motions in the transverse direction. Due to the time-varying characteristics of the seismic ground motions, the torsional effect on the SS may, in some cases, change from a de-amplification to an amplification of the displacement demand.

The co-shape oscillator

Each COSO is constructed from the two-degree-of-freedom (2DOF) modal properties of the two specific vibration modes of a one-way asymmetrical building. These two vibration modes consist of an identical number of stationary points in their mode shapes. In addition, the normalized mode shapes of these two vibration modes are very similar. These same unique characteristics of the mode shapes of each pair of vibration modes are the key reasons to name the proposed oscillator as COSO. The first task in developing the COSO is to establish its physical model and its corresponding inelastic properties. The second task is to construct the COSOs representing higher-mode pairs of the multistory asymmetrical building in order to consider the higher-mode effects on its seismic responses.

The concept of using COSOs to estimate the seismic responses of asymmetrical buildings is shown in Fig. 1. The equation of motion for the COSO is:

$$\mathbf{M}^*\ddot{\mathbf{u}}^* + \mathbf{C}^*\dot{\mathbf{u}}^* + \mathbf{K}^*\mathbf{u}^* = -\mathbf{M}^*\iota\ddot{u}_g(t) \tag{4}$$

where:

$$\mathbf{M}^* = \begin{bmatrix} m^* & 0 \\ 0 & I^* \end{bmatrix} = \begin{bmatrix} 1 & 0 \\ 0 & 1 \end{bmatrix}, \quad \mathbf{u}^* = \begin{bmatrix} u_z^* \\ r^* u_\theta^* \end{bmatrix} \quad \iota = \begin{bmatrix} 1 \\ 0 \end{bmatrix}$$
$$\mathbf{K}^* = \begin{bmatrix} m_1\omega_1^2 + m_2\omega_2^2 \;, & sym. \\ -\sqrt{m_1 m_2}\left(s_2\omega_1^2 + s_1\omega_2^2\right) & I_1\omega_1^2 + I_2\omega_2^2 \end{bmatrix} \tag{5}$$

$\ddot{u}_g(t)$ is the ground acceleration record, and r^* is the mass radius of gyration. The parameters m_n, I_n, and ω_n, where n = 1 and 2, denote the mass, mass moment of inertia, and the circular vibration frequency of the two targeted vibration modes of the original N-story asymmetrical building, respectively. The two targeted vibration modes are the first translational-dominant and the first rotational-dominant vibration modes of the original building. The quantities m_n and I_n, where n = 1 and 2, are computed as:

$$m_n = \boldsymbol{\varphi}_{zn}^T \mathbf{m} \boldsymbol{\varphi}_{zn}, , \; I_n = \boldsymbol{\varphi}_{\theta n}^T \mathbf{I} \boldsymbol{\varphi}_{\theta n}, \quad n = 1, 2 \tag{6}$$

where **m** and **I** are the $N \times N$ mass matrix and the $N \times N$ mass moment of inertia matrix of the original building, and $\boldsymbol{\varphi}_{zn}$ and $\boldsymbol{\varphi}_{\theta n}$ are the $N \times 1$ sub-vectors of the nth mode shape of the original building. In Eq. (5), the values of s_1 and s_2, which are equal to either 1 or −1, are determined from the directions of the mode shapes of the two targeted vibration modes. When the directions of the translational component $\boldsymbol{\varphi}_{zn}$ and the rotational component $\boldsymbol{\varphi}_{\theta n}$ of the targeted vibration mode are the same, the corresponding s_n equals 1. Conversely, when $\boldsymbol{\varphi}_{zn}$ and $\boldsymbol{\varphi}_{\theta n}$ have opposite directions, the corresponding s_n equals −1. The elastic and inelastic properties of the springs and dashpots of the COSO are given by Lin *et al.* (2013). The relationships between the seismic responses of the COSO and those of the original multi-story building are also given by Lin *et al.* (2013).

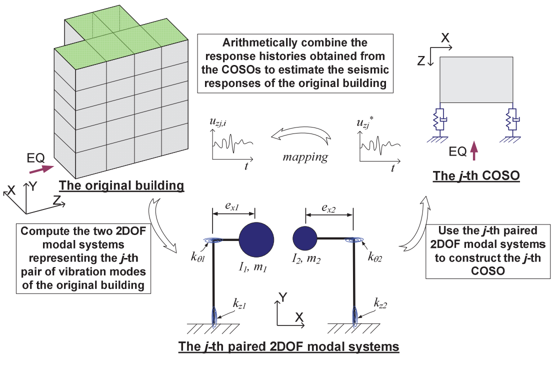

Fig. 1 The concept of using COSOs to estimate the seismic responses of asymmetrical buildings.

Conclusions

This study provided an effective alternative explanation of some of the trends in torsional effects in asymmetrical buildings using the characteristics of 3DOF modal systems. Among the characteristics of the 3DOF modal systems, the modal eccentricities and the non-proportionality between the modal translations and the modal rotation are the keys to reaching the explanations behind the trends in torsional effects.

The properties of each pair of vibration modes pertaining to multistory asymmetrical buildings are used to construct the associated COSO. The COSO consists of a rigid mass block, which has unit mass and unit mass moment of inertia, connected with two spring–dashpot sets. Each spring–dashpot set of the COSO preserves the modal properties belonging to one of the two associated vibration modes. The conventional SDOF oscillator is usually used to represent a single vibration mode of a building, whereas the COSO simultaneously represents a pair of vibration modes in an asymmetrical building. The COSO also possesses an advantage of computational efficiency similar to the conventional SDOF modal oscillator.

References

Fajfar, P., Kilar, V., Marusic, D., Perus, I. (2005), “Torsional effects in the pushover-based seismic analysis of buildings”, *Journal of Earthquake Engineering*, 9: 831-854.

Han S.W., Chopra A.K. (2006), “Approximate incremental dynamic analysis using the modal pushover analysis procedure”, *Earthquake Engineering and Structural Dynamics*, 35: 1853-1873.

Krawinkler H., Lignos D.G., Putman C. (2011), “Prediction of nonlinear response — pushover analysis versus simplified nonlinear response history analysis”, Structures Congress, Las Vegas, Nevada.

Lin, J.L., Tsai, K.C. (2008), “Seismic analysis of two-way asymmetric building systems under bi-directional seismic ground motions”, *Earthquake Engineering and Structural Dynamics*, 37: 305-328.

Lin, J.L., Tsai, K.C. and Chuang, M.C. (2012), “Understanding the trends in torsional effects in asymmetric-plan buildings”, *Bulletin of Earthquake Engineering*, 10: 955-965.

Lin, J.L., Tsai, K.C. and Chuang, M.C. (2013), “Effective oscillators for the seismic analysis of inelastic one-way asymmetric-plan buildings”, *Engineering Structures*, (in press, DOI 10.1016/j.engstruct.2013.02.007).

The Study of the Safety Factor of the Pushover Analysis Procedure Based on the Capacity Spectrum Method

Yeong-Kae Yeh [1] and Te-Kuang Chow [2]

葉勇凱 [1]、周德光 [2]

Abstract

At present, engineers often use pushover analysis based on the capacity spectrum method to work on detailed seismic evaluation of structures in Taiwan. The performance target of the ground acceleration is used to compare with the site peak ground acceleration of a design earthquake with a 475-year return period to evaluate the sufficiency of a structure's seismic capacity. These evaluated results are too conservative as stated in FEMA 440. In this report, the nonlinear dynamic analysis of a single degree structure is used to study the inherent safety factor of the capacity spectrum method and its relationship with the elastic stiffness of the structure, the dispersive hysteretic energy, and the characteristic of input seismic record. From the analysis results, this safety factor is found to be larger than 2 and to have a larger value for less stiff structures. It is also found to be independent of the dispersive hysteretic energy, and to be influenced by the characteristic of the input seismic record.

Keywords: detailed seismic evaluation, nonlinear pushover analysis, capacity spectrum method, nonlinear dynamic analysis,

Introduction

Detailed seismic evaluation procedures are often used to confirm the seismic capacity of existing buildings. Currently the most widely used detailed evaluation method is nonlinear pushover analysis to obtain the capacity curves of structures, namely the establishment of the relationship between the base shear and roof displacement. Based on the building's performance needs, a performance point is set on the capacity curve through a specific procedure to seek a design earthquake that can cause this performance-point roof displacement. This performance target earthquake is presented by its associate 475 year design response spectrum and maximum ground acceleration. The above procedures can be divided into two categories: one is the capacity spectrum method suggested by ATC 40 (ATC, 1996); the other is the coefficient method suggested by FEMA 356 (FEMA, 2000).

In Taiwan the most popular detailed seismic evaluation methods are the "Seismic Evaluation of Reinforced Concrete Structure with Pushover Analysis" developed by the National Center for Research on Earthquake Engineering (NCREE) and the "Seismic Evaluation of RC Buildings (SERCB)" developed by the team led by Prof. I-Chau Tsai from the National Taiwan University. Both of these two methods are based on the capacity spectrum method of ATC 40. The pushover analysis based on the capacity spectrum method is an approximation method to simulate the roof displacement of the structure calculated by nonlinear dynamic analysis. In the FEMA 440 (FEMA, 2005) report, the capacity spectrum method of ATC 40 is noted to be too conservative. The Capacity spectrum method has been widely used in the seismic evaluation and retrofitting of existing buildings in Taiwan, so it is necessary to study the implicit safety factor of the method, and its relationship with the elastic stiffness of the structure, the hysteretic energy dissipation of its elements, and the characteristic of input seismic records.

The analysis results of the capacity spectrum method are dependent on the vertical distribution of the lateral loading and the reference mode (ATC,

[1] Researcher, National Center for Research on Earthquake Engineering, ykyeh@ncree.narl.org.tw

[2] Assistant Technologist, National Center for Research on Earthquake Engineering, tkchow@ncree.narl.org.tw

1996). In order to simply study the relationship between the nonlinear pushover analysis and the dynamic analysis, we use a single degree of freedom structure system as the subject of analysis, so that choice of lateral loading distribution and reference mode can be avoided.

The third edition of the NCREE technology handbook is used to define the nonlinear hinges of the structure, and the software packages ETABS and PERFORM3D are adopted to perform the nonlinear pushover analysis and the nonlinear dynamic analysis respectively.

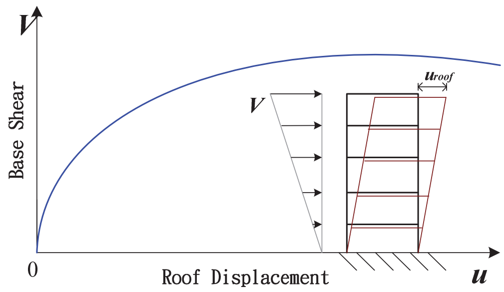

Fig. 1 Capacity curve of the pushover analysis

Capacity Spectrum Method

The actual structure subject to the 475-year design earthquake will develop nonlinear deformation. In order to understand the mechanical behavior of the buildings during the earthquake excitation, the most direct approach is nonlinear dynamic analysis. The most familiar seismic design is to adopt the static elastic analysis where the ductile capacity of the structure is assumed to reduce the design seismic forces. It also uses the elastic response spectrum and the peak ground acceleration to represent the design earthquake. Engineers are more accustomed to static analysis than nonlinear dynamic analysis. So, the static pushover analysis is more commonly used in seismic evaluation to simulate the displacement response of the structure in earthquakes.

The capacity spectrum method for seismic evaluation is suggested by ATC 40 and is also widely adopted by the engineering community. It is based on the nonlinear pushover analysis of a planar frame to establish the capacity curve of the structure. This is done by setting a performance point at the capacity curve and seeking the performance object earthquake that can cause this performance object displacement. The peak ground acceleration of this performance object earthquake is used to compare with the peak ground acceleration of a 475-year design earthquake. If the value of the performance object earthquake is larger, the structure has adequate seismic capacity. Otherwise, the structure needs to be retrofitted to reduce the nonlinear displacement in earthquakes.

The above mentioned capacity curve is developed by the pushover analysis. According equation (1) to set up the lateral loading, the force-deformation curve relating base shear V to roof displacement u_{roof} can be found from a graph as shown in Fig. 1.

$$V_j = V\frac{m_j\phi_{j1}}{\sum_{i=1}^{N} m_i\phi_{i1}} \tag{1}$$

where, m_i is the mass of the i-th floor and ϕ_{i1} is the amplitude of the i-th floor of the first mode.

The capacity curve is then transformed into the capacity spectrum, namely the relation curve of the spectral displacement S_d and the spectral acceleration coefficient S_a. The transform equations are shown as:

$$S_d = \frac{u_{roof}}{PF_1\phi_{roof,1}} \tag{2}$$

$$S_a = \frac{V}{\alpha_1 \cdot W} \tag{3}$$

where, PF_1 and α_1 are the participation factor and the modal mass coefficient for the first mode of the structure respectively; W is the weight of the structure.

Each performance point (S_{dp}, S_{ap}) of the capacity spectrum can be treated as a response to an equivalent single degree of freedom system at a different level earthquake with an equivalent period and damping ratio. The seismic evaluation procedure seeks a high damping ratio response spectrum which intersects the capacity spectrum at the performance point. The peak ground acceleration (PGA) of this high damping ratio response spectrum is named the performance object ground acceleration A_p. A_p can be calculated as:

$$A_p = \begin{cases} S_{ap} \Big/ \left[1+\left(\frac{2.5}{B_S}-1\right)\frac{T_{eq}}{0.2T_0}\right] & for\, T_{eq} \le 0.2T_0 \\ \frac{B_S}{2.5}S_{ap} & for\, 0.2T_0 < T_{eq} \le T_0 \\ \frac{B_S T_{eq}}{2.5T_0}S_{ap} & for\, T_0 < T_{eq} \end{cases} \tag{4}$$

where, $T_0 = (S_{D1}B_S)/(S_{DS}B_1)$ is the parting between the short and middle period ranges; S_{DS} is the short period design spectral acceleration at the site; S_{D1} is the site one second period design spectral acceleration; B_S and B_1 are the damping ratio modification coefficients defined in the design code which are dependent on β_{eq} .

Pushover Analysis of a Single Degree of Freedom Structure

As shown in Fig.2, the four-column four-beam single-span single-floor structure is 450 cm long, 450 cm wide, and 330 cm high. The site is set in the eastern part of Tainan City and the site ground is class 2. The reference lines of the columns and beams are the middle centerlines. The offsets of the columns and beams are assumed to be rigid. The properties of the panel zones are the same as the columns. The flexural rigidity EI of the crack section along the weak axis of the columns is 149.4×108 kgf • cm^2. The flexural rigidity EI of beams' crack section is 573.8×108 kgf • cm^2. The properties of the nonlinear moment hinges at both ends of the columns along the weak axis and beams are shown in Fig. 3. The floor has a 12 cm thickness and is set as a rigid diaphragm. The vertical load comes from the self-weight of members and the floor's uniform loading is set at 0.01 kgf/cm^2. The story mass and the mass moment of inertia are 14850 kg and 1.503×109 kg • cm^2 respectively.

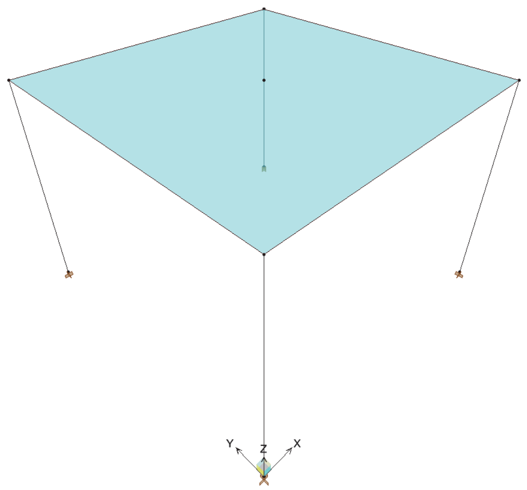

Fig. 2 The four-column four-beam single-span single-floor structure

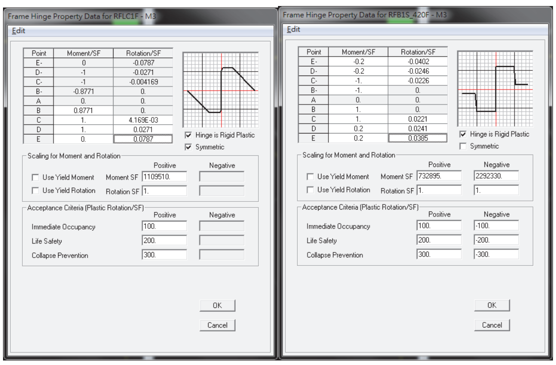

Fig. 3 The moment hinges of the columns and beams

The model is set up in the software ETABS. At first, the vertical loading is applied under force control. Then, under displacement control, the lateral forces are applied at the mass centers of each floor along the X-direction. The capacity curve is shown in Fig. 4. A roof displacement of 7.5 cm is chosen as the performance object displacement. According to the capacity spectrum method, the performance object ground acceleration is calculated as 1.156g, which corresponds to a roof displacement of 7.5 cm in an earthquake with a PGA of 1.156g for this structure. However, the real roof displacement in an actual earthquake will be smaller. The ratio between the estimated roof displacement and the actual is the studied safety factor.

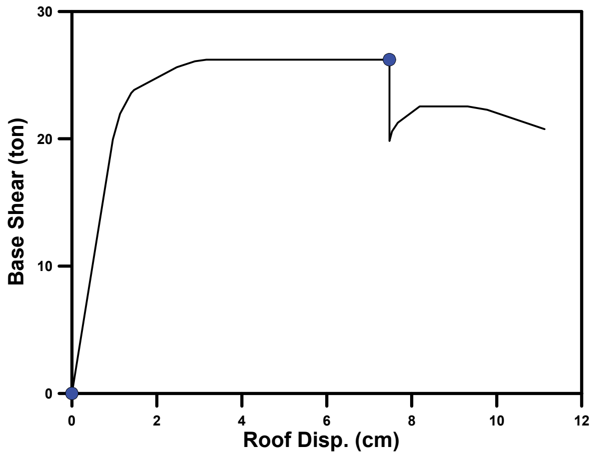

Fig. 4 Capacity curve of the single-span single-floor structure

Nonlinear Dynamic Analysis of a Single Degree of Freedom Structure

The software PERFORM3D is used to perform the nonlinear dynamic analysis for this study. The model is same as that used in the pushover analysis. We have two types of hysteretic behavior: one where the stiffness does not degrade during the analysis as shown in Fig.5, and another where the stiffness does degrade as shown in Fig. 6.

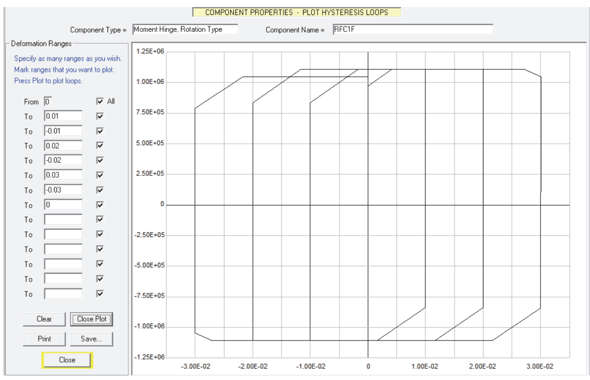

Fig. 5 Hysteretic behavior of nonlinear hinge of columns with no stiffness degradation

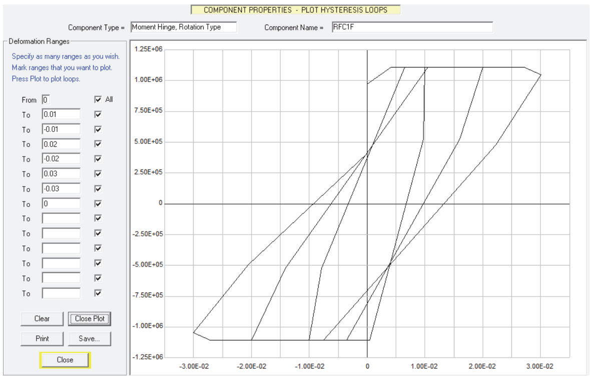

Fig. 6 Hysteretic behavior of nonlinear hinge of columns with stiffness degradation

The input earthquakes are chosen from the seismic databank of the Central Weather Bureau. The seismic intensity for all twenty seismic records is larger than 6 and the seismic stations are all located on class 2 ground. The peak ground accelerations of these records lie between 250gal and 550gal. Their response spectrums and the average spectrum are shown in Fig. 7.

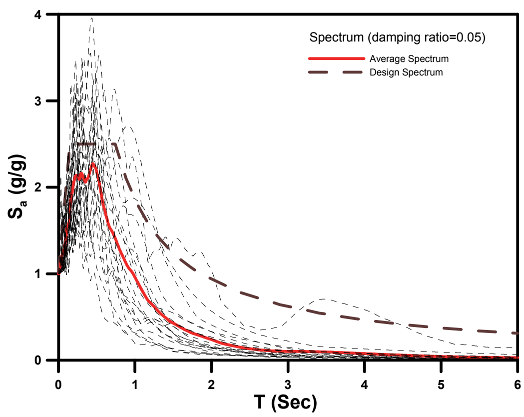

Fig. 7 Response spectrums of 20 chosen earthquakes

As shown in Table 1, the average roof displacement of the cases with no stiffness degradation is 1.64 cm, which is much smaller than the performance object displacement 7.5 cm, and the ratio 4.5 is the implicit safety factor; the average roof displacement of the cases with stiffness degradation is 1.73 cm, which is also smaller than the performance object displacement, and the implicit safety factor is 4.3. From the comparison, we can conclude that conservation of the capacity spectrum method is not dependent on the stiffness degradation.

Conclusions

This study shows the capacity spectrum method to be a very conservative method and to overvalue the importance of stiffness degradation in hysteretic cycles.

Table 1 The analysis of the roof displacements in nonlinear dynamic analyses

Earthquake	Disp.(cm) (No Degradation)	Disp.(cm) (Degradation)
21	1.12	1.12
22	1.32	1.59
23	1.24	1.24
24	1.76	1.87
25	1.37	1.52
26	2.11	2.52
27	2.28	2.38
28	1.35	1.41
29	1.24	1.25
30	1.40	1.40
31	2.00	2.00
32	1.15	1.15
33	1.85	2.26
34	1.55	1.54
35	2.55	2.55
36	2.50	2.70
37	1.27	1.29
38	1.45	1.45
39	1.83	1.83
40	1.56	1.56
AVE	1.64	1.73
STD	0.44	0.50

References

Applied Technology Council (ATC) (1996), "ATC-40 Seismic Evaluation and Retrofit of Concrete Buildings", prepared by the Applied Technology Council, Redwood City, Calif.

Federal Emergency Management Agency (FEMA) (2000), "Prestandard and Commentary for the Seismic Rehabilitation of Buildings (FEMA Publication 356)", prepared by the American Society of Civil Engineers, Washington, D.C.

Federal Emergency Management Agency (FEMA) (2005), "FEMA 440 Improvement of Nonlinear Static Seismic Analysis Procedures", prepared by the Applied Technology Council for the Federal Emergency Management Agency, Washington, D.C.

Verification of Simplified Pushover Analysis of School Buildings by In-Situ Tests

Lap-Loi Chung[1], Lai-Yun Wu[2], Yao-Sheng Yang[3], Ting-Yu Ku[3], Yong-An Lai[3], and Chun-Ting Huang[3]

鍾立來 [1]、吳賴雲 [2]、楊耀昇 [3]、顧丁與 [3]、賴勇安 [3]、黃鈞鼎 [3]

Abstract

During the Chi-Chi Earthquake in Taiwan, 786 school buildings were damaged and 43 school buildings collapsed. Unfortunately, elementary schools and junior high schools sustained the majority of the damage. As there is a lack of seismic capacity for existing school buildings, solving this problem has become an important issue in Taiwan. For this purpose, various seismic evaluation methods were proposed by researchers to determine whether existing school buildings needed retrofitting. However, some of these methods require complicated calculations and packaged software. Therefore, a simple and efficient seismic evaluation method for estimating the seismic capacity of existing school buildings needs to be developed.

Based on post-earthquake reconnaissance reports, school buildings in Taiwan typically collapsed along the direction of the corridor during an earthquake. Therefore, only the seismic resistance along the direction of the corridor is considered in this study. In order to realize how school buildings subjected to lateral forces behave, many in-situ pushover tests of school buildings have been completed in Taiwan by the research team at the National Center for Research on Earthquake Engineering (NCREE).

The Simplified Pushover Analysis (SPA), based on the assumption of shear buildings, is used in this study to verify the seismic capacity of Ruei-Pu elementary school by in-situ pushover tests. The results show that the analytical pushover curves agree with the in-situ pushover tests. Thus, this analysis will benefit engineers when predicting the seismic capacity of typical school buildings in Taiwan.

Keywords: simplified pushover analysis; in-situ pushover test; weak columns and strong beams

Introduction

School buildings in Taiwan are typically two or three stories high, and are classified as low-rise buildings. According to field investigation and in-situ tests after the Chi-Chi earthquake, column failure is the main factor contributing to the fact that school buildings were seriously damaged, while little damage was observed on beams. This phenomenon is called "weak-column-and-strong-beam failure mode". As RC slabs and RC beams are constructed together, the stiffness of beams becomes stronger than expected.

Based on the behavior of weak columns and strong beams, this study uses the Simplified Pushover Analysis (SPA) method, which refers to nonlinear behaviors of concrete columns to predict the seismic capacity of typical school buildings. It is reasonable to assume that typical school buildings in Taiwan can be categorized as shear buildings due to their weak-column-and-strong-beam failure mode.

To verify the feasibility of SPA, the base shear versus roof displacement curve, called seismic capacity, is calculated by the proposed method, and compared with the results obtained from an in-situ pushover test of Ruei-Pu elementary school.

[1] Researcher, National Center for Research on Earthquake Engineering, Professor, National Taiwan University, chung@ncree.narl.org.tw
[2] Emeritus Professor, Department of Civil Engineering, National Taiwan University
[3] Student, Department of Civil Engineering, National Taiwan University

Behavior and Failure Mode of Column

Before implementing the SPA, it is important to characterize the nonlinear behavior of the structure. From observing the school buildings that damaged in Chi-Chi Earthquake, the failure behavior was caused by weak columns and strong beams. Columns played the main role in resisting the earthquake. For this reason, the nonlinear behavior of school buildings is established by the nonlinear behavior of RC columns.

From previous researches, columns are categorized into three different failures conditions: flexural failure, shear failure, and flexural shear failure. The three types of failure conditions are proposed by Elwood and Moehle [1,2], and the failure condition of columns is determined by the ratio between lateral strength due to flexure and that due to shear (V_m / V_n). The lateral strength due to flexure V_m and due to shear V_n can be calculated[3], respectively, using Eqs. (1) to (4):

$$V_m = 2M_n / H \tag{1}$$

$$V_n = V_c + V_s \tag{2}$$

$$V_c = 0.53(1 + P/140A_g)\sqrt{f_c'}bd \tag{3}$$

$$V_s = A_{st} f_{yt} d(\cot\alpha)/s\ . \tag{4}$$

where, M_n is the nominal flexural strength; H is the clear height of the reinforced concrete column; V_n is the nominal shear strength; V_s is the nominal shear strength provided by shear reinforcement; V_c is the nominal shear force provided by concrete; P and A_g are the axial force and the gross area of the reinforced concrete column, respectively; f_c' is the compressive strength of concrete; b and d are the width and the effective depth of the columns, respectively; A_{st} is the area of transverse reinforcement; f_{yt} is the specified yield strength of the transverse reinforcement; s is the transverse reinforcement spacing; and α is the angle of the shear cracks as calculated using Eqs. (5)

$$\alpha = 45^\circ - \frac{1}{2}\tan^{-1}\left(\frac{\sigma}{2f_t\sqrt{(1+\sigma)/f_t}}\right) \tag{5}$$

where, $\sigma = P/A_g$; and f_t ($f_t = 1.06\sqrt{f_c'}$) is the tensile strength of the concrete. The flexure-to-shear force ratio and failure conditions of column are defined as follows:

$$\begin{cases} V_m / V_n < 0.6 & \textit{flexural failure} \\ 0.6 \le V_m / V_n \le 1.0 & \textit{flexural-shear failure} \\ V_m / V_n > 1.0 & \textit{shear failure} \end{cases}$$

In this study, the ratio between the lateral strengths due to flexure and shear of all columns are smaller than 0.6, calculated based on the data collected from in-situ pushover tests of Ruei-Pu elementary school. Therefore, the failure conditions of all columns are flexural failure, and the relationship of lateral force-displacement of columns is defined in Fig 1.

When the flexural strength of a column is developed, the displacement is Δ_y, which can be calculated using Eq. (6):

$$\Delta_y = V_m / k_c \tag{6}$$

where, k_c is lateral stiffness of the column, equal to $0.35\times(12E_cI_g/H^3)$. When the column transits from flexural to shear failure, the displacement is Δ_s which can be calculated using Eq. (7):

$$\frac{\Delta_s}{H} = \frac{3}{100} + 4\rho'' - \frac{1}{40}\frac{v_m}{\sqrt{f_c'}} - \frac{1}{40}\frac{P}{A_g f_c'} \ge \frac{1}{100} \tag{7}$$

where, ρ'' is the ratio of transverse reinforcement defined as A_{st}/bs; and v_m is the maximum nominal shear stress in MPa , defined as V_m / bd.

When the column appears to be in axial failure, the displacement is Δ_a calculated using Eq. (8):

$$\frac{\Delta_a}{H} = \frac{4}{100}\frac{1+(\tan\theta)^2}{\tan\theta + P\dfrac{s}{A_{st}f_{yt}d_c\tan\theta}}\ . \tag{8}$$

where d_c is the depth of the column core from the center line to the center line of the ties; θ ($\theta = \tan^{-1}(H/h)$) is the maximum crack angle, where h is the depth of the column, and θ is less than 65 degrees. The seismic capacity established by column behavior and their failure conditions can be performed using SPA.

Simplified Pushover Analysis

In SPA, the seismic capacity of typical school buildings in Taiwan is obtained by the following procedures:

1. The lateral force-displacement curve of all columns for each story should be established;
2. The lateral force-displacement curve of each story should be established, and the lateral force is obtained by superimposing the lateral force of all the columns in the same story by consistent displacement. It should be noted that the lateral strength of each story is not calculated by adding the maximum strength of all columns in the story directly;
3. When the building is subjected to lateral earthquake loading, the lateral force applied and distributed at each story is in the form of an inverted triangle based on the seismic code in Taiwan and can be calculated using Eq. (9):

$$F_i = \frac{(V_{bs} - F_t)W_i}{\sum_{i=0}^{n} W_j h_j} \quad (9)$$

where, V_{bs} is base shear; W_i and W_j are the weight of level i and j; and for low-rise buildings, F_t is equal to zero. The corresponding lateral force of each story can be calculated using Eq. (10):

$$V_{Fi} = \sum_{k=i+1}^{n} F_{Fk} \quad (10)$$

4. Based on Eq. (10), the corresponding story drift can be obtained. The roof displacement Δ_{RF} is the summation of each story drift Δ_i, which can be calculated using Eq. (11):

$$\Delta_{RF} = \sum_{i=1}^{n} \Delta_i \quad (11)$$

Database of Ruei-Pu Elementary School

The in-situ pushover test of Ruei-Pu elementary school is chosen to be verified by implementing the SPA method. The database of the building is as follows:

Ruei-Pu elementary school is located in Taoyuan, Taiwan. It is a 2-story RC building, with two classrooms and 17 columns in each story. The total length of the school building is 18.6m, and the total width is 10.8m as shown in Fig 2. The height of each story is 3.6m, with a total building height of 7.2m, as shown in Fig 3. Column sections of the specimen are divided into two sizes, C1 with dimension of 35cm×40cm and C2 with dimensions of 24cm×40cm, respectively. The cross section details of columns are shown in Fig 4.

The properties of the materials used are as follows: the compressive strength of concrete is 113kgf/cm^2; the yield strength of longitudinal reinforcements is 3204kgf/cm^2; and the yield strength of transverse reinforcements is 4386kgf/cm^2. These material properties are the average values of the test results.

Test Results

The test result of the school building is shown in Fig. 5. The school building is cut into two sections: one for monotonic testing and the other for cyclic testing, where the latter is used to simulate a real earthquake. The comparison of the maximum base shear shows that the maximum base shear of the cyclic loading test is 97% of that of the monotonic loading test.

Fig. 6 shows the maximum strength of 1FL and 2FL obtained by SPA.

Fig. 7 presents the comparison between results from the pushover test and analysis.

The maximum base shear from the in-situ pushover test was 117.7 tf, as the roof displacement reached 3.78cm. When the base shear was dropped to 0.8 times the maximum base shear, the roof displacement reached 10.73cm.

The maximum base shear from the SPA was 108.4 tf, as the roof displacement reached 2.80cm. When the base shear was dropped to 0.8 times the maximum base shear, the roof displacement reached 6.14cm.

The maximum analysis base shear is 7.9% less than the test one, and the displacement corresponding to the maximum base shear by analysis is 26% less than the test one. The SPA is conservative in its base shear and displacement predictions.

Conclusion

Seismic capacity obtained from the SPA by superposing the lateral force-displacement curves of all columns was verified with in-situ pushover tests of Ruei-Pu elementary school in Taiwan. The verification indicates that

1. The analysis result demonstrates conservative predictions of the base shear and displacement, where the base shear prediction is 92% of the test result, and the displacement corresponding to the maximum base shear from the analysis is 74% of the test value;
2. Most of the columns failed due to flexural failure conditions, which agree with the test results;
3. It is an effective analytical tool to obtain the seismic capacity of shear buildings.

Reference

Elwood, K.J. and Moehle, J.P., "Drift Capacity of Reinforced Concrete Columns with Light Transverse Reinforcement," Earthquake Spectra, Vol. 21, No. 1, pp. 71-89, 2005.

Elwood, K.J. and Moehle, J.P., "Axial Capacity Model for Shear-Damaged Columns," ACI Structural Journal, Vol. 102, No. 4, pp. 578-587, 2005.

ACI Committee 318, Building Code Requirements for Structural Concrete (ACI 318-05) and Commentary (ACI 318R-05). American Concrete Institute, Farmington Hills, MI, 2005.

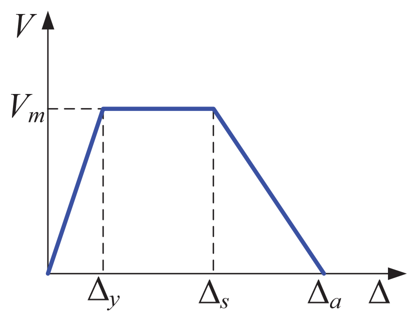

Fig. 1 Lateral Force-Displacement of Flexural Failure

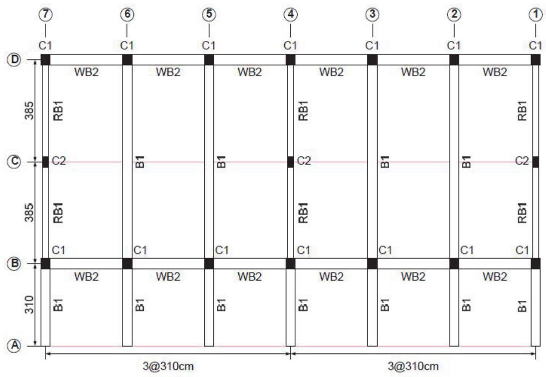

Fig. 2 Plan View of the School Building

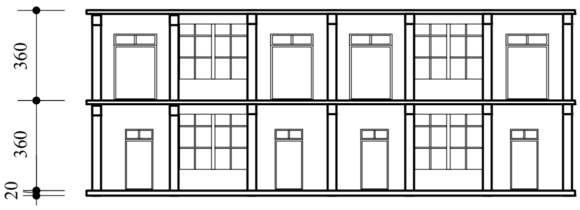

(a) the front of elevation view

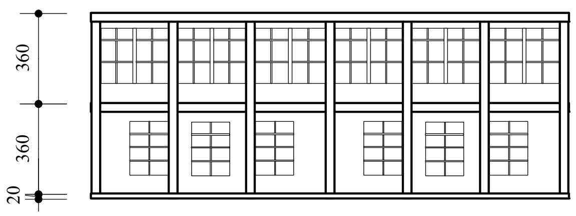

(b) the back of elevation view

Fig. 3 Front and Back Elevation View of the School Building

Serial numbers of columns	C1	C2
Cross-Section detial	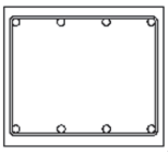	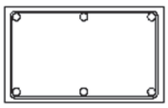
Main reinforcement	∘ 8－D19	∘ 6－D19
Transverse reinforcement	D10@25cm	D10@25cm
Size	$35cm \times 40cm$	$24cm \times 40cm$

Fig. 4 Cross Section Details of Columns

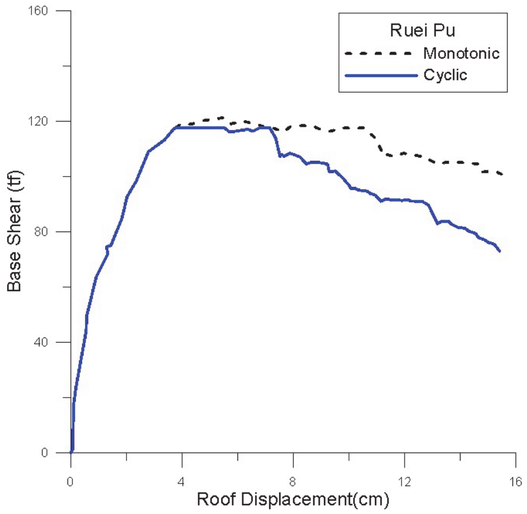

Fig. 5 Experimental Capacity Curve

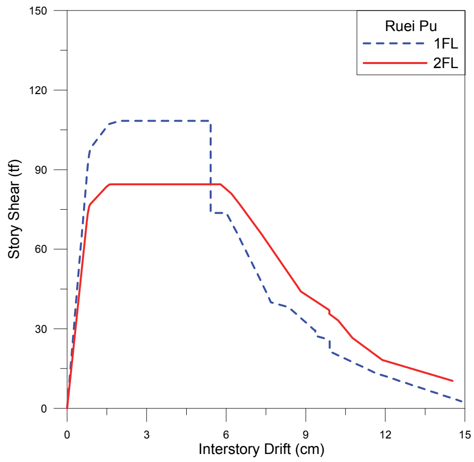

Fig. 6 Analytical Lateral Force-Displacement Curve of Each Story

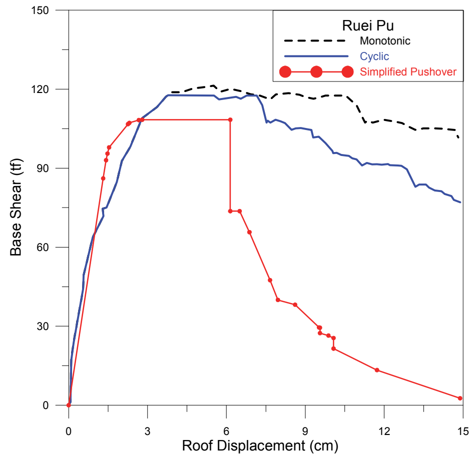

Fig. 7 Comparison between Experimental and Analytical Capacity Curves

Verification of Seismic Preliminary Evaluation of School Buildings by In Situ Tests

Lap-Loi Chung[1], Lai-Yun Wu[2], Kun-Wei Lin [3], and Yao-Sheng Yang[3]

鍾立來 [1]、吳賴雲 [2]、林琨偉 [3]、楊耀昇 [3]

Abstract

Preliminary evaluation is a screening stage for the seismic performance of existing school buildings. This method is simple, fast, objective, and effective to reduce the magnitude of a problem of seismic deficiency. From data regarding the seismic zone, the importance factor, the dimensions of the structure and its members, the seismic capacity and demand of a school building can be estimated by preliminary evaluation. The priority of a school building to enter the next stage, that of detailed evaluation, is determined according to the seismic capacity and demand ratio. However, a preliminary evaluation should be conservative enough to avoid overestimation of the performance of school buildings. Unlike in laboratory tests, the material strength, reinforcement detailing, construction quality, and foundation boundary conditions of in situ tests of a school building are realistic. In this study, the results of in situ pushover tests of Ruei-Pu Elementary School are used. From the configuration and capacity curve (the relationship between lateral force and lateral displacement) of the school building, the ultimate base shear, the weight per unit floor area, the fundamental vibration period, the allowable ductility capacity, and the fundamental seismic performance (the ratio of seismic capacity and demand) are found. Based on the results of the in situ tests of the school building, the results of the preliminary evaluation are examined. Even though the compressive strength of concrete is quite low and the thickness of the concrete cover is quite high in the specimen, the preliminary evaluation of the school building is found to still be conservative.

Keywords: school building, seismic performance, preliminary evaluation, in situ experiments

Introduction

Seismic capacity is a common problem for school buildings currently in use in Taiwan. To reduce risks to students, upgrading the seismic performance of school buildings has become a serious issue. Following the procedures of preliminary evaluation, detailed evaluation, retrofit design and construction, the seismic capacity of school buildings can be upgraded effectively and the risk to teachers and students can be reduced during an earthquake event.

Due to the importance of the safety of the school buildings, the Taiwanese government allocated a budget of $17.6 billion NTD in the economy revival plan to upgrade the seismic capacity of public elementary, junior and senior high school buildings from 2009 to 2011. Preliminary seismic evaluation was one of the procedures in the project.

According to structure types, seismic weakness, failure modes, and experimental data, the National Center for Research on Earthquake Engineering (NCREE) developed an evaluation method that is simple and objective. The main purpose of this method is to quickly determine which school buildings have a lower seismic capacity and to provide school teachers, engineers, and government officials with necessary information to decide on a plan for each school.

[1] Researcher, National Center for Research on Earthquake Engineering, Professor, National Taiwan University, chung@ncree.narl.org.tw
[2] Emeritus Professor, Department of Civil Engineering, National Taiwan University
[3] Student, Department of Civil Engineering, National Taiwan University

Database of Ruei-Pu Elementary School

Located in Taoyuan, Ruei-Pu Elementary School was established in the era of Japanese occupation. In 1979, the two school buildings were rebuilt into a two-story buildings made of reinforced concrete. Each floor consisted of four classrooms and a unilateral hallway without exterior columns.

Each specimen [1] contained two classrooms on a single floor, including three partition brick walls of 25 cm thickness. Each classroom consisted of three spans that lay along the longitudinal direction. Each floor was 3.6 m high; the total length along the corridor was 18.8 m and the transverse width was about 8 m. The specimen had seventeen columns on a single floor with two different types of sectional detailing: fourteen C1-columns with dimensions of 35 cm × 40 cm, and three C2-columns, located in the three brick walls, with dimensions of 24 cm × 40 cm. There were three types of beams: an RB1- beam with dimensions of 24 cm × 35 cm, a WB2- beam with dimensions of 40 cm × 40 cm, and a B1- beam with dimensions of 35 cm × 60 cm. The compressive strength of the concrete was 113 kgf/cm^2, and the yielding strength of the rebar and stirrup were 3204 and 4386 kgf/cm^2, respectively. A photo, structural plan, and an elevation plan are shown in Fig. 1.

The two buildings were used as specimens for a monotonic loading test and a cyclic loading test, respectively [2]. Comparing the capacity curves of the monotonic test and the cyclic loading test in Ruei-Pu Elementary School, the maximum base shear of the cyclic loading test was 97% of that of the monotonic test. After the maximum base shear was reached, the increment of roof displacement of the specimen under the cyclic loading test was half of that under the monotonic loading test. In this study, the capacity curve under a monotonic loading test was modified to simulate the cyclic one and used to verify the seismic preliminary evaluation.

Maximum Base Shear of School Building

The seismic performance of the school buildings can be evaluated from their seismic capacity to demand ratio [3]. The seismic capacity of the school buildings is computed by superimposing the shear strength of various vertical members, such as walls and columns. The seismic demand is determined from the weight and location of the school building. In order to simplify the evaluation method, fundamental assumptions, based on the characteristics of typical school buildings in Taiwan, are made. Transverse to the corridors, classrooms are typically partitioned by walls, which are continuous in the direction of gravity. However, along the corridors, there are windows and doors for entrances and provision of natural light. Because the walls are seldom continuous in the direction of gravity, damage and collapse of school buildings occurs only along the corridors.

Thus, seismic performance is evaluated along the corridor direction only. Since the demand of seismic shear force at the first story is larger than at other stories, and as school buildings are quite regular from story to story, the seismic resistance of the first story is the most critical. Therefore, the seismic vulnerability of the first story needs to be evaluated. Due to the presence of the concrete slab and the lintel above the window, the beams were strongly confined, becoming stronger and stiffer than the columns. School buildings are often founded to be damaged or collapsed due to the failure of the vertical members. Therefore, only columns and walls are taken into account in the evaluation of seismic resistance. The total base shear strength $V_{\mathrm{bs,PE}}$ from preliminary evaluation is shown below:

$$V_{\mathrm{bs,PE}} = \beta(\tau_{\mathrm{CI}} A_{\mathrm{CI}} + \tau_{\mathrm{CII}} A_{\mathrm{CII}} + \tau_{\mathrm{CIII}} A_{\mathrm{CIII}}) \quad (1)$$

where $\beta = 0.9$ is the reduction factor; and τ_{CI}, τ_{CII}, and τ_{CIII} are the ultimate strengths per unit cross sectional area of the classroom columns (at the front and back frame of the classroom), corridor columns (at the exterior side of the corridor), and partition columns (embedded in the partition wall) in the first floor, respectively. Meanwhile, A_{CI}, A_{CII}, and A_{CIII} are the total cross-sectional areas of the classroom columns, corridor columns, and partition columns in the first floor, respectively.

In Ruei-Pu Elementary School, the total cross-sectional area of the classroom columns was 19,600 cm^2 and that of the partition columns was 2,880 cm^2. The maximum base shear strength from preliminary evaluation was 140.80 tf. From the in situ test, the maximum base shear of the specimen was 117.71 tf. Therefore, the preliminary evaluation overestimates the maximum base shear strength; it is found to be 119.6% of the experimental value.

Weight of School Building

The actual weights of the roof and the second floor were calculated to be 145.27 and 168.46 tf, respectively. The total weight of the specimen was 313.73 tf. The actual weights per unit floor area on the roof and the second floor were $w_{\mathrm{RF,EX}} = 723$ and $w_{\mathrm{2F,EX}} = 839\,\mathrm{kgf/cm^2}$, respectively.

From preliminary evaluation, the total weight of school building can be estimated as:

$$W_{\mathrm{PE}} = \sum_{i=2}^{N_{\mathrm{F}}} w_{i\mathrm{F,PE}} A_{i\mathrm{F}} + w_{\mathrm{RF,PE}} A_{\mathrm{RF}} \quad (2)$$

where $A_{i\mathrm{F}}$ is the floor area on the i-th floor and $w_{i\mathrm{F,PE}}$ is the weight per unit floor area on the i-th floor. In the preliminary evaluation, the weight per unit floor area on the roof and the i-th floor are assumed to be $w_{\mathrm{RF,PE}} = 750$ and $w_{i\mathrm{F,PE}} = 900\,\mathrm{kgf/cm^2}$, respectively.

The total weight of the building estimated from the preliminary evaluation was 331.45 tf, 105.7% of the actual weight. The weight per unit floor area on the roof and the second floor estimated from preliminary evaluation were 103.7% and 107.3% of the actual values.

Fundamental Vibration Period

The first mode shape of the school building can be assumed to be $\boldsymbol{\varphi}_1 = [1 \quad 0.5]^{\mathrm{T}}$. The first modal weight $\overline{W}_1$ can be calculated as:

$$\overline{W}_1 = \boldsymbol{\varphi}_1^{\mathrm{T}} \mathbf{W} \boldsymbol{\varphi}_1 = W_{\mathrm{RF,EX}} + 0.25 W_{\mathrm{2F,EX}} \tag{3}$$

In the in situ test, the proportion of the applied lateral force on the roof and the second floor was $F_{\mathrm{RF}} : F_{\mathrm{2F}} = 1 : 0.5$. The relationship between the lateral force and the displacement can be shown as:

$$\begin{bmatrix} F_{\mathrm{RF}} \\ F_{\mathrm{2F}} \end{bmatrix} = \mathbf{K}\boldsymbol{\varphi}_1 \Delta_{\mathrm{RF}} = \mathbf{K}\begin{bmatrix} 1 \\ 0.5 \end{bmatrix} \Delta_{\mathrm{RF}} \tag{4}$$

where $\mathbf{K}$ is the stiffness matrix of the building. And Δ_{RF} is the roof displacement.

After pre-multiplying by $\boldsymbol{\varphi}_1^{\mathrm{T}}$, the above equation can be transformed to:

$$1.25 F_{\mathrm{RF}} = \overline{K}_1 \Delta_{\mathrm{RF}} \tag{5}$$

where $\overline{K}_1$ is the first modal stiffness of the structure. The base shear V_{bs} is the summation of the lateral forces on the roof and second floor:

$$V_{\mathrm{bs}} = 1.5 F_{\mathrm{RF}} = \frac{1.5 \overline{K}_1 \Delta_{\mathrm{RF}}}{1.25} \tag{6}$$

From Eqs. (3) to (6), the actual fundamental vibration period from the in situ test is:

$$T = 2\pi \sqrt{\frac{1.5(W_{\mathrm{RF}} + 0.25 W_{\mathrm{2F}})\Delta_{\mathrm{RF}}}{1.25 \mathrm{g} V_{\mathrm{bs}}}} \tag{7}$$

In the in situ test, as the base shear V_{bs} developed to 0.7 times the maximum base shear $V_{\mathrm{bs,EX,max}}$, the corresponding roof displacement was $\Delta_{\mathrm{RF}} = 1.739\,\mathrm{cm}$. The actual fundamental vibration period was $T_{\mathrm{EX}} = 0.437\,\mathrm{s}$.

Since the school building was a reinforced concrete structure without reinforced concrete walls or stiffened members, the fundamental vibration period of the building was estimated in the preliminary evaluation as:

$$T = 0.070 h_n^{3/4} \tag{8}$$

where h_n is the height of the structure. The structural period of the building was estimated in the preliminary evaluation to be $T_{\mathrm{PE}} = 0.308\,\mathrm{s}$, 70.4% of the experimental value.

Allowable Ductility Capacity

The capacity curve can be transformed to an equivalent elastic, perfectly plastic curve. The slope of the curve is determined by the secant stiffness when the base shear rises to 0.7 times the maximum base shear. When the base shear has already reached its maximum value and drops to 0.8 times the maximum base shear, the corresponding roof displacement is the ultimate displacement $\Delta_{\mathrm{RF,u}}$. The ductility capacity $R_{\mathrm{EX}} = \Delta_{\mathrm{RF,u}} / \Delta_{\mathrm{RF,y}}$ is the ratio of the equivalent ultimate roof displacement and the yielding displacement. From the in situ test results, the ductility capacity R_{EX} can be obtained as:

$$\frac{1}{R_{\mathrm{EX}}} = 1 - \sqrt{1 - \frac{2 U_{\mathrm{V\Delta}} \Delta_{\mathrm{RF,0.7Vmax}}}{0.7 V_{\mathrm{bs,EX}} \Delta_{\mathrm{RF,u}}^2}} \tag{9}$$

The school building was located at the site other than in the Taipei Basin, so the allowable ductility capacity $R_{\mathrm{a,EX}}$ was:

$$R_{\mathrm{a,EX}} = 1 + (R_{\mathrm{EX}} - 1)/1.5 \tag{10}$$

In the in situ test, as the base shear V_{bs} rose to 0.7 times the maximum base shear, the corresponding roof displacement was $\Delta_{\mathrm{RF,0.7Vmax}} = 1.739\,\mathrm{cm}$. As the base shear dropped to 0.8 times of the maximum base shear, the corresponding roof displacement was $\Delta_{\mathrm{RF,u}} = 10.728\,\mathrm{cm}$. The experimental and allowable ductility capacity are $R_{\mathrm{EX}} = 4.515$ and $R_{\mathrm{a,EX}} = 3.343$, respectively. From the preliminary evaluation, the allowable ductility capacity is assumed to be $R_{\mathrm{a,PE}} = 2.2$, 65.8% of the experimental value.

Fundamental Seismic Performance

According to the seismic design code [4], the design lateral strength can be calculated as:

$$V = \frac{S_{\mathrm{aD}} I}{1.4 \alpha_{\mathrm{y}} F_{\mathrm{u}}} W \tag{11}$$

where S_{aD} is the design spectral acceleration. I is the importance factor. W is the total weight of the building. α_{y} is the amplification factor for the first yielding in the building, and F_{u} is the reduction factor due to the structural system. After rearranging the above equation, the capacity-to-demand ratio can be expressed as below:

$$R_{\mathrm{CD}} = \frac{1.4 \alpha_{\mathrm{y}} V}{S_{\mathrm{aD}} IW / F_{\mathrm{u}}} = \frac{V_{\mathrm{bs}}}{S_{\mathrm{aD}} IW / F_{\mathrm{u}}} \tag{12}$$

In order to express this more clearly, the capacity-to-demand ratio is enlarged 100 times the fundamental seismic performance index E:

$$E = 100 R_{\mathrm{CD}} = (100) \frac{V_{\mathrm{bs}} F_{\mathrm{u}}}{S_{\mathrm{aD}} IW} \tag{13}$$

In the in situ test, the maximum base shear was $V_{\mathrm{bs}} = 117.71\,\mathrm{tf}$. The importance factor was $I = 1.25$ for a normal school building. The total weight of the specimen was $W = 313.73\,\mathrm{tf}$. The structural period of the specimen T was 0.437 s. The spectral response acceleration parameters at short period, $S_{\mathrm{S}}^{\mathrm{D}}$, and at 1-s period, S_1^{D}, were 0.6 and 0.35, respectively. The near-fault modification factors, N_{A} and N_{V}, were

1.0. The site coefficients were $F_a = 1.1$ and $F_v = 1.4$. Therefore, the design spectral response acceleration parameters at short period, S_{DS}, and at 1-s period, S_{D1}, were 0.66 and 0.49, respectively. The corner period of the design spectrum was $T_0^D = S_{D1}/S_{DS} = 0.742\,\mathrm{s}$. The design spectral response acceleration was $S_{aD,EX} = 0.66$. The allowable ductility capacity $R_{a,EX}$ was 3.343, so that the reduction factor due to the structural system F_u is 2.385. The fundamental seismic performance E can be calculated to be 108.5.

In the preliminary evaluation, the maximum base shear $V_{bs,PE}$ was 140.80 tf. The total weight of the specimen W_{PE} was 331.45 tf. The design spectral response acceleration $S_{aD,PE}$ was 0.66. The allowable ductility capacity $R_{a,PE}$ is 2.2. The reduction factor due to the structural system $F_{u,PE}$ was 1.844. The fundamental seismic performance E can be estimated to be 94.9, 87.5% of the experimental one.

Conclusion

In this paper, the results of an in situ test on Ruei-Pu Elementary School was used to verify the accuracy of the preliminary seismic evaluation. Because the actual compressive strength of concrete was less than that assumed for the preliminary evaluation and as the clear cover of column was too thick, the maximum base shear found in the preliminary evaluation was slightly larger than the experimental value. The allowable ductility capacity assumed for the preliminary evaluation was 65.8% of the calculated value. The total weight in the preliminary evaluation was 105.7% of the actual weight. As a whole, the fundamental seismic performance from the preliminary evaluation was 87.5% of that from the experiments. Therefore, the preliminary evaluation is confirmed to be conservative.

Reference

Chung LL, Wu LY, Lin KW, Yang YS, Lien KH. Verification of Seismic Preliminary Evaluation of School Buildings by In situ Tests. Journal of the Chinese Institute of Civil and Hydraulic Engineering 2012; 24(3):299- 311.(In Chinese)

Weng YT, Lin KC, Hwang SJ, Chiou TC. In situ pseudo-dynamic test and cyclic pushover test of existing school buildings. Report number NCREE 08-004, National Center for Research on Earthquake Engineering, Taiwan, 2008. (In Chinese)

Su, Keng-Li, "Preliminary Seismic Evaluation Method for Typical School Buildings in Taiwan", National Taiwan University, 2008. (in Chinese)

Construction and Planning Agency, "Seismic Design Specifications and Commentary of Buildings", Ministry of the Interior, Taiwan, 2004. (in Chinese)

(a) Photo of specimen

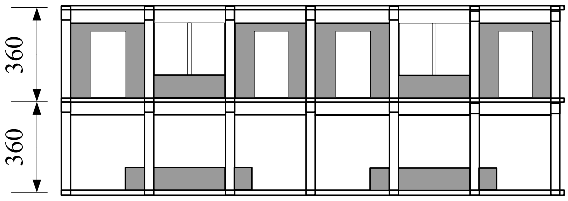

(b) Elevation plan

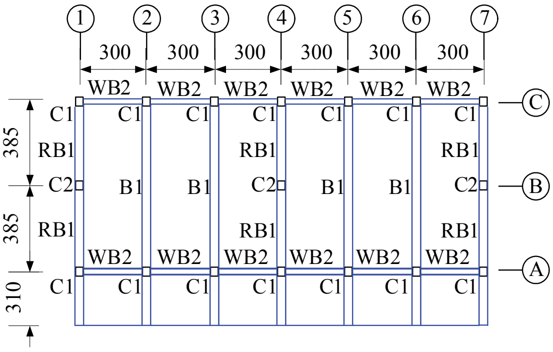

(c) Structural plan

Fig. 1 (a) Photo, (b) elevation plan and (c) structural plan of the building specimen

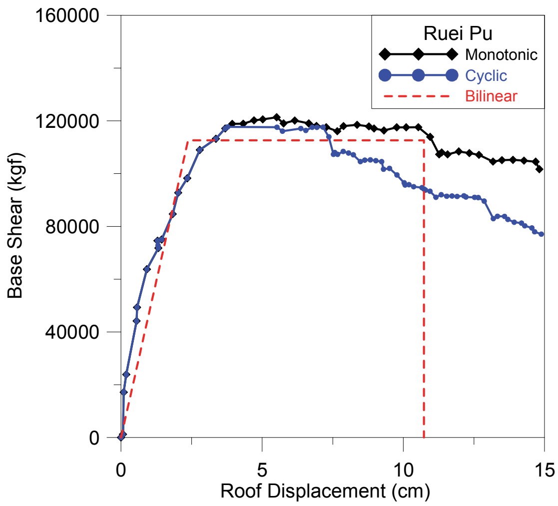

Fig. 2 Capacity curve of the building specimen

Dazhi Bridge Safety Monitoring Demonstration Project

Zheng-Kuan Lee [1]

李政寬

Abstract

Technology for the real-time monitoring of bridge safety is required by bridge management authorities and one task the National Center for Research on Earthquake Engineering (NCREE) has continually researched and developed. How to conduct real-time monitoring of long-range, multi-span bridges economically and effectively has remained the most significant challenge for related research and development. The NCREE has significantly improved the manufacturing of fiber optic sensor instruments, fiber optic welding technology, and communication capabilities in recent years, allowing the center to conduct real-time monitoring of long-range, multi-span bridges. Last September NCREE obtained approval from the Taipei City government to establish a fiber optic monitoring system on Dazhi Bridge. We hope that by using this project as an example, we can introduce a new generation of comprehensive full-bridge fiber optic monitoring technology to bridge management authorities throughout Taiwan.

Keywords: optic fiber sensors, bridge health monitoring, cable-stayed bridge, bridge elevation profile

Bridge Situation in Taiwan

Currently, approximately 28,000 bridges exist in Taiwan. These bridges are subjected to frequent earthquakes and typhoons, in addition to overloading and material fatigue. Concerns are growing regarding the durability and safety of bridges. Thus, bridge safety inspections are becoming increasingly important. Therefore, the development of an economical monitoring system is needed to monitor bridges simultaneously at all times and facilitate bridge safety inspections. This study, as an example of optic-fiber bridge monitoring system, demonstrates the integrated FBG-sensors applied on Dazhi Bridge.

Introducing Dazhi Bridge

Dazhi Bridge crosses the Keelung River, connecting to Binjiang Street in the south and Dazhi District in the north. It is an important bridge in the Zhongshan District of Taipei City. The bridge was completed and opened to traffic on June 23, 2002. Dazhi Bridge is beige with a total of 11 spans. The three spans in the north are box-shaped steel beams and the five spans in the south are pre-stressed concrete box-shaped beams. The middle three spans are fishing rod-style cable-stayed steel beams. The cable-stayed bridge section features striking red steel cables, and is considered a landmark of Taipei (Fig. 1).

Fig. 1 Dazhi Bridge landscape

Introducing the Comprehensive Full-Bridge Fiber Optic Monitoring System Developed by the NCREE

To fulfill the safety monitoring requirements for long-range, multi-span bridges, the NCREE developed a comprehensive full-bridge fiber optic monitoring system following years of research, development, and integration. The goal was to assist bridge management authorities in controlling

[1] Associate Researcher, National Center for Research on Earthquake Engineering, zklee@ncree.narl.org.tw.

the state of bridge safety at all times, which includes managing the flood levels, expansion joint distance changes, bridge elevation, the steel cable tension of the cable-stayed section, and other monitoring data directly related to safety (Fig. 2).

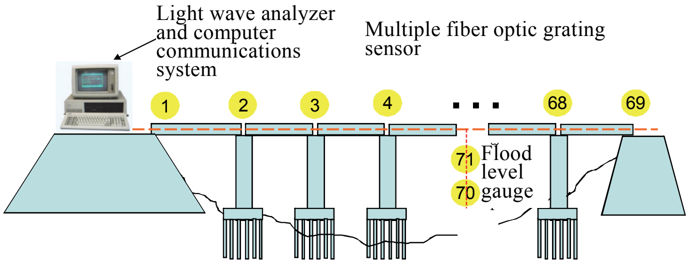

Fig. 2 Long-range, multi-span bridge safety monitoring

The comprehensive full-bridge fiber optic monitoring system can be used to monitor bridges for (1) routine bridge testing operations; (2) earthquake and post-earthquake bridge safety; and (3) flooding and post-flood bridge safety. This monitoring system can be considered specifically designed for disaster prevention and rescue management (Fig. 3).

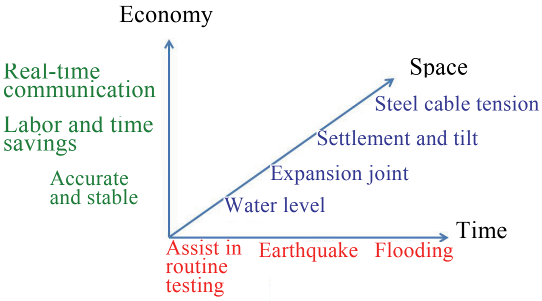

Fig. 3 Monitoring system characteristics

Table 1 Comparisons on the current commercial optical sensors and those sensors developed this study

	Current commercial product	Features of this study
Charts and comparisons	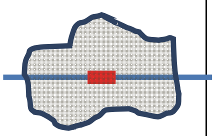	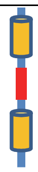
	Gratings are attached to or embedded into the bridge as a strain gauge	Prestressed-clamp FBG in the instrument components, combining physical principles to assemble the sensor
Numbers of gratings	On-site welding a single optical fiber cable with more than ten gratings is relatively difficult because of adverse circumstances	This research improves the welding techniques. One optical fiber cable possesses up to thirty gratings
Features and signal interpretation	Receiving the strain of the local structures; however, monitoring the performance of the entire bridge is difficult	The designed sensor possesses physical meanings. Numerous sensors facilitates the safety control of long bridges

Introducing Fiber Optic Settlement and Tilt Sensor Gauge

Fiber optic settlement and tilt sensor gauge can monitor bridge elevation, which is the monitoring system's most prominent characteristic. This system applies the communicating vessels principle and the buoyancy principle to monitor changes in bridge elevation (Fig. 4). According to the design dimensions, the instrument accuracy is up to 1 mm, and the high resolution is extremely beneficial for monitoring the bridge pier settlement or tilt.

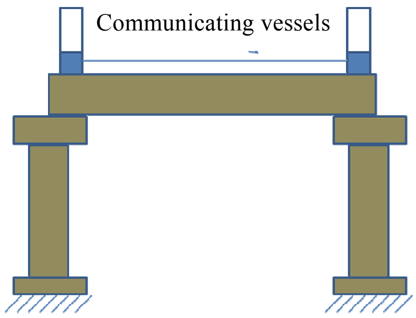

Fig. 4 Fiber optics settlement and tilt sensor gauge

Layout of the Comprehensive Full-Bridge Fiber Optic Monitoring System for Dazhi Bridge

This study installed steel-cable vibration meters, bridge Altimeter, angle gauges, expansion joint displacement meters, and flood level gauges throughout Dazhi Bridge. The instantiation and layout are shown in Table 2, Fig. 5(a) and Fig. 5(b).

Table 2 The instrument type, purpose, and quantity installed throughout Dazhi Bridge

Sensor	Purpose	Quantity
Steel cable vibration meter	Tension analysis	22
Altimeter (Fig. 5)	The girder's elevation and bridge pier settlement	7
Two-axis gauge	Bridge pier tilt	3
Displacement meter	Expansion joint displacement	10
flood level gauge	Warning flood level Action flood level	2

Displacement gauge Flood level gauge

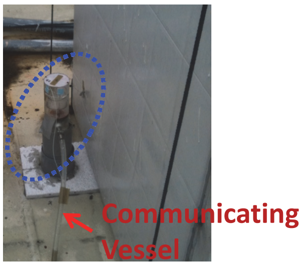

Altimeter (Subsiding and tilting) Vibration meter

Fig. 5(a) The installation of FBG sensors on Dazhi Bridge

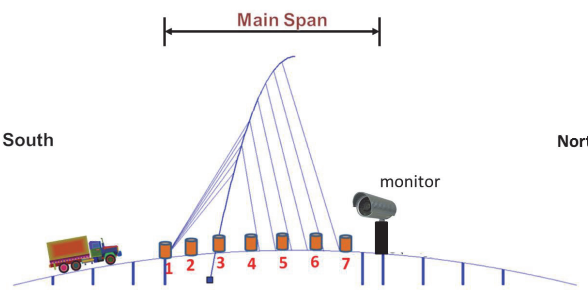

Fig. 5(b) Altimeter layout

Monitoring Data Analysis

After data transmission to the NCREE, the real-time monitoring data are immediately analyzed. The monitoring data are illustrated in Fig. 6(a). The top image is the vibration of the longest steel cable, the middle image shows the rotation of the girder in the traffic direction, and the bottom image shows the elevation profile of the girder. Dynamic messages are rendered in real time. Fig. 6(b) shows those real-time signal and image on mobile devices.

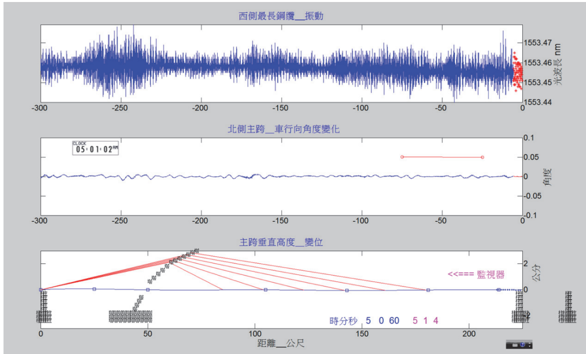

Fig. 6(a) Illustration of monitoring data: the top image shows the steel cable vibration, the middle image shows the girder's rotation, and the bottom image shows the girder's elevation

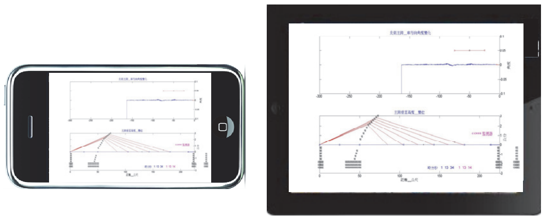

Fig. 6(b) The real-time signal and bridge elevation profile on mobile devices

Cost and Effect

The cost of this system is approximately half to one third that of conventional electronic monitoring systems. In Taiwan domestic market, currently the conventional electronic monitoring systems are imported, whereas the software and hardware of the studied system, excluding the datalog, are developed and manufactured by NCREE. In addition, the following techniques of this new system are unprecedented in Taiwan, and currently no similar product can be found domestically: automatic elevation measuring system, visualization of the dynamic deformation response for the bridge structure, synchronous measurement of the vibrations of multiple cables, and monitoring the expansion joints of long bridges with multiple spans.

Practical Application in the Future

The integrated sensing system could be applied to various transportation systems with verdict bridges, such as the high-speed railway, the highways, the Metro, the railways.

Conclusion

After many years of research, development and system integration, the NCREE can finally self-produce sensors and integrate communication systems, facilitating the achievement of long-range, multi-span bridge safety monitoring.

The Development of a Smart Sensing System for Bridge Health Monitoring

Kung-Chun Lu [1], Chin-Hsiung Loh [2] and Pei-Yang Lin[3]

盧恭君 [1]、羅俊雄 [2] 林沛暘 [3]

Abstract

Bridges are very important types of infrastructure that connect communication and transportation between cities. In recent years, torrential rain has induced damage to the structural safety of cross-river bridges; therefore, health monitoring and damage detection of bridges is of utmost importance. A pioneering step in the study of this issue is to collect and observe structural response signals under different environmental conditions. A flexible sensing solution is required to provide an effective and robust way to collect the structural response of bridges under harsh climate conditions. The objective of this paper is to develop a Smart Sensing System to provide a flexible sensing solution for bridge health monitoring. The Smart Sensing System was developed to fulfill the requirements of bridge health monitoring, which include 1) a flexible and reliable data transmission in a field environment; 2) autonomous and long-term measurement under harsh climates; 3) high sensitivity signal sampling to extract structural ambient responses; 4) on-site signal processing and analysis. The performance of the Smart Sensing System was examined during a field experiment at Niudou Bridge during the FANAPI typhoon period.

Keywords: wireless sensing, structural health monitoring, bridge monitoring

Introduction

In recent years, increasingly serious natural hazards have endangered the structural safety of bridges; therefore, bridge health monitoring has become an important issue in the mitigation of the effects of natural hazards on the transportation infrastructure as well as the protection of the lives and property of citizens. The first step in monitoring a bridge structure is to assess its dynamic behavior; a flexible long-term measurement system is required for this purpose. The application of wireless sensing technology on civil infrastructure was initially proposed by Straser and Liremidjian,1998, and several structural health monitoring (SHM) applications with wireless sensors have been developed using both scale models and full-scale structures. Moreover, Lynch et al., 2002, have extended their work to include computational microcontrollers in the hardware design of wireless sensors so that various system identification and damage detection algorithms can be embedded for local execution by the sensor. Through these pioneering studies, the concept of wireless sensing is widely accepted in the monitoring of civil infrastructure. For example, wireless sensing has been used in the monitoring of the Alamosa Canyon Bridge (New Mexico), the Geumdang Bridge (Korea), the WuYuan Bridge (China), and the Voigt Bridge (California). Recently, Hongki Jo, et al., 2012, proposed the concept of a wireless smart sensor network and Junhee Kim, et al., 2012, proposed the concept of a smart wireless sensor network, where both studies examined the production of a wireless sensor for the realistic application of SHM. The aim of this study is the development of a smart sensing system and is focused on the integration of software (SHM analysis) and hardware (long-term monitoring system).

In this study, the concept of a smart sensing system was applied to bridge health monitoring. The Sensor Node (NTU-WSU) of a smart sensing system

[1] Assistant Researcher, National Center for Research on Earthquake Engineering, kclu@ncree.narl.org.tw.

[2] Professor, National Taiwan University, lohc0221@ntu.edu.tw

[3] Researcher, National Center for Research on Earthquake Engineering, pylin@ncree.narl.org.tw

was adapted to version 0.2b in order to consider bridge monitoring and the use of a medium cost accelerometer instead of a high cost ambient velocity-meter.

The Concept of the Smart Sensing System

The Smart Sensing System (S^3) was designed for civil engineering applications. We must first define the function of the Smart Sensing System before deciding on the hardware. **Figure 1** shows the concept of the Smart Sensing System; there are three nodes in this system, the Sensor Node, the Server Node and the User Node. Based on the application scenario of automatic bridge health monitoring, the structural vibration responses of the bridge is routinely measured and buffered by the Sensor Node. In order to implement the arranged health monitoring procedure, the Sensor Node offers distributed computing functions and wireless communication to process the measured data and communicate with the Server Node. Therefore, the Sensor Node is a smart sensor that includes three major functions: signal sampling, distributed computing, and wireless communication.

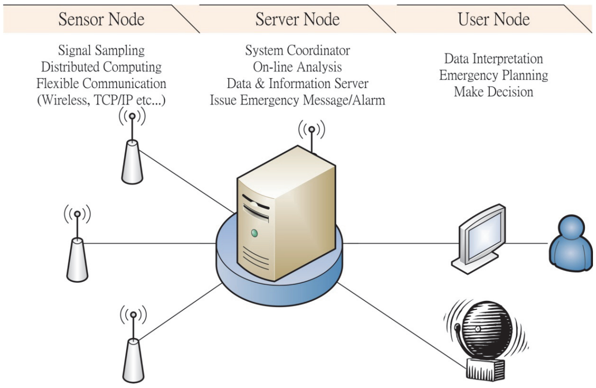

Fig. 1 The concept of the Smart Sensing System

From past experiences, bridges are considered to be large-scale structures and most of them are subjected to heavy traffic loading; these conditions make both instrumentation and maintaining a traditional wired sensing system on a bridge structure difficult. Linking the sensors to a central data logger on a large-scale structure requires lengthy signal cables that are very expensive and expend a lot of manpower on the installation and maintenance of the cables. Noise disturbance and signal attenuation effects of the lengthy signal cables are difficult to constrain; moreover, these effects cause a serious deterioration in the quality of sensor signals, especially when the measured target is a very weak signal, for example, structural ambient vibration responses. The sensor network of the Smart Sensing System adopts wireless communication technology to avoid the above deficiencies of a wired system; also, wireless communication provides an efficient and economical way to link the Sensor Node and the Server Node of the Smart Sensing System and overcome the communication limitations of large-scale bridge structures.

The system coordinator of the Smart Sensing System is a Server Node that coordinates the wireless sensor network and manages the system status and the assigned working procedure. After the Sensor Node feeds the data back to the Server Node, the arranged on-line SHM analysis is executed to calculate the monitoring results and the identified structural information on the Server Node. Two information distribution pathways are built into the Server Node: 1) Issue the emergency message or alarm, and 2) Data and Information Server. The User Node is an interface for engineers and others who are interested in the structural safety status. To provide a conventional interface for the user, the User Node is designed to be a common general-purpose electoral information machine (e.g., PC, Laptop, PDA, Smart Phone) that allows the user to easily retrieve information from the Smart Sensing System, i.e., the interface between the Smart Sensing System and the Wide Area Network must follow standard internet protocols (e.g.. TCP/IP, FTP, Webpage).

The Revised Sensor Node (WSU_V02b)

The following section focuses on the hardware improvements made to the Smart Sensing System.

Most SHM methods are based on the analysis of structural vibration responses; furthermore, many output-only system identification methods use the assumptions of the white noise process. The structural ambient responses are closest to these assumptions; its frequency contents are mainly distributed over the low frequency band (in general, it is around 0.1 ~ 30Hz), and the peak-to-peak range is generally smaller than 1gal. Therefore, the transducer of the Sensor Node must be a sensitive vibration sensor that satisfies the specifications of high sensitivity and the broad-frequency band. In order to keep costs at a minimum, this new wireless sensing unit (WSU) version was integrated with a medium cost accelerometer (AS-2000). In order to adopt the AS-2000 sensor into the ambient structural vibration measurement, a signal conditioner is required to prevent high frequency noise and the anti-aliasing effect.

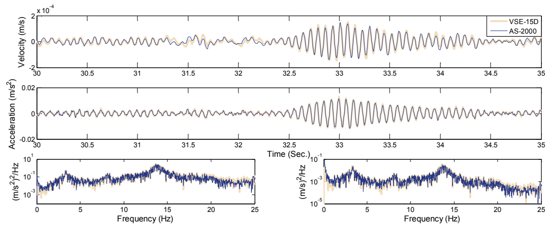

Fig. 2 A signal comparison of the VSE-15D and AS-2000

An analog low-pass filter whose filter type and implemented topology are 8^{th} order butter-worth (fc = 50Hz) and the Sallen-Key topology was integrated into the Smart Sensing System to enhance the performance of the AS-2000 sensor in the measurement of ambient structural responses. To evaluate the sensor performance, the VSE-15D and AS-2000 with a signal conditioner were collocated, and these two signals were recorded by the Sensor Node (NTU-WSU V0.2b). Figure 2 shows a comparison of these two sensors.

The main improvement in the signal sampling of version 0.2b is the oversampling process. This process achieves ADC sampling with a rarely encountered high speed (the speed is limited by the performance of the ADS8341EB and is about 100 kHz) and reduces the sample by the process of downsampling to the configured sampling rate (Fs). The oversampling process has three advantages for signal sampling: avoiding aliasing, improving resolution, and reducing noise. Version 0.2b provides 5 different sampling rates, Fs, (50, 100, 200, 500, 10k Hz) and when the oversampling function is achieved, the oversampling number D is 128 for 50Hz, 64 for 100Hz, 32 for 200Hz, 16 for 500Hz, and 1 for 10kHz. Figure 3 shows the oversampling process of the Sensor Node; the output signal of the AS-2000 accelerometer is first filtered by a low-pass filter to avoid the aliasing effect; this filtered signal is held and quantized by an analog-to-digital converter (ADC) with the sampling rate D*Fs; the microcontroller unit (MCU) processes these digitalized data using the oversampling process (averaging and down-sampling), and generates the row data.

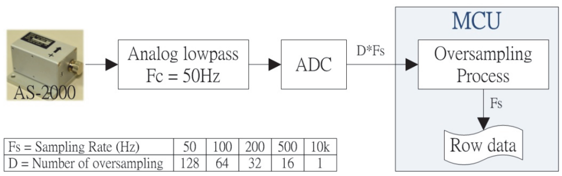

Fig. 3 Oversampling process of WSU

Considering the sensor signal sampling, the new version 0.2a provides two signal adjustment stages. The first stage is an amplifying signal with optimal gain and the second stage is a scaling and shifting signal to the sampling range of the ADC. There are four sensor input channels in the Sensor Node and all of them have the same amplification gain settings which are controlled by the general purpose input/output (GPIO) (PD6 and PD7) of the ATmega128; this does not make sense in real application scenarios where each channel should be adjusted individually to get the best signal quality. Version 0.2b is capable of this requirement. In version 0.2b, each channel is controlled by the ATmega128 with individual GPIO pins and each channel is set through the software interface of the Server Node.

Version 0.2b also places emphasis on the wireless communication performance; the data rate and the RF signal strength are improved in this version. The universal asynchronous receiver/transmitter (UART) is the interface between the microcontroller and the wireless module, and its data rate depends on the clock frequency of the MCU. The data rate capacity of the UART interface of the 9XTend module is 115.2kbps, but this capacity is constrained by the mapping error of the UART interface of the MCU and is only 57.6kbps in version 0.2a. To obtain the maximum data rate, version 0.2b adopts a 16MHz oscillator to replace the original one (8MHz) in version 0.2a. This increases the data rate of version 0.2b to 115.2kbps, twice as fast as version 0.2a and six times faster than a wireless modular monitoring system (WiMMS); this faster data rate shortens the data collection time of the Smart Sensing System considerably. Another issue is the RF signal strength; in order to obtain the highest transmission power of the 9XTend module, the power system of the Sensor Node was revised and is shown in Figure 4.

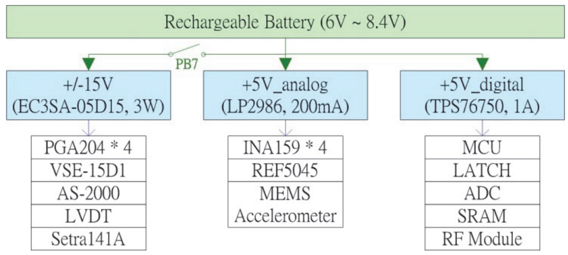

Fig. 4 The power system of the Sensor Node

The revised power system of the Sensor Node is divided into three power circuits, +5V for the analog device, +5V for the digital device, and +/-15V for the sensing interface, to prevent the noise effect which is produced by the current sink. The 5V digital power source was designed according to the requirements of the 9XTend module, and a 1-A low-dropout voltage regulator, TPS76750, was adopted in this power circuit. The main feature of TPS76750 is its ultralow typical quiescent current (85μA) which improves the power efficiency of the Sensor Node and also allows the 9XTend achieve the highest transmission power. To reduce the power consumption of the sensors, the sensor power of Version 0.2b is switched by the GPIO (PB7) of the MCU, and the Sensor Node turns the sensor off when a sensor signal is not requested; this mechanism extends the battery life of the Sensor Node substantially.

Field Experiment at Niudou Bridge

Niudou Bridge crosses the Lanyang River and is located in Sanxing Township, Yilan County, Taiwan. Niudou Bridge is a dangerous bridge with serious foundation soil scouring. The bridge is a simple supported bridge with 7 spans and 6 piers; the length of the deck in each span is 36.5m and the total length of this bridge is 256m; the width of this bridge is 5m.

FANAPI was a medium-strength typhoon; its center made landfall in the Hualien area and its storm hit Taiwan between the 19^{th} and the 21^{st} of

September 2010. The typhoon's outer bands gave rise to extremely heavy rain in the east and southeast of Taiwan, and the Lanyan River became swollen as a result.

Fig. 5 Photos of the Smart Sensing System on Niudou Bridge

The objective of this field experiment was to collect the structural responses of the Niudou Bridge under serious flood loading to obtain the foundation soil scouring and the flood loading induced structural vibration characteristics. There were a total of 5 NTU-WSU units installed on the 2nd to 6th deck of the Niudou Bridge and a local site (Host Node) was installed on this bridge. Each NTU-WSU was connected to two ambient sensors that measured the vertical and transverse vibrations at the center point of the deck, and a total of 10 ambient sensors were installed on this bridge. The site of the Niudou Bridge has 3G Mobile Internet (Chunghwa Telecom) signal coverage, with a signal strength of about 30%. The position of the user node was not limited; in this experiment, the user node was a laptop installed in a hotel at Niudou.

This system was installed before the land warning of FANAPI, and continuously collected the structural responses of the Niudou Bridge during the typhoon period. The system was set to collect data every 15 minutes and each record had 15000pts (@ 200Hz) of structural responses. The data was saved as a MS EXCEL file and labeled with the current time and date. A remote user could observe the system status and the recorded data over the internet from a safe place during this typhoon period.

Figure 5 shows photos of the Smart Sensing System on the Niudou Bridge; Figure 5(a) shows the Sensing Node installed on the deck of the Niudou Bridge, (b) shows the Server Node, and (c) shows the contents of the Sensing Node, which includes a NTU-WSU, two VSE-15D sensors, and a Li battery (which supplied over 3 days of power with full loading of the Sensing Node); an acrylic housing with an aluminum plate was used to protect the Sensing Node and was mounted on the bridge deck. Figure 5(d) shows the serious flood acting on the foundations of the Niudou Bridge.

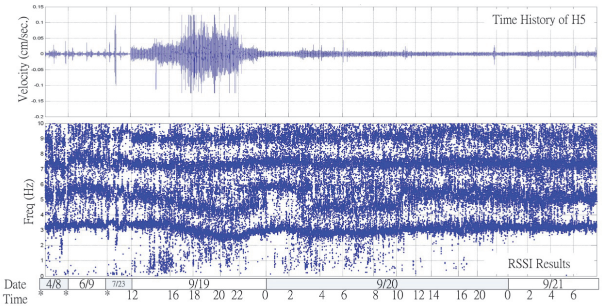

Fig. 6 The time history of H5 and the analysis results of RSSI

The structural responses of the Niudou Bridge were collected during the FANAPI typhoon event with the reference database established before this event. Based on the data, Figure 6 shows the rough results of the RSSI analysis which was performed by Dr. J. H. Weng who also worked on this project. In this figure, the response data includes 4/8, 6/9, 7/23, and the period during typhoon FANAPI. The RSSI results show that the frequencies of the Niudou Bridge changed during the typhoon period.

Conclusions

The new version of the Sensor Node, NTU-WSU V0.2b, provides: 1) a more flexible adjustment range of the sensor signal; 2) high quality and accurate signal sampling through the oversampling process; 3) high speed data rates for wireless communication, twice as fast as Version 0.2a; 4) more reliable wireless communication and a larger RF transmission range through the enhanced power design of the Sensor Node; 5) a low cost measuring solution of ambient structural responses through the extended compatibility of the medium cost accelerometer, AS-2000. Through this study, the concept of the Smart Sensing System was extended to cover the application of bridge health monitoring. Such a flexible monitoring system is a good solution for bridge structures. The experiment at the Niudou Bridge during the FANAPI typhoon period demonstrates that the Smart Sensing System is fit for field experiments in harsh climate conditions. The modifications of the system design (software and hardware) of the Smart Sensing System were shown to be successful during this experiment. The system setup on the Niudou Bridge only took about 30 minutes, and the robustness of the system allowed for its continuous function during the FANAPI period, which was approximately three days.

References

Kung-Chun Lu, Chin-Hsiung Loh, "Development of Wireless Sensing System for Structural Health Monitoring", Earth&Space 2010, 12th International Conference on Engineering, Science, Construction, and Operations in Challenging Environments, Honolulu, Hawaii, March 14-17.

Phase Controlled Semi-active Tuned Mass Dampers for Vibration Reduction under Base Excitation

Lap-Loi Chung[1], Yong-An Lai[2], Ting-Yu Ku[2], Lai-Yun Wu[3]

鍾立來 [1]、賴勇安 [2]、顧丁與 [2]、吳賴雲 [3]

Abstract

The vibration suppression effect of phase controlled semi-active tuned mass dampers (SATMD) under base excitation is proposed in this study. The phase control algorithm applies the variable friction force to slow down the mass block at specific moments when the phase lag of the SATMD with respect to the structure is off the optimal 90 degrees, returning the SATMD back to the desired phase lag, i.e., a -90 degree phase deviation, so that the SATMD has maximum power flow to reduce the structural vibration. A single-degree-of-freedom structure with phase controlled SATMD is simulated to be subjected to sinusoidal base acceleration, random base acceleration, and earthquakes. Under the sinusoidal base acceleration, the results show that the SATMD has a broader range of excitation frequency in reducing structural vibration than the optimal passive tuned mass damper. The SATMD also has better robustness of its design parameters especially the frequency ratio under random base accelerations. The earthquake excitation shows that although the SATMD is not very effective in reducing the peak value of structural response but it is still able to reduce root-mean-square responses.

Keywords: tuned mass damper, phase control, semi-active control, base excitation

Introduction

According to the power flow theory (Soong, and Dargush, 1997), tuned mass dampers (TMD) have the best performance in suppressing the vibration when the TMD has a 90° phase lag (or -90° phase deviation) to the structure. Therefore, attempts have been made to control the phase of TMD (Chung, et al., 2012). To induce the TMD mass block movement to have a 90° phase lag to the structure, a variable friction force is applied to slow down the TMD mass block velocity. The effectiveness of the proposed control algorithm is observed.

In this paper, the device for a semi-active tuned mass damper (SATMD) is assumed to be a variable friction device with a variable normal force to slow down the mass block velocity. This semi-active friction device acts like a brake mechanism to create friction force to adjust the phase lag. A single-degreed-of-freedom (SDOF) structure with SATMD phase control is simulated to be subject to sinusoidal base accelerations, random base accelerations, and earthquakes. Under the sinusoidal base acceleration, the results show that the SATMD has broader range of excitation frequencies to reduce the structural vibration than the optimal passive tuned mass damper. The SATMD is also found to have better robustness in its design parameters especially in the frequency ratio under random base accelerations. The earthquake excitation shows that although the SATMD is less effective in reducing the peak value of the structural response, it is still able to reduce the root-mean-square responses.

Motion Equation

As a SATMD is attached to a SDOF structure, as shown in Fig. 1, it becomes a 2DOF system. The equation of motion of the system can be expressed as:

[1] Researcher, National Center for Research on Earthquake Engineering,
Professor, National Taiwan University, chung@ncree.narl.org.tw
[2] Student, Department of Civil Engineering, National Taiwan University
[3] Emeritus Professor, Department of Civil Engineering, National Taiwan University

$$\mathbf{M}\ddot{\mathbf{x}}(t)+\mathbf{C}\dot{\mathbf{x}}(t)+\mathbf{K}\mathbf{x}(t)=\mathbf{b}u(t)+\mathbf{e}w(t) \quad (1)$$

where $\mathbf{M}=\begin{bmatrix} m_d & 0 \\ 0 & m_s \end{bmatrix}$ is the mass matrix of the system, m_d is the TMD mass, m_s is the SDOF structural mass; $\mathbf{C}=\begin{bmatrix} c_d & -c_d \\ -c_d & c_d+c_s \end{bmatrix}$ is the damping matrix of the system, c_d is the TMD damping coefficient, c_s is the SDOF structural damping coefficient; $\mathbf{K}=\begin{bmatrix} k_d & -k_d \\ -k_d & k_d+k_s \end{bmatrix}$ is the stiffness matrix of the system, k_d is the TMD stiffness and k_s is the SDOF structural stiffness; $\mathbf{x}(t)=\begin{bmatrix} x_d(t) \\ x_s(t) \end{bmatrix}$ is the displacement vector of the system, $x_d(t)$ and $x_s(t)$ are, respectively, the TMD displacement and the SDOF structural displacement; $u(t)$ is the semi-active friction force; $\mathbf{b}=\begin{bmatrix} 1 \\ -1 \end{bmatrix}$ is the friction force location vector; $w(t)$ is base acceleration; $\mathbf{e}=\begin{bmatrix} -m_d \\ -m_s \end{bmatrix}$ is the base excitation location vector.

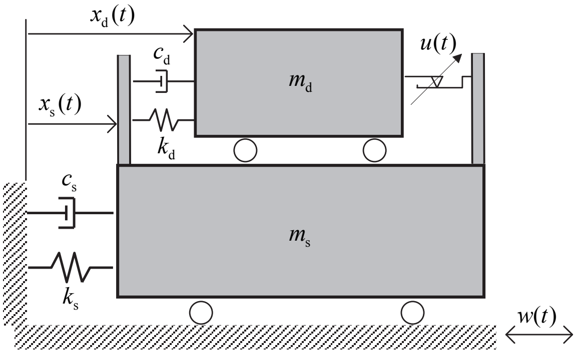

Fig. 1 Model of SDOF structure with the attached SATMD

The motion equation can be expressed as state-space form:

$$\dot{\mathbf{z}}(t)=\mathbf{A}\mathbf{z}(t)+\mathbf{B}u(t)+\mathbf{E}w(t) \quad (2)$$

where $\mathbf{z}(t)=\begin{bmatrix} \mathbf{x}(t) \\ \dot{\mathbf{x}}(t) \end{bmatrix}$ is the state vector; $\mathbf{A}=\begin{bmatrix} \mathbf{0} & \mathbf{I} \\ -\mathbf{M}^{-1}\mathbf{K} & -\mathbf{M}^{-1}\mathbf{C} \end{bmatrix}$ is the system matrix; $\mathbf{B}=\begin{bmatrix} \mathbf{0} \\ \mathbf{M}^{-1}\mathbf{b} \end{bmatrix}$ is the state-space friction force location vector; $\mathbf{E}=\begin{bmatrix} \mathbf{0} \\ \mathbf{M}^{-1}\mathbf{e} \end{bmatrix}$ is the state-space wind force location vector.

It can be assumed that the semi-active friction force, $u(t)$, and the base acceleration, $w(t)$, in a single sampling period, Δt, both are piecewise constants. The discrete-time state-space equation can be expressed as:

$$\mathbf{z}[k+1]=\mathbf{A}_d\mathbf{z}[k]+\mathbf{B}_d u[k]+\mathbf{E}_d w[k] \quad (3)$$

where $\mathbf{A}_d=e^{\mathbf{A}\Delta t}$ is the discrete-time system matrix; $\mathbf{B}_d=\mathbf{A}^{-1}(\mathbf{A}_d-\mathbf{I})\mathbf{B}$ is the discrete-time friction force location vector; $\mathbf{E}_d=\mathbf{A}^{-1}(\mathbf{A}_d-\mathbf{I})\mathbf{E}$ is the discrete-time base excitation location vector.

Phase Control Algorithm

When the external force resonates with the structure, the TMD has the best performance at a 90° phase lag to the structure. For this case, the flowing characteristic is observed: when the displacement of the structure is 0, the relative displacement (stroke) of the TMD is at a maximum (the relative velocity of the TMD is 0). Once the external force stops resonating with the structure, the TMD loses its efficacy. In this case, the phase deviation of the TMD to the structure is no longer at -90°. When the frequency of the external sinusoidal force is lower than the natural frequency of the structure, the phase deviation is between -0° and -90° (phase leading). When the frequency of the external force is higher than the natural frequency of structure, the phase deviation is between -90° and -180° (phase lagging). Therefore, the control strategy for the SATMD to bring the mass block back to a 90° phase lag for the cases of "phase leading" and "phase lagging" is proposed as follows:

1. The responses of the TMD relative displacement and structural displacement when the external frequency is 0.95 times of the structural frequency are shown in Fig. 2 (a). At specific moments (A) and (B) in Fig. 2 (a), the TMD relative displacement is at a maximum (the TMD relative velocity is 0) and the structural displacement is still decreasing but not at 0. At these moments, the phase of the TMD to the structure is between -0° and -90° (phase leading), not simply a 90° phase lag. Therefore, a friction force is applied to stop the TMD motion at these moments in order to keep the TMD relative velocity at 0 until the structural displacement is 0. Thus, the TMD will return to a 90° phase lag to the structure.

2. The responses of the TMD relative displacement and structural displacement when the external frequency is 1.05 times of the structural frequency are shown in Fig. 2 (b). At specific moments (C) and (D) in Fig. 2 (b), the structural displacement is 0 but the TMD's relative displacement is still increasing (the TMD relative velocity is decreasing, but not 0). The phase of the TMD to the structure is between -90° and -180° (phase lagging). Thus, the friction force is applied to stop the TMD motion at these moments in order to decrease the TMD relative velocity to 0. Therefore, the TMD will head back towards the 90° phase lag to the structure.

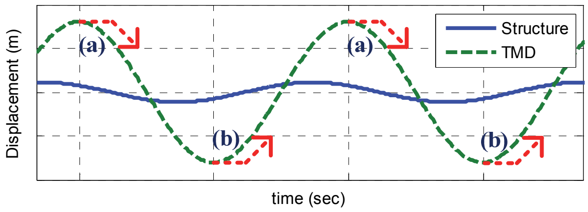

(a) Phase leading

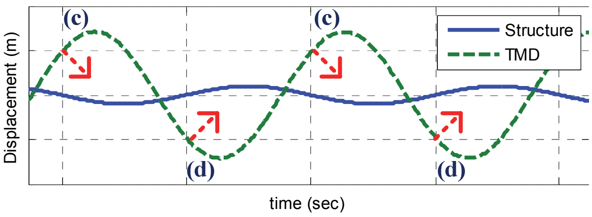

(b) Phase lagging

Fig. 2 TMD relative displacement (stroke) and structural displacement time history

Therefore, no matter whether the TMD is "phase leading" or "phase lagging", it is found that a friction force can be applied to slow down the TMD relative velocity to 0 at specific moments: "the signs of structural displacement and the TMD relative velocity are opposite, and the signs of the structural velocity and the TMD relative displacement are also opposite". To determine this, the sign convention, G is introduced as:

$$G = \frac{1}{2}\{1-\mathrm{sgn}(\dot{x}_s[k+1])\times \mathrm{sgn}(x_d[k+1]-x_s[k+1])\}\times \frac{1}{2}\{1-\mathrm{sgn}(x_s[k+1])\times \mathrm{sgn}(\dot{x}_d[k+1]-\dot{x}_s[k+1])\} \tag{4}$$

When $G=1$, the control force is applied to stop the TMD movement ($u[k]\neq 0$). When $G=0$, no control force is applied ($u[k]=0$).

To determine whether the friction force is to be applied at the current step k, the states of the next step $\hat{\mathbf{z}}[k+1]$ are estimated by neglecting the external disturbances to be:

$$\hat{\mathbf{z}}[k+1] = \mathbf{A}_d \mathbf{z}[k] \tag{5}$$

By eq. (5), the estimated structural displacement $x_s[k+1]$, TMD relative velocity $\dot{x}_d[k+1]-\dot{x}_s[k+1]$, structural velocity $\dot{x}_s[k+1]$ and TMD relative displacement $x_d[k+1]-x_s[k+1]$ can be calculated. Then the control opportunity can be determined by eq. (4).

Next, the friction force $u[k]$ can be calculated by assuming the next step (k+1-th step) in the TMD relative velocity to be 0:

$$\mathbf{d}_1 \mathbf{z}[k+1] = 0 \tag{6}$$

where $\mathbf{d}_1 = [0 \quad 0 \quad 1 \quad -1]$ is the TMD relative velocity location vector.

Substituting eq. (3) into eq. (6), the friction force $\hat{u}[k]$ is estimated by neglecting the external disturbances term to be:

$$\hat{u}[k] = -(\mathbf{d}_1\mathbf{B}_d)^{-1}\mathbf{d}_1(\mathbf{A}_d\mathbf{z}[k]) \tag{7}$$

The semi-active device output power may not achieve the estimated friction force. For this reason, the actual outputs of the semi-active friction force have to be limited by the maximum output u_{max}:

$$u[k] = \frac{1}{2}\hat{u}[k]\times\left[1+\mathrm{sgn}(u_{max}-|\hat{u}[k]|)\right] + \frac{1}{2}\mathrm{sgn}(\hat{u}[k])u_{max}\times\left[1+\mathrm{sgn}(|\hat{u}[k]|-u_{max})\right] \tag{8}$$

Therefore, the control strategy is as follows: once measuring the states at the current step, by eq. (5) to estimate one step states, by eq. (4) to judge whether the friction force is applied or not, then by eq. (6) to eq. (8) to calculate and apply the friction force.

Numerical Verification

A SDOF structure with structural frequency 0.33 Hz and structural damping ratio 0.02 is installed with a SATMD and subjected to sinusoidal base acceleration, random base acceleration, and earthquakes, respectively. In order to show the effect of SATMD, a linear optimal passive tuned mass damper (PTMD) is also simulated for comparison. The PTMD and SATMD design parameters are show in Table 1.

Table 1 PTMD and SATMD design parameters

PTMD mass ratio	0.02
PTMD frequency ratio	0.9678
PTMD damping ratio	0.0702
SATMD mass ratio	0.02
SATMD frequency ratio	1
SATMD damping ratio	0.01

Sinusoidal Base Acceleration Excitation

A SDOF structure is subjected to sinusoidal base accelerations to plot the frequency response functions. The sinusoidal base accelerations frequency range is assigned to be 0.8 to 1.2 times of the structural frequency. Fig. 3 shows the structural displacement and absolute acceleration frequency response functions. The frequency response of the SATMD is always smaller than the optimal PTMD and the peak of frequency response of the SATMD is almost only half of the optimal PTMD. Like MTMDs (Multiple Tuned Mass Dampers), the effective range of SATMD is broadened to 0.88 to 1.15 times of the structural frequency.

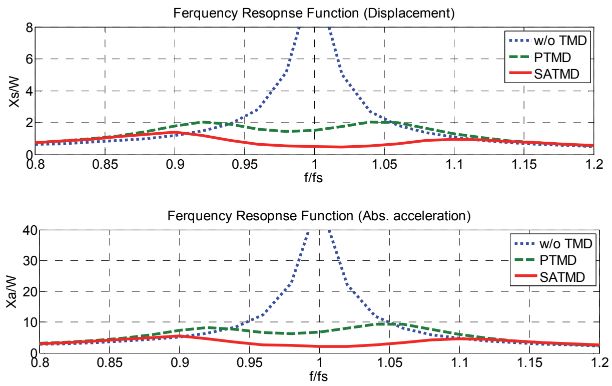

Fig. 3 Frequency response functions of the structural displacement and absolute acceleration

Random Base Acceleration Excitation

The SDOF structure is subjected to random base accelerations to study the design parameter sensitivity. As Fig. 4 shows, the SATMD is less sensitive to the frequency ratio. The off-tuned effect can be minimized. The SATMD friction device can fully replace the damping device in its energy dissipation function. The defect can be overcome if the design damping is less than optimal.

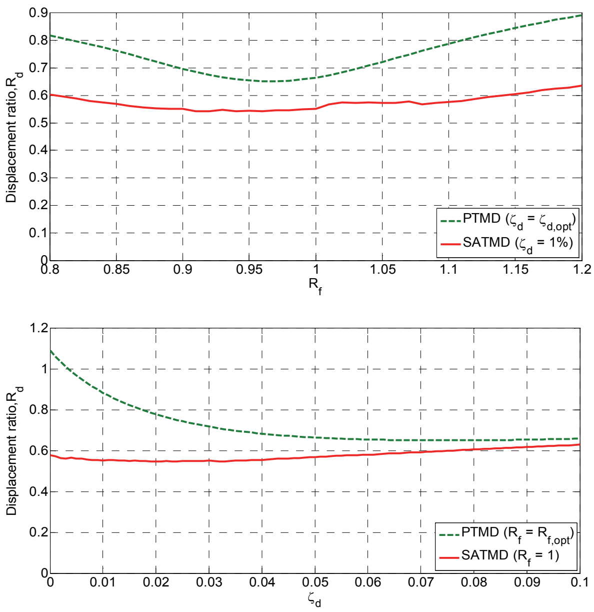

Fig. 4 Sensitivity analysis of frequency ratio and damping ratio

El Centro Earthquake Excitation

The responses under El Centro earthquake excitation are shown in Fig. 5. Without the use of the TMD, the peak values of the structural displacement and absolute acceleration are 0.3854 m and 1.6923 m/s^2 respectively. The root mean square of the structural displacement and absolute acceleration are 0.1759 m and 0.7723 m/s^2. After installing the PTMD, the peak value of the structural displacement and absolute acceleration are 0.2674 m and 1.1660 m/s^2. The root mean square of the structural displacement and absolute acceleration are 0.1013 m and 0.4556 m/s^2. After installing the SATMD, the peak value of the structural displacement and absolute acceleration are 0.2644 m and 1.1522 m/s^2. The root mean square of the structural displacement and absolute acceleration are 0.0874 m and 0.3935 m/s^2. The SATMD therefore, seems to be less effective in reducing the peak value of the structural responses but is able to reduce the root-mean-square responses.

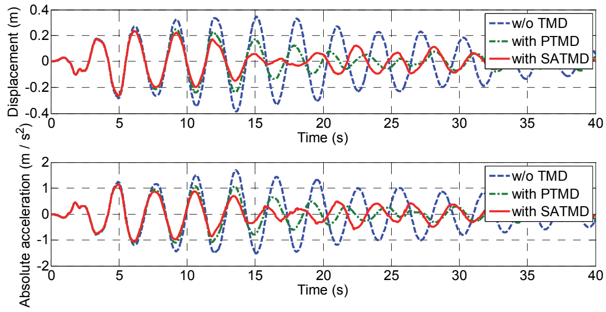

Fig. 5 Time histories of the structural displacement and absolute acceleration under El Centro earthquake

Conclusion

In this paper, the phase control for semi-active tuned mass dampers (SATMD) is presented under base excitation. According to the results of the numerical simulations, the phase controlled SATMD have good performance and the conclusions that are drawn are as follows:

1. The frequency response functions of the SATMD with phase control are smaller than optimal PTMDs and the peak of frequency response functions of the SATMD are only half of that of optimal PTMDs. The effective frequency range of SATMD can be broadened under a phase control like the MTMD.

2. According to the sensitivity study under random base acceleration excitation, SATMD with phase control can improve the weakness of PTMDs in their sensitivity to the frequency ratio. Thus, the off-tuning effect can be minimized.

3. The El Centro earthquake simulation results show that the SATMD is less effective in reducing the peak value of structural responses but is able to reduce root-mean-square responses.

Reference

Soong, T.T. and Dargush, G.F., Passive Energy Dissipation Systems in Structural Engineering. Wiley, New York, 1997.

Chung, L.L., Ku, T.Y., Lai, Y.A. and Wu, L.Y., Application of Optimal Passive and Phase-Control Semi-active Tuned Mass Dampers for Vibration Reduction under Base Excitation. NCREE-12-004, 2012.

Shaking Table Tests on Sloped Rolling-Type Isolation Devices

Shiang-Jung Wang[1], Chia-Yi Shiau[2], Wang-Chuen Lin[3], Jenn-Shin Hwang[4] and Kuo-Chun Chang[5]

汪向榮[1]、蕭佳益[2]、林旺春[3]、黃震興[4]、張國鎮[5]

Abstract

Seismic simulation tests on sloped rolling-type isolation devices with different design parameters such as sloping angles and supplemental sliding friction capabilities, together with a isolated raised floor system were conducted in this study. Not only is the efficiency of the isolation devices in seismically protecting the objects studied, but also a validation of the derived theory in predicting the seismic responses of the isolation devices is experimentally investigated. From the study, it is evident that the sloped rolling-type isolation device has excellent potential for the mitigation of seismic risks posed to critical equipment and facilities.

Keywords: Seismic isolation, Sloped rolling-type isolation device, Isolated raised floor, Twin-flag mathematical model, Shake table test, Numerical verification

Introduction

Based on the derived theory for sloped rolling-type isolation devices (Wang et al., 2012; 2013), a simplified twin-flag mathematical model to represent the hysteretic characteristics of the isolation bearing has been developed. In the isolation device, both surfaces of the intermediate bearing plate are V-shaped sloping while the upper and lower bearing plates have either V-shaped sloping surfaces (Type A isolation device) or flat surfaces (Type B isolation device) in contact with cylindrical rollers, as shown in Figure 1. A total of four equations of motion were derived for Type A and Type B isolation devices along the horizontal direction. For Type A isolation devices, when the roller is moving within the fixed curvature range, the equation of motion is given by:

$$\begin{aligned} &M\ddot{x}_1 + \frac{1}{2R}M\left(g+\ddot{z}_g\right)\mathrm{sgn}(x_1)x_1 \\ &+\left(\mu_r N + F_D\right)\mathrm{sgn}(\dot{x}_1) = -M\ddot{x}_g \end{aligned} \tag{1}$$

When the roller is moving away from the fixed curvature range, it is written as:

$$\begin{aligned} &M\ddot{x}_1 + \frac{1}{2}M\left(g+\ddot{z}_g\right)\sin 2\theta\,\mathrm{sgn}(x_1) \\ &+\left(\mu_r N + F_D\right)\cos\theta\,\mathrm{sgn}(\dot{x}_1) = -M\ddot{x}_g \end{aligned} \tag{2}$$

For Type B isolation devices, when the roller is moving within the fixed curvature range, it is given by:

$$\begin{aligned} &M\ddot{x}_1 + \frac{1}{4R}M\left(g+\ddot{z}_g\right)\mathrm{sgn}(x_1)x_1 \\ &+\left(\mu_r N + F_D\right)\mathrm{sgn}(\dot{x}_1) = -M\ddot{x}_g \end{aligned} \tag{3}$$

When the roller is moving away from the fixed curvature range, it is written as:

$$\begin{aligned} &M\ddot{x}_1 + \frac{1}{2}M\left(g+\ddot{z}_g\right)\sin\theta\,\mathrm{sgn}(x_1) \\ &+\left(\mu_r N + F_D\right)\cos\theta\,\mathrm{sgn}(\dot{x}_1) = -M\ddot{x}_g \end{aligned} \tag{4}$$

where $\ddot{x}_g$ and $\ddot{z}_g$ are the horizontal and vertical acceleration excitations, respectively; x_1, $\dot{x}_1$ and $\ddot{x}_1$ are the horizontal relative displacement, velocity and acceleration responses of the protected object,

[1] Associate Researcher, National Center for Research on Earthquake Engineering, sjwang@ncree.narl.org.tw
[2] Assistant Researcher, National Center for Research on Earthquake Engineering, cyshiau@ncree.narl.org.tw
[3] Assistant Researcher, National Center for Research on Earthquake Engineering, wclin@ncree.narl.org.tw
[4] Deputy Director General, National Center for Research on Earthquake Engineering, jshwang@ncree.narl.org.tw
[5] Director General, National Center for Research on Earthquake Engineering, kcchang@ncree.narl.org.tw

respectively; g is the acceleration due to gravity; M is the total seismic reactive mass of the protected object together with the device components; μ_r is the ratio of the rolling resistant coefficient (δ) to the roller radius (r) (Shames, 1996); N is the normal force acting between the bearing plate and the roller, which can be approximated as Mg; F_D is the sliding friction force acting parallel to the slope of the bearing plate; R is the curvature radius in the range between two inclines of the V-shaped surface of the bearing plate; and θ is the sloping angle of the V-shaped surface of the bearing plate.

In this study, Type A and Type B isolation devices with multi-rollers (Chang et al., 2011) and an isolated raised floor system were tested using a shaking table. In addition to experimentally investigating the dynamic behavior of the isolation devices with different design parameters, the efficiency of the isolation devices in their seismic protection of the equipment and the validity of the proposed simplified hysteretic model in predicting the seismic responses of the isolation devices are demonstrated.

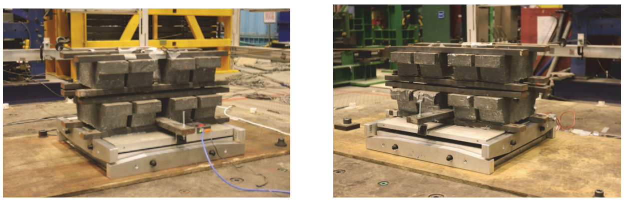

(a) Type A (b) Type B

Fig. 1 The sloped multi-roller isolation devices (Test Scheme I)

Seismic Simulation Test

The upper, intermediate and lower bearing plates of the tested sloped multi-roller isolation devices, as shown in Figure 1, are made of aluminum with heat treatment. The bearings have a plan dimension of 600*mm* by 600*mm*. The cylindrical rollers are made of stainless steel and have a sectional radius (r) of 17.5*mm* and a longitudinal length of 600*mm*. The maximum allowable displacement of the isolation devices is designed to be 250*mm*. An arc length of 19*mm* (±9.5*mm*) with a curvature radius (R) of 100*mm* is provided at the intersection of the two inclines of the V-shaped surfaces of the bearing plates to prevent undesired instant pounding as the rollers pass through the sharp angles of the V-shaped surfaces.

The supplemental friction damping mechanism is composed of a vulcanized rubber pad with a thickness of 2*mm* attached to the surfaces of the upper, intermediate and lower bearing plates sliding against the stainless steel surface of the side plate. The tested dynamic friction coefficient varies approximately between 0.2 and 0.25. The friction mechanism can be renewed effortlessly if needed by replacing the rubber pad. The required normal force for the supplemental sliding friction is provided by the compression of linear spring modules installed in the side plates.

A total of two test schemes were conducted in this study. In Test Scheme I, four sloped multi-roller isolation devices including Type A and Type B bearings, respectively denoted as Bearings A-1, A-2, B-1 and B-2 hereafter and detailed in Table 1, are designed to investigate the effects of the design parameters on the seismic performance of the isolation devices. The difference between Bearings A-1 and A-2 as well as Bearings B-1 and B-2 is that supplemental friction damping mechanism is provided in Bearings A-2 and B-2. In Bearings A-2 and B-2, two sets of linear spring modules with a constant compression length of 6*mm* are installed in each side plate so that the normal force for sliding friction applied to each side plate is about 332.52*N*. The to-be-protected equipment above the isolation devices is simulated by lead blocks with a total seismic reactive mass of 500 $N-sec^2/m$. The setup is shown in Figure 1.

Table 1 Design parameters of different sloped multi-roller isolation devices

Bearing No.	Design parameter		
	Sloping angle of V-shaped surface		Sliding friction
	Upper and lower bearing plates	Intermediate bearing plate	
A-1	6.25 degrees	6.25 degrees	w/o
A-2	6.25 degrees	6.25 degrees	with
B-1	flat	6.25 degrees	w/o
B-2	flat	6.25 degrees	with

As summarized in Table 2, the recorded ground motion of the 1940 El Centro earthquake, denoted as I-ELC270 hereafter, is used for the seismic simulation test. In addition, two generated acceleration histories compatible with the required response spectra of AC156, denoted as AC156-TAP090 and AC156-TCU054 hereafter, are also adopted in the test.

Table 2 Acceleration excitation program

Test name	Excitation direction		Targeted input peak acceleration (g)
I-ELC270	Unilateral	X	0.36
	Bilateral	X/Y	0.36/0.21
AC156-TAP090	Unilateral	X	0.50
	Bilateral	X/Y	0.50/0.45
AC156-TCU054	Unilateral	X	1.00
	Bilateral	X/Y	1.00/0.96

The comparison of the horizontal acceleration and displacement response histories together with the hysteresis loops for Bearings A-1, A-2, B-1 and B-2 under unilateral I-ELC270 is illustrated in Figure 2.

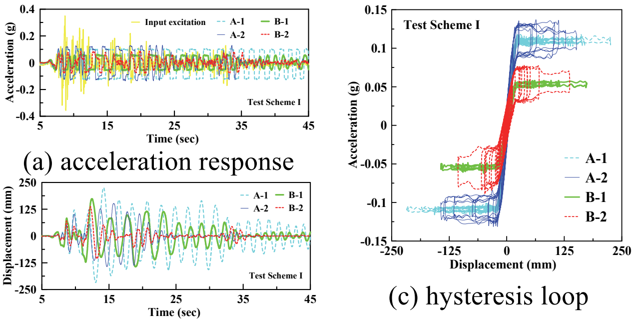

(a) acceleration response

(b) displacement response

(c) hysteresis loop

Fig. 2 Comparison of seismic responses of the isolation devices with different design parameters subjected to unilateral I-ELC270

It is of no surprise that the increase in supplemental sliding friction mechanism (i.e. energy dissipation capability) will lead to a reduction in maximum horizontal displacement responses but will also result in the augmentation of the maximum horizontal transmitted acceleration responses. In addition, the oscillations after the input excitations will be damped out more quickly. As a consequence, the displacement and acceleration performances should be mutually compromised when designing the supplemental damping mechanism. Furthermore, it was indicated (Wang et al., 2012; 2013) that without considering rolling and sliding friction for the isolation device, the horizontal transmitted acceleration responses can essentially remain constant corresponding to the constant inclined surface angle (θ) when the roller moves away from the fixed curvature range. Besides, the dynamic behavior of Type A isolation devices in which the roller is sandwiched between two V-shaped surfaces with a sloping angle of θ is identical to that of Type B isolation devices in which the roller is sandwiched between a flat surface and a V-shaped surface with a sloping angle of 2θ. In this test program, assuming that the rolling friction contribution is very limited, the maximum horizontal transmitted acceleration response of Bearing A-1 is larger than and about twice ($\sin(2\theta)/\sin(\theta) \approx 2$ where θ is 6.25 degrees) that of Bearing B-1.

More importantly, the test results show that the maximum horizontal displacement response of Type B isolation devices is less than that of Type A isolation devices under the same excitations. It implies that an increase in the sloping angle of bearing plates (or potential energy capability) may not result in the reduction of maximum horizontal displacement responses of the isolation device, which agrees with the previous analytical results for highway bridges equipped with sloped rolling-type isolation bearings (Ou et al., 2010). This may be clarified using the definition of the equivalent damping ratios (ξ_{eq}) shown in Equation (5) and Figure 3, in which E_D is the total energy dissipated by the isolation device and E_S is the maximum potential (or strain) energy of the isolation device. When Type A and Type B isolation devices have the same horizontal displacement responses (that is, when D_1 and D_2 respectively represent the rollers moving within and away from the fixed curvature range), the calculated equivalent damping ratios of Type B isolation devices ($\xi_{eq,B}$) are found to be more significant than those of Type A isolation devices ($\xi_{eq,A}$) due to the smaller strain energy in Type B isolation devices. In other words, under the same damping conditions, Type B isolation devices should have a smaller horizontal displacement response than Type A isolation devices.

$$\xi_{eq} = E_D / 4\pi E_S \tag{5}$$

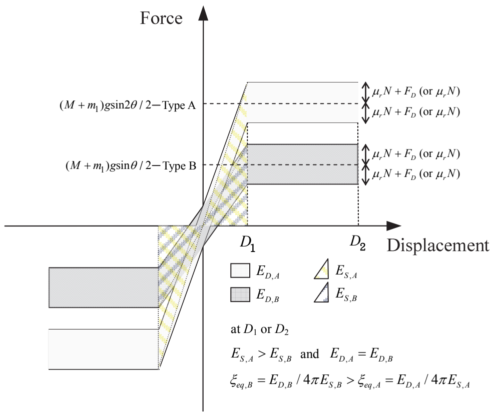

Fig. 3 Approximation of equivalent damping ratios for Type A and Type B isolation devices

In Test Scheme II, the effectiveness of Type B devices with the supplemental friction mechanism is investigated on a seismically isolated raised floor system with a plane dimension of 3m by 3m. For the four isolation devices underneath the raised floor system, the sloping angle (θ) of the V-shaped surfaces of the intermediate plate is designed to be 6 degrees. A steel frame composed of 200×150×6×9 (mm) H beams is designed to connect the raised floor to the isolation devices. The total seismic reactive mass of the raised floor system is about 1420 $N-sec^2/m$. The equipment to be protected, placed above the isolated raised floor system, is simulated by lead blocks with a total seismic reactive mass of 1000 $N-sec^2/m$. The setup is shown in Figure 4.

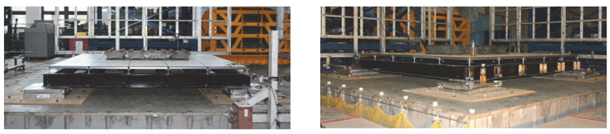

Fig. 4 Isolated raised floor system in Test Scheme II

The X directional acceleration response histories transmitted to the isolated raised floor system and the X directional hysteresis loops of the isolated raised floor system under bilateral AC156-TAP090 and bilateral AC156-TCU054 are depicted in Figures 5 and 6, respectively. It is evident that the maximum acceleration response transmitted to the isolated raised floor system can be drastically reduced in comparison to the input peak acceleration and can reveal an acceptably steady level. Since the supplemental sliding friction is engaged, the hysteresis loops shown in Figure 6 reveal an excellent energy dissipation capability. The test results also disclose that the isolated raised floor system has an excellent plane rotation control.

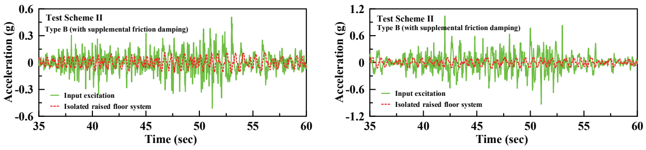

(a) AC156-TAP090 (b) AC156-TCU054

Fig. 5 X directional acceleration response histories of isolated raised floor system

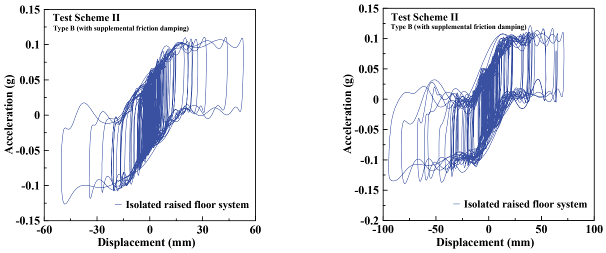

(a) AC156-TAP090 (b) AC156-TCU054

Fig. 6 X directional hysteresis loops of isolated raised floor system

Numerical Verification

When the test models are subjected to horizontal acceleration excitations, the dynamic behavior of a single degree of freedom (SDOF) system equipped with the sloped multi-roller isolation devices can be numerically predicted using the simplified twin-flag hysteretic model (Wang et al., 2012; 2013). The comparison of the experimental results and the numerical predictions for Bearing B-2 subjected to unilateral AC156-TAP090 is presented in Figure 7. It is found that the numerical predictions using the proposed simplified mathematical hysteretic model have an excellent agreement with the seismic simulation test results, including the predictions of amplitude and phase responses.

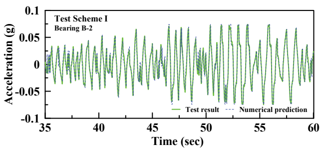

(a) acceleration response

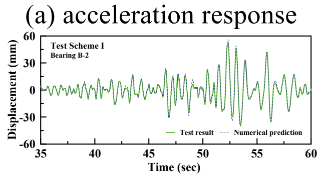

(b) displacement response

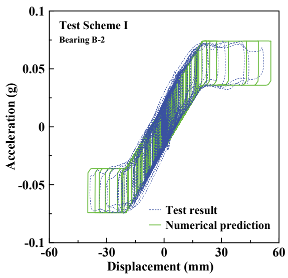

(c) hysteresis loop

Fig. 7 Comparison of experimental results and numerical predictions

Conclusions

The sloped rolling-type isolation device features a standardized design irrespective of input motions, which addresses one of the most important design concerns for critical equipment or facilities if the maximum acceleration response is selected as the seismic performance criterion. In this study, a series of seismic simulation tests on isolation devices with different design parameters and an isolated raised floor system subjected to the recorded ground motion and spectrum compatible floor acceleration histories were conducted to demonstrate the seismic performance of the isolation device. The high efficiency of employing the isolation devices in reducing seismic demands (or seismic damage potential) of the protected objects is experimentally verified. The test results also clarify the influences of different sloping angles and supplemental sliding friction on the dynamic behavior of the isolation devices. Moreover, the excellent agreement between test results and numerical predictions shows a validity and practical applicability of the proposed twin-flag mathematical model in characterizing the hysteretic behavior of the isolation devices. As a consequence, the sloped rolling-type isolation device is capable of effectively mitigating seismic risks posed to the critical equipment and facilities.

References

Chang KC, Hwang JS, Wang SJ, Hwang CH, Tsai MS. Adaptable Seismic Isolation Bearing System. Patent Application 100125835, WOOD & WU Patent and Trademark Office, Taiwan, 2011.

Ou YC, Song J, Lee GC. A parametric study of seismic behavior of roller seismic isolation bearings for highway bridges. Earthquake Engineering and Structural Dynamics, 2010; 39(5): 541-559.

Shames IH. Engineering Mechanics: Dynamics. 4th Ed, Eaglewood Cliffs (NJ): Prentice-Hall Inc., 1996.

Wang SJ, Chang KC, Hwang JS, Tsai MS, Hsiao JY, Yu CH. Development of Sloped Rolling-Type Isolation Devices for Seismic Protection of Important Equipment and Facilities. Proceedings of the 15th World Conference on Earthquake Engineering (15WCEE), Lisbon, Portugal, September 24-28, 2012.

Wang SJ, Hwang JS, Chang KC, Shiau CY, Tsai MS, Hong JX. Sloped rolling-type isolation devices for seismic protection of equipment and facilities: theoretical study. Earthquake Engineering and Structural Dynamics, 2013. (under review)

Feasibility Study of Smart Carbon Fiber Reinforced Concrete for Structural Monitoring

Fang-Yao Yeh[1], Kuo-Chun Chang[2], Wan-Yu Lien[3] and Wen-Cheng Liao[4]

葉芳耀 [1]、張國鎮 [2]、連婉佑 [3]、廖文正 [4]

Abstract

Structural monitoring systems are important in civil engineering. Traditional structural monitoring systems have some disadvantages such as a shorter sensor life span than the structures. This research uses CFRC (Carbon Fiber Reinforced Concrete) as a structural monitoring sensor to extend the life of the sensor to match that of the structure. There are some known advantages of carbon fiber reinforced concrete, such as high tensile strength and high ductility which increases the seismic capacity and security of structures. However, CFRC has functionality similar to piezoresistive materials which can be used as a self-sensing material for strain measurement and damage detection. This property is based on the reversible effect of the strain on the volume of electrical resistivity and the irreversible effect of material damage on its resistivity. The strain sensing behavior is such that the resistivity decreases reversibly upon compression due to the slight inward push of crack-bridging fibers and the consequent decrease in the contact electrical resistivity of the fiber-cement interface. Similarly, the resistivity increases reversibly upon tension due to the slight outward pull of crack-bridging fibers and the consequent decrease in the contact resistivity. To consider the economic benefits, the fiber content is only 0.2 vol. % which is less than half of the amount used in other references (0.48 vol. %). The experimental results show that the conductivity of current materials is significantly improved by CFRC and that it can be used for strain measurement and damage detection with fiber content of 0.2 vol. %. Moreover, the experimental results of CFRC coated beams can be kept in a database for applications in the future.

Keywords: CFRC, Self-sensing, Strain measurement, Damage detection

Introduction

This article shows that once carbon fiber is added to concrete to become carbon fiber reinforced concrete (CFRC) it has functionality similar to piezoresistive materials that can be used as self-sensing materials for strain measurement and damage detection. This functionality is based on pairing the reversible effect of strain on the volume's electrical resistivity with the irreversible effect of damage to the resistivity. The strain sensing behavior is such that the resistivity decreases reversibly upon compression due to the slight inward push of crack-bridging fibers and the consequent decrease in the contact electrical resistivity of the fiber-cement interface. Similarly, the resistivity increases reversibly upon tension due to the slight outward pull of crack-bridging fibers and the consequent decrease in the contact resistivity [Wen and Chung, 2007; Han and Ou, 2007]. The self-sensing ability of CFRC cement-based composites has been well demonstrated under compression and under flexure. Using the electrical resistance change of CFRC and the appearance of structural cracks, we are able to derive an integration of sensors, and which possesses the material smartness quotient of self-sensing, stability, and repetitiveness.

[1] Researcher, National Center for Research on Earthquake Engineering, fyyeh@ncree.narl.org.tw

[2] Director, National Center for Research on Earthquake Engineering, kcchang@ncree.narl.org.tw
Professor, Department of Civil Engineering, National Taiwan University, ciekuo@ntu.edu.tw

[3] Master, Department of Civil Engineering, National Taiwan University, quietskycrystal@gmail.com

[4] Assistant Professor, Department of Civil Engineering, National Taiwan University, wcliao@ntu.edu.tw

Experimental Investigations

Preparation of Materials

The design concrete strength was set to 500 kgf/cm^2. The cement was a blended Portland cement and the specimens were made from a mix with the following ratios: water-cement ratio (w/c) = 0.4; sand-cement ratio (s/c) = 0.75; silica fume 15% by weight of cement; methylcellulose 0.4% by weight of cement and carbon fiber 0.2% by of total volume. The fiber diameter was 7μm. The nominal fiber length was 15mm. A standard mixing procedure was used. A rotary mixer with flat beater was used for mixing. After pouring the mix into oiled molds, an external electric vibrator was used to facilitate compaction and decrease the amount of air bubbles.

Specimens and Test Setup

From the aforementioned concrete mixture, 5 CFRC bone-shaped specimens, 4 CFRC cylinders and 8 different styles of CFRC beams were produced for testing at 28 days of age. The bone-shaped specimens had dimensions of 455×50×20mm and were prepared for uniaxial tension testing. The cylinders had dimensions of 100×200mm and were prepared for uniaxial compression testing. With the same concrete mixture, 8 concrete beams were produced. These beams had dimensions of 550×150×150mm and were prepared for three-point bending testing. The test setup is shown in Fig. 1.

Uniaxial Tension Test

A monotonous tensile loading was applied to the specimen shown in Fig. 1(a). The tensile strain of the CFRC specimen was measured using an LVDT under a gauge length of 105mm. The electrical resistance measurements were conducted using the four-probe method, with silver paint in conjunction with copper wires for electrical contacts and the electrode distance was 75mm (Fig. 1(a)). A Keithley 2000 digital multimeter was used to measure the electrical resistance of the specimens.

Uniaxial Compression Test

A monotonous compressive loading was applied to the specimen shown in Fig. 1(b). The compressive strain of the CFRC specimen was measured by an LVDT under a gauge length of 100mm. The electrical resistance measurements were also conducted using the four-probe method, with silver paint in conjunction with copper wires for electrical contacts and the electrode distance was 90mm (Fig. 1(b)).

Three-point Bending Test

Cyclical loading was applied to the CFRC beam specimen shown in Fig. 1(c). The dynamic strain of the CFRC beam was measured by the strain gauge, the central deformation was measured by an LVDT, and the electrical resistance was measured by the Keithley 2000 digital multimeter under a gauge length of 120mm (Fig. 1(c)).

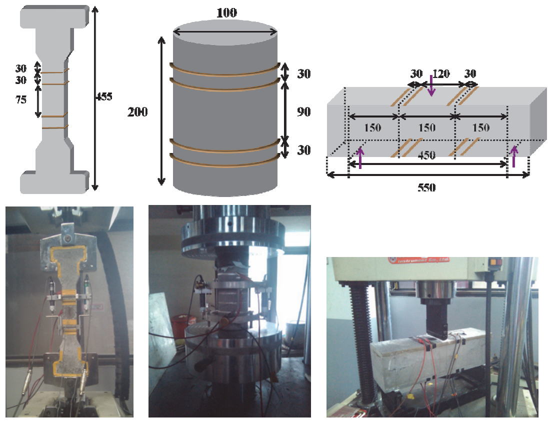

(a) (b) (c)

Fig. 1 Test setup, (a) uniaxial tension test, (b) uniaxial compression test, and (c) bending test

Results and Discussion

Uniaxial Tension Test

The test results of the 28 day old specimens are shown in Fig. 2. Fig. 2(a) shows the relationships between the fractional change in electrical resistance of the CFRC and the strain measured by LVDT at the middle portion of the specimens. This data depicts a linear relationship between the fractional change in electrical resistance of the CFRC and the strain measured by LVDT before a proportional limit. If the limit is exceeded, the fractional change in the electrical resistance decreases due to the increase in electrical resistance in the CFRC specimen caused by microstructure changes. This causes the micro crack density to increase and damage occurs.

In order to relate the fractional change in electrical resistance to tensile strain, we define the gauge factor (GF) as being the fractional change in electrical resistance per unit strain. When under the proportional limit, there is a strong linear relationship ($R^2 \fallingdotseq 1$) between the fractional change in electrical resistance and the tensile strain in the T1 to T5 specimens (Fig. 2(a)). The similarity between the fractional change in the electrical resistance and tensile strain under uniaxial tension testing means that CFRC can be used as a kind of self-sensing material for strain measurement within the proportional limit.

Based on the different variations in the fractional change in electrical resistance, three regions are considered in this paper: (1) region-I - the linear region where strain sensing via fractional change in electrical resistance has a linear relationship and is reversible; (2) region-II - the plastic region where the strain sensing via fractional change in electrical resistance is still with some proportional relationship and partial reversibility, owing to crack occurrence and damage accumulation in the specimen, but is not as obvious in the tensile specimens; (3) region-III - the damaged region where the strain sensing via fractional change in electrical resistance is meaningless, owing to the damage and material failure in the specimen. The fractional change in the electrical resistance changes very rapidly and can be used for damage detection.

Fig. 2(b) shows the variation in tensile stress and the fractional change in electrical resistance with tensile strains. The fractional change in electrical resistance has a linear relationship with tensile strain in region-I and rapidly decreases in region-III because of the fast electrical resistance increase, due to damage accumulation. The slope of fractional change against tensile strain is a good indicator for damage detection under tensile loading.

The test results are summarized in Table 1. Before the proportional limit, there exists a strong linear relationship between the fractional change in electrical resistance and tensile strain. The range of the R^2 values is between 0.93 and 0.97. The similarity of the fractional change in electrical resistance and tensile strain under uniaxial tension tests means that CFRC can be used for strain measurement. The gauge factors are 9.5 to 19.5 and the measurement ranges are 57.8% to 83.33% of the ultimate tensile strain.

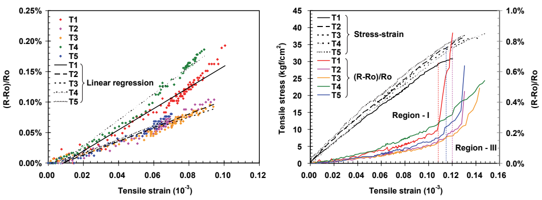

(a) (b)

Fig. 2 Tension test, (a) comparison between the fractional change in electrical resistance and strain measured by LVDT in linear region, and (b) variation of the tensile stress and fractional change in electrical resistance with tensile strain

Table 1 Results of the uniaxial tension tests

Unit / Spec.	f_t (kgf/cm^2)	ε_u (10^{-3})	Ro (Ω)	GF	R^2	$(\Delta R/Ro)_L$ (10^{-3})	MR %
T1	30.79	0.120	26.47	15.4	0.95	0.1	83.33
T2	37.29	0.173	25.03	10.0	0.94	0.1	57.80
T3	32.14	0.137	29.23	9.5	0.96	0.1	72.99
T4	38.22	0.147	36.54	19.5	0.97	0.1	68.03
T5	37.70	0.130	24.87	11.5	0.93	0.1	76.92

Uniaxial Compression Test

The test results from the 28 day old specimens are shown in Fig. 3. Fig. 3(a) shows the relationships between the fractional change in electrical resistance of the CFRC and the strain measured by the LVDT at the middle of the specimens. This data showed a bi-linear relationship between the fractional change in electrical resistance of the CFRC and the strain measured by the LVDT before the proportional limit. If the proportional limit is exceeded, the fractional change in electrical resistance decreases due to an increase in electrical resistance in the CFRC specimen caused by the microstructure changes. In addition, micro crack density increases and damage occurs.

When under the proportional limit there is a bi-linear relationship between the fractional change in electrical resistance and the compressive strain. Fig. 3(b) shows that the relation between the fractional change in electrical resistance and compressive strain is smaller than 2×10^{-4} and that the gauge factor of the C1 to C4 specimens are 200 to 250. Fig. 3(c) shows the relation between the fractional change in electrical resistance and the compressive strain to be between 5×10^{-4} and the proportional limit and that the gauge factor of the C1 to C4 specimens are 20 to 30. The similarity in the fractional change in electrical resistance and the compressive strain under uniaxial compression tests demonstrates that CFRC can be used as a self-sensing material for strain measurement within a proportional limit.

Fig. 3(d) shows the variation in the compressive stress and fractional change in electrical resistance as compressive strain varies. The fractional change in electrical resistance has a linear relationship with the compressive strain in region-I and region-II where GF1 and GF2 are used for compressive strain measurement. The fractional change in electrical resistance rapidly decreases in region-III because the electrical resistance increases quickly due to the damage accumulation. The slope of the curve is a good indicator for damage detection under compressive loading.

The test results are summarized in Table 2. Before reaching the proportional limit, there exists a strong bi-linear relationship between the fractional change in electrical resistance and compressive strain. The range of R^2 values is greater than 0.94. The similarity between the fractional change in electrical resistance and compressive strain under uniaxial compressive testing can be used for strain measurement. The gauge factors range from 187.1 to 240.6 (for GF1) and 20.9 to 24.9 (for GF2) and the measurement range lies between 71.15% and 88.32% of the ultimate compressive strain.

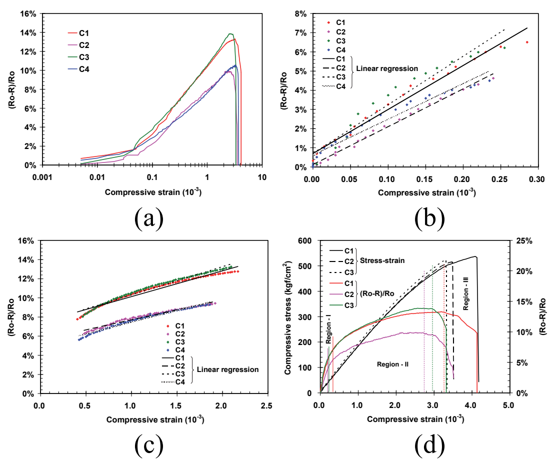

Fig. 3 Compression test, (a) comparison between the

fractional change in electrical resistance and strain measured by LVDT, (b)(c) comparison between the fractional change in electrical resistance and the strain measured by LVDT in linear region, and (d) variation of compressive stress and fractional change in electrical resistance as compressive strain changes

Three-point Bending Test

The test results of 28 day old three-point bending specimens are shown in Table 3. The different types of specimen shown in Table 3 include a pure CFRC beam without steel reinforcement (P), a pure CFRC beam with steel reinforcement (PS), a concrete beam coated with a CFRC layer without steel reinforcement (Co) and a concrete beam coated with a CFRC layer with steel reinforcement (CoS).

From Table 3, the following results were observed: (1) from a comparison of the two pure CFRC beams, the strain in both the tension and compression side of the P specimens are found to be smaller than the PS specimens, but the electrical resistance (Ro) and gauge factor (GF) are found to be larger in the P specimens; (2) from a comparison of the two CFRC coated beams, the gauge factor of the CoS specimens are found to be greater than the Co specimens; (3) from a comparison between the pure CFRC beams and the CFRC coated beams, the gauge factor of the CFRC coated beams (Co and CoS) are found to be larger in the pure CFRC beams (P and PS). Generally, the CoS specimens were found to have the greater gauge factor.

Summary and Discussion

To consider the economic benefits, the fiber content of the CFRC is only 0.2 vol. % which is less than half the amount used in the cited references (0.48 vol. %). The experimental results of the uniaxial tension tests, the uniaxial compression tests and the three-point bending tests show that the conductivity of materials significantly improved and that CFRC can be used for strain measurement and damage detection at a fiber content of 0.2 vol.%.

From the tension tests, we observed that due to the similarity between the fractional change in electrical resistance and tensile strain under uniaxial tension testing, the material can be used as a self-sensing material for strain measurement within the proportional limit. The slope of the fractional change against tensile strain curve is a good indicator for damage detection under tensile loading.

From the compression tests, we also observed that due to the similarity between the fractional change in electrical resistance and compressive strain under uniaxial compression testing, the material can be used as a self-sensing material for strain measurement within the proportional limit. The slope of the fractional change against compressive strain curve is a good indicator for damage detection under compressive loading.

From the three-point bending tests, the gauge factor of the concrete beams coated with a CFRC layer with steel reinforcement was found to be greater than that of a concrete beam coated with a CFRC layer but without steel reinforcement and pure CFRC beams with or without steel reinforcement. Moreover, the experimental results of the coated beams can be kept in the database for applications in the future.

Self-sensing of the tensile strain, compressive strain, and damage detection was found to be effective in CFRC under monotonous loading. The self-sensing ability of CFRC, as shown in the sensing of strain and damage detection, is demonstrated in this paper.

References

Sihai Wen and D. D. L. Chung "Piezoresistivity-based strain sensing in carbon fiber-reinforced cement", *ACI Materials Journal,* Vol. 104, No. 2, pp 171-179, 2007.

Baoguo Han and Jinping Ou "Embedded piezoresistive cement-based stress/strain sensor", *Sensors and Actuator*, A138, pp 294-298, 2007.

Table 2 Results of the uniaxial compressive tests

Unit / Specimen	E	f'_c	ε_u	Ro	GF1	R^2	GF2	R^2	$(\Delta R/Ro)_L$	MR
	(tf/cm^2)	(kgf/cm^2)	(10^{-3})	(Ω)					(10^{-3})	%
C1	178.18	536.77	4.09	19.63	240.6	0.98	24.9	0.97	2.91	71.15
C2	181.18	514.87	3.49	31.38	197.2	0.99	20.9	0.97	2.57	73.64
C3	189.66	523.62	3.30	31.17	253.0	0.94	29.3	0.98	2.89	87.58
C4	179.65	519.65	3.68	19.93	187.1	0.95	24.7	0.98	3.25	88.32

Table 3 Results of the three-point bending tests

Bending		Specimen	Strain (10^{-3})		Ro (Ω)		GF		R^2		Force
			c	t	c	t	c	t	c	T	kN
CFRC	w/o Rebar	P1	-0.08	0.040	36.8	53.3	175	220	0.97	0.81	7
	w Rebar	PS1	-0.17	0.075	14.7	18.9	52	87	0.96	0.90	10
		PS2	-0.15	0.075	15.3	15.9	78	89	0.92	0.89	10
Coated	w/o Rebar	Co1	-0.11	0.075	54.1	51.1	252	160	0.97	0.91	8.5
		Co2	-0.15	0.060	31.9	35.7	49	78	0.88	0.95	8.5
	w Rebar	CoS1	-0.15	0.060	81.9	49.7	1031	497	0.95	0.94	13
		CoS2	-0.06	0.045	40.6	84.3	603	844	0.98	0.93	13
		CoS3	-0.08	0.050	31.8	47.8	445	516	0.94	0.93	13

Development of Damage Evaluation Techniques for Geotechnical Structures (II) - A Case Study of the old Jhong-Jheng Bridge in Hsinchu

Yung-Yen Ko[1] Ya-Han Hsu[2]

柯永彥[1]、許雅涵[2]

Abstract

This report presents a verification of damage evaluation techniques for geotechnical structures based on structural dynamic responses developed in previous years through an actual case study. In Taiwan, several failures of highway bridges related to foundation scour occurred in recent years, which have caused considerable casualties and property loss. Therefore, the focus of this study is on the damage evaluation of bridge foundations, and the old Jhong-Jheng Bridge in Hsinchu, of which the caisson foundations have suffered severe exposure due to scouring, was adopted as the object of study. Firstly, microtremor measurements were made on the superstructure of the bridge, and the influence of foundation scouring was revealed by spectrum analysis and modal analysis. In addition, because the design drawings were unavailable and the foundation depth is thus unknown, the impulse response method was utilized to estimate the depth of the caisson foundation and a satisfactory result was obtained. According to all the above results, the feasibility of the non-destructive testing methods in the damage evaluation of structural foundations can be validated.

Keywords: geotechnical structures, damage evaluation, foundation scour, microtremor measurement, impulse response

Introduction

In Taiwan, several major highway bridge failures occurred in recent years. The majority of these failures were related to the exposure of the pier foundation due to scouring, which reduces its bearing capacity. For example, a pile foundation of the Kao-Ping Bridge settled in 2000, and a caisson foundation of the Hou-Fong Bridge tilted in 2008, causing the collapse of their superstructures. In both cases, the foundations were significantly exposed due to scouring. In 2009, Typhoon Morakot hit Taiwan with record-breaking rainfalls. An over 200-year-recurrence flood occurred in the watershed of the Kao-Ping River, and several bridges, including the Liu-Gui Bridge, the Ci-Wei Bridge, the Da-jin Bridge, and the Shuang-Yuan Bridge, experienced severe scour and were destroyed.

These disasters led to considerable casualties and property loss, yet they could have been preventable if the damage or insufficient capacity of the foundation could have been detected in advance, and repairs and retrofitting works or the implementation of restraints on the usage of the bridge were timely executed. Although it is possible to inspect the exposure of the foundation using instruments installed on it, these instruments might be destroyed in flood conditions. Therefore, it is necessary to develop indirect damage evaluation techniques for the foundations.

The geotechnical structure can be regarded as a soil-structure system. Its structural dynamic responses exhibit the global characteristics of the system and also reflect the boundary conditions. Thus, measuring the dynamic responses of a geotechnical structure helps to detect its damage. This kind of damage evaluation is classified as non-destructive testing. It is easy to perform, data processing is well developed, and many vulnerability indices have been proposed. Hence, it is a research subject worthy of development. Since the disaster mitigation of bridges has become an important issue, the focus is on bridge foundations.

[1] Associate Researcher, National Center for Research on Earthquake Engineering, yyko@ncree.narl.org.tw
[2] Assistant Researcher, National Center for Research on Earthquake Engineering, yhhsu @ncree.narl.org.tw

The old Jhong-Jheng Bridge in Hsinchu, which crosses the Tou-Cian River, used to be a vital roadway and has been in operation for more than 30 years. The riverbed nearby is mainly composed of mudstone or inter-layered mudstone and sandstone. Thus, scouring and erosion has formed many gullies and has caused several piers to suffer foundation exposure (NCTU, 2005). Although many anti-scour protective works for the bridge foundations have been completed, the strong current induced by the heavy rainfall of Typhoon Saola in August 2012 still caused the caisson foundation of pier P9 to be severely exposed, as shown in Fig. 1. Because of the possible insufficiency of the structural stability, this bridge has been closed since then, and a new bridge is to be constructed.

Taking advantage of this opportunity, microtremor measurements were performed on the superstructure of the old Jhong-Jheng Bridge during the closed period to investigate the influence of the foundation exposure on the dynamic behavior of the bridge. In addition, the impulse response method was utilized to examine the length of the caisson foundation. Through this case study, non-destructive testing methods for the damage evaluation of foundations can be verified.

Fig. 1 The scouring condition of the old Jhong-Jheng Bridge (August 2012)

Testing and Analysis Methods

The testing techniques adopted in this study and their corresponding analysis methods are as follows:

1. Microtremor Measurement:

Microtremors are randomly generated by natural and civilian activities in the environment and have a wide frequency range. If the input microtremors and the excited structural responses are simultaneously measured, the transfer function can be deduced for system identification. If no input motion is available, the structure can be characterized only by its excited response, assuming microtremors as the white noise.

The vibration characteristics of a structure, such as its natural frequency, damping, and modal shape, are related to its structural properties and integrity. Since damage of a structure lowers its natural frequency due to stiffness reduction, the natural frequency is often adopted for damage evaluation. Moreover, the modal shape of a damaged structure would be changed because of the stiffness redistribution. Therefore, the modal shape would help to locate the damage.

In order to identify the dynamic properties of the bridge–foundation–ground system using microtremor measurements, the analysis methods adopted include:

(a) Average spectrum analysis

When long-term field vibration measurements are made, the vibration characteristics at various moments show a certain variance since the environment and the vibration source are not consistent. To eliminate the dispersion, the concept of Samizo et al. (2007) was used. Sections with a fixed duration are extracted from the overall record, and each is partially overlapped with the next. The Fourier spectrum is calculated in each section and an averaged spectral curve is then obtained as a representative as shown in Fig. 2. Thus, the influence of abnormal events can be diluted and the structural characteristics are better described.

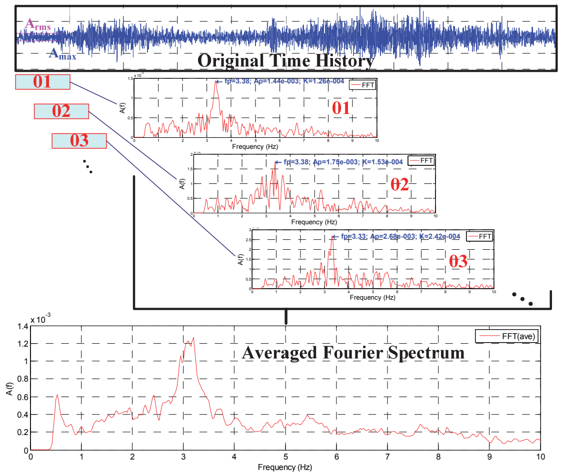

Fig. 2 Procedures of average spectrum analysis.

(b) Modal analysis

In this study, the correlation analysis method is adopted for modal analysis. Considering the time histories of two random vibration signals, $x(t)$ and $y(t)$, their cross-correlation is defined by the function:

$$r_{yx}(t) = \int_{-\infty}^{\infty} y(\tau)x(t+\tau))d\tau \qquad (1)$$

The cross-correlation of $x(t)$ with itself is usually called as auto-correlation.

If the Fourier transform is performed on the cross-correlation function, a cross-power spectrum can be obtained, which is exactly the dot product of $x(t)$ and $y(t)$ in the frequency domain:

$$S_{yx}(\omega) = \int_{-\infty}^{\infty} r_{yx}(\tau)e^{-i\omega t}d\tau = Y(\omega)\cdot\overline{X}(\omega) \qquad (2)$$

where $Y(\omega)$ and $X(\omega)$ are the Fourier transform of $x(t)$ and $y(t)$, and $\overline{X}(\omega)$ is the conjugate of $X(\omega)$.

Similarly, if the auto-correlation function is transformed into the frequency domain, the auto-power spectrum is acquired, which is exactly the dot product of $x(t)$ and itself in the frequency domain.

Accordingly, a reference point is first chosen. Then the cross- and auto-power spectra of the vibrations in a certain direction at all the measuring points (including the reference point) with respect to the vibration of the reference point are calculated. Thus, the mutual peaks of these power spectra are considered to be the fundamental (natural) frequencies of the principal modes of the system. Based on the amplitude ratio and the phase differences among all the points at the fundamental frequency of a specific mode, the corresponding modal shape is obtained.

2. Impulse Response Method:

The impulse response method is based on the recognition of the reflected compressive wave and is often used to inspect the pile integrity. As shown in Fig. 3, the pile top is impacted by an impulse hammer, inducing a transient impulse propagating downward along the pile. When the impulse reaches the discontinuities of the pile, such as the pile tip or the deflections in the pile body, reflection occurs. Then, the pile length or the location of the deflections can be estimated according to the response of the reflected wave measured by the accelerometer on the pile head.

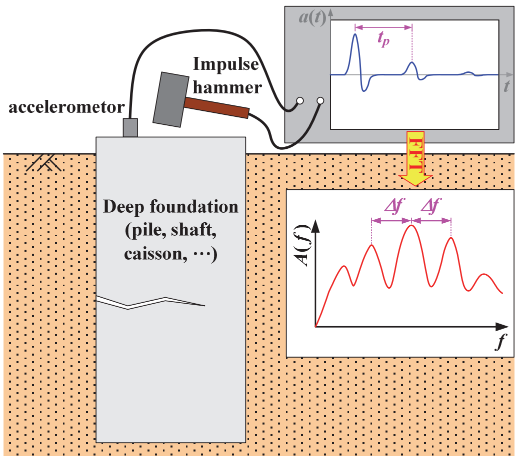

Fig. 3 Test scheme of the impulse response method.

The data processing procedures for the impulse response method are described as follows:

(a) Time domain analysis

Since the stiffness of the pile body is relatively higher than the supporting soil below the pile tip or the deflections, the reflected wave induced by these discontinuities will be in phase with the incident wave, as shown in Fig. 3. The travelling distance of the impulse can be calculated by the time lag between the incident and reflected waves passing the pile head and the P-wave velocity in the pile. Thus, the pile length or the location of deflections can be deduced.

The time lag between incidence and reflection can be estimated directly by the peaks on the time-history curve. However, the reflected waves may not be easily recognized due to environmental conditions, impact quality, and material inhomogeneity. In this case, Eq. (1) can be introduced to perform an auto-correlation analysis for the measured response, and the maximum of the correlation function, apart from the one at $t = 0$, can be identified at $t = t_p$. Then, t_p is considered to be the duration of the impulse travelling back and forth along the pile. If the discontinuity is at the pile tip, then the pile length L can be calculated as below:

$$L = \frac{v_P t_P}{2} \tag{3}$$

where v_p is the propagating velocity of the impulse.

(b) Frequency domain analysis

Based on elastic theory, a prismatic pile has a consistent interval between the intrinsic frequencies of the resonant modes, which is a function of L and v_p, provided that the induced wavelengths are greater than the diameter of the pile. Therefore, if the Fourier spectrum of the impulse response on the pile head is obtained, then the frequency interval Δf can be estimated accordingly, as shown in Fig. 3. Then the pile length L can be calculated by the following equation (Finno and Gassman, 1998):

$$L = \frac{v_P}{2\Delta f} \tag{4}$$

Microtremor Measurement of the old Jhong-Jheng Bridge

During the closed period of the old Jhong-Jheng Bridge, a microtremor measurement was conducted on its superstructure. The measuring points were located at pier P9, where the foundation exposure was the most severe, and at neighboring piers P10 and P11, as shown in Fig. 1. Velocity-type vibro-sensors were adopted and were installed on the deck beside the expansion joint. At the measurement, the exposed depth of the caisson of pier P9 was estimated at around 15 m using a plumb bob and measuring tape.

Using an averaging scheme, the average Fourier spectrum of the horizontal transverse (HT, parallel to the flow direction) vibrations can be obtained, as shown in Fig. 4. A majority of the vibrations at piers P10 and P11 are concentrated in the frequency range of 2–4 Hz, with predominant frequencies of 2.8 Hz and 3.3 Hz, respectively. For pier P9, an obvious peak is noted at the frequency of 1.5 Hz. The predominant frequency of P10 is found to be lower than that of P11, where the protective works remained intact, probably because the protective work was partially damaged. Meanwhile, pier P9, which was severely scoured, has a lower predominant frequency than P10 and P11. It is therefore concluded that the exposure of the foundation will cause the predominant frequency of vibration of the pier to be apparently decreased.

In addition, modal analysis was performed using the microtremor measurement data. The fundamental frequency of the 1st mode is found to be 1.47 Hz, conformable to the predominant frequency of the microtremors of pier P9. The corresponding modal shape is shown in Fig. 5, in which the maximum vibration amplitude is observed for pier P9. Consequently, the stiffness of pier P9, which had suffered severe scour and significant foundation exposure, is found to belower than the neighboring piers as expected. Thus, it will show a larger response when subjected to external loads, leading to stability concerns in terms of settlement and overturning.

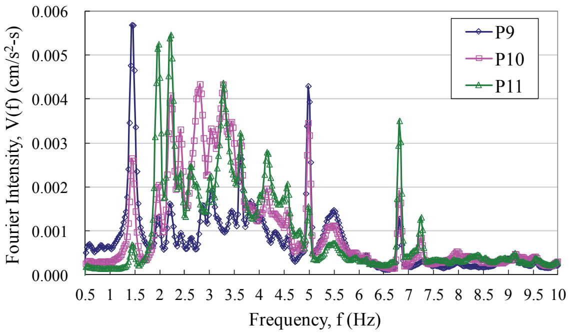

Fig. 4 Average Fourier spectra of HT vibrations.

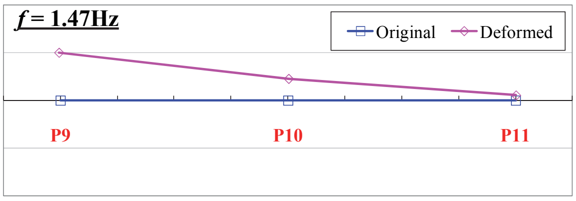

Fig. 5 Modal shapes of the bridge section P9~P11

Impulse Response Testing on the Caisson Foundation of the old Jhong-Jheng Bridge

The caisson foundations were used for the old Jhong-Jheng Bridge. However, the design drawings are unavailable and the foundation depth is unknown, so the influence of the foundation exposure on the stability of the pier cannot be evaluated. Therefore, the impulse response method was adopted for the testing of the caisson length of pier P11. The test situation is as shown in Fig. 6. An impulse hammer was used to hit the top of the caisson, an accelerometer was placed on the top to measure the incidence and reflection of the induced impulse wave, and another accelerometer was installed on the side of the caisson 1.85 m below the top to estimate the wave velocity.

Fig. 7(a) depicts the time history of the impulse response at the top of the caisson. The waveforms of the incident and reflected waves are identifiable and t_p can be obtained using the correlation method. Several high-quality hits were chosen to obtain an average $t_p = 1.053\times10^{-2}$ s as a representative. In addition, from the time lag of the impulse passing between the two accelerometers, the v_p can be estimated to be around 4975 m/s. From this, the length of the caisson can be calculated by Eq. (3), and is about 26.2 m. Fig. 7(b) gives the Fourier spectrum of the impulse response. Similarly, an average Δf of about 96.0 Hz was acquired. Then the caisson length was calculated using Eq. (4), and is 25.9 m, close to that found from the time domain analysis.

As mentioned, the exposed depth of the P9 caisson was close to 15 m. If the length of the P9 caisson is the same as that of P11, the exposure exceeds half of the caisson length. Therefore, the foundation stability of pier P9 might be insufficient.

Fig. 6 Impulse response testing on P11caisson.

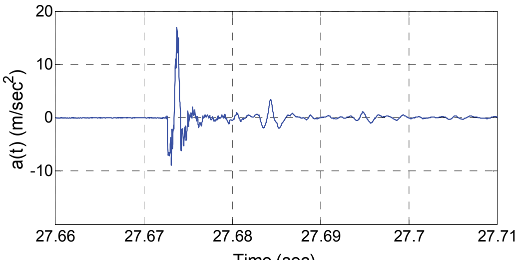

(a)

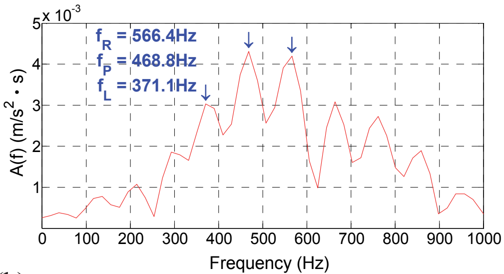

(b)

Fig. 7 Impulse response on the top of P11 caisson: (a) time history curve; (b) Fourier spectrum.

References

Finno, R.J., and Gassman, S.L. (1998), “Impulse response evaluation of drilled shafts”, J. Geotech. Geoenviron. Eng, ASCE, 124(10), pp. 965-975.

NCTU (2005), The Study on the Impact of Jhong-Jheng Bridge and the Other Existing Flood Control Structures to the Overall Characteristics of Tou-Cian River, MOEA/WRA Report.

Samizo M, Watanabe S, Fuchiwaki A and Sugiyama T. (2007), “Evaluation of the structural integrity of bridge pier foundations using microtremors in flood conditions”, Quarterly Report of the Railway Technical Research Institute, 48(3), pp. 153-157.

Shaking Table Tests on Model Pile in Saturated Sloping Ground

Chia-Han Chen[1], Tzou-Shin Ueng[2] and Cheng-Hsing Chen[3]

陳家漢[1]、翁作新[2]、陳正興[3]

Abstract

For the study of soil-structure interaction, including the effect of lateral spreading, in a saturated sloping ground during earthquake, shaking table tests on a model pile in an inclined large biaxial laminar shear box filled with saturated clean sand were conducted at the National Center for Research on Earthquake Engineering (NCREE), in Taiwan. The pile tip was fixed at the bottom of the shear box to simulate the condition of a pile foundation embedded in a firm stratum. The pile top was mounted with 6 steel disks to simulate the superstructure. Input shakings including sinusoidal and recorded earthquake accelerations were imposed either perpendicular or parallel to the slope direction. Strain gauges and accelerometers were placed on the pile surface to obtain the response of the pile under shaking. The near-field and far-field soil responses, including pore water pressure changes, accelerations, and settlements were also measured. The lateral spreading displacement of the soil and pile behavior were observed and evaluated while soil liquefaction was triggered under shakings in either direction.

Keywords: shaking table test, liquefaction, lateral spreading, pile

Introduction

Pile foundations within liquefiable and laterally spreading ground have suffered extensive damages in many large earthquakes such as the 1964 Niigata Earthquake, the 1989 Loma Prieta Earthquake, the 1995 Kobe Earthquake, the 1999 Chi-Chi Earthquake, the 2011 Christchurch Earthquake and the 2011 Great East Japan Earthquake. Previous studies on soil-pile interactions have been conducted in order to understand the mechanism of the dynamic loading on the piles (soil-pile interaction) and their responses under earthquake loading. Lateral loading tests in the field or in the laboratory and shaking table tests on model piles within soil specimens, under either 1 g or centrifugal condition, have been used to investigate the pile behaviors and soil-pile interaction in saturated soil (e.g. Dobry et al. 2003, Tokimatsu et al., 2005, Ashford et al., 2006, Brandenberg et al., 2006, Cubrinovski et al., 2006, Madabhushi et al., 2010, Ueng and Chen, 2010). The results of these studies, including failure mechanisms, bending moments of pile in laterally spreading ground, pore water pressure variation around the piles, p-y relations for soil-pile interaction, and pile cap effect, can provide information on performance criteria for aseismic design of structures with pile foundations.

However, there are still uncertainties concerning the soil-pile interaction issues in laterally spreading ground, including (1) the kinematic loading on pile foundation due to lateral spreading; (2) the relationship between the mobilized lateral pressure and the ground displacement; and (3) the transient responses of the surrounding soil and pile during soil liquefaction. In this study, a large biaxial laminar shear box developed at the National Center for Research on Earthquake Engineering (NCREE) was used as the soil container and an instrumented aluminum model pile was installed inside the shear box filled with saturated sand. The biaxial shear box with the model pile in a saturated sloping ground was placed on 1 g shaking table and one dimensional sinusoidal and recorded earthquake accelerations were applied perpendicularly or parallel to the slope direction. The soil and pile responses and their

[1] Assistant Researcher, National Center for Research on Earthquake Engineering, chiaham@ncree.narl.org.tw
[2] Professor Emeritus, Department of Civil Engineering, National Taiwan University
[3] Professor, Department of Civil Engineering, National Taiwan University

interaction, including the inertial and kinematic actions on the model pile, under these types of shakings were studied.

Model Pile and Sand Specimen

The model pile was made of an aluminum alloy pipe, with a length of 1600 mm, an outer diameter of 101.6 mm, and a wall thickness of 3 mm. Its flexural rigidity, EI = 75 kN·m^2, was obtained by flexural testing. Strain gauges and mini-accelerometers were placed at different locations to respectively measure bending strains and accelerations along the model pile. The shear box was inclined 2° to the horizontal, simulating a mild infinite slope. The sloping direction of this model was in the X-direction. The pile was vertically fixed at the bottom of the shear box. Hence, this physical model can be used to simulate the condition of a vertical pile embedded in sloping rock or within a sloping stratum of firm soil. In addition, 6 steel disks, 226.14 kg, were attached to the top of the model pile to simulate the superstructure.

A clean fine silica sand (G_s = 2.65, D_{50} = 0.31 mm) from Vietnam was used in this study for the sand specimen inside the laminar shear box. The maximum and minimum void ratios are 0.918 and 0.631, respectively. The sand specimen was prepared using the wet sedimentation method after the placement of the model pile and the instruments inside the shear box. The sand was rained down into the shear box filled with water to a pre-calculated depth. The size of the sand specimen is 1.880 m × 1.880 m in plane and about 1.31 m in height before shaking tests. The relative density of the sand is about 10 %. Details of the biaxial laminar shear box and the sand specimen preparation are described in Ueng et al. (2006).

Shaking Table Tests

Shaking table tests were first conducted on the model pile without sand specimen in order to evaluate the dynamic characteristics of the model pile itself. Sinusoidal and white noise accelerations with amplitudes from 0.03 to 0.05 g were applied in X- and/or Y-directions. In the two-dimensional (multidirectional) sinusoidal shakings, there is a 90° phase difference between the input acceleration in X- and Y-directions, i.e., a circular or ellipse motion was applied. The model pile in saturated sloping ground was then tested under one dimensional sinusoidal (1-8 Hz) and the recorded accelerations during Chi-Chi Earthquake and Kobe Earthquake with amplitudes ranging from 0.03 to 0.15 g. Input motions were mainly imposed perpendicular to the slope direction for the study of kinematic effect on the pile foundation (lateral spreading force) independently, and also tested in another direction parallel to the slope to investigate the resultant force on the pile foundation including the inertial and kinematic effect. White noise accelerations with amplitude of 0.03 g were also applied in both the X- and Y-directions to evaluate the dynamic characteristics of the model pile within the soil and the sand specimen. Figure 1 shows a picture of the shaking table test on a model pile with 6 steel disks on its top.

Fig. 1 A model pile with 6 steel disks on its top in saturated sloping ground on the shaking table

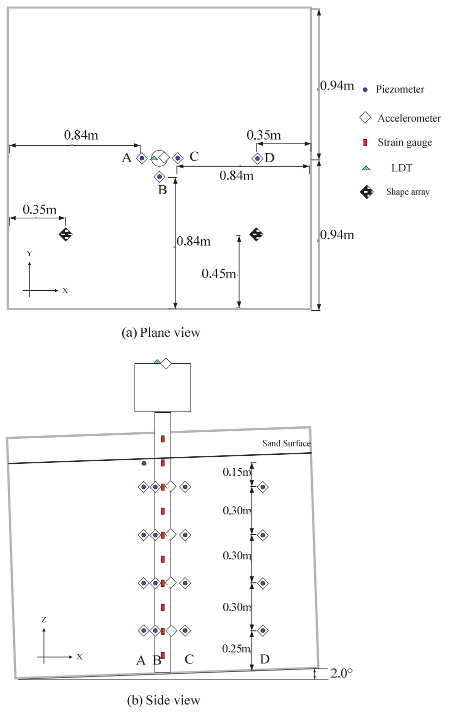

Fig. 2 Instrumentation on the pile and within the sand specimen

The pile top displacements, strains and accelerations at different depths on the pile, and the pore water pressures and accelerations in the sand specimen (near-field and far-field) were measured during each shaking, as shown in Fig. 2. In addition, the frame movements at different depths of the laminar shear box were also recorded to evaluate the responses and liquefaction of the sand specimen using displacement transducers and accelerometers. Pore water pressures inside the sand specimen were measured continuously until sometime after the end of shaking to observe the dissipation of the water pressures. The height of the sand surface after each test was obtained for the settlement and density of the sand specimen. Soil samples were taken using short thin-walled cylinders at different depths and locations after completion of the shaking tests to obtain the densities of the sand specimen.

Preliminary Results

Characteristics of model pile

Shaking table tests on the model pile without sand specimen were conducted to evaluate the dynamic characteristics of model pile itself. The behavior of model pile on the shaking table can be regarded as a single-degree viscously damped system. Hence, the amplification curve was obtained from the Fourier spectral ratio of the measured acceleration of the pile top and the input motion. Table 1 lists the predominant frequencies of the model pile according to the test data. The damping ratio of the model pile ranges from 0.7 % to 1.2 % obtained by the back-calculations from the free vibration and forced vibration.

Table 1 Predominant frequencies of the model pile

Mass on pile top	Aluminum pile
	Freq., Hz
No mass	22.9
6 steel disks	2.1

Dynamic characteristics of soil and soil-pile system under small amplitude of shaking

The dynamic characteristics of soil stratum and soil-pile system were evaluated by a series of shaking table tests on the model pile within the saturated sand specimen with small amplitude. Table 2 lists the predominant frequencies of the soil and the soil-pile system for the model pile (with 6 steel disks on its top) in soil of various relative densities. It can be seen that the predominant frequency of soil increases with the relative density, but that of pile increase slightly with the relative density. In addition, the predominant frequency of soil-pile system is significantly lower than that of the soil specimen. Comparing the predominant frequencies of the model pile without and within soil specimen (Table 1 and Table 2, respectively), one can find that, except for the case without mass on the pile top, the predominant frequencies of the model pile in the soil specimen were higher than those without soil due to the constraint of the soil on the pile. Hence, the response of the pile was mainly governed by the inertia force from the 6 steel disks.

Table 2 Predominant frequencies of the soil and the aluminum pile in soil of different relative densities

Density of soil	Predominant frequency , Hz	
Dr, %	Soil	Pile in soil
11.9	10.92	4.61
26.0	11.7	4.64
42.4	12.7	4.65
70.1	13.8	4.67

Response of model pile under laterally spreading

A shaking table test under one-dimensional sinusoidal acceleration with frequency of 8 Hz and amplitude of 0.068 g in the Y-direction (i.e. the input motion was imposed perpendicular to the slope direction) was conducted to study the kinematic effect on the pile foundation in a saturated sloping ground with relative density of 13.6 %. The depth of liquefaction was determined based on the measured pore water pressures in the sand specimen and accelerometers on the frames (Ueng et al., 2010). In this test, the liquefied depth of the sand specimen reached about 112.6 cm. Figure 3 shows a distinct lateral spreading displacement after the shaking. (Compared with Figure 1)

Fig. 3 Liquefaction-induced lateral spreading displacement in X direction

The time histories of relative displacement and trajectory of the pile top are shown in Fig. 4. The X-displacement of the model pile is mainly caused by lateral spreading, whilst the displacement in the other direction is induced by the shaking. Hence, the force exerted on the model pile due to lateral spreading (X-direction) can be extracted from this kind of test. It is also observed that the pile response in the X-direction can be divided into three stages during the shaking. (i) The first stage is only small movement and rebound at 2.2 to 3 seconds. The response of pile is due to the small amount of movement and softening at the shallower depth of soil. (ii) The second stage, pile has the maximum displacement and rebound again at 3 to 4.2 seconds. At this stage, the model pile suffers the majority of liquefaction-induced lateral ground displacement (Fig. 5), and it has its maximum displacement at 3.618 seconds. After this time, the pile rebounds again because of the reduction in lateral force on the pile when the specimen was liquefied. (iii) The pile response at this stage demonstrates a free vibration motion at 4.2 to 8 seconds. The predominant frequency of the acceleration on the pile top in the X-direction is about 2 Hz. Comparing this result with the predominant frequency of the model pile without soil specimen (Table 1), one can find that the predominant frequency of the model pile within liquefied soil was almost the same as that of model pile without soil specimen. This inferred that the stiffness of the soil had nearly dissipated when soil liquefaction occurred.

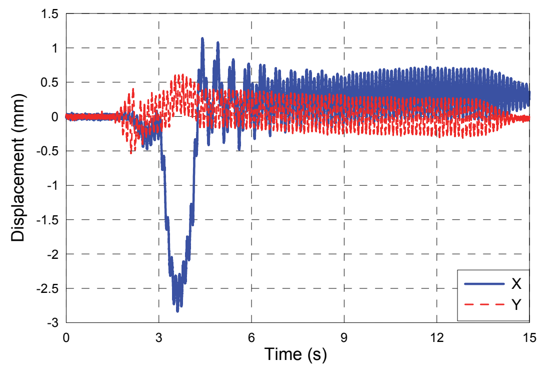

Fig. 4 The time histories of relative displacement of the pile top

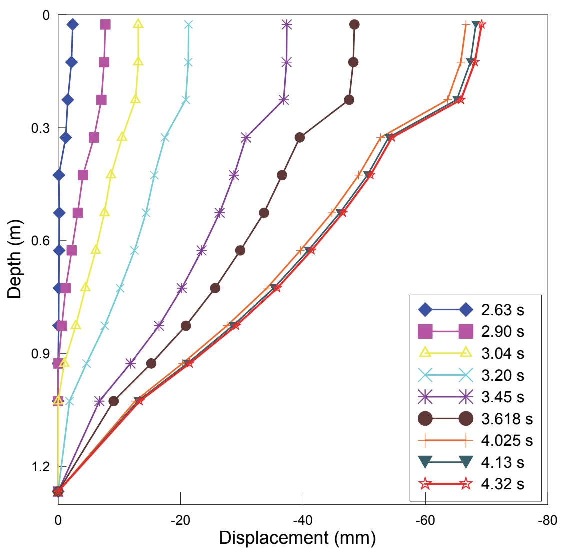

Fig. 5 Profiles of free-field ground at various times in X direction

Conclusions

Shaking table tests were conducted on an aluminum model pile in saturated sloping ground using the biaxial laminar shear box. Analyses of the dynamic behavior of the model pile and the soil stratum were conducted during the shaking tests according to observations. Lateral spreading displacements of the soil and pile behavior were observed while soil liquefaction was triggered under the shaking. It was also found that the kinematic loading on the model pile due to lateral spreading during shaking can be separated individually in a suitable way by using the biaxial shear box. Further analyses of the test data will be performed to obtain more information on the relationship between the mobilized lateral pressure on the pile and the ground movement and the evaluation of bending moment of pile in design.

References

Ashford, S. A., T. Juirnarongrit, T. Sugano and Hamada, M. (2006). "Soil–pile response to blast-induced lateral spreading I: Field Test," Journal of Geotechnical and Geoenvironmental Engineering, Vol.132, No.2, pp.152-162.

Brandenberg, S. J., Boulanger, R. W., Kutter, B. L., and Chang, D. D. (2005). "Behavior of pile foundations in laterally spreading ground during centrifuge tests," Journal of Geotechnical and Geoenvironmental Engineering, Vol.131, No.11, pp.1378-1391.

Cubrinovski, M., Kokusho, T., and Ishihara, K. (2006). "Interpretation from large-scale shake table tests on piles undergoing lateral spreading in liquefied soils," Soil Dynamics and Earthquake Engineering, Vol.26, No.2-4, pp.275-286.

Dobry, R., Abdoun, T., O'Rourke, T. D., and. Goh, S. H.(2003). "Single piles in lateral spreads: field bending moment evaluation," Journal of Geotechnical and Geoenvironmental Engineering, Vol.129, No.10, pp.879-889.

Haigh S. and Madabhushi, G.(2005). "The effects of pile flexibility on pile-loading in laterally spreading slopes," Seismic performance and simulation of pile foundations in liquefied and laterally spreading ground. Vol I.

Madabhushi, G., Knappett, J., and Haigh S. (2010). Design of pile foundations in liquefiable soils, Imperial College Press, U.K.

Tokimatsu, K., Suzuki, H. and Sato, M. (2005). "Effect of inertial and kinematic interaction on seismic behavior of pile with embedded foundations," Soil Dynamics and Earthquake Engineering, Vol.25, No.7-10, pp.753-762.

Ueng, T. S., Wang, M. H., Chen, M. H., Chen, C. H., and Peng, L. H. (2006). "A large biaxial shear box for shaking table tests on saturated sand," Geotechnical Testing Journal, Vol.29, No.1, pp.1-8.

Ueng, T. S., and Chen, C. H. (2010). "Multidirectional shaking table tests on model piles in saturated sand," Seventh International Conference on Physical Modelling in Geotechnics, Vol II pp.1445-1450.

Ueng, T. S., Wu, C. W., Cheng, H. W., and Chen, C.H. (2010). "Settlements of saturated clean sand deposits in shaking table tests," Soil Dynamics and Earthquake Engineering. Vol.30, No.1-2, pp.50-60.

Using the ANSYS/LS-DYNA to Investigate the Seismic Response of Dry Storage Facility for Spent Nuclear Fuel

Cheng-Hsing Chen[1] Hsuan-Chih Yang[2] Yung-Yen Ko[3] Shang-Yi Hsu[4]

陳正興 [1]、楊炫智 [2]、柯永彥 [3]、許尚逸 [4]

Abstract

The management and storage of the high radioactive waste has always been an important subject to maintain the security and running continuously of nuclear power plants. The planning of spent fuel storage including three steps: (1) short term storage; (2) interim storage; and (3) long-term storage. The concept of dry storage system means the spent fuel was stored in cask which is freestanding on a concrete pad. This leads to stability concerns in terms of sliding, rocking or tipping over in an earthquake event. In this study, the ANSYSLS/LS-DYNA code is adopter to analyze the seismic response of the dry storage facility. A 3D coupled finite element model was established, which consisted of a freestanding cask, a concrete pad, the interface friction coefficient and an artificial earthquake. The results show that there is a threshold value of friction coefficient control the fist move of cask to slide or rotation. The friction coefficient between freestanding cask and concrete pad will influence the seismic behavior of cask. The cask will slide and rotation but not tip over during the artificial earthquake. The design and analysis of dry storage facility need to consider the influence of friction coefficient.

Keywords: dry storage facility, friction coefficient, ANSYSLS/LS-DYNA

Introduction

The management and storage of highly radioactive waste has always been an important issue in the safe and continuous operation of nuclear power plants. In Taiwan, the available space of spent fuel pools for short-term storage will be exhausted in a few years, and the location of the final disposal facility has yet to be decided. Therefore, the installation of dry storage facilities for interim storage is necessary. In dry storage facilities, the spent fuel is stored in dry-type storage casks or modules, and these casks/modules are usually free-standing on a concrete pad rather than anchored like other ordinary civil structures. This leads to stability concerns in terms of sliding and rocking in the event of an earthquake [1]. The main considerations for the seismic safety of the free-standing casks/modules are the possible collision between casks/modules due to their horizontal displacement and tipping-over due to the rocking response of the cask during an earthquake [2]. The coefficient of friction must be greater than the breadth-height ratio of the body in order to initiate rocking motions. If the coefficient of friction at the interface is small enough, a rigid block resting on a floor subjected to a strong horizontal ground motion will not jump. A strong dependency relationship between the stability, the aspect ratio (h/r), and size (R) has been established [3、4]. Rabbat etc. also indicate that the coefficient of friction can be influenced by the presence of the mill scale on the steel surface, as well as by the normal pressure applied to the interface [5]. According to previous studies, the coefficient of friction at the interface between the cask and the pad is crucial when determining the seismic response of a free-standing vertical cylindrical cask. However, the difference in the value of the coefficient of friction is considerable between different materials.

In this paper, the seismic behavior of a free-standing vertical cylindrical cask (VCC), which has been widely used in practice, will be investigated

1 Professor, Department of Civil Engineering, National Taiwan University
2 Associate Researcher, National Center for Research on Earthquake Engineering
3 Associate Researcher, National Center for Research on Earthquake Engineering
4 Associate Researcher, National Center for Research on Earthquake Engineering

for various coefficients of friction. Firstly, a quasi-static equilibrium analysis of the cask was performed to examine the basic physics of a VCC. Then, the ANSYS/LS-DYNA code was adopted to analyze the seismic response of a dry storage facility with a VCC. A 3D finite element (FE) model consisting of a VCC and a concrete pad was established with the simulation of the nonlinear frictional contact at their interface. Artificial earthquake motions, which are compatible with the design spectra, was adopted as input motions. The characteristics of the seismic response of a VCC and the influence of the coefficient of friction at the cask/pad interface will be presented and discussed herein.

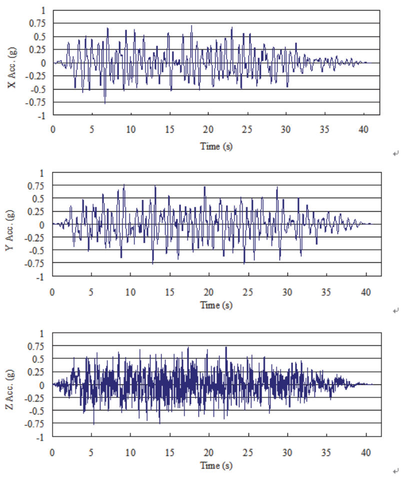

Fig. 1 Pad motions based on the design spectrum in the X, Y, and Z directions

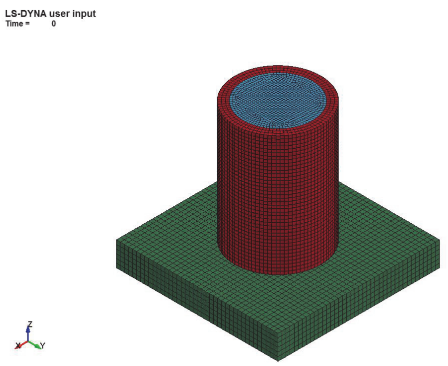

Fig. 2 Finite element model of a cask standing freely on a pad.

Analysis Model and Parameters

Although it is well known that ground motions are one of the most important factors affecting the dynamic response of a shaken system, only one set of time-histories will be specified and inputted to the pad in the current analyses. A 40 second duration artificial earthquake compatible with the design spectrum was established. This is compatible with the design response spectrum of a selected VCC project in Taiwan as shown in Fig. 1. The peak ground accelerations in the X-, Y-, and Z-directions were all scaled to 0.78 g. This is considered to be a very conservative value for this parameter.

A prototype VCC that will be used in Taiwan was selected as an example VCC. The VCC is of a cylindrical type with a diameter of 4.25 m and a height of 5.95 m. It is assumed to be standing freely on a rigid concrete pad with dimensions of 8 m × 8 m and a thickness of 1.2 m. An FE mesh of the model is shown in Fig. 2. The minimum element length was about 0.1 m and the time step for explicit time integration was 2.84×10^{-5} sec. Both of these satisfy the basic requirements for numerical accuracy and stability. In order to save computational effort, the material in the inner cylinder of the cask was assumed to be rigid (Φ3.83 m) and the outer part was assumed to be elastic concrete. Concerning the modeling of the highly nonlinear contact behavior at the interface between the cask and the pad, the "contact_automatic_single_surface" algorithm provided in the LS-DYNA code was used, and Coulomb's law of friction was adopted for the modeling of friction. The coefficients of friction chosen in this analysis were 0.2, 0.5, and 0.8

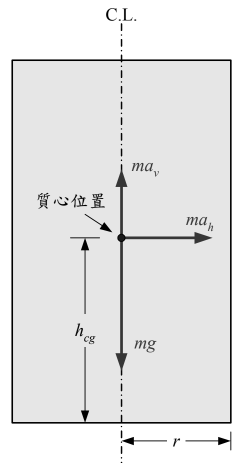

Fig. 3 Free body diagram of a free-standing cask

Fig. 3 shows the free body diagram of a cylindrical cask. The height from the cask base to the center of gravity (CG) is denoted as h_{cg}, and the radius of the cask is denoted as r. The forces applied to the cask include the gravitational force, mg, the horizontal seismic inertial force, ma_h, and the vertical seismic inertial force, ma_v; where m denotes the mass of the cask, g is the acceleration due to gravity, a_h is the horizontal ground acceleration, and a_v is the vertical ground acceleration. The more conservative case of an upward a_v is considered here, and the effective compressive normal force acting on the cask base is $m(g-a_v)$.

When the horizontal seismic inertial force on the cask exceeds the maximum static frictional force at the cask/pad interface, the cask will slide relative to the pad, i.e.,

$$ma_h \geq \mu(mg - ma_v) \;\Rightarrow \mu \leq \frac{a_h}{g - a_v} = a_c \tag{1}$$

When the overturning moment generated by the horizontal seismic inertial force on the cask exceeds the stabilizing moment provided by the effective weight of the cask, one side of the cask will be lifted (rocking) against the contact point between the two bodies, i.e.,

$$ma_h h_{cg} \geq (mg - ma_v)r \quad \Rightarrow \frac{r}{h_{cg}} \leq \frac{a_h}{g - a_v} = a_c \tag{2}$$

For cases with $\mu > (r/h_{cg})$, the rocking motion of the cask will be induced whenever $a_c > (r/h_{cg})$. For the VCC model selected, since r=2.125 m and h_{cg}=2.975 m, the ratio of r/h_{cg} is 0.714 in this case. According to the quasi-static equilibrium analysis, this can be regarded as a borderline value of the frictional coefficient, differentiating the motion type of the cask between sliding and rocking. Therefore, the response of the cask is pure sliding without any tip-over for cases with μ = 0.2 and 0.5, while it is dominated by a rocking type motion at μ = 0.8. This can be verified via the dynamic analysis.

Seismic Responses of the VCC

For the corresponding cases, the loci of horizontal displacements at the center of the base and the center of the top of the cask are plotted in Fig. 4, in which the solid line represents the loci of horizontal displacements at the center of the base of the cask, and the dotted line represents the loci of horizontal displacements at the center of the top of the cask. For all analyzed cases, the maximum and residual translational displacements at the center of the base of the cask are summarized in Table 1. The maximum rocking angle and the maximum and residual rotational angles of the cask were also calculated and are shown in Table 1.

To characterize the response of the cask under the conditions of various coefficients of friction, the key response to be considered is the vertical (Z) displacement. From the results shown in Figs. 4 and Table 1, it can be noted that the vertical (Z) displacements at the center of the base of the cask are equal to zero for cases with μ = 0.2 and 0.5, and are not equal to zero for cases with μ = 0.8. The former means that the cask's motion type is purely sliding and the latter means that the cask's motion includes the rocking response

Table 1 Maximum and residual seismic responses of the cask

	Relative displacement (m)					Rocking angle (deg)	
μ	X		Y		Z	X-dir.	Y-dir.
	Max	Final	Max	Final	Max		
0.2	0.40	-0.12	0.40	0.03	-	-	-
0.5	0.17	0.02	-0.12	0.08	-	-	-
0.8	-0.41	0.21	-0.27	0.03	0.28	7.16	-4.90

Fig. 4(a) and 4(b) show that the loci of horizontal displacements at the center of the top of the cask coincide with those at the center of the base of the cask. Therefore, the responses of the cask are almost purely sliding with minimal rocking motion for cases with μ = 0.2 and 0.5. When μ = 0.2 and 0.5, the magnitude of the maximum horizontal displacement of the cask decreases significantly as the coefficient of friction increases. This is due to the fact that the resisting force of friction at the cask/pad interface increases with the magnitude of the coefficient of friction. However, no significant relationship between the residual displacement and the coefficient of friction was observed. Since the residual displacement is the accumulation of the dynamic response (back and forth) of the cask during the foundation excitation, it is not necessarily related to the coefficient of friction.

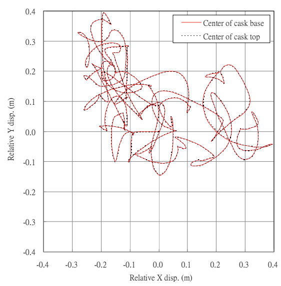

(a) μ = 0.2

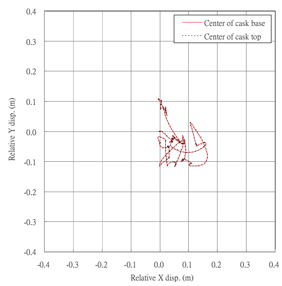

(b) μ = 0.5

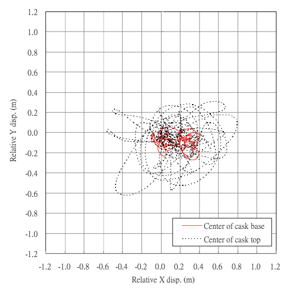

(c) μ = 0.8

Fig. 4 Horizontal displacement locus of the cask for μ = 0.2, 0.5 and 0.8

.

Fig. 4(c) shows the loci of horizontal displacements at the center of the top and the center of the base of the cask for the case of $\mu = 0.8$. The larger Z-displacement implies that the response of the cask was dominated by the rocking motion, yet the significant horizontal displacements may not result from sliding. The cask top experienced a much larger displacement than the base due to the rocking motion. In addition, the cask exhibited a rolling behavior following the rocking motion. That is, when the cylindrical cask was uplifted on one side, it could roll along the circumference of the cask's bottom edge.

As mentioned in the previous section, the ratio r/h_{cg} is a borderline value of the coefficient of friction that differentiates the motion type of the cask at the onset of motion between sliding and rocking from the rigid-body quasi-static equilibrium analysis. For the cask adopted in this case study, the value of r/h_{cg} was 0.714. Therefore, from the results of the dynamic analysis, the motion of the VCC during the excitation changed from a sliding to a rocking response when the coefficient of friction changed from 0.6 to 0.8.

Conclusions

Based on the results obtained in this study, some general conclusions can be drawn as follows:

1. According to the rigid-body quasi-static equilibrium analysis, the r/h_{cg} value of a vertical cylindrical cask (VCC) represents a borderline value of the coefficient of friction that differentiates the motion type of the cask at the onset of motion between sliding and rocking.
2. The results of the case study show that for $\mu = 0.2$ and 0.5, the cask response was almost purely sliding, and the maximum horizontal displacement of the VCC decreased significantly as the coefficient of friction increased.
3. For the aseismic design of a dry storage cask, it is suggested to allow the sliding motion but to prevent the rocking motion. This can be achieved by setting an appropriate coefficient of friction at the cask/pad interface

References

Toshiari Saegusa, Genki Yagawa, and Masanori Aritomi, "Topics of research and development on concrete cask storage of spent nuclear fuel," Nuclear Engineering and Design, Vol. 238, pp. 1168-1174 (2008).

Yuji Ishiyama, "Motions of Rigid Bodies and Criteria for Overturning by Earthquake Excitations," Earthquake Engineering and Structural Dynamics, Vol. 10, pp. 635-650 (1982).

Lin Yanheng and Shi Baoping, "Response of 3D Free Axisymmetrical Rigid Objects under Seismic Excitations," New Journal of Physics, arXiv:0807.2101v3 (2008).

Antonio Scalia and Mezhlum A. Sumbatyan, "Slide Rotation of Rigid Bodies subjected to a Horizontal Ground Motion," Earthquake Engineering and Structural Dynamics, Vol. 25, pp. 1139-1149 (1996).

B. G. Rabbat, M. ASCE and H. G. Russell, "Friction Coefficient of Steel on Concrete or Grout," Journal of Structural Engineering. ASCE, Vol. 111, No. 3, pp. 505-515 (1985).

Centrifuge Shaking Table Tests on the Seismic Responses of Geosynthetic Reinforced Earth Embankments

Wen-Yi Hung [1] , Yi-Zeng, Chiou[2], Jin-Hung Hwang[3], Chung-Jung Lee[4] and Jiunn-Shyang Chiou[5]

洪汶宜 [1] 邱益增 [2] 黃俊鴻 [3] 李崇正 [4] 邱俊翔 [5]

Abstract

A series of centrifuge shaking table tests are performed to study the seismic behavior of geosynthetic reinforced earth (GRE) embankments. From the test results, for an 8-m-high GRE embankment, the natural frequency is found to be about 5.7 Hz and has no significant relationships with the reinforcement material, the reinforcement arrangement, or the facing batter. The amplification of the acceleration increases with increasing elevation and with increasing frequency of the input motion. At the same elevation, the amplification inside the reinforced earth zone is found to be larger than that inside the retained soil zone.

Keywords: Centrifuge; embankment; natural frequency; amplification

Introduction

Reinforced earth is generally constructed with backfill and manufactured materials, such as metal strips, geosynthetic sheets or grids, known as reinforcements. The reinforcements sustain the forces resulting from the deformation of reinforced earth structures and external loadings. The biggest advantage of reinforced earth structures over reinforced concrete structures is in their flexibility and capacity to absorb deformation due to poor foundations and seismic loadings. A series of centrifuge modeling tests were performed by Viswanadham and Kong (2009) to investigate the effect of differential settlement in the foundation on a reinforced earth slope with a flexible facing. The advantages of geosynthetic reinforced structures were verified from the test results. It was indicated that even after inducing a differential settlement of 1.0 m in prototype dimensions, the reinforced soil structure was not found to experience a collapse failure.

In addition, observations made after the Chi-Chi earthquake in Taiwan or the Hanshin-Awaji earthquake in Japan showed that most reinforced soil structures survived without serious damage, demonstrating an earthquake-resistant capability. The seismic behaviors of reinforced earth walls and slopes were studied by Nova-Roessig and Sitar (2006) using a centrifuge shaking table. The models were subjected to maximum input accelerations of up to 1.08 g. The experimental results showed that reinforced slopes move under small input motions and that significant lateral and vertical deformations occur under strong shaking, but the distinct failure surfaces were not observed. The magnitude of the deformations is related to the backfill density, the reinforcement stiffness and spacing, and the slope inclination.

It was also found from other past studies that the design of the reinforcement, including its length, spacing, and strength, significantly affects geosynthetic reinforced earth (GRE) structures (Hu et al., 2010; Chen et al., 2007). Therefore, in this research, a series of centrifuge shaking table tests was performed in a 50 g acceleration field to investigate the effects of the reinforcement design on the seismic response of GRE embankments, including the natural frequency and the amplification of acceleration.

[1] Associate technologist, National Center for Research on Earthquake Engineering, wyhung@ncree.narl.org.tw
[2] Master, Department of Civil Engineering, National Central University, h87727@yahoo.com.tw
[3] Professor, Department of Civil Engineering, National Central University, hwangjin@ncu.edu.tw
[4] Professor, Department of Civil Engineering, National Central University, cjleeciv@ncu.edu.tw
[5] Researcher, National Center for Research on Earthquake Engineering, jschiou@ncree.narl.org.tw

Testing Equipment and Materials

This experimental work was undertaken in the centrifuge modeling laboratory at the National Central University (NCU) of Taiwan. The NCU centrifuge has a nominal radius of 3 m and a one-dimensional servo-hydraulically controlled shaker is installed in a swing basket. It has a maximum nominal shaking force of 53.4 kN with a maximum table displacement of ±6.4 mm and it operates at up to an 80 g centrifugal acceleration with a model weight of 400 kg. The operating frequency range is 0 Hz to 250 Hz. A rigid model container with inner dimensions of 767 mm × 355 mm × 400 mm (L × W × H) is used for dry soil models.

The sand used to prepare the uniform sandy model consists of fine quartz. The quartz sand is pluviated into the rigid model container and the falling height was maintained at 0.6 m to prepare the uniform models with a relative density of about 60%. Two very weak geosynthetic materials with tensile strengths, T_u, of 1.25 kN/m and 2.24 kN/m were selected to simulate the prototype reinforcement materials with strengths of 62.5 kN/m and 112.0 kN/m, respectively, in a 50 g acceleration field.

Table 1 The configurations of GRE embankment models

No.	Width (m)	Height (m)	Slope	s_v (m)	T_u (kN/m)
GREE4	18.35	8.0	1:1.0	0.8	112.0
GREE5	18.35	8.0	1:0.5	0.8	112.0
GREE6	18.35	8.0	1:0.5	0.8	62.5
GREE8	18.35	8.0	1:1.0	0.5	112.0
GREE9	18.35	8.0	1:0.5	0.5	112.0

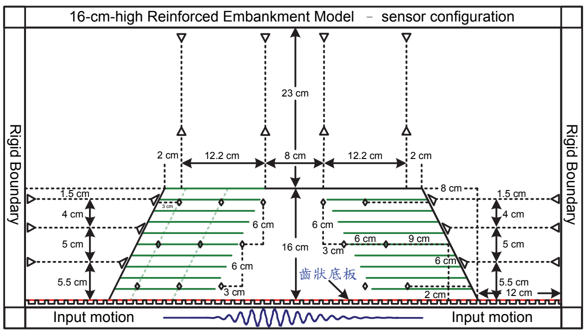

Fig. 1 The profile and the configuration of sensors for model GREE5

Model Setup and Testing Procedures

The GRE embankment models were wrapped-face with 100% coverage of reinforcement material. The purpose of this study was to investigate the effects of the reinforcement spacing, s_v, and the face inclination on the seismic response of the GRE embankment induced by different input motions. In the design of GRE embankment models, the external and internal stabilities of the structure must be ensured. Consequently, a tooth-shaped aluminum alloy plate was installed at the bottom of the rigid model container to prevent the model sliding during shaking. Above the tooth-shaped plate, the 10-mm-thick sandy foundation was firm.

The configurations of five GRE embankment models are shown in Table 1 in prototype scale. The height and the top width of the GRE embankment models were made to be 160 mm and 367 mm, respectively, to scale the model to GRE embankment prototype, which is 8-m-high and 18.35-m-wide. The reinforcement length was 0.71 times the height and the overlap length was 0.4 times the reinforcement length. Two face inclinations of 1.0:1.0 (vertical:horizontal) and 1.0:0.5 (vertical:horizontal) and two reinforcement spacings of 16 mm and 10 mm, which correspond to 0.8 m and 0.5 m in the prototype, respectively, were selected.

For instance, Figure 1 shows the profile and the configuration of the sensors for model GREE5. For each model, seven accelerometers were installed, including one fixed onto the shaking table to monitor the input motion, and two accelerometer arrays were instrumented inside the retained soil zone (A6–A4–A12) and inside the reinforced earth zone (A11–A13–A10). Eight linear variable differential transformers were placed to measure the settlement on top of the embankment and the horizontal displacement of the facing.

During the construction of the GRE embankment model, several pieces of hard Styrofoam boards were piled up in front of the model to provide lateral support. For each reinforcement layer, the reinforcement material was placed first followed by pluviating the sand to construct the retained soil and the reinforced earth zones until the desired reinforcement spacing was attained. The accelerometers were placed in their proper positions inside the model simultaneously. Then the reinforcement was wrapped to produce the facing and embedded into the backfill. This process was repeated until it reached the design height. Finally, the weight of the model was measured to check its relative density. The completed model was then put on the platform and fixed on the shaking table to start the centrifuge modeling processes.

The completed model was accelerated stepwise to 50 g, with an increment of acceleration in each step of 10 g. The model was maintained and preserved for 3 minutes at each step to ensure the consolidation of the sand model at the current overburden pressure. At 50 g, the model was then excited with a series of one-dimensional seismic events. First, white noise input motion was applied to detect the natural frequency of the GRE embankment system. Next, two series of seismic events with frequencies of 1 Hz and 4.8 Hz (in the prototype) were applied to the models with a sinusoidal input motion consisting of 15 cycles.

Natural Frequency of the GRE Embankment

The acceleration histories obtained from the white noise input motion were adopted and the Fast Fourier Transform was used to transfer the data to the frequency domain. Then, the Fourier spectrum of each accelerometer was divided by that of the base input motions to create transfer function, which gives the amplification of the acceleration at different frequencies. The frequency at the first peak of the transfer function was at the natural frequency of the GRE embankment system. Based on these calculations, it was found that the natural frequency for all the models was about 5.7 Hz, meaning that the reinforcement spacing and the face inclination did not affect the natural frequency of the GRE embankment. Thus, the natural frequency for an 8-m-high GRE embankment is also about 5.7 Hz. On the other hand, the transfer function at the 1 Hz input motions for different elevations were close to 1, illustrating that the acceleration was not amplified. At a 4.8 Hz frequency, significantly different values of the transfer functions were observed, leading to different amplifications of acceleration at varying elevations. In the following section, the amplifications of accelerations are calculated directly from the acceleration responses of different seismic events.

Amplification of Acceleration of the GRE Embankment

There are 30 data points for each accelerometer in each seismic event, including the positive and negative peaks of the 15 cycles. The peak values of input motion and the measurements by the accelerometer are converted to absolute values and plotted in Figures 2, 3, and 4 according to the top, middle, and bottom of the GRE embankment, respectively. Figures 2(a) and 2(b) indicate the relationships between the base input motion and the responses of acceleration at the top of the retained soil zone and reinforced earth zone, respectively. In these figures, the circular, triangular, diamond and inverted triangular symbols represent the peak accelerations for the models GREE4, GREE5, GREE8, and GREE9, respectively. The hollow and solid symbols represent the input motions of 1 Hz and 4.8 Hz, respectively. If the symbols are located at the left of the solid black line, this means that the acceleration was amplified. By comparing Figures 2, 3, and 4, it can be seen that the trends of all the hollow symbols are almost parallel to the solid line. Consequently, the different reinforcement spacing and the face inclination do not seem to affect the amplification of the acceleration significantly for GRE embankments subjected to 1 Hz seismic loadings.

On the other hand, when comparing Figures 2(a), 3(a), and 4(a), or Figures 2(b), 3(b), and 4(b), it can be seen that the accelerations are amplified with increasing elevations inside either the retained soil zone or the reinforced earth zone for GRE embankments subjected to 4.8 Hz seismic loadings. Nevertheless, the amplifications inside the reinforced earth zone were slightly larger than those inside the retained earth zone. There are several solid symbols located in the intermediate zone surrounded by a red ellipse in Figures 2(a), 2(b), 3(a), and 3(b). These are the first peak accelerations of seismic events with a frequency of 4.8 Hz and are usually smaller than the peak values in the other cycles. Aside from the data points of the first cycle, the trend for all solid symbols seems to lie on a line that is steeper than the black line. This shows that the seismic response of the GRE embankment is not related to the reinforcement spacing and the face inclination.

The measurements of each seismic event are divided into the responses of the retained soil zone and the reinforced earth zone, as shown in Figures 5 and 6, respectively. Figure 5 shows the relationships between the elevation normalized by height and the mean values of the amplification for the retained soil zone. The hollow symbols in Figures 2, 3, and 4 are graded into three input motions with a frequency of 1 Hz. These grades are relative: small, middle, and large accelerations which correspond to mean accelerations of 0.056 g, 0.111 g and 0.199 g labeled in the figures as hollow circles, squares, and triangles, respectively. It can be seen that the mean amplifications increase slightly with increasing elevation. In addition, a smaller input acceleration seems to lead to larger amplification. The maximum amplification was found to be about 1.3 at the top of the retained soil zone for an 8-m-high GRE embankment subjected to 1 Hz at an approximately 0.056 g seismic loading. The solid symbols in Figures 2, 3, and 4 are also graded into three input motions with a frequency of 4.8 Hz. The mean accelerations are 0.015 g, 0.037 g, and 0.086 g and are labeled by solid circles, squares, and triangles, respectively. It can be observed that, in these tests, the mean amplification increases dramatically with increasing elevation when the input motion frequency was raised to 4.8 Hz. The amplification at the top was about 4.5 for the input motion of 0.037 g, which is larger than that for the input motion of 0.086 g.

Figure 6 shows the relationships between the elevation normalized by height and the mean values of the amplification for the reinforced earth zone. It also can be seen that the mean amplifications increase slightly with increasing elevation. The smaller input acceleration leads to the larger amplification with a maximum value of 1.4 at the top of the reinforced earth zone for an 8-m-high GRE embankment subjected to 1 Hz and 0.056 g seismic loadings. The mean amplification increases dramatically with increasing elevation for input motions with a frequency of 4.8 Hz. The maximum amplification at the top is about 5.5 for the input motion of 0.037 g.

Consequently, if a constant amplification of acceleration is used to design a GRE embankment, the results would underestimate the seismic behavior at the top portion of the GRE embankment as the frequency of the input motion is close to the natural frequency of system.

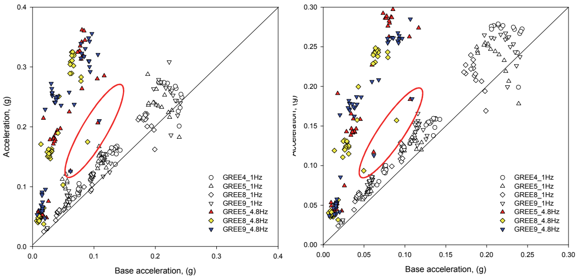

Fig. 2 The relationships of the base input motion and the acceleration measured at the top of (a) retained soil zone; (b) reinforced zone

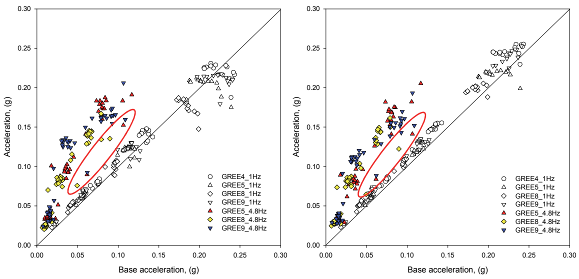

Fig. 3 The relationships of the base input motion and the acceleration measured at the medium of (a) retained soil zone; (b) reinforced zone

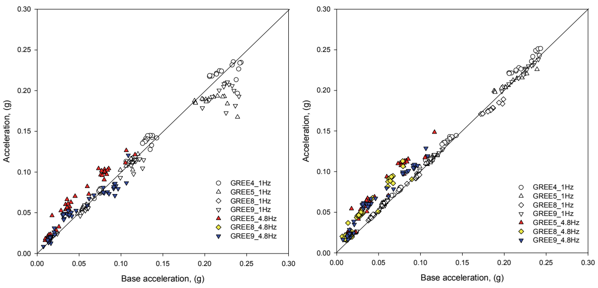

Fig. 4 The relationships of the base input motion and the acceleration measured at the bottom of (a) retained soil zone; (b) reinforced zone

Conclusions

A series of centrifuge shaking table tests was performed to investigate the seismic response of geosynthetic reinforced earth (GRE) embankment with different reinforcement spacing and face inclination. The test results show that for an 8 m-high GRE embankment, the natural frequency is about 5.7Hz and has no significant relationships with the reinforcement material, the reinforcement arrangement and the batter of facing. The amplification of acceleration increases with the increasing elevation and with the increasing frequency of input motion. At the same elevation, the amplification inside the reinforced earth zone is larger than that inside the retained soil zone. It tells that the uniform distribution of amplification with height assumed in the current design guidelines may underestimate that at top of GRE embankment and result in overestimating the local stability.

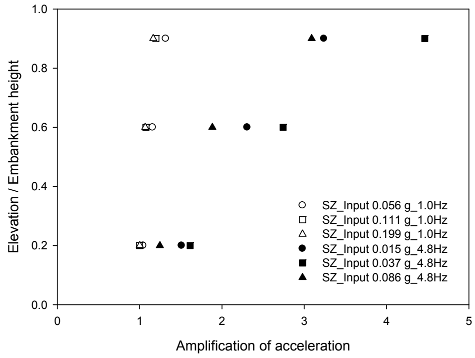

Fig. 5 The amplification of acceleration inside the retained soil zone for different input motions

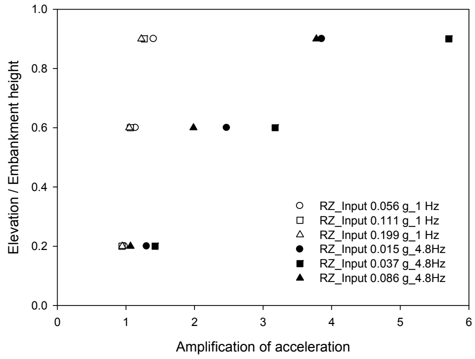

Fig. 6 The amplification of acceleration inside the reinforced zone for different input motions

References

Chen, H.T., Hung, W.Y., Chang, C.C., Chen, Y.J and Lee, C.J, (2007) “Centrifuge modeling test of a geotextile-reinforced wall with a very wet clayey backfill.” *Geotextiles and Geomembranes*, 25(6), pp. 346–359.

Hu, Y., Zhang, G., and Lee, C.F., (2010) “Centrifuge modeling of geotextile-reinforced cohesive slopes,” *Geotextiles and Geomembranes*, 28, pp.12-22.

Nova-Roessig, L., and Sitar, N., (2006) “Centrifuge model studies of the seismic response of reinforced soil slope,” *Journal of Geotechnical and Geoenvironmental Engineering*, ASCE, 132(3), pp.388-400.

Viswanadham, B.V.S., and Kong, D., (2009) “Centrifuge modeling of geotextile-reinforced slopes subjected to differential settlements,” *Geotextiles and Geomembranes*, 27, pp.77-88.

Earthquake Source Parameters of Active Faults for Seismic Potential Assessment in the Chianan Region of Taiwan

Che-Min Lin[1], Tao-Ming Chang[2], Hung-Hao Hsieh[3], Yi-Zen Chang[4], Chun-Hsiang Kuo[5], and Kuo-Liang Wen[6]

林哲民 [1]、張道明 [2]、謝宏灝 [3]、張議仁 [4]、郭俊翔 [5]、溫國樑 [6]

Abstract

The Chiayi and Tainan (Chianan) regions in southwestern Taiwan are scattered by several active faults that have induced massive earthquakes. The seismicity is generally quite high and widespread in this region. The potential of disastrous earthquakes is expected to be high in the near future. Therefore, the present study aims to monitor micro-earthquakes activity in the Chianan region for three years. The monitoring data will provide important information about recent seismicity and the source parameters of active faults, which are indispensable in assessing the seismic potential for the Chianan region. Twenty-one highly-sensitive broadband stations were installed to develop a regional network covering the Chiayi County and City, Tainan City, and adjacent foothills, as well as the adjoining major seismogenic area. Almost 1,200 earthquakes were observed by this network in the first two years. The data were processed and analyzed periodically to evaluate the seismicity of the Chianan region. The earthquake relocations and focal mechanism solutions were also studied to understand the probable seismogenic structures and source ruptures.

Keywords: earthquake monitoring, active fault, earthquake location, focal mechanism

Introduction

The Chiayi and Tainan (Chianan) region in southwestern Taiwan has witnessed numerous serious disasters caused by massive earthquakes, including the Meishan Earthquake in 1906, Chungpu Earthquake in 1941, Hsinhua Earthquake in 1946, Paiho Earthquake in 1964, Rueyli Earthquake in 1998, and the Chiayi Earthquake in 1999, all occurring within the last century. More recently, the Jiasian Earthquake occurred in Kaohsiung with a magnitude of M_L 6.7 and also caused damage to some buildings in the Chianan region. According to the paleoseismological research of the National Science Council (NSC), the Meishan Fault in Chiayi has the highest short-term probability of experiencing a characteristic earthquake amongst all active category one faults in Taiwan. The probabilities of earthquakes from faults with magnitudes of 7 or more within 10 and 50 years are respectively 9.75 % and 45 %. Additionally, there are still four other active category one faults of the first category and four category two faults rooted in the Chianan region. Since potential disastrous earthquakes in the region are expected in the near future, it is imperative to understand the characteristics of the active faults in the Chianan region.

Based on the Central Weather Bureau (CWB) earthquake catalog and the micro-earthquake monitoring in the Southern Taiwan Science Park from the end of 2006 to 2010 (Lin et al., 2010), the seismicity was widely distributed over the Chianan region. The earthquakes were not restricted only to the faults but occurred frequently between the foothills on the east side and the coastal plain on the west. The

[1] Associate Researcher, National Center for Research on Earthquake Engineering, cmlin@ncree.narl.org.tw
[2] Associate Researcher, National Center for Research on Earthquake Engineering, tmchang@ncree.narl.org.tw
[3] Assistant Researcher, National Center for Research on Earthquake Engineering, hhhsieh@ncree.narl.org.tw
[4] Assistant Researcher, National Center for Research on Earthquake Engineering, yzchang@ncree.narl.org.tw
[5] Associate Researcher, National Center for Research on Earthquake Engineering, chkuo@ncree.narl.org.tw
[6] Professor, Dep. of Earth Science, National Central University and Division Manager, National Center for Research on Earthquake Engineering, wenkl@ncree.narl.org.tw

western seismicity beneath the coastal plain was thought to result from the tectonic escape behavior of plate collision. However, the thick alluvial cover on the surface limits understanding of the underground seismogenic structures.

Therefore, this study planned to monitor micro-earthquakes in the Chianan region for three years. The objects that were monitored were not only the active faults, but also blind faults and other seismogenic structures beneath the wide coastal plain. A study of micro-earthquakes will help researchers to understand the probable fault planes and rupture mechanisms of major faults. The source parameters of characteristic earthquakes will be estimated to assess the seismic potential of the Chianan region. The preliminary results of the monitoring in the first two years will be discussed in this article.

Micro-Earthquake Monitoring Network in the Chianan Region

The development and planning of the micro-earthquake monitoring network in the Chianan region was based on the distributions of historical earthquakes and major fault lines. Twenty-one stations were installed to develop the network in the second half of 2011. In addition, several real-time stations were also installed in the Chianan region. Each real-time station was installed with a broadband velocimeter and an accelerometer. The combined monitoring data provides complete ground motion information for the region.

Figure 1 shows the distributions of all seismic stations, including the National Center for Research on Earthquake Engineering (NCREE) strong-motion and micro-earthquake networks, used in this study. Because the seismicity was widely distributed over the Chianan region, the integrated network covered the Chiayi County and City, Tainan City, and adjacent foothills over which the faults were spread. The network provides a complete ability to monitor the seismicity for research on the characteristics of faults and seismic sources in the Chianan region.

This study benefitted from the rich experience that the group acquired conducting installations and monitoring of micro-earthquakes in the Science Parks over the past few years. A standard operating procedure was created to avoid artificial noise. The station locations were all chosen with caution and the background noise was continuously accounted for to ensure the data quality. Then, the seismometer, set in a bucket, was buried at a depth of at least 1 m. To increase the quality of the incident seismic waves, a cement foundation sat on the bottom of the bucket and several long nails were used to fix the bucket in the bottom of the hole. In doing so, the rims of the bucket, in which the seismometer was placed, were able to avoid touching the surrounding soils of the hole and decrease the surface noise. The moisture proofing and heat insulation aided in keeping a stable monitoring operation.

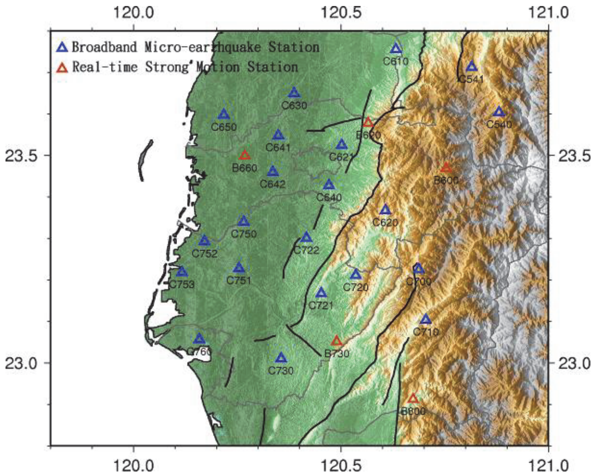

Fig. 1 The distribution of the monitoring networks in the Chianan region

Because this project concentrated on small earthquakes with magnitude lower than 3 in order to observe potential insignificant tremors related to the faults, high-sensitivity broadband seismometers (CMG-6TD, Guralp Systems Ltd) were used in the micro-earthquake network to collect the weak seismic waves. The recording was carried out continuously with a sampling rate of 100 points per second to avoid missing any micro-earthquakes. A set of solar energy equipment and a GPS antenna were installed at each station to supply electricity and correct the internal clock of the seismometer. The photos in Fig. 2 show the installation set up of a station in the field. For a real-time strong motion station, a broadband seismometer and an extra accelerometer (Etna, Kinemetrics), which was installed in a FRP station, were set up together.

Fig. 2 Photos of the micro-earthquake monitoring stations

Data Processing

The data processing was based on a program developed by NCREE for the micro-earthquake monitoring network (Chang, 2009). The data conversion, earthquake selection, arrival time picking and earthquake location are all included in the program. The preliminary location for each earthquake was determined using the program HYPO 71 (Lee and Lahr, 1972) to estimate the origin time, epicenter location, focal depth and duration magnitudes (M_d) based on the arrival times of the P- and S-waves. Every two months, the data were collated and processed to locate any observed micro-earthquakes. The monthly micro-earthquake activity was compared against the CWB seismic catalog to assess the current status and any variation in the seismicity in the Chianan region.

To reduce location errors, a double-difference hypocenter location program (hypoDD) was used to relocate the earthquakes observed by the network. This program incorporates ordinary absolute travel-time measurements and cross-correlation P- and S-wave differential travel-time measurements to determine high-resolution hypocenter locations for an earthquake sequence. The location method collapses diffuse locations into sharp images of seismicity and reveals seismogenic structures.

Micro-earthquake Activity

Figure 3 shows the distribution of almost 1200 micro-earthquakes located by the Chianan network before November, 2012. The micro-earthquakes observed this year exhibited a widespread and frequent distribution within the monitoring scope of the network, as expected. In the northern part of the monitoring region, the Chiayi region, the earthquakes concentrated in the eastern side of the Tachienshan and Chukou Faults. Some earthquakes also took place east of Chiayi City. Meanwhile, the seismicity was quiet near the Meishan and Hsinhua Faults, which were dislocated and have induced destructive earthquakes in the past. In Tainan City, in the southern part of the region, high seismicity was heavily located along the Chukou, Muchiliao, and Liuchia Faults and extended to the southeast of the northern Chishan Fault. Earthquakes occurred on both sides of these faults and were uniformly concentrated along the fault traces to form a wide NW–SE trending seismic zone. The seismic zone extends to the border between Kaohsiung and Taitung. The high seismicity may result from a broken local structure.

The mainshock region of the Jiasian earthquake, which occurred on 3rd March 2010, in the south of the network continued to induce small earthquakes. The small earthquakes show a NW–SE trend from the middle of the Chishan Fault that crosses the Liukuei and Chaochou Faults. It indicated that the seismogenic structure of the Jiasian earthquake is still active to release the tectonic stress.

Some 368 earthquakes were relocated by hypoDD and are shown in Fig. 4. There are two obvious lines of relocated earthquakes, including the seismicity along the east side of the Chukou Fault and the mainshock region, which has just been discussed. The Chukou Fault is an active thrust category one fault. The revised length of this fault is 28 km. It connects with the Tachienshan Fault at the northern end. The original southern part of the Chukou Fault, with the length of 48 km, has been renamed as the Lunghou Fault and is believed to be inactive. The east side of the Chukou and Lunghou Faults shows dense seismicity in comparison to the west side. The earthquake linearity begins at the northern end of the Chukou Fault and stops at the Zengwun River at southern Lunghou fault.

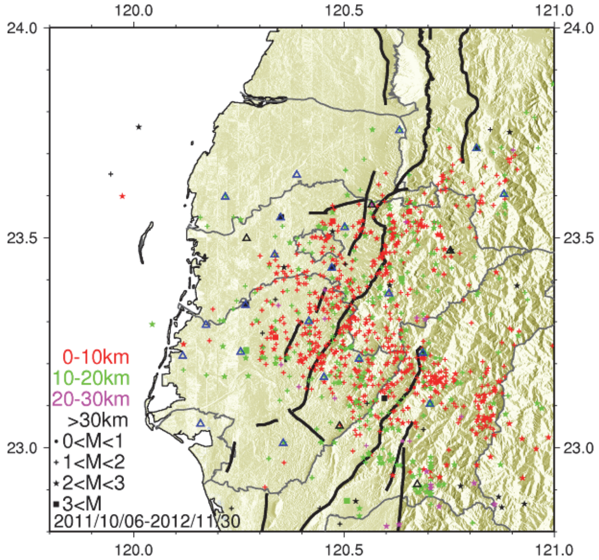

Fig. 3 The earthquakes located by the Chianan micro-earthquake monitoring network before November, 2012

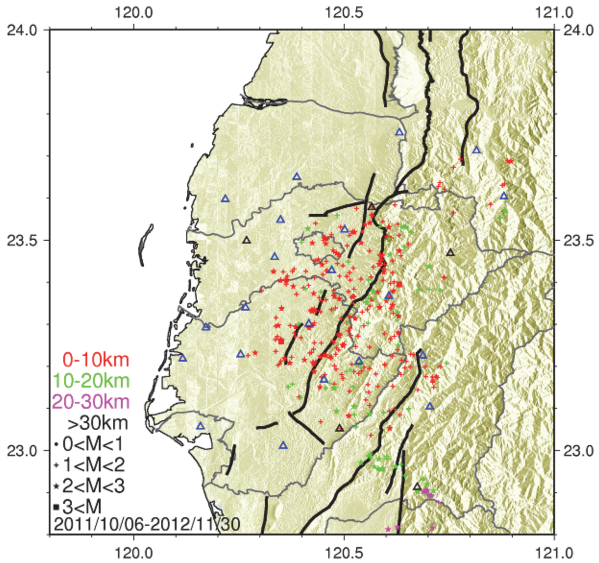

Fig. 4 Double-difference locations of earthquakes

Furthermore, a M_L 4.2 earthquake occurred at the eastern side of the northern end of the Chukou Fault on 18th January 2012 (Fig. 5). The Chianan micro-earthquake monitoring network observed some aftershocks over the next few days. The mainshock focal mechanism and the double-difference hypocenter relocations of the aftershocks are shown in Fig. 6. An E–W cross-section view of the hypocenters is shown in Fig. 7. The relocated aftershocks indicate an E–W–striking source rupture plane dipping toward the east with a high angle. The rupture plane agrees with the mainshock focal mechanism. The upward extension of the plane is close to the fault trace of the Chukou Fault on the surface. These verify that the M_L 4.2 earthquake and its aftershocks were induced by the partial activity of the Chukou Fault.

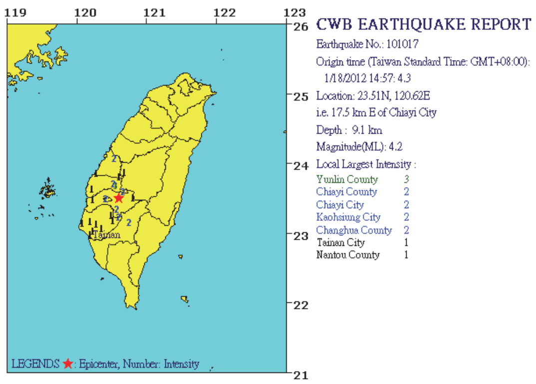

Fig. 5 The CWB report for the M_L 4.2 earthquake that occurred on 18th January 2012

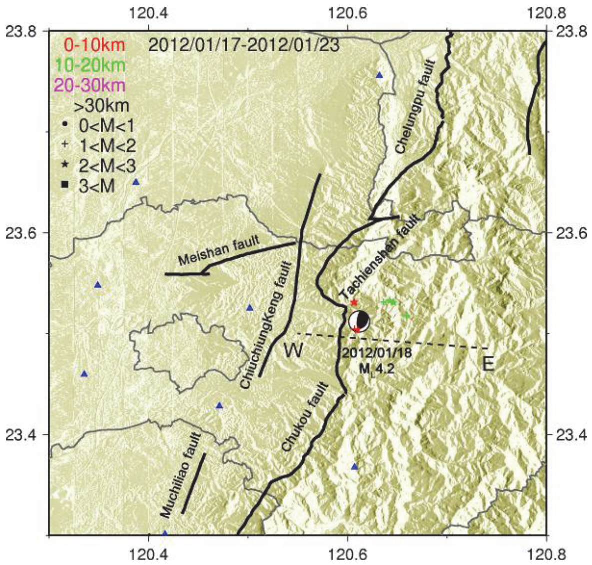

Fig. 6 The CWB mainshock focal mechanism and aftershocks, relocated by this study, of the 18th January 2012 M_L 4.2 earthquake.

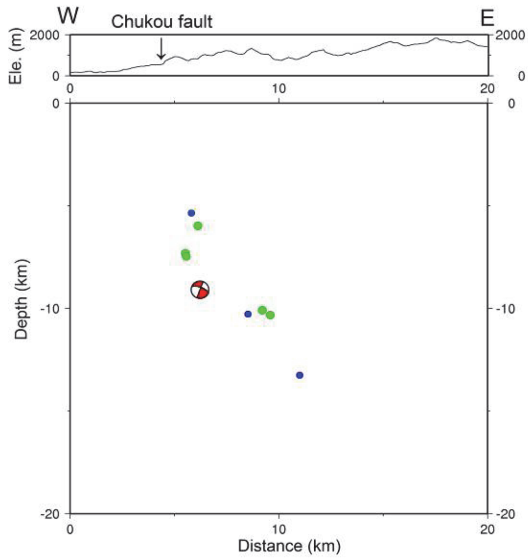

Fig. 7 The E–W cross-section of the dashed line in Fig. 6

Conclusions

The establishment of the Chianan micro-earthquake monitoring network has been accomplished for long-term, high-resolution, seismic monitoring. The network is currently able to detect abnormal seismicity in order to achieve the goals of disaster prevention. The earthquake relocations and the focal mechanism solutions were also studied to understand the seismogenic structures and source ruptures in the region. The monitoring data will provide important information on recent seismicity and the source parameters of active faults that will be indispensable in assessing the seismic potential for the Chianan region.

References

Chang, T. M. (2009), "Earthquake data processing system installation and using guide", NCREE Rep., NCREE-09-066. (In Chinese)

Lee, W.H.K. and Lahe, J. C. (1972), "Hypo71：A computer program for determining hypocenter, magnitude, and first motion pattern for local earthquakes", USGS open file Rep., 100pp.

Lin, C. M., Chang, T. M., Wen, K. L., Hsienh, H. H., Chen, A. B., Chang, L. C., and Kuo, C. H. (2010), "Micro-Earthquake Monitoring of Science Parks in Taiwan", NCREE Rep., NCREE-10-020. (In Chinese)

Waldhauser, F. and Ellsworth, W. L. (2000), "A double-difference earthquake location Algorithm: method and application to the northern Hayward fault, California", Bull. Seism. Soc. Am., 90, 1353-1368.

Analysis of Site Effects using Microtremor in Kaohsiung and Pingtung

Chun-Hsiang Kuo[1], Kuo-Liang Wen[2], Che-Min Lin[3], and Hung-Hao Hsieh[4]

郭俊翔 [1]、溫國樑 [2]、林哲民 [3]、謝宏灝 [4]

Abstract

Microtremor is one of noninvasive methods which are usually used to estimate site effects. The Engineering Geological Database for TSMIP (EGDT) was used in this study as well as measured microtremor at free-field strong motion stations in Kaohsiung and Pingtung to analyze site effects. The dominant frequencies of the Horizontal to Vertical Spectral Ratio (HVSR) of microtremor were proportional to the Vs30 value. The stations considered in this study are classified according to the Building Seismic Safety Council (BSSC). The Vs30 values indicate that differences exist between shear wave velocities (Vs) in the shallow part of thick sediments at stations of class D and E, but this is difficult to estimate using HVSR. The main advantage of HVSR is its ability to detect discontinuities in velocities such as the interfaces of engineering bedrock and seismic bedrock. Most of the strong motion stations are located in plane areas and are classified as class D, showing no significant variation in Vs at depths. Stations of class C are mainly distributed in piedmonts and show a larger variation in their Vs values. Vs values at class B stations are relatively low; only one station in this study had a Vs30 value higher than 1000 m/s. Two stations from the total 62 drilled stations in this area are classified as class E. The distribution pattern of dominant frequencies was found to be comparable with the Vs30 map provided by the EGDT. The dominant frequency was lower than 2 Hz in the plane area, over 4 Hz in the mountains, and lower than 1 Hz for several near the coast. One exception was the station labeled KAU003 which had a coastal location and a dominant frequency of over 10 Hz. This exception is due to the limestone geology at this station. The similarity between the dominant frequency and Vs30 maps demonstrates that HVSR can recognize different seismic site conditions by indicating changes in sedimentary depths.

Keywords: HVSR, microtremor, free-field strong motion stations, S-wave velocity, site classification

Introduction

The so called site effect is the study of seismic wave amplification by local unconsolidated sediments at specific frequencies during strong ground motions. It is an important consideration in both seismology and earthquake engineering. The fact that different seismic site conditions are able to cause varied site effects was first recognized in the 19th century (Milne, 1898). It was noted that “it is an easy matter to select two stations within 1000 feet of each other where the average range of horizontal motion at the one station shall be five times, and even ten times, greater than it is at the other”. This indicates that the site effect can be evident even at two nearby stations.

Microtremors are caused by various natural and artificial signals. These signals exist perpetually and thus the time of measurements is very short in comparison with that for earthquakes. After Nakamura (1989) proposed the HVSR method, microtremor became a popular tool to assess site response to

[1] Associate Researcher, National Center for Research on Earthquake Engineering, chkuo@ncree.narl.org.tw
[2] Professor, Dep. of Earth Science, National Central University and Division Manager, National Center for Research on Earthquake Engineering, wenkl@ncree.narl.org.tw
[3] Associate Researcher, National Center for Research on Earthquake Engineering, cmlin@ncree.narl.org.tw
[4] Assistant Researcher, National Center for Research on Earthquake Engineering, hhhsieh@ncree.narl.org.tw

ground motions, i.e., the resonance frequency and amplification factor at a specific site. The EGDT was constructed by the NCREE and CWB, and includes logging data at over 400 stations. The Vs30 data and site classification of the drilled stations has also been accomplished (Kuo et al., 2011; 2012) according to the criteria of BSSC (2001). The site classification is a pre-requisite for the present study of developing HVSR models for different seismic site conditions in this study.

In this study, microtremors were measured at 74 free-field TSMIP stations in Kaohsiung and Pingtung (Fig. 1). Old data from the EGDT in the area was reviewed, the Vs30 of KAU048 was corrected, and the site was reclassified from class E to class D. The Vs30 value of the station KAU086 was derived from the N-value and was classified as class D. Finally, the Vs30 data for 62 stations in the area was used in this study. This included 6 stations of class B, 10 stations of class C, 44 stations of class D, and 2 stations of class E.

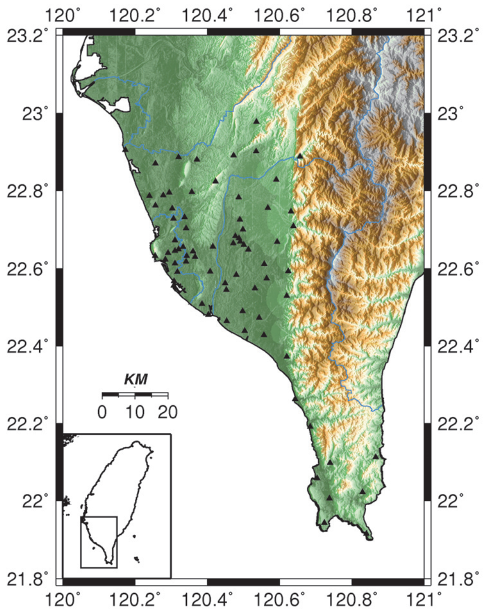

Fig. 1 Distribution of the measured stations (black triangles) in the KaoPing area

Microtremor Measurements and Data Processing

A SAMTAC-801B (recorder) and a VSE311C (sensor) manufactured by Tokyo Sokushin were the instruments used in the study. The sampling rate was 200 points per second and the recording period was 18 minutes for each measurement. The microtremor measurements were located at the side of each station to ensure that the geological conditions were identical. The instrumental response was eliminated in the HVSR procedure. Multi-windows with a length of 8192 points were utilized to partition the microtremor recordings, and a 6% cosine taper was implemented at both ends of each window. The recordings should be checked so that the windows contaminated by unusual noise can be deleted in advance; however, the number of selected windows should be more than 20 to make sure that the averaged result will be stable. A geometric mean of the horizontal Fourier spectra was calculated, smoothed 5 times, and then divided by the smoothed vertical Fourier spectrum to derive a single HVSR. After averaging the single HVSR of each window, the mean HVSR at a station was finally derived.

Properties of Microtremors

In the studied area, most of the strong motion stations are located in plane area and are classified as class D without significant variation in Vs at depths. Stations of class C are mainly distributed in piedmonts with larger variations in Vs. Class B stations have relatively low velocities; only one station has a Vs30 higher than 1000 m/s (Fig. 2).

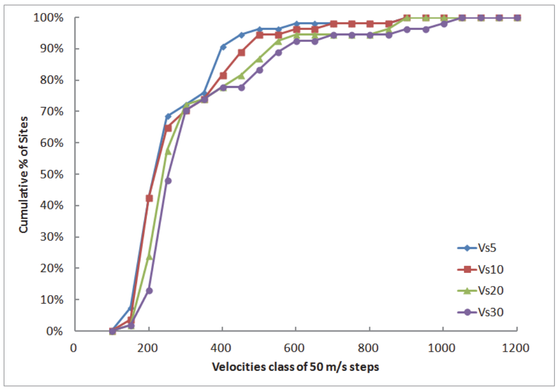

Fig. 2 Cumulative percentage of sites in velocity steps of 50 m/s

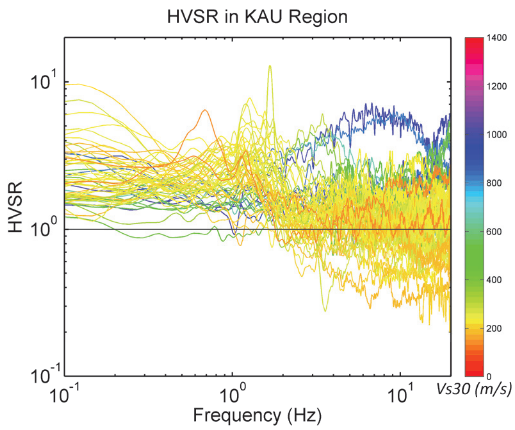

Fig. 3 HVSR of the 61 measured stations at different seismic site conditions with different colors corresponding to Vs30

HVSRs at the 61 strong motion stations were derived following the standard data processing steps introduced in the above section. The HVSRs were plotted using different colors according to the Vs30 values from logging data (Fig. 3). The dominant frequencies increased with Vs30. Moreover, these HVSRs were categorized into classes of B, C, D, and E according to the site classification of Kuo et al. (2011; 2012); in addition, two stations were reclassified by N-value as explained above (Fig. 4). The similarity of HVSRs in each class is consistent and the differences between each class are also quite clear.

Stations in class B are situated on hard rocks or sometimes covered with a thin regolith and therefore the dominant frequencies of HVSR are unremarkable or relatively higher than those at other stations. The stations of class C, which are situated on soft rocks or stiff soils, have obvious amplification at comparatively lower resonant frequencies than those of class B. The HVSRs of classes D and E are evidently amplified at relatively lower resonant frequencies.

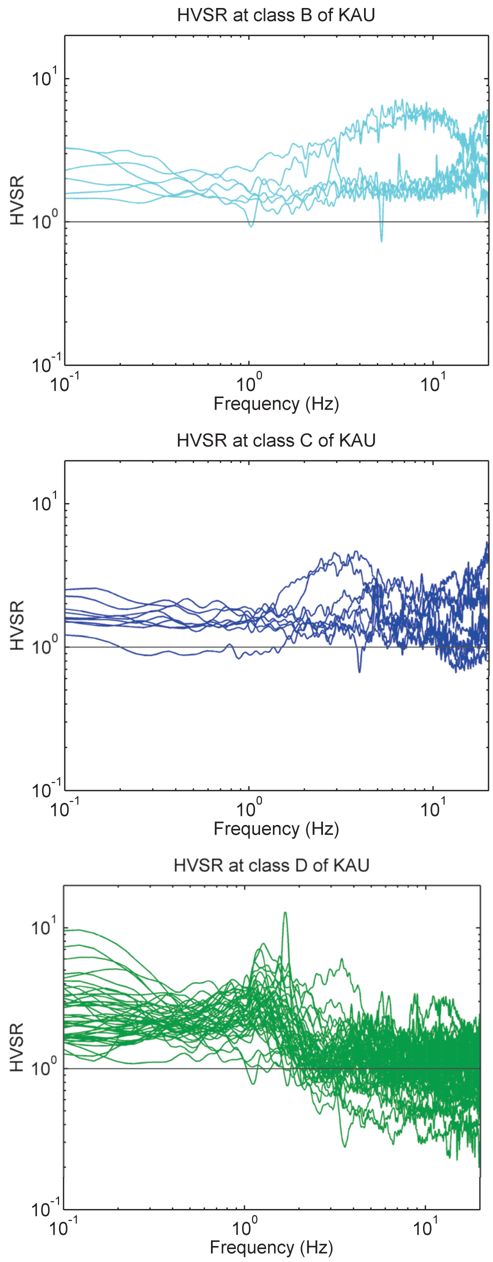

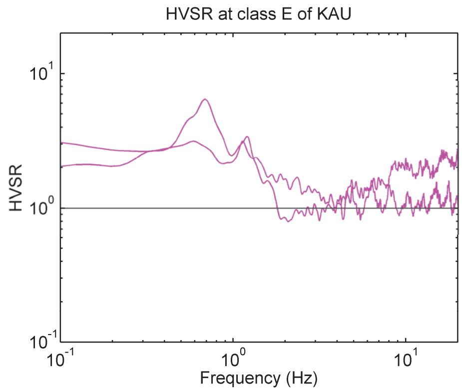

Fig. 4 The categorized HVSR curves according to logging data. From top to bottom, they are class B, class C, class D, and class E

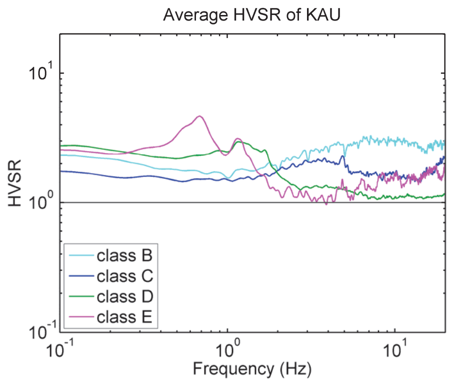

Fig. 5 Averaged HVSRs of each class

Additionally, Fig. 4 also shows the phenomenon of "deamplification", which could be observed in many of the HVSR curves in class D, class E, and several class C (Kuo et al., 2013).

Fig. 5 shows the average HVSR of the four classes. In this figure, the difference in shape and dominant frequencies are very clear. However, the HVSR of class E was only available at two stations; therefore the average HVSR in this class may not be very reliable. The deamplification of HVSRs was also averaged but cannot be seen in Fig. 5. However, the trend of decreasing ratios is still apparent in the average curves of class D and E.

Dominant frequency and Vs30 maps

The dominant frequencies of the microtremor HVSRs are proportional to the measured Vs30 values in the KaoPing area as shown in Fig. 6. Our recent study (Kuo et al., 2013) in the Taipei area showed the outstanding reliability of site classification using HVSRs of microtremor. This approach analyzed the similarity of HVSRs between the site of interest and the average HVSRs of each class using the Spearman's rank correlation coefficient as well as adopting the dominant frequency, deamplification, and relative amplification as weightings to assess the site class of a station. The accuracy of this approach is better than previous results using surface geology parameters.

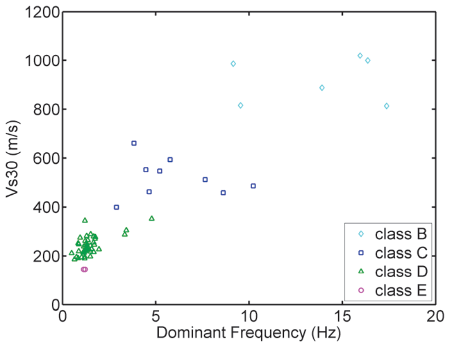

Fig. 6 The correlation between Vs30 and the dominant frequency

Conclusions

This study conducted microtremor measurements in Kaohsiung and Pingtung, and considered the EGDT logging data to analyze the site effects. Fig. 7 shows the distribution of the dominant frequencies of microtremor at 74 measured KAU stations. The pattern is comparable with the surface geology in Fig. 1. The dominant frequency was lower than 2 Hz in the plane area, over 4 Hz in the mountains, and lower than 1 Hz for several near the coast. One exception is station KAU003 that is located near the coast but had a dominant frequency of over 10 Hz. The geology at the station is mainly limestone with higher velocity characteristics.

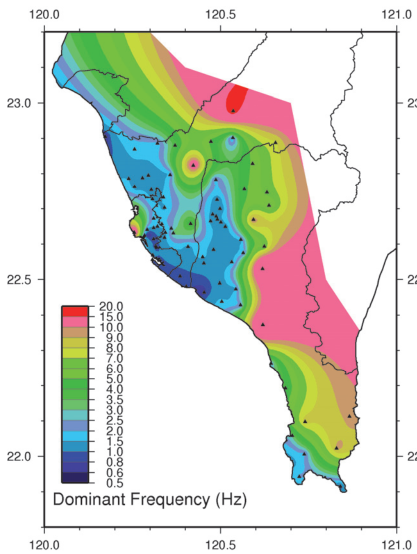

Fig. 7 Dominant frequency map from 74 measured KAU stations

The Vs30 map (Fig. 8) in this area was plotted using the results of Kuo et al. (2012). However, it also includes the stations in Tainan and Taitung. It also displays similarities to the distribution pattern in Fig. 7, indicating that the dominant frequencies of microtremor are able to detect the variation in the main interface of different velocities. When the sedimentary depth of a site is less than 30 meters, it may be class B or C; on the contrary, when the sedimentary depth becomes larger than 30 meters, it may be class D or E. The HVSRs indicate several stations with dominant frequencies lower than 1 Hz near the coast. This may be caused by very thick sediments in this region and also demonstrates a better recognition than Vs30 for deeper interfaces.

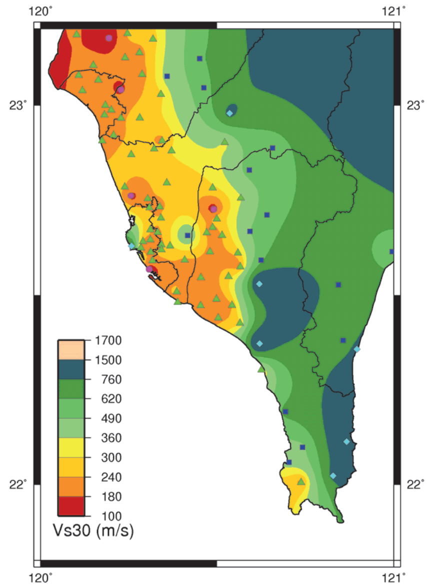

Fig. 8 Vs30 map derived from the EGDT results

References

Building Seismic Safety Council, BSSC (2001), "NEHRP Recommended Provisions for Seismic Regulations for New Buildings and Other Structures", Washington, DC.

Kuo, C. H., K. L. Wen, H. H. Hsieh, C. M. Lin, and T. M. Chang (2011), "Characteristics of Near-Surface S-wave Velocity", National Center for Research on Earthquake Engineering, NCREE-11-022, 82 p. (In Chinese)

Kuo, C.H., Wen, K.L., Hsieh, H.H., Lin, C.M., Chang, T.M., and Kuo, K.W. (2012), "Site Classification and Vs30 estimation of free-field TSMIP stations using the logging data of EGDT", *Engineering Geology*.

Kuo, C. H., Wen, K. L., Lin, C. M., Huang, J. Y., and Chang, T. M. (2013), "Analysis of HVSR of Microtremor on Different Seismic Site Conditions", *10CUEE Conference Proceedings*, 151-157, Tokyo, Japan.

Milne, J. (1898), Seismology. London, K. Paul, Trench, Trubner & co., ltd. 320 p.

Nakamura, Y. (1989), "A method for dynamic characteristics estimation of subsurface using microtremor on the ground surface", *Quarterly Report of Railway Technical Research Institute*, 30 (1), 25-33.

Ground Motion Selection for Engineering Applications

Hsun-Jen Liu[1] , Wen-Yu Jean[2] , and Yu-Wen Chang[3]

劉勛仁 [1]、簡文郁 [2]、張毓文 [3]

Abstract

In practice, for new structures of major importance (rock-filled dams, nuclear power plants), complexity (soil-structure systems, irregular buildings), inelasticity and geometrical nonlinearity (base-isolated structures), dynamic time-history analysis is very beneficial for obtaining inelastic structural responses that are close to reality. In the past, dynamic time-history analysis frequently used records from significant earthquakes, such as El Centro (1940), Kobe (1995), and Chi-Chi (1999), or used artificial records based on random vibration theory. During the last decade, however, due to experience of severe earthquakes and massive earthquake records, modern seismic codes prescribe general guidelines that input motions, either real or artificial, must be selected to represent regional seismicity and must conform to design earthquakes. This paper aims to use real earthquake records to establish magnitude-distance (M–R) bins for different site conditions, and to match these with target spectral shapes defined by ten corner periods (T_c). Comparisons of record spectra from M–R bins for different hazard sources, and a review of record spectra versus design spectra from the Taiwan Building Code are discussed. The results of applied ground motion selection for the Taiwan region are presented.

Keywords: selection of real records, spectral matching, design spectra, seismic code

Introduction

The main purpose of ground motion selection is to select real records that satisfy both design levels and seismic hazards. In other words, the selection of real records should reflect site conditions and anticipated earthquake scenarios, so that the reliability, safety, and economy of seismic design can be improved. With advances in technology, new systems and special construction methods have been widely used in the building industry, so that dynamic analysis using smooth response spectra is insufficient to understand the nonlinear behavior of such structures. According to current seismic design trends, linear or nonlinear dynamic analysis requires recorded time histories as seismic input.

In this study, magnitude-distance (M–R) bins for different site conditions have been developed to estimate the characteristics of response spectra corresponding to various hazard sources. M-R bins can also be used as seed motions for response analyses. Meanwhile, ten target response spectra with different corner periods (T_c) from the Taiwan Building Code have been employed to select ground motions for spectral matching and, as such, can be utilized in the framework of performance-based design.

Code for Seismic Input

Most contemporary seismic codes, such as the New Zealand Standards (NZS 1170.5), the Italian Code (OPCM 3274), the Greek Seismic Code (EAK 2000) and Eurocode 8, describe relatively similar procedures for seismic inputs to be used as dynamic loadings in structures. Most frequently, seismic inputs can be represented by real, artificial, or simulated records, while some important seismological parameters, such as earthquake magnitude, distance, the seismotectonic environment, and the local soil conditions, should reflect local seismic scenarios.

In the scope of the nuclear industry, the regulatory or standards such as RG 1.208, NUREG-0800, and NUREG/CR-6728 by NRC, and ASCE 4-98 and

[1]Assistant Researcher, National Center for Research on Earthquake Engineering, hjliu@ncree.narl.org.tw
[2] Researcher, National Center for Research on Earthquake Engineering, wychien@ncree.narl.org.tw
[3]Assistant Researcher, National Center for Research on Earthquake Engineering, ywchang@ncree.narl.org.tw

ASCE/SEI 43-05 by ASCE, require more criteria for developing seismic inputs. For example, RG 1.208 requires ground motions that are generated to “match” or “envelop” given design response spectral shapes and should comply with the majority of the following:

(1) The average ratio of the spectral acceleration calculated from the recorded time history to the target, *i.e.*, the record-to-target ratio (RTR), where the ratio is calculated frequency-by-frequency, is only slightly greater than one.

(2) Time histories should have a time increment of at most 0.01 seconds, and a total duration of 20 seconds. The total duration of the record can be increased by zero-packing to satisfy these frequency criteria.

(3) The computed 5 percent damped response spectrum of the average of all accelerograms should not fall more than 10 percent below the target spectrum at any one frequency, and should not exceed the target spectrum at any frequency by more than 30 percent. That is, the RTR at any frequency should be between 0.9 and 1.3.

(4) To be considered statistically independent, the directional correlation coefficients between pairs of time histories should not exceed 0.16.

Ground-Motion Database

For ground motion selection and M–R bins development, the use of an informed ground-motion database is important. The earthquake data used in this study are from Taiwan Strong Motion Instrumentation Program (TSMIP), which is operated by the Central Weather Bureau (CWB). The TSMIP system, composed of more than 700 stations that are spaced approximately 5 km apart in populated areas, is widely used in the Taiwan area.

The station information is from the Engineering Geological Database for TSMIP (EGDT), which is co-established by both the CWB and the National Center for Research on Earthquake Engineering (NCREE). CWB and NCREE carried out a free-field strong-motion station drilling project to construct the EGDT (Kuo *et al*., 2011). Up to 2010, the site investigation at 469 TSMIP stations was completed and all of the results of this investigation were systematically organized in the EGDT project. With a detailed subsurface soil profile and quantitative soil properties (SPT-N values and wave velocities) at a station site, the site effect of the ground motions can be thoughtfully analyzed for a certain class of site conditions.

According to data sufficiency and the designed ground motion level, the earthquake records in the ground-motion database complied with the following two conditions: (1) the earthquake events included were from 1991 to 2010 and (2) the local magnitude (M_L) was greater than 4.5. Considering engineering applications, some ground motion parameters are also included in the ground-motion database, such as cumulative absolute velocity (CAV), strong motion duration (T_d), and Arias intensity (I_a).

Response Spectra Characterization

Ground-motion frequency content is one of the most important aspects of free-field motion as it affects structural responses, and is strongly dependent on specific factors pertaining to both the earthquake and the site. Three particularly important characteristics of ground motions are earthquake magnitude, epicentral distance, and the average shear-wave velocity in the top 30 m (V_{s30}). Therefore, the response spectra characterization of hazard-consistent scenario earthquakes is very important for

Table 1 M–R bins of V_{s30} between 360 and 760 m/s.

距離(R, km) / 規模(M)	0 – 25	25 – 50	50 – 75	75 – 100	100 – 125	125 – 150	150 – 175	175 – 200
5.50 – 5.75	[Total Data] 71 [$\overline{M}_L$] 5.65 [$\overline{R}$, km] 12.80 [V/A, sec] 0.019 ~ 0.176 [PGA_{GM}, g] 0.056 ~ 0.658 [S_{as}] 0.076 ~ 1.193 [S_{a1}] 0.036 ~ 0.682 [CAV_{GM}] 0.067 ~ 1.018	[Total Data] 35 [$\overline{M}_L$] 5.66 [$\overline{R}$, km] 34.16 [V/A, sec] 0.019 ~ 0.077 [PGA_{GM}, g] 0.053 ~ 0.142 [S_{as}] 0.025 ~ 0.104 [S_{a1}] 0.011 ~ 0.051 [CAV_{GM}] 0.059 ~ 0.361	[Total Data] 10 [$\overline{M}_L$] 5.66 [$\overline{R}$, km] 60.66 [V/A, sec] 0.013 ~ 0.031 [PGA_{GM}, g] 0.063 ~ 0.087 [S_{as}] 0.012 ~ 0.035 [S_{a1}] 0.006 ~ 0.017 [CAV_{GM}] 0.103 ~ 0.248	[Total Data] 4 [$\overline{M}_L$] 5.68 [$\overline{R}$, km] 77.64 [V/A, sec] 0.023 ~ 0.041 [PGA_{GM}, g] 0.063 ~ 0.072 [S_{as}] 0.007 ~ 0.017 [S_{a1}] 0.003 ~ 0.008 [CAV_{GM}] 0.096 ~ 0.212	N/A	[Total Data] 1 [$\overline{M}_L$] 5.58 [$\overline{R}$, km] 130.39 [V/A, sec] 0.050 ~ 0.050 [PGA_{GM}, g] 0.054 ~ 0.054 [S_{as}] 0.003 ~ 0.007 [S_{a1}] 0.001 ~ 0.003 [CAV_{GM}] 0.146 ~ 0.146	N/A	N/A
5.75 – 6.00	[Total Data] 35 [$\overline{M}_L$] 5.88 [$\overline{R}$, km] 14.22 [V/A, sec] 0.016 ~ 0.121 [PGA_{GM}, g] 0.053 ~ 0.609 [S_{as}] 0.104 ~ 1.228 [S_{a1}] 0.051 ~ 0.717 [CAV_{GM}] 0.104 ~ 1.253	[Total Data] 28 [$\overline{M}_L$] 5.86 [$\overline{R}$, km] 33.57 [V/A, sec] 0.017 ~ 0.091 [PGA_{GM}, g] 0.056 ~ 0.337 [S_{as}] 0.035 ~ 0.141 [S_{a1}] 0.017 ~ 0.070 [CAV_{GM}] 0.076 ~ 0.945	[Total Data] 2 [$\overline{M}_L$] 5.98 [$\overline{R}$, km] 54.40 [V/A, sec] 0.032 ~ 0.068 [PGA_{GM}, g] 0.064 ~ 0.068 [S_{as}] 0.017 ~ 0.050 [S_{a1}] 0.008 ~ 0.024 [CAV_{GM}] 0.103 ~ 0.325	N/A	N/A	N/A	N/A	N/A
6.00 – 6.25	[Total Data] 95 [$\overline{M}_L$] 6.14 [$\overline{R}$, km] 15.27 [V/A, sec] 0.025 ~ 0.188 [PGA_{GM}, g] 0.056 ~ 0.609 [S_{as}] 0.141 ~ 1.265 [S_{a1}] 0.070 ~ 0.753 [CAV_{GM}] 0.130 ~ 2.145	[Total Data] 62 [$\overline{M}_L$] 6.12 [$\overline{R}$, km] 35.71 [V/A, sec] 0.017 ~ 0.216 [PGA_{GM}, g] 0.052 ~ 0.240 [S_{as}] 0.050 ~ 0.187 [S_{a1}] 0.024 ~ 0.096 [CAV_{GM}] 0.111 ~ 0.825	[Total Data] 21 [$\overline{M}_L$] 6.12 [$\overline{R}$, km] 59.46 [V/A, sec] 0.029 ~ 0.108 [PGA_{GM}, g] 0.053 ~ 0.145 [S_{as}] 0.025 ~ 0.071 [S_{a1}] 0.012 ~ 0.035 [CAV_{GM}] 0.103 ~ 0.364	[Total Data] 5 [$\overline{M}_L$] 6.18 [$\overline{R}$, km] 82.34 [V/A, sec] 0.033 ~ 0.088 [PGA_{GM}, g] 0.055 ~ 0.069 [S_{as}] 0.015 ~ 0.037 [S_{a1}] 0.007 ~ 0.018 [CAV_{GM}] 0.136 ~ 0.330	N/A	N/A	N/A	N/A
6.25 – 6.50	[Total Data] 43 [$\overline{M}_L$] 6.42 [$\overline{R}$, km] 16.49 [V/A, sec] 0.018 ~ 0.164 [PGA_{GM}, g] 0.070 ~ 1.039 [S_{as}] 0.187 ~ 1.302 [S_{a1}] 0.096 ~ 0.791 [CAV_{GM}] 0.156 ~ 3.408	[Total Data] 49 [$\overline{M}_L$] 6.44 [$\overline{R}$, km] 38.05 [V/A, sec] 0.018 ~ 0.192 [PGA_{GM}, g] 0.054 ~ 0.328 [S_{as}] 0.071 ~ 0.243 [S_{a1}] 0.035 ~ 0.128 [CAV_{GM}] 0.108 ~ 2.118	[Total Data] 41 [$\overline{M}_L$] 6.47 [$\overline{R}$, km] 63.04 [V/A, sec] 0.039 ~ 0.107 [PGA_{GM}, g] 0.056 ~ 0.220 [S_{as}] 0.037 ~ 0.098 [S_{a1}] 0.018 ~ 0.050 [CAV_{GM}] 0.158 ~ 0.491	[Total Data] 9 [$\overline{M}_L$] 6.38 [$\overline{R}$, km] 87.92 [V/A, sec] 0.028 ~ 0.121 [PGA_{GM}, g] 0.057 ~ 0.110 [S_{as}] 0.022 ~ 0.052 [S_{a1}] 0.011 ~ 0.026 [CAV_{GM}] 0.144 ~ 0.334	N/A	[Total Data] 1 [$\overline{M}_L$] 6.48 [$\overline{R}$, km] 132.78 [V/A, sec] 0.042 ~ 0.042 [PGA_{GM}, g] 0.069 ~ 0.069 [S_{as}] 0.011 ~ 0.022 [S_{a1}] 0.005 ~ 0.011 [CAV_{GM}] 0.175 ~ 0.175	N/A	N/A
6.50 – 6.75	[Total Data] 27 [$\overline{M}_L$] 6.57 [R, km] 15.70 [V/A, sec] 0.025 ~ 0.135 [PGA_{GM}, g] 0.070 ~ 1.039 [S_{as}] 0.243 ~ 1.341 [S_{a1}] 0.128 ~ 0.832 [CAV_{GM}] 0.156 ~ 2.118	[Total Data] 78 [$\overline{M}_L$] 6.65 [$\overline{R}$, km] 39.43 [V/A, sec] 0.023 ~ 0.224 [PGA_{GM}, g] 0.055 ~ 0.620 [S_{as}] 0.098 ~ 0.311 [S_{a1}] 0.050 ~ 0.168 [CAV_{GM}] 0.170 ~ 1.172	[Total Data] 105 [$\overline{M}_L$] 6.65 [$\overline{R}$, km] 59.16 [V/A, sec] 0.033 ~ 0.163 [PGA_{GM}, g] 0.053 ~ 0.237 [S_{as}] 0.052 ~ 0.133 [S_{a1}] 0.026 ~ 0.069 [CAV_{GM}] 0.163 ~ 0.724	[Total Data] 25 [$\overline{M}_L$] 6.70 [$\overline{R}$, km] 84.33 [V/A, sec] 0.043 ~ 0.091 [PGA_{GM}, g] 0.055 ~ 0.170 [S_{as}] 0.032 ~ 0.073 [S_{a1}] 0.016 ~ 0.038 [CAV_{GM}] 0.195 ~ 0.484	[Total Data] 1 [$\overline{M}_L$] 6.70 [$\overline{R}$, km] 103.62 [V/A, sec] 0.052 ~ 0.052 [PGA_{GM}, g] 0.062 ~ 0.062 [S_{as}] 0.022 ~ 0.046 [S_{a1}] 0.011 ~ 0.023 [CAV_{GM}] 0.158 ~ 0.158	N/A	N/A	N/A
6.75 – 7.00	[Total Data] 23 [$\overline{M}_L$] 6.90 [$\overline{R}$, km] 19.55 [V/A, sec] 0.054 ~ 0.162 [PGA_{GM}, g] 0.091 ~ 0.698 [S_{as}] 0.311 ~ 1.381 [S_{a1}] 0.168 ~ 0.874 [CAV_{GM}] 0.347 ~ 1.247	[Total Data] 48 [$\overline{M}_L$] 6.87 [$\overline{R}$, km] 40.36 [V/A, sec] 0.024 ~ 0.150 [PGA_{GM}, g] 0.052 ~ 0.384 [S_{as}] 0.133 ~ 0.389 [S_{a1}] 0.069 ~ 0.217 [CAV_{GM}] 0.203 ~ 1.004	[Total Data] 86 [$\overline{M}_L$] 6.84 [$\overline{R}$, km] 61.99 [V/A, sec] 0.028 ~ 0.224 [PGA_{GM}, g] 0.053 ~ 0.354 [S_{as}] 0.073 ~ 0.179 [S_{a1}] 0.038 ~ 0.095 [CAV_{GM}] 0.188 ~ 0.897	[Total Data] 20 [$\overline{M}_L$] 6.87 [$\overline{R}$, km] 86.08 [V/A, sec] 0.041 ~ 0.270 [PGA_{GM}, g] 0.057 ~ 0.143 [S_{as}] 0.046 ~ 0.102 [S_{a1}] 0.023 ~ 0.053 [CAV_{GM}] 0.207 ~ 0.599	[Total Data] 22 [$\overline{M}_L$] 6.87 [$\overline{R}$, km] 114.56 [V/A, sec] 0.047 ~ 0.204 [PGA_{GM}, g] 0.059 ~ 0.115 [S_{as}] 0.032 ~ 0.066 [S_{a1}] 0.016 ~ 0.034 [CAV_{GM}] 0.221 ~ 1.095	[Total Data] 21 [$\overline{M}_L$] 6.82 [$\overline{R}$, km] 136.54 [V/A, sec] 0.082 ~ 0.363 [PGA_{GM}, g] 0.055 ~ 0.147 [S_{as}] 0.023 ~ 0.046 [S_{a1}] 0.012 ~ 0.023 [CAV_{GM}] 0.177 ~ 0.553	[Total Data] 2 [$\overline{M}_L$] 6.99 [$\overline{R}$, km] 170.71 [V/A, sec] 0.041 ~ 0.048 [PGA_{GM}, g] 0.052 ~ 0.062 [S_{as}] 0.018 ~ 0.034 [S_{a1}] 0.009 ~ 0.017 [CAV_{GM}] 0.304 ~ 0.366	N/A
7.00 以上	[Total Data] 13 [$\overline{M}_L$] 7.30 [$\overline{R}$, km] 17.29 [V/A, sec] 0.057 ~ 0.306 [PGA_{GM}, g] 0.158 ~ 0.800 [S_{as}] 0.389 ~ 1.381 [S_{a1}] 0.217 ~ 0.874 [CAV_{GM}] 1.561 ~ 3.598	[Total Data] 27 [$\overline{M}_L$] 7.30 [$\overline{R}$, km] 40.01 [V/A, sec] 0.111 ~ 0.508 [PGA_{GM}, g] 0.095 ~ 0.833 [S_{as}] 0.179 ~ 0.389 [S_{a1}] 0.095 ~ 0.217 [CAV_{GM}] 0.917 ~ 2.882	[Total Data] 22 [$\overline{M}_L$] 7.30 [$\overline{R}$, km] 64.27 [V/A, sec] 0.064 ~ 0.448 [PGA_{GM}, g] 0.063 ~ 0.436 [S_{as}] 0.102 ~ 0.179 [S_{a1}] 0.053 ~ 0.095 [CAV_{GM}] 0.342 ~ 1.821	[Total Data] 34 [$\overline{M}_L$] 7.30 [$\overline{R}$, km] 82.83 [V/A, sec] 0.080 ~ 0.431 [PGA_{GM}, g] 0.063 ~ 0.510 [S_{as}] 0.066 ~ 0.102 [S_{a1}] 0.034 ~ 0.053 [CAV_{GM}] 0.378 ~ 1.399	[Total Data] 19 [$\overline{M}_L$] 7.24 [$\overline{R}$, km] 109.69 [V/A, sec] 0.044 ~ 0.433 [PGA_{GM}, g] 0.056 ~ 0.153 [S_{as}] 0.046 ~ 0.066 [S_{a1}] 0.023 ~ 0.034 [CAV_{GM}] 0.236 ~ 0.825	[Total Data] 19 [$\overline{M}_L$] 7.24 [$\overline{R}$, km] 135.00 [V/A, sec] 0.040 ~ 0.420 [PGA_{GM}, g] 0.052 ~ 0.153 [S_{as}] 0.034 ~ 0.046 [S_{a1}] 0.017 ~ 0.023 [CAV_{GM}] 0.203 ~ 3.118	[Total Data] 6 [$\overline{M}_L$] 7.27 [$\overline{R}$, km] 159.16 [V/A, sec] 0.022 ~ 0.265 [PGA_{GM}, g] 0.074 ~ 0.147 [S_{as}] 0.026 ~ 0.034 [S_{a1}] 0.013 ~ 0.017 [CAV_{GM}] 0.468 ~ 0.765	[Total Data] 3 [$\overline{M}_L$] 7.10 [$\overline{R}$, km] 185.87 [V/A, sec] 0.040 ~ 0.061 [PGA_{GM}, g] 0.059 ~ 0.094 [S_{as}] 0.020 ~ 0.026 [S_{a1}] 0.010 ~ 0.013 [CAV_{GM}] 0.293 ~ 0.325

seismic design.

Based on the statistics method of time histories that is adopted in NUREG/CR-6728, Table 1 shows M–R bins for V_{s30} between 360 and 760 m/s. Each bin represents the total data, mean of the magnitude and epicentral distance, range of V/A ratio, PGA, $S_{a(0.3s)}$, $S_{a(1.0s)}$, and CAV. The observations are as follows: (1) according to data scattered in the M–R bins, the hazard-consistent earthquake scenario should consider the larger magnitude with both close-field and far-field; (2) larger M_L values were accompanied by a higher V/A ratios, so large earthquake events obviously induce a long-period effect; and (3) the closer the distance and the larger the magnitude, the higher the PGA, V/A ratio, CAV, and S_a.

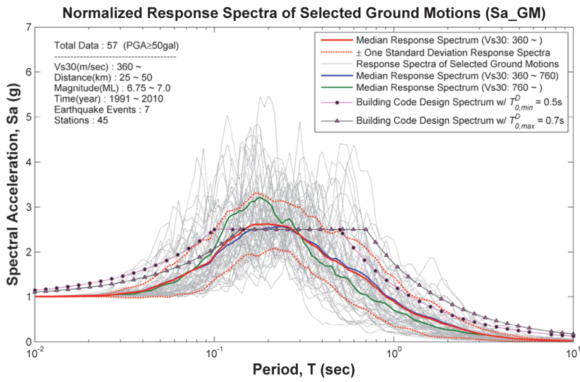

Fig. 1 Design response spectra (T_c = 0.5 s, 0.7 s) *vs*. recorded response spectra from M–R bins (M: 6.75–7.0, R: 25–50 km).

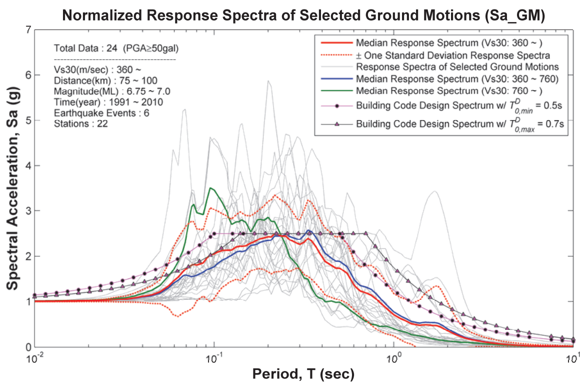

Fig. 2 Design response spectra (T_c = 0.5 s, 0.7 s) *vs*. recorded response spectra from M–R bins (M: 6.75–7.0, R: 75–100 km).

In order to estimate the characteristics of the response spectra for various seismic hazards in terms of earthquake magnitudes and distances, Fig. 1 and Fig. 2 show comparisons between design response spectra (T_c = 0.5 s, 0.7 s) based on the Taiwan Building Code and recorded response spectra from the M–R bins. The observations are as follows: (1) the average record spectrum is close to code-based spectra, so it seems that design spectra from the Taiwan Building Code can be applied for firm sites; (2) lower V_{s30} values are characterized by narrow-banded response spectra and high frequencies in comparison to higher V_{s30} values; and (3) the farther the distance of large-magnitude earthquake event, the higher the predominant period.

Applied Ground Motion Selection

Spectral matching is a commonly used code-based selection process. In this procedure, two parameters should be used: (1) the scale factor (F), a mean value of all RTRs applied to the entire recorded response spectrum; and (2) the mean squared error (MSE), represents a difference between the target spectrum and the recorded response. The MSE and scale factor were calculated in terms of the natural logarithm scale as follows:

$$F = \sum_{i}^{N} \left[\ln\left(SA_{target}(t_i) - \ln\left(SA_{record}(t_i)\right)\right) \right] \Big/ N \tag{1}$$

$$MSE = \sum_{i}^{N} \left[\ln\left(SA_{target}(t_i)\right) - \ln\left(F \times SA_{record}(t_i)\right) \right]^2 \Big/ N \tag{2}$$

In the above, 87 points were near-uniformly spaced over the log period scale from 0.01 s to 10 s, so the value of N will change in different period ranges.

The design spectra, as defined by the Taiwan Building Code, satisfied the following conditions: the return period of 475 years, full site classification, and no consideration of near-fault effects. As above, ten target spectral shapes defined by T_c have been grouped as shown in Table 2. The corner period can not only be used to judge the frequency content and site conditions, but also can be used instead of the parameters S_s and S_1 related to the spectral shape to illustrate the response spectrum.

Table 2 The T_c groups of code-based design spectra.

Site Class	S_S^D	S_1^D	F_a	F_v	S_{DS}	S_{D1}	T_c	Zone	Section Point of T_c
TAP1	--	--	--	--	0.60	0.96	1.60	TAP1	1.60
TAP2	--	--	--	--	0.60	0.78	1.30	TAP2	1.30
TAP3	--	--	--	--	0.60	0.63	1.05	TAP3	1.05
SC1	0.6	0.30	1.0	1.0	0.60	0.30	0.50	SC1-P1	0.50
	0.7	0.35	1.0	1.0	0.70	0.35	0.50	SC1-P1	0.50
	0.8	0.40	1.0	1.0	0.80	0.40	0.50	SC1-P1	0.50
	0.8	0.45	1.0	1.0	0.80	0.45	0.56	SC1-P2	0.60
	0.7	0.40	1.0	1.0	0.70	0.40	0.57	SC1-P2	0.60
	0.6	0.35	1.0	1.0	0.60	0.35	0.58	SC1-P2	0.60
	0.5	0.30	1.0	1.0	0.50	0.30	0.60	SC1-P2	0.60
	0.5	0.35	1.0	1.0	0.50	0.35	0.70	SC1-P3	0.70
SC2	0.8	0.40	1.0	1.3	0.80	0.52	0.65	SC2-P3	0.70
	0.6	0.30	1.1	1.5	0.66	0.45	0.68	SC2-P3	0.70
	0.8	0.45	1.0	1.2	0.80	0.54	0.68	SC2-P3	0.70
	0.7	0.35	1.0	1.4	0.70	0.49	0.70	SC2-P3	0.70
	0.6	0.35	1.1	1.4	0.66	0.49	0.74	SC2-P4	0.80
	0.7	0.40	1.0	1.3	0.70	0.52	0.74	SC2-P4	0.80
	0.5	0.30	1.1	1.5	0.55	0.45	0.82	SC2-P5	0.85
	0.5	0.35	1.1	1.4	0.55	0.49	0.89	SC2-P6	0.90
SC3	0.6	0.30	1.2	1.8	0.72	0.54	0.75	SC3-P4	0.80
	0.7	0.35	1.1	1.7	0.77	0.60	0.78	SC3-P4	0.80
	0.8	0.40	1.0	1.6	0.80	0.64	0.80	SC3-P4	0.80
	0.6	0.35	1.2	1.7	0.72	0.60	0.83	SC3-P5	0.85
	0.7	0.40	1.1	1.6	0.77	0.64	0.83	SC3-P5	0.85
	0.8	0.45	1.0	1.5	0.80	0.68	0.85	SC3-P5	0.85
	0.5	0.30	1.2	1.8	0.60	0.54	0.90	SC3-P6	0.90
	0.5	0.35	1.2	1.7	0.60	0.60	1.00	SC3-P7	1.00

An example case for comparison between the design spectrum of the second microzonation of the Taipei basin (TAP2) and all horizontal records in the ground-motion database is presented in Fig. 3. It seems that the top five recorded spectra of the best spectral fit to the target spectrum can be applied as seismic input, but some problems obviously can occur, as follows: (1) the stations do not belong to TAP2 and (2) the higher the scale factor, the smaller the spectral amplitude of the record compared to the design level. This shows that the MSE is applied to select the conformed ground motions along with the target spectrum, not to select the records appropriate to the anticipated earthquake scenario. In other words, some criteria and parameters consistent with characteristics for the controlling earthquake and site conditions should accommodate the selection.

Fig. 4 shows the selection results, according to records from the Taipei basin, with PGA greater than 50 gal, and periods range from 0.07 s to 3 s. The results ranked in ascending order of MSE are shown in Table 3. This information could be provided to develop seismic inputs for dynamic analyses. In order to estimate the criteria for developing time histories in RG 1.208 applied to a real case, Fig. 4 also shows 1.3 and 0.9 times the target spectral shapes in the period range from 0.07 s to 3 s in order to represent the restricted RTR. It is obvious that real records cannot comply with any RTR between 0.9 and 1.3. Even if the upward scale factor to satisfy the most parts of criteria, it is still hard to satisfy the criteria with any RTR lower than 1.3.

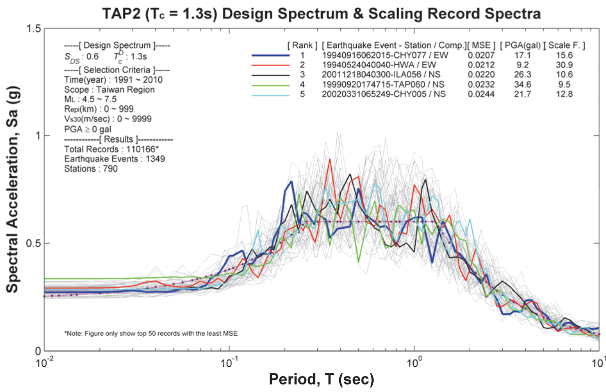

Fig. 3 Comparisons of TAP2 design spectra *vs*. all record spectra of the database (T: 0.01–10 s).

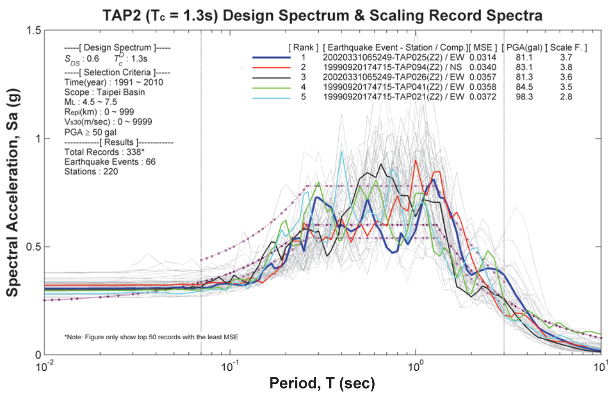

Fig. 4 Comparisons of TAP2 design spectra *vs*. record spectra of the Taipei basin (T: 0.07–3 s)

Table 3 The top twenty selection results for TAP2.

[Design Spectrum] TAP2 (S_{DS} = 0.6, T_c = 1.3s) [Period Range] 0.07s~3.0s [PGA]≥50gal [Sorting By] MSE

Rank	Matching Index		Earthquake Parameters				Station Parameters			Ground Motion Parameters					
	MSE	Scale Factor	Time (UTC)	M_L	R_{epi} (km)	Depth (km)	Station (zone)	Comp	V_{s30} (m/s)	PGA (gal)	PGV (cm/s)	PGD (cm)	CAV (gal-sec)	V/A (sec)	T_d (sec)
1	0.0314	3.7	2002/03/31 06:52:49	6.8	120.7	13.8	TAP025 (2)	EW	251.6	81.1	18.4	8.2	0.49	0.23	29.5
2	0.0340	3.8	1999/09/20 17:47:15	7.3	158.4	8.0	TAP094 (2)	NS	408.2	83.1	17.0	8.3	0.58	0.21	25.8
3	0.0357	3.6	2002/03/31 06:52:49	6.8	119.2	13.8	TAP026 (2)	EW	201.7	81.3	15.0	6.3	0.49	0.18	26.7
4	0.0358	3.5	1999/09/20 17:47:15	7.3	160.1	8.0	TAP041 (1)	EW	374.1	84.5	20.6	24.1	0.60	0.24	30.9
5	0.0372	2.8	1999/09/20 17:47:15	7.3	151.3	8.0	TAP021 (1)	EW	167.0	98.3	28.6	12.3	0.76	0.29	28.6
6	0.0379	4.4	1999/09/20 17:47:15	7.3	160.1	8.0	TAP041 (2)	NS	374.1	63.0	18.1	11.5	0.53	0.29	29.3
7	0.0398	2.9	2002/03/31 06:52:49	6.8	120.4	13.8	TAP100 (1)	EW	--	114.6	22.7	10.7	0.51	0.20	23.2
8	0.0402	5.2	2002/03/31 06:52:49	6.8	131.9	13.8	TAP002 (2)	NS	389.7	61.0	15.5	5.8	0.42	0.25	30.3
9	0.0407	5.6	2002/03/31 06:52:49	6.8	129.1	13.8	TAP096 (2)	NS	162.7	51.6	12.5	5.3	0.36	0.24	22.8
10	0.0409	3.7	2002/03/31 06:52:49	6.8	126.3	13.8	TAP006 (2)	NS	202.8	87.8	20.1	7.0	0.42	0.23	16.6
11	0.0415	3.4	1999/09/20 17:47:15	7.3	156.1	8.0	TAP042 (2)	EW	--	86.5	17.2	14.1	0.60	0.20	22.2
12	0.0436	2.8	1999/09/20 17:47:15	7.3	153.3	8.0	TAP014 (1)	EW	194.6	106.8	27.4	10.1	0.85	0.26	28.8
13	0.0446	4.3	1999/09/20 17:47:15	7.3	152.9	8.0	TAP051 (2)	NS	409.1	62.6	16.0	12.6	0.50	0.26	26.4
14	0.0453	4.9	2002/03/31 06:52:49	6.8	126.3	13.8	TAP006 (1)	EW	202.8	67.2	12.9	5.2	0.34	0.19	21.8
15	0.0471	3.2	2002/03/31 06:52:49	6.8	118.3	13.8	TAP109 (1)	NS	--	88.6	16.8	4.7	0.50	0.19	17.4
16	0.0479	4.1	2002/03/31 06:52:49	6.8	139.3	13.8	TAP041 (1)	EW	374.1	73.2	25.7	10.6	0.41	0.35	20.9
17	0.0479	2.4	2002/03/31 06:52:49	6.8	118.3	13.8	TAP109 (2)	EW	--	147.3	28.4	8.8	0.55	0.19	15.3
18	0.0486	4.8	2002/03/31 06:52:49	6.8	121.9	13.8	TAP019 (2)	EW	229.9	64.0	14.8	6.3	0.45	0.23	25.2
19	0.0487	3.9	1999/09/20 17:47:15	7.3	156.1	8.0	TAP042 (1)	NS	--	95.0	15.6	10.5	0.51	0.16	34.3
20	0.0507	2.5	2002/03/31 06:52:49	6.8	118.7	13.8	TAP015 (2)	EW	209.5	127.5	32.2	8.3	0.62	0.25	19.6

Conclusions

In this study, magnitude–distance (M–R) bins of different site conditions and the application of ten target spectra to select ground motions have been presented. Several comments can be made as follows:

(1) M–R bins can be used to assess the characteristics of controlling earthquake. In addition, M–R bins and the selection results of ten target spectra defined by T_c can be applied to develop seismic inputs for dynamic analyses.

(2) Spectral matching between the design spectrum and the response spectrum of a selected record is commonly required in practice. However, with some parameter settings, these criteria should be considered in the selection process.

(3) Because of ground motion diversity, it is difficult to comply with RG 1.208 criteria. The issue of how to select time histories appropriately and to modify ground motion to serve as seismic input will be discussed in future research.

References

Kuo, C. H., Wen, K. L., Hsieh, H. H., and Kuo, K. W. (2011). “Introduction of the Geological Database for TSMIP,” *8CUEE Conference Proceedings*, Tokyo, Japan, pp. 157-163.

McGuire, R. K., Silva, W. J., and Costantino, C. J. (2001). “Technical Basis for Revision of Regulatory Guidance on Design Ground Motions: Hazard- and Risk-Consistent Ground Motion Spectra Guidelines,” NUREG/CR-6728, *U.S. Nuclear Regulatory Commission*.

RG 1.208, (2007). “A Performance-Based Approach to Define the Site-Specific Earthquake Ground Motion,” *U.S. Nuclear Regulatory Commission*.

CPAMI, (2011). “Seismic Design Code for Buildings in Taiwan”, Construction and Planning Agency, Ministry of the Interior, Taiwan. (in Chinese)

De-Noising the Influence of Meteorological Parameters on Geochemical Monitoring Data: Pre-processing for Earthquake Precursory Research

Vivek Walia [1] Arvind Kumar [2] Baldev Raj Arora [3] Shih-Jung Lin [4]
Hsiao-Hsien Chang [5] Tsanyao Frank Yang [6] Kuo-Liang Wen [7]

瓦里亞 [1] 亞耳文 [2] 艾若拉 [3] 林世榮 [4] 張效賢 [5] 楊燦堯 [6] 溫國樑 [7]

Abstract

The present work is focused to investigate the relation of geochemical precursors to earthquakes through a network soil-gas radon stations in the multiple-plate collision setting of Taiwan. Geochemical variations of soil-gas composition are recorded at established geochemical observatories along the Hsincheng fault (HC) in Hsinchu area, Hsinhua fault (HH) in Tainan and at Jaosi in Ilan areas of Taiwan, respectively, to determine the influence of enhanced concentrations of soil gases on the tectonic activity in the region and to test the proposed tectonic setting based model from data generated at earthquake monitoring stations during the observation period. In addition to the continuous monitoring, in an effort to reduce the noise level which may be due to meteorological parameters especially for the rainfall, statistical filters have been applied to a selected data segment for both HC and HH monitoring stations. An attempt has been made to derive noise free synthetic curve on the data segment of the HC monitoring station.

Keywords: Soil-gas, Earthquake, Radon, Meteorological Parameters, Singular Spectral Analysis (SSA), Single Value Decomposition (SVD)

Introduction

Studies on earthquake precursory signals related to soil-gas anomalies have accelerated during the past few decades. Gases like radon, helium and carrier gases like carbon dioxide, nitrogen, methane etc. with different origins in soil have been used to trace various fault systems (Fu et al., 2005; Walia et al, 2009a, 2010) and in earthquake precursory studies (Kumar et al., 2009; Walia et al., 2005; Yang et al., 2006). The process of gases migration in the soil is apparently controlled by the interaction of geological, pedological, climatic and meteorological factors. Radon concentration variations have been established as a major contributor for seismic surveillance. While other gases have also been considered as possible earthquake precursors, however, bulk of reports in the scientific literature is focused on radon. As the stress build-up increases, the rocks in the impending focal zone experience opening of micro-cracks. With the opening of the cracks exposed surface area of rocks increases that leads to enhanced emanation of radon. If this increase in radon intensity can be measured at the surface, it can serve as a possible precursor to earthquakes. Diffusion is the simplest mechanism, but owing to its short half-life, radon cannot travel more than a few meters. The second mechanism, the advection mechanism, is mostly dominated in fault zones and fractured systems and convection can occur when a sufficient thermal gradient is available

---

[1] Researcher, National Center for Research on Earthquake Engineering, walia@ncree.narl.org.tw
[2] Associate Researcher, National Center for Research on Earthquake Engineering, kumar@ncree.narl.org.tw
[3] Visiting Professor, National Center for Research on Earthquake Engineering, arora@ncree.narl.org.tw
[4] Assistant Researcher, National Center for Research on Earthquake Engineering, sjlin@ncree.narl.org.tw
[5] Assistant Researcher, National Center for Research on Earthquake Engineering, seanchang@ncree.narl.org.tw
[6] Professor, Department of Geosciences, National Taiwan University, tyyang@ntu.edu.tw
[7] Professor, National Center for Research on Earthquake Engineering, wenkl@ncree.narl.org.tw

within the soil, depending on many local parameters, such as viscosity, porosity, permeability and so on. The transport by means of a carrier gas (Yang et al., 2003, 2011) is particularly important inside a volcanic edifice, where gases, such as, CO_2, H_2 SO_2 and H_2S etc. are abundantly present and can be good carriers of radon, reaching the surface at very high rates. Radon monitoring across the seismic active zone is motivated by these physical processes. In addition, change of soil moisture (capping effect), squeezing of water (rinsing effect) and the rise & fall of water table following the events of rainfall produce fluctuations in radon intensity. The real assessment and quantification of these influences is a major pre-requisite in the isolation of precursory signals.

Taiwan is a product of the arc-continent collision between Philippine Sea plate and Eurasian plate which makes it a region of high seismicity. In the southern part of the island, the Eurasian plate is subducting under the Philippine Sea plate while in the northern part of the island, the Philippine Sea plate bounded by the Ryukyu trench is subducting beneath the Eurasian plate. Behind the Ryukyu trench, the spreading Okinawa trough has developed. The northern part of Taiwan Island is located at the western extrapolation of the Okinawa trough. These collisions are generally considered to be the main source of tectonic stress in the region which is, thus, densely faulted and seismically active.

In last few years, we focused on the temporal variations of soil-gas composition at established geochemical observatories along the Hsincheng fault (HC) in Hsinchu area, Hsinhua fault (HH) in Tainan and at Jaosi (JS) in Ilan areas of Taiwan, respectively, to determine the influence of enhanced concentrations of soil gases to monitor the tectonic activity in the region and to test the previously proposed tectonic setting based model (Walia et al, 2009b, Walia et al, 2012) from data generated at earthquake monitoring stations during observation period. The stress-induced variations due to impending earthquakes in radon are contaminated by meteorological changes (i.e. atmospheric temperature, pressure, precipitation etc.) and, hence assessment and quantification of these influences is a major pre-requisite in the isolation of precursory signals. The present study is aimed at the appraisal and filtrations of these environmental/ meteorological parameters. Detailed geology and tectonic features of the monitoring stations are reported elsewhere (see the previous reports).

Methodology

Temporal soil-gases compositional variations were measured regularly at continuous earthquake monitoring stations using RTM2100 (SARAD) for radon and thoron measurement following the procedure as described in Walia et al, 2009b. Seismic parameters (viz. earthquake parameters, intensity at a monitoring station etc.) and meteorological parameter data were obtained from Central Weather Bureau of Taiwan (www.cwb.gov.tw).

To carry out the present investigation, a segment of soil-gas radon data for the station HC and HH was selected for its continuity, availability of corresponding atmospheric pressure, temperature, humidity and rainfall data from Central Weather Bureau. Single Value Decomposition (SVD) in the form of Singular Spectral Analysis (SSA) was applied to isolate respective variations.

Results and Discussions

Long term time series data are fundamental to try various numerical tools to quantify the influences of meteorological parameters as well as critical to re-validate the developed methodology using some recent segments of the data. As per the present practice, the data from various stations are examined synoptically to evaluate earthquake precursory signals against the backdrop of rainfall and other environmental factors (see the previous reports). Various guidelines are developed to identify the nature of precursory signals almost in real time. A tectono-physical model to isolate precursory radon signals and to issue a provisional forecast for future academic assessment and integration with other precursory signals has already been proposed (Walia et al, 2009b, Walia et al, 2012). In earthquake prediction research it is extremely important to estimate the size and shape of the earthquake preparation zone. We calculated effective/strain radius (D) for the earthquake preparation zone using Dobrovolsky (1979) formula:

$$D=10^{0.43M}$$

where, M is the magnitude of the earthquake.

Taiwan is one of the most active seismic regions of the world with an average of about 20,000 earthquakes occurring every year in or around as reported by the Central Weather Bureau of Taiwan (www.cwb.gov.tw). Therefore, it is essential to define some selection criteria to identify threshold earthquakes for this study. Based on the anomalous signatures from particular monitoring stations we are in a state to identify the area for impending earthquakes of magnitude ≥ 5. For selection criteria, earthquakes having local intensity ≥ 1 at the monitoring stations with epicentral distance (R) < 150 kms having D/R ratio ≥ 1 with focal depth < 40 kms are considered.

After careful examination of all available data from a network of 3 stations, a segment of soil-gas radon data for the station HC, corresponding to a period of about 7 months, i.e., from August 11, 2009 to March 5, 2010, was selected for applying the statistical filtrations. The 15 minute data were carefully edited for rare duplicate sampling, gaps and discontinuous jump following intervals of mal-functioning of equipments. Since allied meteorological data were available with hourly sampling, 15-min radon were also reduced to hourly averages. It is to note that time series is dominated by two classes of variations; (i) periodic variations at diurnal frequencies, (ii) aperiodic signals with a time scale of less than 30 days, the formulation of Single Value Decomposition (SVD) in the form Singular Spectral Analysis (SSA) was applied to isolate respective variations. The decomposed eigen values in the radon show absence of variations determined by earth tides. Aperiodic signals in radon, in period band of 2-30 days, show some control of temperature, pressure and rainfall (Fig. 1). It has been noted that sharp changes in radon are correlated with rainfall occurrence, although with some phase lag. However, it has been observed that radon variations are not significantly influenced by temperature and pressure variations.

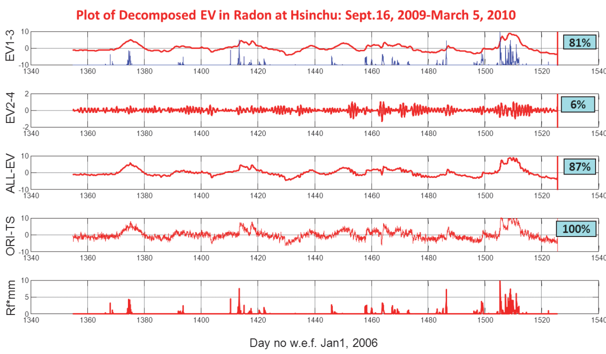

Fig. 1 Sum Plots of aperiodic (EV1&EV3) and periodic (EV2&EV4) decomposed Eigen Values (EV) together with the sum of all EV and original time series (ORO-Ts) in Radon at station Hsinchu during September 16, 2009 - March 5, 2010. The lower panel shows the distribution of rainfall (Rf). Percentage variance accounted for by combined EV are shown in boxes.

With an objective to identify earthquake related perturbation in radon, the residual radon variations corrected for temperature, pressure and rainfall indicated changes are compared in relation to earthquake occurrence. Amongst the various meteorological parameters, the influence of rainfall on radon is found to be the strongest. Radon at the onset of rainfall shows a step-jump that attain peak in 12-15 hours. This is attributed to increased flow of radon to measuring chamber as increased soil moisture prevents escape of radon into the atmosphere (capping effect). After the rainfall, radon shows regular recession in a complex manner. The intensity of radon decreases rapidly first and then shows slow decrease which continued for the next several days. In addition, radon variation shows long-term modulations which appear to be due to ground level variations. After testing linear and exponential decay pattern, the overall recession could be approximated in terms of double exponential decay and internal loading could reproduce the most salient perturbation seen during the intervals of rainfall (Fig. 2a). The residual radon series shows some definite deviations in respect of earthquake occurrences which are in agreement with

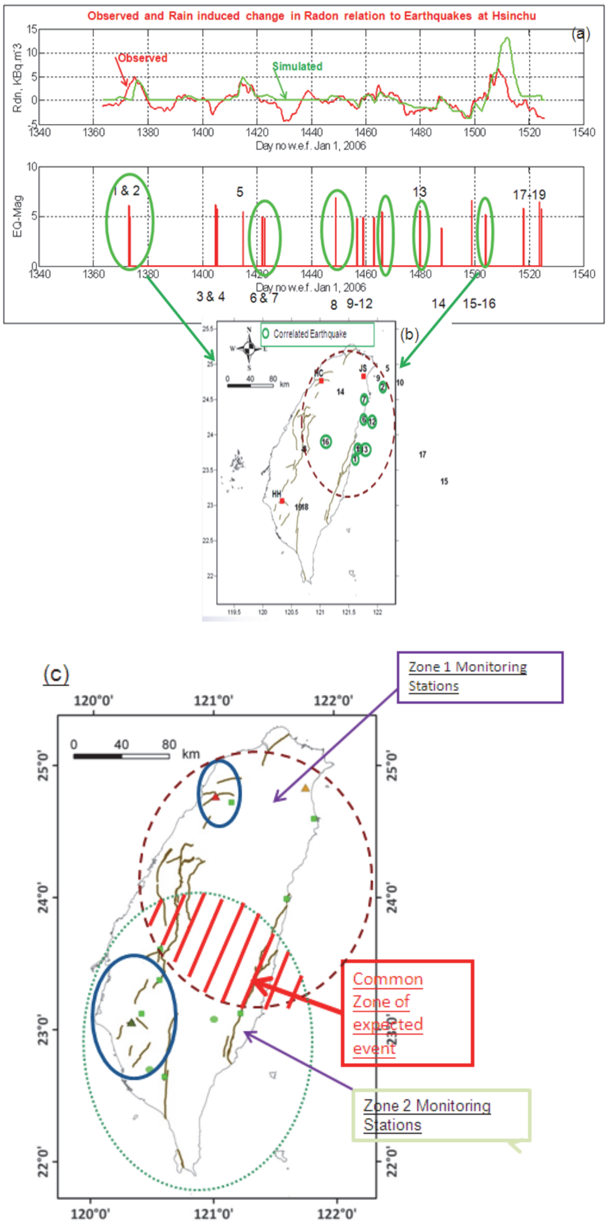

Fig. 2 (a) Relation of significant perturbations in observed and rainfall induced changes in radon with 19 earthquakes occurring within radius of 150 km of the monitoring station at Hsinchu during the selected observation period (b) Corelated earthquakes with radon monitoring station at Hsinchu (c) Proposed tectonic based model.

the signatures inferred from long term synoptic observations (Fig. 2). It can be noted that many of the strong perturbations in radon are the manifestation of the rainfall induced effects. Allowing for these correspondences, still a number of anomalies can be related to earthquake occurrences. It is obvious that all earthquake occurrences within 150 km of the recording stations produce anomalies. Some of the significant anomalies are consistent with earthquakes numbered 1, 2, 6, 7, 8, 12, 13 as well as 15-16 (Fig. 2b) and these fit well in the proposed model (Fig. 2c).

In order to check the efficiency of applied methodology, we have also applied SSA filter to a selected data segment (i.e. Nov. 2011 to Feb 2012) for the HH monitoring station (Fig. 3). The The singular value decomposition (SVD) results show that radon varations at HH stations is more influenced by periodic variations corresponding to diurnal and semi-diurnal variation (about 25%) which are found to be less at HC monitoring station (6%) data. It may be attributed to the daily temperature variations. Further, it has been noted that radon variation is not much effected by rainfall during the observation period, although no heavy rainfall was recorded during that period. Same kind of synthetic curve will be developed for this and other monitoring stations.

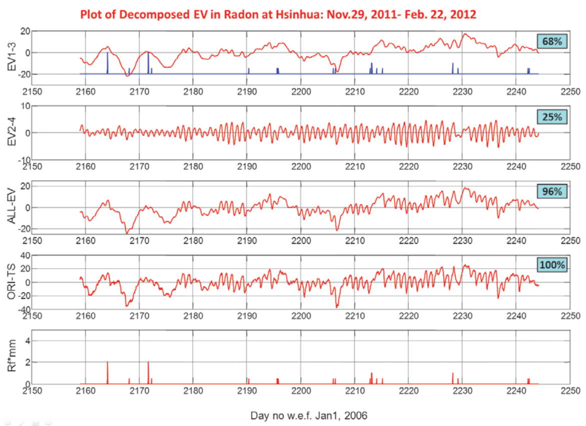

Fig.3 Sum Plots of aperiodic (EV1&EV3) and periodic (EV2&EV4) decomposed Eigen Values (EV) together with the sum of all EV and original time series (ORO-Ts) in Radon at station Hsinhua during November 29, 2011 – Feburary 22, 2012. The lower panel shows the distribution of rainfall (Rf). Percentage variance accounted for by combined EV are shown in boxes.

References

Etiope G., Calcara, M., Quattrocchi, F. (1997). "Seismogeochemical algorithms for earthquake prediction: an overview". *Annali Di Geofisica*, 40(6), 1483-1492.

Dobrovolsky, I.P., Zubkov, S.I. and Miachkin, V.I. (1979). "Estimation of the size of earthquake preparation zones". *Pure and Appl. Geophys*., 117, 1025-1044.

Kumar, A., Singh, S., Mahajan, S., Bajwa, B.S., Kalia, R., Dhar, S., (2009). "Earthquake precursory studies in Kangra valley of North West Himalayas, India, with special emphasis on radon emission". Appl. Radiat. Isot. 67, 1904-1911.

Fu, C.C., Yang, T.F., Walia, V., Chen, C.H. (2005). "Reconnaissance of soil gas composition over the buried fault and fracture zone in southern Taiwan". *Geochemical Journal*, 39,427-439.

Walia, V., Yang, T.F., Lin, S.J., Hong, WL., Fu, C.C., Wen, K-L.,Chen, C-H. (2009a). "Geochemical variation of soil-gas composition for fault and earthquake precursory studies along Hsincheng fault in NW Taiwan". *Appl. Radiat. Isotopes, 67, 1855- 1863*.

Walia, V., Yang, T.F., Lin, S.J., Hong, W.L., Fu, C.C., Wen, K.L.,Chen, C.H. (2009b). "Continuous temporal soil.gas composition variations for earthquake precursory studies along Hsincheng and Hsinhua faults in Taiwan". *Radiat. Meas.,* 44, 934.939.

Walia, V., Virk, H.S., Yang, T. F., Mahajan, S., Walia, M. and Bajwa, B.S. (2005). "Earthquake prediction studies using radon as a precursor in N.W Himalayas, India: a case study". *TAO*, 16(4), 775.804.

Walia, V., Lin, S-J.,Yang, T.F., Fu, C-C., Hong, W-L., Wen, K-L.,Chen, C-H. (2010). "Soil-gas monitoring: A tool for fault delineation studies along Hsinhua Fault (Tainan) Southern Taiwan." *Applied Geochemistry, 25,* 602-607.

Walia, V., Yang, T.F., Lin, S-J., Kumar, A., Fu, C-C., Chiu, J-M., Chang, H-H., Wen, K-L.,Chen, C-H. (2012). "Temporal variation of soil gas compositions for earthquake surveillance in Taiwan." *Radiat. Meas.,* http://dx.doi.org/10.1016/j.radmeas.2012.11.007.

Yang, T.F., Chou, C.Y., Chen, C.H, Chyi, L.L., Jiang, J.H. (2003). "Exhalation of radon and its carrier gases in SW Taiwan". *Radiat. Meas.* 36, 425.429.

Yang, T.F., Fu, C.C., Walia, V., Chen, C.H., Chyi, L.L., Liu, T.K., Song, S.R., Lee, M., Lin, C.W., Lin, C.C., (2006). Seismo-geochemical variations in SW Taiwan: multi.parameter automatic gas monitoring results, *Pure Appl. Geophys.*, 163, 693.709.

Yang, T.F., Wen, H.-Y., Fu, C.-C., Lee, H.-F., Lan, T.F., Chen, A.-T., Hong, W.-L., Lin, S.-J., Walia, V., (2011). "Soil radon flux and concentrations in hydrothermal area of the Tatun Volcano Group, Northern Taiwan". *Geochem. J.*, 45, 483-490.

From P Wave Attenuation to Study 2006 Taitung Earthquake

Yi-Zeng Chang [1] and Strong Wen [2] and Chau-Huei Chen [3] and Kou-Liang Wen [4]

張議仁 [1]、溫士忠 [2]、陳朝輝 [3]、溫國樑 [4]

Abstract

Amplitude attenuation and attenuation dispersion are the two main methods used in the study of seismic wave attenuation, especially the attenuation dispersion obtained from single stations. When the seismic wave is propagating, its geometric spread and inelastic absorption would affect the amplitude as well as related factors such as the rock porosity, lithology, temperature and pressure conditions, rock particle size, viscosity, and the saturation of the medium. According to the continuous relaxation model, based on the assumption that the attenuation material is a linear viscoelastic solid, we picked up the first cycle of the P arrival wave from the vertical component in a single station to calculate the delay time of the group velocity using the multiple filter technique and then adopted the Genetic Algorithm (GA) method to investigate the related parameters of the Qp value. In this study, we calculated the temporal variation of Qp with the stations near to the 2006 Taitung earthquake epicenter (M6.2). We explored each quadrant of the Qp value changes with different stations and the consistency in different orientations of the stations. The results confirmed each other to enhance the observable characteristics of strong earthquake forecasting.

Keywords: Attenuation dispersion, Qp

Introduction

The purpose of this study is to make use of the attenuation dispersion of seismic waves to investigate the characteristics of the medium before a strong earthquake event. This includes the study of the differences in regional characteristics, how the size of the main shock shows the correlation between a strong earthquake and the dispersion property, the relationship between the size of the main shock and the Q value, the temporal variation in Q value anomaly distribution, the Q value abnormal direction and many other related issues. If a correlation between a strong earthquake event and the Q value can be found, a seismogenic zone could be detected through surveying. Since real-time waveform data and related earthquake information cannot be obtained immediately, this study firstly investigated large historic earthquakes. Enough stations were located near the main shock, allowing the production of good quality data that could be used to analyze bigger magnitude events. Since the crust medium exhibits non-uniform and non-elastic characteristics, the use of the attenuation property of the seismic wave can help us obtain information when seismic waves passing through the path bring out the medium component, status, and the temperature distribution. The study of attenuation dispersion is suitable for the study of smaller events. In that way, more of the available seismic data can be used and the distribution of small earthquake locations, depths, and epicenter distances can make our study more comprehensive.

Methodology

The attenuation dispersion model was based on the continuous relaxation model, which was proposed by Correig and Mitchell (1989). The Q value can be

[1] Assistant Researcher, National Center for Research on Earthquake Engineering, yzchang@ncree.narl.org.tw

[2] Associate Researcher, National Center for Research on Earthquake Engineering, scwen@ncree.narl.org.tw

[3] Professor, Dept. of Earth and Environment Sciences, National Chung Cheng Univ., seichen@eq.ccu.edu.tw

[4] Professor, Dept. of Earth Science, National Central Univ.,wenkl@ncree.narl.org.tw

expressed by the following equation：

$$Q^{-1}(\omega) = \frac{2}{\pi} Q_m^{-1} \arctan \left[\frac{\omega(\tau_1 - \tau_2)}{1 + \omega^2 \tau_1 \tau_2} \right] \qquad (1)$$

ω : Angular Frequency

τ_1, τ_2 : Long and Short Relaxation Times

Q_m^{-1} : Constant representing the flat part of the spectrum (Liu et al., 1976)

If the attenuation medium can be referred as the linear viscoelastic solid, then the phase velocity can be showed as (Ben-Menahem and Singh, 1981)：

$$C(\omega) = C_\infty \left\{ 1 + \frac{1}{\pi} Q_m^{-1} \left[\ln\frac{\tau_1}{\tau_2} + \frac{1}{2}\ln\left(\frac{1+\omega^2\tau_2^2}{1+\omega^2\tau_1^2} \right) \right] \right\}^{-1} \qquad (2)$$

C_∞ : Phase Velocity at Infinite Frequency (the Perfectly Elastic Case)

Correig (1991) used formula (1) to express the relationship between group velocity and phase velocity ：

$$U(\omega) = \frac{C(\omega)}{1 - \frac{\omega}{C(\omega)} \frac{dC(\omega)}{d\omega}} \qquad (3)$$

Then, the delay time of group velocity is the following:

$$\Delta t_g = t_g(\omega) - t_g(\omega_r) \quad \text{(Correig, 1991)：}$$

$$\Delta t_g = \frac{t}{\pi Q_m} \left[\frac{1}{2} \ln \frac{(1+\omega^2\tau_2^2)(1+\omega_r^2\tau_1^2)}{(1+\omega^2\tau_1^2)(1+\omega_r^2\tau_2^2)} + \frac{\omega^2(\tau_1^2-\tau_2^2)}{(1+\omega^2\tau_1^2)(1+\omega^2\tau_2^2)} - \frac{\omega_r^2(\tau_1^2-\tau_2^2)}{(1+\omega_r^2\tau_2^2)(1+\omega_r^2\tau_2^2)} \right] \qquad (4)$$

t : The Travel Time of the Signal at Infinite Frequency

ω_r : Reference Frequency

We obtain the delay time of the group velocity from multiple filter techniques and apply this to formula (4) with the travel time of the P wave. Finally, we can obtain Q_m, τ_1 and τ_2 through the Genetic algorithm (GA) inversion。

Data processing

In Figure 1, the study area is illustrated along with the station distribution (the blue triangles), the red star indicates as the location of epicenter of the 2006 Taitung earthquake (2006/04/01, M6.2) and the red lines are the fault traces. This study used the data from the CWBSN to search the attenuation parameters.

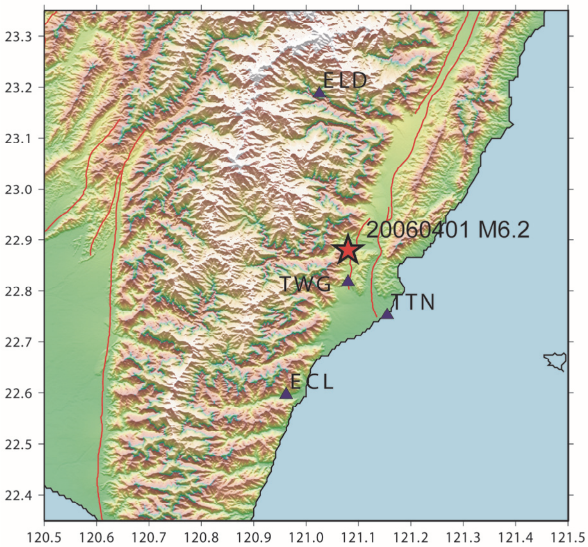

Fig. 1 The study area where includes Taitung earthquake and the related stations.

1. Choosing data

We choose the vertical component data having a magnitude lower than 3 from October 2005 to March 2006 for each station. We must take into account that the larger the earthquake, the lower the angular frequency becomes. Therefore, even while using smaller events, the angular frequency can still fall into the frequency range. As a side-note, a relatively large number of smaller events can help us study the surrounding environment of the measuring stations. The main factor of high frequency energy attenuation is the propagation distance so the data accessed was for the selected epicenter and the focal depth was within 30 km of the station. Regional stress accumulations are within a limited range before a strong earthquake hits, and longer wave propagation paths tend to weaken the seismic waves to bring abnormal characteristics from seismogenic areas. But for these factors, this study would have used ECL and ELD stations that were over 30 km from the epicenter. Therefore, the epicenter distance of these two stations are changed to 40 and 50 km, respectively. In addition, the seismic data received by the TTN station exhibited a high noise ratio, so the poor quality data from this station cannot be used in this study. Figure 2 shows the selected events near the TWG station.

2. Resample and filter the signal

The waveform was resampled at 1000 points by using the Newton Interpolation method and the band-pass filter.

3. Cut the first cycle of P wave

According to the theory in Cong and Mejia (2000) and Correig (1991), the first cycle of the P wave is enough to obtain information on the medium and is quite resilient to interference from other phase signals. Therefore, we cut the first cycle of the P wave in our calculations. In Figure 3, the waveform of the first cycle of the P wave with duration of 0.1~0.2 seconds is shown.

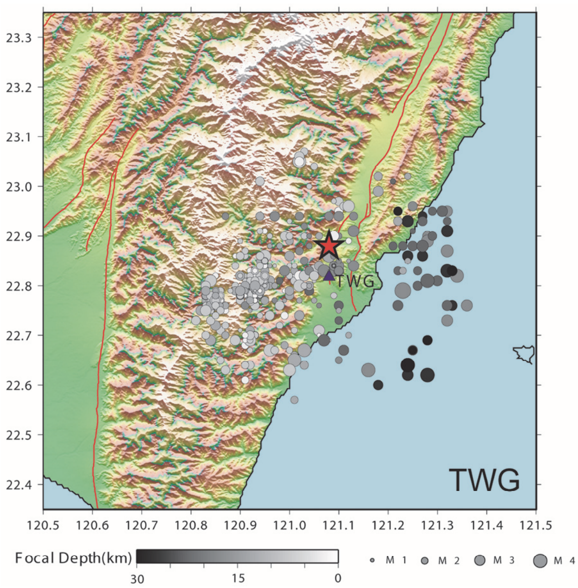

Fig. 2 The distribution of earthquakes near by TWG station

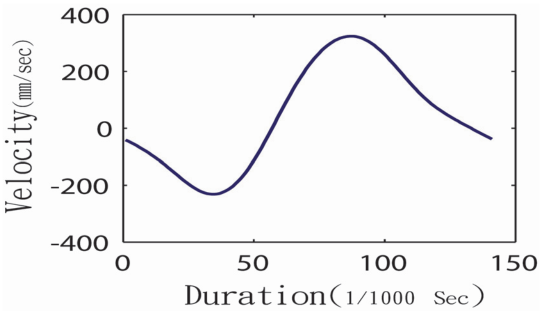

Fig. 3 Cutting the first cycle of P wave

4. Calculating the Group Velocity Delay Time Spectrum from Multiple Filter Method and using GA to Invert the Attenuation Factors Qp

The interception of the first cycle of the P wave would adopt multiple filters to obtain the group-velocity delay time-frequency spectrum. In Figure 4, the horizontal axis is the frequency, and the ordinate is the time, the red circle represents the magnitude of the energy corresponding to the different frequencies. If the waveform data is disturbed, then the time-frequency spectrum would exhibit chaotic behavior and the data would not be used. Finally, we use GA to search for optimal solutions (shown in red lines) to produce , and in formula (4). Finally, each seismic Q value statistic obtained by the stations is converted into a distribution diagram corresponding to its time and an appropriate average is taken to show the temporal variation in attenuation factor changes due to the tectonic seismogenic process in the station's vicinity before strong earthquakes.

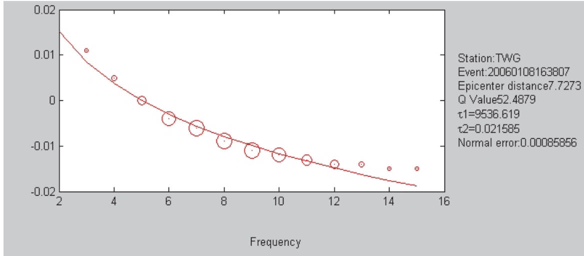

Fig. 4 The spectrum with the group velocity delay time

Results and Discussions

In this study, the chosen stations (TWG, ECL, and ELD) were near the 2006 Taitung earthquake epicenter (M6.2) but the TTN station was not used due to poor quality waveform data. The distances of the ECL and ELD stations from the epicenter of the Taitung earthquake (M6.2) are more than 30 and 40 km, respectively, thus, these results in a smaller weighting on the path of the seismic wave propagated through the source area of the strong earthquake and the selected events are weighted less. Therefore, since the variation of the Qp value is not as obvious, this report omitted the results of the two stations.

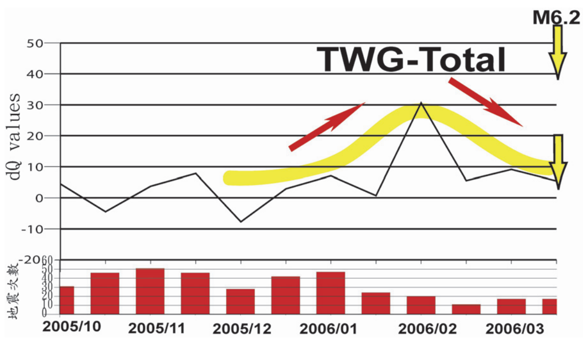

Fig. 5 TWG station: The variation of temporal average in δQ . The yellow arrow indicates the occurrence of the Taitung earthquake and the red histogram indicates the number of events.

According to the Qp study in Cong et al (2000), the Qp value increases with epicenter distance. Therefore, this study adopted linear regression to obtain a linear trend with the epicenter distance erasing the effect of epicenter distance to obtain the residual of Qp (see Figure 5). Moreover, in order to investigate the change in the path effect related to the δQ , we used the station as the center to divide the seismic data into different orientations to explore the changes in δQ (see Figure 6).

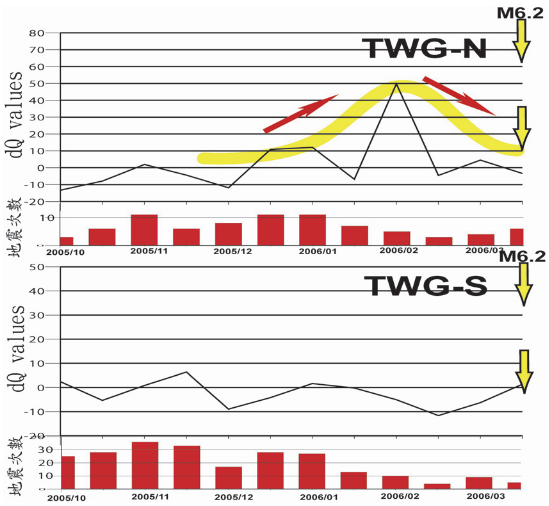

Fig. 6 The variation of δQ in TWG station.

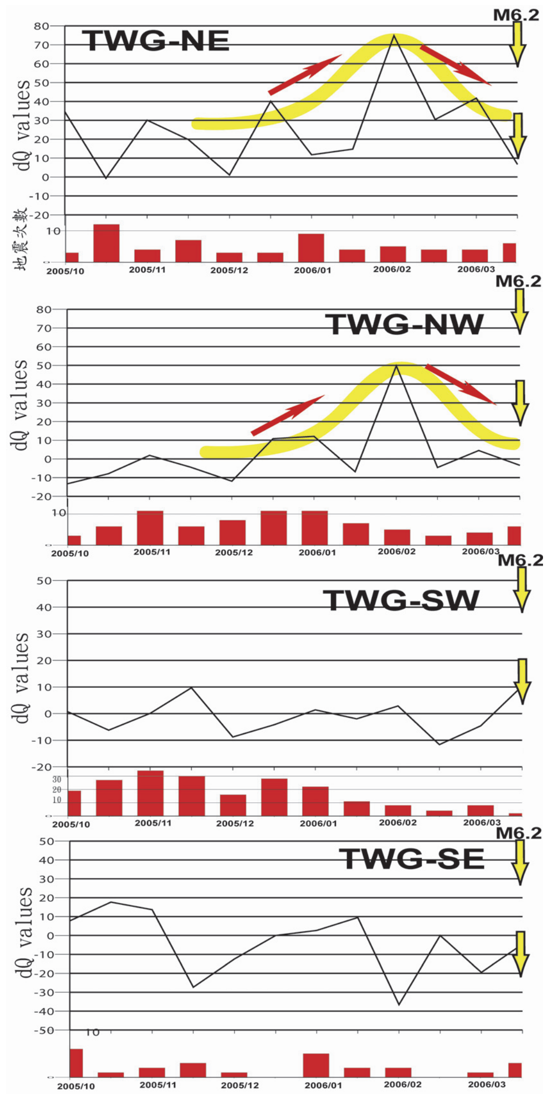

Fig. 7 The azimuth variation of δQ in TWG station.

The study adopted the temporal average of 0.5 months as a unit to display the variation of δQ. This value is mainly related to the number of earthquakes because the finer sorting corresponds to the number of events. Figure 5 shows the value to be slightly higher in February since the Qp value is related to the path. Therefore, we try to separate the north side from the south side based on the TWG station in Figure 6. From the results, the peak value becomes more apparent in north side of TWG in February while the south side is relatively stable. In the study area, the Taitung earthquake (M6.2) is located to the north of the TWG. This makes it reasonable for the north side to exhibit anomalies in its data. This also confirms the high values that the TWG station observed in February (Figure 5), and their absence in the south side. For finer classification, the azimuth is mainly limited by time - number of earthquakes. This study further divided the data into four regions to analyze (Figure 7). In Figure 7, the TWG-NE and TWG-NW both appear to have high values in February. This phenomenon is understood to occur from the Taitung earthquake (M6.2) being located in the north side of the TWG station.

Conclusions

In this study, the high quality of waveform data is a necessity, and having a sufficient number of earthquakes within the time unit is also important. Using small-scale earthquakes to increase the number of natural earthquakes can make this data useful in enhancing the data quality. Moreover, analyzing real time seismic data is also a major problem owing to the limitations in data processing, which includes the data download and location procedures. If more stations were available to monitor the study area, we could use the azimuth variation in δQ to identify the same area with different stations. This can provide us with important information of precursors to strong earthquakes.

References

Ben-Menahem, A., and S. J. Singh (1981). Seismic Waves and Sources,Springer-Verlag, New York, 1108 pp.

Correig, A. M., and B. J. Mitchell (1989). Attenuative dispersion at La Cerdanya, eastern Pyrenees, Phys. Earth Planet. Int. 57, 304-310.

Correig, A. M. (1991). On the measurement of body wave dispersion, J. Geophys. Res. 96, 16,525-16,528.

Cong L, J. Mejia, B. J. Mitchell（2000）. Attenuation dispersion of P waves in near the New Madrid seismic zone, Bull. Seism. Soc. Am. 90（3）, 679-689.

Liu, H. P., D. L. Anderson, and H. Kanamori (1976). Velocity dispersion due to anelasticity: implications for seismology and mantle composition, Geophys. J. R. Astron. Soc. 47, 41-58.

Rapid on-site peak ground acceleration estimation based on SVM and P-wave features in Taiwan

Ting-Yu Hsu[1] , Shieh-Kung Huang[2], Yu-Weng Chang[3], Chun-Hsiang Kuo[4], Che-Min Lin[5], Tao-Ming Chang[6], Kuo-Liang Wen[7], Chin-Hsiung Loh[8]

Abstract

This study extracts pressure wave (P-wave) features from the first few seconds of recorded vertical ground acceleration at a single station. These features include the predominant period, peak acceleration amplitude, peak velocity amplitude, peak displacement amplitude, cumulative absolute velocity, and the integral of the squared velocity. The support vector regression method is employed to establish a regression model, which can predict the peak ground acceleration according to these features. Some representative earthquake records of the Taiwan Strong Motion Instrumentation Program from 1992 to 2006 are used to train and validate the support vector regression model. Then the constructed model is tested using entire earthquake records from the same period as well as the 2010 Kaohsiung earthquake with a magnitude of 6.4 ML. The effects on the performance of the regression models using different P-wave features and different lengths of time window to extract these features are studied. The results illustrate that, if the first three seconds of the vertical ground acceleration are used, then the standard deviation of the predicted peak ground acceleration error for the entire 15 years of earthquake records tested is 20.89 gal. The time window can be shortened, e.g., to 1 second, increasing the prediction error slightly, in order to lengthen the lead-time before destructive shear waves reach the station.

Keywords: earthquake early warning, single station method, on site, support vector machine, peak ground acceleration

Introduction

In an earthquake early warning system, an on-site warning issues an alarm within a few seconds after triggered, based on initial pressure wave (P-wave) motion at a single station. Nakamura (1988) developed an earthquake early warning system named UrEDAS that predicted potential damage according to the estimation of magnitude and location based on the calculated predominant frequency, back azimuth, vertical-to-horizontal ratio, and amplitude level. Nakamura (1998) further developed the Compact UrEDAS which estimated potential damage based on the calculation of destructive intensity defined as the logarithm of the absolute value of the inner product of acceleration and velocity. Odaka et al. (2003) tested another approach to estimate magnitude and epicenter distance based on the P-wave amplitude and the fitting parameter of the waveform envelope. Kanamori (2005) proposed another predominant frequency of P-wave which is similar to the one developed by Nakamura (1988) to estimate the magnitude. He proposed the combination of both the predominant frequency and peak ground displacement (PGD) of the P-wave measured in the vertical direction to recognize damaging earthquakes. Bose et al. (2012) estimated

[1] Associate Researcher, National Center for Research on Earthquake Engineering, dysheu@ncree.narl.org.tw.
[2] Assistant Researcher, National Center for Research on Earthquake Engineering, sghuang@ncree.narl.org.tw.
[3] Assistant Researcher, National Center for Research on Earthquake Engineering, ywchang@ncree.narl.org.tw.
[4] Associate Researcher, National Center for Research on Earthquake Engineering, chkuo@ncree.narl.org.tw.
[5] Associate Researcher, National Center for Research on Earthquake Engineering, cmlin@ncree.narl.org.tw.
[6] Associate Researcher, National Center for Research on Earthquake Engineering, tmchang@ncree.narl.org.tw
[7] Professor, Department of Earth Sciences and Institute of Geophysics, National Central University, wenkl@earth.ncu.edu.tw.
[8] Professor, Department of Civil Engineering, National Taiwan University, lohc0220@ntu.edu.tw

the magnitude, epicenter distance and peak ground velocity (PGV) based on the three-component waveforms of acceleration, velocity and displacement. In summary, in the above-mentioned literature, an on-site earthquake early warning is issued according to the estimated magnitude, location, PGV, and/or vulnerability of the earthquake.

However, the peak ground acceleration (PGA) is also a representative parameter for earthquake early warning. Following an earthquake, the seismic intensity scale measured at each station can be calculated according to the measured PGA. For example, in Taiwan, the Central Weather Bureau calculate the seismic intensity scale based on an equation of the form $I = a\log(PGA) + b$, where *a* and *b* are constants. Similarly, the Japan Meteorological Agency also reports the earthquake intensity level based on the ground acceleration. The United States Geological Survey can also report the Modified Mercalli Intensity (MMI) scale at each station for smaller events based on the measured PGA using the relationship developed by Worden et al. (2012). Besides, for practical concerns, the PGA threshold is one of the main criteria for earthquake emergency reactions in many applications. For instance, the Taiwan high-speed rail uses PGA as the main criterion for emergency stops. Nuclear power plants also use PGA as the criterion for emergency shutdowns.

Therefore, in this study, PGA is chosen as the target to be estimated. The P-wave features including predominant frequency, peak ground acceleration, peak ground velocity, peak ground displacement, cumulative absolute velocity, and integration of the squared velocity, will be extracted from the initial P-wave motion of the vertical component at a single station. The support vector regression (SVR) method is employed to establish a regression model to predict the PGA according to these P-wave features. In order to gain more lead-time on the on-site warning, the effect of the length of the initial P-wave motion on the performance of the SVR model is also studied.

In addition, the databases used in the literature to establish and validate an empirical regression model between the initial P-wave motion and the final peak ground motion is usually limited to some selected records of some representative events; the epicenter distance is also restricted in some cases. As a result, the applicability of the established empirical regression model could be restricted to only the selected events. Furthermore, since the established empirical regression model has never been validated through the earthquake events of an entire period, e.g., 10 years, the estimated error in practice has never been revealed. Therefore, in this study, earthquake records between 1992 and 2006 from the Taiwan Strong Motion Instrumentation Program (TSMIP) (Liu et al. 1999) will be used to test the proposed approach. The database includes the catastrophic 1999 Chi-Chi earthquake and several damaging earthquake events as well as more than ten thousands records of non-damaging earthquakes.

Methodology

The on-site earthquake early warning technique takes advantage of the different velocities of propagation of P-waves and S-waves. In other words, the expected ground shaking dominated by S-waves can be estimated based on the recorded early informative P-wave of a single station. This is usually accomplished through empirical regressions between the P-wave features extracted from the measurements of the first few seconds and the final earthquake intensity at the same site. Satriano et al. (2011) reviewed the concepts, methods and physical backgrounds of earthquake early warning systems. The P-wave features used to estimate the final earthquake size were also summarized in the same paper. These P-wave features include the peak measurement, predominant period and integral quantities. The P-wave features used to estimate final earthquake intensity in this study are briefly introduced in the following paragraphs.

Firstly, the peak measurement of acceleration, velocity and displacement in the vertical direction t_p seconds after the P-wave's arrival are considered. These features are denoted as P_a, P_v, and P_d, respectively and can be calculated in a straightforward manner. These parameters correlate to the PGA, PGV and PGD of the entire measured time history of ground motion at the same station. Next, the effective predominant period T_c proposed by Kanamori (2005) is employed. This parameter is correlated to the earthquake magnitude. Finally, two more integral quantities are used; the cumulative absolute velocity (CAV) and the integral of the squared velocity (IV2). The CAV is used as a threshold value to determine whether a damaging earthquake is coming. The IV2 is correlated to earthquake magnitude. In this study, the above-mentioned six P-wave features extracted from the vertical component of ground motion after P-wave arrival are used for rapid estimation of PGA.

SVR, which is a supervised learning method based on statistical learning theory, is very effective for solving multivariate problems. Moreover, it has outstanding advantages over other methods, such as no local minimum problem and reliability at underfitting, overfitting, or in high noise conditions. Owing to these merits, this paper employs the SVR algorithm to establish a nonlinear regression model between several P-wave features and PGA. The details for employing SVR to establish a regression model are given by Hsu et al. (2013).

Earthquake data and preprocessing

Approximately fifteen years of TSMIP data between the 29th of July 1992 and the 31th of December 2006 recorded by the Central Weather Bureau are employed in this paper. A total of 91,142 sets of data, named “Testing Earthquake Data”, are used in this study to estimate the general performance of the proposed approach. In order to reduce the time required for training the SVR model, 71 earthquake events with local magnitudes, M_L, between 3.0 and 7.3 are selected for all focal depths (2.8 ~ 282.8 km). In this study, only half of the strong ground motion records of the 71 earthquake events will be used to train the SVR model. As a result, the database for training the SVR model consists of 4,166 sets of data, which are named “Representing Earthquake Data”. The original strong ground motion records are acceleration signals. The zero-mean normalization of the records was applied. The records were integrated once and twice to obtain velocity and displacement signals, respectively. The second-order 0.075Hz high-pass Butterworth filter was applied to remove the low-frequency drift after integration. The Short-Term Average/Long-Term Average algorithm was applied to determine the P-wave arrival time automatically.

Results and conclusions

Figure 1 compares the real PGA and the predicted PGA for the “Testing Earthquake Data” using the SVR model of all six P-wave features. The regions enclosed by the blue lines and the red lines are within zero- and one-level difference of the seismic intensity scale of Taiwan for reference, respectively. It can be observed in the figure that the predicted PGA approximates the real PGA. The standard deviation of the predicted PGA errors is 20.89 gal, and the ratio of the predicted PGA located within one-level difference from the real PGA is 99.22%. Note that the predicted PGA is generally lower than the real PGA, which means the predicted PGA of the SVR model is in the non-conservative side. The predicted PGA could be scaled up to the conservative side for practical application, which is not considered in this paper.

Next, the effect of the length of time window t_p was studied. Although a longer t_p achieves higher reliability, the lead-time of early warning is sacrificed. As discussed, the lead-time is the crucial factor in an effective earthquake early warning system which should issue an early warning before the arrival of destructive seismic waves, instead of issuing an alarm with very high reliability after or during the incoming destructive seismic waves.

The length of the time window t_p ranges from 0.1 to 10 seconds in intervals of 0.1 second. The results show that the standard deviation of the predicted PGA errors of the “Testing Earthquake Data” decreases as t_p increases, as shown in Figure 2. The standard deviation of predicted error diminishes very quickly from about 34 gal to 23 gal within the first second. It continues to decrease gradually thereafter to less than 18 gal. In addition, the ratios of the predicted PGA located within one-level difference from the real PGA are also plotted in the same figure. The one-level predicted ratios increase dramatically from about 91% to 97% within the first 0.4 seconds and then continue to increase rapidly to almost 99% until $t_p = 1$, which is already quite close to the maximum value saturated at around $t_p = 4$. It appears that t_p could be less than 3 seconds for practical application using the proposed approach. Thus, the extent of the region without lead-time could be reduced and valuable response time could be gained.

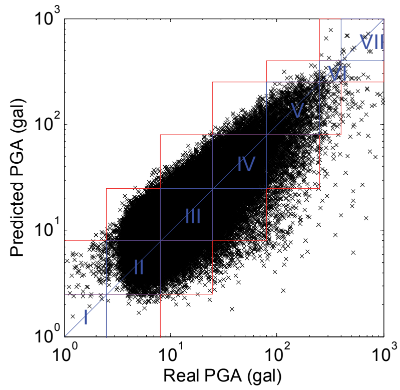

Fig. 1 Real PGA and the predicted PGA of the 91,142 sets of “Testing Earthquake Data” using the SVR model of six P-wave features with $t_p = 3$. The Roman numerals “I” to “VII” represent the seismic intensity scale in Taiwan. The regions enclosed by the blue lines represent the fact that seismic intensity of the predicted PGA is the same as the real one, while the regions enclosed by the red lines represent the seismic intensity of the predicted PGA is within ±one-scale of the real one.

Finally, the feasibility of the proposed SVR model is studied through the application of the 2010 Kaohsiung earthquake which is absent from the “Testing Earthquake Data”. The Kaohsiung earthquake with magnitude $M_L = 6.4$ and focal depth 22.6 km caused injuries to 96 people and different levels of damage to hundreds of buildings. The maximum PGA was 463.03 gal measured at the CHY062 station about 30.48 km from the epicenter, while the minimum PGA was 5.16 gal measured at the TAP057 station about 254.46 km from the epicenter. Again, the overall approximate relationship between real PGA and the predicted PGA can be observed.

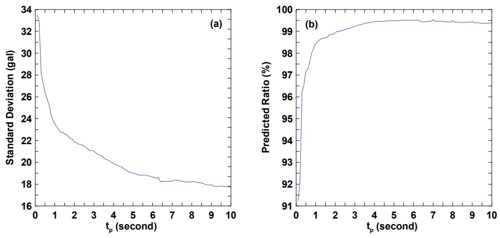

Fig. 2 The performance of the SVR model of the "Testing Earthquake Data" using different length of time window: (a) standard deviation of the predicted PGA errors and (b) ratio of the predicted PGA located within one-level difference from the real PGA.

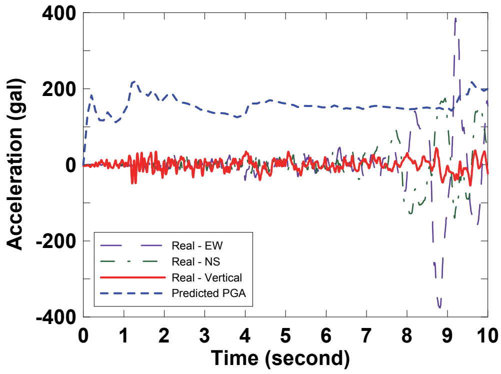

Fig. 3 The predicted PGA of the SVR models with t_p ranges between 0.1 and 10 seconds in intervals of 0.1 second at station: (a) KAU020, (b) KAU018, (c) CHY062, and (d) CHY063. The measured acceleration time-history of three directions at each station is also plotted.

The performances of the SVR models at several stations close to the epicenter are also studied. According to the reconnaissance report of the National Center for Research on Earthquake Engineering in Taiwan (NCREE), four stations, i.e. KAU020, KAU018, CHY062 and CHY063, within a short distance from the epicenter of 18.46, 24.8, 30.5 and 37.2 km, respectively, were accompanied by severe or moderate damage of nearby buildings and non-structural items (NCREE 2010). The predicted PGA at the CHY063 station using the SVR models with different lengths of time window, i.e. $t_p = 0$ to $t_p = 10$, and the measured acceleration time-history of three directions is plotted together in Figure 3. It can be observed that after the arrival of a P-wave, the predicted PGAs at different times are larger than 80 gal or 92 gal, which corresponds to intensity V on the Taiwan scale and intensity VI on the MMI scale (Worden et al. 2012), respectively. In other words, if the warning is issued based on these intensities, the region close to the station could be alerted directly after the arrival of a P-wave. However, in practice, due to the higher uncertainty of the predicted PGA using less P-wave information, the warning could be postponed until the first second if a higher reliability is required. Furthermore, if the warning is issued at the first second after the arrival of a P-wave, the response time before the strike of the largest seismic wave of the station is about 6 seconds.

References

Böse M, Heaton T, Hauksson E (2012) Rapid estimation of earthquake source and ground-motion parameters for earthquake early warning using data from a single three-component broadband or strong-motion sensor. Bull Seism Soc Am 102(2): 738–750.

Kanamori H (2005) Real-time seismology and earthquake damage mitigation. Annu. Rev Earth Planet Sci 33: 195–214.

Liu KS, Shin TC and Tsai YB (1999) A free-filed strong motion network in Taiwan: TSMIP TAO 10(2): 31-50.

Nakamura, Y. (1988). On the urgent earthquake detection and alarm system (UrEDAS). Proc 9th World Conf Earthquake Eng (7): 673–678.

Nakamura Y (1998) A new concept for the earthquake vulnerability estimation and its application to the early warning system. Proc Early Warning Conf Potsdam, Germany.

National Center for Research on Earthquake Engineering (2010) Reconnaissance report on Jiaxian earthquake in Kaohsiung on March 4, 2010. Taipei, NCREE-10-010 (in Chinese).

Odaka T, Ashiya K, Tsukada S, Sato S, Ohtake K, Nozaka D (2003) A new method of quickly estimating epicentral distance and magnitude from a single seismic record. Bull Seism Soc Am 93(1): 526–532.

Satriano C, Wu YM, Zollo A, Kanamori H (2011) Earthquake early warning: Concepts, method and physical grounds. Soil Dyn Earthq Eng 31: 106-118

Vapnik VN (1995) The nature of wtatistical learning theory. Berlin, Springer-Verlag

Worden CB, Gerstenberger MC, Rhoades DA, Wald DJ (2012) Probabilistic relationships between ground-motion parameters and Modified Mercalli Intensity in California. Bull Seism Soc Am 102(1): 204–221.

Hsu T.Y., Huang S.K., Chang Y.W.,Kuo C.H., Lin C.M., Chang T.M., Wen K.L., Loh C.H., "Rapid on-site peak ground acceleration estimation based on support vector regression and P-wave features in Taiwan." Soil Dynamics and Earthquake Engineering (2013), Volume 49, June 2013, Pages 210 – 217, DOI: 10.1016/j.soildyn.2013.03.001.

Investigation of Buried Pipelines under Large Fault Movements by Small-Scale Testing and Numerical Methods

Tsu-Jung Lin (林祖榕)[1]

Abstract

This paper investigates the responses of buried pipelines under large fault movements using numerical models and small-scale experiments. Well-designed small-scale shear boxes experiments can induce the soil-pipeline interaction under fault displacements. Numerical models built by the ABAQUS commercial software were able to simulate the behavior of small-scale shear box experiments at different soil depths. Comprehensive and reliable numerical simulation of this problem requires experimental data to calibrate and verify the three dimensional responses of pipelines subjected to axial and flexural loadings. Finally, recommendations and future works are proposed for the design of small-scale experiments and numerical models.

Keywords: small-scale experiment, fault movement, pipeline, local buckling

Introduction

Earthquakes can damage pipelines near the fault influencing the function of the water supply system. Thus, the structural behavior of buried pipelines under fault lines has gained attention from engineers and researchers. O'Rourke et al. (2008) addressed the large-scale testing of pipeline responses to earthquake-induced ground ruptures and pipeline system performance after earthquakes. Vazouras et al. (2010) presented a rigorous FEM model to investigate the mechanical behavior of buried steel pipelines under strike-slip faults. In Vazouras' research, the interacting soil-pipeline system was modeled by finite elements, which can account for large strains and displacements, nonlinear materials and special contact on the soil and pipelines interface. Due to the high cost and time consumption of large-scale experiments, such as the one shown in Fig. 1, small-scale experiments are often used since they are more convenient to set up and can be conducted as preliminary experiments to large-scale experiments. In this study, small-scale experiments were conducted in National Center for Research on Earthquake Engineering (NCREE) laboratory. Only strike-slip fault movements were applied by the shaking table. The selection of pipelines in the experiment has some limitations with regard to the materials and sizes due to the size restrictions of the small-scale experiments. The axial strains of pipelines and fault movement displacements can be measured during the experiments. The responses of the buried pipelines subjected to large strike-slip fault movements are investigated by finite element analysis (ABAQUS 2011). Geometric and material nonlinearities are taken into account in the simulation.

Fig.1 Large-scale soil-pipeline test at Cornell University

Test Set-up

The small-scale soil-pipeline tests were set-up at the laboratory at the National Center for Research on Earthquake Engineering (NCREE). The shear boxes used were 60 cm in length, 23 cm in width, and 32 cm in height. Fig. 2 shows that one of the shear boxes was placed on a small shaking table with a small hydraulic structural actuator (maximum forces

[1] Associate Researcher, National Center for Research on Earthquake Engineering, tjlin@ncree.narl.org.tw

of 15kN allowed) which can provide a one-way stroke displacement of 14 cm. Another shear box was set up on a small manufactured platform that can be adjusted to the same height as the shear box on the shaking table. The two shear boxes were fabricated to ensure good contact in order to prevent sand leaking issues and also to allow free movement under fault displacements. The shear boxes were initially offset to allow for maximum soil pressure acting on the pipelines, as shown in Fig. 3.

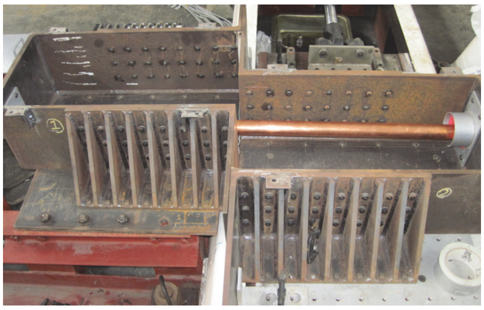

Fig.2 Shear boxes set-up

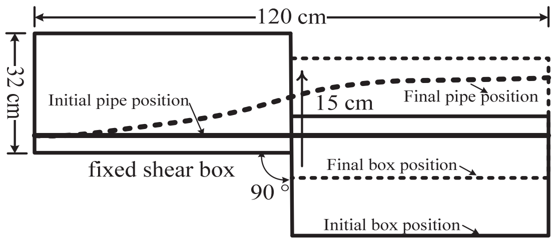

Fig. 3 Plan view of the small-scale pipeline test with key dimensions and geometry

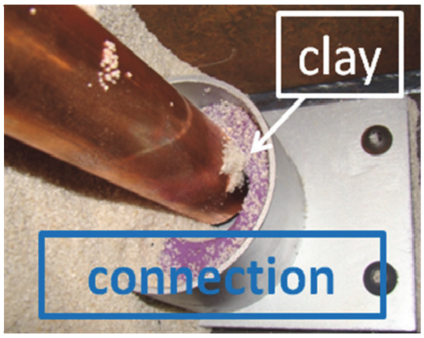

Fig. 4 The end of the pipeline.

Fig. 5 Shear boxes with loadings on the top of the sand surface.

Test Methods

All tests were conducted with partially saturated silica sand imported from Vietnam. During production, the full test set-up was completed by the following steps: 1) pipeline installation in the test basin, 2) structure adjustment at the boxes, 3) soil placement and compaction. Tests were performed using the static monotonic loading method at a 0.5mm/sec speed (slow). Twenty instances of data per second could be recorded. A long steel strip was placed on the bottom of the shear boxes to prevent sand leaking outside the boxes from the location of fault movement.

Compared to large-scale experiments, the small-scale soil-pipeline interaction experiments may bring size effect issues. The choice of pipeline size, soil properties in the small shear boxes and boundary conditions at the ends of the pipeline needed to be considered in the test set-up. The pipeline size chosen in the current tests was 40 mm in diameter with a 0.5 mm copper thickness. The buried depth was 125 mm. Both ends of the pipeline were surrounded by soft clay in order to appropriately reflect the real site situation, as shown in Fig.4. Several lead weights (each one 54 Kg) were placed on the top of rigid plates to increase the soil pressure surrounding the pipelines, as shown in Fig. 5. Eleven strain gauges were placed on each side of the pipeline surface including two yield strain gauges to detect large deformations.

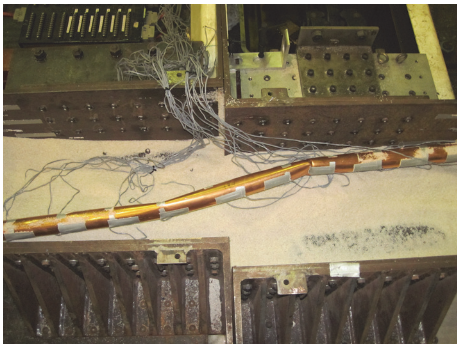

Fig. 6 Local buckling occurred on the pipeline.

Test results

In this case, five lead weights were placed on the top of each shear box. The total lead weight was equal to 270Kg, which gave an additional 0.96m buried depth if the density of dry sand is 1.56. From Fig. 6, local buckling behavior can be observed occurring on the pipeline at both sides of the faults. In Fig. 7(a) and (b), it can be seen that the local buckling occurred at around 20 cm to the fault. The maximum compressive strain occurred at a fault movement of 7 cm. After this movement, the compressive strain decreased gradually because the pipeline had been extended by the fault movement.

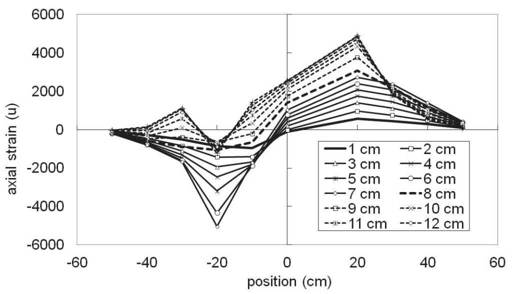

(a)

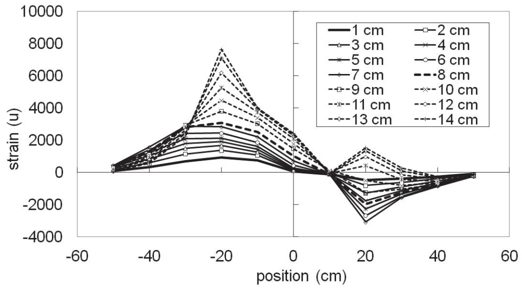

(b)

Fig. 7 The relationship between axial strain and position under different fault movements.

Numerical model and results

The commercial finite element package software ABAQUS was adopted to numerically simulate the mechanical behavior of the buried pipe. The surrounding soil medium and the soil-pipeline interaction were studied in a rigorous manner with consideration to the nonlinear geometry of the soil and the pipe. An elongated prismatic model was considered, as shown in Fig. 8, in which the pipelines were embedded in the soil. The eight-node reduced-integration brick elements (type C3D8R) were used to simulate the surrounding soil. The seismic fault plane divided the soil in two equal parts and was considered perpendicular to the pipeline axis at the middle section of the pipeline. The pipeline was modeled by four-node reduce-integration shell elements (S4R) which easily expressed the local buckling behavior of the pipelines. The pipeline axis was assumed to be horizontal and normal to the fault plane.

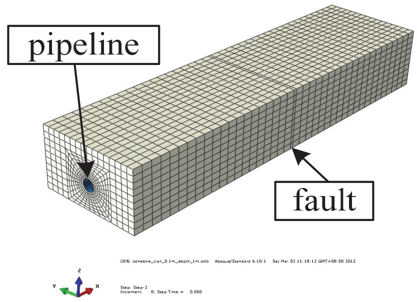

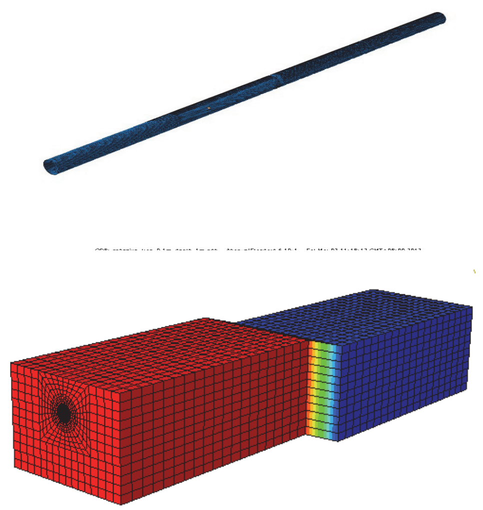

Fig. 8 Numerical model: soil (brick elements); pipeline (shell elements); gap opening at the soil-pipe interface induced by fault movement.

Fig. 9 depicts the shape of the deformed pipeline at a fault displacement of d = 8 cm in the area near the fault where localized deformation at point A is referred to as local buckling. Due to the skew-symmetry of the problem, a similar local deformation occurred at point B, on the hidden side of the pipeline.

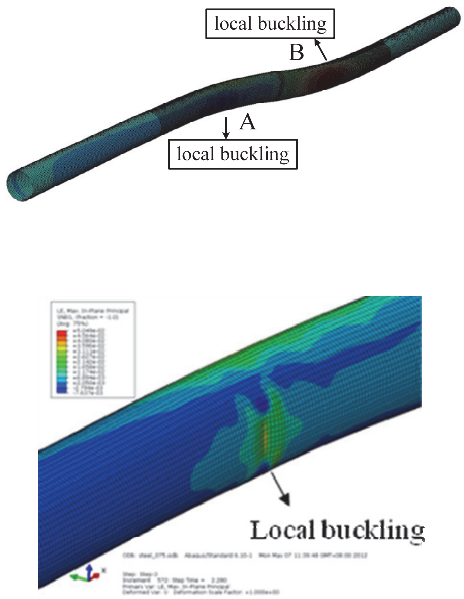

Fig. 9 Local buckling at the pipeline

By conducting the small-scale pipeline-soil interaction tests, the structural behavior of the buried pipeline crossing the strike-slip fault was investigated. Through the commercial FEM software, the effects of the size of the shear boxes, soil material properties and boundary conditions, which might affect the behavior of pipelines, can be discussed in the future. Besides, the parameter calibration of the numerical models can be achieved by using experimental data.

Conclusions

By conducting small-scale pipeline-soil interaction tests, the structural behavior of buried pipelines crossing a strike-slip fault was investigated. However, size effects, which might affect the behavior of pipelines such as, the size of pipelines, soil pressures, and boundary conditions set up at both ends of the pipeline, needed to be considered in the small-scale experiments. In the set up of the current tests, some problems that needed to be considered were: 1) the reduction of the thickness of the pipelines, a characteristic that might be helpful in the observation of local buckling behavior of pipelines; 2) the introduction of steel plates on the top of soil surfaces to produce adequate soil pressure, as well as designing devices to accurately measure the soil pressure; 3) the shaping of the boundary conditions at the two ends of the pipeline in order to simulate the real world behavior of endless pipelines. Using advanced finite element simulation tools, the numerical models of the soil (solid elements) and pipelines (shell elements) were built by the ABAQUS commercial software. The contact algorithm between the soil and pipeline was taken into account. This model can be used to complete the investigation of several soil and pipe parameters on the pipeline deformation and strength. As small-scale experiments are limited to the size of the shear boxes, numerical models are a relatively convenient method to investigate the size effect, which will be part of the future work of this study. The realistic soil material properties of sand measured accurately from the shear boxes will also be applied to the numerical model. A parametric study of the numerical model can be calibrated by using the experimental data in the future.

References

ABAQUS version 6.10 (2011). Analysis Users Manual. Providence, RI: Dassault Systèmes Simulia Corporation.

Abdoun, T. H., Ha, D., O'Rourke, M. J., Symans, M. D. O'Rourke, T. D. Palmer, M. C. and Harry, E. S. (2009). Factors influencing the behavior of buried pipelines subjected to earthquake faulting. *Soil Dyn. Earthqu. Eng.* **29:3**, 415-427.

American Lifelines Alliance-ASCE (2001). Guidelines for the design of buried steel pipe (with addenda through February 2005).

Elhmadi, K. and O'rourke, M. J. (1990). Seismic damage to segmented buried pipelines. *Earthqu. Eng. Struct. Dyn.* **19:4**, 529-539.

Joshi, S., Prashant, A., Deb, A. and Jain, S. K. (2011). Analysis of buried pipelines subjected to reverse fault motion. *Soil Dyn. Earthqu. Eng.* **31:7**, 930-940.

Ha, D., Abdoun, T. H., O'Rourke, M. J., Symans, M. D. O'Rourke, T. D., Palmer, M. C. and Harry, E. S. (2008a). Buried high-density polyethylene pipelines subjected to normal and strike-slip faulting-a centrifuge investigation. *Can. Geotech*. J. 45(12), 1733-1742.

Ha, D., Abdoun, T. H., O'Rourke, M. J., Symans, M. D. O'Rourke, T. D. Palmer, M. C. & Harry, E. S. (2008b). Centrifuge modeling of earthquake effects on buried high-density polyethylene (HDPE) pipelines crossing fault zones, *ASCE J. Geotech. Geoenviron. Eng.* **134:10**, 1501-1515.

Karamitros, D. K., Bouckovalas, G. D. and Kouretzis, G. P. (2007). Stress analysis of buried steel pipelines at strike-slip fault crossings. *Soil Dyn. Earthqu. Eng.* **27:3**, 200-211.

Kennedy, R. P., Chow, A. W. and Williamson, R. A. (1977). Fault movement effects on buried oil pipeline. J. Transp. *Eng. Div.*, ASCE. **103:15**, 617-633.

Newmark, N. M. and Hall, W. J., (1975). Pipeline Design to Resist Large Fault Displacements, Proc. US National Conference on Earthquake Engineering, Ann Arbor, Michigan.

Olson, N. (2009). Soil Performance For Large Scale Soil-Pipeline Tests. PhD, Thesis. Cornell University.

O'Rourke, T. D., Jezerski, J. M., Olson, N. A., Bonneau, A. L., Palmer, M. C., Stewart, H. E., O'Rourke, M. J., Abdoun, T. (2008). Geotechnics of pipeline system response to earthquakes, *Proceedings of the Geotechnical Earthquake Engineering and Soil Dynamics IV Congress.*

Palmer, M. C., O'Rourke, T. D., Olson, N. A., Abdoun, T. H., Ha, D. and O'Rourke, M. J. (2009). Tactile pressure sensors for soil-structure interaction assessment, *ASCE J. Geotech. Geoenviron. Eng.* **135:11**, 1638-1645.

Trifonov, O. V. and Chernify, V. P. (2010). A semi-analytical approach to a nonlinear stress-strain analysis of buried steel pipelines crossing active faults. *Soil Dyn. Earthqu. Eng.* **30:11**, 1298-1308.

Vazouras, P., Karamanos, S. A. and Dakoulas, P. (2010). Finite element analysis of buried steel pipelines under strike-slip fault displacements. *Soil Dyn. Earthqu. Eng.* **30:11**, 1361-1376.

Wang, L. R. L. and Yeh, Y. (1985). A refined seismic analysis and design of buried pipeline for fault movement. *Earthqu. Eng. Struct. Dyn.* **13:1**, 75-96.

Seismic Damage Estimation and Database Construction for the Railway Transportation System in Taiwan

Chin-Hsun Yeh[1], Gee-Yu Liu[2], Lee-Hui Huang[3] and Hsi-Hung Chang[4]

葉錦勳 [1]、劉季宇 [2]、黃李暉 [3]、張錫宏 [4]

Abstract

The objective of this study is to evaluate the seismic risk and retrofit feasibility of railway bridges and to improve the safety of the entire railway system for the Taiwan Railways Administration (TRA). The around-Taiwan railway system is a ring network with some branches. It comprises structural elements such as rail tracks, bridges, tunnels, station buildings, and electrical facilities. The railway database was constructed according to structural elements types, and the relevant parameters were adjusted according to actual damage results and earthquake damage assessments of the railway system. Based on the developed seismic scenario simulation technology and refer to the framework of the Thway (TELES for highway system) software, an integrated software (Trail) was developed for application in the estimation of earthquake damage and economic loss for the railway transportation system. The software is primarily used to evaluate railway bridge damage and turnover loss caused by interruptions to railway bridges following an earthquake event.

Keywords: Railway system, Seismic damage estimation, Turnover loss.

Introduction

The TELES (Taiwan Earthquake Loss Estimation System) software has been developed by the National Center for Research on Earthquake Engineering (NCREE) over many years. It is used to assess potential earth science hazards and possible damage and loss induced by earthquakes. The framework of TELES includes modules of seismic hazard analysis, structural damage assessment, earthquake-induced secondary disaster evaluation, and social economic loss estimation. Traditionally, the analysis modules for buildings, bridges, the water system, and so forth, are all integrated into the TELES software. Each module was often divided into sub-modules for specific research purposes or according to the needs of TELES users. Subsequently, even though its performance has been upgraded continually, the operation of the software has become more complicated. This is sometimes inconvenient for users. Moreover, most users only made use of certain parts of the TELES's functions and modules, with other parts never being used. This may reduce the willingness of users to use the TELES software since time is lost in learning how to operate all the functions and modules of TELES.

Recently, the TELES software has been further developed to allow customization depending on the specific needs of users. For example, an earthquake risk assessment (ERA) module has been developed to meet the unique demand of the Taiwan Residential Earthquake Insurance Fund (TREIF). This module can provide objective evaluations of residential earthquake exposure and calculate the insurance premiums and references for insurance brokers. Similarly, a module for earthquake loss assessment of the water system (Twater) was developed as a standalone module from TELES. It provides hydraulic model analysis and post-earthquake performance assessment for use by water departments of the government.

With participation in research projects such as the "Seismic assessment and retrofit feasibility for highway bridges" (Directorate General of Highways, MOTC, 2009), and the "Development of early seismic

[1] Researcher and Division Manager, National Center for Research on Earthquake Engineering, chyeh@ncree.narl.org.tw
[2] Associate Researcher, National Center for Research on Earthquake Engineering, karl@ncree.narl.org.tw
[3] Assistant Researcher, National Center for Research on Earthquake Engineering, lhhuang@ncree.narl.org.tw
[4] Associate Researcher, National Center for Research on Earthquake Engineering, hhchang@ncree.narl.org.tw

loss estimation module and database for highway bridges" (Liu, et al., 2010), TELES now has the ability to estimate the seismic damage of highway bridges. In this study, the seismic damage estimation module for railway bridges was constructed mainly based on the development experience obtained from the analysis module for highway bridges. However, the superstructures of railway bridges are different from those of highway bridges, as they include rail tracks, roadbeds, electrical facilities, loading types, and so on. Hence, parameters such as the replacement cost, damage ratio, repair time, and the fragility curve have to be modified appropriately for the railway system. At this stage, TELES has included 708 railway bridges, rail tracks, and turnover data for the damage assessments of railway bridges and rail tracks, as well as the estimation of the turnover loss caused by interruption to railway bridges after an earthquake.

Database Construction

Recently, with the participation in the TRA project, "Planning of total examination and seismic retrofit of railway bridges", which was primarily executed by Sinotech Engineering Consultants, the structural database of 708 railway bridges and the GIS database of bridge culverts, rail tracks, and train stations has been obtained. These databases are sufficient for the development of seismic damage estimation of railway bridges and tracks in the railway system, in which the structural elements of culverts and underground passages are a major part of the railway bridge database. Since the properties of these structural elements are different from the regular bridge classification in the highway system, one extra class was added for the culverts and the underground passages in the bridge classification of the railway system.

Regarding the economic loss estimation of the railway system, a simplified module was applied to calculate the distribution of the average daily turnover between any pair of train stations using the TRA annual turnover data of all train stations. Accordingly, one can then obtain the possible turnover loss of the disconnected train stations caused by interruption to railway bridges after an earthquake.

In order to examine the reliability of the estimation parameters and the outcomes of the damage and the turnover loss assessment modules for railway bridges, some survey reports of the railway system suffering from earthquake and typhoon disasters in recent years, including the cases of the 921 Chi-Chi Earthquake in 1999, Typhoon Morakot, and Typhoon Parma in 2009, were also collected for analysis. By comparing the compiled information of damage states, restoration times and repair costs of the railway bridges following actual disasters with the scenario simulation results from the assessment modules, reasonable and reliable parameters for the analysis modules of the railway system were then drawn up.

Damage Estimation of Railway Bridges

The methodology and analysis procedure of seismic damage estimation for railway bridges are similar to those for highway bridges. However, the characteristics and basic requirements of the seismic capacity, replacement cost, restoration time, and repair time between these two engineering structures are different. Hence, it is necessary to appropriately review and modify the relevant parameters of damage assessment for railway bridges.

The classification of bridges is primarily based on the following structural characteristics: seismic design, span continuity, and abutment type. Before 1999, there was no seismic design code in place for railway bridges in Taiwan. In order to understand the seismic capacity of domestic railway bridges, Sinotech Engineering Consultants selected 38 railway bridges with different seismic designs and structural types for the seismic capacity analysis using the pushover method, in which the analysis of railway bridges before 1999 are carried out according to the version of the 1987 seismic design code for highway bridges. After comparing these results with the real damage situation that occurred during the 921 Chi-Chi Earthquake, one can define the fragility parameters of railway bridges, culverts, and underground passages for the railway system.

In contrast to highway bridges, the replacement cost of railway bridges comprises the costs of both civil structures and track facilities, which are denoted by C_{str} and C_{track}, respectively. In other words, the track facilities of rail tracks, roadbeds and electrical facilities in the railway system could be damaged from ground shaking and ground failure in addition to the civil structures. Similar to the estimation formula for the highway system, the replacement cost of the civil structures for each bridge type is given by:

$$C_{str} = A_{bridge} \times C_{unit} , \tag{1}$$

in which A_{bridge} denotes the bridge area, and C_{unit} is the replacement cost per unit deck area.

The replacement cost of the track facilities includes the costs of roadbeds, rail tracks, and electrical facilities. According to practical experience, the replacement cost is NT$30,000 per meter per track for regular roadbeds and rail tracks, and is about NT$35,000 per meter per track for concrete roadbeds. The replacement cost of the electrical facilities is NT$23,500 per meter per track. When a railway bridge requires rebuilding, a temporary rail track would have to be established beside the bridge in order to retain the normal operation of the railway transportation. Thus, it is necessary to include the cost of the temporary track in this situation. Furthermore, when the segment of the rail track on a bridge is damaged and needs to be replaced, other rail tracks nearby would also be affected and need to be replaced concurrently. In this study, we assume that the segment length of the affected rail tracks is about 150 meters. As a result, the total value of rebuilt tracks for the track facilities includes the temporary tracks and the nearby affected tracks. The replacement cost is given by:

$$C_{track} = (L_{bridge} \times (N_{track} + 1) + 150) \times (3.5 + 2.35), \quad (2)$$

where N_{track} represents the number of rail tracks to be replaced and L_{bridge} denotes the length of a damaged railway bridge.

The definition of the damage ratio is the proportion of the repair cost to the replacement cost of a structural system. The relevant parameters of the damage ratio are determined according to the actual loss of each damage state for different types of railway bridges from field investigation. Under the assistance of the TRA, material data and information regarding the damage situations of railway bridges suffering from earthquake and typhoon disasters (such as the 921 Chi-Chi Earthquake, Typhoon Morakot and Typhoon Parma) in recent years were collected from the construction sections, and were compiled in a database in an appropriate format for TELES. According to the practical experience of the TRA, the repair cost of rail tracks and electrical facilities subjected to slight, moderate, or extensive damage is very small. The major repair cost is spent on civil structures in these damage states. However, the difference among the repair costs of bridge structures, rail tracks, roadbeds, and electrical facilities are not significant in the complete damage state. Herein the damage ratio is determined based on the above rules in order to evaluate the economic loss to the railway bridges under different kinds of damage states.

Restoration Time or Intercept Time

The definition of the intercept time (or the restoration time) is the time period for the restoration of damaged railway bridges. The intercept time has an important influence on the operation of the railway transportation system: the longer the intercept time, the more turnover loss is produced. It is therefore necessary to assess the intercept time caused by the interruption to railway bridges after an earthquake before evaluating the turnover loss of the railway transportation system.

The railway transportation system in Taiwan is a ring network. When a railway bridge on a certain section of the railway system is damaged, all the trains that pass through this section will be affected. When a railway bridge located on a section between two adjacent train stations is damaged, the passage between these two train stations will fail. In other words, the greater the number of railway bridges located on a section between two adjacent train stations, the greater the demand of the average intercept time since each railway bridge on this section may be damaged by an earthquake event. Under the assumption that the intercepts of damaged railway bridges are sample events independent of each other and without considering the damage probabilities of the rail tracks or the other facilities, the failure probability of one section is a function of the failure probabilities of the railway bridges on this section only. The failure probability of the section can be expressed as follows:

$$\hat{p}_f = 1 - \prod_k (1 - p_f^k), \quad (3)$$

where p_f^k denotes the failure probability of the k th railway bridge.

Eq. (3) implies that the passage probability of a section is the product of the passage probabilities of all the railway bridges on that section. Assume that the average intercept time of one section under the failure condition, $\hat{T}_f$, is defined by the weighting average of the average intercept times of all the railway bridges on the section under the failure condition, we have

$$\hat{T}_f = \frac{\sum_k p_f^k \cdot T_f^k}{\sum_k p_f^k}, \quad (4)$$

from which the average intercept time of the section is given by

$$\hat{T}_1 = \hat{p}_f \cdot \hat{T}_f. \quad (5)$$

Moreover, if one of the railway bridges on a section requires a long time to be restored, the average intercept time of this whole section may be controlled by this one railway bridge. This implies that another way to determine the average intercept time of one section is to choose the maximum average intercept time among the railway bridges on the section, yields

$$\hat{T}_2 = \max(p_f^k \cdot T_f^k, \quad \forall k). \quad (6)$$

In summary, in this study, the larger value from Eq. (5) and Eq. (6) is chosen to be the average intercept time of one failed section.

The existence of a failed section would interrupt the passage between any pair of train stations that pass through this section. Specifically, when the railway segment between one pair of train stations contains many sections, any section's failure would interrupt the passage of the railway segment. Similar to the calculation of the average intercept time of a failed section containing many railway bridges, the average intercept time of a failed railway segment containing many sections can be evaluated accordingly. The average intercept time of the railway segment between any pair of train stations can be displayed in the form of a matrix, as shown in Table 1.

Table 1 Average intercept time of railway segment between pairs of train stations under failure conditions

	Taipei	Taoyuan	Hsinchu	Taichung	Chiayi	Tainan	Kaohsiung
Taipei	0	$T_{r,21}$	$T_{r,31}$	$T_{r,41}$	$T_{r,51}$	$T_{r,61}$	$T_{r,71}$
Taoyuan	0	0	$T_{r,32}$	$T_{r,42}$	$T_{r,52}$	$T_{r,62}$	$T_{r,72}$
Hsinchu	0	0	0	$T_{r,43}$	$T_{r,53}$	$T_{r,63}$	$T_{r,73}$
Taichung	0	0	0	0	$T_{r,54}$	$T_{r,64}$	$T_{r,74}$
Chiayi	0	0	0	0	0	$T_{r,65}$	$T_{r,75}$
Tainan	0	0	0	0	0	0	$T_{r,76}$
Kaohsiung	0	0	0	0	0	0	0

Turnover Loss Evaluation

To evaluate the turnover loss caused by interruption to railway bridges, the transportation revenues between pairs of train stations were obtained by analyzing the 2011 transportation revenue of each train station provided by the TRA. The transportation revenue between each pair of train stations along a main railway line is expressed in a matrix form, and is called the Daily Turnover Matrix. According to the railway transportation operation type, the Taiwan railway system is divided into four main railway lines: West-sea line, West-mountain line, East line, and South line. As such, one can construct the daily turnover matrices for the four main railway lines, in which each element represents the daily turnover between one pair of train stations.

For example, if one section between the Taoyuan and Hsinchu stations fails, it is necessary to suspend all the trains travelling through this section. As shown by the red circle in Table 2, the trains that set out from the Taipei or the Taoyuan station toward the southern stations after the Hsinchu station are required to be suspended, and vice versa for the trains travelling in the direction to the northern stations. The trains not passing through the failed section will remain in operation. The summation of the turnovers in the red circle in Table 2 represents the total turnover loss caused by the failed section between the Taoyuan and Hsinchu stations.

Table 2 Turnover loss for a failed section between the Taoyuan and Hsinchu stations

	Taipei	Taoyuan	Hsinchu	Taichung	Chiayi	Tainan	Kaohsiung
Taipei	0	L_{21}	L_{31}	L_{41}	L_{51}	L_{61}	L_{71}
Taoyuan	0	0	L_{32}	L_{42}	L_{52}	L_{62}	L_{72}
Hsinchu	0	0	0	L_{43}	L_{53}	L_{63}	L_{73}
Taichung	0	0	0	0	L_{54}	L_{64}	L_{74}
Chiayi	0	0	0	0	0	L_{65}	L_{75}
Tainan	0	0	0	0	0	0	L_{76}
Kaohsiung	0	0	0	0	0	0	0

Conclusions

Regarding the transportation system, the TELES software already contains a module to estimate the earthquake damage of the highway system. This study developed the evaluation methodology of economic loss for railway bridges, railway turnover loss, and the average intercept time for each railway section of the Taiwan railway system. However, the damage estimation module of tunnel structures for the railway and highway systems has not yet been established due to the lack of a database relevant to the tunnel structures. Hence, in order to improve the integrity of the transportation system module for TELES, data collection and the development of the damage estimation of tunnel structures will be the primary focus of work in the future.

References

RMS (Risk Management Solutions, Inc.), 1999, Earthquake Loss Estimation Method -HAZUS99 Technical Manual, National Institute of Building Sciences, Washington, D.C.

Directorate General of Highways, MOTC (2009). *Seismic Assessment and Retrofit Feasibility for Highway Bridges*, Final report, CECI Engineering Consultants, Inc., Taipei. (in Chinese)

Liu, G.-Y., Yeh, C.-H., Chang, K.-C., Jao, C., Hung, H.-Y., Huang, L.-H., Liu, Y.-N., Chen, C.-L., Lin, C.-C. (2010). *Development of Early Seismic Loss Estimation Module and Database for Highway Bridges*, Institute of Transportation, Ministry of Transportation and Communications, Taipei. (in Chinese)

Yeh, C.-H. (1999). *Application of Geographical Information System on Seismic Hazard Analysis and Loss Estimation*, Technical Report NCREE-99-035, National Center for Research on Earthquake Engineering, Taipei. (in Chinese)

Yeh, C.-H. (2002). *Integration Study on the Earthquake Disaster Scenario Simulation and its Application Software*, Technical Report NCREE-02-009, National Center for Research on Earthquake Engineering, Taipei. (in Chinese)

Seismic Testing and Grading of Ductile Iron Water Pipes

Gee-Yu Liu[1], Lap-Loi Chung[2] and Pao-Ching Chou[3]

劉季宇 [1]、鍾立來 [2]、周寶卿 [3]

Abstract

Ductile iron is widely adopted as a material for buried water pipes due to its mechanical and chemical properties, such as its high toughness, strength, and resistance to corrosion. Ductile iron pipes (DIP) are fabricated in segments, normally 6 meters long, in workshops, and are connected by joints one-by-one on site. During an earthquake, they are inevitably subjected to ground shaking and deformation. Damage may occur in the pipe wall or at the pipe joint under excess seismic actions. In this research, seismic testing of DIPs is performed. DIPs with three different joint types, namely K-type, A-type, and flange, are tested. Pipe specimens filled with pressurized water were deformed separately under tension, compression, and bending loads. It is observed that DIPs with either a K-type or an A-type joint have good deformation capacity, but fail to prevent disengagement at the pipe joint under very small tensile action. DIPs with a flange joint, albeit with very high strength, have very poor deformation capacity and may leak easily once opened or bent slightly. Finally, according to the classification suggested by ISO 16134, the seismic capacity of DIPs with each of the three joints is classified with respect to their expansion, contraction, slip-out resistance, and joint deflection performance, respectively.

Keywords: water pipes, ductile iron, seismic capacity, ISO 16134

Introduction

Taiwan is located in an earthquake-prone area. Disastrous inland earthquakes take place every 10 years on average. The expected earthquake losses have become increasingly significant as a result of a highly developed environment. The seismic safety of the water system is evidently critical to the welfare of citizens. Ductile iron is a widely adopted material used for buried water pipes, due to its mechanical and chemical properties, such as its high toughness, plasticity, and resistance to corrosion. Ductile iron pipes (DIP) are fabricated in segments, normally 6 meters long, in workshops, and are connected by joints one-by-one on site. During an earthquake, DIPs are inevitably subjected to ground shaking and deformation. Damage may occur in the pipe wall or at the pipe joint under excess seismic action. Evidence from the 1999 Chi-Chi earthquake showed that DIPs were mostly damaged at the joints. The vulnerability of DIPs is highly dependent on pipe size and joint type.

ISO 16134 now serves as a major reference for the earthquake- and subsidence-resistant design of DIPs; following this reference, practitioners can design a water pipe according to the seismic demands of a site. Nevertheless, very limited research work has focused upon how to quantify the seismic capacity of a pipe through a testing process. In this study, a testing process to determine the seismic capacity of ductile iron water pipes with various types of joints was investigated experimentally. Pipe specimens with a nominal diameter of 400 mm were assembled using K-type, A-type, and flange joints, as illustrated in Fig. 1. Recently in Taiwan, pipes with a K-type joint have become widely used in water pipes. However, pipes with A-type joints outnumber those with K-type joints due to the fact that the former have been used for a long time in buried DIPs. Flange joints are commonly used for the connection of valves and meters.

For each type of joint, six specimens were prepared for testing under different types of loading: two for tension, two for compression, and two for

1 Associate Researcher, National Center for Research on Earthquake Engineering, karl@ncree.narl.org.tw

2 Researcher, National Center for Research on Earthquake Engineering, chung@ncree.narl.org.tw

3 Assistant Researcher, National Center for Research on Earthquake Engineering, pcchou@ncree.narl.org.tw

bending. The specimens were closed with end plates and filled with pressurized water. The water pressure was controlled to maintain a prescribed level. Failure of the specimen was defined as the point at which leakage occurred and the water pressure could not be kept at this prescribed level. The stiffness, strength, ductility, and failure mode of each joint were investigated. The seismic performance of each joint was classified, in terms of resistance to tension, displacement capacity, and rotation capacity according to ISO 16134.

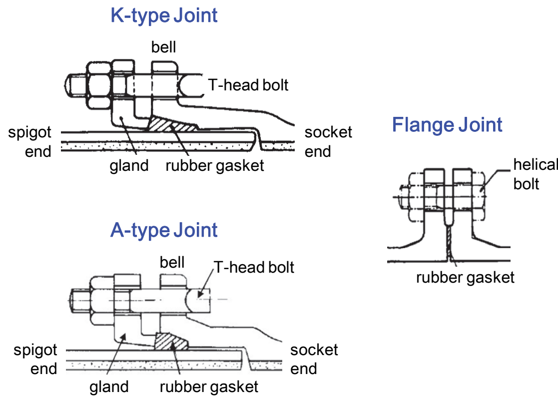

Fig. 1 DIPs with various types of joints

Test Methods

For the tension and compression tests, the specimens had a length of four times their nominal diameter (4DN). Each specimen consisted of a pair of pipes, one with a socket end and the other with a spigot end. After the assembly of the pipes at a joint, the edge of the socket end was positioned exactly at the mid-height of the specimen. It was mounted vertically to the universal testing machine with a capacity of 500 tf through fixtures, as depicted in Fig. 2. The test was conducted under displacement control. During testing, the specimen's axial force and displacement were measured using the internal load cell and the LVDT of the universal testing machine. The relative displacements at the two sides of the pipe joint were measured by a pair of external LVDTs. Knowing that K-type and A-type joints both have very low slip-out resistance, an additional 50-tf load cell was installed with the same alignment during the tension tests to ensure that the measurement of the axial force had adequate resolution.

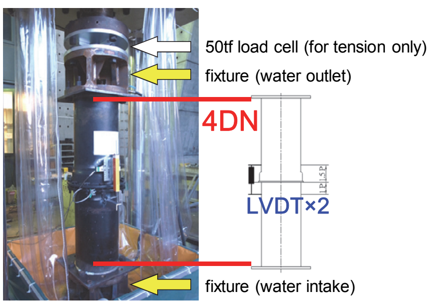

Fig. 2 Setup of the tension and compression tests

For the bending tests, the specimens had a length of eight times their nominal diameter (8DN). Again, each specimen consisted of a pair of pipes, one with a socket end and the other with a spigot end, and the edge of the socket end was positioned exactly at the mid-span of the specimen after the assembly of the pipes at the joint. The specimen was mounted horizontally at the ends on a pair of hinge supports. With a portal frame, a cross beam and a 100-tf actuator, the test was set up in such a way that the specimen was loaded with four-point bending, as depicted in Fig. 3. The 100-tf actuator gradually extended and the specimen was bent in a flexural way. During testing, the actuator load and extension were measured using its internal load cell and LVDT. Four 50-tf load cells were employed to measure the reaction of each hinge support. The bent specimens were also instrumented with tilt meters to record the rotation along the pipes' springline.

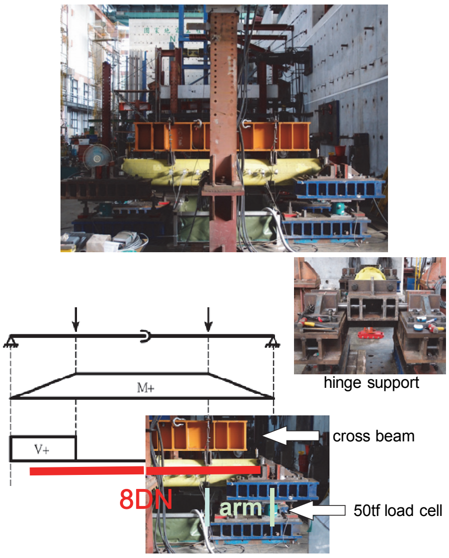

Fig. 3 Setup of the bending test

Since the A-type joint is very old and no longer used in new pipeline installations, the only available socket ends for this kind of joint were from the cross pipes with an A-type joint in stock. Therefore, the specimens were actually an assembly of such cross pipes and the spigot ends of straight DIPs, as depicted in Fig. 4. The pipe thickness of the former was about twice that of the latter. In addition, the cross pipes weren't fabricated by centrifugal casting, which resulted in a poor precision of the sockets' geometry.

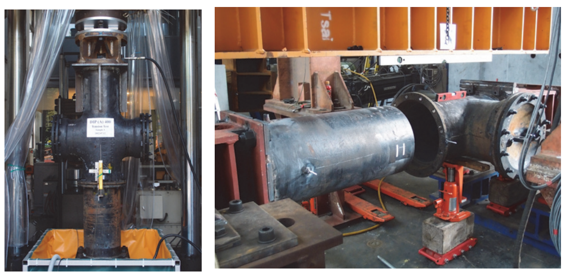

Fig. 4 DIP specimens with an A-type joint.

During each test, the specimen was filled with water that was then pressurized. This was achieved by using a water pressure control system specially fabricated for this study, as depicted in Fig. 5. The deformation of the specimen (axial displacement or rotation) was increased monotonically until the specimens began to leak and the water pressure was no longer maintained. According to ISO 2531 (2009), the leak-tightness of DIP joints to internal pressure should be tested at a pressure of (1.5 × PN + 5) bar. Taking 2 kgf/cm^2 for the working pressure PN, water pressure throughout the testing was supposed to be within 8 ± 0.5 kgf/cm^2, with an additional tolerance of 0.5 kgf/cm^2 to accommodate for the variation of water pressure in the specimen due to the change of its volume during deformation.

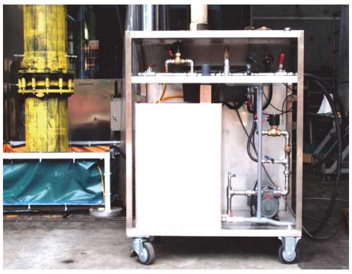

Fig. 5 Water pressure control system

Test Results and Pipe Grading

The detailed test results of this experimental study can be found in the technical reports of the Taipei Water Department (2012) and the Water Resource Agency, MOEA (2012). Regarding the quantitative results, Fig. 6 depicts the axial force–specimen displacement curves of DIP specimens under tension, while Table 1 further summarizes all the test data in detail. It can be seen that both K-type and A-type joints have good deformation capacities. The former can withstand deformations of up to around 110 mm without any leakage (K-1 and K-2), and the latter 75 mm (A-1 and A-2). However, these specimens failed to prevent disengagement at the pipe joint under very small tensile actions of around 40 kN, which is merely the friction between the rubber gasket and the spigot end. Flange joints, although having very high strength, have very poor deformation capacity and may leak easily once opened slightly (F-1 and F-2).

Regarding the qualitative results, in K-type joints, water tightness was achieved in such a way that the rubber gasket was pressed firmly into the socket by the gland. The tensile strength of this joint was low but the tensile deformation capacity was fully developed. Water tightness was maintained until the axial displacement was as large as the splice length of the spigot and socket ends. The compressive strength was high but the compressive deformation was limited. The bending strength was low but the rotation deformation capacity was good.

As mentioned earlier, in the specimens with an A-type joint, the socket end was actually a cross pipe and the spigot end was a straight pipe. The thickness of the former was about twice that of the latter. The tensile strength of the specimen was very low, and once the strength reached its maximum, it degraded very fast. The compression results of the two specimens were very different. The compatibility of the two different pipes connected together may be the reason for the variation of the test results. The bending strength was very low.

In the specimen with a flange joint, two single flange pipes were connected with a rubber gasket as the interface. Because the resilience of the rubber gasket was bad, the tension and bending deformation capacities were very small, not exceeding 1 mm and 0.15°, respectively, and the corresponding tension and bending strengths were very low. The compressive strength was high but water began to leak from the pipe when the compression force was totally unloaded.

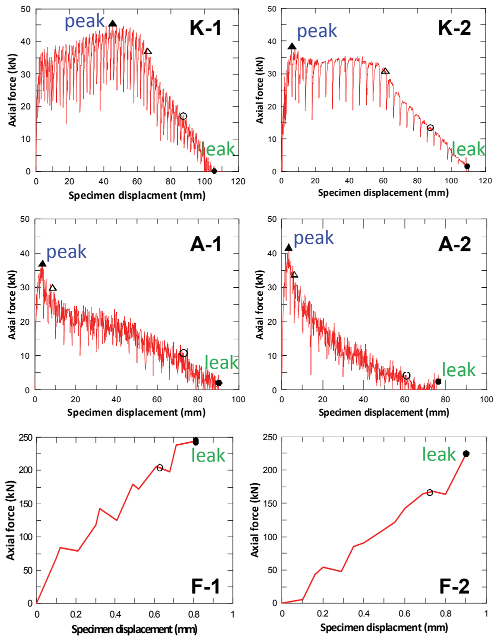

Fig. 6 The axial force-specimen displacement curves of DIP specimens under tension

In the technical report of the Water Resource Agency, MOEA (2012), a procedure was proposed to grade DIPs and joints seismically according to ISO 16134 (2006). It is based upon the reduced deformation capacity of the pipe and joint, which can be decided from the pipe's deformation at peak load and the moment it begins to leak. Following this procedure, the seismic grading of all DIP specimens can be determined as shown in Table 2. For example, the K-type joint's reduced deformation capacity has proven to be larger than 1% of the pipe's nominal length (6000 mm) in the tension test. Its expansion capacity can be graded as S-1. However, its slip-out resistance is well below 0.75d or 300kN, and can only be graded as D.

Table1 Test results for the DIPs.

Joint Type	Test Type	Speci. No.	Peak Load	Peak Deform.	Leak Load	Leak Deform.
K-Type Joint	Tension	1	45.24	45.53	1.64	111.45
		2	38.19	5.98	0.32	109.25
	Comp.	1	2698	7.56	1881	17.43
		2	2594	9.67	1885	17.07
	Bending	1	20.81	10.14	3.86	14.85
		2	28.29	14.20	5.90	17.18
A-Type Joint	Tension	1	37.1	3.59	3.15	90.35
		2	41.95	3.49	3.6	76.2
	Comp.	1	2815	12.45	615	23.01
		2	-	-	96.15	2.09
	Bending	1	9.62	7.85	0.78	9.34
		2	4.4	3.04	1.88	9.39
Flange Joint †	Tension	1	‡	‡	243.5	0.81
		2	‡	‡	223.4	0.92
	Comp.	1				
		2				
	Bending	1	‡	‡	18.89	0.06
		2	‡	‡	44.23	0.14

†: compressive strength beyond capacity of testing machine and too high to be decided
‡: no peak load or deformation
Units: kN (peak load and leak load in tension and compression testing), kN-m (peak load and leak load in bending testing), mm (peak deformation and leak deformation in tension and compression testing), degree (peak deformation and leak compression in bending testing).

Table 2 Seismic grading of the DIPs.

Joint Type			K-Type Joint		A-Type Joint		Flange Joint †	
Specimen No.			1	2	1	2	1	2
Item	Seismic Class.	Range						
Expansion Capacity δ (mm)	S-1	δ≥1%L	√	√				
	S-2	0.5%L≤δ<1%L						
	S-3	δ<0.5%L			√	√	√*	√*
Contraction Capacity δ (mm)	S-1	δ≥1%L						
	S-2	0.5%L≤δ<1%L						
	S-3	δ<0.5%L	√	√	√	√		
Slip-out Resistance F (kN)	A	F≥3d						
	B	1.5d≤F<3d						
	C	0.75d≤F<1.5d						
	D	F<0.75d	√	√	√	√	√*	√*
Joint Deflection Capacity θ (deg)	M-1	θ≥15°						
	M-2	7.5°≤θ<15°	√	√				
	M-3	θ<7.5°			√	√	√	√

L: nominal pipe length (mm)
d: nominal pipe diameter (mm)
†: compression strength too high to be decided;
*: leak load/deformation while failing to maintain water pressure.

Conclusion

According to the test results, K-type joint ductile iron pipes (DIP) are so flexible that their tensile and bending deformation capacities are good but their corresponding strengths are low. A-type joint DIPs are easily disengaged under either axial tension or bending loads. Flange-joint DIPs, due to extremely high joint rigidity, have very low tensile and flexural deformation capacities, and leakage may occur as a result of the poor elasticity of the rubber gaskets. Due to their poor seismic performance, existing A-type joint DIPs should be replaced as soon as possible. Flange-joint DIPs, due to poor deformation capacity, should not be used for the purposes of water transmission and distribution; regarding other usages, their water tightness should be inspected regularly.

References

ISO 16134, 2006, "Earthquake- and Subsidence-Resistant Design of Ductile Iron Pipelines", First Ed.

ISO 2531, 2009, "Ductile Iron Pipes, Fittings, Accessories and Their Joints for Water Applications", Sixth Ed.

Taipei Water Department, 2012, "Seismic Deflection and Leakage Testing of Segmented Water Pipes," Technical Report, Project No. 10131056S04, Taipei.

Water Resource Agency, MOEA, 2012, "A Study on Upgrading Earthquake Loss Estimation Technology for Water Utilities and Seismic Testing Platform and Procedure for Water Pipes," Technical Report, Project No. MOEAWRA-1010381, Taipei.

Seismic Damage Simulation on Taiwan Water Supply Networks with Negative Pressure Treatment

Kuang-Wu Chou[1], Gee-Yu Liu[1], and Chin-Hsun Yeh[2]

周光武[1]、劉季宇[1]、葉錦勳[2]

Abstract

This work is to develop a tool for simulating seismic damages on water supply networks in Taiwan. The tool is based on TELES's potential earth science analysis and a Taiwan-applicable pipeline repair rate formulation proposed by Liu et al. (2012). The development of the tool follows the seismic damage simulation methods from GIRAFFE, especially the negative pressure treatment. The EPANET library is integrated into the tool to create, update, and analyze the hydraulic model of a water supply network. Graph Theory is employed to remove the solution obstacle: no-flow sub-networks derived by either the modeling of network seismic damages, or the removal of negative pressures.

Keywords: hydraulic analysis, EPANET, GIRAFFE, boost, Graph Theory, TELES

Introduction

EPANET as the industrial standard is reliable to solve the hydraulic behaviors of water supply systems. The software, however, couldn't conduct seismic damage simulation on water supply networks. For damaged pipes in such simulation, the modeling of leaks or breaks could cause water loss that greatly exceeds the whole water supply of the network; negative pressures would thus occur in the EPANET solution of the hydraulic analysis. Negative pressures are incorrect prediction unless the network keeps air-tight (any damaged water system with leaking or broken pipes cannot be air-tight). If those negative pressures cannot get some treatment, the network's ability of supplying water will be misestimated.

Ballantyne et al. (1990) assumed that all nodes with negative pressures have no flow to pass through. Shinozuka et al. (1981) suggested removing such nodes and their adjacent links before running the hydraulic analysis. Markov et al. (1994) classified the negative-pressure nodes as no-flow or partial-flow. The no-flow nodes are to remove, and the no-flow node of the highest negative pressure is removed first. The pressure of each partial-flow node will be modified towards 0 by decreasing the roughness of the full-flow pipe walls. The node removal and pressure modification repeat until no negative pressure is shown. GIRAFFE (Cornell University, 2008) proposed a simpler procedure that removes only the node of the highest negative pressure as well as its adjacent links, and then runs the hydraulic analysis again. The procedure repeats unless negative pressure disappears. GIRAFFE, however, couldn't be directly applied to the water systems in Taiwan, because it is based on the experience of seismic damages of the water systems in USA. So there is a need to develop a tool that utilizes Taiwan's experience to grasp the serviceability of Taiwan's water systems after earthquake. This work tries to fulfill the need by following the seismic damage simulation methods that GIRAFFE proposed.

Seismic Damage Simulation for Water Supply Networks

As shown in Fig. 1, this work proposes a method of simulating seismic damages on a water supply network. The first step is to create the network's hydraulic model by using the EPANET library to read an input text that describes the model. To this model, the Monte Carlo method is applied, which performs a loop of 100 random simulations. The entry of the loop is the pipeline seismic damage simulation that is based

[1] Associate Researcher, National Center for Research on Earthquake Engineering

[2] Researcher and the Head of the Earthquake Disaster Simulation Division, National Center for Research on Earthquake Engineering

on a Taiwan-applicable pipeline repair rate formulation proposed by Liu et al. (2012). The step utilizes the result of TELES's potential earth science hazards (PESH) analysis, the pipe diameter, and the pipe material type to randomly determine if the pipe is undamaged, broken, or in leakage. The outcome of the pipeline damage determination will be used in the damage modification of the hydraulic network model.

In the step of modifying the network model, the pipeline damage modification applies GIRAFFE's hydraulic models that simulate pipe breaks and leaks. Because the break model works by cutting a pipe, a network where any pair of nodes are connected may be divided into several sub-networks that are mutually disconnected (on the other hand, it won't change the connectivity of the network to apply the leak model). As long as any sub-network without water supply exists, the whole network cannot be solved in hydraulic analysis. Fortunately, removing all such no-flow sub-networks may make the network solvable again. In this work, the no-flow sub-networks can get identified; they are removed from the network model in the step of modifying the network model. How to identify no-flow sub-networks will be explained in the section of no-flow sub-network identification.

After all no-flow sub-networks get removed, the hydraulic analysis may be carried out on the trimmed network model without obstacle in solution. The hydraulic solution of a damaged network, however, would contain negative pressures that need to be conducted after hydraulic analysis.

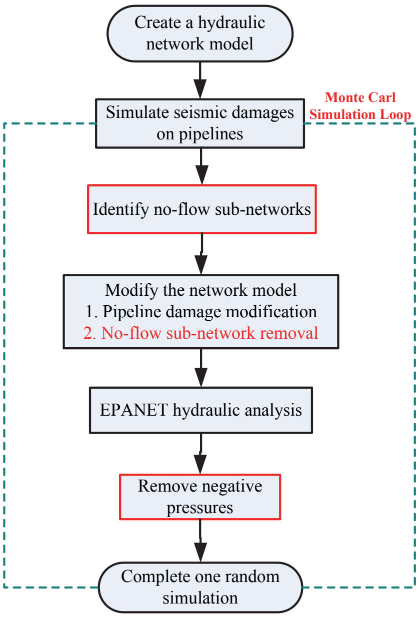

Fig. 1 Procedure of simulating seismic damages on a water supply network

Negative Pressure Removal

The negative pressure removal, at first, finds the node owning the minimum pressure from the result of the hydraulic analysis on a network model modified with seismic damages (See Fig. 2). The removal procedure completes if the minimum is not negative. Otherwise, the node and its adjacent links (including pipes and pumps) are removed from a graph copy of the current network model (why we employ the graph copy here will be explained in the section of no-flow sub-network identification). But as cutting a pipe, removing links may cut the current network into sub-networks containing no-flow ones so that the network cannot be solved in hydraulic analysis. As a result, identifying and then removing the no-flow sub-networks are also required for modifying the network model in the procedure of removing negative pressures.

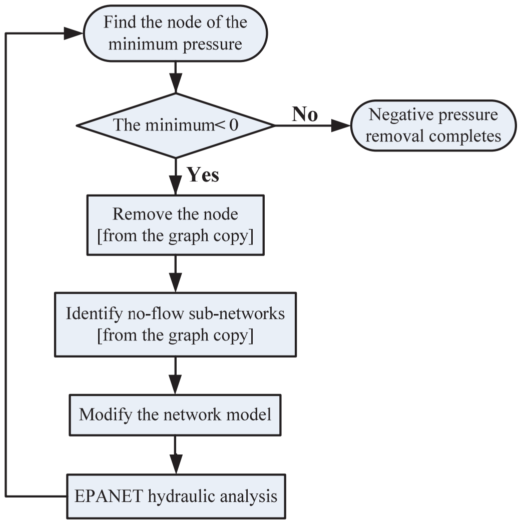

Fig. 2 Procedure of removing negative pressures

EPANET and Hydraulic Network Model Modification

EPANET offers an application, source code files, and a dynamic link library. The dynamic link library, as the EPANET programmer's toolkit, is used in this work. Still, the library needs reading an EPANET input to create a hydraulic network model. Updating a model also requires modifying the EPANET file and then feeding the library with the modified file. In Fig. 1, the library creates a hydraulic network model by reading an EPANET file. In Fig. 1 and Fig.2, the library modifies a hydraulic network model by reading and writing EPANET input files. That means reading or writing files could be performed over one thousand times by the Monte Carlo loop that executes 100 random simulations; if more than 10 negative-pressure nodes are removed in each simulation. In fact, it consumes most file operations in the network seismic damage simulation to repeat trimming the network model within the negative pressure removal procedure.

No-flow Sub-network Identification

Graph Theory is utilized to identify sub-networks resulting from cutting or removing pipes. This theory helps find from a network graph all the connected components as the sub-networks. The required procedures are implemented with the boost graph library (BGL).

The first step of identifying sub-networks is to create a graph copy for the hydraulic network. each vertex and each edge of the graph copy have one-to-one correspondence with each node and each link of the network. Thus the removal of a vertex or edges from the graph copy may simulate removing a node or cutting pipes from the network, respectively. The trimmed graph copy is then given to BGL's connected_component method. This method will find out all the connected components or sub-networks. The method returns the number of sub-networks, and labels each vertex a number that is used to identify which sub-network where this vertex belongs.

The final task is to pick out the sub-networks without water supply. A simple approach is employed as what follow: ask each node about if it is a tank or reservoir; if the condition is true the sub-network where the node resides is identified as having water supply. After all nodes are visited, the sub-networks never confirmed as owning water supply are considered no-flow (without water supply).

Example

A seismic damage simulation is carried out on the water supply network in Taiwan's Lan-Yang area. A simplified hydraulic network model is employed, which was proposed by Sinotech engineering consultants (2009). In the simplified model, 358 nodes and 439 links (comprising pipes and pumps) are defined; 85 nodes are given demands, responsible for supplying water.

An earthquake is simulated by TELES with a Richter magnitude 7.3. The epicenter is at latitude 24.48°N and longitude 121.88°E, in Yilan's offshore. The focal depth is 20Km. The earthquake source is described as a north-south-trending line source. Fig. 3 shows the result of TELES's PESH analysis on the earthquake, the result in the Lan-Yang area.

The outcome of the seismic damage simulation is presented with the serviceability of the water supply network. The serviceability is obtained by dividing the summation of all demands of the model of an undamaged system by that of all available demands of the system model trimmed and modified with damages.

Given the PESH analysis result, the seismic damage simulation brings out the serviceabilities of the water supply network subjected to the simulated earthquake. Fig. 4 shows the town serviceabilities averaged from the 100 Monte Carlo random simulations. The right part of Fig. 4 presents the town serviceabilities computed after the whole simulation procedure is completed. The left part represents the town serviceabilities computed before the negative pressure removal. And the serviceability computation follows the negative pressure treatment proposed by Ballantyne et al. (1990): the demands of all negative-pressure nodes are disregarded in demand summation. Besides, the right and the left of Fig. 4 show the same tendency. The worst serviceabilities are in Touching (頭城), 0.4346 and 0.2552. The second worst are in Jiaoxi (礁溪), 0.6664 and 0.5951. The smaller in any of the two pairs are by the negative pressure removal.

In the 100 Monte Carlo simulations, the 44-th and the 93-th brings out the maximum serviceability of the whole network and the minimum: 0.9555 and 0.7670. Their town serviceabilities are shown in Fig. 5. Fig. 6 shows the maximum's model modifications before and after the negative pressure removal, Fig. 7 the minimum's. As expected, the network gets greater modification after the negative pressure removal than it gets before. In addition, the model modification with the minimum serviceability is more severe than that with the maximum.

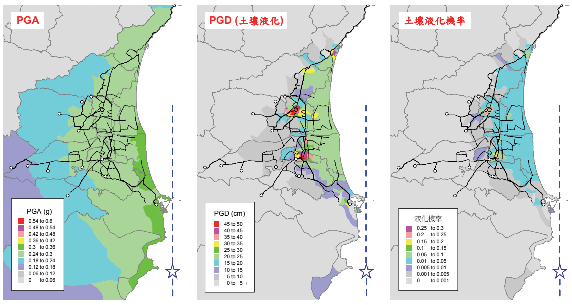

Fig. 3 Distributions of the simulated PGAs, PGDs by soil liquefaction, and soil liquefaction probabilities over the Lan-Yang area (from left to right)

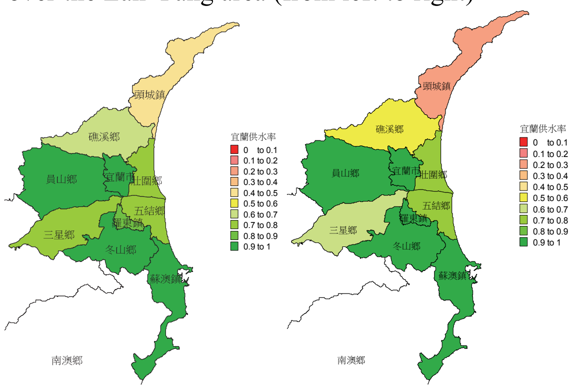

Fig. 4 Town serviceabilities in the Lan-Yang area (left: the negative pressure removal is by-passed)

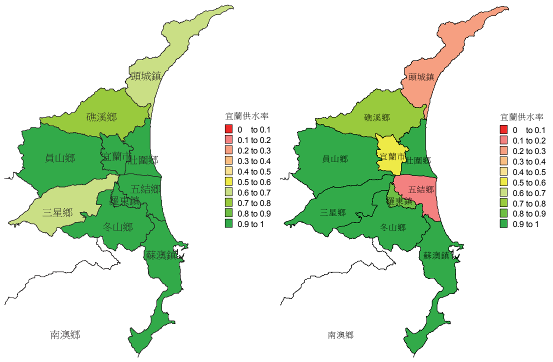

Fig. 5 Town serviceabilities with the maximum whole-network serviceability (left) and that with the minimum (right)

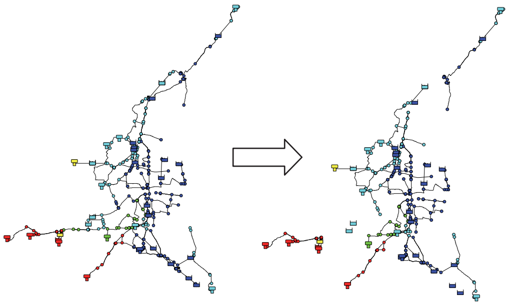

Fig. 6 Network model modification before and after the negative pressure removal, with the maximum whole-network serviceability

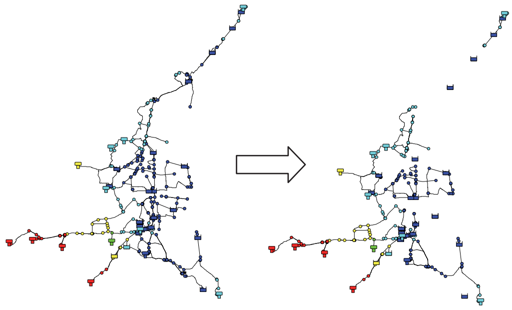

Fig. 7 Network model modification before and after the negative pressure removal, with the minimum whole-network serviceability

Conclusions

A tool for simulating seismic damages on Taiwan's water supply networks is developed. The tool could modify a hydraulic network model modification and remove negative pressures as GIRAFFE does. GIRAFFE couldn't identify no-flow sub-networks itself, however. GIRAFFE needs to run an EPANET hydraulic analysis that finds the disconnected nodes or links for GIRAFFE to remove. The tool works with a different approach. The tool applies Graph Theory to damaged networks so that the tool can identify and then remove no-flow sub-networks from a hydraulic network model. With the help of Graph Theory, the tool depends less on EPANET than GIRAFFE does, and could seize the connectivity of any water supply network.

Nevertheless, the employment of the reliable EPANET library confines the efficiency of modifying a hydraulic network model. The model modification must be performed through reading and writing files that consumes more CPU time than the memory operations do. In this work, the time consumption is observable. We will try to resolve this issue to improve the performance of the tool. Application of the EPANET source codes might be considered.

References

Ballantyne, D. B., Berg, E., Kennedy, J., Reneau, R., and Wu, D. (1990), "Earthquake Loss Estimation Modeling of the Seattle Water System", Technical Report, Kennedy/Jenks/Chilton, Federal Way, WA.

Cornell University (2008). GIRAFFE User's Manual, School of Civil & Environmental Eng., Cornell University, Ithaca, NY.

Markov, I., Grigoriu, M., and O'Rourke, T. (1994), "An Evaluation of Seismic Serviceability Water Supply Networks with Application to the San Francisco Auxiliary Water Supply System", Technical Report NCEER-94-0001, National Center for Earthquake Engineering Research, Buffalo, NY.

Shinozuka, M., Tan, R. Y., and Toike, T. (1981), "Serviceability of Water Transmission Systems under Seismic Risk", Lifeline Earthquake Engineering", the Current State of Knowledge, ASCE, New York, NY.

Liu, G.-Y., Chung, L.-L., Yeh, C.-H., Chou, K.-W., Chang, K.-C., Hung, H.-Y., Chou, P.-C., Lin, T.-J., Chou, C.-H., Chen, J.-C., Chen, C.-H, Kuo, C.-W., and Uang, P.-Y. (2011), "A Study on Upgrading Earthquake Loss Estimation Technology for Water Utilities and Seismic Testing Platform and Procedure for Water Pipes", Technical Report MOEA- WRA-1010381, Water Resources Agency, Ministry of Economic Affairs, Taipei.

Sinotech Engineering Consultants (2009), "Establishment Planning for the Surface-Ground Water Allocation and Management System in Lan-Yang Area", Technical Report MOEA-WRA-0980193, Water Resources Planning Institute, Water Resources Agency, Ministry of Economic Affairs, Taichung.

Constructing Scour Fragility Curves for Piled Bridge Piers from Flume Experiment Data

Chun-Chung Chen [1], Chi-Ying Lin [2], Kuo-Chun Chang [2], and Ming-Yi Shen [2]

陳俊仲 [1]、林其穎 [2]、張國鎮 [3]、沈明毅 [4]

Abstract

The escalating scale of natural disasters increasingly threatens civil infrastructure. In particular, earthquakes and floods are two major types of disasters that can result in damage to key civil structures such as bridges. This preliminary study proposes a procedure for constructing scour fragility curves from flume experiment data for piled bridge piers. Several experiments were conducted and the variation in the scouring process was observed. The scour depths observed were used to develop scour fragility curves for the piled bridge piers. A methodology to construct the scour fragility curves was presented. The main purpose of this paper is to show how to use the flume experiment data to build the scour fragility curves defined as a function of the pile length embedded ratio. The measured trend of the curve is consistent with the general scouring process and the realistic behavior of the piled bridge pier damage sequence. This paper has shown a feasible methodology to construct the scour fragility curves from flume experiment data. However, further studies are necessary in order to find solutions for the problems mentioned in the preliminary study.

Keywords: bridge scour, flume experiment, fragility curves,

Introduction

Earthquakes and floods are two major types of disasters that severely affect bridge structures. Floods can intensify the scouring to bridges and the submerged debris deepens the scour depth. In Taiwan, most bridges cross the river so scouring has been a leading possibility of failures. Therefore, predicting bridge damage due to scouring is much needed and fragility curves can help us to express the probability of damage due to the effects of certain hazards.

A methodology to construct the scour fragility curve from flume experimental data was presented. The scour fragility curve is defined as a function of the pile length embedded ratio. A piled bridge pier model was set up in the flume for scour testing under certain flows. The variations in scour depth and the pier settlement were recorded. Afterwards, the settlement was used to define the damage states. The fragility surface giving a conditional probability of exceeding different scour states given the occurrence of specific flow conditions at certain flow velocities and water levels was constructed in this paper.

Scour Fragility Curves

Applying the fragility curve to predict the possible extent of earthquake-induced damage has been developing for a long time in earthquake engineering. This curve shows the probability of structural damage as a function of the seismic parameter. Conducting a seismic fragility curve requires synergistic use of the following methods (Shinozuka et al, 2001): (1) professional judgment, (2) quasi-static and design code consistent analysis, (3) utilization of damage data associated with past earthquakes, and (4) numerical simulation of bridge seismic responses. Due to the complex condition of bridge scouring, much time and

[1] Associate Researcher, National Center for Research on Earthquake Engineering, ccchen@ncree.narl.org.tw.
[2] Research Assistant, Department of Civil Engineering, National Taiwan University
[3] Director, National Center for Research on Earthquake Engineering
Professor, Department of Civil Engineering, National Taiwan University
[4] Student, Department of Civil Engineering, National Taiwan University

effort is required to simulate the real scouring mechanism. For this reason, few studies have focused on developing the fragility curves for scoured bridges. The procedure to develop seismic fragility curves is a good template for finding scour fragility curves.

The numerical and the empirical approach are two ways to estimate seismic fragility. In the numerical approach, ground motion records were selected and a bridge pier model was constructed. The fragility curve was generated by damage probabilistic analysis (Karim et al, 2001 and Chiou et al, 2011). In the empirical approach, the actual damage data were selected (Sarabandi et al, 2004), and the damage data and seismic parameters were sorted into damage ranks. By relating each damage rank with their damage ratio, the empirical fragility curve could be constructed (Yamazaki et al, 2000).

This paper established its scour fragility curve by a similar procedure to the empirical approach through a series of experiments. Since the fragility curve is a function of defined damage parameters and exceeding probability of specified failure, defining the damage states is the first step in this work. In this study, the vertical displacement of the bridge pier is selected to discriminate the damage states because it correlates to the scouring around the pile. Once the displacement changes and the scour depths are recorded, we can then define the damage states. It can be anticipated that more severe critical damage states would lead to a deeper scour depth. Repeating the experiment provides the experimental data to develop the scour fragility curves.

For the preliminary study, the data includes the mean and the standard deviation of the pile length embedded ratio, R_l, which is equal to the embedded depth of the pile, L_e, over the full length of the pile, L. As the scour depth, D_S, was observed and recorded, at the moment when the vertical displacement of the bridge pier reaches the value of the defined damage state, we can obtain:

$$R_{l,i} = \frac{L_{E,i}}{L} = \frac{(L - D_{S,i})}{L} \tag{1}$$

The parameter i indicates the experiment number. The experimental statistical data, the mean and the standard deviation of the pile length embedded ratio are calculated more precisely as we increase i. As mentioned, the vertical displacement of the pier is selected to discriminate the damage states. Three differentiated damage states were defined: 1mm, 3mm and 5mm. Generally, the structure is considered to be at failure when the vertical displacement exceeds 10 percent of the pile diameter. But owing to the scale effect of the scale model experiments, this factor is not clearly understood. This study takes the broader range of the displacement of the pile into the consideration.

The cumulative probability P_f of the occurrence of the damage states according to the pile length embedded ratio is given as:

$$P_f = \Phi\left[\frac{lnR_{l,j} - \lambda_j}{\xi_j}\right] \tag{2}$$

where, Φ is the standard normal distribution; j indicates the specific damage rank; λ and ξ are the mean and the standard deviation of $\ln R_l$. These two parameters are obtained to develop the scour fragility curves. A detailed description of the procedures can be found in Karim et al, 2001.

Flume Experiments

The experimental setting is simplified so that we can focus on the bridge pier structure failure behaviors. The material strength and the column tilt are relatively unnecessary. Bearing capacity failure is the most controllable failure mode. The self-weight and the soil conditions are the major factors affecting the bearing capacity. The load transfer mechanisms of the pile structure are the point bearing capacity and the friction between the pile and the sediment. The soil bearing capacity fails mostly through punching.

The reduced scale model that was used in this study is shown in Figure 1. It includes a bridge column (2.5cm in diameter) and a cap beam (25cm in length, 5cm in width, 5cm in height) made from stainless steel, and an acrylic pile cap (10cm in length x 10 cm in width x 5cm in height) on top of four replaceable stainless steel piles (1cm in diameter and 20cm in length). An inner camera was installed to observe the scour depth. The hydraulic flume is 0.6 meter wide by 1 meter high with a total length of 7 meters (see Figure 2). The average flow velocity is 0.3 m/sec and the water level is 20 cm above the initial sediment level. Mass blocks were added to provide the vertical loading to accomplish the failure mode of the scoured bridge pier. A weight of 25kg was evaluated and used in this study.

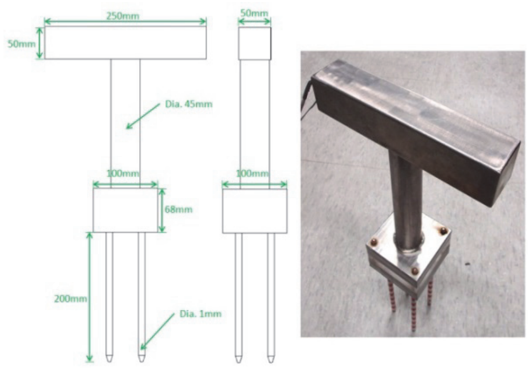

Fig. 1 Pile foundation bridge pier model used in the flume experiment

Figure 3 shows the measuring instruments. The scour depth was recorded by the inner camera. Two magnetic displacement transducers were installed on the top of the cap beam to record the vertical translational displacement. Ambient vibration sensors were also deployed in the experiments, but the change of the dynamic properties of the pier during the scouring process is not discussed in this paper. Some photos of the experiments are shown in Figure 4.

Fig. 2 The hydraulic flume used in this study (Left) Top view of flume channel (Right) Test section of the experimental flume

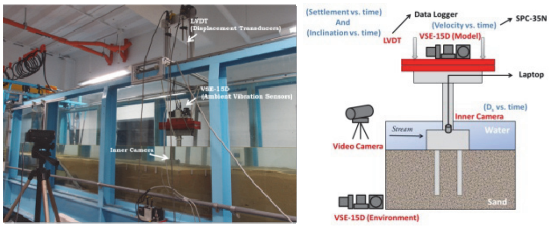

Fig. 3 Layout of the measuring instruments (Left) Measuring instruments (Right) Sketch of the instruments

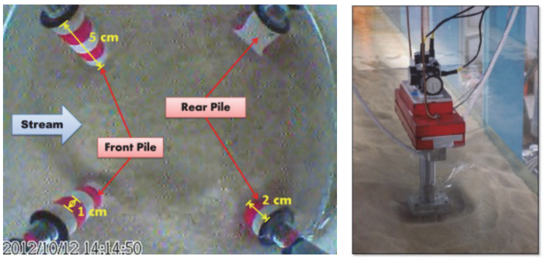

Fig. 4 Photos of the flume experiments (Left) View from the inner camera (Right) Bridge model

Preliminary Results and Discussions

The recorded curves of the embedded length ratio of the pile (R_l) versus time are shown in Figure 5. Only three repeated flume experimental results are presented in this paper because more experiments are still being conducted. The result shows a feasible methodology to construct the scour fragility curve. Figure 6 shows the curves of the vertical translational displacement versus time measured during the experiment. Note that the recorded starting time is the same for the embedded length change observation as it is in the displacement measurement.

Figure 5 indicates that the embedded length will decrease during the experiment. This trend is consistent with the general scour process. The curves also show the variation in the data that accounts for the unavoidable uncertainty of the boundary conditions while setting up the model. The jumps of each curve are caused by the lack of bearing capacity at the pile. The record time of each jump that corresponds to the time of the discontinuities of slope in the vertical translational displacement curves are shown in Figure 6. About 9% - 24% of the depth of the initial sediment around the pier was washed away. The curves of Experiment No. 1 and 2 have similar trends but the curves in Experiment No.3 show a different result. There are several minor settlement events in Experiment 1 and 2. However, Experiment 3 only shows one major settlement event. Thus, it is difficult to find a proper numerical model with natural variability for the full process of bridge scouring. Also, the failure mechanisms of the structure are quite complicated.

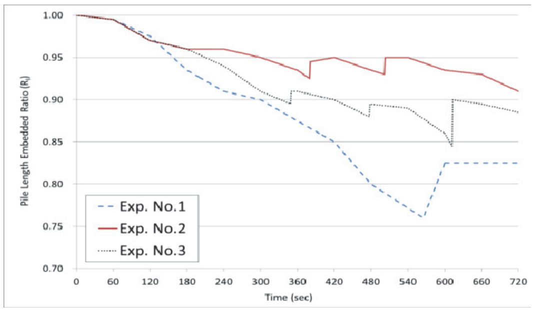

Fig. 5 Curves of the embedded length ratio of the pile versus time

Vertical translational displacement increases along with the movement of the pier. As it can be seen in Figure 6, the settlement occurs in sequence, which describes the realistic behavior of bridges. In Figures 5 and 6, one can see a similar outcome for the different experiments conducted.

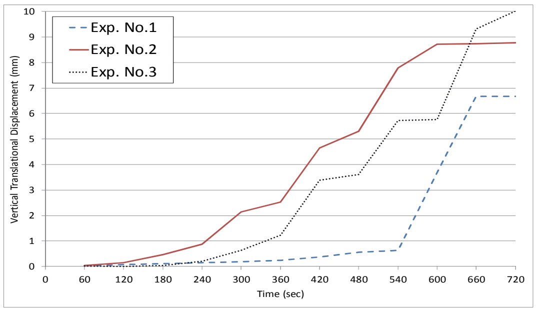

Fig. 6 Curves of the vertical translational displacement versus time

The maximum vertical translational displacement is between 6.8mm to 10mm. If we define the major damage rank directly using the maximum value of the displacement, the damage state of the piled bridge might be overestimated. As mentioned previously, the discriminated values of vertical displacement are 1mm, 3mm and 5mm. These values correspond to minor scour damage, moderate scour damage and major scour damage respectively. We can then obtain the time of occurrence for each of the defined damage ranks from Figure 6 and find the corresponding pile length embedded ratios from Figure 5. Then the experimental statistical properties, the mean and the standard deviation, are calculated to develop the fragility curve by using Equation 2. Finally, the cumulative probability of occurrence for each of the damage states can be obtained. The constructed scour fragility curves are shown in Figure 7. This figure shows the plots of the fragility curves for the defined damage states for the bridge pier model with respect to the embedded length ratio of the pile. In Figure 7, the range of the pile embedded length ratio is from 0.60 to 1.10, where 1.10 is the embedded length of the pile is over the length of the pile itself, which does not happen in reality.

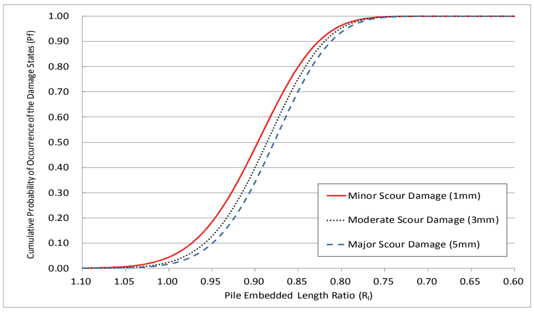

Fig. 7 Scour fragility curves constructed from experimental data in this study

One of the possible reasons why the ratio exceeded 1.0 is that experimental data used in this paper is limited as it was from only three experiments. More experiments are currently being conducted to provide more data to construct the fragility curves. Another possible reason could be that there is an inevitable inaccuracy in the procedure of developing the fragility curves. The simplest solution for the inaccuracy is to set a lower limit for the pile embedded length ratio so that the starting point of the fragility curve would be at 1.0. Further studies are necessary in order to find conclusive solutions for the problems mentioned.

Discussing the preliminary results in this paper, it can be seen (Figure 7) that the developed fragility curves of the minor scour damage (1mm), moderate scour damage (3mm) and major scour damage (5mm) show a different level of damage probability with respect to the pile embedded length ratio. As the pile embedded length ratio decreases, the constructed fragility curves of the major damage rank show a lower level of damage probability compared to that of the moderate damage rank and the minor damage rank in an understandable order. An interesting result was also observed in Figure 7 regarding the spacing between each of the fragility curves with the same level of damage probability. The difference between each discriminated value of the vertical translational displacement is the same but the spacing between fragility curves was not constant. The moderate damage curve is closer to the major damage curve than the minor damage curve. This indicates that the level of minor damage probability is more sensitive to the damage rank criteria. Furthermore, the cumulative probability of occurrence of the damage state reaches 1.0 as long as the pile embedded length ratio is not over 0.75. In other words, we can say that the bridge model will have at least a 5mm vertical translational displacement as the scour depth reaches 25% of the pile length.

Summary and Remarks

A methodology to construct the scour fragility curves from flume experimental data was presented in this preliminary study. The main purpose of this paper is to show how the flume experimental data were used to build the scour fragility curve defined as a function of the pile length embedded ratio. The curve of the embedded length ratio of the pile over time and the curve of the vertical translational displacement over time were observed and recorded through flume experiments. The measured decreasing trend of the curve is consistent with the general scouring process and the realistic behavior of the piled bridge pier damage sequence. The constructed fragility curves were presented and discussed. This paper has shown a feasible methodology to construct the scour fragility curve from flume experiment data. However, further studies are necessary in order to find solutions for the problems mentioned in the preliminary stage.

Reference

Reddy, D. R., 2006, “Bridge Scour Detection”, Proceedings of National Conference on Advanced in Bridge Engineering (ABE), March 24-25.

Shinozuka, M., Feng, M. Q., Kim, H., Uzawa, T., Ueda, T. 2001 “Statistical Analysis of Fragility Curves.” Technical Report MCEER, Department of Civil and Environmental Engineering, University of Southern California Los Angeles, California 90089-2531

Karim, K. R., Yamazaki, F. , 2001,“Effect of earthquake ground motions on fragility curves of highway bridge piers based on numerical simulation.” Earthquake Engng Struct. Dyn., 30:1839-1856

Chiou, J. S., Chiang, C. H., Yang, H. H., Hsu, S. Y. , 2011, “Developing fragility curves for a pile-supported wharf.” Soil Dynamics and Earthquake Engineering, 31:830-40

Sarabandi, P., Pachakis, D., King, S., Kiremidjian, A. ,2004, “Empirical Fragility Functions from Recent Earthquakes.” 13th World Conference on Earthquake Engineering, Paper No.1211

Yamazaki, F., Motomura, H., Hamada, T., 2000, “Damage Assessment of Expressway Networks in Japan based on Seismic Monitoring.” 12th World Conference on Earthquake Engineering, CD-ROM, Paper No. 0551

Modal Analysis of a Nuclear Reinforced Concrete Containment Vessel

Shu-Hsien Chao[1], Chiun-Lin Wu[2], Hsuan-Chih Yang[3] and Kuo-Chun Chang[4,5]

趙書賢 [1]、吳俊霖 [2]、楊炫智 [3]、張國鎮 [4,5]

Abstract

In this study, a finite element model of a reinforced concrete containment vessel (RCCV) in an advanced boiling water reactor (ABWR) was constructed using the commercial program ABAQUS ver.6.12. The modal analysis was performed to derive the modal properties of an RCCV, such as the frequency and mode shape of each mode, in order to clarify the dynamic behavior of the RCCV while it is subjected to earthquake excitation. The effect of different mesh sizes and element types on the modal analysis results was examined. The modal frequencies of the first four dominant modes are 7.3Hz, 15.2Hz, 18.2Hz, and 23.6Hz, with the first one representing the horizontal mode, the second being the torsional mode, the third being the inner-shell deformation mode, and the fourth being the vertical mode. It is suggested that the mesh size can be defined as half of the RCCV thickness, and the quadratic element with a reduced integration point can be used to derive accurate results under the limitations of the hardware environment.

Keywords: finite element method, modal analysis, advanced boiling water reactor, reinforced concrete containment vessel

Introduction

The safety of a nuclear power plant is always an issue of major public concern, especially after the Japanese earthquake on the 11th March 2011. The earthquake induced a tsunami which caused devastation to the Fukushima plant in Japan. The impact of the damage to the Fukushima plant on society, life, the economy, and the environment was massive. Therefore, assessing and re-evaluating the seismic capacity of structures, components, piping systems, and equipment in a nuclear power plant has become essential. In the past, the seismic demand of components, piping systems, and equipment in a nuclear power plant was determined through linear time history analysis using a simplified lumped mass model. However, many general dynamic properties, such as 3-D mode, torsional mode, and torsion-coupled mode cannot be represented by this simplified lumped mass model.

In this study, a finite element model of a reinforced concrete containment vessel (RCCV) of an advanced boiling water reactor (ABWR) was constructed using the commercial program ABAQUS ver.6.12. The modal analysis was performed to derive the modal properties of an RCCV, such as the frequency and the mode shape of each mode, to clarify the dynamic behavior of the RCCV while subjected to earthquake excitation. The effect of different mesh sizes and element types on the modal analysis result was also studied.

Description of Structure and Model

Fig. 1 shows a sketch of the advanced boiling water reactor building [1]. It is a 7-story building with a total height of 63.4m. It comprises an underground section (3-story, 25.7m height) and an aboveground section (4-story, 37.7m height). The dimensions of the basemat are 60m×57m. The building contains an

1 Assistant Researcher, National Center for Research on Earthquake Engineering, shchao@ncree.org.tw
2 Associate Researcher, National Center for Research on Earthquake Engineering, clwu@ncree.org.tw
3 Associate Researcher, National Center for Research on Earthquake Engineering, hcyang@ncree.org.tw
4 Director, National Center for Research on Earthquake Engineering, kcchang@ncree.org.tw
5 Professor, Department of Civil Engineering, National Taiwan University

RCCV, an outer reinforced concrete (RC) box wall, and inner RC shear walls. The entire RCCV and a section of the basemat were considered in this study. The RCCV is a cylindrical wall structure, with an inner diameter of 29m and an outer diameter of 31m. The thickness of the cylindrical wall is 2m. The RCCV should resist earthquake excitation and other types of loading in order to keep harmful radiation inside it during a reactor core accident. It is the final line of defense of a nuclear power plant's safety system. The height of the RCCV is 31.9m and the height of the basemat is 5.5m.

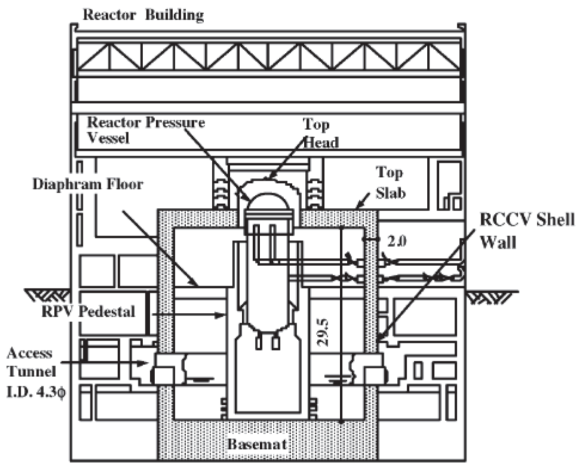

Fig.1 A sketch of the Advanced Boiling Water Reactor Building [1]

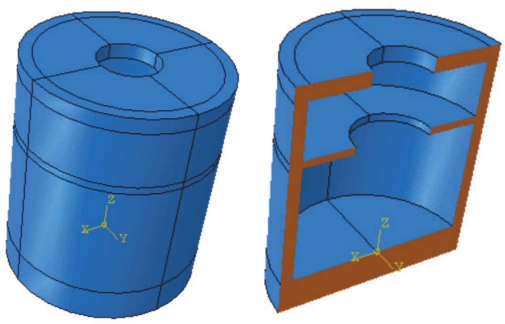

Fig. 2 Illustration of the RCCV model

A finite element model of the RCCV using real dimensions including a part of the basemat was constructed using ABAQUS, as shown in Fig. 2. The analysis model was assumed to be composed of an isotropic linear elastic material. The elastic modulus and Poisson's ratio were assumed based on the design concrete properties. The ultimate compressive strength of the design concrete, f_c', of the RCCV was 350kgf/cm^2. According to design codes [2], the elastic modulus of concrete can be derived as:

$$E_c = 15000\sqrt{f_c'} \quad \cdots\cdots\cdots\cdots\cdots\cdots \quad (1)$$

where the unit of f_c' is kgf/cm^2 and the Poisson's ratio of the concrete was assumed to be 0.2. Only the self-weight of the structure was considered in the model. The density of concrete was assumed to be 2.4t/m^3. The displacement at the bottom of the basemat was assumed to be zero during the modal analysis. All modal properties associated with modal frequencies from 0Hz~33Hz were evaluated.

Mesh and Element Type

Generally, more accurate results can be derived by using a finer mesh size; however, a finer mesh size is accompanied by a larger amount of nodes and elements in the model, which will increase computational efforts. Due to hardware capability limitations, it is unwise to make the mesh size arbitrarily finer. Therefore, it is very important to investigate the effect of the mesh size on the modal analysis results and to determine the appropriate mesh size for a particular engineering problem. In this study, a finite element model with four different mesh sizes was constructed. The outline of this model along with the four different mesh sizes is shown in Fig. 3. The mesh size was defined according to the thickness of the RCCV cylinder wall. The element sizes of mesh type I~IV as shown in Fig. 3 correspond to 200%, 100%, 50%, 25% of the RCCV cylindrical wall thickness respectively.

In ABAQUS ver. 6.12, the solid element is classified into linear elements and quadratic elements according to the element node number. A linear solid element has 8 nodes, and a quadratic solid element has 20 nodes, as shown in Fig. 4. According to the number of integration points, the solid element is classified into full integration and reduced integration elements, as shown in Fig. 4. Therefore, four kinds of solid elements can be used in ABAQUS ver. 6.12. They are:

1. Linear element with reduced integration (C3D8R): this element has 8 nodes and 1 integration point for each face.
2. Linear element with full integration (C3D8): this element has 8 nodes and 4 integration points for each face.
3. Quadratic element with reduced integration (C3D20R): this element has 20 nodes and 4 integration points for each face.
4. Quadratic element with full integration (C3D20): this element has 20 nodes and 9 integration points for each face

In this study, a total of 16 finite element models were constructed for the RCCV according to different mesh sizes and element types. The number of nodes and elements of each model is shown in Table 1. The computational effort for the full integration element is heavier than that for the reduced integration element even if the number of elements is the same. As shown in Table 1, if the mesh size is reduced to 50%, the number of nodes and elements increases by four to five times, and will result in a considerable increase in computational effort.

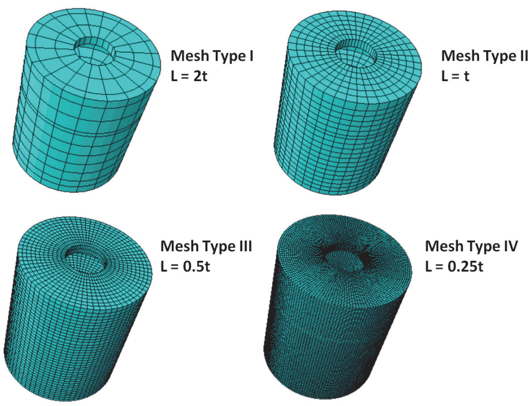

Fig. 3 Different Mesh Types

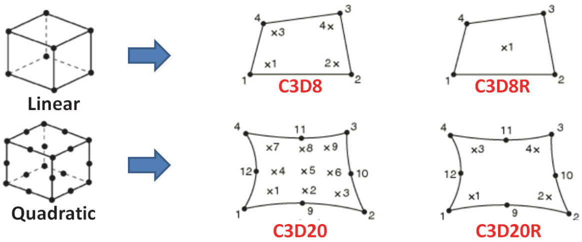

Fig. 4 Linear and quadratic solid elements with full and reduced integration points [3]

Table 1 Number of nodes and elements for 16 different finite element models

	Mesh Type I	Mesh Type II	Mesh Type III	Mesh Type IV
Number of Node				
C3D8R C3D8	775	3044	16085	116128
C3D20R C3D20	2719	10807	59719	444956
Number of Element				
C3D8R C3D8	408	1700	11508	96661
C3D20R C3D20	408	1700	11508	96661

Modal Analysis Result

The modal frequencies of the first four dominant modes for each model are shown in Fig. 5(a) ~ 5(d) respectively. From these figures, it is found that:

(1) The modal frequency analysis results of the quadratic element are more stable than those of the linear element. The mesh size of mesh type II, III, or IV for the quadratic element with full or reduced integration can be used to derive an accurate analysis result.

(2) The modal frequency calculated from the linear element with reduced integration proves lower because of the element's hourglass problem [3]. This makes the analyzed model more flexible than its real counterpart. Besides, higher modes (third mode and fourth mode) cannot be well represented when the mesh size is too coarse (mesh type I and type II). One should use a fine mesh (mesh type IV) to derive an accurate analysis result while using this element.

(3) The modal frequency calculated from the linear element with full integration proves higher because of the element's shear locking problem [3]. The analyzed model has higher stiffness while using this element type and a fine mesh (mesh type IV) is necessary to derive accurate results.

The parametric analysis results suggest that the quadratic element with reduced integration (C3D20R) is favorable for modeling the RCCV. The mesh size can be selected as a half of the RCCV cylinder wall thickness. In this way, accurate results together with affordable computational effort can be assured. In the next section, the analysis result of the C3D20R model with mesh type II is used to illustrate the RCCV modal properties.

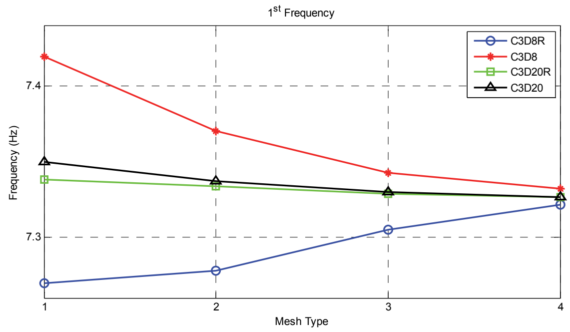

Fig. 5(a) 1st modal frequency of 16 different finite element models

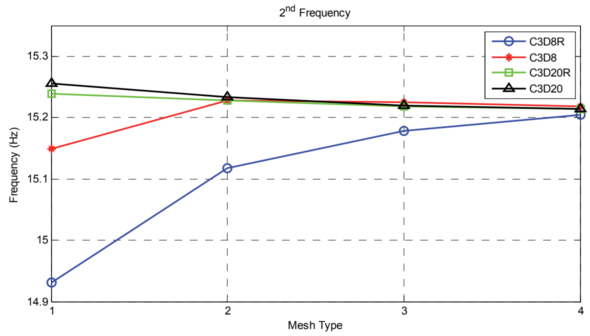

Fig. 5(b) 2nd modal frequency of 16 different finite element models

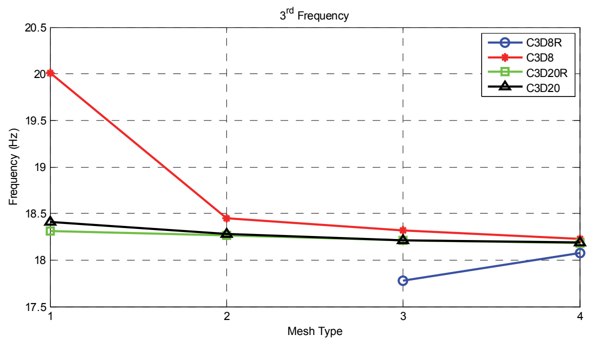

Fig. 5(c) 3rd modal frequency of 16 different finite element models

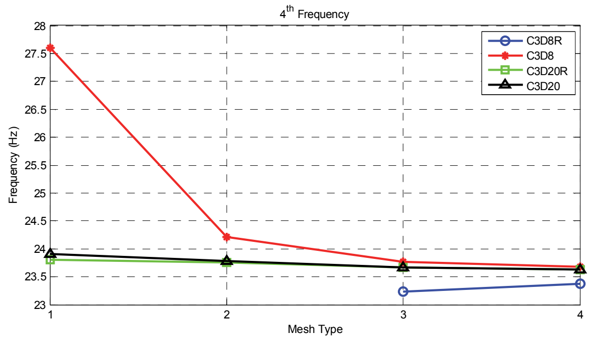

Fig. 5(d) 4th modal frequency of 16 different finite element models

Figure 6 shows the mode shapes of the first four dominant vibration modes of the RCCV. The modal frequencies are 7.3Hz, 15.2Hz, 18.2Hz, and 23.6Hz, respectively. The first mode corresponds to the horizontal mode, and the second represents the torsional mode; the third is the inner-shell deformation mode, and the fourth is the vertical mode.

A key parameter of the concrete material yield function is the von Mises stress. Therefore, the von Mises stress of each element is discussed in this study. The definition of the von Mises stress is:

$$\sigma_{mises} = \sqrt{\frac{(\sigma_1 - \sigma_2)^2 + (\sigma_2 - \sigma_3)^2 + (\sigma_1 - \sigma_3)^2}{2}} \quad \ldots\ldots(2)$$

where $\sigma_1 \sim \sigma_3$ is the first, second, and third principal stress at the integration point. Figure 7 shows the maximum von Mises stress distribution of each element for each mode. The results show that the stress is concentrated at the bottom of the RCCV for the first and second modes, at the middle plate of the RCCV for the third mode, and at the top plate and the bottom of the RCCV for the fourth mode.

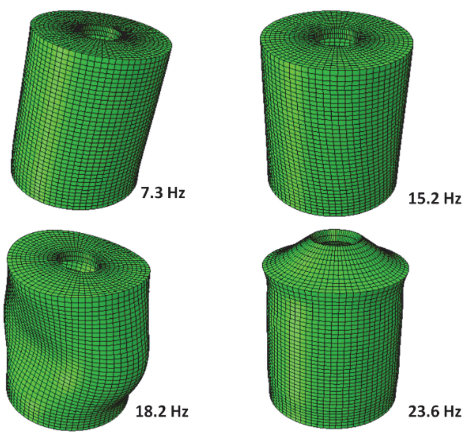

Fig. 6 Mode shape of each mode

Conclusions

In this study, a finite element model of a reinforced concrete containment vessel (RCCV) of an advanced boiling water reactor (ABWR) was constructed using the commercial program ABAQUS ver.6.12. The modal analysis was performed to derive the modal properties of the RCCV, such as the frequency and mode shape of each mode, to clarify the dynamic behavior of the RCCV while subjected to earthquake excitation. The effect of different mesh sizes and element types on the modal analysis result was studied. The modal frequencies of the first four dominant vibration modes are 7.3Hz, 15.2Hz, 18.2Hz, and 23.6Hz. The first is the horizontal mode, the second is the torsional mode, the third is the inner-shell deformation mode, and the fourth is the vertical mode. It is suggested that the mesh size can be defined as a half of the RCCV thickness, and the quadratic element with reduced integration point can be used to derive accurate results under hardware limitations.

In this study, only the RCCV substructure from an ABWR building was investigated. In the near future, a finite element model for a complete ABWR building will be considered to realize its dynamic behavior comprehensively. The differences between the analysis results of the finite element model and the simplified lumped mass model will be discussed to validate the application of the simplified lump mass model in our subsequent studies.

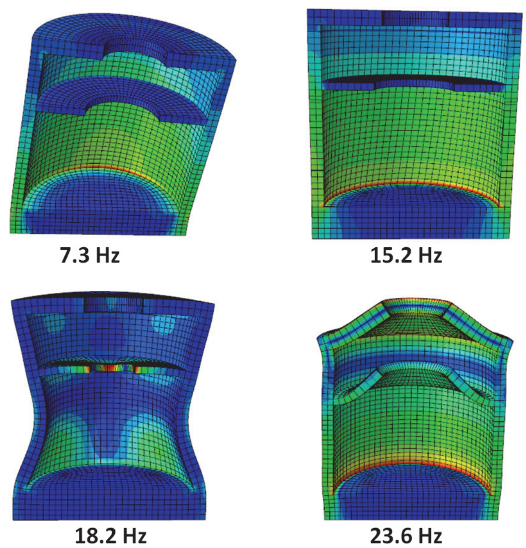

Fig. 7 Stress distribution of each mode

References

Hirama T. et al. (2005a). “Seismic proof test of a reinforced concrete containment vessel (RCCV) Part 1: Test model and pressure test.” *Nuclear Engineering and Design*, 235, 1335–1348.

土木 401-93 (2004)，“混凝土工程設計規範與解說”，中國土木水利工程學會，ISBN: 957-655-394-6.

Hibbitt, Karlsson and Sorensen, Inc. “Abaqus Analysis User’s Manual”, Version. 6.3.

Seismic Probabilistic Risk Assessment of Nuclear Power Plants

Chang-Ching Chang[1], Ying-Hsiu Shen[2], Yin-Nan Huang[3] and Kuo-Chun Chang[4]

張長菁 [1]、沈盈琇 [2]、黃尹男 [3]、張國鎮 [4]

Abstract

Seismic Probabilistic Risk Assessment (SPRA) determines the annual frequency of unacceptable seismic performances of a nuclear power plant (NPP), such as core melt and release of radiation, and has been recognized as an important tool for assessing the seismic risk of NPPs. In this study, the procedures of conventional SPRA methodologies are explored and the seismic risk of a sample NPP for one of the accident sequences is computed using conventional SPRA methodologies. SPRA methodologies typically involve the use of component fragility curves defined as a function of ground-motion parameters, such as peak ground acceleration and spectral acceleration. In future studies, the conventional SPRA procedure will be compared with the new SPRA procedure proposed by Huang et al. (2011), where the component fragility curves are defined as a function of structural-response parameters, such as floor spectral acceelration, and the advantages and disadvantages of those two methodologies are discussed.

Keywords: seismic probabilistic risk assessment, fragility curve, nuclear power plant.

Introduction

The United States Nuclear Regulatory Commission (USNRC) issued Supplement 4 to Generic Letter No. 88-20 (USNRC 1991) in 1991 requiring nuclear power plant (NPP) utilities to perform an Individual Plant Examination of External Events (IPEEE). They also issued NUREG-1407 (Chen et al. 1991) to help guide the IPEEE. NUREG-1407 identified Seismic Probabilistic Risk Assessment (SPRA) as an acceptable methodology for the examination of earthquake-induced risks. The purpose of a SPRA is to determine the probability distribution of the frequency of occurrence of adverse consequences (e.g. core damage, radiological release and off-site consequences). In conventional SPRA methodologies, fragility curves express the conditional probability of failure of a structure or component for a given ground-motion parameter, such as peak ground acceleration (PGA) or spectral acceleration.

In this study, the prodedures of conventional SPRA methodologies are explored, and the seismic risk of a sample NPP for one of the accident sequences is computed using conventional SPRA methodologies. In future work, the conventional SPRA prodedure will be compared with the new SPRA procedure proposed by Huang et al. (2011), where the component fragility curves are defined as a function of structural-response parameters, such as floor spectral acceelration. The results of risk computed using conventional and new SPRA methodologies are compared and the advantages and disadvantages of the new methodology will be futher discussed.

Steps in Seismic Probabilistic Risk Assessment

NUREG/CR-2300 (USNRC 1983) provides general guidance for performing SPRA for NPPs. The

[1] Assistant Researcher, National Center for Research on Earthquake Engineering, ccchang@ncree.narl.org.tw.
[2] Assistant Researcher, National Center for Research on Earthquake Engineering.
[3] Assistant Professor, Department of Civil Engineering, National Taiwan University.
[4] Professor, Department of Civil Engineering, National Taiwan University & Director, National Center for Research on Earthquake Engineering.

guideline describes two SPRA methods: (1) "Zion" and (2) the "Seismic Safety Margin Research Program" (SSMRP). The Zion method requires less computational effort than the SSMRP method and is currently the most popular SPRA procedure. In the Zion method, the component fragility curves are defined in terms of ground-motion parameters, such as peak ground acceleration and spectral acceleration at a given period. The four steps of SPRA are briefly described in the following subsections.

1. Seismic Hazard Analysis

The seismic hazard used in a SPRA is characterized using Probabilistic Seismic Hazard Analysis (PSHA). A PSHA generates a family of hazard curves, which describe the frequency of exceedance for a ground-motion parameter (e.g., PGA and spectral acceleration at a given period) at a specific site. The following four steps that comprise a seismic hazard analysis are as below: (1) identify of sources of earthquakes; (2) evaluation of earthquake history in the region surrounding the site; (3) development of ground motion attenuation relationships; and (4) integration of the above to obtain the frequency of exceeding different ground motion intensities.

2. Plant-System and Accident-Sequence Analysis

There may be a series of elements in a NPP that are required to function in order to prevent core damage. These elements are analogous to the links in a chain. If one link in the chain fails, then the chain fails to perform its function and if a further element fails, then core damage occurs. More formally, the plant logic model takes the form of event trees and fault trees. Event trees display the success or failure of various safety systems leading to a failure event. On the other hand, fault trees answer the question of how a particular system fails. Thus, for each of the systems in an event tree, there is a corresponding fault tree that relates the various structure and equipment failures in a logical manner. The branches of a fault tree proceed downward in increasing refinement, until the most basic failure events are reached. Through the logic of the event and fault trees, the fragilities of the basic events are related by a Boolean equation for the failure event under consideration. Thus, the frequency of failure for the individual structures and equipment are combined to produce the frequency of failure, such as core melt.

3. Component Fragility Evaluation

Seismic fragility curves for structural and nonstructural components in NPPs are needed in a SPRA to estimate the frequencies of occurrence of initiating events and the failures of different safety systems. The lognormal distribution has become the most widely used distribution for developing fragility curves. A lognormal distribution for a random variable can be fully defined by two parameters: the median and logarithmic standard deviation. The latter parameter represents the dispersion in the variable. The sources of the dispersion are distinguished into two types for developing fragility curves for structural and nonstructural components in NPPs: (1) "epistemic uncertainty", for the variability due to the lack of knowledge for the procedure and variables used in the analysis process, for example, the variability in the strength of a shear wall, which could be tested to eliminate the uncertainty; and (2) "aleatory randomness", for the variability that is inherent in the used variables and cannot be reduced practically, for example, the variability in peak ground acceleration for a given earthquake magnitude and distance.

Reed and Kennedy (1994) presented a methodology for developing fragility curves used in a SPRA, and apply a double lognormal model in order to consider the two types of variability separately. The model is shown as:

$$A = \overline{A} \cdot \varepsilon_r = \hat{a} \cdot \varepsilon_u \cdot \varepsilon_r \tag{1}$$

where A is the random variable for the capacity of the component and the capacity is defined in terms of a ground-motion parameter, such as peak ground acceleration or spectral acceleration at a given period; $\overline{A}$, which is equal to $\hat{a} \cdot \varepsilon_u$, is a random variable for the median capacity of the component; $\hat{a}$ is a deterministic value representing the median of $\overline{A}$; and ε_u and ε_r are two lognormally distributed random variables with medians both equal to one and logarithmic standard deviations of β_u and β_r, respectively. Variables ε_u and ε_r represent the uncertainty and randomness in A, respectively. In this model, the median capacity of the component is considered uncertain. The model of (1) can be used to generate a family of fragility curves for each structure, system and component (SSC) in NPPs. As an example, the fragility curve is developed as shown in Fig. 1. The conditional failure frequency for a peak ground acceleration of $2g$ is calculated as 0.29.

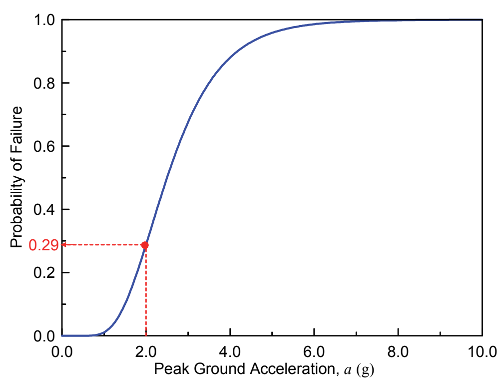

Fig. 1 Component Fragility Curve

In estimating the fragility parameters, it is convenient to work in terms of an intermediate random variable called the factor of safety. The factor of safety, F, on ground acceleration capacity above the safe shutdown earthquake level specified for design, A_{SSE}, is defined as follows:

$$A = F \cdot A_{SSE} \tag{2}$$

The basic variables are presented for structures first and are followed next by a discussion of the basic variables that effect equipment.

(1) Basic Fragility Analysis Variables for Structures

For structures, the factor of safety can be modeled as the product of three random variables:

$$F = F_S F_\mu F_{RS} \tag{3}$$

where the strength factor, F_S, represents the ratio of ultimate strength or strength at loss-of-function to the stress calculated for A_{SSE}; the inelastic energy absorption factor, F_μ, accounts for the fact that an earthquake represents a limited energy source and many structures or equipment are capable of absorbing substantial amounts of energy beyond yield without loss-of-function; and the structure response factor, F_{RS}, is modeled as a product of factors influencing the response variability.

$$F_{RS} = F_{SA} F_{GMI} F_\delta F_M F_{MC} F_{EC} F_{SSI} \tag{4}$$

where F_{SA} is the spectral shape factors; F_{GMI} is the ground motion incoherence factor; F_δ is the damping factor; F_M is the modeling factor; F_{MC} is the mode combination factor; F_{EC} is the earthquake component combination factor; and F_{SSI} is the factor to account for the effect of soil-structure interaction including the reduction of input motion with depth below the surface.

(2) Basic Fragility Analysis Variables for Equipment

For equipment and other components, the factor of safety is made up of three parts consisting of a capacity factor, F_C; a structure response factor, F_{RS}; and an equipment response factor, F_{RE}. Thus,

$$F = F_C F_{RE} F_{RS} \tag{4}$$

The capacity for the equipment may be evaluated as the product of the strength factor, F_S and the inelastic energy absorption factor, F_μ. The equipment response factor, F_{RE}, is the ratio of equipment response calculated in design to the realistic equipment response. Both the responses are calculated for the design floor spectra. F_{RE} is the factor of safety inherent in the computation of equipment response. It depends upon the response characteristics of the equipment, as it is influenced by some of the variables listed under Eq. (4). These variables differ according to the seismic qualification procedure. For equipment qualified by analysis, the important variables that influence response and variability are qualification method, spectral shape, modeling, equipment damping, combination of modal responses, and combination of earthquake components. The structural response factor, F_{RS}, is based on the response characteristics of the structure at the location of the component (equipment) support. The applicable variables are spectral shape, ground motion incoherence factor, damping, modeling, mode combination, and soil-structure interaction effect including the reduction with depth of seismic input, and are almost the same as Eq. (4).

4. Consequence Analysis

Once the hazard curves for the site and the fragility curves for a failure event are obtained, two curves, one from each of the two sets, are selected to compute the frequency of the failure event, P_f, using the following equation:

$$P_f = -\int_0^\infty P_{f/a} \left| \frac{d\lambda_H(a)}{da} \right| da \tag{5}$$

where $P_{f/a}$ is the fragility curve that characterizes the probability of the occurrence of the failure event for a given a value of the parameter a; and λ_H represents the seismic hazard curve. The range of integration should be wide enough to cover all of the earthquake intensities with significant contributions to P_f. The use of (5) requires that the fragility and seismic hazard curves be a function of the same parameter.

Example of Seismic Risk Calculations for One of the Accident Sequences in NPPs

In this study, the seismic risk of a sample NPP for one of the accident sequences is computed using conventional SPRA methodologies. The hazard curve for this sample NPP is shown as Fig. 2.

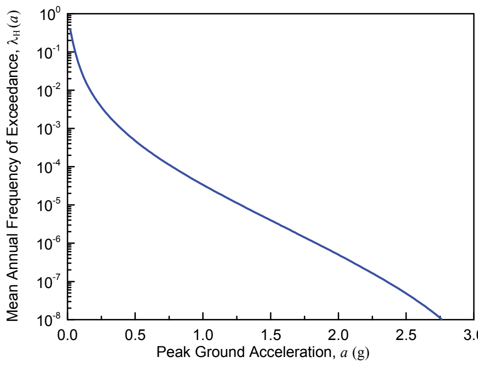

Fig. 2 Hazard Curve for the Sample NPP

One of the accident sequences for the sample NPP is presented in Fig. 3. The accident sequence starts from a seismic event, ends at core damage and consists of a series of safety systems in between. The accident sequence is triggered by a seismic event, which results in a loss of off-site power (LOP). Although all the safety-related structures maintain their integrity during the earthquake, the service water system (SW) fails, which results in the failure of emergency diesel generator. The swing diesel generator has its own service water system and survives in this accident sequence. Scram succeeds in representing that the process of safety control rod insertion is finished. Under these conditions, the Reactor Core Isolation Cooling System (RCIC) provides core cooling for approximately 8 hours as designed. Subsequently, the reactor is depressurized to permit the AC Independent Water Addition System (ACIWA) to inject water into the reactor. In the accident sequence of Fig. 3, ACIWA fails which results in core damage. Therefore, the failure event is LOP, SW, and ACIWA in the sample accident sequence.

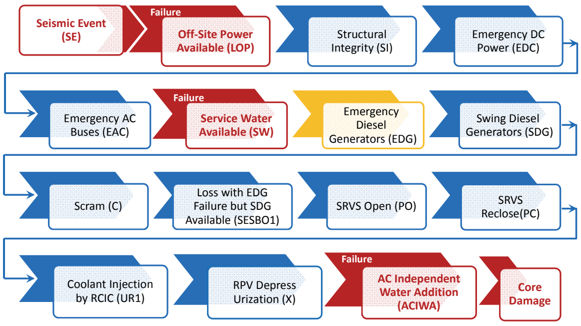

Fig.3 Accident Sequence

In this example, fragility curves express the conditional probability of failure of a structure or component for a PGA using the Zion method. For the accident sequence of Fig. 3 in the sample NPP, the fragility curve is calculated as shown in Fig. 4. Then, the seismic risk P_f can be obtained by numerical convolution of the seismic hazard curve and fragility curve, using Eq. (5). In this sample, the frequency of core damage for this accident sequence is calculated as 8.78×10^{-6}.

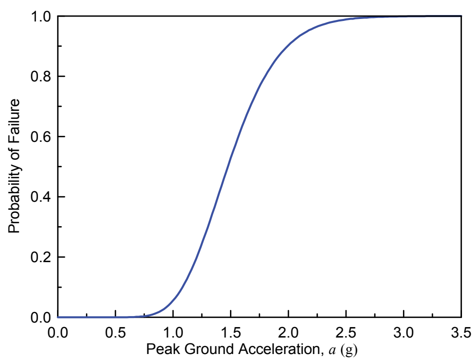

Fig. 4 Fragility Curve for the Accident Sequence

Conclusions

In conventional SPRA methodologies, fragility curves express the conditional probability of failure for a structure or component for a given ground-motion parameter, such as PGA or spectral acceleration. In this study, the seismic risk for one of the accident sequences in NPPs is calculated and the component fragility curves are defined in terms of PGA. However, the damage and failure of NPP components are more closely tied to structural response parameters than to ground motion parameters. The use of ground motion parameters greatly increases the dispersion in the fragility curves. Moreover, the median and dispersion of a component fragility curve expressed in terms of ground-motion parameters are dependent on both the capacity of the component and the response (demand) of the structure where the component is attached.

In future studies, the conventional SPRA procedure will be compared with the new SPRA procedure proposed by Huang et al. (2011), where the component fragility curves are defined as a function of structural-response parameters, such as floor spectral acceleration. The results of risk computed using conventional and new SPRA methodologies are compared and the advantages and disadvantages of the new methodology will be further discussed.

References

Chen, J. T., Chokshi, N. C., Kenneally, R. M., Kelly, G. B., Beckner, W. D., McCracken, C., Murphy, A. J., Reiter, L., and Jeng, D., "Procedural and submittal guidance of individual plant examination of external events (IPEEE) for severe accident vulnerabilities." NUREG-1407, U.S. Nuclear Regulatory Commission, Washington, D.C., 1991.

Huang, Y.-N., Whittaker, A. S., and Luco, N., "A probabilistic seismic risk assessment procedure for nuclear power plants: (I) Methodology." *Nuclear Engineering and Design*, 241(9), pp3996-4003, 2011.

Huang, Y.-N., Whittaker, A. S., and Luco, N., "A probabilistic seismic risk assessment procedure for nuclear power plants: (II) Application." *Nuclear Engineering and Design*, 241(9), pp3985-3995, 2011.

Pickard, Lowe, and Garrick, Inc., and Westinghouse Electric Corporation, Fauske & Associates, Inc., "Zion Probabilistic Safety Study." prepared for Commonwealth Edison Company, Chicago, 1981.

Reed, J. W., and Kennedy, R. P., "Methodology for developing seismic fragilities." TR-103959, Electric Power Research Institute, Palo Alto, CA. 1994

U.S. Nuclear Regulatory Commission (USNRC). "PRA procedures guide." NUREG/CR-2300, USNRC, Washington, D.C., 1983.

NARLabs
National Center for Research on Earthquake Engineering
200, Sec. 3, Xinhai Rd., Taipei 106, Taiwan, R.O.C.
Tel: +886-2-6630-0888 Fax: +886-2-6630-0858
http://www.ncree.org.tw

ISBN：978-986-89629-1-0